University of Southampton

Faculty of Engineering and Applied Science

Department of Civil and Environmental Engineering

FINITE ELEMENT ANALYSIS OF CONFINED CONCRETE IN BUILDING FRAME COMPONENTS AND JOINTS

by

Mingchao Guo

(BEng, MEng)

A thesis submitted for the degree of

Doctor of Philosophy

in Structural Engineering

May 1998

UNIVERSITY OF SOUTHAMPTON

ABSTRACT

FACULTY OF ENGINEERING AND APPLIED SCIENCE

DEPARTMENT OF CIVIL AND ENVIRONMENTAL ENGINEERING

Doctor of Philosophy

FINITE ELEMENT ANALYSIS OF CONFINED CONCRETE IN BUILDING FRAME COMPONENTS AND JOINTS

by Mingchao Guo

This thesis describes numerical investigations of the semi-rigid behaviour of the joints in precast concrete building frames. This research was one of three co-ordinated projects funded by EPSRC and carried out at Nottingham, Southampton and City Universities. It developed standardised finite element analysis techniques for modelling of reinforced concrete structures, improving the method of adding the smeared concrete material to overcome the early crushing phenomenon of the concrete elements. A number of experimental connections and precast concrete joints were numerically analysed to calibrate the finite element analysis techniques. Internal mechanism of the joints, such as cracking and crushing status of concrete components, stress distribution of the connectors and failure modes of the joints, all had to agree for the techniques to be acceptable. This calibration used connections tested in European Union countries through the COST initiative, including a T-stub connection, a bolt in concrete joint, and six billet-welded plate joints tested in the University of Nottingham.

Sensitivity analyses defined the mechanical behaviour of the billet-welded plate joints when a wide range of parameters were varied within realistic engineering limits. Simplified calculations for defining the characteristics of the joints were proposed for use in semi-rigid analysis of complete building frames.

Finally, the finite element analysis techniques were extended to the modelling of the innovative fibre reinforced plastic tube confined concrete columns tested at the University of Southampton.

The smeared concrete technique developed was shown to be effective for modelling the performance of locally cracked, and crushed, concrete components with limited confinement. The technique is also effective for the analysis of completely confined concrete up to approximately double the normal uniaxial compressive strain, after which an analysis based on the crushed concrete's equivalent granular material properties was found to be more suitable.

Acknowledgements

The financial support of this research programme by the EPSRC under Contract No. GR/K30360 is gratefully acknowledged.

I would like to take this opportunity to express my sincere gratitude to my supervisor Dr C K Jolly for his knowledgeable and skilful guidance and constructive criticism throughout this research programme. His ready advice and constructive comments greatly contributed to the steady progress of the project.

Special thanks are given to Dr A C Lock for his helpful assistance with the computer and modelling related programmes.

Comments made by Professor K S Verde, City University, and Dr K S Elliott, Nottingham University, regarding the work are much appreciated.

I am particularly grateful for the friendly assistance given by Mr D Lillistone and Mr M Foster in the research programme.

Thanks are extended to all colleagues within the Department for their useful advice and fruitful discussions.

Finally, but not least, I gratefully acknowledge the ever-present encouragement and generosity of my parents. Their affection, sacrifice and moral support have made the successful completion of this work possible.

Dedication

To My Wife

Who Contributed So Much And Received So Little.

Contents

Chapter 1

Introduction

1.1 General

Precast concrete is used in a large proportion of buildings including load bearing and non load bearing structures and systems[1~5]. Precast concrete members possess high quality in strength, stiffness and durability. They provide a wide variation in spans, shapes and bearing capacities. Also architectural precast concrete has found its place as one of the best technologies for high-quality facades. Because they offer fast construction and the consequent economy of the whole building process, precast concrete elements in load bearing structures and systems are widely used. Precast concrete building frames represent a large proportion of this kind of structure.

Basically a precast concrete building frame consists of beams, columns, joints which combine beams and columns together to form a structure, and slabs. Lateral actions are resisted either by cores and/or shear walls or by the frame itself. A frame designed to withstand vertical actions only is simply named a no-sway frame, while one designed to withstand both vertical and lateral actions is named a sway frame.

Joints are important elements in building structures, especially in precast concrete frames. Joints transmit forces between structural members, and they are designed to have higher capacities in strength than other adjacent members, such as beams and columns. In precast concrete building frames, due to the good manufacturing conditions in production plants that results in high quality of the precast concrete members, design and construction of joints become uncommonly significant. The joints carry high and complex internal forces concentrated from neighbouring beams and columns.

Construction of the joints, however, is difficult because of the complicated details in the limited space and the in-situ fabrication condition. Thus more attention has been paid to design and construction of the joints [6~9].

There are three main types of joints used commercially in the UK in precast concrete building frames[10~25]. These involve the use of corbels, cast-in steel billet-welded plates, or sleeve-bolted cleats. Their practical design method has not been covered in detail by current design standards. A few references [8] deal with design of the joints based on the assumption of pinned connections. Semi-rigid potential of the joints, however, naturally exists and offers certain advantage of structural behaviour. Consequently, research has been carried out to identify the semi-rigid nature of the joints so that it can be reliably utilised in engineering practice [10~30]. Three co-ordinated research projects at Nottingham, Southampton and City Universities, funded by EPSRC, had been conducted in this field [16, 18 and 19].

In the research work, theoretical analysis of the mechanical behaviour of the joints is not easy, because of the complex and unclear stress and deformation distribution, as well as the deviation and difficulty of determination of material properties of both steel and concrete. Experimental study is thus an essential approach for such a research field. Nevertheless, large scale specimen tests are very expensive. Usually series of numerous tests with variable parameters are not economically realisable. In addition, it is impossible to measure the detailed distribution and variation of stress and strain inside of the joints with normal experimental facilities. Consequently, finite element analysis (FEA) serves as a very useful approach too. Using this method the mechanical behaviour of the joints in a wide range of geometry and material can be economically investigated.

In the present research which is one of the three co-ordinated projects, the semi-rigid behaviour of joints which are commercially used in the UK for precast concrete frames will be accurately modelled using the FEA method. Standard FEA techniques for reinforced concrete structures will be proposed firstly. After calibrations to match existing test results, the techniques will be used in sensitivity analyses for the semi-rigid behaviour of the joints of a wide range of geometry and material parameters. Then predictions of future joint characteristics, and recommendations to improve engineering practice can be made. Finally, application of the techniques will be extended to model

the confinement behaviour of concrete circular columns encased in fibre reinforced plastic tubes.

1.2 Joints in precast concrete building frames

In monolithic reinforced concrete frames, the term *frame joint* generally means the location including the zone where beams and columns intersect together and the adjacent ends of beams and columns where the section properties differ from the majority of the span. In a precast concrete frame, details of beam-column connection are quite different, normally beams bear on to columns, and the *intersection zone* is part of the column. In the present research, *joint* is used to indicate the wide zone of the intersection of precast members as in a monolithic frame. The components linking beams and columns together are named *connectors*, and the physical interface between two components is refereed to as a *connection*.

According to their locations, four basic types of joints exist in a plane frame. These are: external joint on top level of a frame (╔), internal joint on top level of a frame (╦), external joint (╠) and internal joint (╬), see Fig. 1.1. If the beams in the perpendicular direction of the plane frame are considered, more repeats of these types of joint will appear[29].

Depending on the capacity of internal force resistance and the stiffness, the joints in a precast concrete frame can be distinguished into three types. One is the joint which is capable of continuously transmitting moment with a rigid stiffness the same as a monolithic joint. It is called a hard joint, moment continuous joint or rigid joint. The joint is not truly rigid, so the term moment continuous joint is preferred in this thesis. Fig. 1.2 shows a typical example of a moment continuous joint. In contrast, many types of joint are those which are designed to transmit shear forces from beams to columns, and can resist a limited amount of moment with some rotation stiffness. It is called a soft joint, simple joint or semi-rigid joint. Semi-rigid joint is the term used in this thesis. If the moment capacity is very small, then the semi-rigid joint is assumed to behave as a pinned joint.

Moment continuous joints are reliable but difficult and expensive to build. Normally they are used in the frames for the purpose of resisting severe actions, such as an earthquake. These frames are required to have adequate capacity to dissipate energy, that is, to have

enough strength, stiffness, ductility and stability. Semi-rigid joints are convenient for construction, and also can meet particular functional requirements by carefully design.

1.3 Structural effects of semi-rigid joints

The mechanical properties of joints will significantly affect the distribution of internal forces as well as the mechanical behaviour of a frame. Compared with the frame with beams simply supported on the columns, frames with semi-rigid joints have the following advantages:

a. The moment at span centre of a beam reduces incrementally with the increase of the moments at beam ends. The failure mode will be changed from at the span centre only to at both span centre and/or beam ends. The capacity of preventing cracking has been improved. Thus the beams can contribute to the load reaction more efficiently and economically. The moment along the height of a column may redistribute in the two different directions. Overturning moment will be resisted by the whole structure whilst producing additional axial forces in the columns. This will reduce the magnitude of the moments in the columns.

b. Deflection at span centre of a beam will decrease greatly, since the stiffness of the beam has been increased. Stiffness and stability of the columns will be enhanced, thus stiffness and stability of whole frame will be improved.

All of the benefit can be achieved based on adequate capacities of moment resistance and rotation stiffness of the joints, which may be obtained by efficient and accurate design.

1.4 General considerations of connection design

The basic principle in selection and design of connections for joints in precast concrete building frames is that the connections will not be the weak links of the structures. In other words, the connection will not fail before other members in the frames. In order to realise this principle, the following general conditions should be satisfied:

a. Structural function

Connections must have adequate strength to resist the actions in both erection and service phases. The actions may include forces, such as compression, tension, shear, bending, and torsion, caused by loads and such effects as creep, shrinkage, temperature

change and settlement. The concentration effect of local stresses should also be considered.

The connector stiffness in the direction of the joints should be high enough to meet the requirements of function in both construction and service phases.

Rotation capacity of connectors is also required to improve the ductility and stability of the whole structures.

b. Construction

Manufacturing of connections should be simple and technically feasible, so maximum economy and quality of precast concrete construction can be achieved. Standardisation of components and connections are recommended for precast concrete structures.

The connections should be rapidly made and have an immediate strength and stability so that temporary supports are not required. Enough space should be provided for erection, and tolerance should be limited within a suitable range. Field welding should be kept to a minimum or avoided, since its quality is not easy to control and it is expensive. Where cast in-situ concrete is required for the joints, the members of the joints should be, where possible, self shuttering.

c. Durability

Connections should be capable of resisting corrosion and fire. Suitable concrete cover should be provided to protect all steel elements against both corrosion and fire.

d. Appearance

It is desirable for a built up structure to have an invisible connection, a neat and clean finish.

1.5 Connections in semi-rigid joints

The types of connections in precast concrete frames are numerous, hence it is impossible to describe all of them in full detail. However, the identical characteristics of all types is that the columns are the supports of the beams, and the beams bear onto connectors fixed on the columns. The fundamental functions of the connectors are to withstand the vertical forces from the beams. Cantilevers projecting from the surfaces of columns

therefore are the essential members of the connections to support the shear forces. The cantilevers can be made of different kinds of materials with different details.

To increase the stability of both the beams and the frame, additional connectors are often used to connect the top of the beams to the columns. Because these connections have large eccentricities from the corresponding main shear connection between the beam and the column, enhanced moment resistance and rotational stiffness are generated in the joints. The connections are not designed specially to resist certain moments, thus the capacities of moment resistance and the rotation stiffness are not as high as that in the moment continuous joints. This creates the semi-rigid behaviour of some moment capacity being developed at significant rotation in the joints.

Typical examples of semi-rigid joints which are applied commercially in the UK are summarised as follows:

1.5.1 Reinforced concrete corbels

Reinforced concrete corbels are the connections widely used in precast concrete frames, especially in industrial building constructions. As cantilever members the corbels are monolithically cast together with, and thus do not detract from the strength of, the columns. Special details are designed to transfer the forces from the beams to the corbels. The connections between the beams and corbels are made by welding or bolting together steel plates embedded in the two precast members, see Fig. 1.3, for instance.

Reinforced concrete corbels possess advantages of higher capacities of load resistance, reliable transmissions of forces, rigid stiffness and convenient construction, etc.. However the corbels often project from the frames into the occupied space, and this is not expected in civil buildings. Alternatively, the corbels may be designed within the beam geometry as a halving joint, so that an invisible connected structure can be achieved.

To reduce the complex reinforcement detailing in the corbels, some kinds of steel fibres are sometimes included into the concrete to increase the shear strength and avoid congestion of stirrups[30].

1.5.2 Steel inserts

In these connections, the cantilevers are made up of steel members which are embedded into the columns. In some case steel inserts also can be incorporated into beams. The steel insert may be a solid billet or some kind of formed steels, such as H, Π, or rectangular hollow section steel, etc.. Of these possibilities, the billet is the most popular.

Compared with reinforced concrete corbels, steel inserts offer connections with simple details, much smaller sections, and higher ductility. Thus it is easy to keep the connection within the depth of the beam, and hence an uniform construction depth can be obtained. However, special consideration is required to minimise the voids formation under the embedded members during casting. In addition, particular care is also needed with the projecting parts during handling and lifting to avoid their distortion.

Recessed beam ends are normally used to hide the steel inserts within the beam depths. Steel plates incorporated into the beam ends are commonly used to ensure the reliability of connection between beams and columns. Fig. 1.4 shows a typical example of a joint with billet and welded steel plate connection.

1.5.3 Steel bolted cleats

In this kind of connection steel bolts and cleats are used similar to those used in steel frame assembly, see Fig. 1.5. The bottom cleat serves as the cantilever member which bears the vertical shear force from the beam end, and the lateral force caused by the moment at the beam end. This lateral force is transmitted through the dowel action of the vertical bolt and the friction between the beam end concrete and the cleat seat. The top cleat provides lateral force to create the moment at the beam end, and stability and torsion restraint to the beam end. All of the cleats are attached to the columns by bolts (normally grade 8.8 high-tensile steel bolts) which pass through sleeved holes in the columns and are thus fitted on site immediately prior to frame assembly. The precast beam has halving joints at the ends, and the reduced beam depth bears onto the seat cleat to derive immediate support. Special details strengthen the reduced beam section at the end. A vertical bolt passes through the top cleat, the beam end and the bottom cleat to fasten the beam to the column both at top and bottom. As mentioned above, this vertical bolt transmits lateral forces to the top and bottom cleats as well. The small gap

left at the joint is shuttered and filled with expanding grout to form a fairly rigid, flush joint, adding considerably to the structure's stability during continued frame erection. The grout also provides corrosion and fire protection.

1.6 Research background

Semi-empirical design guidance (ISE) was developed from test programmes carried out in the 1960's and 1970's by, for example, Somerville, G.[8].

More recent relevant research on precast concrete joints conducted in the UK can be summarised as follows.

Mechanical behaviour of sleeve bolted cleat connections has been experimentally and numerically investigated in the University of Southampton[10, 11]. A set of precast concrete subframes with sleeve bolted cleat connections have been tested[12, 13]. Additionally, a data base of experimental results of joints in precast concrete frames has been developed.

In the University of Nottingham, semi-rigid behaviour of sway joints with corbel, billet and welded plate connections in precast concrete frames has been studied. A series of effective length charts based on an elastic analysis using stability functions were developed[14].

City University made a computer program SWANSA which was especially used to analysis precast concrete frames with semi-rigid connections. This program was validated against experimental results obtained in both Nottingham and City Universities[15].

Lately the three universities carried out co-ordinate research projects funded by EPSRC, on the semi-rigid behaviour of joints in precast concrete frames. Full scale no-sway subframes with and without slabs tested in the University of Nottingham[16, 17]. City University developed a new design method which utilises a simple frame analysis, and modelled some joints tested in the University of Nottingham[18]. The task of Southampton University was to accurately model the performance of the joints, and this was the fundamental work addressed in this thesis[19~25].

1.7 Scope of the present research

The above research background shows that the semi-rigid behaviour of some typical joints have been investigated experimentally and numerically. However, both accurate and extensive analyses using FEA techniques are essential to study the internal mechanism and variations to a wide range of parameters of the joints. Thus predictions for characteristics of the joints and recommendations for improved engineering practice can be made. This defines the scope of the present research.

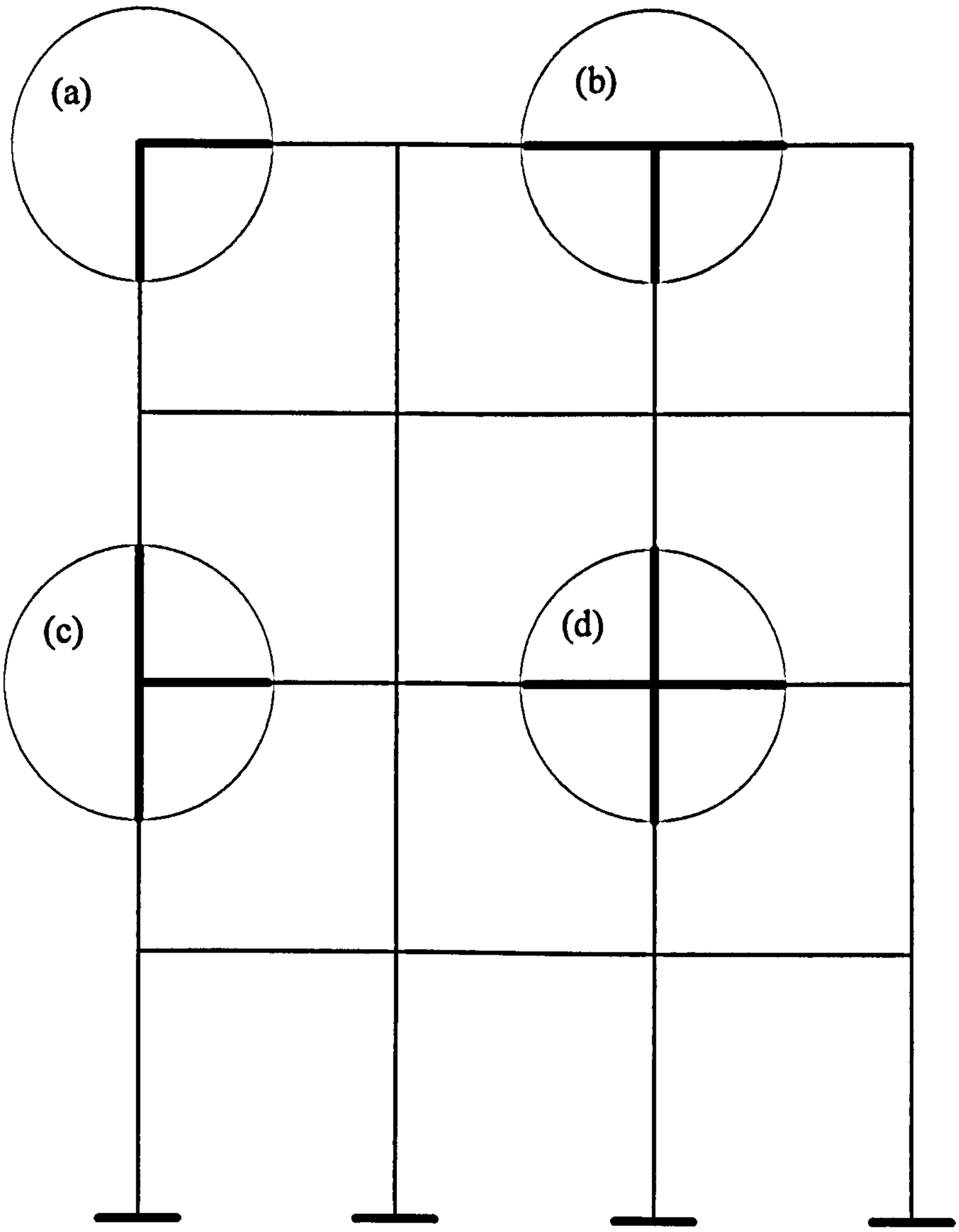

(a) External joint on top level

(b) İnternal joint on top level

(c) External joint

(d) Internal joint

Figure 1.1 *Joint types in building frames*

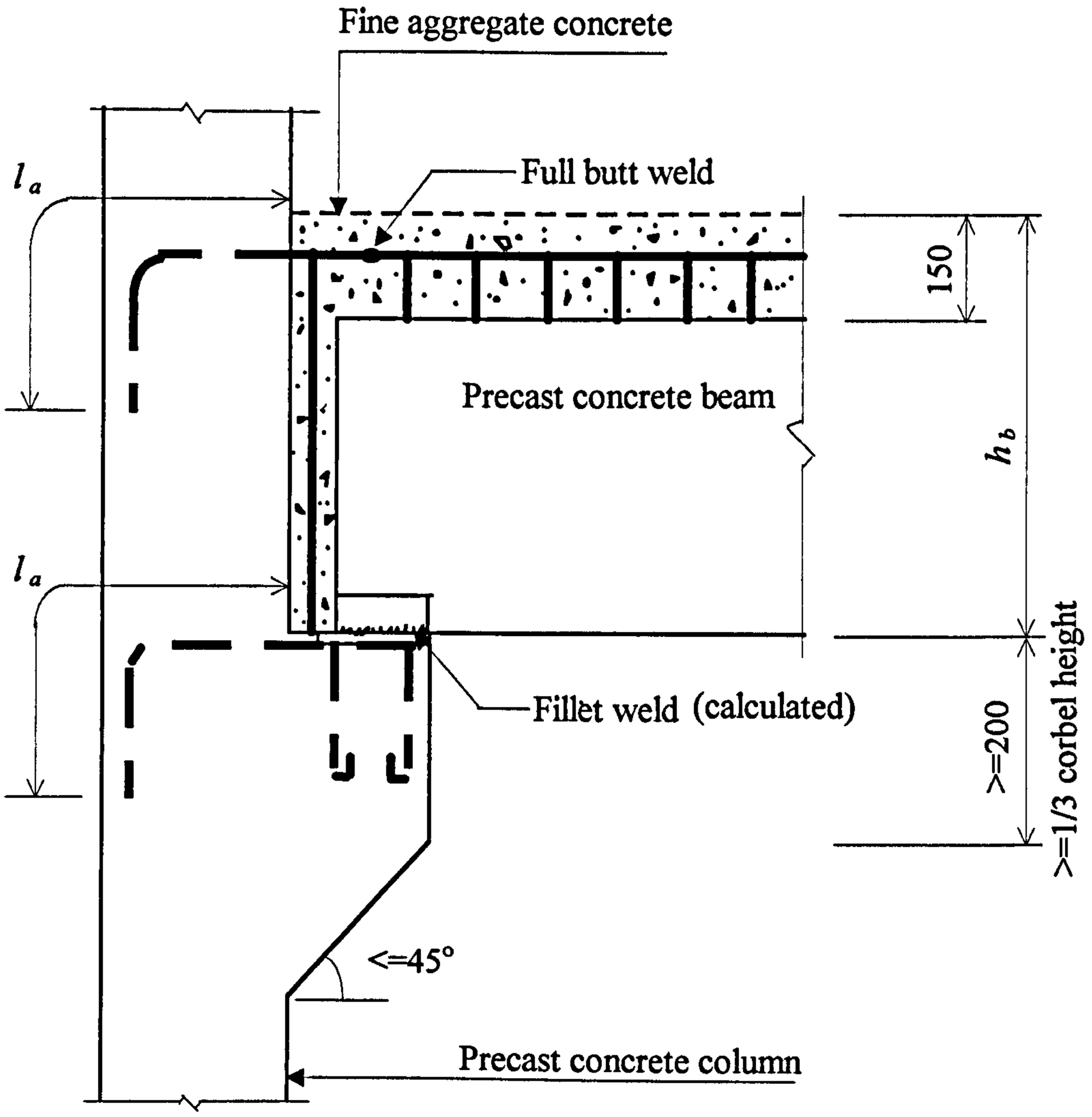

Note: l_a is the anchorage length of reinforcement in earthquake resistance design

Figure 1.2 *Moment continuous reinforced concrete corbel joint*

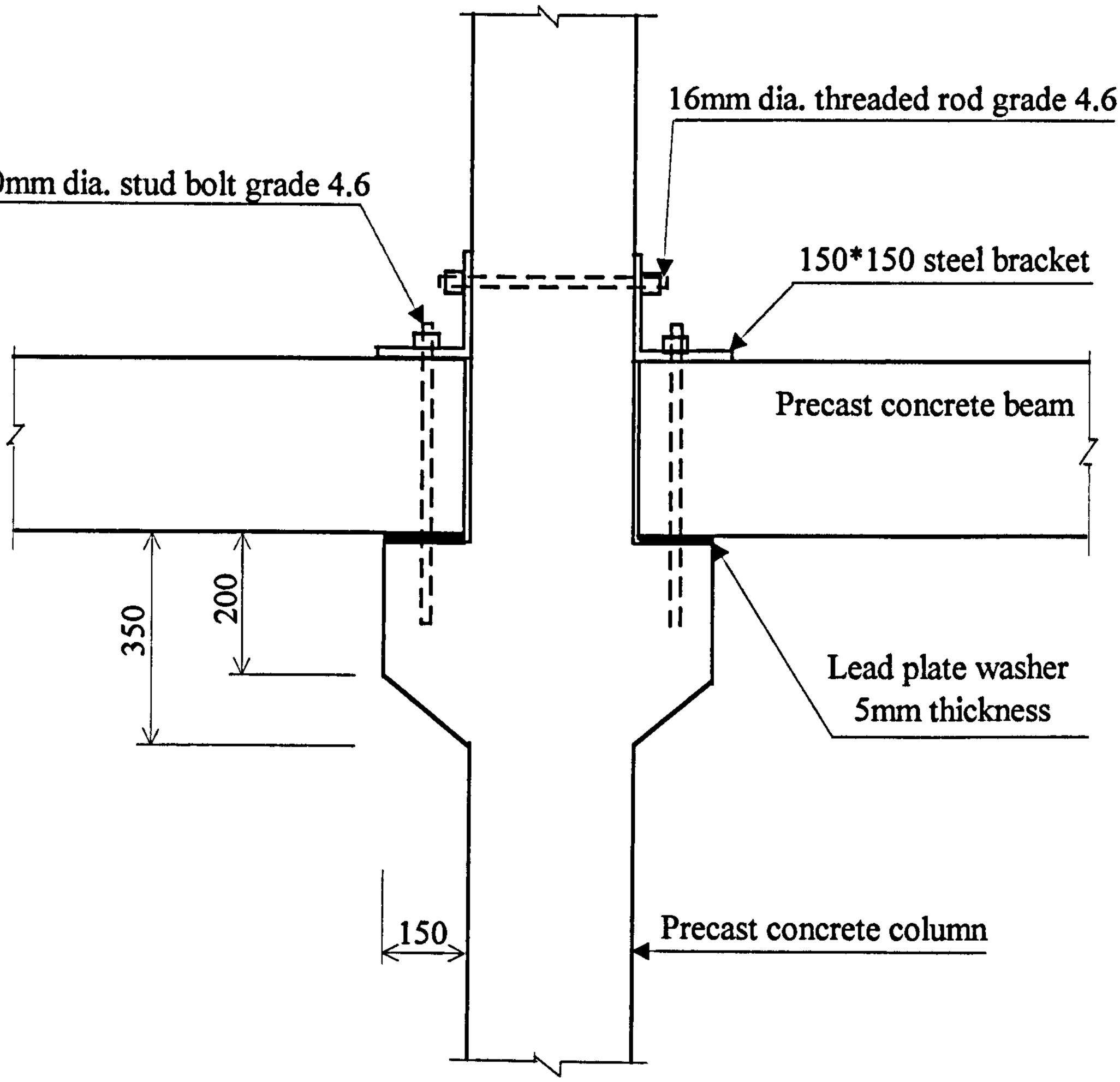

Figure 1.3 *Reinforced concrete corbel connection*

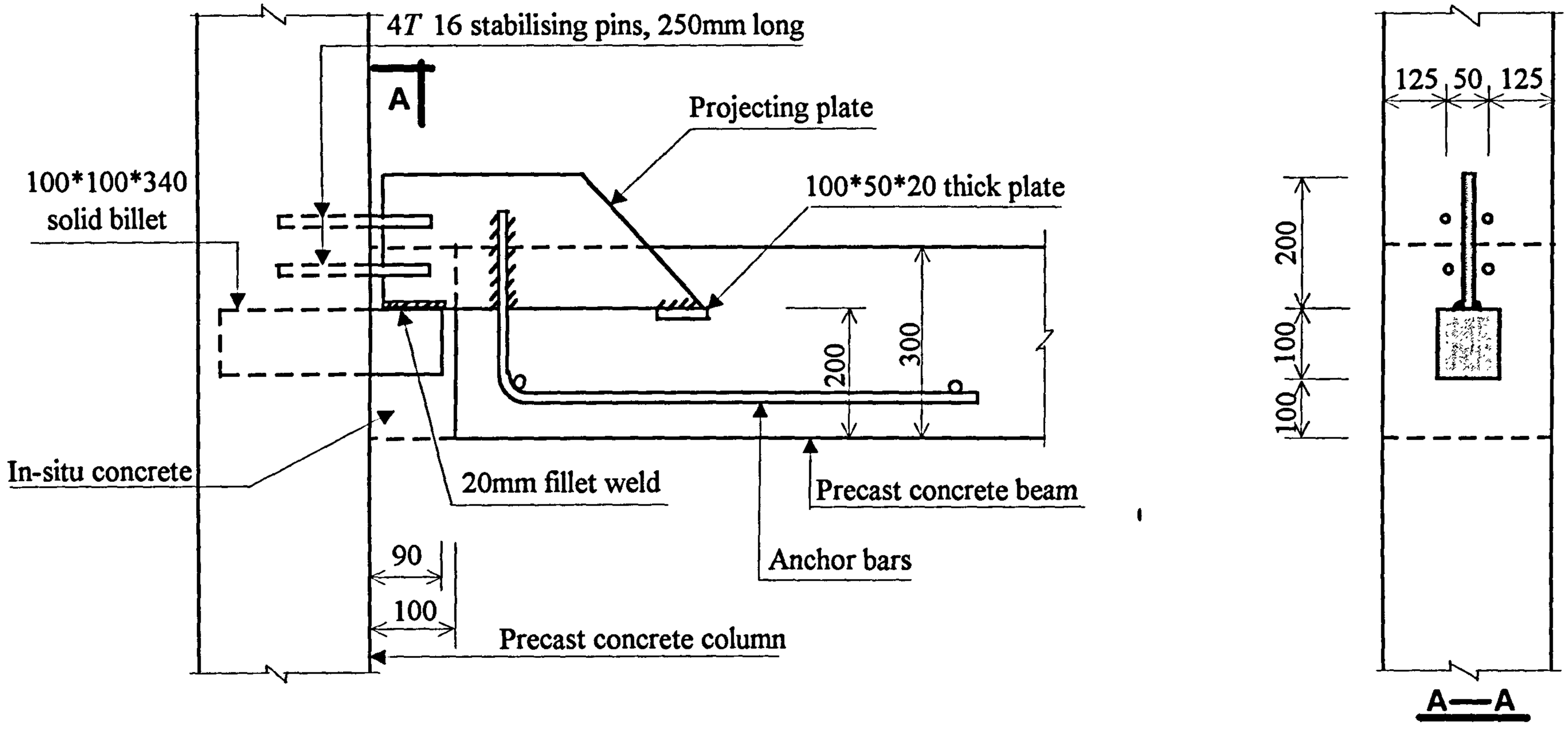

Figure 1.4 *Steel billet-welded plate connection*

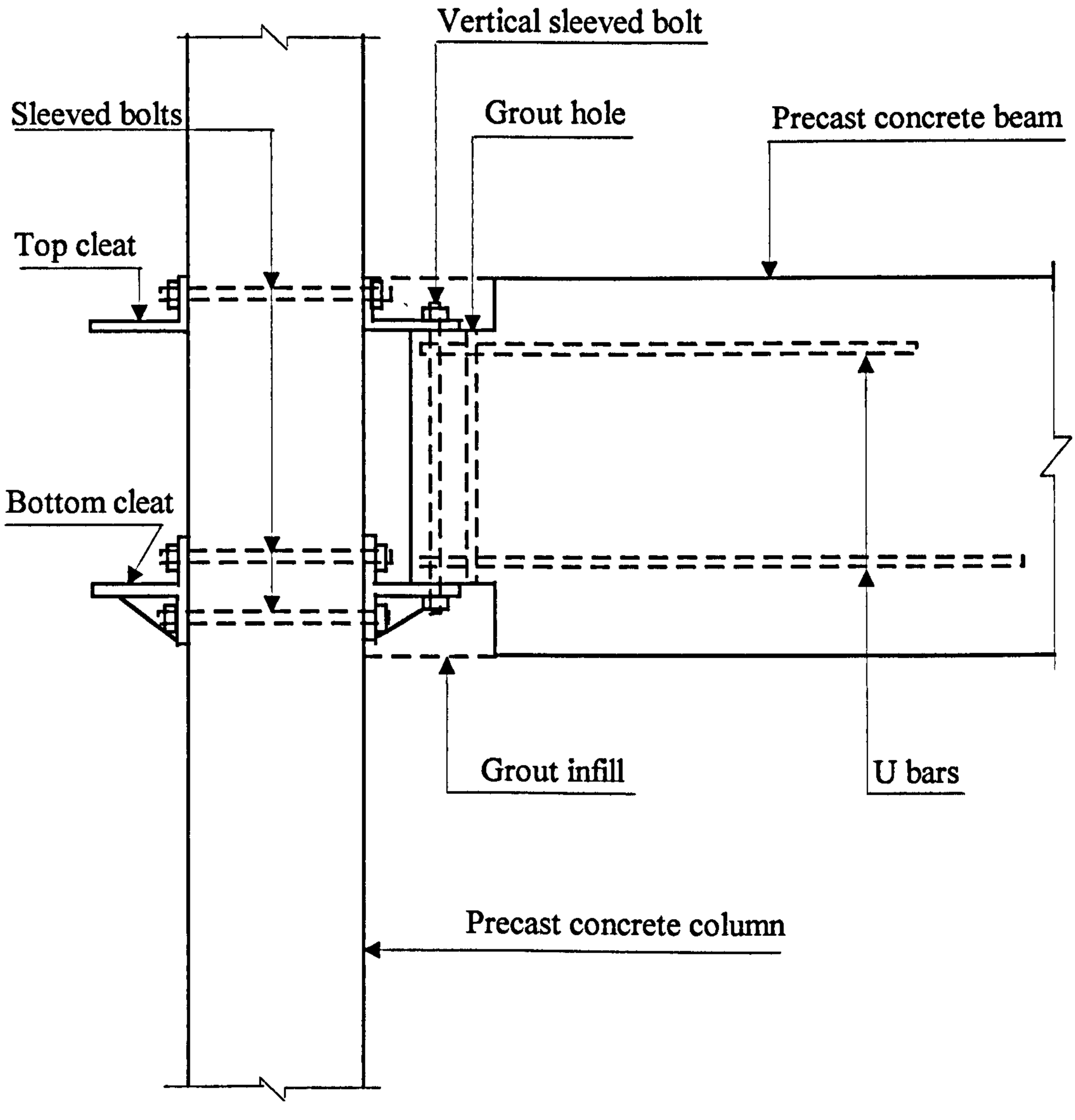

Figure 1.5 *Sleeve bolted cleat connection*

Chapter 2

Theory and Method of Finite Element Analysis

2.1 Introduction

Finite element analysis techniques have been introduced into reinforced concrete structures since the 1960's. Today, particular element types tailored for the analysis of reinforced concrete can be found in most popular commercial FEA packages. Since the nonlinearity, variability, cracking, crushing and creep nature of concrete material is complex, application of FEA techniques to concrete structures is still limited to some extent, especially in the analyses of large and complex three dimensional components and structures. Investigations for details of the modelling techniques in this area are essential. A standardisation of FEA techniques for reinforced concrete structures is aimed to be established in the present research, which is expected to be used subsequently in any general reinforced concrete structures.

A series of prerequisites are required for any finite element analyses. These prerequisites will be the foundation of the standardisation. Normally the prerequisites include choice of program, simplification of the analysed system, design and generation of model, treatment of particular problems, and selection of solution method. This chapter introduces the choices of these items. Once the items have been determined, they will be kept unchanged and applied to all of the modelling in the present work. The items selected only for particular applications will be described in the relevant chapters.

2.2 The ANSYS programme

Computer program ANSYS is a general purpose program introduced by Dr John Swans and Swans Analysis Systems, Incorporated(SASS), in 1970[31]. Today, possessing the latest finite element analysis and design technology, ANSYS is widely used by researchers and engineers. ANSYS can be used for almost any type of finite element analysis. In the other words, the program can be used in all kinds of subjects. For structural engineering analysis, it can deal with static, dynamic, buckling, etc. problems in both linear and non-linear states. Mainly because of these features, the ANSYS program (revision 5.0) is chosen as a basic tool for the present research.

The ANSYS program consists of two basic levels. One is the *begin* level that acts as a gateway of the program. The other is the *processor* level containing several processors. Each processor serves a special purpose, from pre-processing, loading and solving, to post-processing. ANSYS offers a library of over 100 standard elements including many specialised elements that can be used for most kinds of structural engineering analyses. There are over 800 commands in the program, each acts as a specific function. ANSYS can be run either in interactive mode or batch mode. The program works with one large database that stores all input data and output data in an organised fashion. Thus it is quick and easy to list, display, modify, or delete any specific data item. Details of characteristics of the program can be found in the ANSYS user's manual[31].

2.3 Model geometry

One of the fundamental decisions taken when planning an analysis is how to represent and simplify the geometry of the model. The basic rules recommended for the analyses of problems within this research programme are:

a. Main dimensions of the components must be represented as exactly as possible because they will significantly control the mechanical behaviour of a model. Herein the *main dimensions* means extents of section and length or height of components, such as beams, columns, bolts, billets, steel plates, etc., of an analysed specimen.

b. When both the geometry and the loading have a common axis of symmetry, it should be used to simplify the problem. Frequently only half, a quarter, or even one eighth of a

specimen needs to be modelled, if there are one, two, or three axes of symmetry, respectively. This will significantly save both space and time required to run the model.

c. Dimensions of some small or special components will affect the mechanical behaviour of an analysed specimen slightly, but exact representation of their geometry will cause the whole modelling process to become much more complex. Some simplifications are necessary for these components. For example, both the main reinforcements and links will be modelled by spar elements that can only be subjected to axial forces in either compression or tension. Details of the elements are described in the relevant chapters.

2.4 Mesh generation

2.4.1 Method of mesh generation

The ANSYS programme provides two ways to generate meshes for models. The first is *solid modelling* with which the program generates all the nodes and elements automatically following the described geometric boundaries, using the established size and shape of elements. The second method is *direct generation* by which the location of every node, the size, shape and connectivity of every element is determined manually. Although *solid modelling* is an easy way to generate mesh for models, it sometimes uses large amounts of CPU time, and 'fails' to generate a valid mesh under certain circumstance. In order to control accurately the meshing of a model, *direct generation* is selected as the preferred method for the present work.

2.4.2 Fineness of mesh

It is generally recognised that the finer the mesh, the higher the accuracy of an analysis. A compromise, however, must be considered between the fineness of mesh and the time taken to obtain a solution when analysing full scale structures. In areas of stress concentration the element needs to be finer to accurately represent the rapidly changing stress gradient. Transitions between fine and coarse meshes must be effected smoothly.

In the modelling of the joints in precast concrete building frames, the stress concentration areas are at the steel connectors and the surrounding concrete. Therefore,

a finer mesh is only applied to the connectors and the concrete which withstands complex and high stresses.

The element mesh is also arranged to coincide with the load path and boundary conditions, so that it is easy to apply load and constrain boundaries.

2.4.3 Transitions between fine mesh and coarse mesh

Transitions between zones with a fine mesh to zones with a coarse mesh are best achieved by incrementing the element geometry in alternate planes. This is illustrated in Fig. 2.1. No internal element boundary should terminate at an orthogonal boundary. Effectively, alternate layers of elements contain both rectangular and triangular prisms. The numerical accuracy of this arrangement is greater than the alternative of a single layer of elements containing tetrahedral.

Normally, wedge elements will be required to achieve the transitions. Application of this kind of elements, however, should be kept to a minimum and in lower stress gradient. A warning message appears during the checking phase to indicate the presence of such degenerated element.

2.4.4 Shapes of solid elements

The aspect ratio of each solid element should be maintained within the range of 0.33 to 3.00 whenever possible. This constraint forces consistency of numerical errors in the three orthogonal directions. This condition can be met in most of the mesh elements, especially in the fine mesh region. However, in some places where elements of different components contact to each other, or shapes of the elements coincide with shapes of the components, it is difficult to keep the aspect ratio within the required range. Numerical tests of some standard concrete specimen show that slender concrete element normally gives lower capacity of resisting compression, see section 4.7.

The internal angles in any surface should be within the range of $90° \pm 45°$, or a warning message will appear during the checking phase.

2.4.5 Concrete element mesh

Concrete element boundaries should coincide with the centreline of the reinforcing bars. Thus positions of both the main reinforcements and links dictate some of the nodal positions. Intermediate nodal positions are fixed by the required shapes of solid elements.

2.5 Node numbering

Normally, nodes should first be numbered along the axis which contains the fewest nodes. Parallel arrays of nodes should be numbered starting at the same end as the first array, and progressing in the direction of the axis which contains the second lowest number of nodes. This numbering system will generally minimise the stiffness matrix bandwidth, thereby also reduce both the space and the time required to run the model. However, when there is only localised contact between adjoining components, the nodes should be numbered with the nodes on the interfacial boundary being sequential. This constraint overrides the normal numbering sequence.

2.6 Main element types

Each element has its special capabilities and properties. Depending on the mechanical function and material composition, each component requires to be modelled by elements with specific characteristics. The ANSYS program possesses a large element library that supplies a wide range of element types. Determination of element types selected in the present work is described as follows.

2.6.1 Steel components

Steel items in the joints, such as bolts, bolt sleeves, billets, plates, and welded-plate cleats, will be subjected to complex stresses. They will significantly affect the behaviour of the joints, locally. Thus they should be modelled by some kind of three-dimensional solid element. An eight-node isoparametric solid, named SOLID45 in ANSYS, is selected for all of the steel components. This element has capabilities of plasticity, stress stiffening, large deflection, large strain, etc.. It not only can represent the mechanical behaviour of steel members effectively, but comparing with the related twenty-nodes

element (SOLID95), it is also simple and economic to be run in the programme. Additionally, node number of this element is compatible with that recommended for concrete modelling, described subsequently in Chapter 2.6.3. This coincidence of node number between adjacent elements is essential, and also convenient for mesh generation of models.

2.6.2 Reinforcement

In finite element analysis there are three approaches to represent reinforcements in concrete. One is to add spar elements along the central line of the reinforcement. The second is to add reinforcement as smeared material in anything up to three directions. The third is to use two or three dimensional solid elements. In the first two methods it is assumed that bond between the reinforcement and the surrounding concrete is complete, and the reinforcement is subjected only to axial tension or compression so that the modelling is simplified. In the third method, full stress distribution can be modelled. Additionally, slip characteristics between reinforcement and concrete, and dowel action of reinforcement can be modelled. The latter method is suitable for the special local behaviour analysis, and requires more elements. The first approach is preferred because spar elements are more accurate in modelling the reinforcement behaviour in complex stress situations than the smeared material capability of the element. The smeared material option for modelling reinforcement has been found to be accurate only if the member is acting primarily in bending.

The principal contribution of main reinforcements and links is to resist axial forces. This can be best represented by using the three-dimensional spar element LINK8 in ANSYS. This element type has capabilities of plasticity, stress stiffening, etc.. Only two nodes on the reinforcement axis are required to defined this element geometrically, and these nodes coincide with corner nodes of the surrounding concrete element.

2.6.3 Concrete

Concrete is a particular kind of material that behaves non-linearly in its stress-strain relationship, with cracking in tension and crushing in compression. In the ANSYS programme a special three-dimensional element, SOLID65, is supplied to represent the

properties of solids with or without reinforcing bars (rebars). This element offers both cracking and crushing capabilities, and additionally it will represent plasticity and creep. The rebars may be added as smeared material in up to three directions, each with the capabilities of plastic deformation and creep. The element has eight nodes and is assumed to have isotropic material properties. Consequently, this element was selected at the start of this research for the concrete modelling. This element remains the one recommended by ANSYS at the conclusion of the research, and has the same element functions in the most recent update revision ANSYS 5.3.

2.6.4 Contact element

In the joints of precast concrete frames, gaps may occur between precast components as they are assembled, or may develop between components as they are loaded. The gap or contact problems needs to be modelled by using contact elements.

The ANSYS programme provides several choices for contact element types which transfer load only when the materials are in contact at the gap interface. These are point to point or point to surface contact elements, with either two or three degrees of freedom. In the present work, where the mesh of the model will be created by direct generation, it is very easy to ensure the contact surfaces of the two components are designed with compatible mesh. The two degrees of freedom elements can only be applied in a plane problem, while three dimensional analysis is required in the present research. Therefore, the three dimensional point to point contact element, CONTACT52, is chosen.

Most interfaces between adjoining components are initially in contact with each other, that is, the initial gap is zero. Zero gap, however, is not applicable to element CONTACT52. A value of 10^{-5} mm is used when the gap between the contact surfaces is zero. If the value is less than 10^{-5} mm, the value will be treated as 0.00 by the program.

The stiffness of contact elements will not affect the results significantly, and a value of the order of the related spring stiffness is recommended[31]. The higher the stiffness

value, the more accurate the results, but the longer the running time required. The parameters used in the contact element are listed in Table 2.1.

The nodes at each end of the contact elements must be arranged geometrically so that they tend to approach each other as load-induced deflections occur. For plane contact surfaces all nodes on each side of an interface must occupy the same geometry locations. For interface surfaces which diverge, such as those with differently radiused, curved surfaces, however, the nodes must be aligned in the deflection direction. Fig. 2.2 shows the cross-section of a bolt which is located vertically within a sleeve of different material. The nodes around the bolt perimeter are located vertically about those of the sleeve, and not in the apparently more logical arrangement of being located at equal angles from the centre of the circle.

2.7 Simplified modelling of circular sections

In the precast concrete joints some components have circular sections. A steel bolt is a typical example. When their behaviour does not influence the performance of the joints significantly, they will be modelled simply, see Chapter 2.3. In the simplification, a quadrant section of the component is represented by a quadrilateral element. Generally, the circular section is simultaneously subjected to moment, shear force and axial force. The displacement of the component in the perpendicular direction of the section consists of the deformations caused by bending and shearing. Therefore, the shape of the quadrilateral element is determined by following the rule, that both the area and the second moment of area in the loading direction must be equal to those of the quadrant section.

To simplify the calculation, the lengths of the sides in both x and y axes are taken to be equal to the radius of the circle r, see Fig. 2.3. Thus, only the co-ordinates of point B in the figure need to be determined.

Assuming that the co-ordinates of point B are x_0 and y_0. The equations for straight lines AB and BC can be derived and expressed as Eqs. 2.1 and 2.2.

Line AB: $$x = x_0 \frac{r - y}{r - y_0} \qquad (2.1)$$

Line *BC*: $$x = x_0 + \frac{(r - y_0)(y_0 - y)}{y_0} \tag{2.2}$$

From the condition of equal area for the two sections, the following equation is obtained:

$$\frac{1}{2}x_0(r - y_0) + \frac{1}{2}y_0(r + x_0) = \frac{1}{4}\pi r^2 \tag{2.3}$$

$$x_0 + y_0 = \frac{1}{2}\pi r \tag{2.3a}$$

From the condition of equal second area for the two sections, the following equation is obtained:

$$\int_0^{y_0} xy^2 dy + \int_{y_0} xy^2 dy = \frac{\pi(2r)^2}{4 \times 64} \tag{2.4}$$

Substituting x in both the first and second items by Eqs. 2.1 and 2.2 respectively and integrating, Eq. 2-4a can be determined:

$$x_0\left(r^2 + ry_0 + {y_0}^2\right) + {y_0}^3 = \frac{3}{4}\pi r^3 \tag{2.4a}$$

Finally the co-ordinates of point B, x_0 and y_0, are obtained by combining Eqs. 2.3a and 2.4a:

$$x_0 = \frac{r}{2}\left(\pi - \sqrt{\frac{3\pi - 2}{\pi - 2} + 1}\right) \approx 0.796r \tag{2.5}$$

$$y_0 = \frac{r}{2}\sqrt{\frac{3\pi - 2}{\pi - 2} - 1} \approx 0.775r \tag{2.6}$$

2.8 Material properties

Normally material properties include constitutive relationships and failure models, and they are extremely fundamental and important in finite element analyses. For the analysis

of reinforced concrete structures the material properties of steel, concrete, and the interfacial bond-slip relationship should be considered.

In the joints of precast concrete building frames, failures normally occur in the connections and the surrounding concrete, while bond failure between the reinforcement and the surrounding concrete seldom happens. Thus complete connection between reinforcement and concrete is assumed in the models.

For the properties of steel and concrete, many input parameters are uncertain because of the nonlinearity and variability of the materials. Therefore, special attention is given to the development of standard methods to determine the parameters for both the materials. These methods can be summarised as follows:

2.8.1 Steel

Usually bar reinforcement is assumed to transfer axial forces only because of its slender shape. Uniaxial stress-strain relationships are adequate for the analyses. A multiaxial stress-strain relationship is required for analyses of the other steel components, but the criterion is based on a uniaxial stress-strain relationship. Thus, a simplified mechanical model for steel in uniaxial tension or compression is proposed, and the factors required by the model can be defined by a set of equations which are created using a statistical approach. Details of this part work are described in Chapter 3.

2.8.2 Concrete

Multiaxial stress-strain relationships are essential for concrete modelling. Parameters required by the ANSYS programme are listed in Table 2.2. It is clear that the properties in uniaxial compression and tension are still the basis of the definition. In the present work, constitutive equations to determine the parameters are recommended, and a simplified mechanical model for concrete in uniaxial compression is proposed. The method using smeared concrete material to avoid earlier failure of the concrete model is completed and improved. Additionally, a large number of numerical tests are carried out to investigate the influences of different variables on the concrete element. Details of this part work are given in Chapter 4.

It should be mentioned that the default values in Table 2.2 are valid only for stress states where following condition is satisfied:

$$|\sigma_h| \leq \sqrt{3} f_c \tag{2.7}$$

$$\sigma_h = \frac{1}{3}\left(\sigma_{xp} + \sigma_{yp} + \sigma_{zp}\right) \tag{2.8}$$

where σ_h is the hydrostatic stress, σ_{xp}, σ_{yp} and σ_{zp} are the principle stresses in principle directions x, y and z, and f_c is the uniaxial compressive strength of concrete. If the condition of Eq. 2.7 is not satisfied and the default values shown in Table 2.2 are assumed, the strength of the concrete material may be incorrectly evaluated.

2.8.3 Material strengths

One choice described here, which is applicable to both steel and concrete, is the material strength used in the finite element analysis. Among the material properties, such as strength, elasticity, ductility, durability, toughness, etc., strength is the most important and sensitive, and therefore it is the dominate factor. Usually the yield stress or proof stress is used to define strength for steel, and the cube or cylinder strength is used to define strength for concrete.

According to the purpose of application, several material strengths can be chosen. These are sample strength, mean strength, characteristic strength and design strength. Sample strength can only be obtained after a physical sample test. This value cannot be used to predict the material strengths of an analysed model because of the randomness of material properties. Mean strength normally is the average value of at least three standard tested samples. It is a statistical value with 50% of failure possibility. Characteristic strength is a statistical value based on large amount of physical test results with 5% possibility of failure, and is a standard value widely used in engineering standards and codes. Design strength is a one used in design work, with much smaller failure possibility and larger safety factor. The relationships of magnitude of the latter three values are that for a particular material strengths, mean strength is the highest, while design strength is the lowest.

In finite element modelling on the behaviour of engineering structures, normally test results should be matched firstly. The safety of the recommended design methods can be considered afterward. Therefore, the standard value of characteristic strength is used as the basic input strength for any kind of material in the present work, unless particular stress states are considered.

2.9 Loading and solving

2.9.1 Load application

In numerical analysis there are two ways to apply load. One is by adding increments of force, while the other is by adding increments of displacement. For non-linear analysis, if the load is applied by equal increments of force, the corresponding displacements become progressively larger. Consequently, there is a high probability that the model fails before the ultimate deformation of the model is obtained. However if load is applied by equal increments of displacement, the increments of force become successively smaller with increased displacement, see Figure 2.4. The second method is selected for the present work, which is realised by moving the boundary constraint in the ANSYS program.

2.9.2 Loading steps

Displacement increments are added in multiples, and the progress of the model can be observed after each displacement step. If the analysis fails during application of a displacement increment, the analysis can be terminated and the previous displacement step solution retrieved. Displacement steps are applied in the *time* option.

Modelling of the response of reinforced concrete structures is a typical non-linear analysis. The energy caused by the input external loads will be dissipated by the analysed system. The system is nonconservative, and the analysis is path dependent. Thus, substeps are required within each loading step. The increments of displacement, or the loading speed, at the critical location in each substep should be small so that a consistent result can be obtained. The magnitude of substeps should be dictated by strain rate. In the steel and concrete systems, non-linear behaviour normally appears earlier in concrete components than in steel components. Therefore, based on the numerical tests of

concrete prisms, displacement increments in the range 1% to 5% of the concrete ultimate strain are recommended, see Chapter 4.

2.9.3 Convergence tolerances

Several choices of convergence tolerances for successive iterations are offered in the ANSYS program. The convergence of a solution can be controlled by tolerances based on forces, moments, displacements, or rotations, or on any combination of these items. The force-based convergence serves as an absolute measurement of convergence, while displacement-based convergence provides only a relative measurement of apparent convergence. Additionally, for a modelling of a system including concrete elements, after crushing occurs at an integration point the strain of concrete at that point increases intensely. This may invalidate displacement-based convergence checking. Consequently, the force-based convergence checking is adopted as the convergence criteria. The values of the criteria are determined for each particular model.

No.	Parameter	Value used
1	Young's modulus, based on stiffness, k, below	Steel E_s: 205 kN/mm^2 Concrete E_c: equations in Table 4.2
2	Poisson's ratio, based on stiffness, k, below	Steel ν_s : 0.30 Concrete ν_c : 0.20
3	Static coefficients of friction, μ	Steel to steel: 0.25[3] Steel to concrete: 0.65[14] Concrete to concrete: 0.80[3]
4	Stiffness of the contact element, k	Greatest of adjoining element stiffness, steel: E_sA_s/l_s, concrete: E_cA_c/l_c. where A_s and A_c are the surface areas of adjacent steel or concrete elements, while l_s and l_c are the relevant thickness.

Table 2.1 *Input parameters of the contact element*

No.	Parameter	Value used
1	Modulus of elasticity for concrete, E_c	Equations, Table 4.2
2	Poisson's ratio of concrete, ν_c	0.20
3	Shear transfer coefficients for an open crack	0.50
4	Shear transfer coefficients for a closed crack	0.60
5	Ultimate uniaxial tensile cracking strength, f_t	Equations, Table 4.3
6	Ultimate uniaxial compressive strength (positive), f_c	Equations, Table 4.1
7	Ultimate biaxial compressive strength (positive), f_{cb}	Default value, $1.2f_c$
8	Ultimate compressive strength for a state of biaxial compression superimposed on hydrostatic stress state, f_1	Default value, $1.45f_c$
9	Ultimate compressive strength for a state of uniaxial compression superimposed on hydrostatic stress state, f_2	Default value, $1.725f_c$
10	Stress-strain relationship in uniaxial compression	The simplified model, Chapter 4

Table 2.2 *Input parameters of the concrete element*

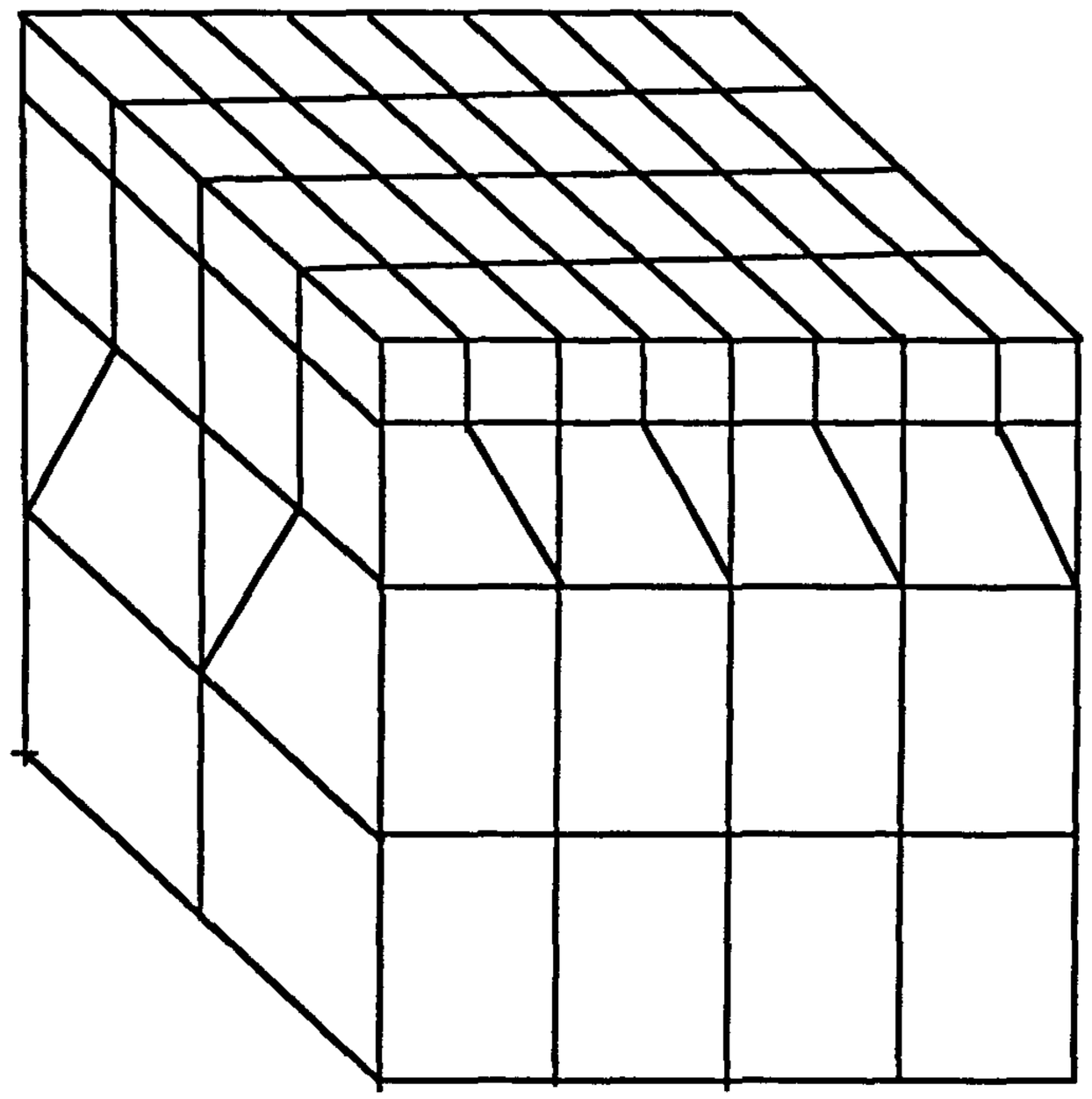

Figure 2.1 *Alternative element transitions*

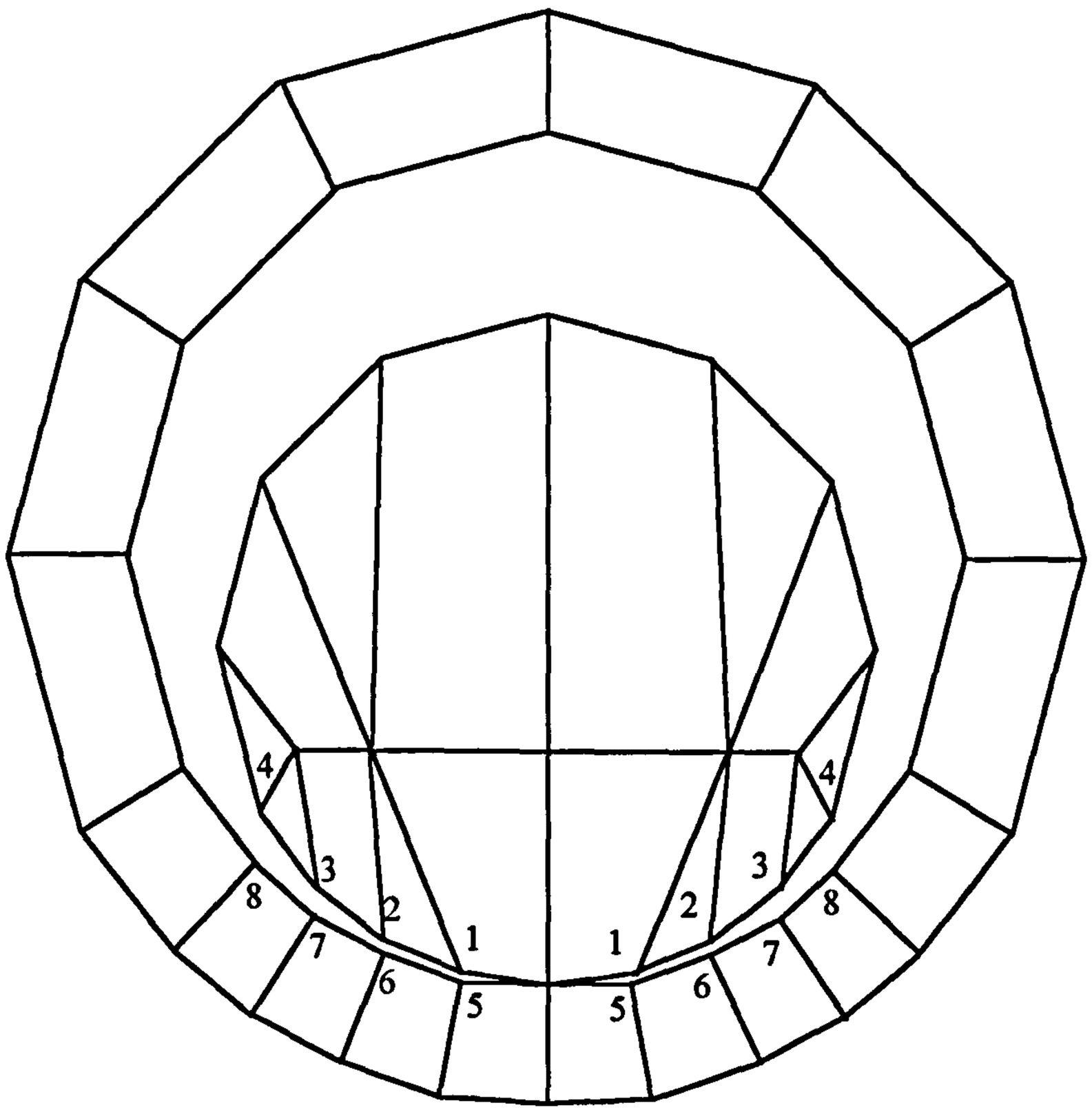

Nodes 1, 2, 3 & 4 and 5, 6, 7 & 8 vertically aligned

Figure 2.2 *Showing gap element orientation*

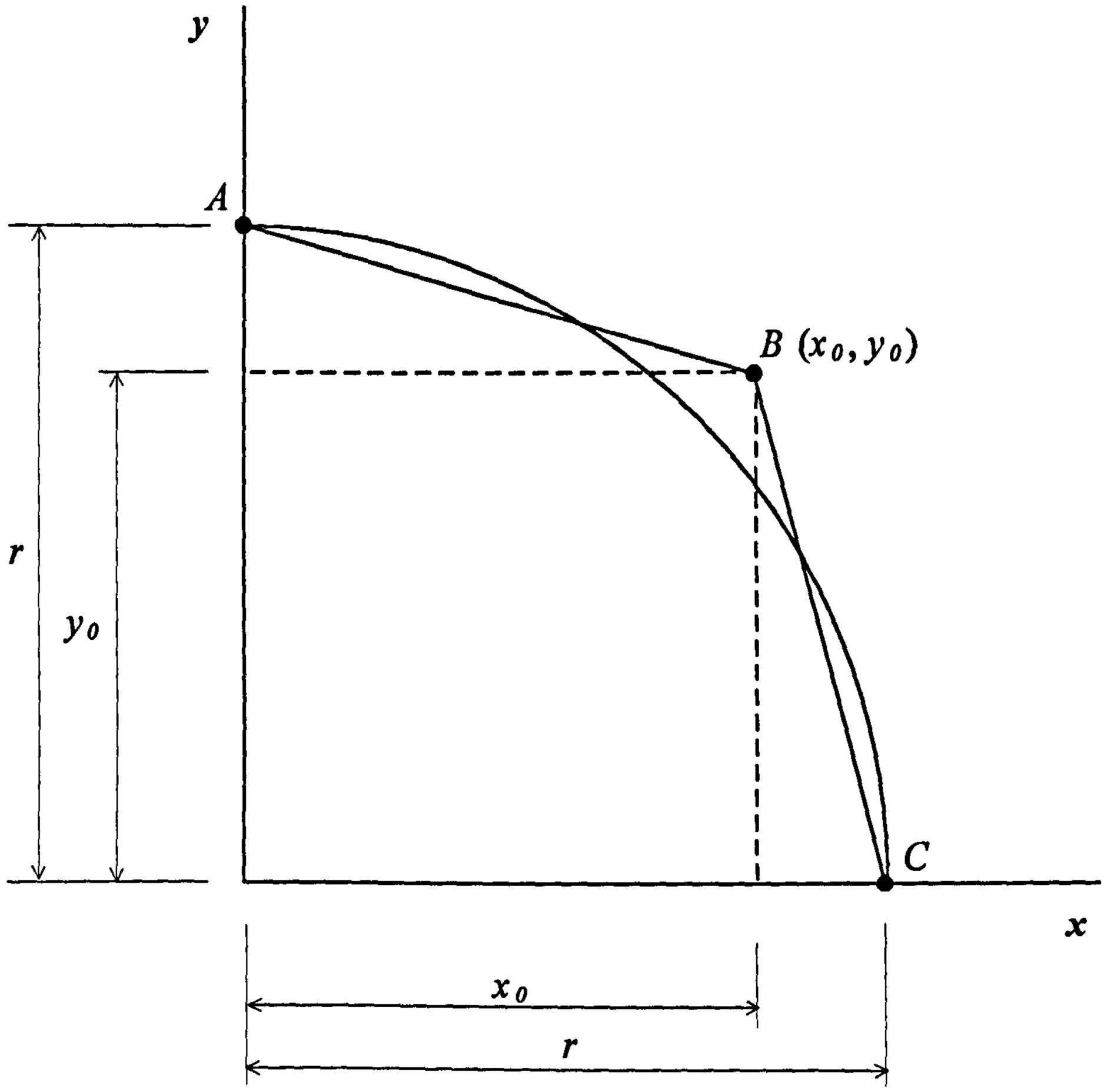

Figure 2.3 *Simplification of a quarter circle section*

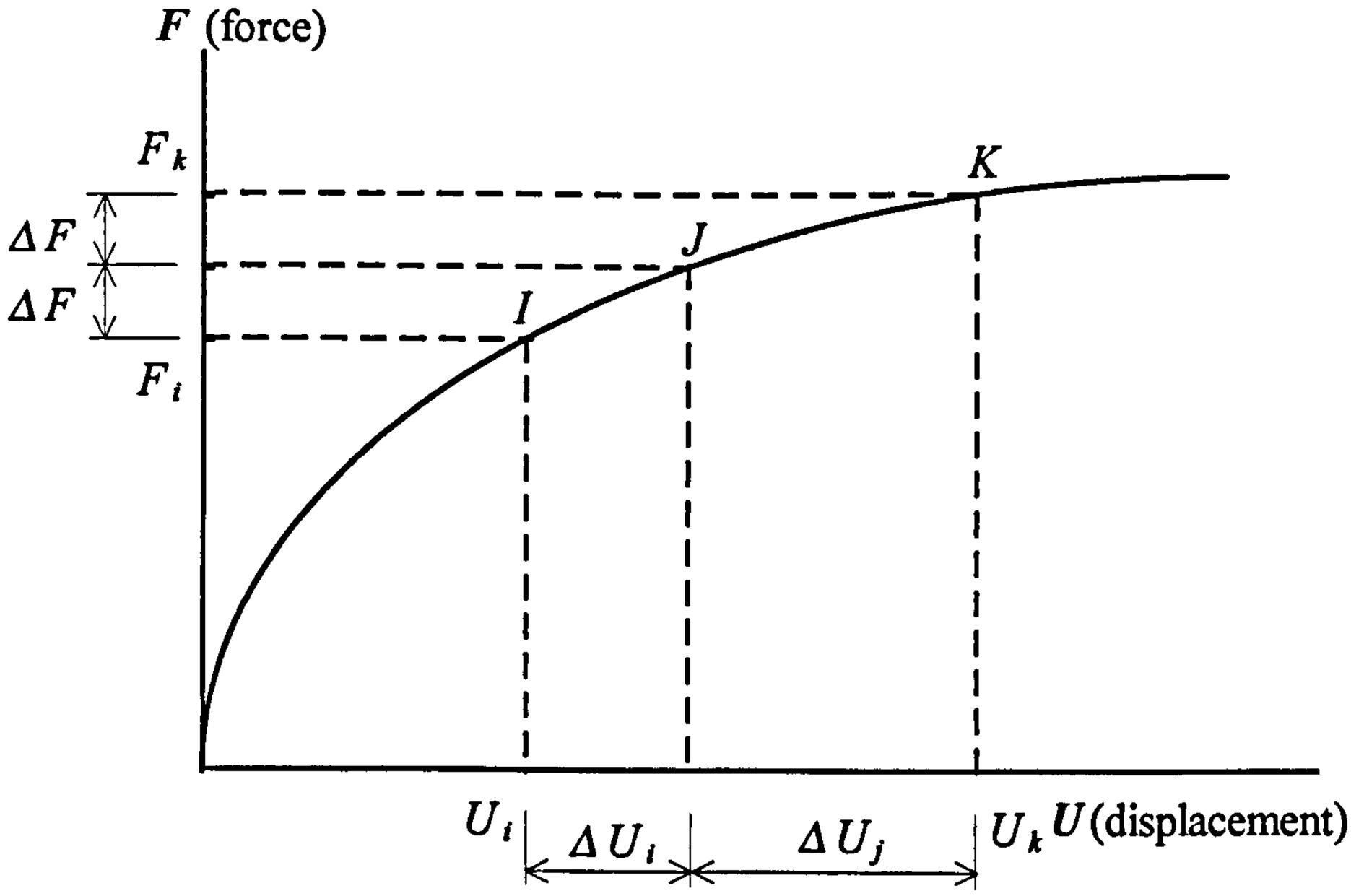

(a) Loading in increments of force

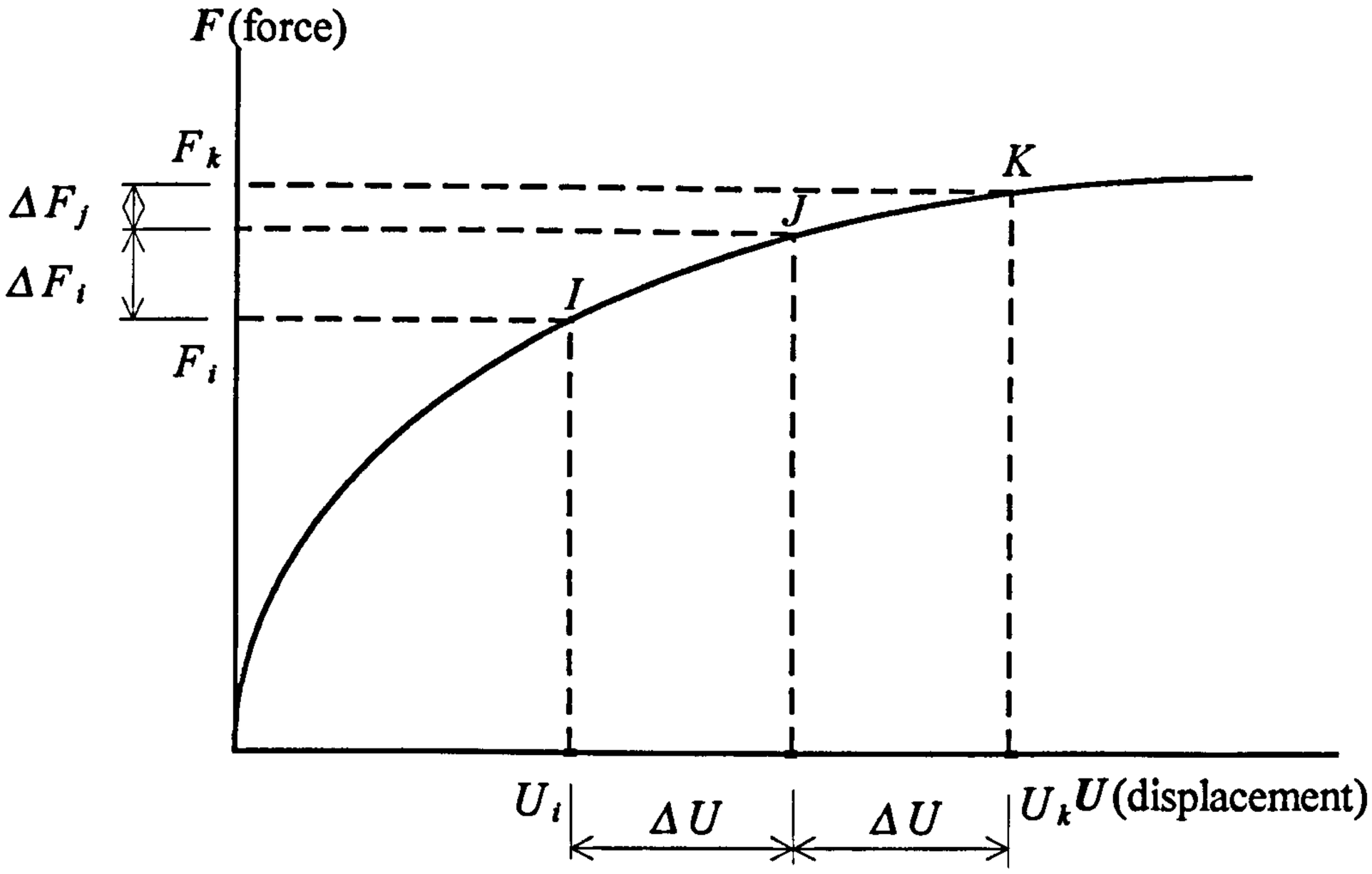

(b) Loading in increments of displacement

Figure 2.4 *Comparison of force with displacement increments loading*

Chapter 3

A Simplified Mechanical Model for Steel

3.1 Introduction

The stress-strain relationship of steel in uniaxial tension (or in uniaxial compression, which is similar to that in tension before the ultimate strength point) presents the fundamental mechanical properties of the material. In finite element analysis, reinforcement is normally modelled using two noded element which is capable of being subjected to an axial force in either tension or compression as if it is a member in a pin-jointed structure. In this case the stress-strain relationship of steel itself is enough to represent the properties. If some other steel components in a multiaxial stress state are analysed, the yield and fracture of the material will be dominated by some characteristics. The characteristics always include the parameters in uniaxial stress-strain relationship. Therefore, only the uniaxial stress-strain relationship, normally in the form of a simplified model, will be required as basic input data in general analyses.

Depending on whether a stress-strain curve has a definite yield point, the steels applied in structural engineering can be divided into two groups. Mild steel and hot rolled high yield steel, for instance, are widely used materials with definite yield points, while cold-worked high yield steel is one without a definite yield point for which the yield strength is defined in terms of a permanent strain, usually 0.2%. The typical stress-strain curves for steels[33~40] are shown schematically in Fig. 3.1.

Normally there are two approaches used to obtain mechanical properties of materials. One is from test results, while the other is from a number of recommended principal parameters in published standards and reference books. The models from test results are

usually very reliable and this is the most direct way. Full test results of mechanical properties of the materials, however, cannot be obtained for every finite element analysis, because test samples of the material may not be accessible. Even if the test is carried out, sometimes the full properties required in analyses cannot be achieved due to limits of capacities or functions of test machines. The models created from the conventionally quoted principal parameters, such as yield point and ultimate stress, can only give an approximate description because of both the randomness of mechanical properties of the materials and the absence of adequate parameters to describe the shape of the entire stress-strain relationship.

According to the requirement of accuracy of an analysis the stress-strain curve of steel can be simplified into different kinds of idealised models. Some typical models are shown in Fig. 3.2[36]. The models in Figs. 3.2a and 3.2b are too simple to give a full description of the curve. The model in Fig. 3.2c, however, is difficult to be realised in the general analyses.

All these factors lead to a need for a consistent means of representing the full mechanical properties of steel simply and effectively. In this chapter a standardised method and the essential factors are proposed. The method is applicable to all finite element packages, and its use is demonstrated in the widely used commercial package ANSYS[31]

3.2 Concept of the simplified mechanical model for steel

It is proposed that the stress-strain curves for all kinds of steel will be represented by a six-straight-line simplified model, as shown in Fig. 3.3. The position of the 6 key points at which the lines connect to each other will be determined by following the rule that in the main part the area under the model equals that under the original curve, that is the model should have same strain energy as that of the original curve. Herein the main part means the part before the ultimate stress point (point 5 in Fig. 3.3). The six straight lines are chosen because they are enough to fully represent the relationship and they just satisfy the limit of point number in the option of MKIN (Multilinear Kinematic Hardening) in the ANSYS programme.

In finite element analyses, if the test curves with full elongation for steel mechanical properties are supplied, the simplified model can be created easily using the definitions and rules given in this chapter. If the test curves are not available or inadequate

parameters are available, the factors of the simplified model can be created using the formulae developed statistically in the following sections of this chapter.

3.3 Principle to determine positions of the key points

3.3.1 Point 1

This point is defined as the limit of linear elastic state of steel. Thus the stress should be the value of limit of proportionality for steel whether with or without a definite yield point. The corresponding strain can be obtained from the ratio of the stress over Young's modulus.

3.3.2 Point 2

This point is one after which the modulus of steel will decrease greatly. For steel with a definite yield point the stress is the yield strength and the strain should be a little bigger than the ratio of yield strength over Young's modulus. For steel without a definite yield point, because the curvature between the point of limit of proportionality and the proof yield point is too big to be indicated by one straight line, this point should be between the two points and its co-ordinates will be determined statistically from test results.

3.3.3 Point 3

This point is at the end of the horizontal plateau for steel with a definite yield point, and at the 0.2% proof strength point for steel without a definite yield point. Therefore, for the steel with a definite yield point the stress should be a little higher than the yield strength and the strain will vary depending on the magnitude of yield strength. Both values will be determined statistically for the simplified model.

3.3.4 Point 4

The curvature between point 3 and ultimate strength point (numbered 5) is so great for most kinds of steel that the curve can not be replaced with accuracy by one straight line. Hence an extra point, numbered 4, should be inserted between the two points. The co-ordinates of this point for all kinds of steel will be determined statistically for the simplified model.

3.3.5 Point 5

This is the peak stress point of the curve. Thus the stress should be the ultimate strength for all kinds of steel, and the strain should be the corresponding value. The co-ordinates of this point for all kinds of steel will be determined statistically for use in the simplified model.

3.3.6 Point 6

This is the point at which a tested sample fractures. The stress is lower than the ultimate value in a general stress-strain curve (see Fig. 3.1, for example) in which the stress is calculated using the original cross sectional area. In fact this stress should be higher than the ultimate value if the calculation is based on the real necked area. In addition, negative modulus is not allowed in some elements in the ANSYS programme and only five points can be input in the option of MKIN. After the fifth point the program will treat the material as having the same stress as point 5 for all further increases of strain up to the ultimate strain. For the model in this chapter the stress is taken as equal to the ultimate strength (equal to that at point 5) and the strain is the fracture, or ultimate, value for all kinds of steel.

3.4 Experimental investigation

3.4.1 Purposes and specimens

Although the fundamental mechanical behaviour of different kinds of steel is well known, it is difficult to find literature describing the properties in detail. The aim of this present work is to build up a uniform model for all kinds of engineering steel statistically, so extensive experimental data will be required. For the purpose of understanding the mechanical properties of engineering steels by first hand experience and adding some data for the statistical work, some steel bars with different strengths and deformation capacities in uniaxial tension have been tested.

The test specimens were square bars, all with same section of 6.3×6.3 mm (1/4×1/4 in) and length of 275 mm, Fig. 3.4. Two typical kinds of widely used engineering steel were tested. These were bright drawn mild steel with and without stress-relief, one giving a definite yield point and the other not. Two specimens were manufactured for each kind

of steel, one to be tested until rupture, while the other test was stopped just before rupture in order to measure more accurately the ultimate elongation.

3.4.2 Test performance

The test was carried out in the Model Structural Laboratory at the University of Southampton. The specimens were marked at several positions before test, since necking might occur anywhere between the two jaws, Fig. 3.4. Therefore, several gauge lengths between the pairs of marks could be measured both before and after the test, giving a number of choices of method for determination of the ultimate elongation and strain for each bar tested.

The INSTRON test machine was used to apply tensile force to the specimen, and to plot the curve of load-crosshead movement automatically at the same time. The loading rate of 2 mm per minute was adopted. Because the deformation of the curve was the total between crossheads which is normally much larger than the deformation of the tested bar and is also non-uniform during the test, it is not suitable to calculate the material strain. Consequently, an extensometer was utilised simultaneously to measure the net deformation of the tested steel bar. The gauge length of the extensometer was 127 mm.

3.4.3 Test results

The stress-strain curves of the tested steel bars are shown in Fig. 3.5 and the key parameters are listed in Table 3.1. The maximum strain that can be measured by the extensometer is 2%, thus only the early parts of the curves were plotted on the basis of the results from the extensometer. The latter parts of the curves were plotted according to the results from the test machine, which were verified by the ultimate elongation between the pairs of marks spanning the fractured or necking areas. Almost all of the yield points occurred between the marks within the extensometer length of 127 mm. In order to permit comparison with other results and be used in the simplified model, the test results in Fig. 3.5 and Table 3.1 have been modified to correspond with the standard gauge length of $5.65\sqrt{S_0}$ (BS18, Part 1, 1970), where S_0 is the original area of cross section of a specimen.

3.5 Determination of parameters in the model

Because the values of Young's modulus and Poisson's ratio vary within only a very narrow range for all kinds of steel, the constants of 205 kN/mm^2 and 0.3 are taken respectively in the model.

The co-ordinates of the six key points are determined by a set of formulae which are derived statistically and will be described below.

3.5.1 Sources of data

The data used for the statistical work come from two sources. Firstly the data from our test mentioned above certainly are used and they are the most detailed ones. Secondly the data from several published standards and reference books also are chosen to enlarge the data base. All of the data used are listed in Table 3.2.

The strain must be a function of the gauge length in test used. The data from different tests have different gauge lengths. For example, the results of reinforcement from Reference 36 have a gauge length of 8 in (203 mm), while those from other references have gauge lengths of 5 diameters for a circular cross-section test piece and 5 widths for a rectangular cross-section test piece. The gauge length of 5 diameters or 5 widths is chosen as standard gauge length in the present work. Therefore, the ultimate strains with gauge length of 8 in have been enlarged by 1.25 times[35]. The reason why the ultimate strains need to be modified is that the gauge length will affect the strain seriously only after the ultimate strength arrives and the necking occurs.

In addition the ultimate strains in some published standards[35] also have been modified by increasing 1.4 times which is the safety factor for strength in those standards, because they are more conservative.

3.5.2 Explanations

a. For the convenience of evaluation, only one independent variable is required in the formulae, namely the yield strength of steel f_y ($\sigma_{0.2}$ for steel without a definite yield point).

b. There is no clear correspondence between the magnitude of yield strength and whether or not any specific steel will have a definite yield point. Normally a steel with a low yield strength will have a definite yield point, whereas a steel with a high yield

strength will be less likely to have a definite yield point. In the statistical work, when the behaviour is extremely distinct between the steels with and without a definite yield point, the formulae are determined separately for each type of steel. Interpolation is then made between the two types of steel. 200 N/mm^2 is chosen as the lowest likely yield strength and this steel is taken as typical of one with a definite yield point. 1200 N/mm^2 is chosen as the highest likely yield strength and this steel is typified as having no definite yield point.

c. In the derivation of the statistical formulae beyond the yield point, the evaluation is carried out net of elastic strain, i.e. using strain values of $\varepsilon_i - f_y/E_s$. Herein, ε_i is the strain of the ith point, f_y and E_s are the yield strength and Young's modulus of steel respectively.

3.5.3 Equations

a. Point 1

As described previously, σ_1 should be the stress of limit of proportionality for all kinds of steel either with or without a definite yield point. For steel with a definite yield point the ratio of σ_1 over f_y varies within the range of 80~90% [35], the average value in our test results is 81%. Consequently the value σ_1 is suggested to be taken as $0.85f_y$. For steel without a definite yield point the average ratio of σ_1 over $\sigma_{0.2}$ is 0.555 in our test results, Fig. 3.6. The value of σ_1 is suggested to be taken as $0.6f_y$.

In the simplified model the resulting formulae for this point are:

$$\sigma_1 = \left(0.85 - \frac{0.25\left(f_y - 200\right)}{1000}\right) f_y \qquad (3.1)$$

$$\varepsilon_1 = \frac{\sigma_1}{E_s} \qquad (3.2)$$

b. Point 2

For steel with a definite yield point σ_2 is taken as the yield strength f_y and ε_2 is suggested to be (σ_2/E_s+0.02%) in the light of our test results.

For steel without a definite yield point σ_2 and ε_2 are suggested to be $0.85\sigma_{0.2}$ and (σ_2/E_s + 0.035%) respectively, from our test results, Fig. 3.6.

In the simplified model the final formulas for this point are:

$$\sigma_2 = \left(1 - \frac{0.15(f_y - 200)}{1000}\right) f_y \tag{3.3}$$

$$\varepsilon_2 = \frac{\sigma_2}{E_s} + 0.0002 + \frac{0.00015(f_y - 200)}{1000} \tag{3.4}$$

c. Point 3

For steel with a definite yield point σ_3 is recommended to be $1.03f_y$ according to the results from our test and Reference 37. The relationship between ε'_3 and f_y is shown in Fig. 3.7, and the statistical formula is:

$$\varepsilon'_3 = 57800 f_y^{-2.6} \tag{3.5}$$

The correlation coefficient of this formula is -0.924.

Depending on the definition of the normal yield point, the unrecovered strain of steel without a definite yield point should be:

$$\varepsilon'_3 = 0.002 \tag{3.6}$$

Thus for this point it is necessary to use the two sets of formulae for the different types of steel. The curves of the two formulae will intersect at a point with co-ordinates of $\sigma =$ 740 N/mm^2 and $\varepsilon = 0.2\%$, see Fig. 3.7. Consequently, in the simplified model the final formulae for this point are:

for $f_y \leq 750$ N/mm^2,

$$\sigma_3 = \left(1.03 - \frac{0.03(f_y - 200)}{550}\right) f_y \tag{3.7}$$

$$\varepsilon_3 = \frac{f_y}{E_s} + 57800 f_y^{-2.6} \tag{3.8}$$

for $f_y > 750$ N/mm^2,

$$\sigma_3 = f_y \tag{3.9}$$

$$\varepsilon_3 = \frac{f_y}{E_s} + 0.002 \tag{3.10}$$

d. Point 4

The relationships of σ_4 - f_y and ε_4 - f_y are illustrated in Figs. 3.8 and 3.9 for steel either with or without a definite yield point. Hence in the simplified model the final formulae for this point are:

$$\sigma_4 = 1.1 f_y + 95 \tag{3.11}$$

$$\varepsilon_4 = \frac{f_y}{E_s} + 700 f_y^{-1.59} \tag{3.12}$$

The correlation coefficients of the two formulae are 0.981 and -0.941 respectively.

e. Point 5

The relationships of σ_5 - f_y and ε_5 - f_y are illustrated in Figs. 3.10 and 3.11 for steel either with or without a definite yield point. Therefore, in the uniform model the formulae for this points are:

$$\sigma_5 = 1.05 f_y + 180 \tag{3.13}$$

$$\varepsilon_5 = \frac{f_y}{E_s} + 127 f_y^{-1.17} \tag{3.14}$$

The correlation coefficients of the two formulae are 0.93 and -0.89 respectively.

f. Point 6

The relationship of ε_6 and f_y is shown in Fig. 3.12 for steel either with or without a definite yield point, and the formula for this point in the simplified model is:

$$\varepsilon_6 = \frac{f_y}{E_s} + 453 f_y^{-1.3} \tag{3.15}$$

The correlation coefficient of this equation is -0.93.

3.6 Summary of the simplified model for steel

3.6.1 List of the equations

For convenience of application the equations of the simplified model described previously are summarised in Table 3.3.

3.6.2 Comparison with some test results

Fig. 3.13 shows the comparison of curves created from the simplified model and test results given in References 36 and 37. It is clearly observed that in Fig 3.13(a) the ultimate strains from the uniform model are a little larger than those from test results, but in Fig. 3.13(b) the ultimate strains from the uniform model are a little smaller. The difference of gauge lengths between different sets of tests still affects the results despite them having been modified. Agreement of the curves is nonetheless acceptable.

Sample	E_s (N/mm^2)	σ_e (N/mm^2)	ε_e (%)	$\sigma_{0.2}$ (N/mm^2)	$\varepsilon_{0.2}$ (%)	$\sigma_{y,l}$ (N/mm^2)	$\varepsilon_{y,l}$ (%)	$\sigma_{y,u}$ (N/mm^2)	$\varepsilon_{y,u}$ (%)	σ_u (N/mm^2)	ε_u (%)	ε_f (%)
S1	211	353	0.17	735	0.54					794	7.16	10.89
S2	195	176	0.09			264	0.18	274	2.75	405	21.44	36.56
S3	203	479	0.24	760	0.58					791	4.99	6.20
S4	204	264	0.13			277	0.15	279	3.36	407	24.67	38.38

Note: E_s is the Young's modulus of steel

σ_e and ε_e are the stress and strain of limit of proportionality respectively

$\sigma_{0.2}$ is the proof stress with plastic strain of 0.2%, $\varepsilon_{0.2}$ is the strain corresponding to $\sigma_{0.2}$

$\sigma_{y,l}$ and $\varepsilon_{y,l}$ are the stress and strain at the lower yield point

$\sigma_{y,u}$ and $\varepsilon_{y,u}$ are the stress and strain at the end of horizontal plateau

σ_u is the ultimate strength, ε_u is the strain corresponding to σ_u and

ε_f is the fracture/ultimate strain.

Table 3.1 *Test results of the steel bars*

Ref.	f_y (N/mm^2)	σ_3 (N/mm^2)	ε_3 (%)	σ_4 (N/mm^2)	ε_4 (%)	σ_5 (N/mm^2)	ε_5 (%)	ε_6 (%)
Test	735	735	0.20	775	1.24	794	7.16	10.89
	760	760	0.20	775	1.23	791	4.99	6.20
	264	274	2.62	373	7.37	405	21.44	36.56
	277	279	3.22	373	7.37	407	24.57	38.38
[33]	240					470		30.80
	345					550		28.00
[35]	230					425		36.40
	360					610		28.00
	315					500		29.40
	380					530		26.60
	800					1000		9.00
	390					660		18.20
[36]	270	270	2.32	410	7.87	470	13.87	24.84
	400	400	0.57	568	3.91	613	7.81	15.89
	545	545	0.29	695	3.23	753	7.13	12.91
	638	638	0.20	826	2.59	889	6.29	11.86
[37]	285	285	2.80	400	8.46	425	15.86	33.86
	396	396	1.54	540	6.01	587	14.41	20.01
	421	421	1.17	596	4.90	643	10.80	13.60
	604	604	0.66	791	3.41	868	9.41	12.11
[38]	244	254	2.38	392	8.88	440	19.88	34.88
	372	379	1.22	490	8.22	558	17.92	24.82
	555	555	0.20	636	2.73	670	6.33	8.93

Table 3.2 *Data used in the statistical work*

Point	Stress σ	Strain ε
1	$\sigma_1 = (0.85\text{-}0.25(f_y\text{-}200)/1000)f_y$	$\varepsilon_1 = \sigma_1/E_s$
2	$\sigma_2 = (1\text{-}0.15(f_y\text{-}200)/1000)f_y$	$\varepsilon_2 = \sigma_2/E_s + 0.0002 + 0.00015(f_y\text{-}200)/1000$
3	for $f_y \leq 750$ N/mm^2,	
	$\sigma_3 = (1.03\text{-}0.03(f_y\text{-}200)/550)f_y$	$\varepsilon_3 = f_y/E_s + 57800f_y^{-2.6}$
	for $f_y > 750$ N/mm^2,	
	$\sigma_3 = f_y$	$\varepsilon_3 = f_y/E_s + 0.002$
4	$\sigma_4 = 1.1f_y + 95$	$\varepsilon_4 = f_y/E_s + 700f_y^{-1.59}$
5	$\sigma_5 = 1.05f_y + 180$	$\varepsilon_5 = f_y/E_s + 127\,f_y^{-1.17}$
6	$\sigma_6 = \sigma_5$	$\varepsilon_6 = f_y/E_s + 453f_y^{-1.3}$

Table 3.3 *Summary of equations in the simplified mechanical model for steel*

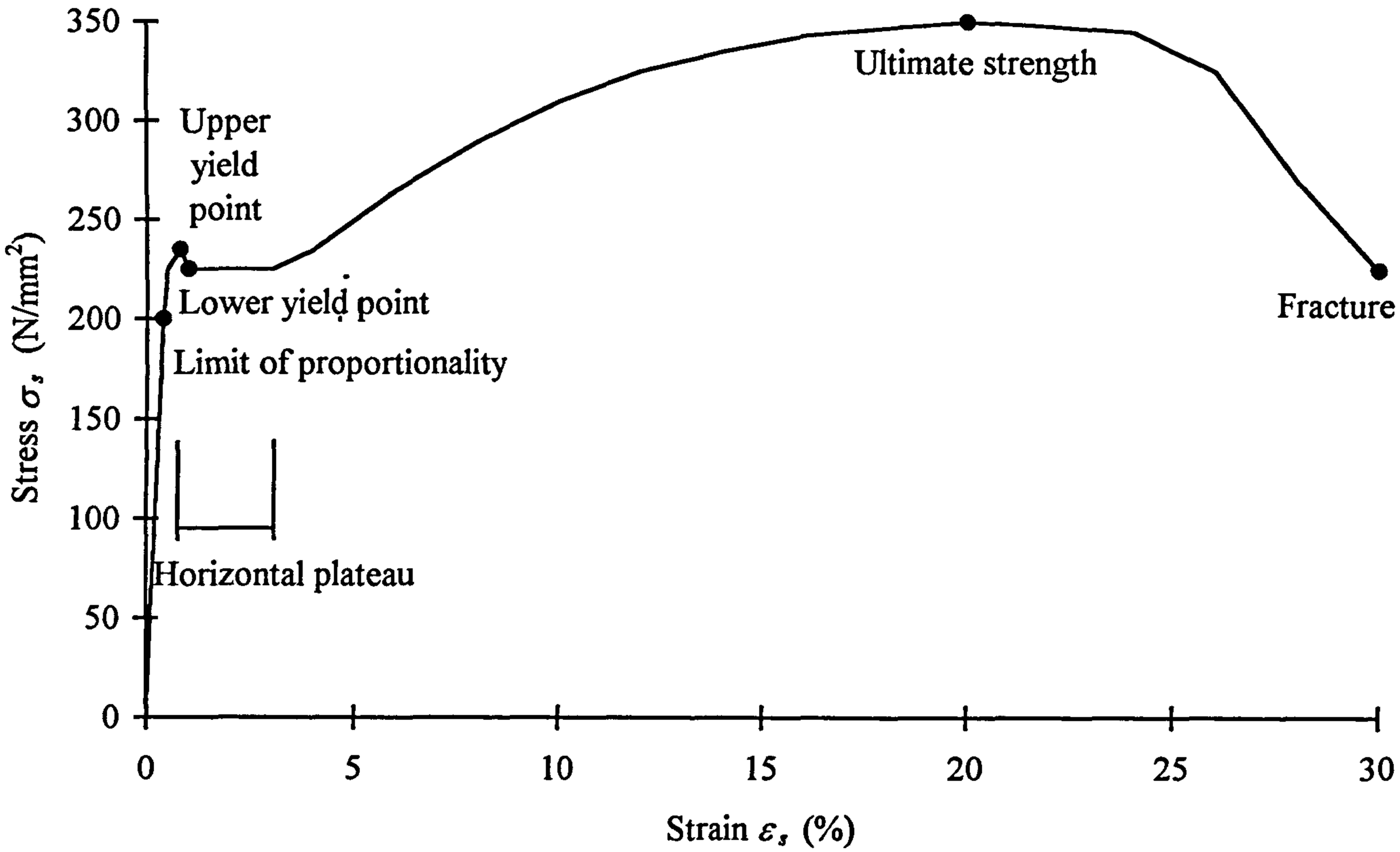

(a) Steel with a definite yield point

Figure 3.1 *Typical stress-strain curves of steel*

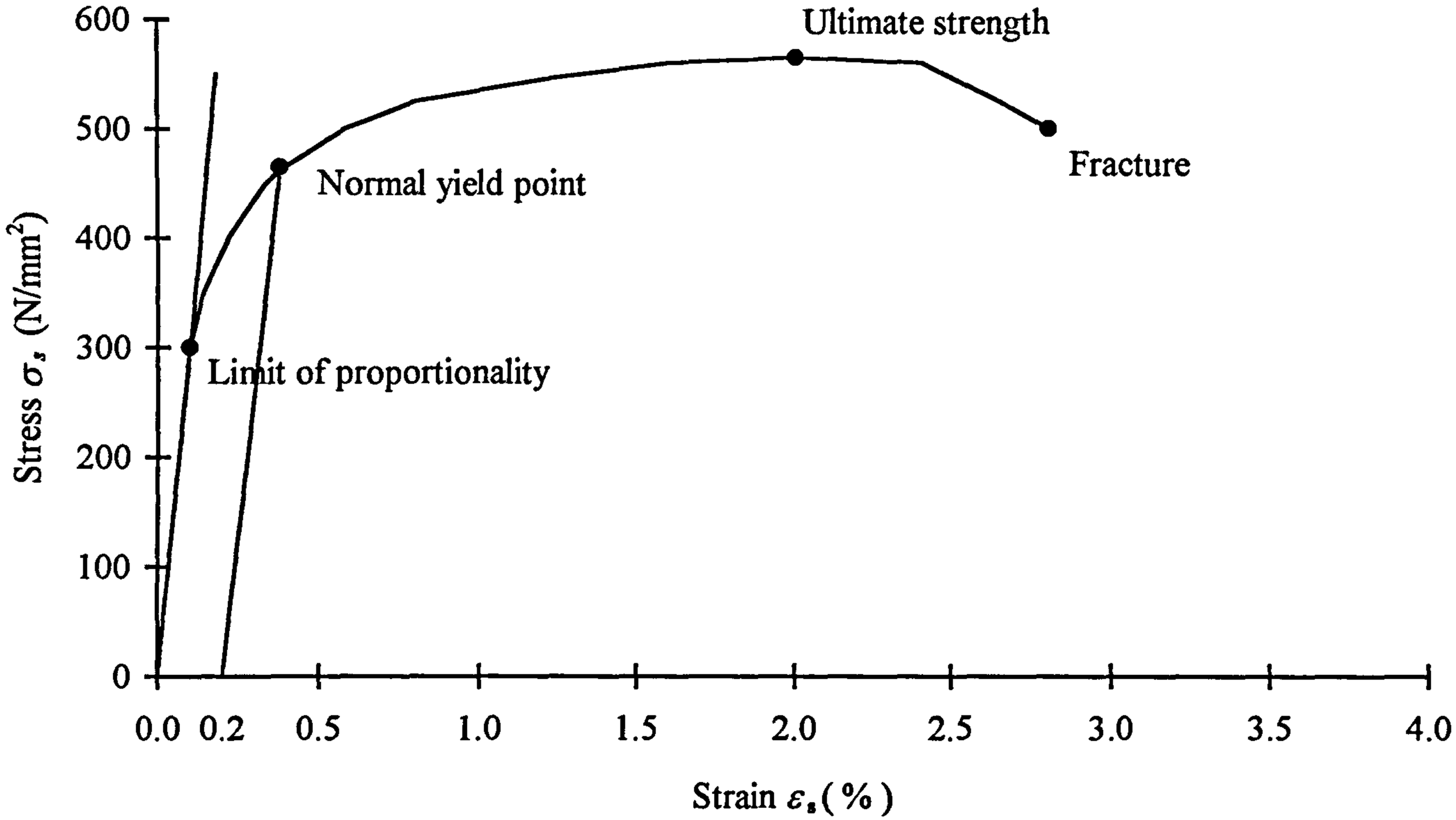

(b) Steel without a definite yield point

Figure 3.1 *Typical stress-strain curves of steel*

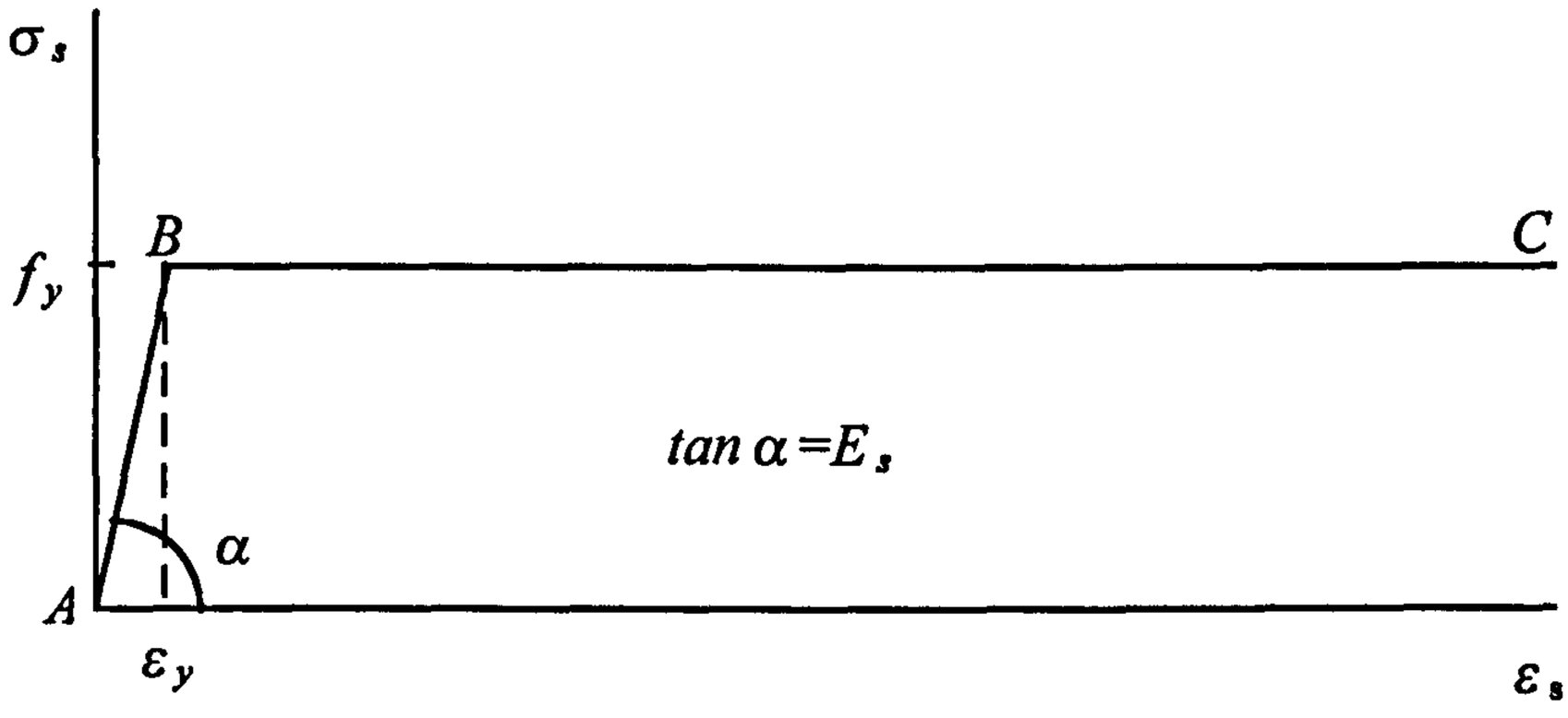

(a) Simplified idealised elasto-plastic

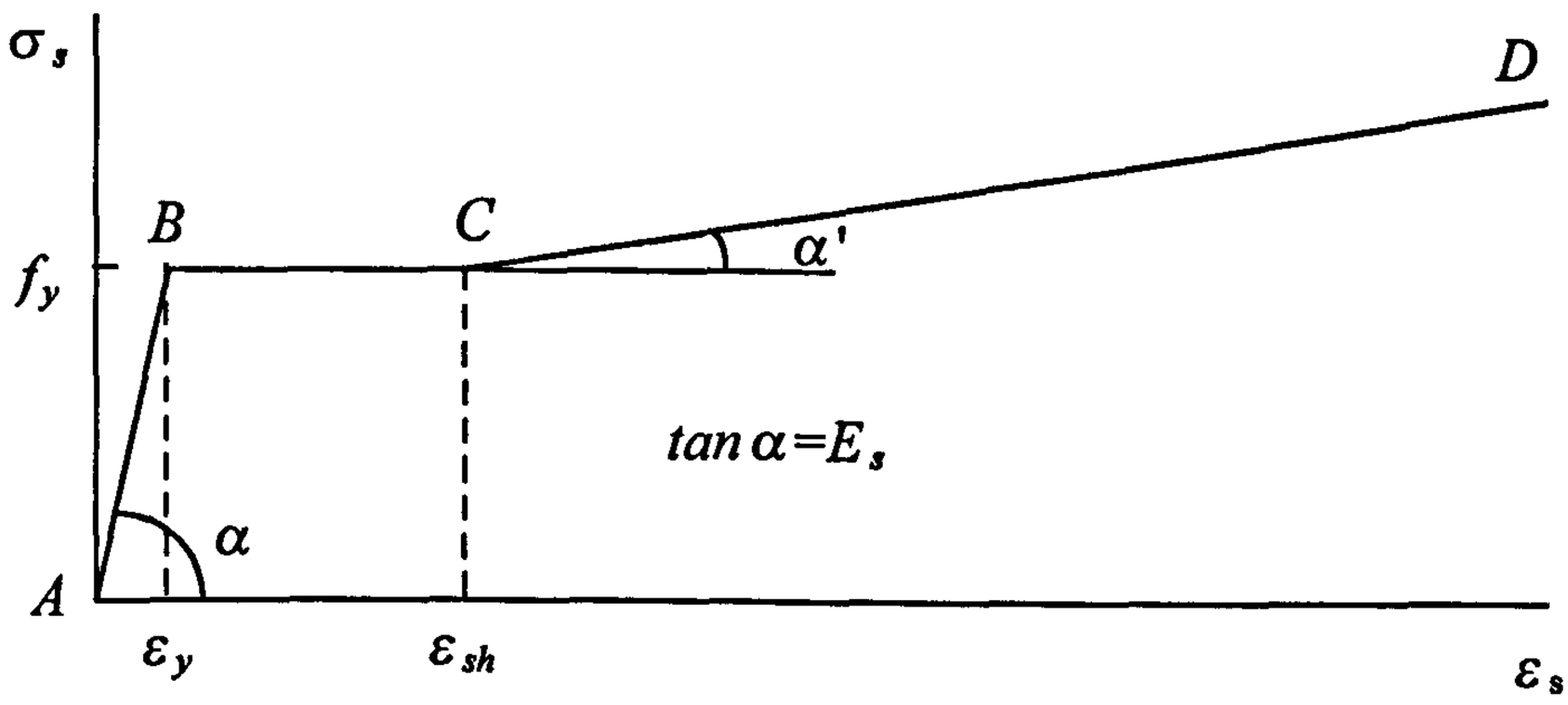

(b) Simplified three straight lines

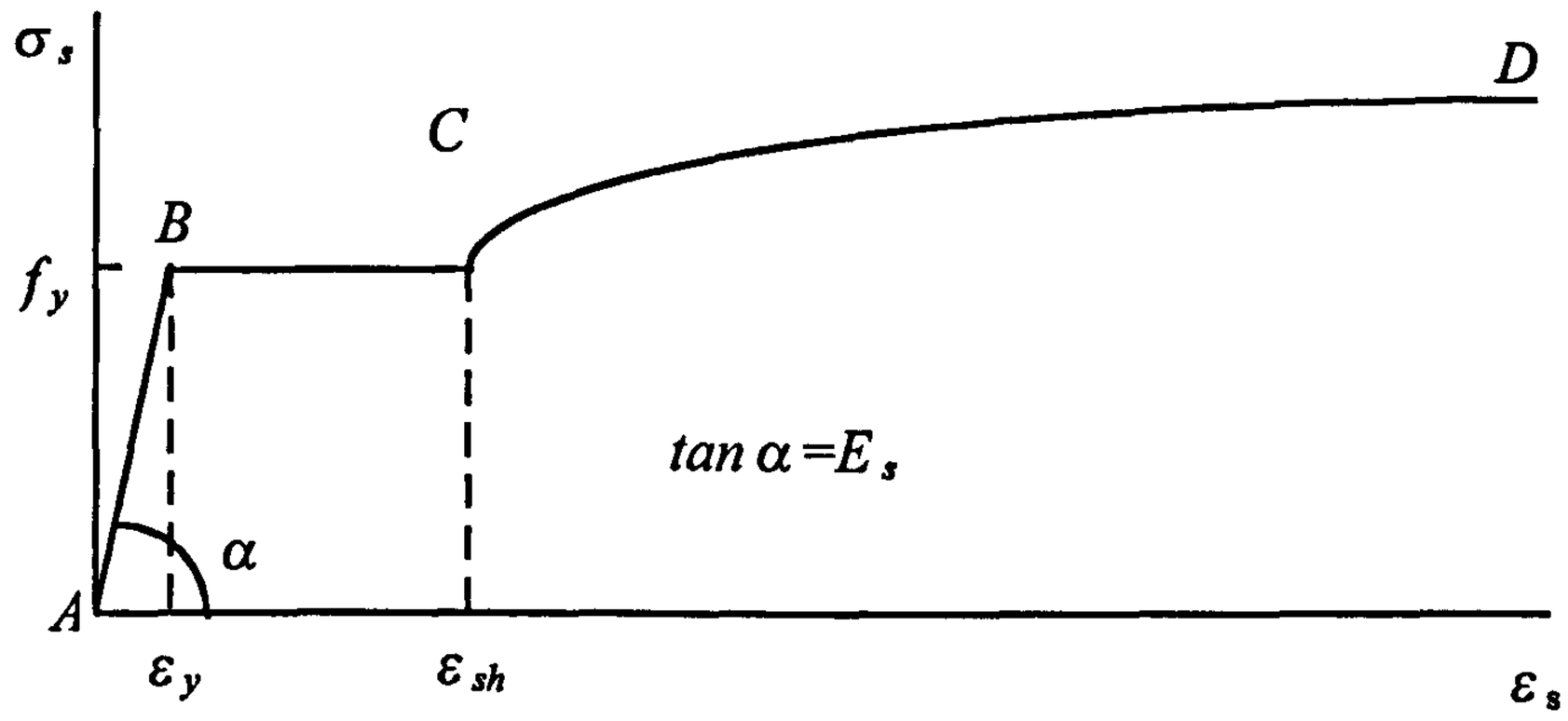

(c) Full curve

Figure 3.2 *Idealised stress-strain curves for steel in uniaxial tension or compression*

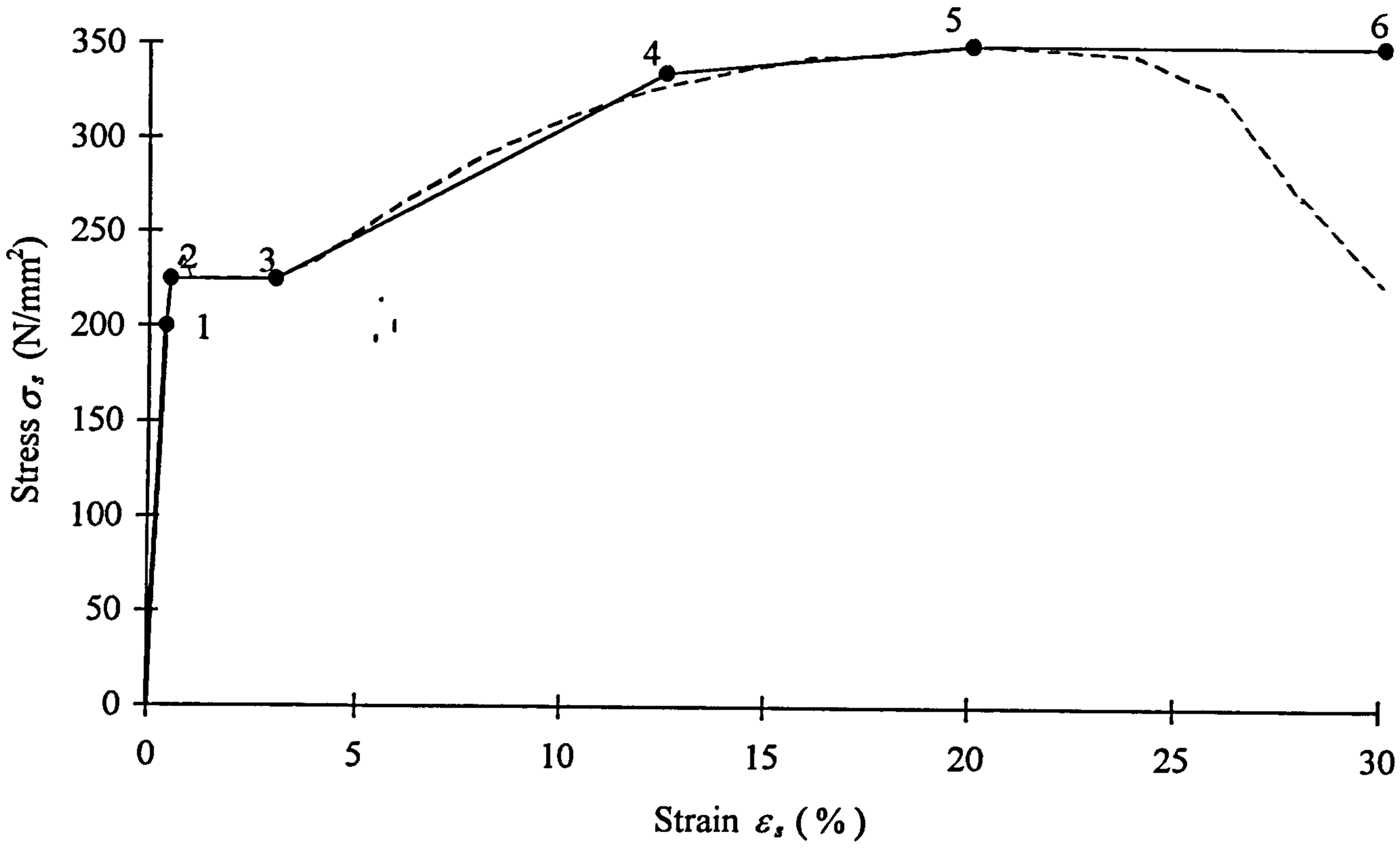

(a) Steel with a definite yield point

Figure 3.3 *Simplified mechanical model for steel*

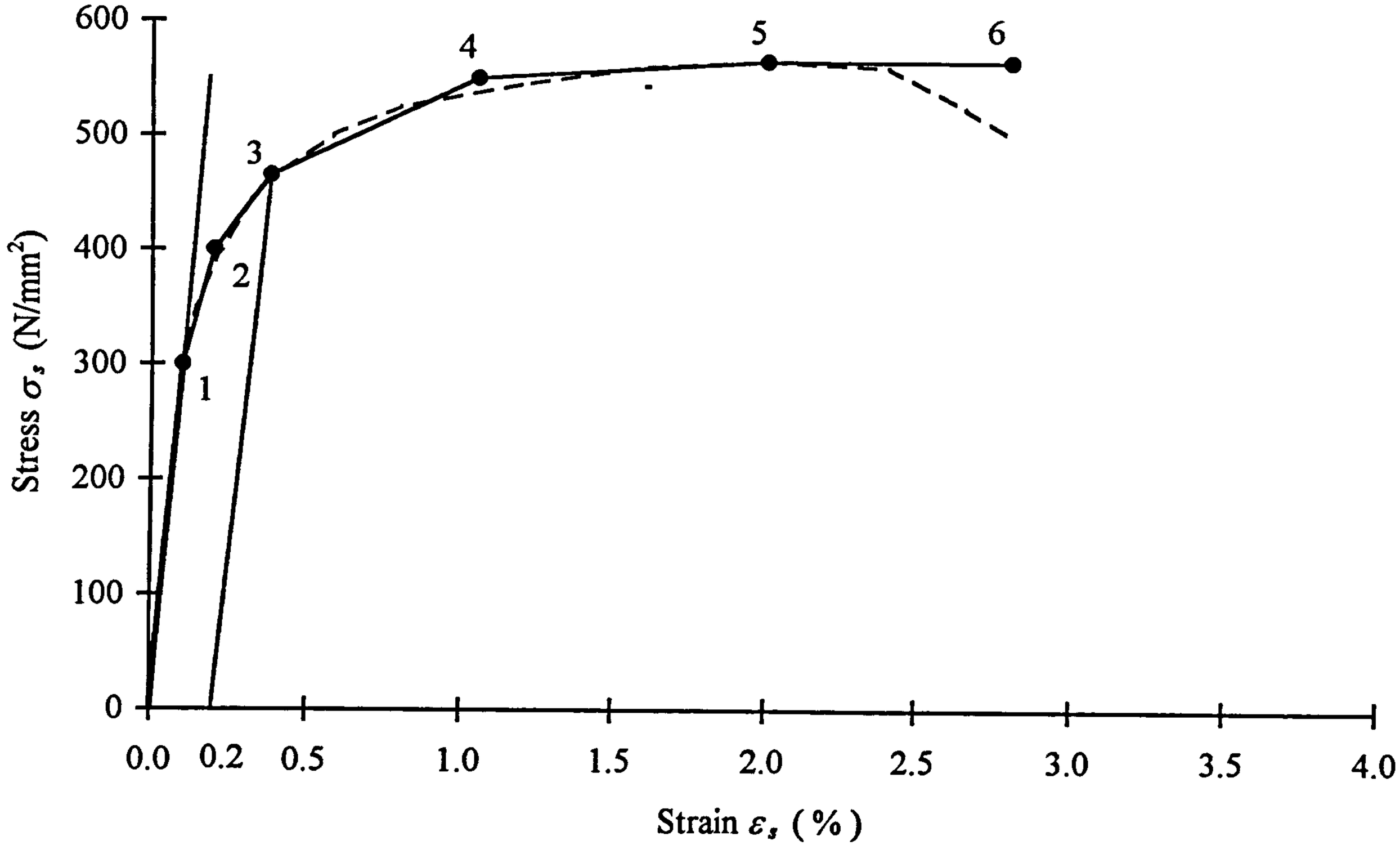

(b) Steel without a definite yield point

Figure 3.3 *Simplified mechanical model for steel*

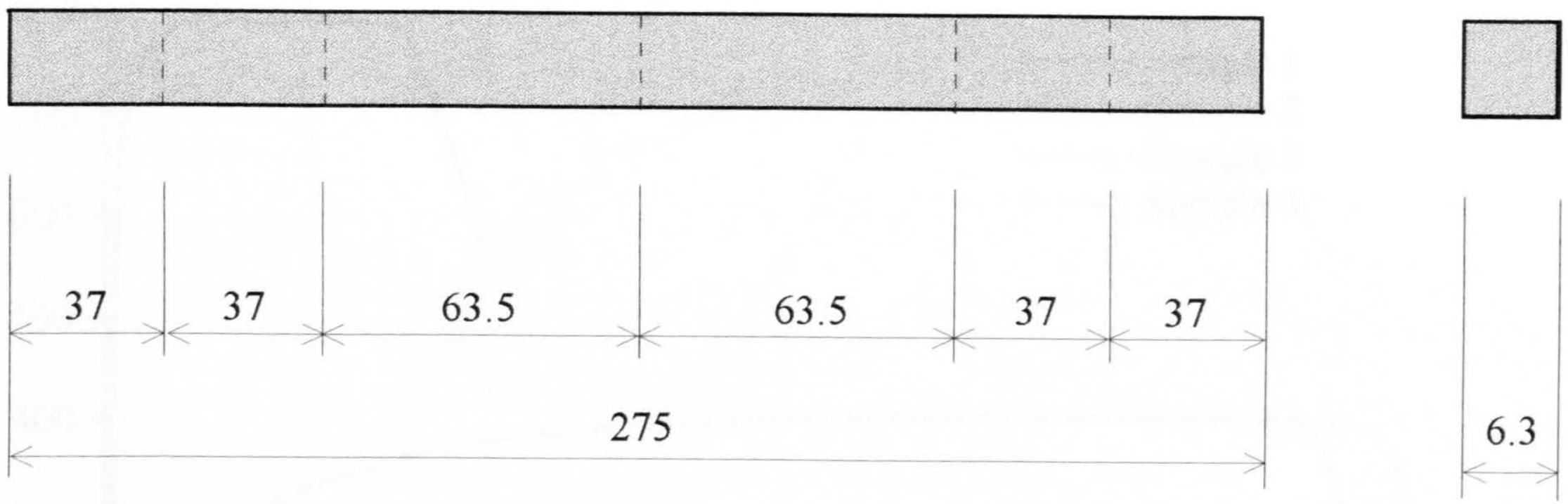

Figure 3.4 *Dimensions of the tested steel bars*

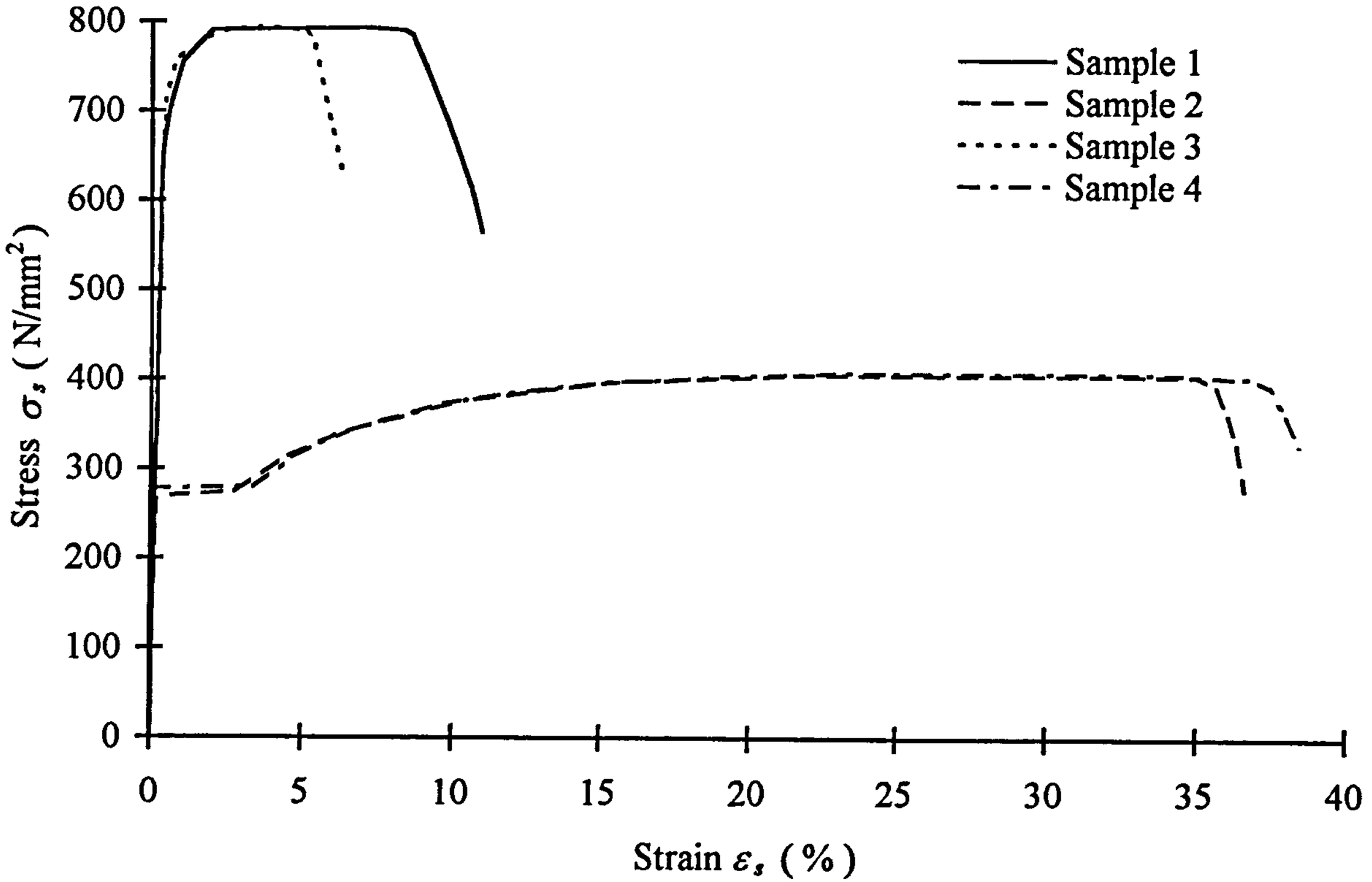

Figure 3.5 *Stress-strain curves of the tested steel bars*

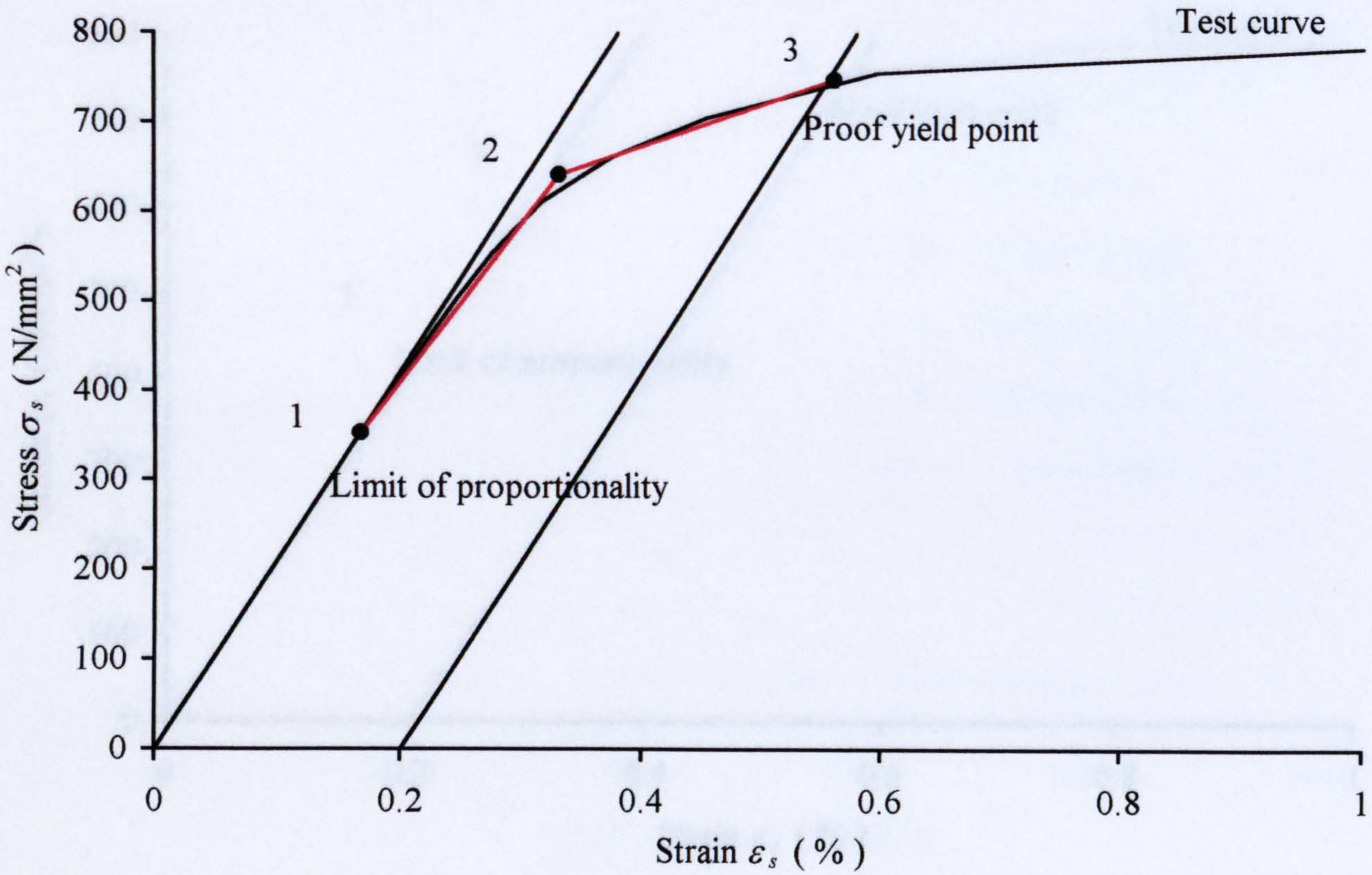

(a) Sample 1

Figure 3.6 *Local view of the test curves for steel without a definite yield point*

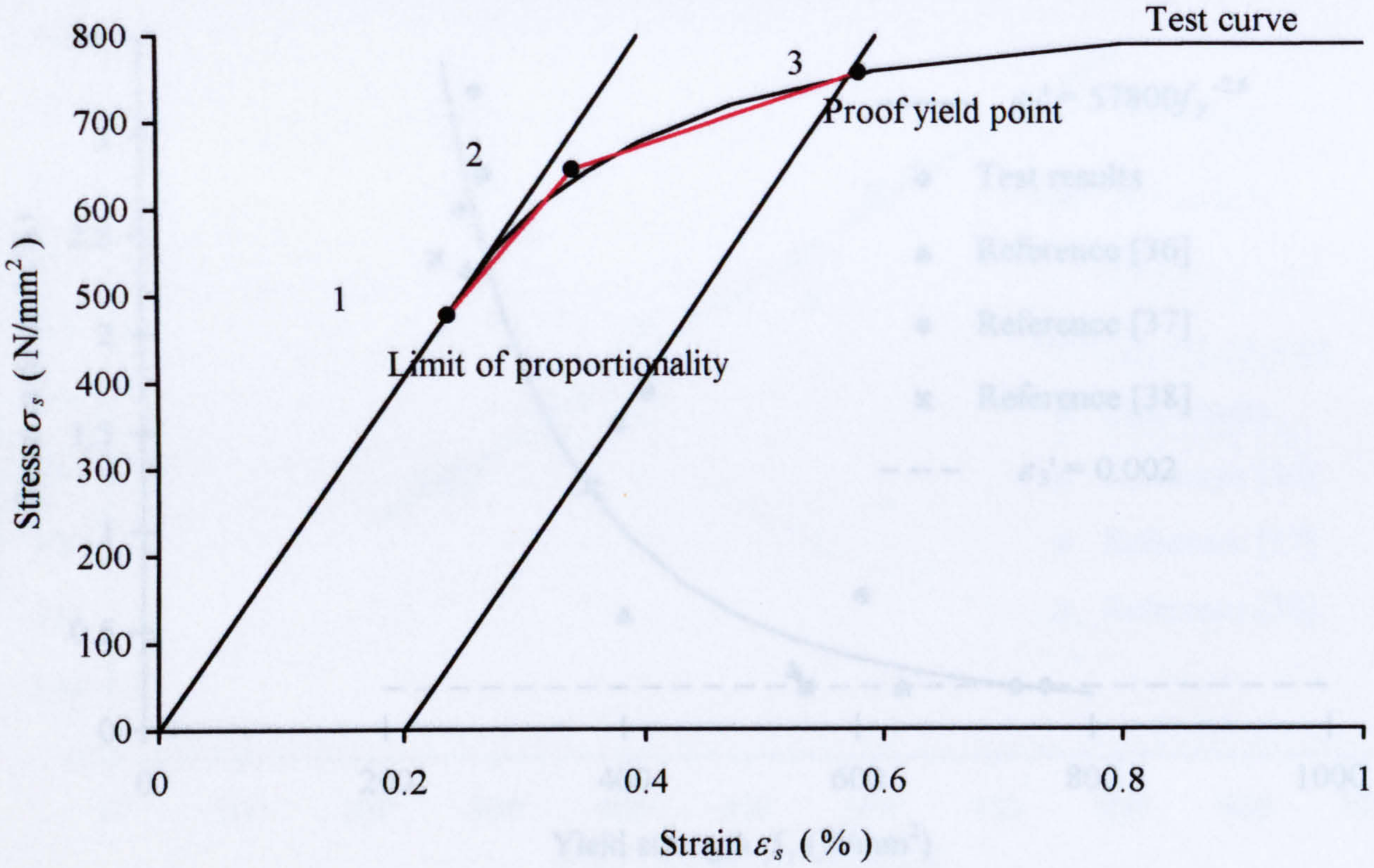

(b) Sample 3

Figure 3.6 *Local view of the test curves for steel without a definite yield point*

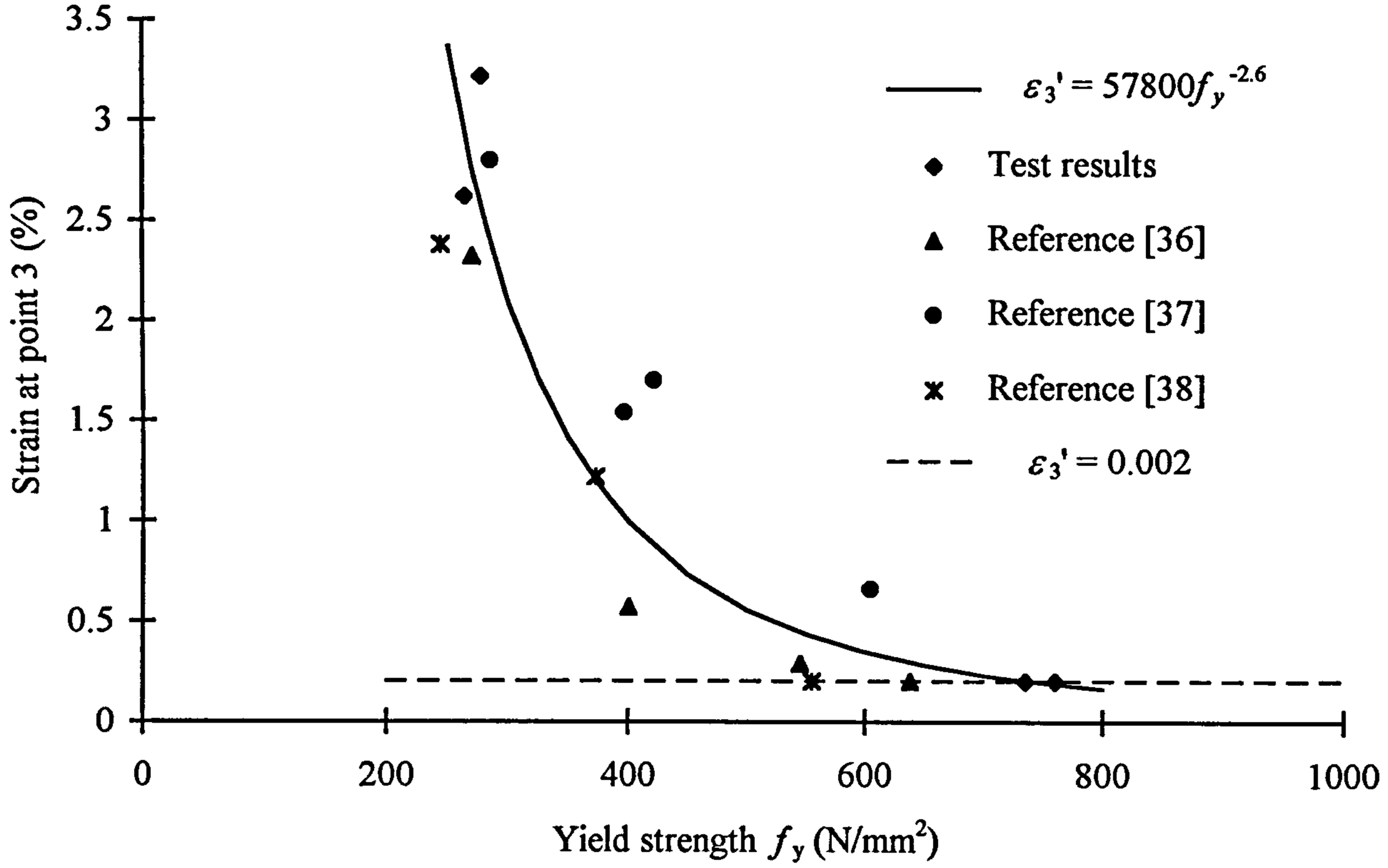

Figure 3.7 *Relationships of ε_3 and f_y*

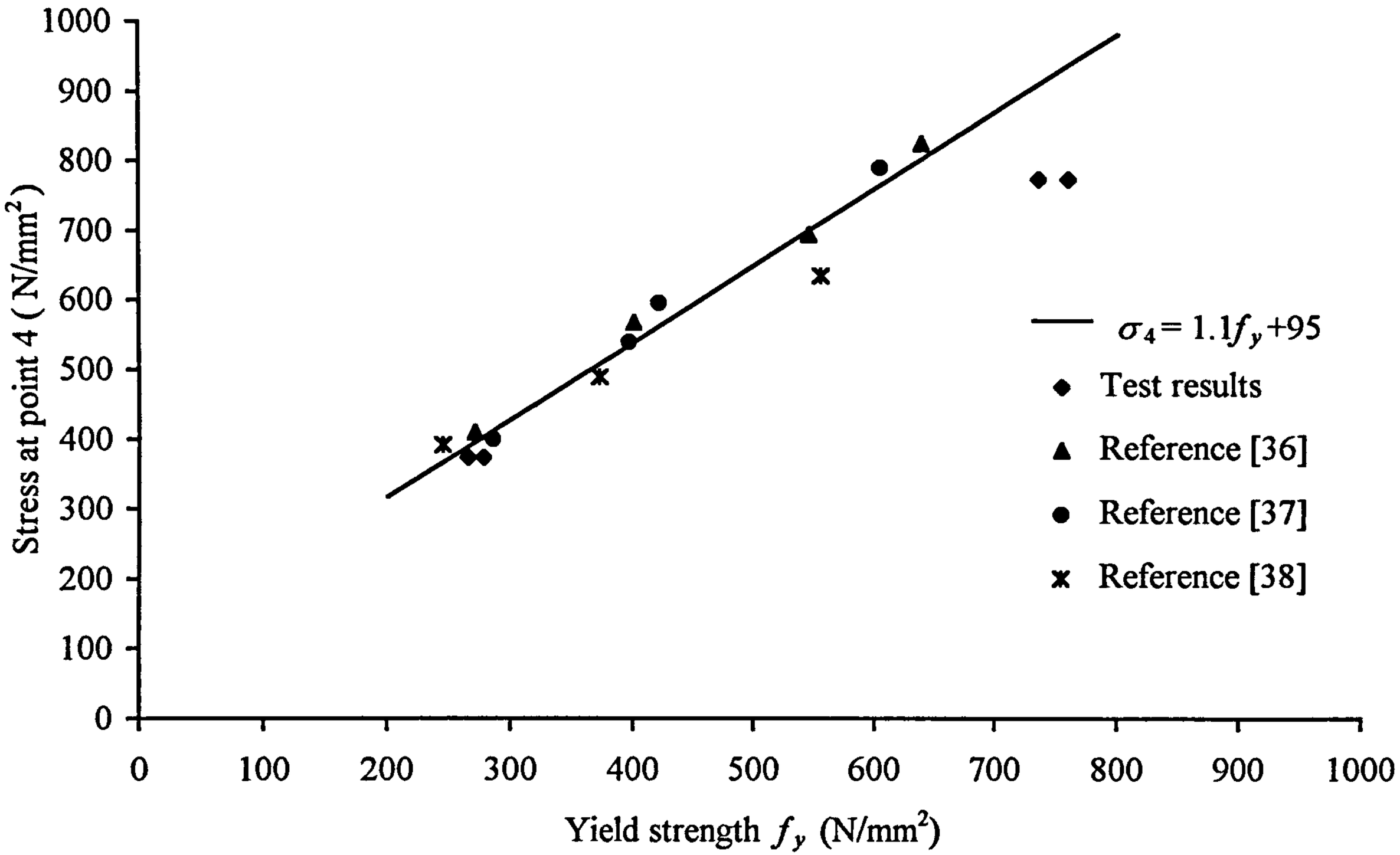

Figure 3.8 *Relationships of σ_4 and f_y*

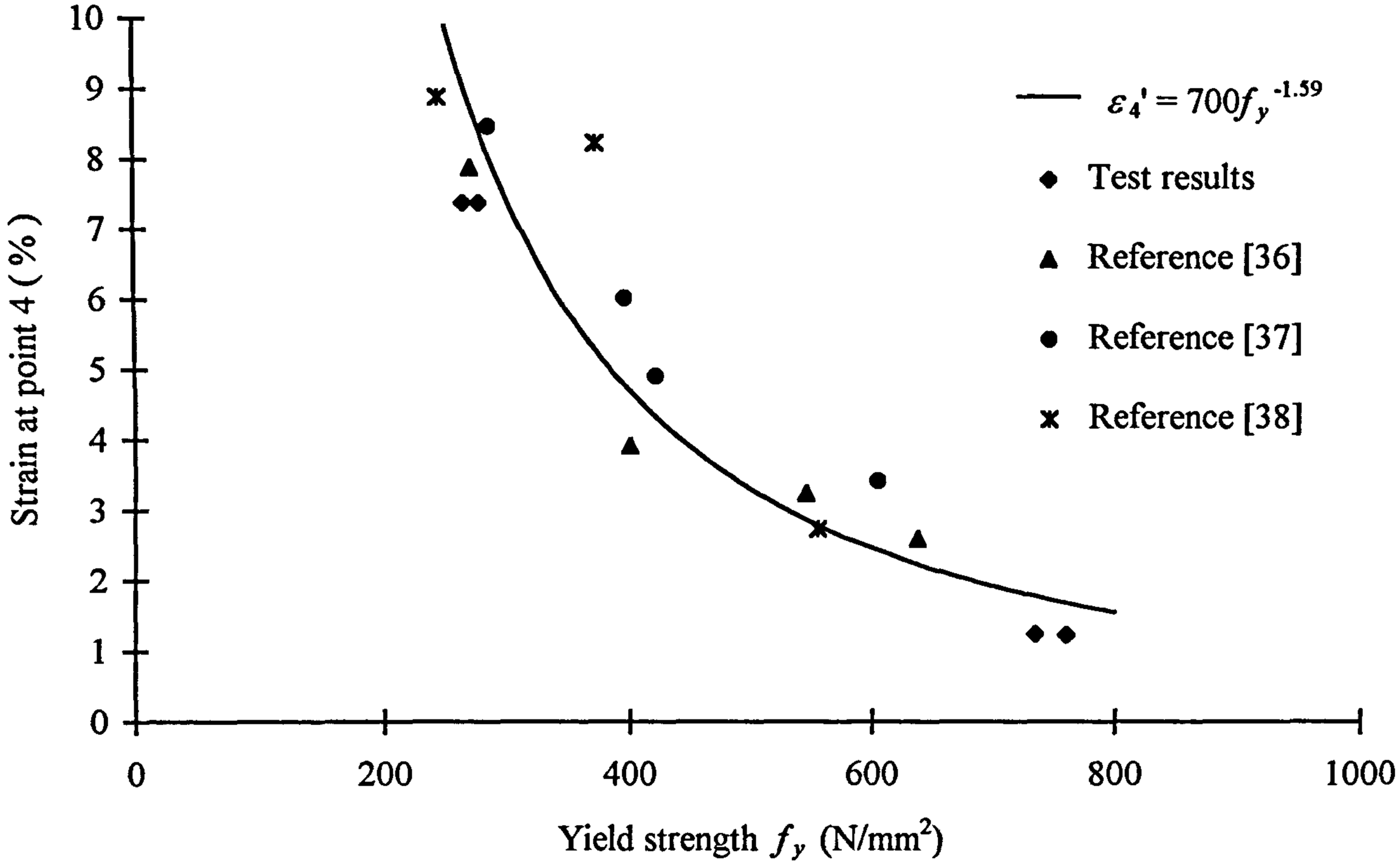

Figure 3.9 *Relationships of ε_4 and f_y*

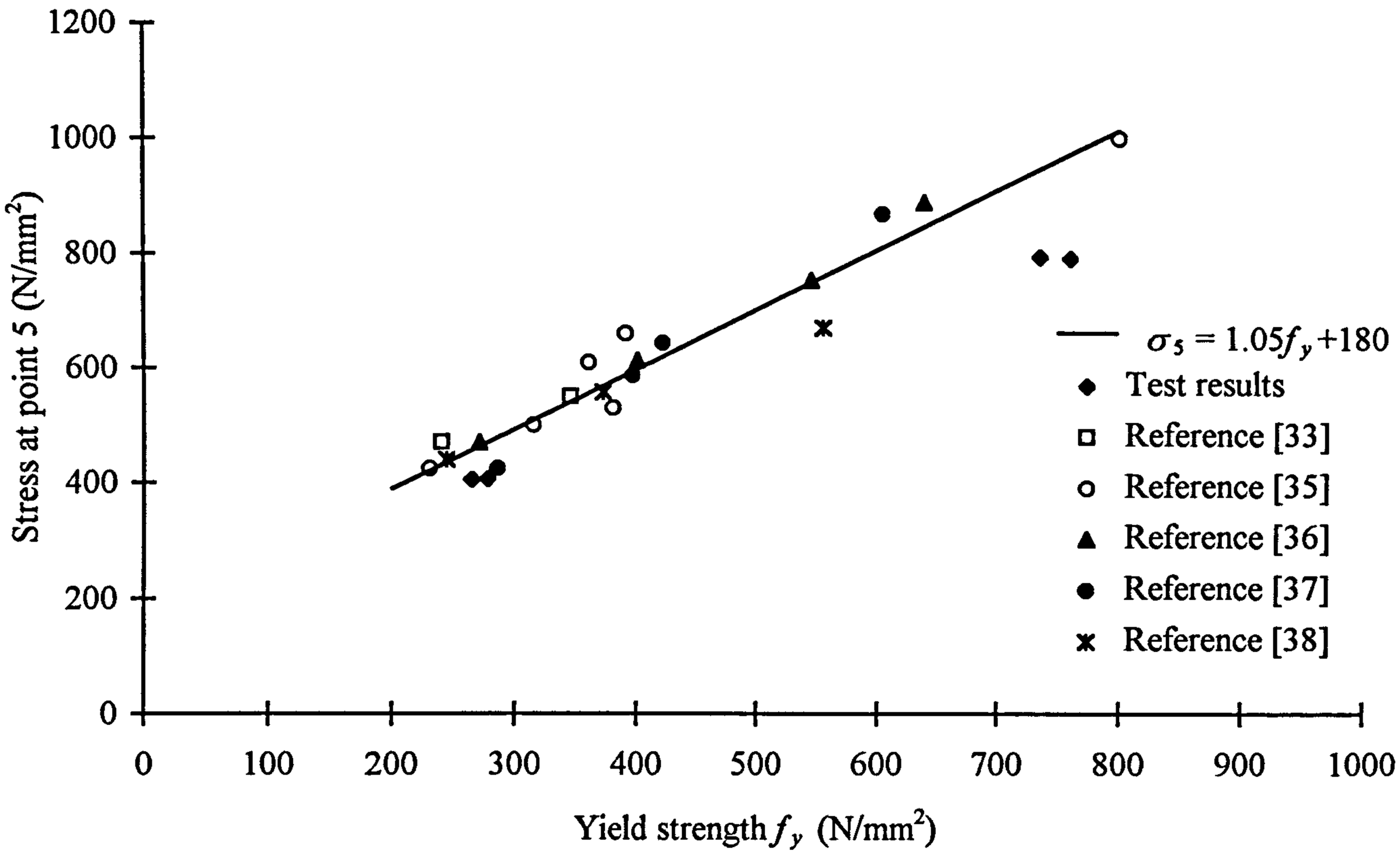

Figure 3.10 *Relationships of σ_5 and f_y*

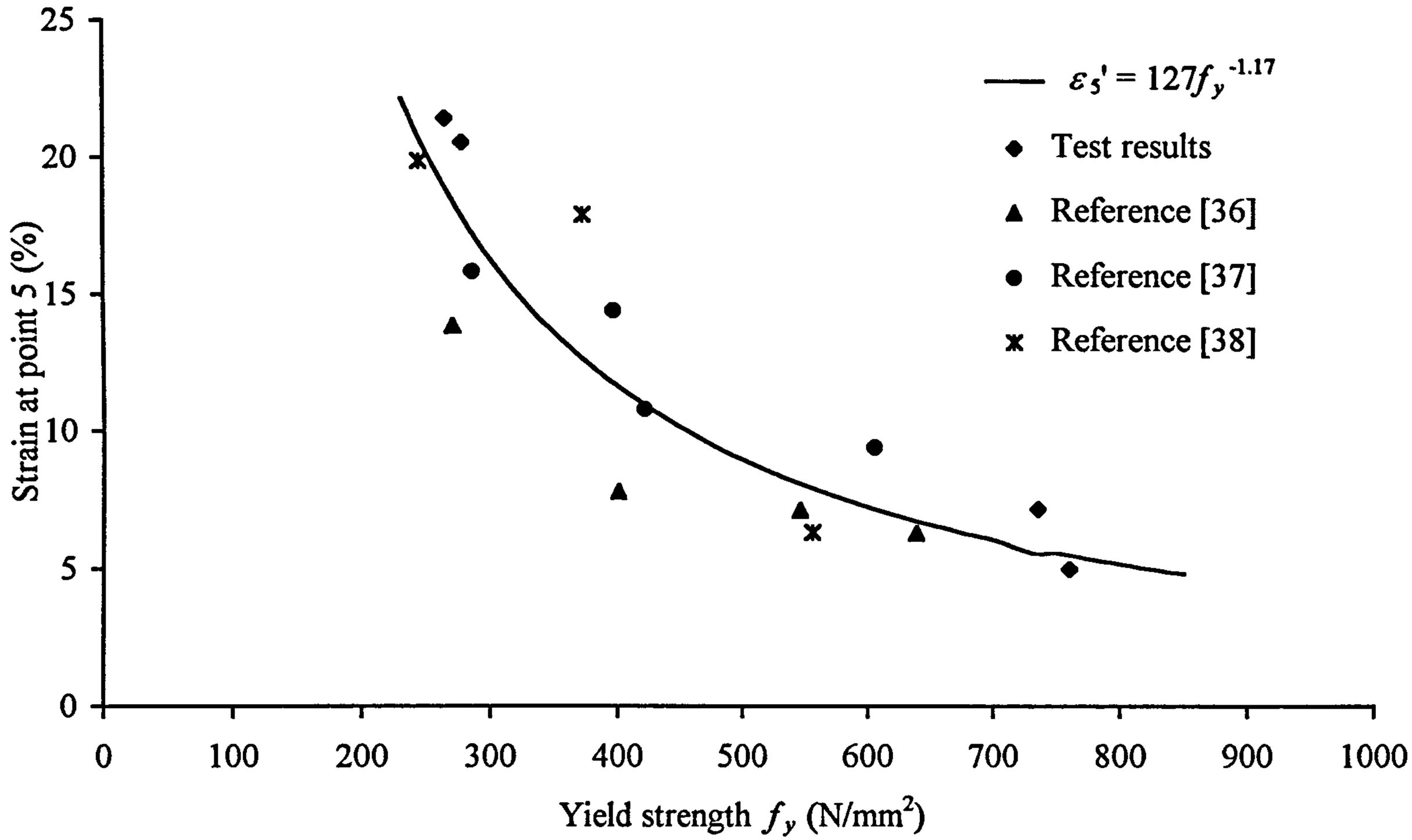

Figure 3.11 *Relationships of ε_5 and f_y*

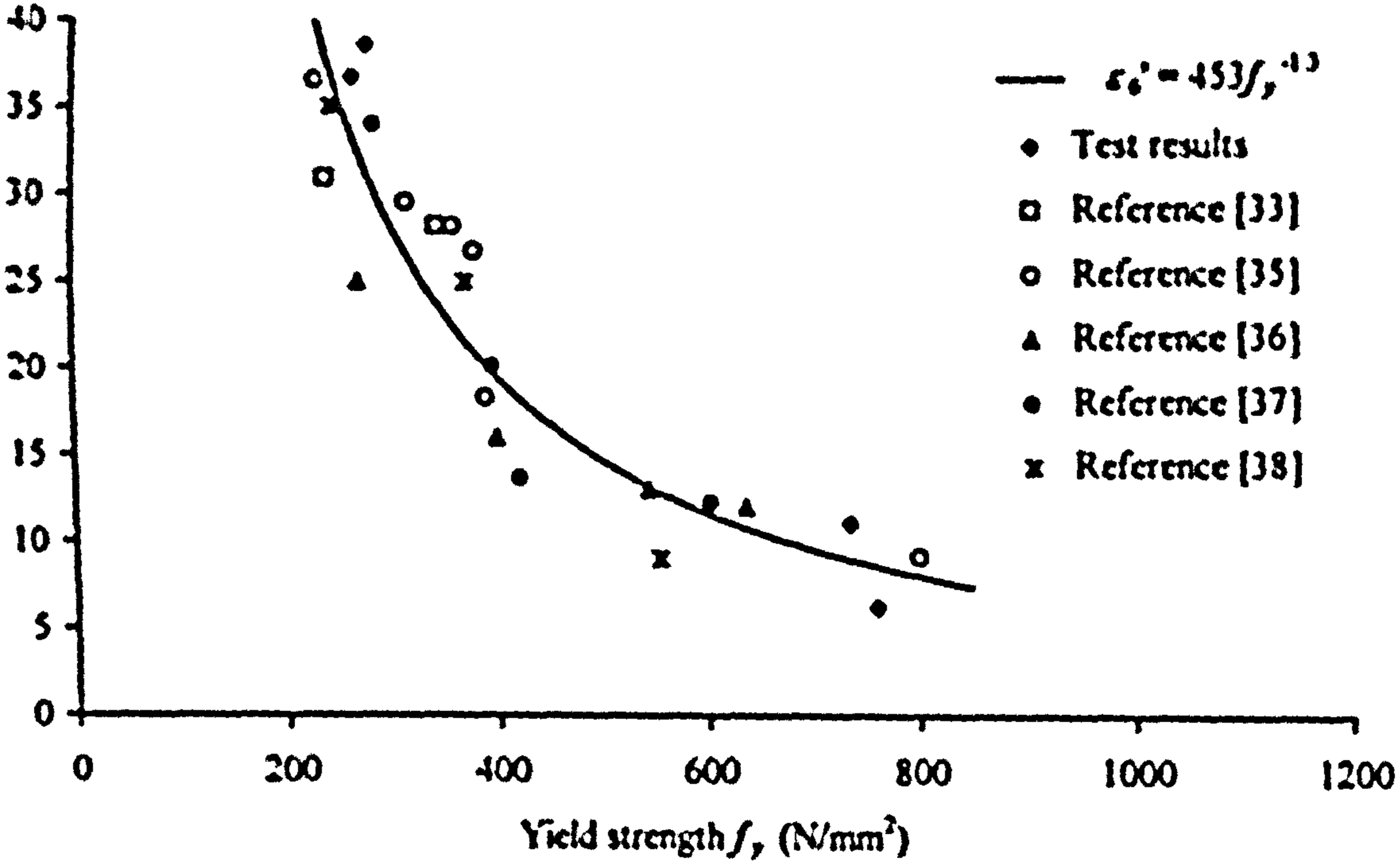

Figure 3.12 *Relationships of ε_6 and f_y*

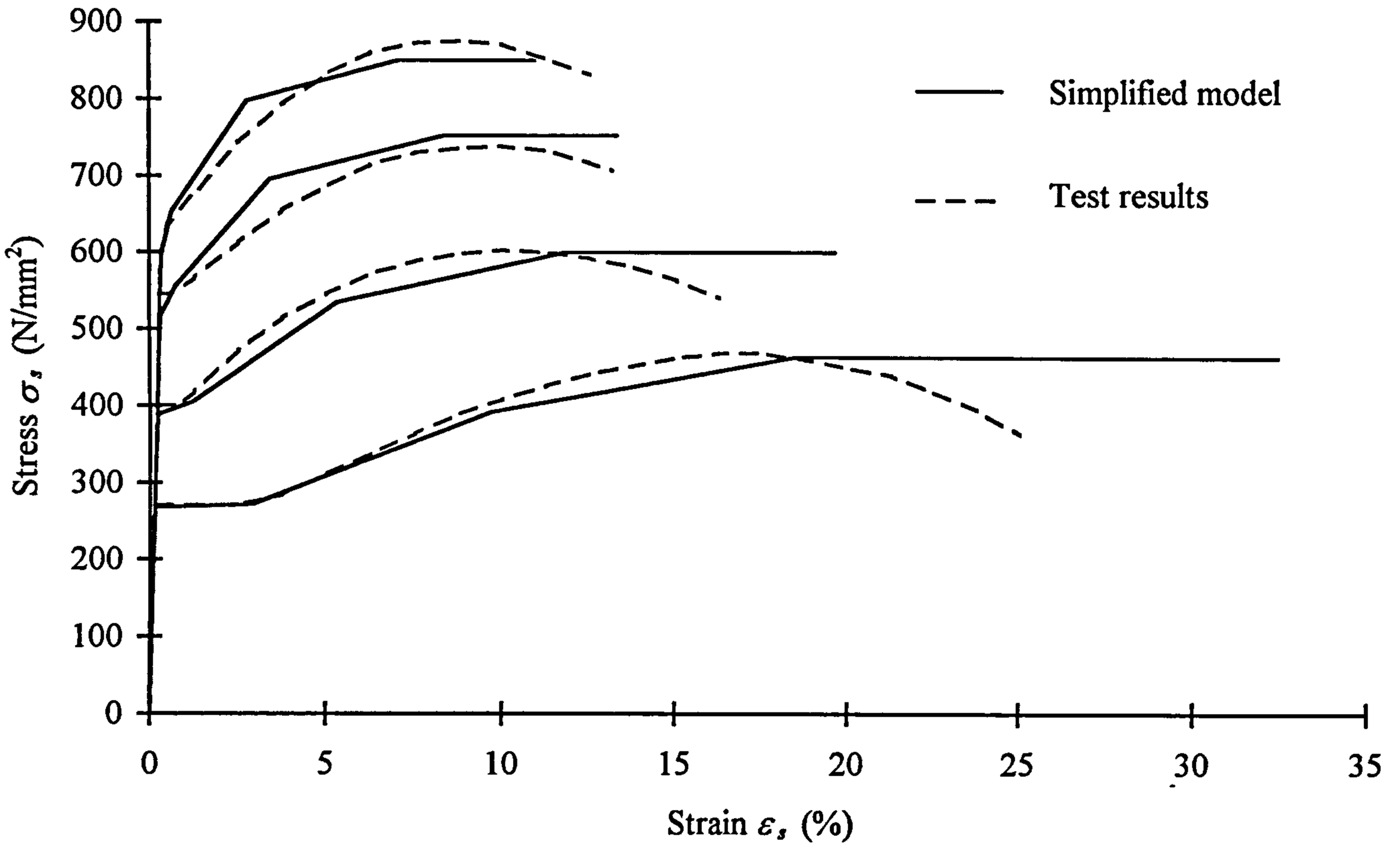

(a) Test results in Reference 36

Figure 3.13 *Comparison of curves derived from the simplified model and the test results*

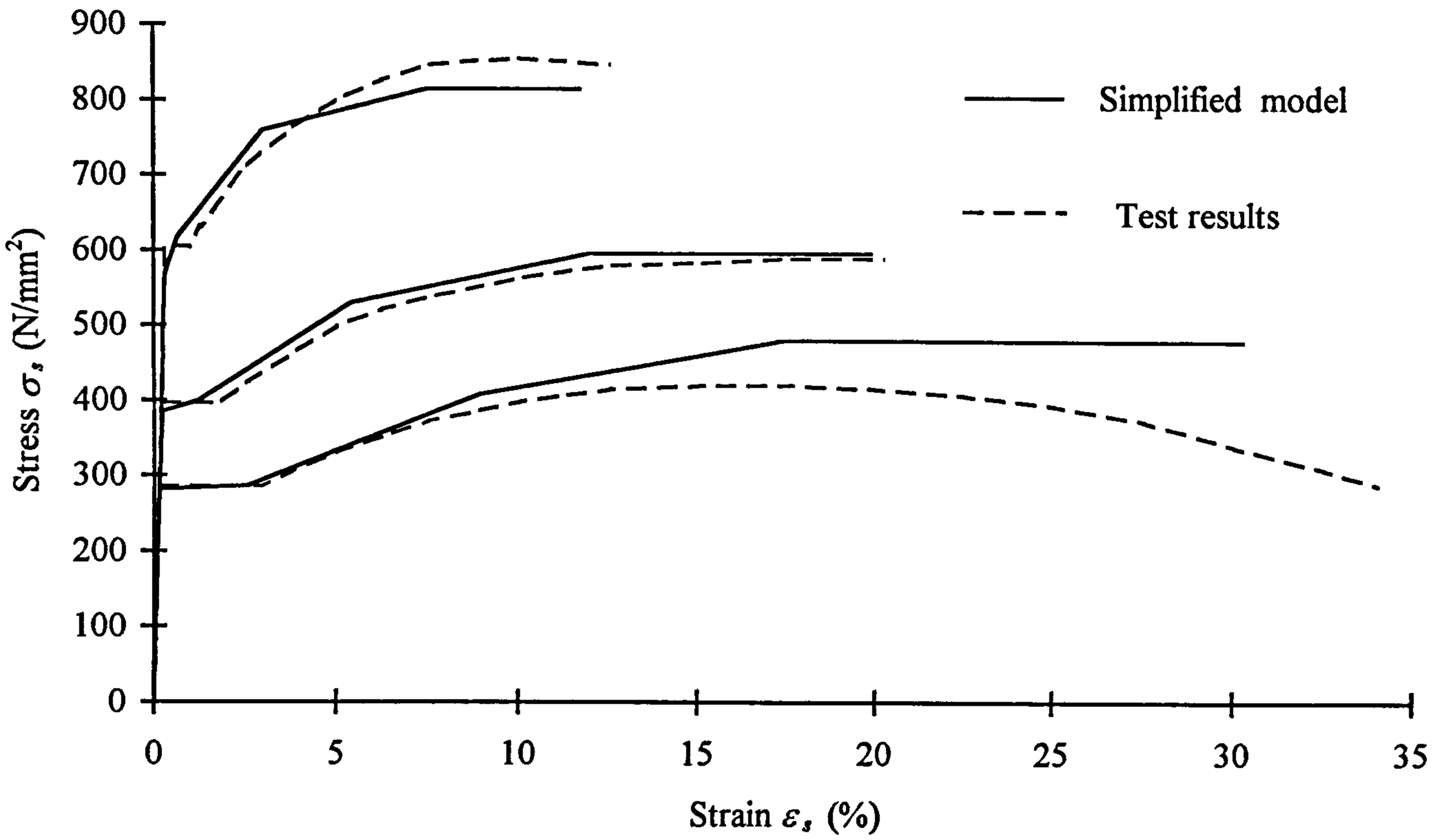

(b) Test results in Reference 37

Figure 3.13 *Comparison of curves derived from the simplified model and the test results*

Chapter 4

Modelling the Mechanical Behaviour for Concrete

4.1 Introduction

As with steel, the mechanical properties of concrete plays an important role in finite element analysis. In addition, because of the nonlinearities and variabilities of this material, constitutive equations and strength failure criteria of concrete have been a more attractive research field for many years. Generally concrete works in the state of multiaxial stress, and the criteria of cracking and crushing are the function of the stress distribution. The stress-strain curve in uniaxial compression however is an essential relationship, which provides fundamental parameters for the criteria. A large number of constitutive equations can be found to describe the uniaxial properties[36, 41~48, 50~52]. The question for finite element analysis is which equations are most reliable and applicable.

In the ANSYS program a special element SOLID65 is provided, which is particularly suitable for the modelling of reinforced concrete, Chapter 2.8.2. It is necessary to do some trial modelling before applying this element into analyses of concrete structures, so that capacities and features of the element can be investigated foremost.

The element SOLID65 possesses the capability of crushing in compression. Once crushing occurs at an integration point, the material strength is assumed to have degraded to an extent such that the contribution to the stiffness of an element at the integration point is ignored[31]. This is a special property of concrete, but sometimes it

causes the model to fail too early to obtain a full solution[11, 21, 23, 24]. A method is required to prevent the unexpected early failure of an analysed model.

In this chapter the constitutive equations and the relevant factors required for using the element SOLID65 are selected first. Then a simplified mechanical model for concrete in uniaxial compression is suggested. Afterwards a series of numerical tests are carried out to investigate the characteristics of the element, and to study the method to overcome the early failure problem of the element.

4.2 Mechanical behaviour of concrete in uniaxial compression

The mechanical behaviour of concrete in uniaxial compression is the most fundamental and important characteristic of the material, and it can be expressed by the stress-strain curve shown in Fig. 4.1. The curve has a nearly linear elastic behaviour up to about 30% of its maximum compressive strength, f_c. For stress above this point, concrete begins to soften and the curve shows a gradual increase in curvature up to about 75~90% of f_c, after which the curve bends more sharply until it approaches the peak point at f_c. Beyond the peak point, the curve has a descending part until crushing failure occurs at some ultimate strain ε_u.

Fig. 4.2 shows the stress-strain curves for concrete with different strengths. The shapes are nearly the same but a high-strength concrete behaves in a linear fashion to a relatively higher stress level than a low-strength concrete, and peak strains increase slightly with the increase of the strength. The ultimate strain for any kind of concrete is much larger than 0.0035[36, 51].

Poisson's ratio of concrete remains a constant within the normal working stress limits, ranging from 0.15 to 0.22. 0.19 or 0.20 is a representative value provided the ratio of the compressive stress σ_c over cylinder strength f_c' is under 0.8. After the ratio σ_c/f_c' exceeds 0.8, micro cracks distinctly develop and the *apparent Poisson's ratio* begins to increase. In some tests values of this ratio over 1.0 have been measured in the unstable crushing phase[51].

4.3 Constitutive equations for concrete in uniaxial compression

The constitutive equations for concrete in uniaxial compression are essential for both the research and the design work. Most parameters used in finite element analysis are determined by using these equations. Typical equations from the literature are listed in Table 4.1. As can be seen from Fig. 4.3, most equations give virtually the same shape for the ascending portion of the curve, the parabolic equation being in the mid-range covered by the curves. In addition, it is found that the curve formed by a parabolic equation gives close agreement with test results[41]. In the commercial package ANSYS negative stiffness is not permitted, so the descending portion can only be modelled by a horizontal line[31]. Hence, equations describing the descending portion of the curve are neglected. Consequently, the mixed parabola and straight line is used as the constitutive equation for concrete in uniaxial compression, and they are listed below.

For $\varepsilon \leq \varepsilon_0$,

$$f = f_c\left[\frac{2\varepsilon}{\varepsilon_0} - \left(\frac{\varepsilon}{\varepsilon_0}\right)^2\right] \qquad (4.1)$$

for $\varepsilon_0 < \varepsilon \leq \varepsilon_u$,

$$f = f_c \qquad (4.2)$$

where f is the compressive stress at any strain ε

f_c is the maximum compressive strength at strain ε_0, evaluation of this strength is discussed in Chapter 4.4.1

ε_0 is the strain at the peak stress point, taken to be 0.002, and

ε_u is the ultimate strain, taken to be 0.0035.

4.4 Determination of the key parameters

4.4.1 Compressive strength in uniaxial compression

Strengths derived from different tests are used to describe the capacity of concrete in uniaxial compression. These are the standard cube strength f_{cu}, the standard cylinder strength f_c' and the standard prism strength f_c. Due to the effect of friction between the surfaces of specimen and platens, the specimen is constrained in the lateral direction whilst it is subjected to uniaxial compression in the vertical direction. Both the cube strength and the cylinder strength are higher than that in an actual component. Test results show that if the ratio of height to width of a prism exceeds approximately 3 to 4, then the effect of the constraint can be ignored. Therefore, the prism strength is close to the actual pure compressive strength of concrete. According to test results, the relationships among the mean values of the three strengths are[37]:

$$f_c' = 0.83 \sim 0.85 f_{cu} \tag{4.3}$$

$$f_c = 0.80 f_{cu} \tag{4.4}$$

The three strengths are normally only used to determine the grade of concrete. Coefficients, typically 0.67 or 0.85, are used to modify the compressive strengths to obtain the required strengths in design or research work.

In this thesis, the prism strength is taken as the compressive strength which is free of the effects of lateral constraints. This compressive strength is taken as 0.8 times the cube strength.

4.4.2 Modulus of Elasticity

There have been numerous empirical equations proposed to determine modulus of elasticity for concrete. Some typical equations are listed in Table 4.2 and graphically expressed in Fig. 4.4. It can be clearly observed that the curves created by the equations in ACI 318/89[49] and BS8110 Part 1[42] have the steepest slopes. They give lower values for lower grade concrete (smaller than 50 N/mm^2), and middle values for higher grade concrete. The curve created by the equation in the CEB-FIP Model Code[43] gives middle values for lower grade concrete but lower values for higher grade concrete.

Therefore, the equation in the CEB-FIP Model Code is chosen to determine modulus of elasticity for concrete with cube strength smaller or equal to 50 N/mm^2, while the equation in ACI 318/89 is selected for concrete with cube strength larger than 50 N/mm^2. That is

for $f_{cu} \leq 50$ N/mm^2,

$$E_{ci} = E_{c0}\left[\frac{f_{ck} + \Delta f}{f_{cmo}}\right]^{1/3} \tag{4.5}$$

where E_{ci} is the modulus of elasticity at a concrete age of 28 days

f_{ck} is the characteristic cylinder strength

$\Delta f = 8$ N/mm^2

$f_{com} = 10$ N/mm^2

$E_{c0} = 2.15 \times 10^4$ N/mm^2, and

$$E_c = 0.85 E_{ci} \tag{4.6}$$

E_c is the reduced modulus of elasticity E_{ci}.

for $f_{cu} > 50$ N/mm^2,

$$E_c = 4730\sqrt{f_c'} \tag{4.7}$$

where f_c' is the specified compressive strength of concrete.

4.4.3 Tensile strength

Some typical equations to determine tensile strength of concrete are given in Table 4.3 and Fig. 4.5. It is evident that the equations derived from bending tests give higher values than those from splitting or direct tension tests. The equation in the CEB-FIP Model Code[43] for the mean value of tensile strength is chosen because it gives average values.

$$f_{ctk,m} = f_{ctk0,m}\left(\frac{f_{ck}}{f_{ck0}}\right)^{2/3} \tag{4.8}$$

where $f_{ctk,m}$ is the mean values of the characteristic tensile strength of concrete

$f_{ck0} = 10$ MPa

$f_{ctk0,m} = 1.4$ MPa, and

f_{ck} is the characteristic cylinder strength of concrete in compression.

4.5 Simplified mechanical model for concrete in uniaxial compression

For the purpose of finite element analysis, the constitutive equations for concrete in uniaxial compression are further simplified into a linearised model, as shown in Fig. 4.6. The strain at any point is increased by a constant incremental value of 0.0005, and the stresses are calculated directly with the selected Eqs. 4.1 and 4.2. The stress at the first point $\sigma_{c,1}$, is determined by Eq. 4.9, since in the option of MKIN in the ANSYS program the initial slope is required to equal the input elastic modulus.

$$\sigma_{c,1} = E_c \times \varepsilon_{c,1} \tag{4.9}$$

where E_c is the modulus of elasticity for concrete and

$\varepsilon_{c,1}$ is the strain at first point in the simplified mechanical model for concrete.

4.6 Improvement on post crushing properties of the element

4.6.1 Problem of post crushing

As mentioned above, when the stress level satisfies the strength failure criterion, crushing occurs at an integration point within an element. The material associated with this integration point loses its strength completely and the stresses are redistributed among the surrounding integration points. Effectively, the material represented by the element disappears since it carries no stress regardless of the strain imposed. The surrounding integration points may crush too during the stress redistribution. If enough integration points crush at the same time, the whole model fails so that a full response of

the model cannot be obtained. This early failure phenomenon can be identically observed in the numerical test on a standard prism in compression as shown in Fig. 4.9. As for the case of plain concrete, the maximum output compressive strength should approximately equal the input compressive strength f_c (= 41.473 N/mm^2 in Fig. 4.9), and the associate strain should approximately equal ε_0 (= 0.002 in Fig. 4.9). In fact, however, because of the earlier crushing of the whole model, only about half f_c maximum compressive stress and half ε_0 associated strain are output.

4.6.2 Method to solve the problem

The idea of using smeared concrete material acting similarly to steel reinforcement to stiffen-up the element was proposed in the previous work to solve the early crush problem[11]. The smeared material has strength in its axis direction only and exhibits the same stress-strain relationship as the concrete in the rest of the element, Fig. 4.6. Crushing is not specified for the smeared material. Hence, when the element concrete has crushed, the smeared material can continue to withstand a certain amount of load.

In the present research, the optimum volume of the smeared material required by the elements to represent the expected material's response is determined by a number of numerical tests. Afterwards the method is modified so that it can also be applied to the modelling of concrete elements under the multiaxial stress state.

4.6.3 Numerical test for optimum value of the smeared material

The models used in the numerical tests are standard cubes (100×100×100 mm^3) and prisms (100×100×300 mm^3). Due to symmetries in the three directions only 1/8 of the cube or prism is modelled, as shown in Figs. 4.7 and 4.8. In both of the models, the top surfaces are laterally constrained to simulate the friction effect of the stiff top platen at the platen-specimen interface. The models are loaded in the z direction, controlled by increments of displacement.

Fig. 4.9 shows a series of curves from prisms with different percentages of smeared material. The curves are average values of all nodes on both the top surface and the middle section. It is evident that as the percentage of smeared material increases, both strength and deformation capacity increase.

When the percentage of smeared material reaches an optimum value, the output maximum stress shows close agreement to the input compressive strength. Beyond this optimum value the output stress-strain curve has no descending branch. This critical percentage of smeared material is a function of a number of parameters including loading increment, shape of model and mesh of element. For example, in the case in Figs 4.7 to 4.9, the loading speed is 175 $\mu\varepsilon$ (equals 5%ε_{cu})/substep and the critical percentage is 9.73%; if the loading increment is decreased to 87.5 $\mu\varepsilon$/substep, the critical percentage is 9.72%; while if the loading speed is increased to 350 $\mu\varepsilon$/substep, the critical percentage is 9.77%. Based on a series of numerical tests, the value of 9.7% is suggested as the optimum percentage which will work effectively in most cases.

4.7 Effect of element aspect ratio

The aspect ratio of the element will affect the solution, and the range from 1 to 3 is suggested for most types of elements[31]. In this study a series of numerical tests have been carried out to investigate the effect of the aspect ratio on the special reinforced concrete element in the ANSYS program.

The model is the standard prism shown in Fig. 4.8. The only independent variable is the aspect ratio of x/z or y/z. Herein, z is the loading direction and x/y always equals unity.

The numerical tests indicate that element aspect ratio is a significant factor affecting the mechanical behaviour of the concrete element. The prism with an aspect ratio of 0.33 only gives 70% of its input compressive strength, while the one with a ratio of 1.67 presents a result without a descending portion, Fig. 4.10. Fig. 4.11 shows that in the range of 0.33 to 1.0, the output maximum stress is proportional to the aspect ratio. With an aspect ratio of 1.0, the output maximum stress is very close to the input value of compressive strength $f_{c,\,input}$. Within the range of 1.0 to 3.0 the output curve extends to an infinite strain. Here, the maximum stress is almost a constant, which is approximately 15% higher than $f_{c,\,input}$.

Two sets of results with different input compressive strengths are shown in Fig. 4.12. In set B, $f_{c\,,\,input}^{B}$ is the sum of the compressive strength in set A, $f_{c\,,\,input}^{A}$ and the difference between $f_{c\,,\,input}^{A}$ and the maximum output stress with an aspect ratio of 0.33. It is clearly

observed that in set *B* the maximum output stress at an aspect ratio of 0.33 is very close to the expected value f_c^A ,input, and the linear progression of set B is almost parallel to that of set *A*. The difference between the maximum output stress with aspect ratio smaller than 1.0, and the input compressive strength, can therefore be used as the increment of the input compressive strength. In other words, the loss of output maximum stress due to the slender shape of the element can be compensated for by increasing the input compressive strength by an amount equal to the loss.

Based on several sets of numerical tests, a relationship between the ratio of the maximum output stress to input compressive strength and the aspect ratio of the element has been obtained. The regression relationship is given in Eq. 4.10, and shown in Fig. 4.13.

$$\frac{\sigma_c}{f_c} = 0.4595\frac{x}{z} + 0.5225 \qquad \left(0.33 \le \frac{x}{z} \le 1.0\right) \tag{4.10}$$

where, σ_c is the output maximum compressive stress of concrete modelled using elements with aspect ratios within 0.33 to 1.0

f_c is the input compressive strength of concrete

x is the element size in the perpendicular direction of loading and

z is the element size in the loading direction.

In finite element modelling a simplified method is suggested. In the method the aspect ratio range of 0.33 to 1.0 is divided into three regions, for which an increased input compressive strength f_{input} is recommended, that is:

for $0.33 \le x / z < 0.55$,

$$f_{input} = 1.35 f_c \tag{4.11}$$

for $0.55 \le x / z < 0.77$,

$$f_{input} = 1.25 f_c \tag{4.12}$$

for $0.77 \leq x / z < 1.0$,

$$f_{input} = 1.15 f_c \tag{4.13}$$

for $1.0 \leq x / z \leq 3.0$,

$$f_{input} = 1.0 f_c \tag{4.14}$$

The relation of these suggested equations and the numerical results can be found in Fig. 4.13.

Fig. 4.14 presents an example of the application of this recommended method. Set *C* is the results of using f_{input} determined with Eqs. 4.10 to 4.14. The results show good correlation with the target input strength

4.8 Relationship between the results from prism test and cube test

As for the physical tests, there should be a relationship between the results from numerical tests on prism and cube models. Fig. 4.15 displays a set of output stress-strain curves from cube tests, whilst the relevant prism test curves can be found in Fig. 4.10. The elements in a cube are more confined than those in a prism, so the curves from cube models indicate higher stress and deformation capacity than those from prism models. The maximum output stress for a cube is about 20~25% greater than that in the corresponding prism. This relationship is similar to that of the physical tests.

4.9 Effect of final slope of the smeared material

As described in Chapter 4.6.2, the smeared material has the same properties as the remainder of the concrete element. Besides the percentage of the smeared material, the only parameter which can be varied is the slope of the curve beyond the peak stress. Fig. 4.16 gives a set of prism model results using different magnitudes of this slope. As the magnitude of the slope increases, the ascending portion of the curve remains unchanged, and only the descending portion shows greater deformation capacity. Therefore, zero stiffness is recommended in future models.

4.10 Consideration of the multiaxial stress state

The analyses in Chapters 4.6 to 4.8 indicate that adding smeared material is a successful approach to avoid the earlier failure problem of the concrete element. Since all of the analyses are based on the condition that the smeared material has same uniaxial stress-strain relationship as that of concrete, conclusions obtained above provide fundamental properties of concrete strengthened by smeared material in the uniaxial stress state. In the application of this method to FEA of concrete structures, however, the effect of the multiaxial stress state should be considered.

In most cases concrete works in a multiaxial stress state. Strength failure criteria of concrete vary corresponding to the stress state suffered by the concrete. A typical failure criteria of concrete in the biaxial stress state is shown in Fig. 4.17, whilst a triaxial one is shown in Fig. 4.18[31, 36, 51]. The key parameters of the failure criteria employed in the ANSYS programme have been listed in Table 2.2. Normally the crushing strength of concrete determined by the failure criteria is higher than the uniaxial compressive strength f_c, but it will never exceed $1.725f_c$ plus the hydrostatic stress, see Table 2.2.

The smeared material is treated as an uniaxial tensile or compressive reinforcement and it possesses its own failure criteria[31]. When concrete reaches a criterion strength which is higher than f_c at a critical integration point, the smeared material may only keep its highest stress equalling the input strength f_c. Therefore the smeared material cannot strengthen the concrete as it crushes, and the early failure will continue to occur.

The problem may be solved by increasing the input compressive strength of the smeared material, $f_{c,s}$, to match the concrete failure strength. It is impossible to estimate the failure strength of concrete at an integration point, however, because it varies according to the stress state of the point. Substitution of concrete with the smeared material eliminates the Poisson relationship between the three axes. Consequently the maximum compressive strength superimposed on ambient hydrostatic stress state of concrete defined by the failure criteria of the program is recommended. That is:

$$f_{c,s} = 1.725 f_c \tag{4.15}$$

where $f_{c,s}$ is the input compressive strength of the smeared material and

f_c is the uniaxial compressive strength of concrete.

Once the compressive strength has been determined, the other parameters required by the stress-strain relationship for the smeared material can be created using the equations described in Chapters 4.3 to 4.5.

The result from a numerical prism test in Fig. 4.19 indicates that as the input compressive strength of the smeared material has been increased by 72.5%, the output of the prism strength is enhanced by about 20%. It should be noted that this enhancement is from the uniaxial compressive prism test, so it must be the maximum increment of concrete compressive strength caused by the higher input compressive strength of the smeared material.

No.	Reference	Equation
1	BS8110 Part 1[42], CEB-FIP[43], GBJ 10-89[44], EC2[45] and NS3473E[46]	for $\varepsilon \le \varepsilon_0$, $f = f_c(2(\varepsilon/\varepsilon_0)-(\varepsilon/\varepsilon_0)^2)$ for $\varepsilon_0 < \varepsilon \le \varepsilon_u$, $f = f_c$ where f is the compressive stress at any strain ε; f_c is the maximum compressive strength at strain ε_0, as a design strength f_c is taken as $0.45f_{cu}$ in all of the design codes with the partial safety factor 1.5, herein f_{cu} is the standard characteristic cube strength; ε_0 is the strain at the peak stress, $2.4\times10^{-4}\sqrt{f_{cu}/\gamma_m}$ in BS8110 Part 1 and 0.002 in the other codes, and ε_u is the ultimate strain, taken to be 0.0033 or 0.0035.
2	E. Hognestad[47]	for $\varepsilon \le \varepsilon_0$, $f = f_c(2(\varepsilon/\varepsilon_0)-(\varepsilon/\varepsilon_0)^2)$ for $\varepsilon_0 < \varepsilon \le \varepsilon_u$, $f = f_c[1-0.15((\varepsilon-\varepsilon_0)/(\varepsilon_u-\varepsilon_0))]$ where $\varepsilon_0 = 0.002$ $f_c = 0.85f_c'$ f_c' is the cylinder strength and $\varepsilon_u = 0.0035$.
3	BS8110 Part 2 [48]	$f = 0.8f_{cu}\left(k\eta-\eta^2\right)/\left(1+(k-2)\eta\right)$ $\eta = \varepsilon/\varepsilon_0 = \varepsilon/0.0022$ $k = 1.4\varepsilon_0 E_c/f_{cu} = 3E_c/f_{cu}$ where E_c is the elastic modulus of concrete in kN/mm^2 $\varepsilon_0 = 0.0022$.
4	P. Desayi and S. Krishnan[41]	$f = E_c\varepsilon/\left(1+(\varepsilon/\varepsilon_0)^2\right)$ where E_c is a constant (same as initial tangent modulus) such that $E = 2f_c/\varepsilon_0$.

Table 4.1 *Typical constitutive equations for concrete in uniaxial compression*

No.	Reference	Equation
1	BS8110, Part 2 [48]	$E_{c,28} = k_0 + 0.2 f_{cu,28}$ where $E_{c,28}$ is the static modulus of elasticity at 28 days $f_{cu,28}$ is the characteristic cube strength at 28 days; k_0 is a constant closely related to the modulus of elasticity of the aggregate (taken as 20 kN/mm^2 for normal weight concrete). The modulus of elasticity of concrete at an age t may be derived from the following equation: $E_{c,t} = E_{c,28}\left(0.4 + 0.6 f_{cu,t} / f_{cu,28}\right)$ where t ≥ 3 days.
2	CEB-FIP[43]	$E_{ci} = E_{c0}\left[\left(f_{ck} + \Delta f\right) / f_{cmo}\right]^{1/3}$ where E_{ci} is the modulus of elasticity at a concrete age of 28 days; f_{ck} is the characteristic cylinder strength $\Delta f = 8$ MPa $f_{com} = 10$ MPa $E_{c0} = 2.15 \times 10^4$ MPa. The reduced modulus of elasticity E_c is taken to be $E_c = 0.85 E_{ci}$
3	ACI318-89[49]	$E_c = 57000\sqrt{f_c'}$ (psi) $= 4730\sqrt{f_c'}$ (MPa) where f_c' is the specified compressive strength of concrete in psi.
4	BS8110 Part 1 [42]	$E_c = 5500\sqrt{\left(f_{cu} / \gamma_m\right)}$ where f_{cu} is the characteristic cube strength of concrete γ_m is the partial safety factor, taken as 1.5 for concrete in flexure or axial load.

Table 4.2 *Typical equations for modulus of elasticity of concrete*

No.	Reference	Equation
5	EC2[45]	$E_{cm} = 9.5(f_{ck} + 8)^{1/3}$ where E_{cm} is the secant modulus of concrete f_{ck} is the characteristic cylinder strength of concrete.
6	GBJ 10-89[44]	$E_c = 100000 / (2.2 + 33 / f_{cu})$ where f_{cu} is the characteristic cube strength of concrete.

Table 4.2 continued *Typical equations for modulus of elasticity of concrete*

No.	Reference	Equation
1	CEB-FIP[43]	$f_{ctk,\min} = f_{ctk0,\min}\left(f_{ck} / f_{ck0}\right)^{2/3}$ $f_{ctk,\max} = f_{ctk0,\max}\left(f_{ck} / f_{ck0}\right)^{2/3}$ $f_{ctk,m} = f_{ctk0,m}\left(f_{ck} / f_{ck0}\right)^{2/3}$ where $f_{ctk,\min}, f_{ctk,\max}, f_{ctk,m}$ is the minimum, maximum and mean values of the characteristic tension strength of concrete $f_{ck0} = 10$ MPa $f_{ctk0,\min} = 0.95$ MPa $f_{ctk0,\max} = 1.85$ MPa $f_{ctk0,m} = 1.40$ MPa and f_{ck} is the characteristic cylinder strength of concrete in compression.
2	C. Z. Wang and Z. M. Teng[37]	$f_r = 7.5 \sim 12\sqrt{f'_c}$ (psi) where f_r is the tensile strength of concrete from bending test and f'_c is the cylinder strength of concrete in compression.
3	C. Z. Wang and Z. M. Teng[37]	$f_t = 0.35 f_{cu}^{3/4}$ (kg/cm^2) where f_t is the tensile strength of concrete from splitting test and f_{cu} is the cube strength of concrete in compression.
4	C. Z. Wang and Z. M. Teng[37]	$f_r = 9.5\sqrt{f'_c}$ (psi) where f_r is the tensile strength of concrete from bending test.
5	C. Z. Wang and Z. M. Teng[37]	$f_t = 0.5 f_{cu}^{2/3}$ (kg/mm^2) where f_t is the tensile strength of concrete from direct tension test.
6	M. Y. H. Bangash[50]	$f_t = 0.55\sqrt{f'_c}$ (MPa) where f_t is the tensile strength of concrete from splitting test.

Table 4.3 *Typical equations for tension strength of concrete*

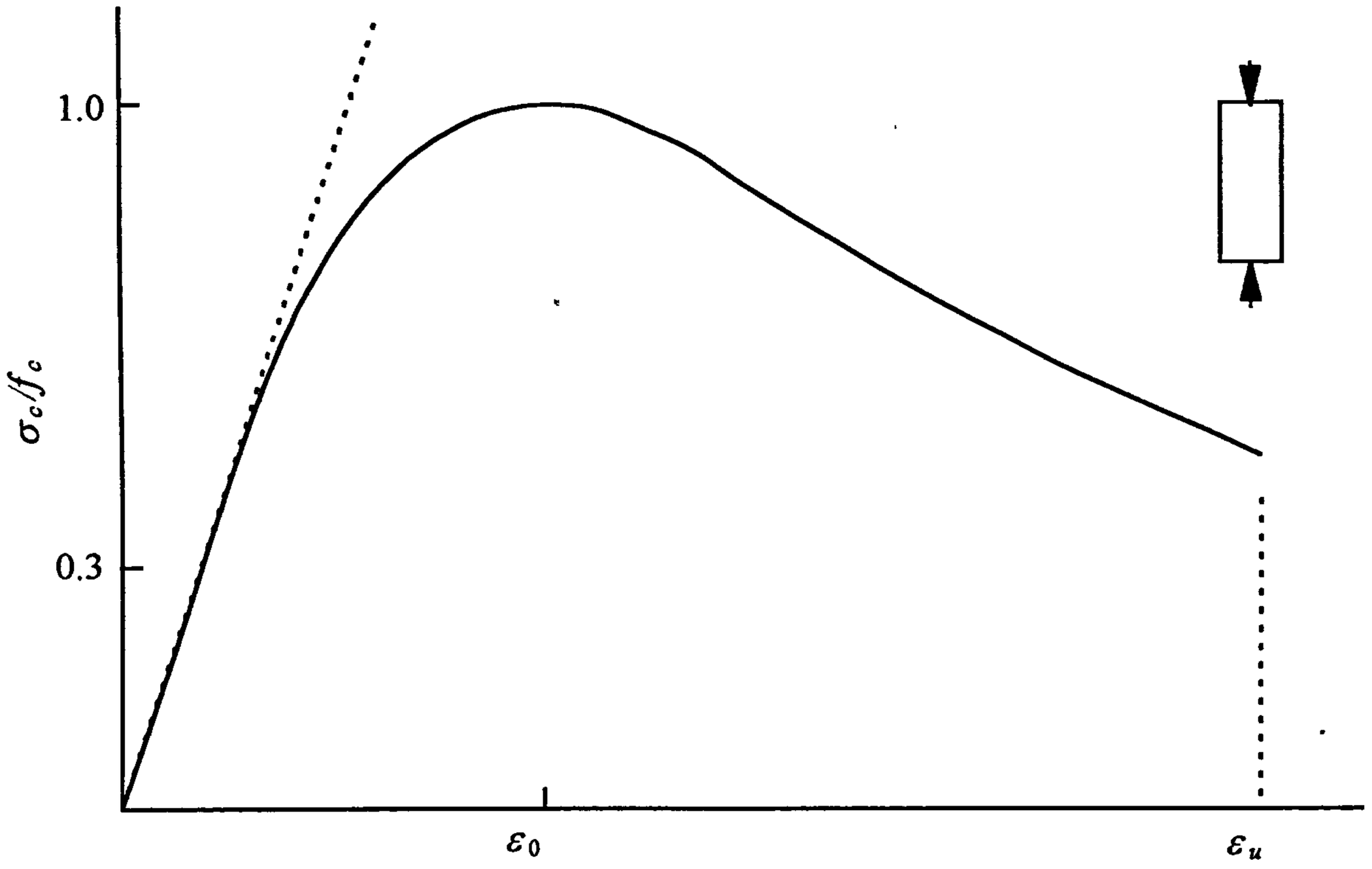

Figure 4.1 *Typical stress-strain curve for concrete in uniaxial compression*

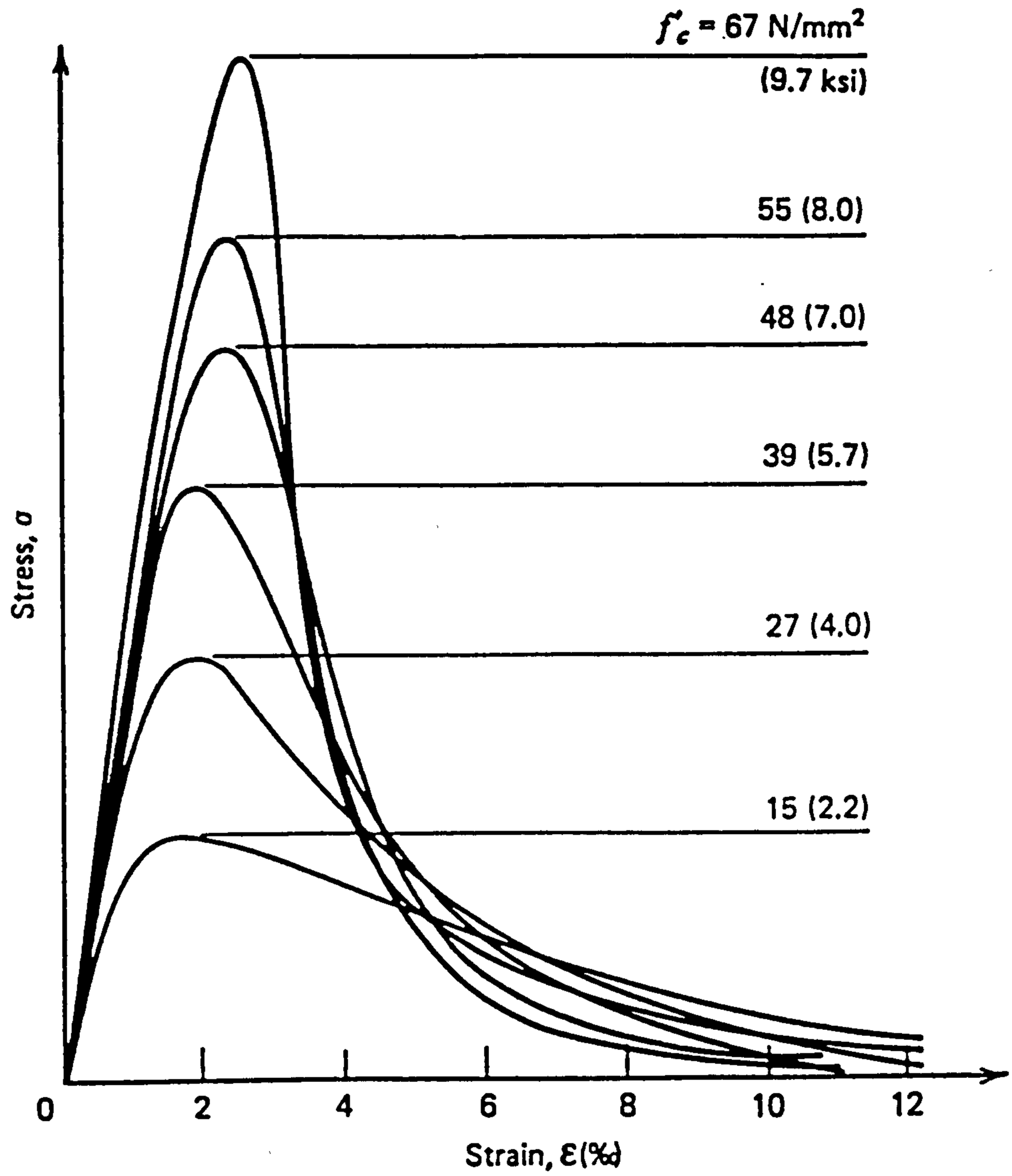

Figure 4.2 *Experimental uniaxial compressive stress-strain curves for concrete of different strengths (from Reference 51)*

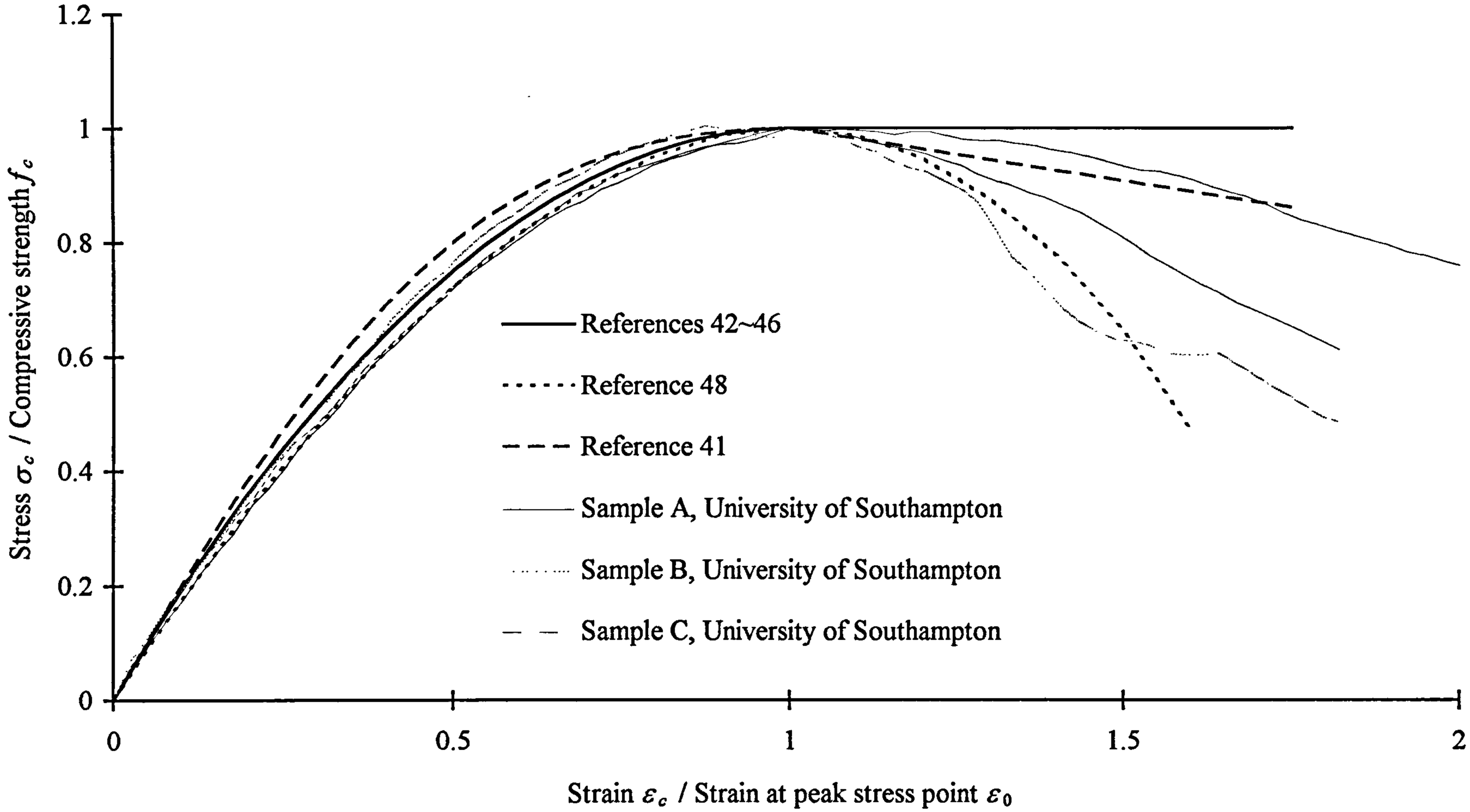

Figure 4.3 *Stress-strain relationships for concrete in uniaxial compression*

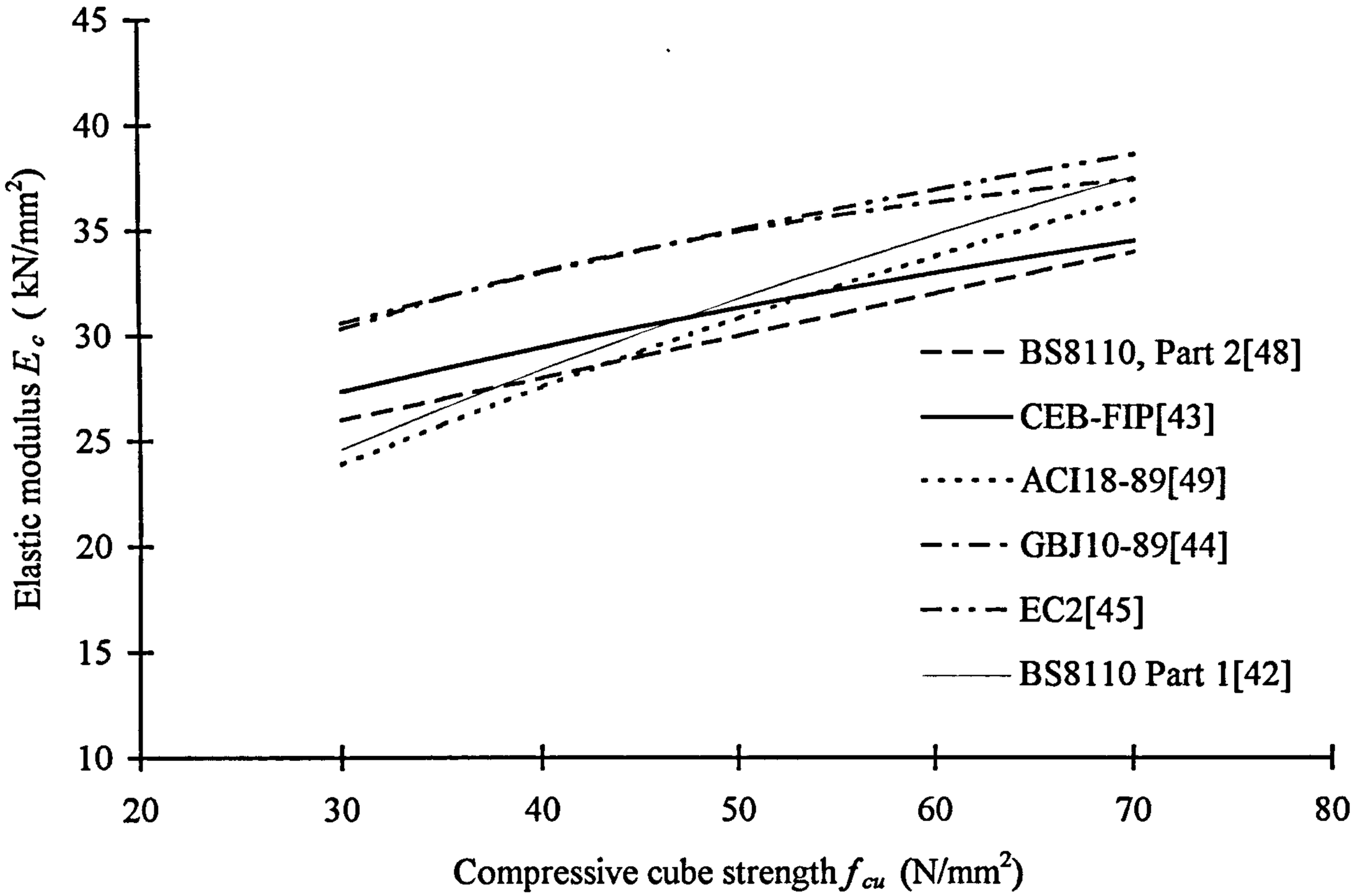

Figure 4.4 *Comparison of elastic moduli given in references*

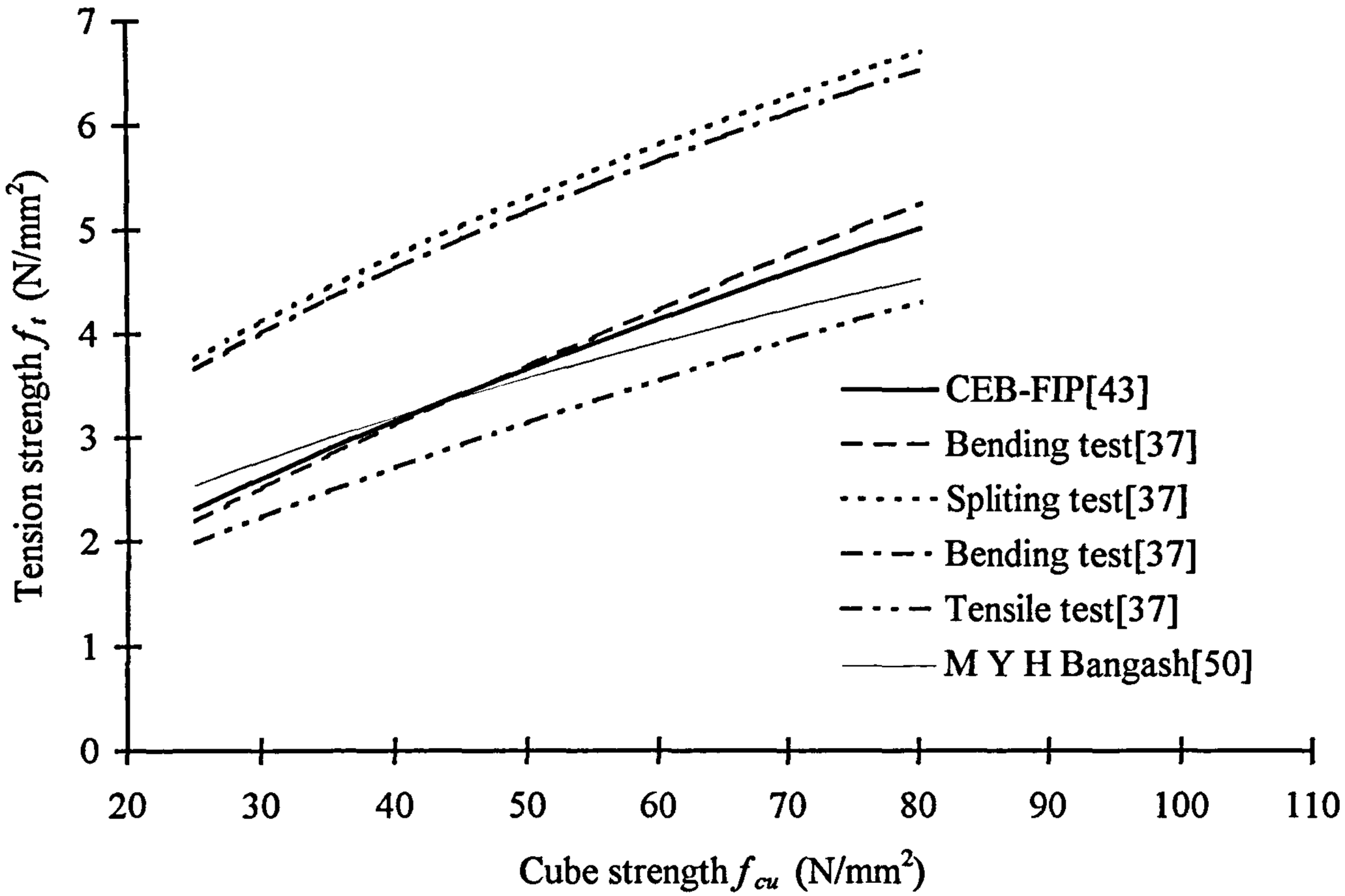

Figure 4.5 *Comparison of tension strengths given in the references*

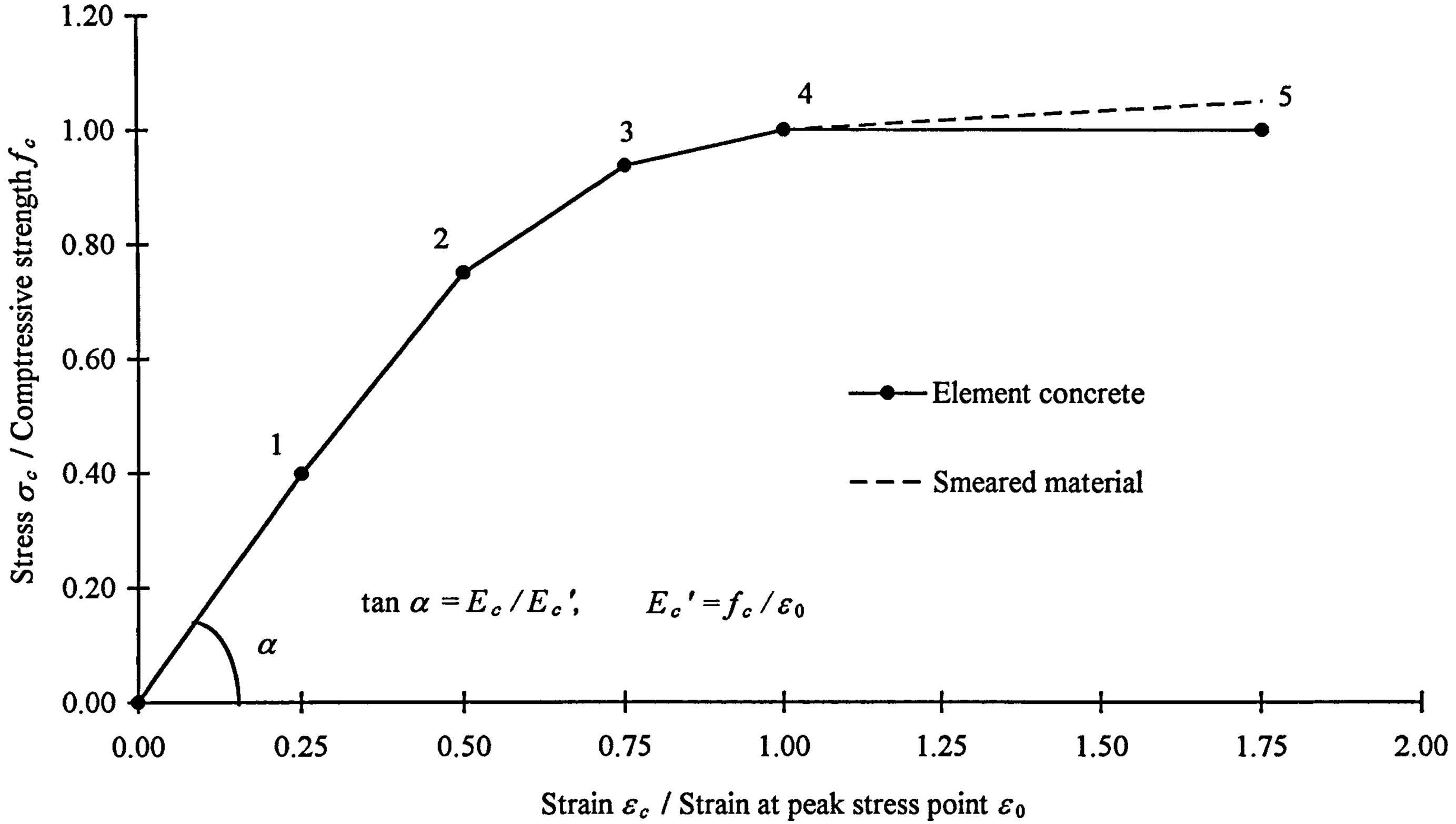

Figure 4.6 *Simplified mechanical model for concrete in uniaxial compression*

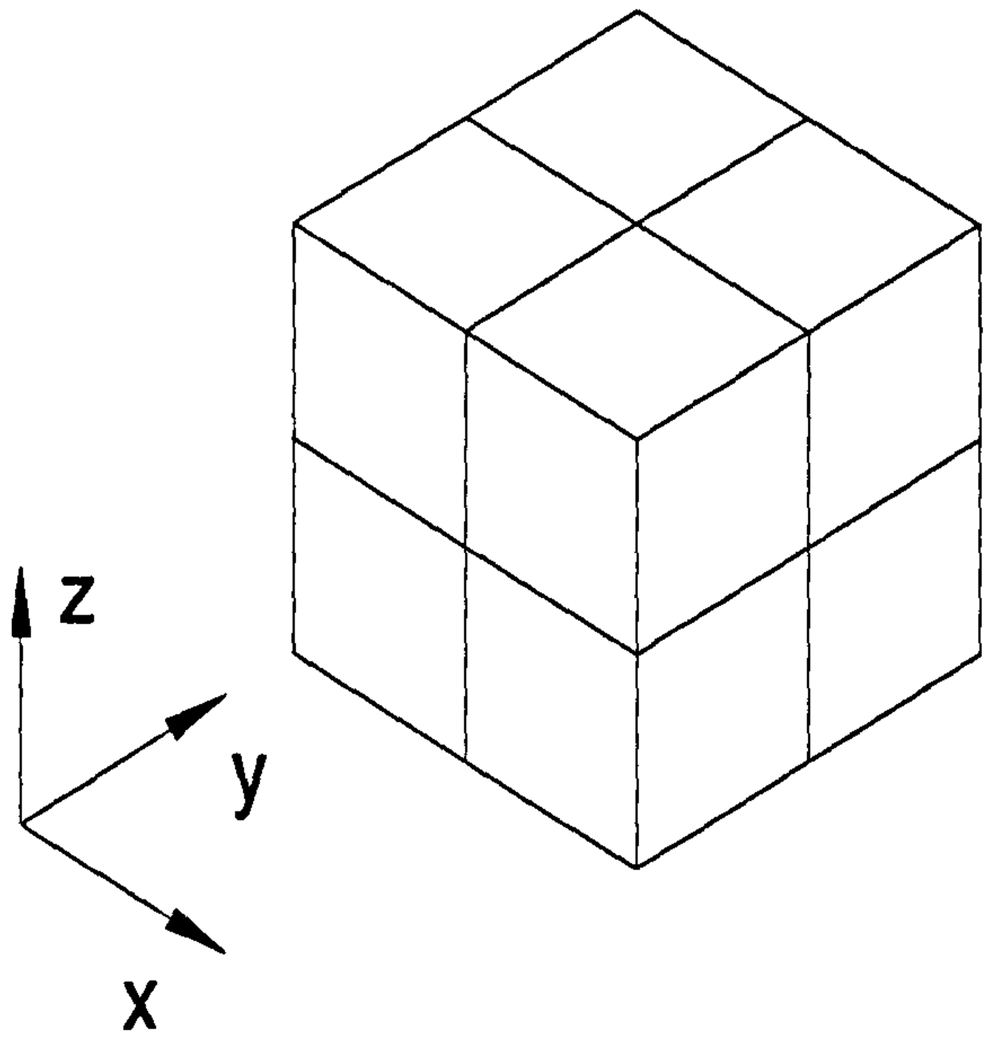

Figure 4.7 *Mesh of the cube*

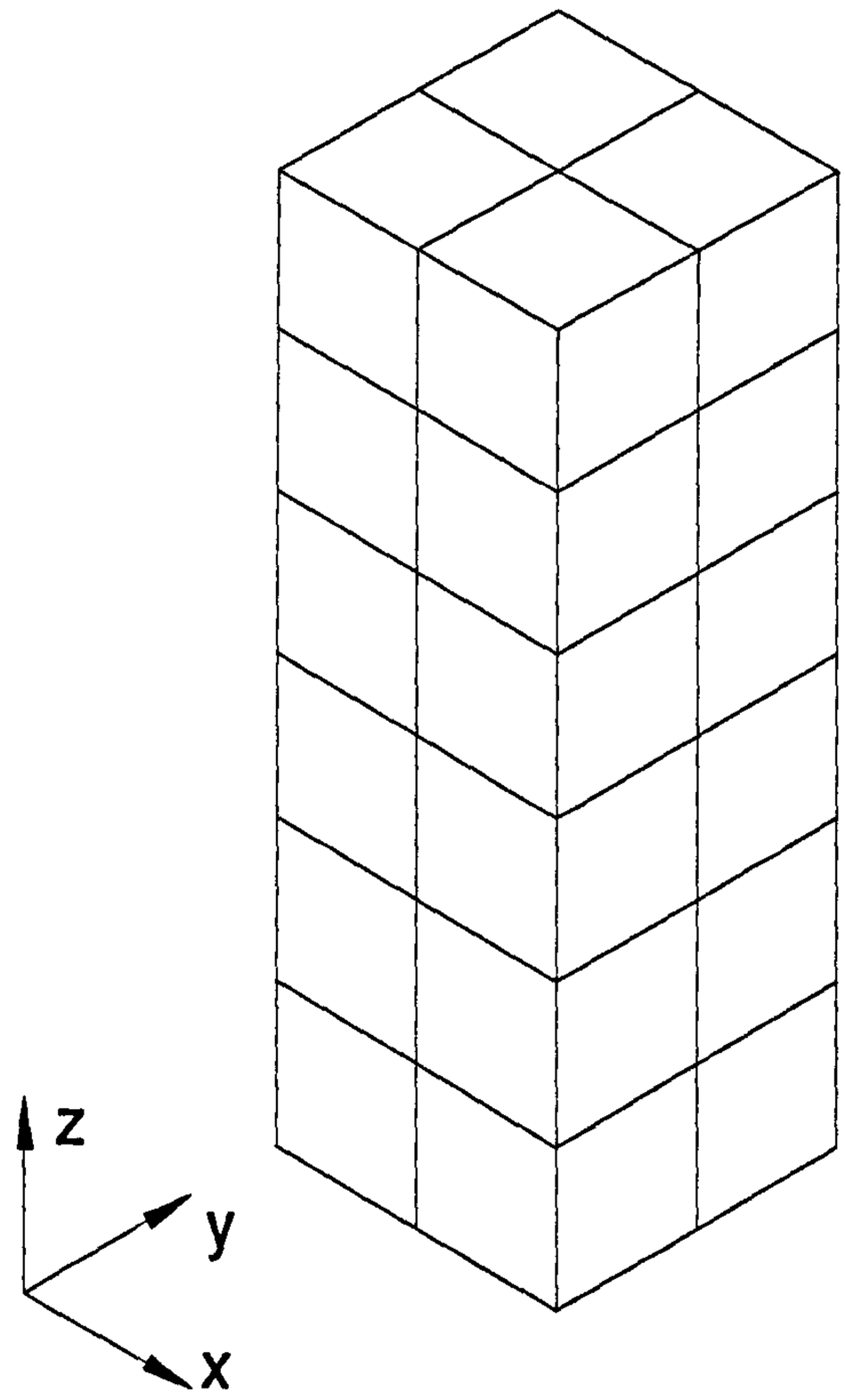

Figure 4.8 *Mesh of the prism*

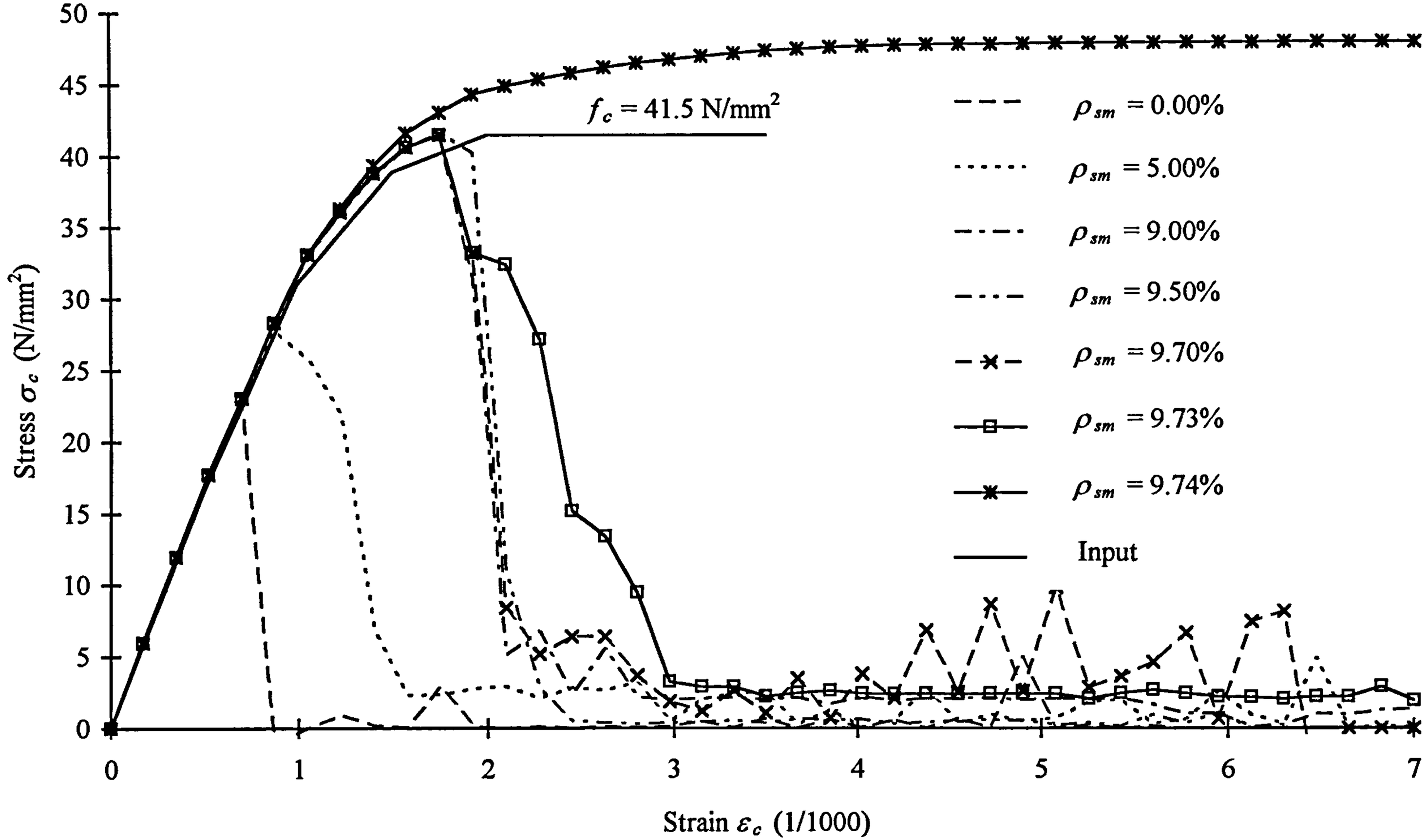

Figure 4.9 *Stress-strain curves of the prism with different percentage of the smeared material (h/d=3, 25*25*25 mm^3 element, f_c =41.5 N/mm^2, v_t = 175 με/substep)*

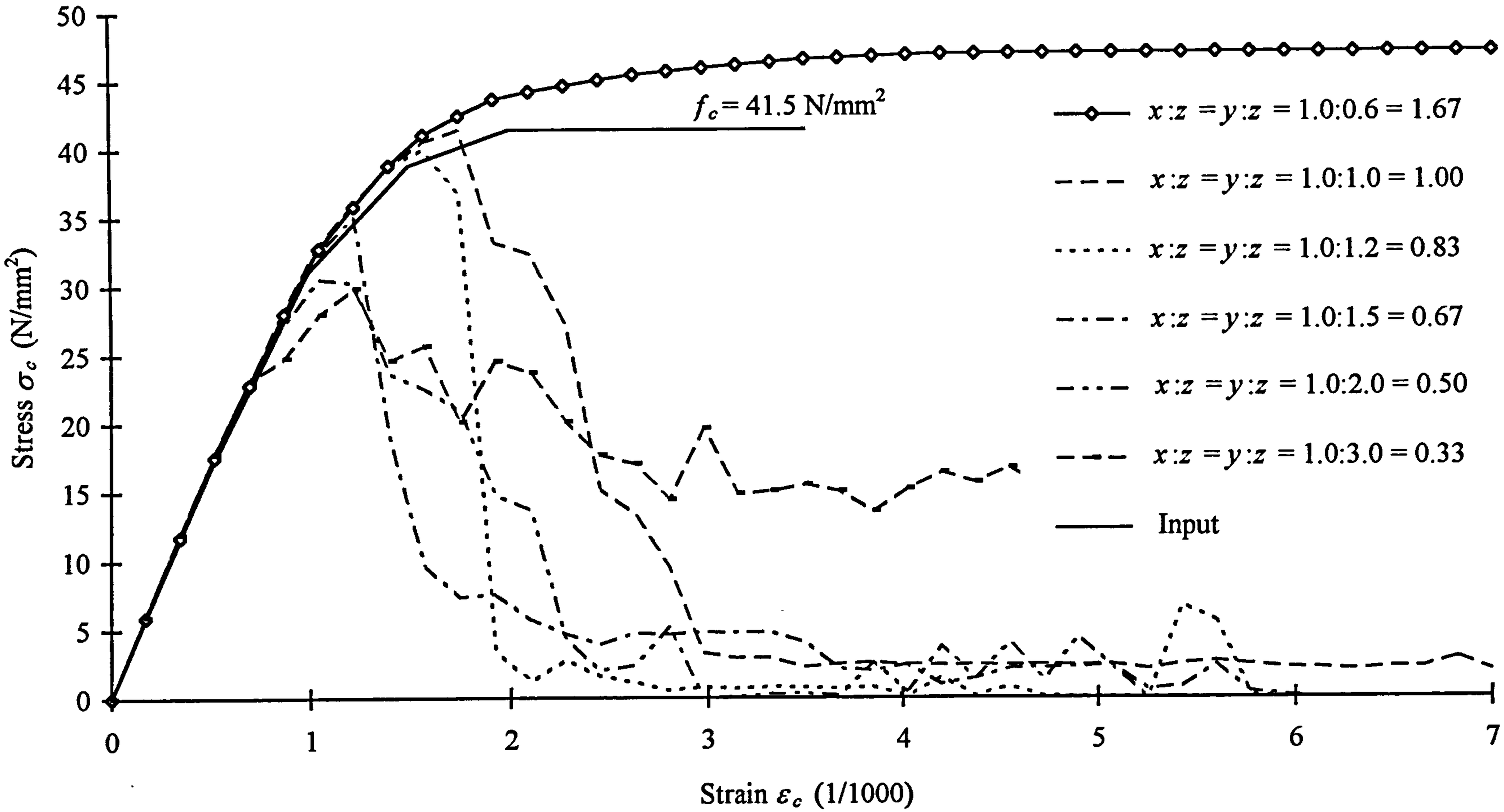

Figure 4.10 *Stress-strain curves of the prism with different element aspect ratios (h/d = 3, ρ_{sm} = 9.73%, f_c = 41.5 N/mm^2, v_l = 175 $\mu\varepsilon$/substep)*

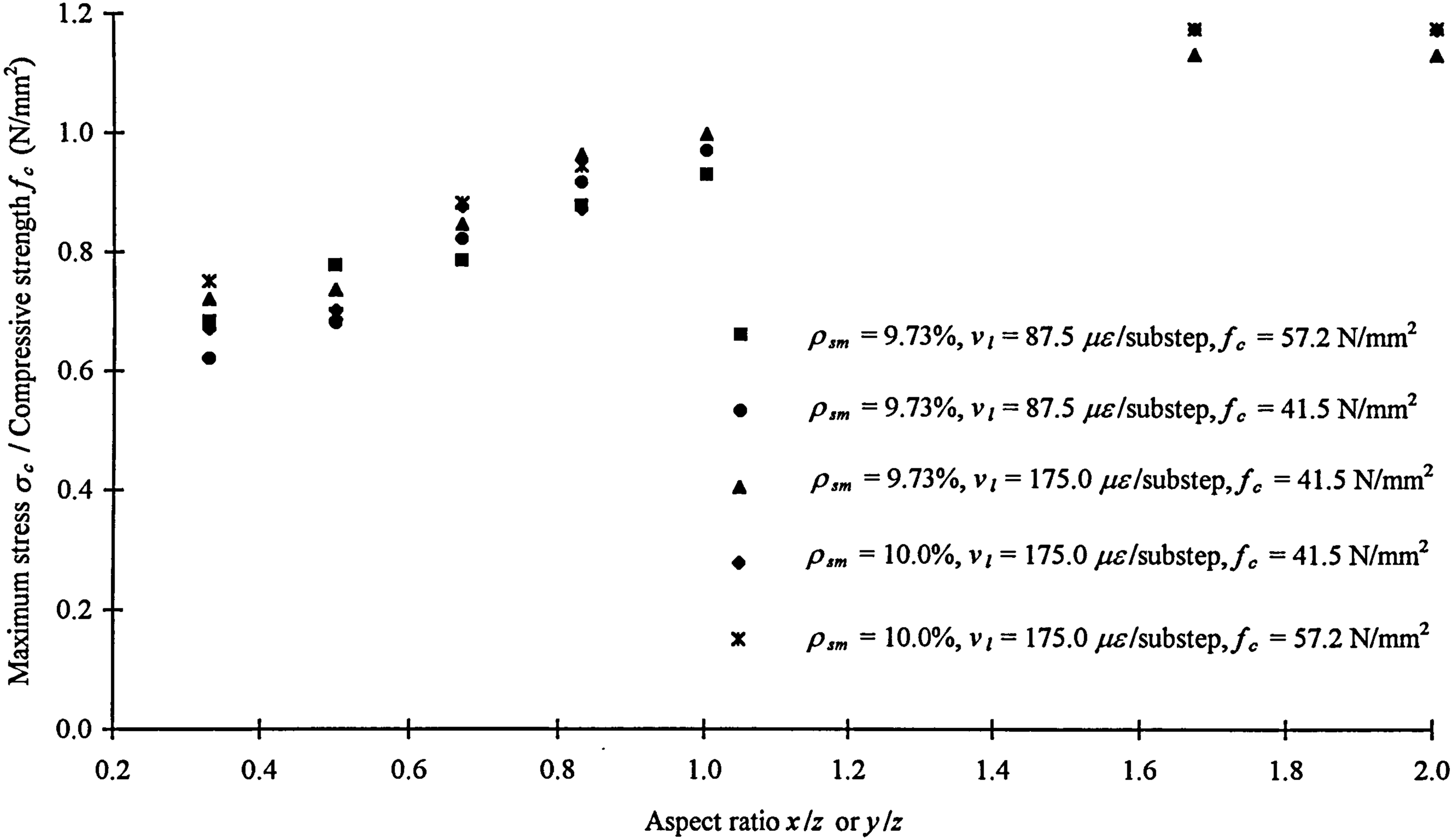

Figure 4.11 *Maximum output stresses versus element aspect ratios of the prism tests (h/d = 3)*

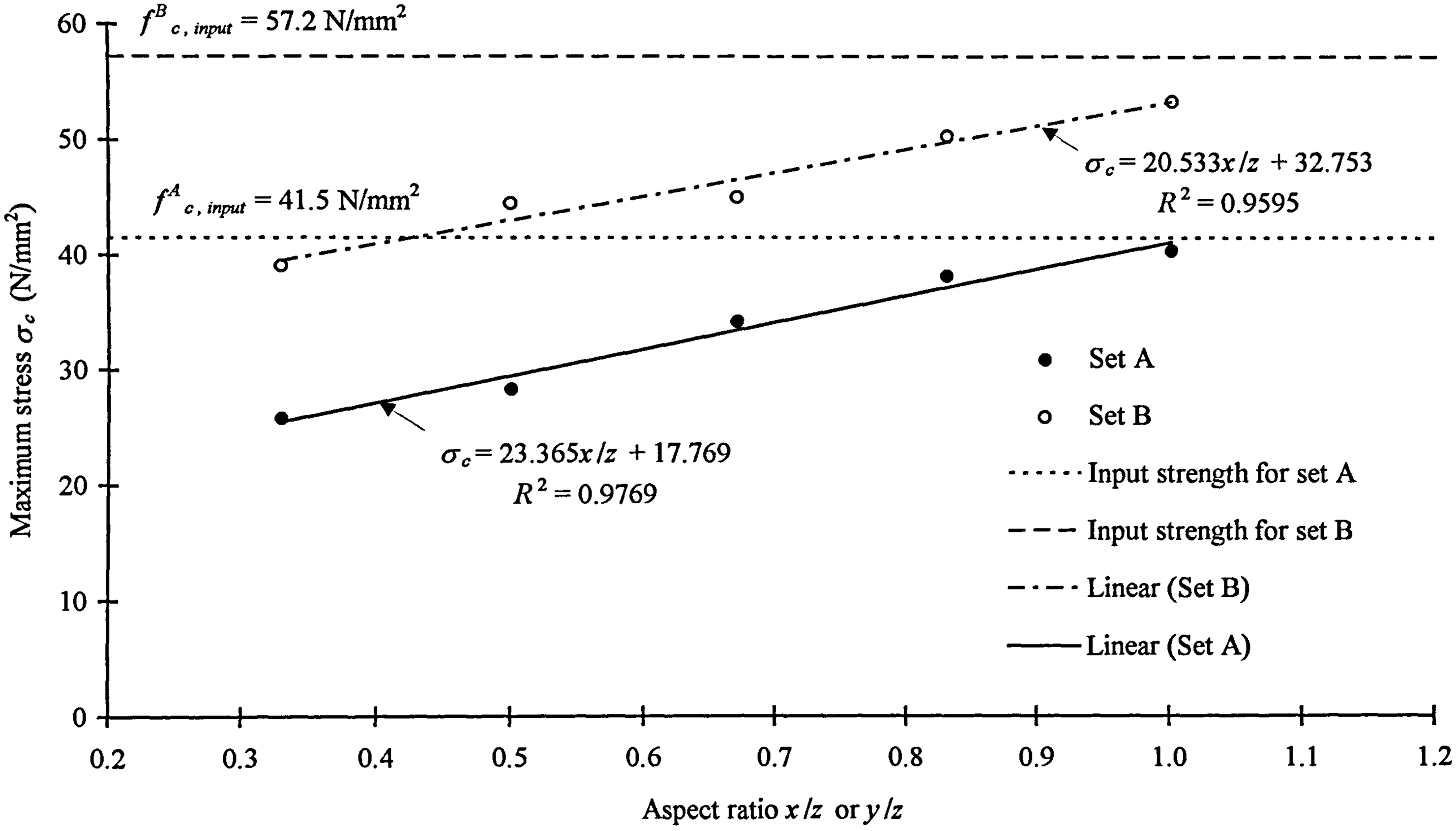

Figure 4.12 *Relationships of maximum stress and element aspect ratio (h/d = 3, 25*25*25 mm^3 element, v_l = 87.5 $\mu\varepsilon$/substep, ρ_{sm} = 9.72%)*

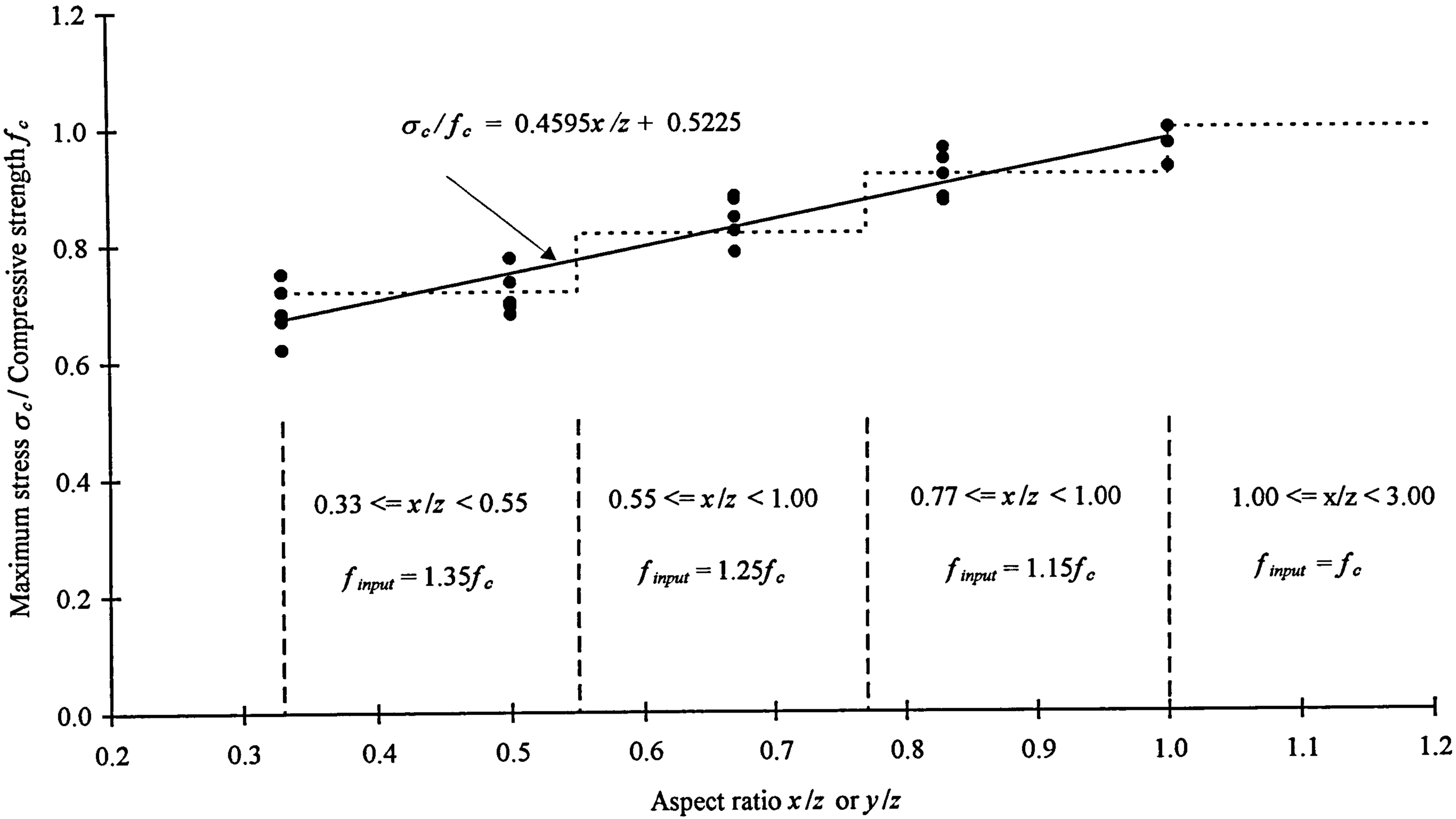

Figure 4.13 *Recommendations of input compressive strengths for elements with aspect ratios smaller than 1.0*

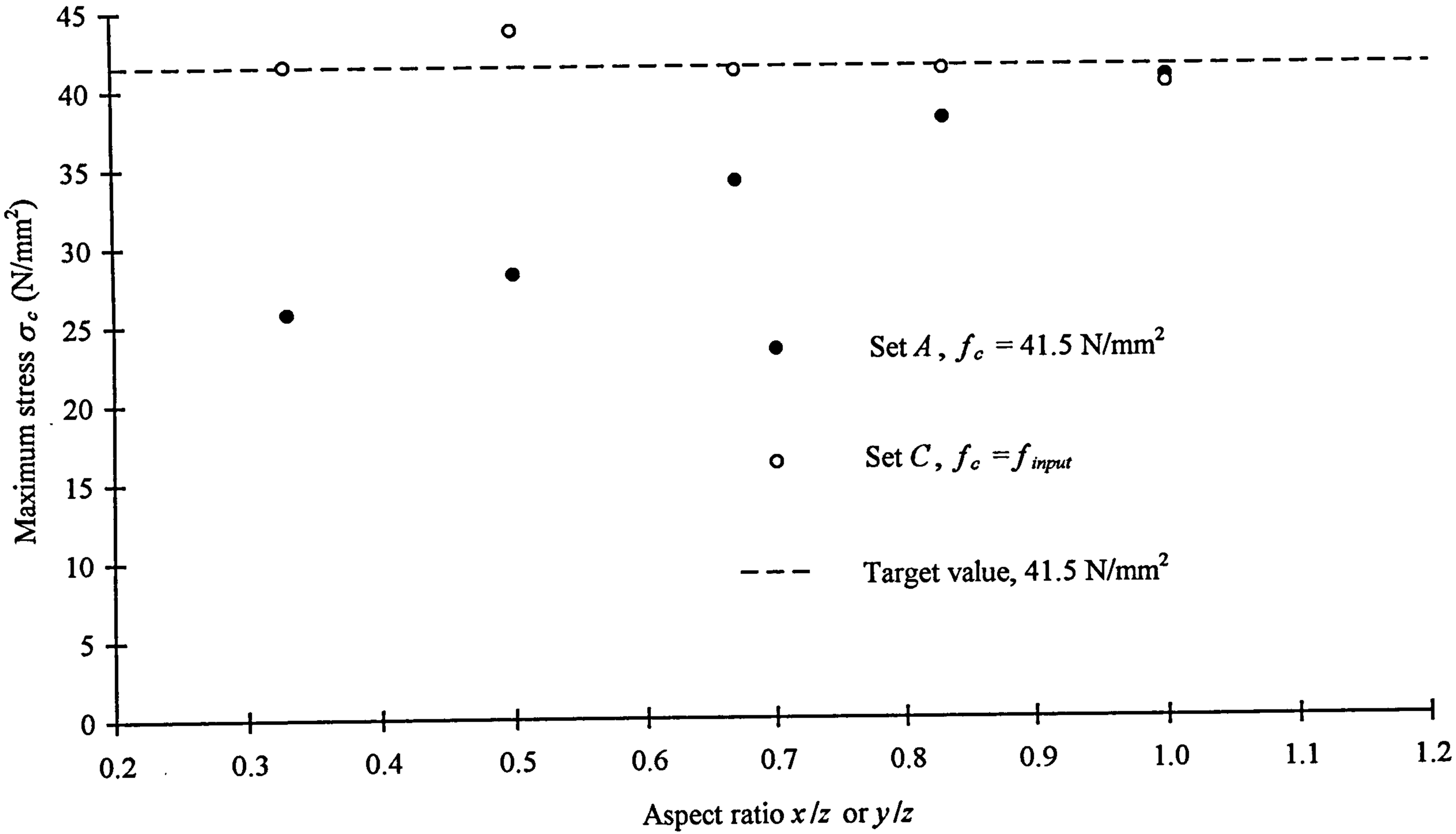

Figure 4.14 *Relationships of input and output stresses versus element aspect ratios (h/d = 3, 25*25*25 mm^3 element, v_t = 87.5 $\mu\varepsilon$/substep, ρ_{sm} = 9.72%)*

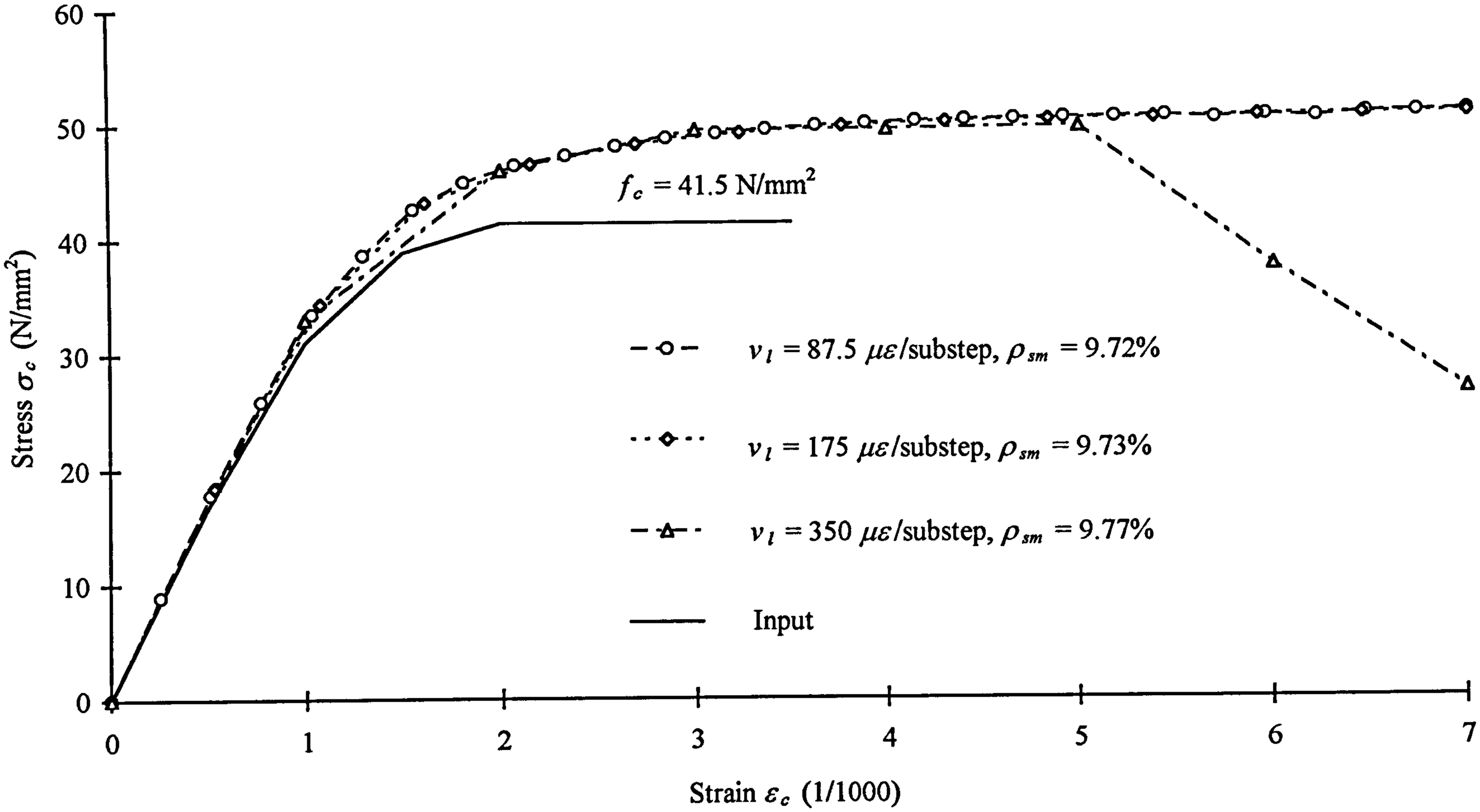

Figure 4.15 *Stress-strain curves of the cube tests (25*25*25 mm^3 element)*

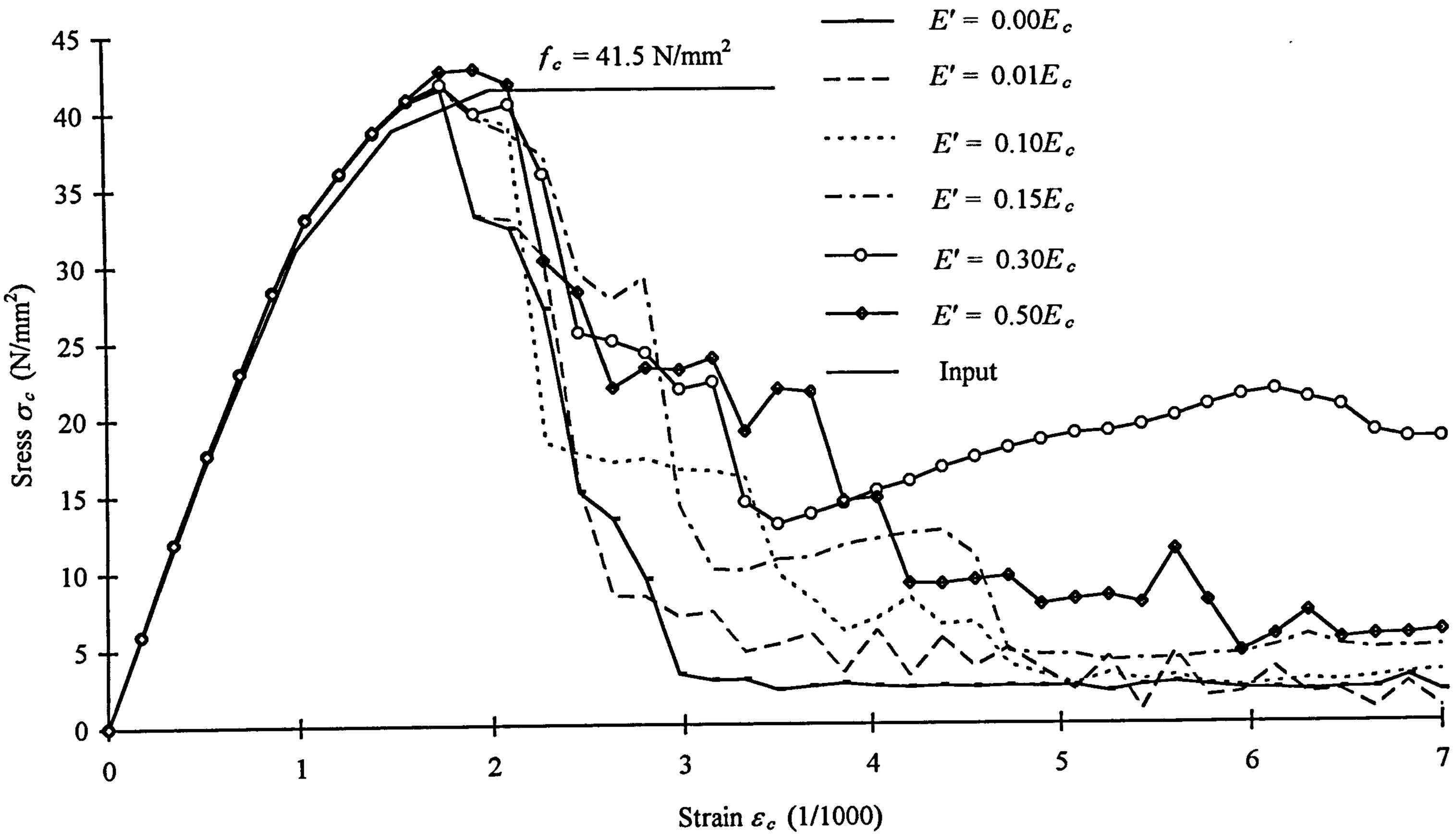

Figure 4.16 *Stress-strain curves of the prism with different final slopes of the smeared material (h/d = 3, 25*25*25 mm^3 element, v_l = 175 $\mu\varepsilon$/substep, ρ_{sm} = 9.73%)*

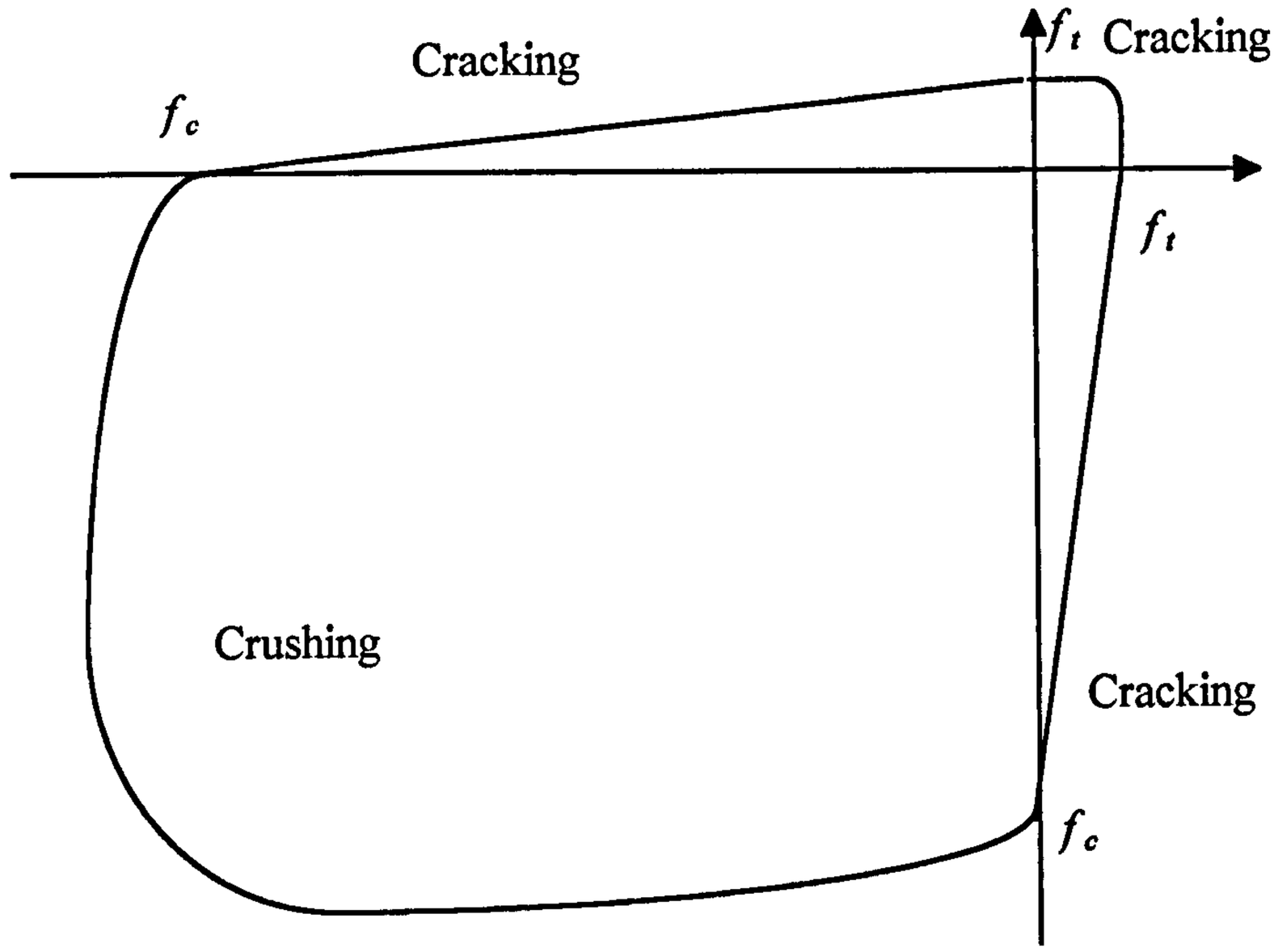

Figure 4.17 *Failure surface of concrete in biaxial stress state*

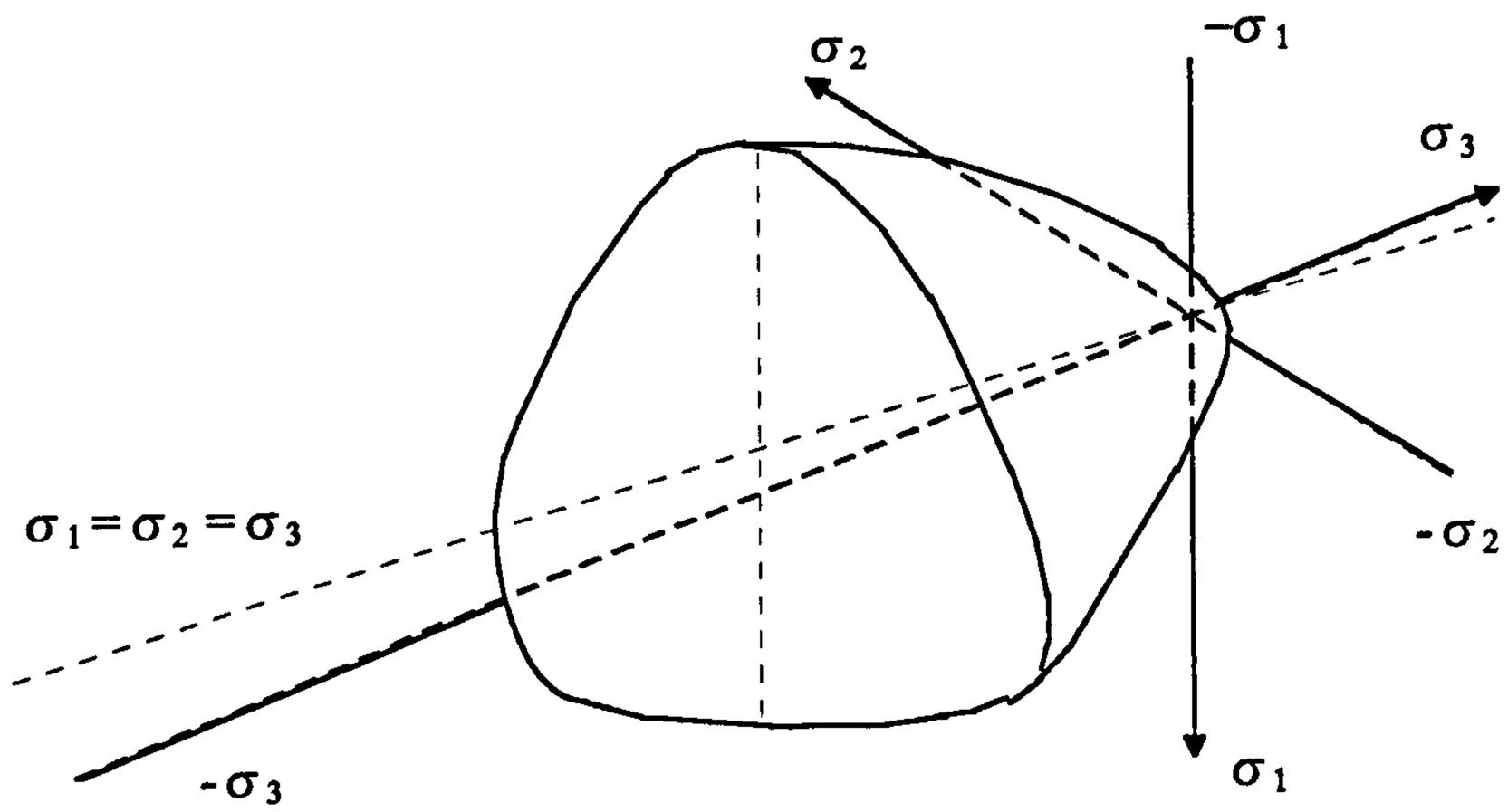

Figure 4.18 *Three-dimension failure surface of concrete in principal stress space*

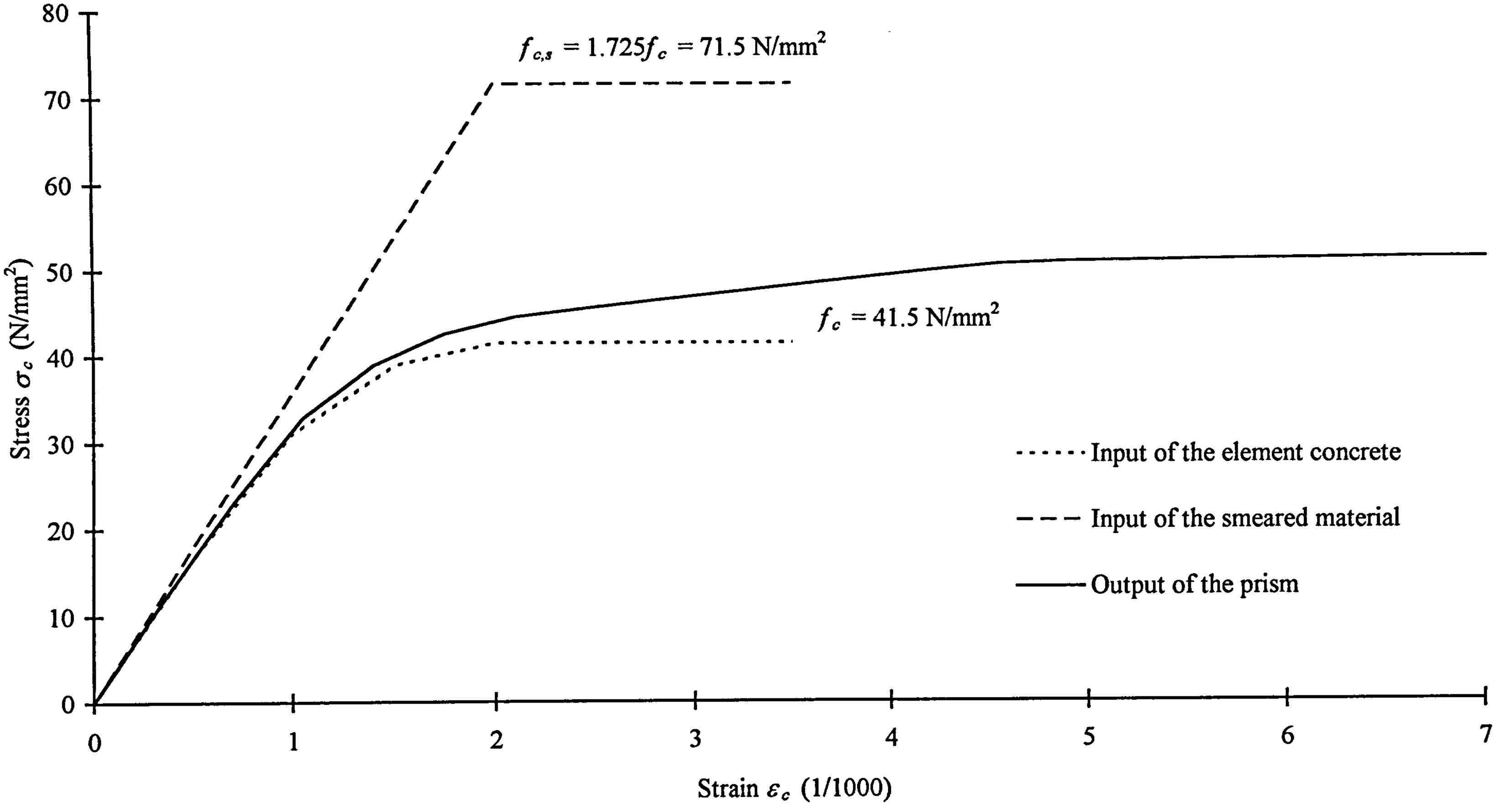

Figure 4.19 *Efficiency of compressive strength of the smeared material ($h/d = 3$, 25*25*25 mm^3 element, $v_l = 175$ $\mu\varepsilon$/substep, $\rho_{sm} = 9.70\%$)*

Chapter 5

Modelling of General Connection Components

5.1 Introduction

Several connection components are modelled to achieve the following aims:

a. Examine the precision of the mechanical models for both steel and concrete and suitability of their application in the ANSYS programme.

b. Check the applicability of the selections for finite element analyses determined in Chapter 2, such as mesh generation, element types, loading and solution.

c. Investigate the behaviour of some well known connections which are tested and modelled by other researchers, so that reliability of the modelling in the present work can be verified.

d. Finally, based on the above work, the standardisation of FEA techniques for reinforced concrete structures can be completed.

The components include a plain steel bar in tension, a T-stub connector in tension, and a steel bolt embedded in joint concrete in shear.

5.2. Steel bar in tension

The first modelling is of the most simple and direct model -- a monotonically loaded tensile steel bar, as shown in Fig. 5.1. Since a simplified element mesh is required for future application in more complex modelling situations, a relatively coarse mesh is utilised in this model. Due to the dual symmetry in the two directions of the 20 mm diameter section, only a quadrant is analysed and it is represented by one SOLID 45 element in ANSYS. Using Eqs. 2.5 and 2.6, the quadrant section is represented by a

quadrilateral section as shown in Fig. 5.2. The gauge length of the bar is 100 mm of which only half is analysed due to symmetry in the longitudinal direction. It is meshed into five elements, see Fig. 5.2.

Fig. 5.3 shows the input stress-strain relationship determined using the simplified mechanical model for steel in Chapter 3, with the yield strength of 270 N/mm^2. The figure also shows the corresponding finite element solution of the stress-strain curve. The excellent agreement of the two curves prove that the simplified model satisfies the requirements of the ANSYS programme well. It can also be noted that although the input is up to the ultimate strength point (point 5) limited by the option of MKIN in the ANSYS programme, the solution can reach a strain as large as required (30% in this numerical test).

The accuracy of the solution leaves little doubt that if the input stress-strain relationship is some other model, for instance a bilinear model, the output curve will give the same shape as that of the input. Therefore it is necessary to represent the mechanical property of each material matching the actual curve as well as possible, especially when the non-linear behaviour of a model is critical.

5.3 T-stub connection

5.3.1 Objective

The second modelling is of the T-stub connection tested in the University of Liege, Belgium[53]. A number of numerical simulations on the behaviour of the connection have been carried out in the Numerical Simulation Working Group of the European Co-operation in the Field of Scientific and Technical Research (COST), in order to compare the capabilities of the available finite element method programmes[54~56]. It is also one example of the finite element analyses on steel structure connections recently carried out within the European countries[57~59]. The specimen is illustrated in Fig. 5.4. Full details of the connection, geometry, material properties, and test results are as described in Reference 53.

Many factors should be considered to achieve an accurate analysis of the connection. These include slips between the nut, washer and flange, yield of the T flange under the nut and washer, bending due to prying of the bolt, local yield at the bearing surfaces of the threads, deformation of nut and washer, bending in the T flange, etc.. Most of the

factors have been considered in the simulations. The influence of mesh fineness and input material properties has been investigated by the authors and reported separately[54]. Only one model with a coarse mesh is introduced herein.

5.3.2 Model

Since all three planes are symmetrical, only one eighth of the connection is modelled and the views of the model are shown in Fig. 5.5. Again the model is meshed as simply as possible because such a component will represent a small part of subsequent structural subframe analyses. The nut constraint on the front face of the T-stub flange is represented by tapered elements through the flange thickness. The front face of the 'nut' has the same area as the washer, whereas the back face of the tapered elements has the same area as the bolt core. The bolt length protrudes behind the flange as shown in Fig. 5.5 to represent the short bolt length through the T-stub flange, which would otherwise derive artificial rigidity from direct contact with the bolt/flange elements if they were fixed at the plane of symmetry.

5.3.3 Results

Fig. 5.6 illustrates the load-displacement curves of both numerical and physical tests. From the comparison it can be concluded that the simplified mechanical model for steel can work well at high stress levels. Although a very simple mesh is used, the model still can present the main non-linear behaviour and the ultimate capacities of both strength and deformation. A more detailed mesh at the corner of the T-stub has been shown [54] to be more accurate at all stress levels.

5.4 Bolt in joint concrete

5.4.1 Objective

The third modelling is of a simple connection of a bolt in joint concrete in shear, which is a portion of a connection in precast concrete structures. The physical test was carried out in the Tampere University of Technology, Finland[60], in order to investigate the connecting response of the bolt and the surrounding concrete. The dimensions and the test arrangements of the test specimen are shown in Fig. 5.7. The general behaviour of the specimen will be analysed as the fundamental purpose of this modelling. The

influence of some factors in finite element analysis, such as the fineness of element mesh and the application of contact elements, are investigated simultaneously.

5.4.2 Models

Three models are constructed with different meshes, with or without contact elements. Due to the dual symmetry, only a quarter of the tested specimen is modelled. Details of the models are described as follows.

5.4.2.1 Model 1

Again, to be consistent with our further modelling, simple element mesh is applied to this model, Fig. 5.8. In this coarsely meshed model the quarter circle section of the bolt is represented by a quadrilateral element. Input the radiator of r = 15.00 mm into the Eqs. 2.5 and 2.6, the co-ordinates of the point (B in Fig. 2.3) are obtained as x_0 = 11.940 mm, y_0 = 11.625 mm. No contact elements are used in this model.

5.4.2.2 Model 2

In the normal direction of the contact surface between steel and concrete, the bond strength in tension is so small that can be neglected in the general analyses. However, if there are no gap or contact elements used in the location, the bond strength will equal the tensile strength of concrete. This overestimates the bond strength and results in stiffer models. Therefore, 8 contact elements are used in this model, located in two rows along the bottom lines of the steel bolt, starting at the end surface of the joint concrete. The other characteristics of this model are the same as those for model 1, see Fig. 5.8.

5.4.2.3 Model 3

Fine meshes are used in this model, see Fig. 5.9, to have a comparison with the coarsely meshed model. No contact elements are used in this model.

5.4.3 Element types

According to the standardisation for finite element analysis described in Chapter 2, element SOLID45 is used for the steel bolt and tube, element SOLID65 with 9.7% of the smeared material for the joint concrete. CONTACT52 is selected as the contact element.

5.4.4 Material properties

According to the test report of Tampere University of Technology[60], the fundamental mechanical property parameters of the materials used in the modelling are those listed in Tables 5.1 and 5.2. The uniaxial stress-strain relationships of the steel bolt, steel tube and joint concrete, Figs. 5.10 to 5.12, are created by using the simplified mechanical models for both steel and concrete proposed in Chapters 3 and 4.

5.4.5 Solution

The models are loaded by applying displacement at the head of the bolt in increments of 0.0286 mm. This incremental value is identical to the value used in the previous models for the behaviour analyses of the concrete element, see Chapter 4.

5.4.6 Results and discussion

The load-displacement relationships from both the numerical analyses and physical tests for the head, middle and base sections of the bolt (as defined in Fig. 5.7) are shown in Figs. 5.13 to 5.15. The curve consists of a pseudo-elastic portion with a high initial stiffness and a transition to a region of plastic deformation and relatively low stiffness. The curves from the numerical analyses have a higher initial stiffness than the curves obtained from test specimens. However, the reaction forces at which the specimens yielded in the numerical analyses were lower than the test results. Additionally, the ultimate reaction forces in the numerical analyses were also less than the ultimate loads obtained in the tests. The differences between the results from the two approaches are small and considered acceptable for adoption of this technique in the analysis of larger and more intricate joints.

Comparison of the curves from models 1 and 2 shows that the introduction of the contact elements has reduced the stiffness of the model. The differences between the curves from model 1 and model 3 are small, although model 1 is slightly stiffer. Hence, coarsely meshed models can give acceptable results, provided the models are carefully designed and the dimensions of elements are not too large.

Fig. 5.16 shows the relationships of bending moment and rotation angle from both the numerical analyses and physical tests at the base section of the bolt. The same

conclusions can be obtained from this figure as those from the load-displacement relationships, but closer agreements are obtained.

From Figs. 5.17 to 5.19 it can be observed that the deformed shape of the bolt in the three models is similar. The use of contact elements, in model 2, results in a larger rotation angle and a gap around the first two elements along the base section of the bolt.

The relationships between principal stress and displacement at the head section of the bolt are illustrated for the three models in Figs. 5.20 to 5.22. During the loading process both the steel and concrete experienced a full elasto-plastic history. As the displacement at the head section of the bolt increased to about 0.5 mm the concrete element on top of the bolt base crushed, Fig. 5.21. Further increased displacement (about 1.8 mm) caused the steel elements around the bolt base to yield, Fig. 5.20, consequently the stiffness of the connection was reduced significantly, Figs. 5.13 to 5.15. From Fig. 5.21 it is also observed that the compressive strength of concrete in the three dimensional stress situations increased to 39.78 N/mm^2 and 40.58 N/mm^2 in model 1 and model 3 respectively. The input uniaxial compressive strength of concrete was 28.24 N/mm^2. In the case without contact elements between the steel and concrete in the tensile zone, higher tensile stresses appeared between the two materials, Fig. 5.22.

Some typical stress distributions of the three models are presented in Figs. 5.23 to 5.29. In the loading direction, i.e. the *y* axis, the highest compressive stresses are initially located in concrete surrounding the top surface of the bolt base, Figs. 5.23 and 5.24. When the added displacement at the head section of the bolt is large enough, the elements with the highest compressive stresses crush, and the highest stresses redistribute to the adjacent elements, see Fig. 5.25. Meanwhile the tube in the loading direction bears the highest tensile stresses to balance the compressive stresses in the concrete (Figs. 5.23 to 5.25).

In the longitudinal direction of the bolt, i.e. the *z* axis, both the maximum tensile and compressive stresses are located around the base of the bolt (Figs. 5.26 to 5.28). In the case including contact elements between the bolt and concrete, the location of maximum tensile stress moves into the joint and the concrete beneath is not subjected to tensile stresses Fig. 5.27).

In the x axis direction the maximum tensile stress occurs at the end of the tube over the base of the bolt. The numerical analyses indicated that this was the last component of the connection to yield, see Fig. 5.29.

5.4.7 Conclusions

As the results from numerical analyses show good agreement with those from physical tests, it is can be concluded that the models have been successfully constructed. Coarsely meshed models can give acceptable results if the models are carefully designed. However, it is necessary to use contact elements to model the interface between steel and concrete. The simplified mechanical models for both steel and concrete proposed in Chapters 3 and 4 have been successfully applied. These successful applications and calibrations corroborate the standardisation of the FEA techniques for reinforced concrete structures.

Results of the numerical analyses show that failure of the connection is initiated by crushing of concrete on the top surface of the bolt near the base section. Further increased load causes yielding of the steel bolt and full plasticity of the connection to be developed. During the latter stages of loading, the edge of the steel tube over the base of the bolt yields also.

	f_y (N/mm^2)	f_u (N/mm^2)	E_s (kN/mm^2)	ν
Steel bolt	350.00	548.00	207.00	0.30
Steel tube	275.00	467.00	205.00	0.30

Note: f_y is the characteristic yield strength

f_u the ultimate strength

E_s the Young's modulus and

ν the Poisson's ratio.

Table 5.1 *Parameters of mechanical properties for steel in the modelling of the bolt in joint concrete*

	$f_{c,\ cylinder}$ (N/mm^2)	f_t (N/mm^2)	E_c (kN/mm^2)	ν
Joint concrete	30.00	3.00	26.35	0.20

Note: $f_{c,\ cylinder}$ is the characteristic cylinder strength

f_t the tensile strength

E_c the modulus of elasticity and

ν the Poisson's ratio.

Table 5.2 *Parameters of mechanical properties for concrete in the modelling of the bolt in joint concrete*

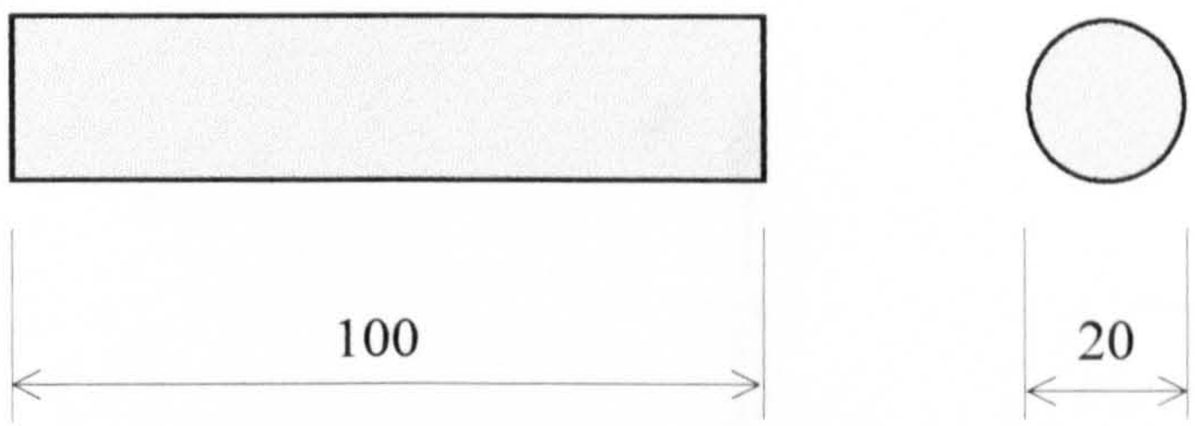

Figure 5.1 *Dimension of the bar*

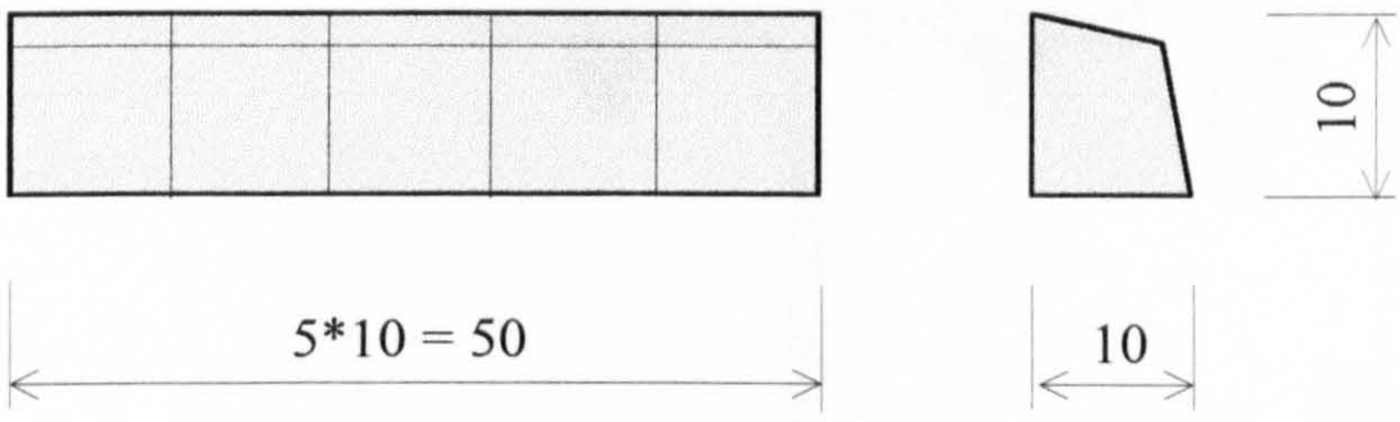

Figure 5.2 *Element mesh of the bar*

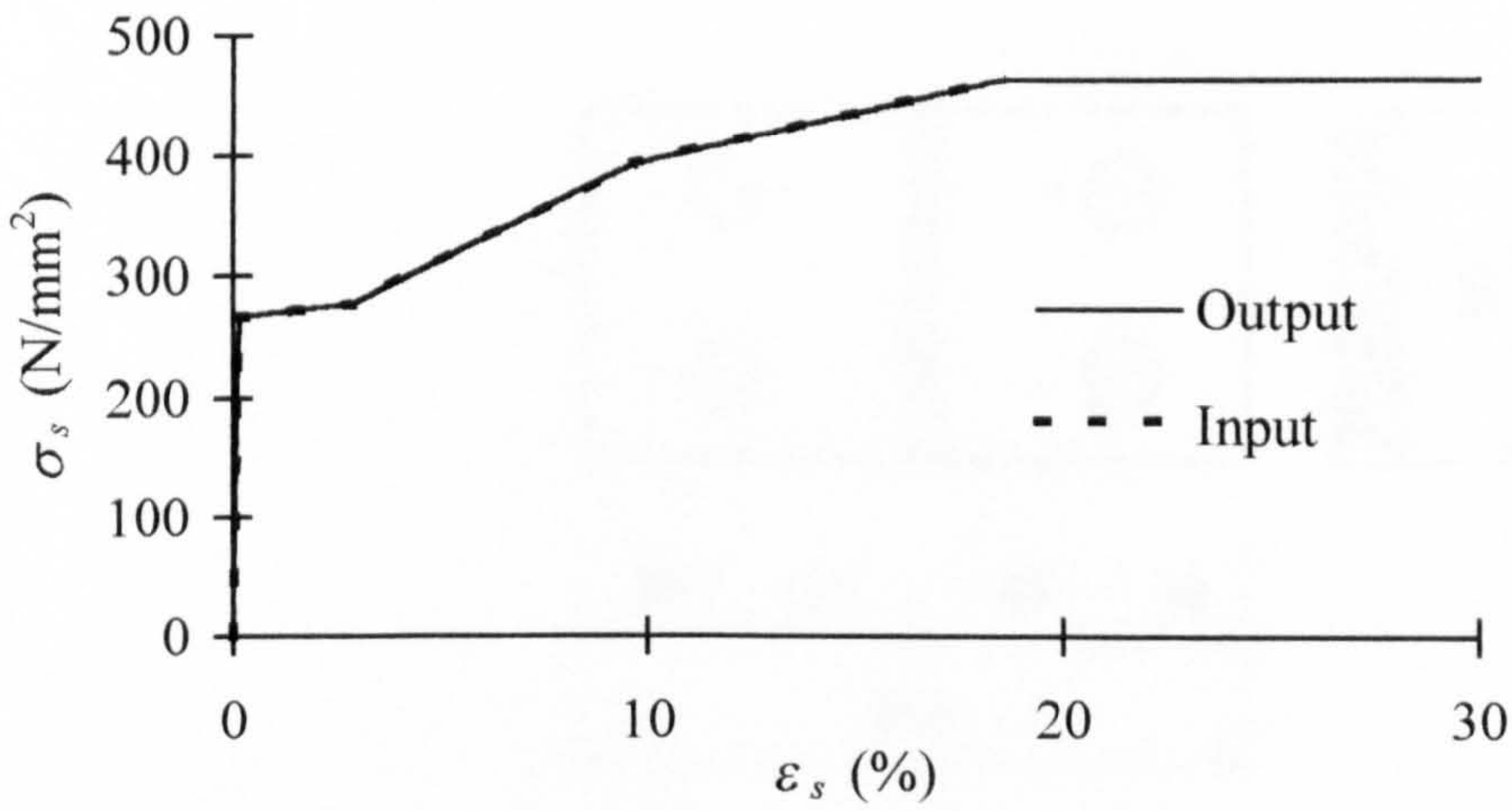

Figure 5.3 *Input and output σ-ε curves of the bar steel in tension*

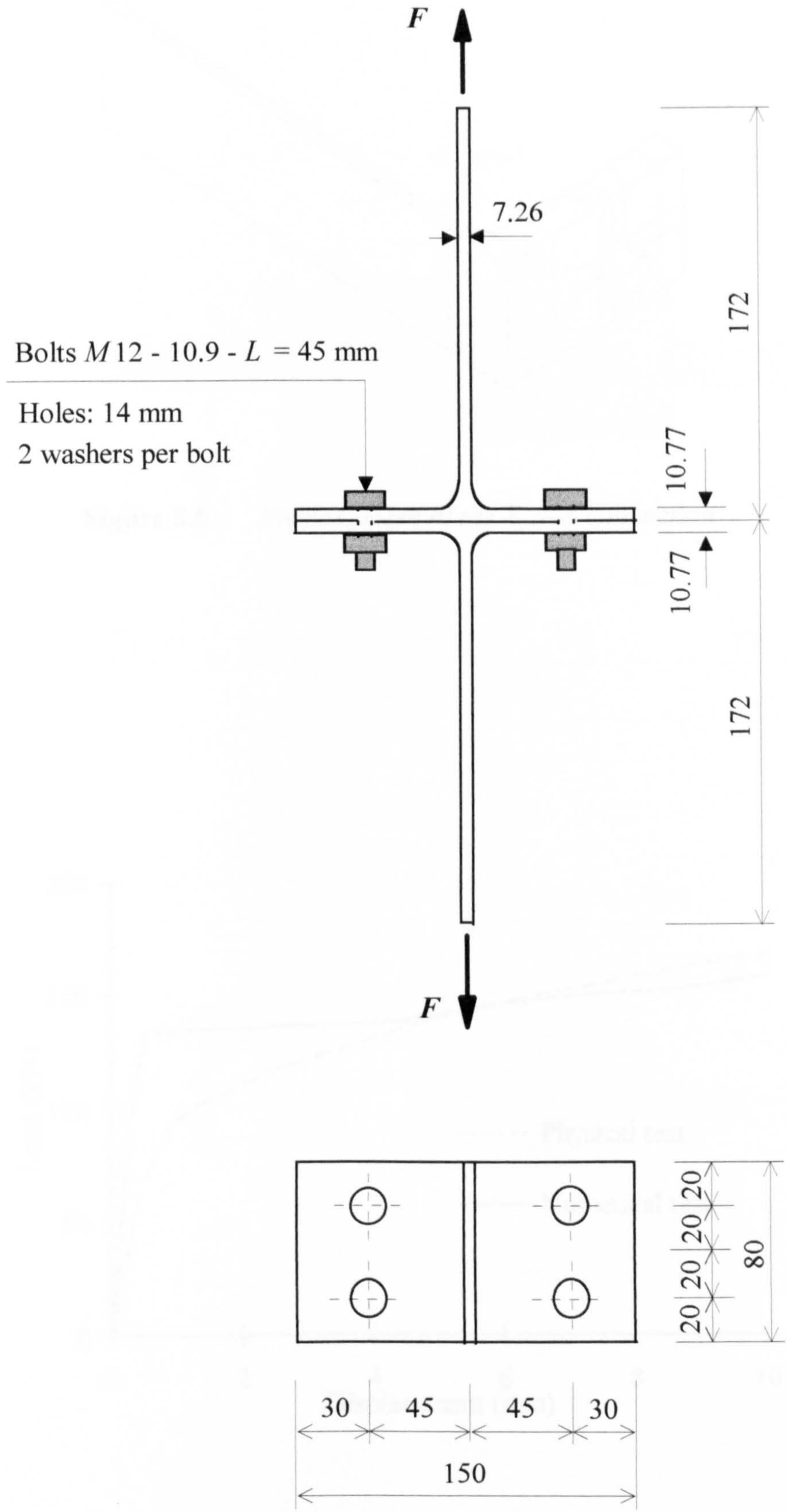

Figure 5.4 *The T-stub dimensions and test arrangements*

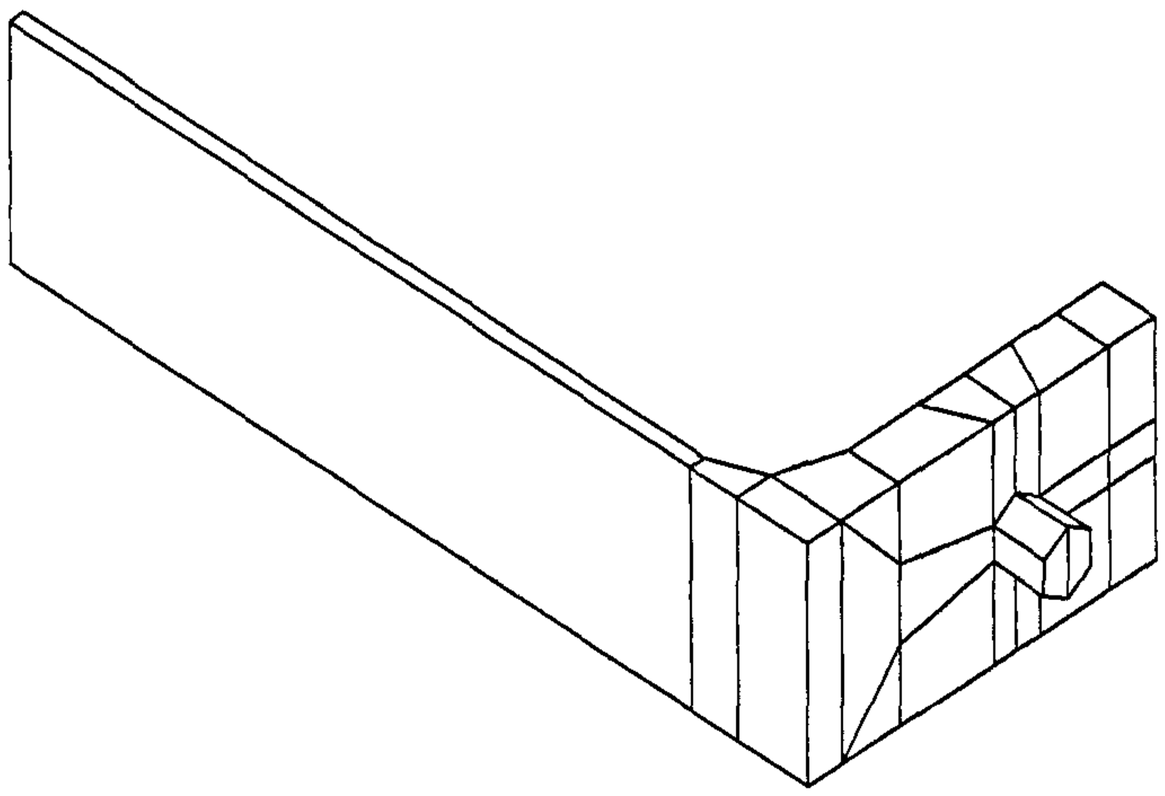

Figure 5.5 *Element mesh of the T-stub connection*

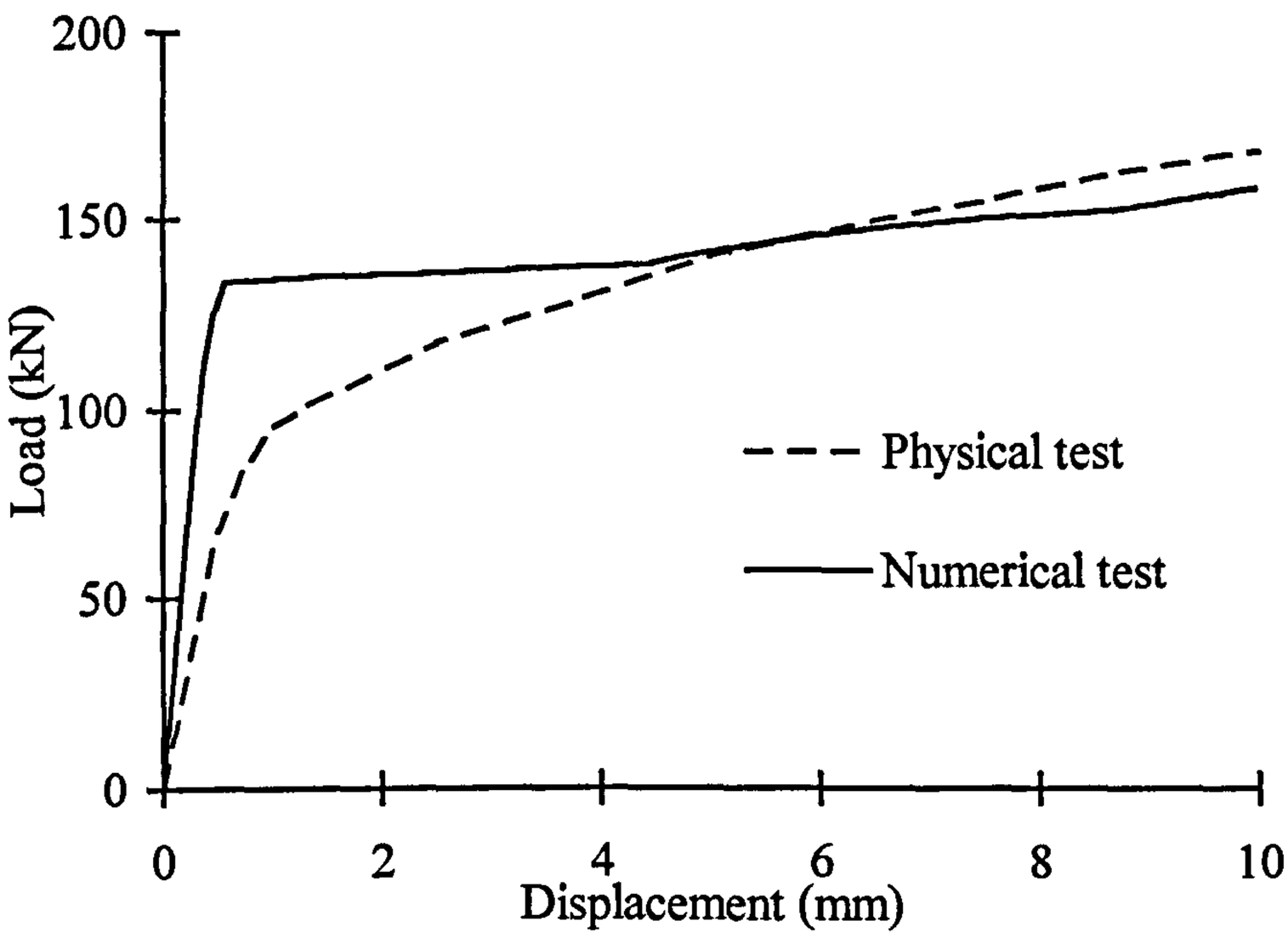

Figure 5.6 *Load-displacement curves of the T-stub connection*

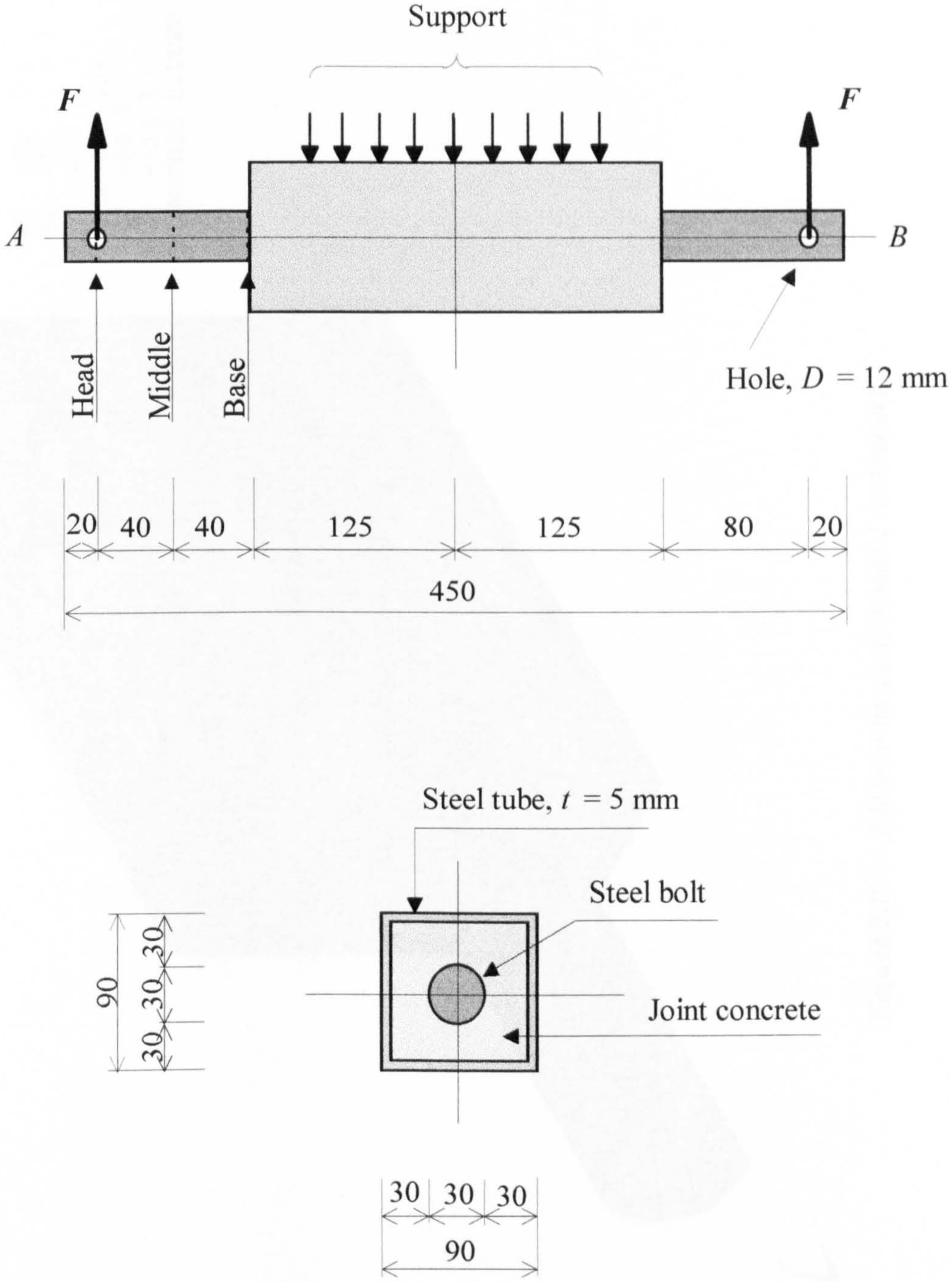

Figure 5.7 *Dimensions of the bolt in joint concrete and the test arrangements*

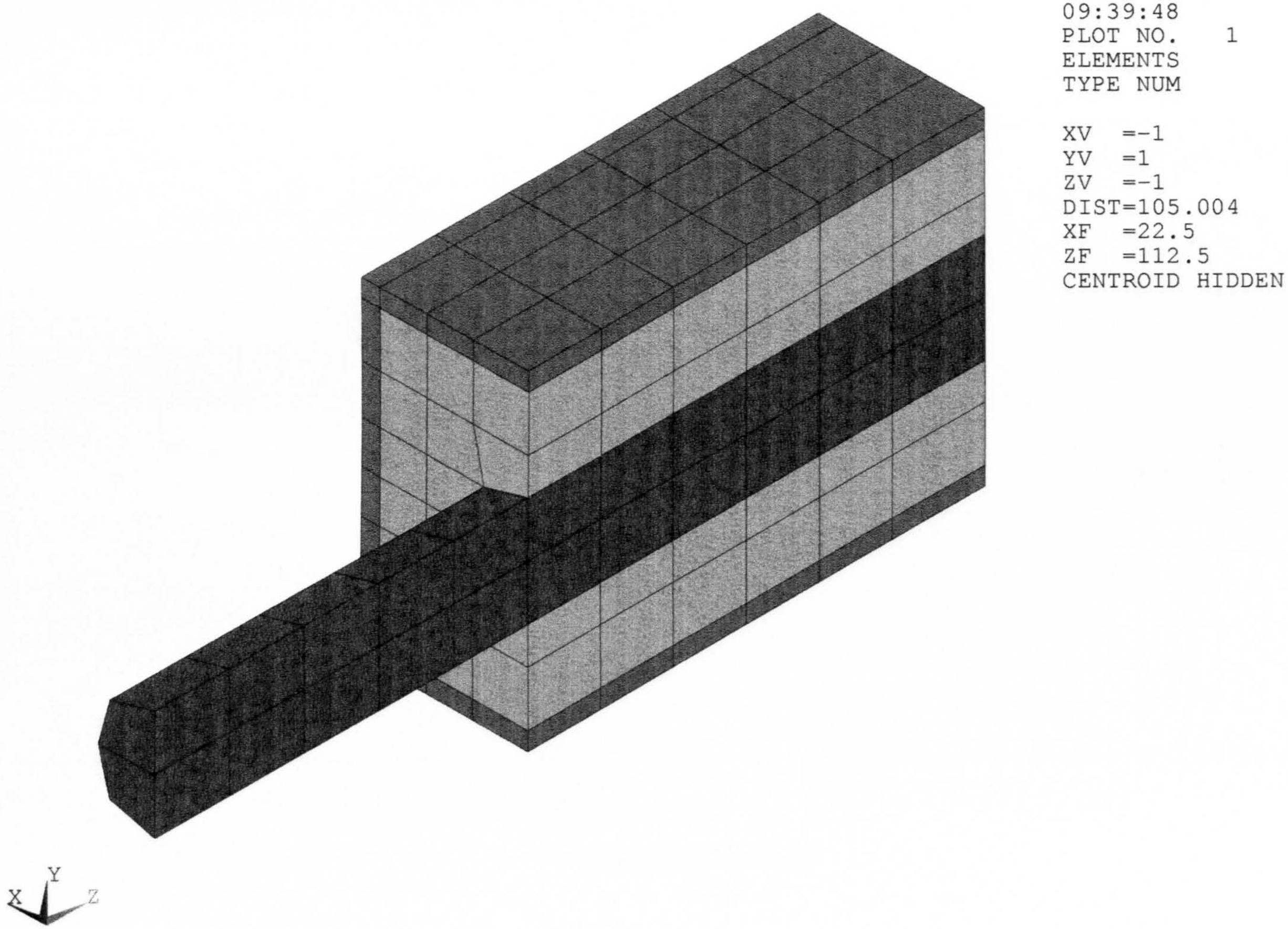

Figure 5.8 *Element mesh of model 1 and model 2*

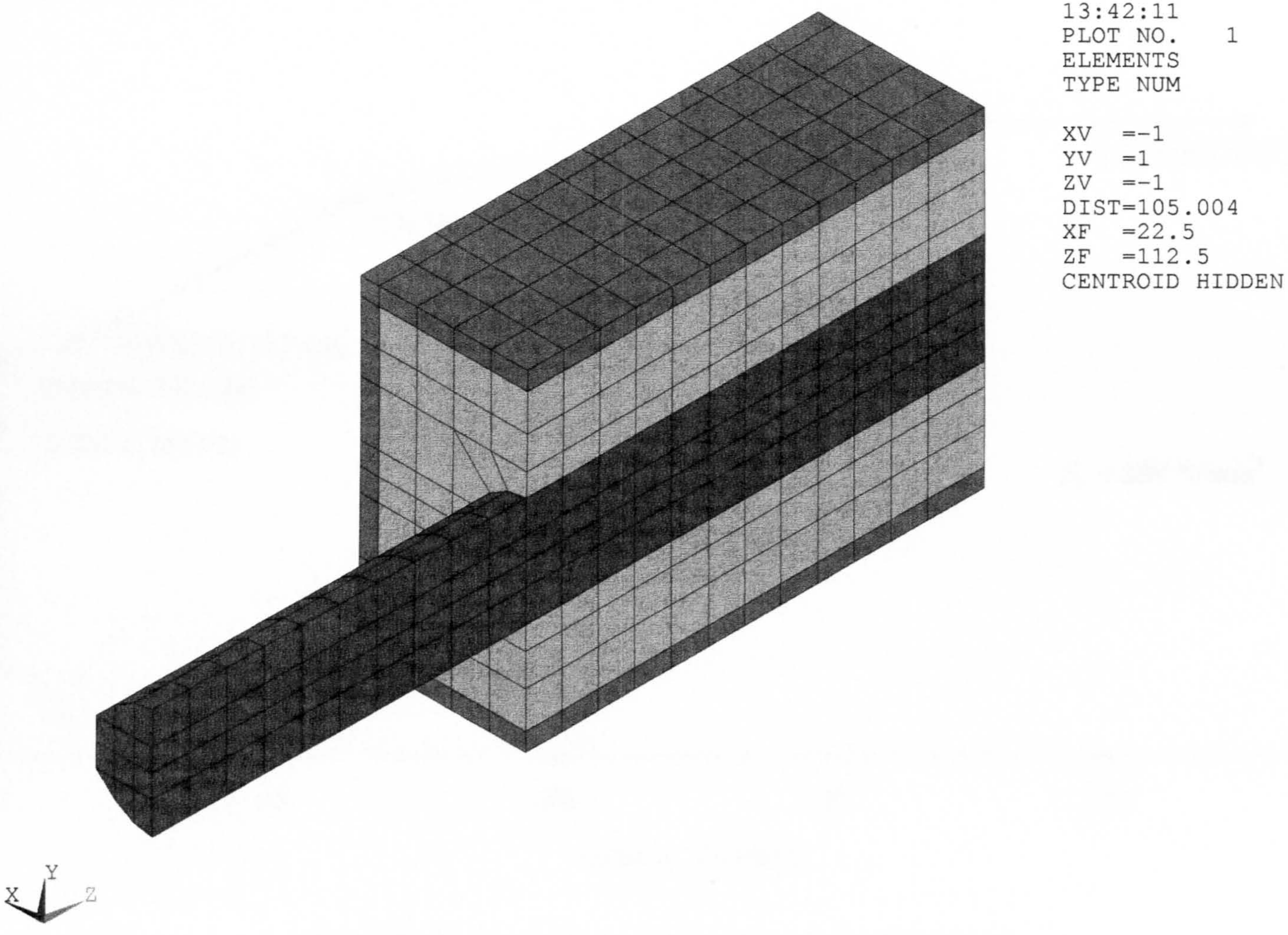

Figure 5.9 *Element mesh of model 3*

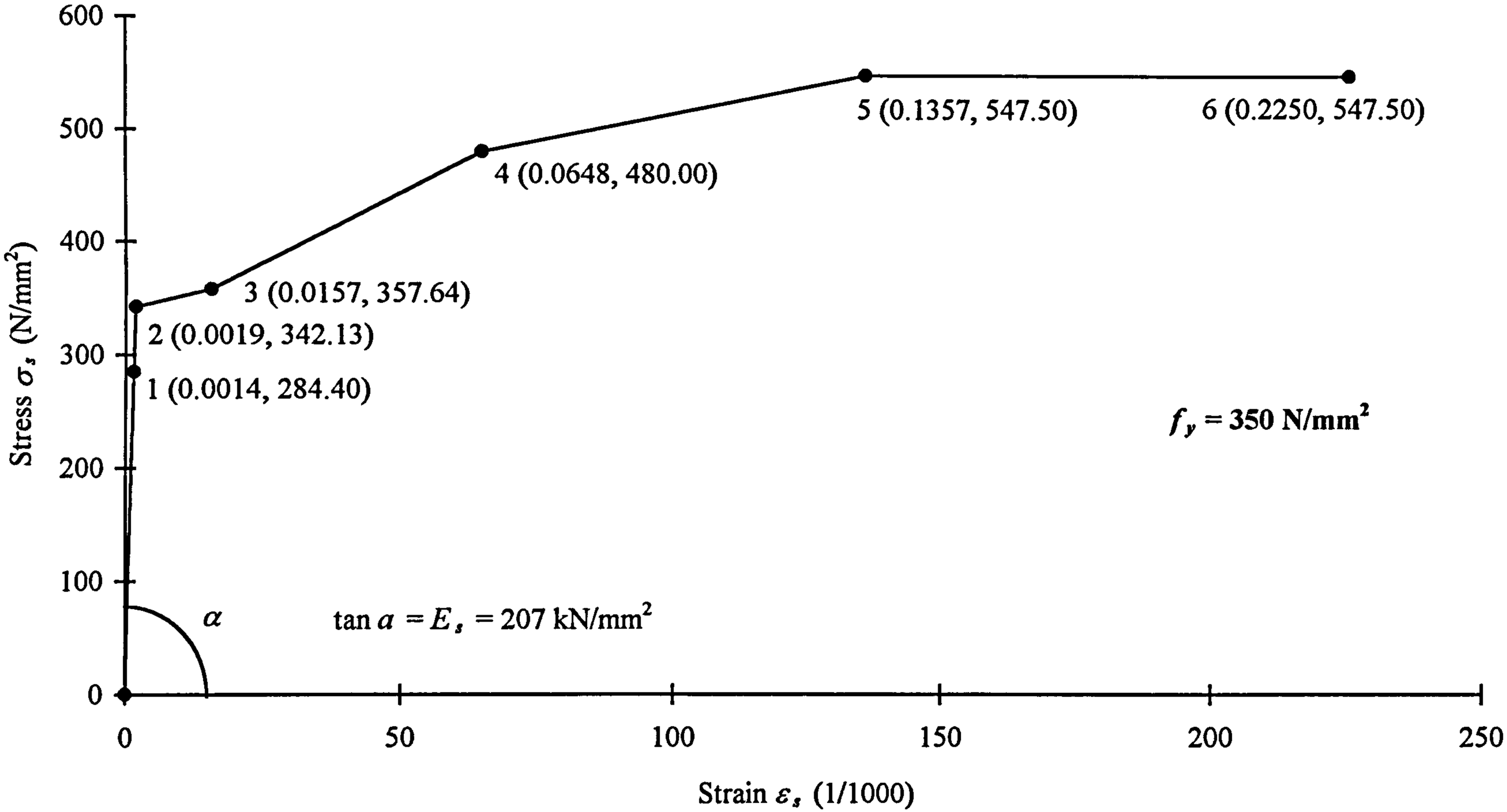

Figure 5.10 *Stress-strain relationship of steel for the bolt*

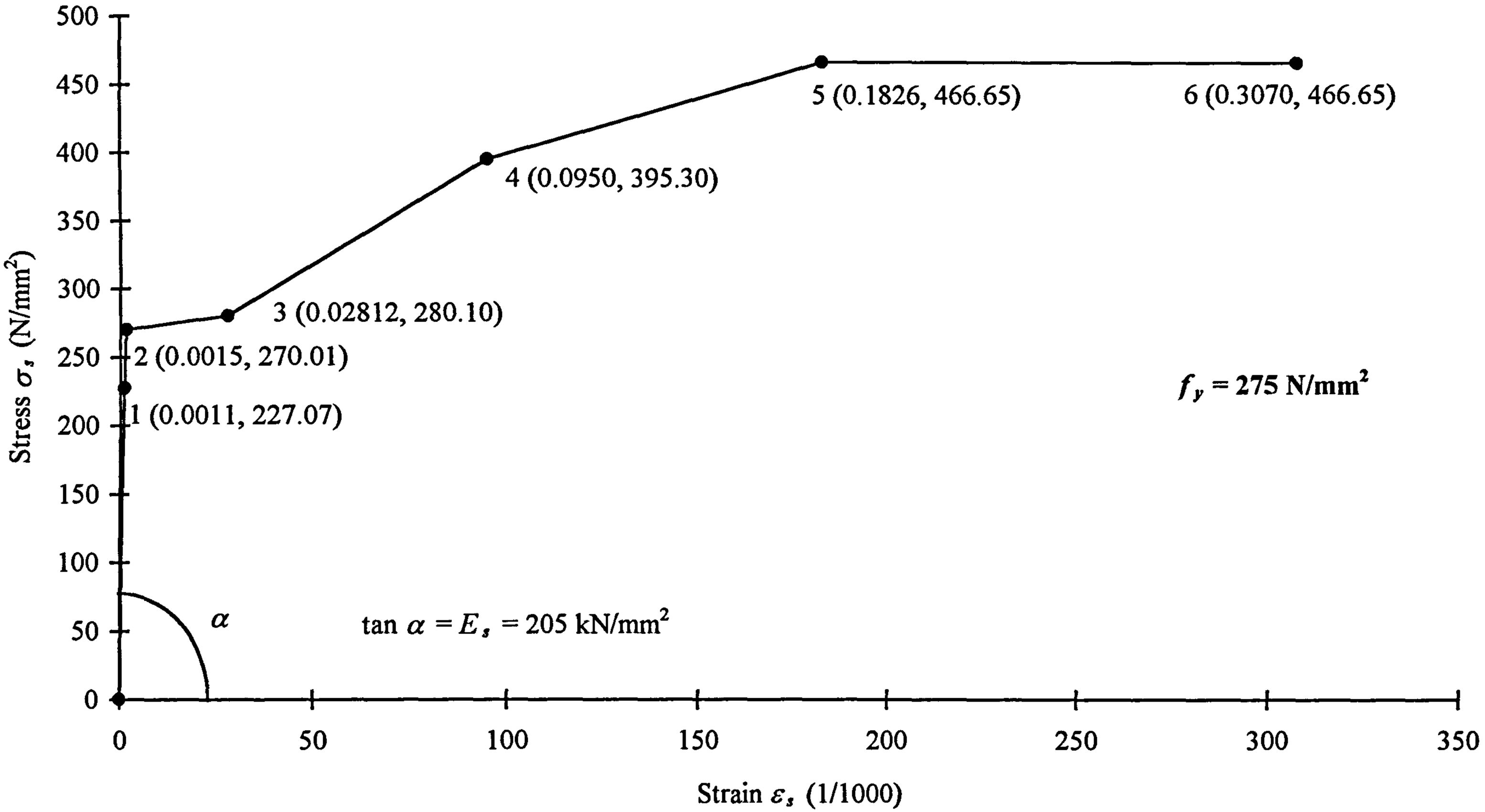

Figure 5.11 *Stress-strain relationship of steel for the tube*

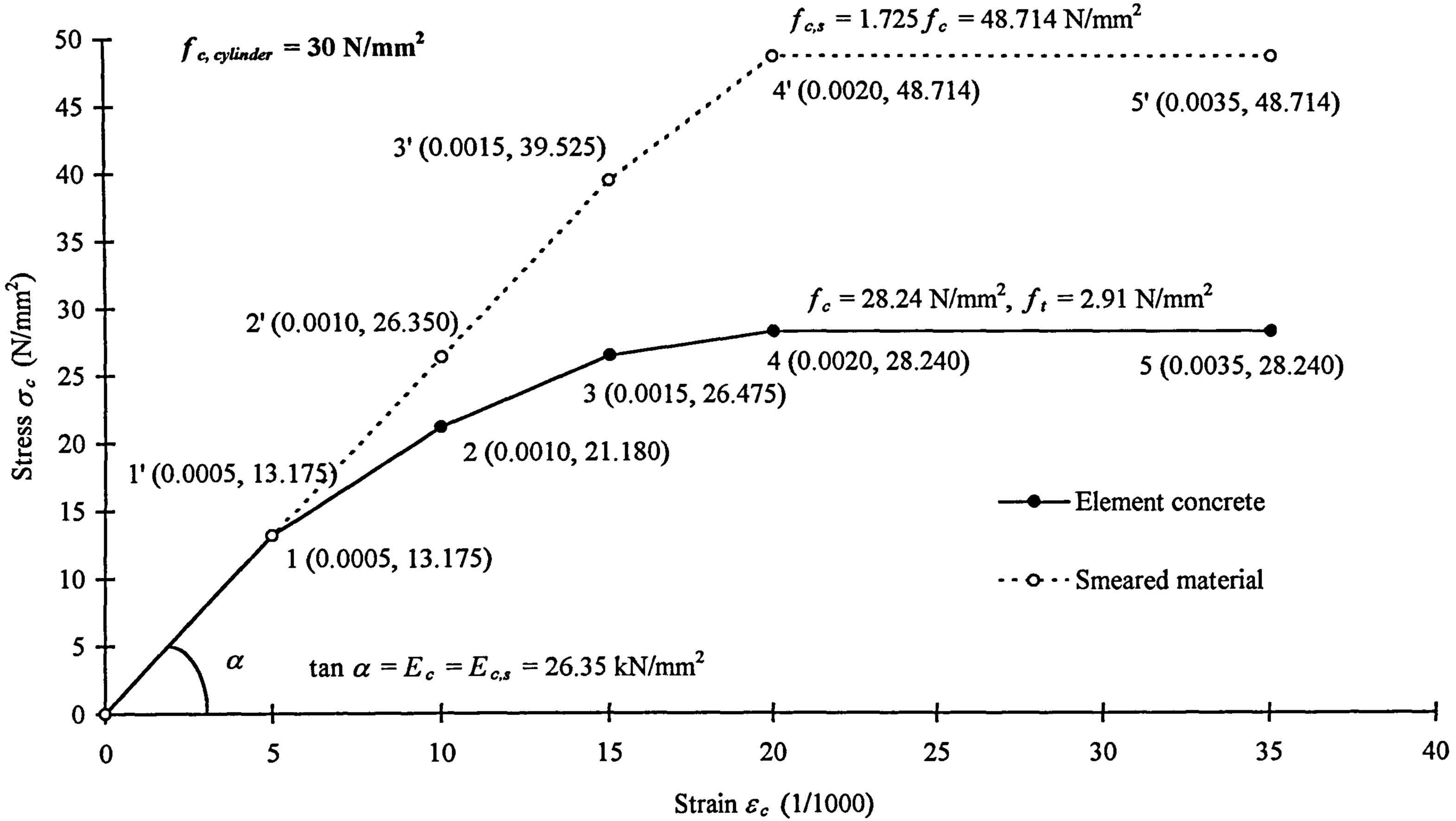

Figure 5.12 *Stress-strain relationship for the joint concrete*

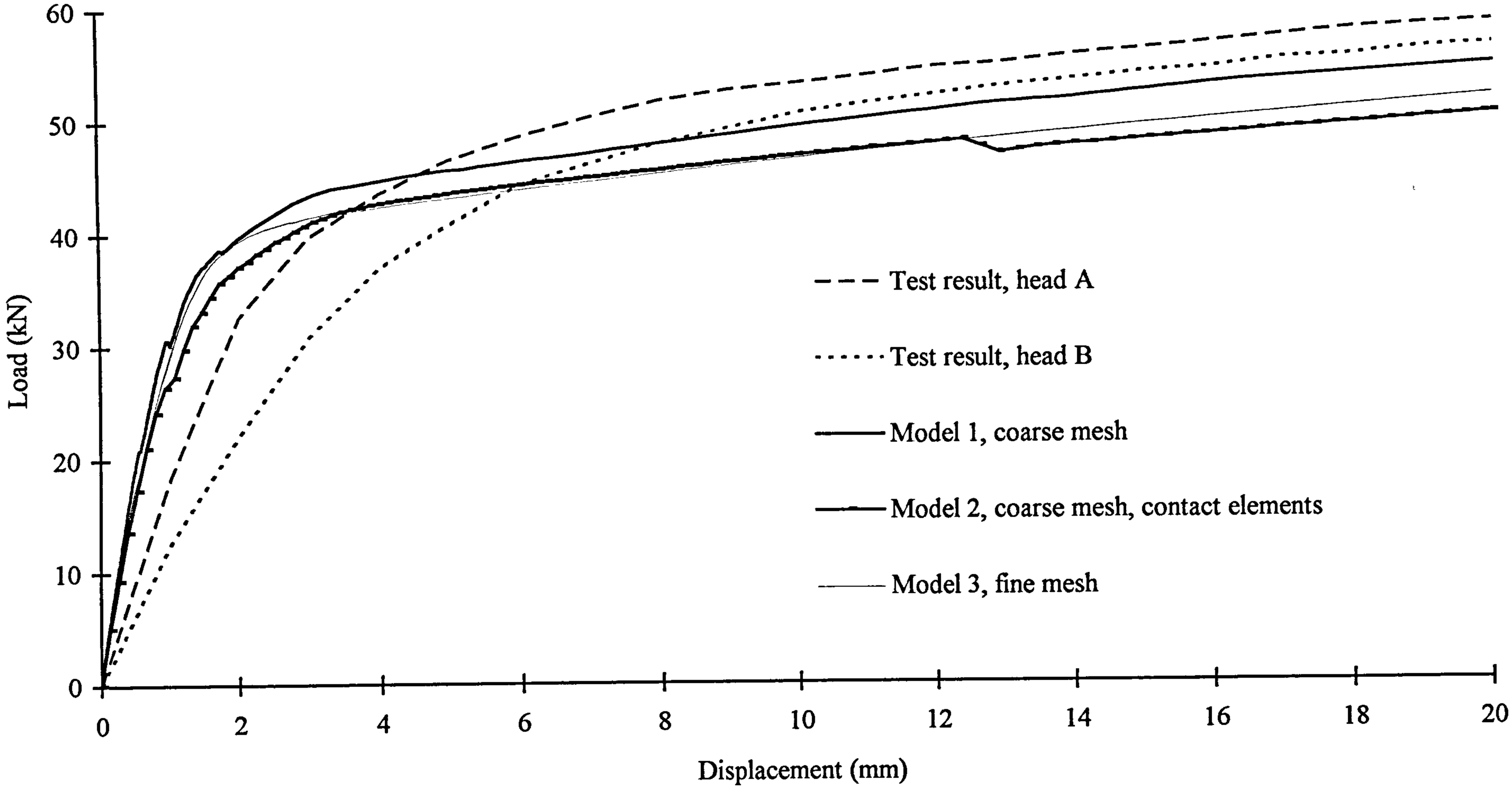

Figure 5.13 *Relationships of load-displacement at the head of the bolt*

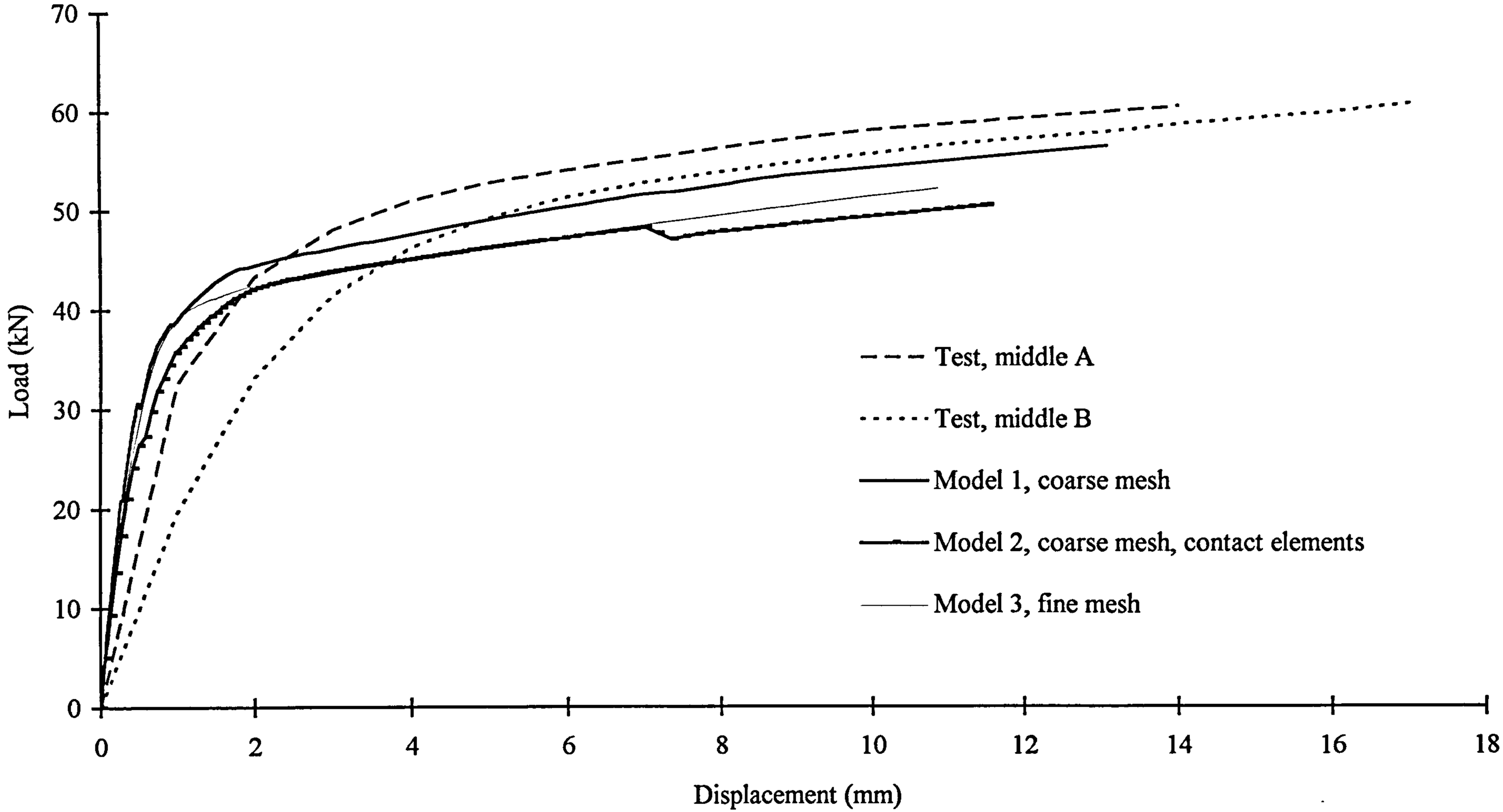

Figure 5.14 *Relationships of load-displacement at the middle of the bolt*

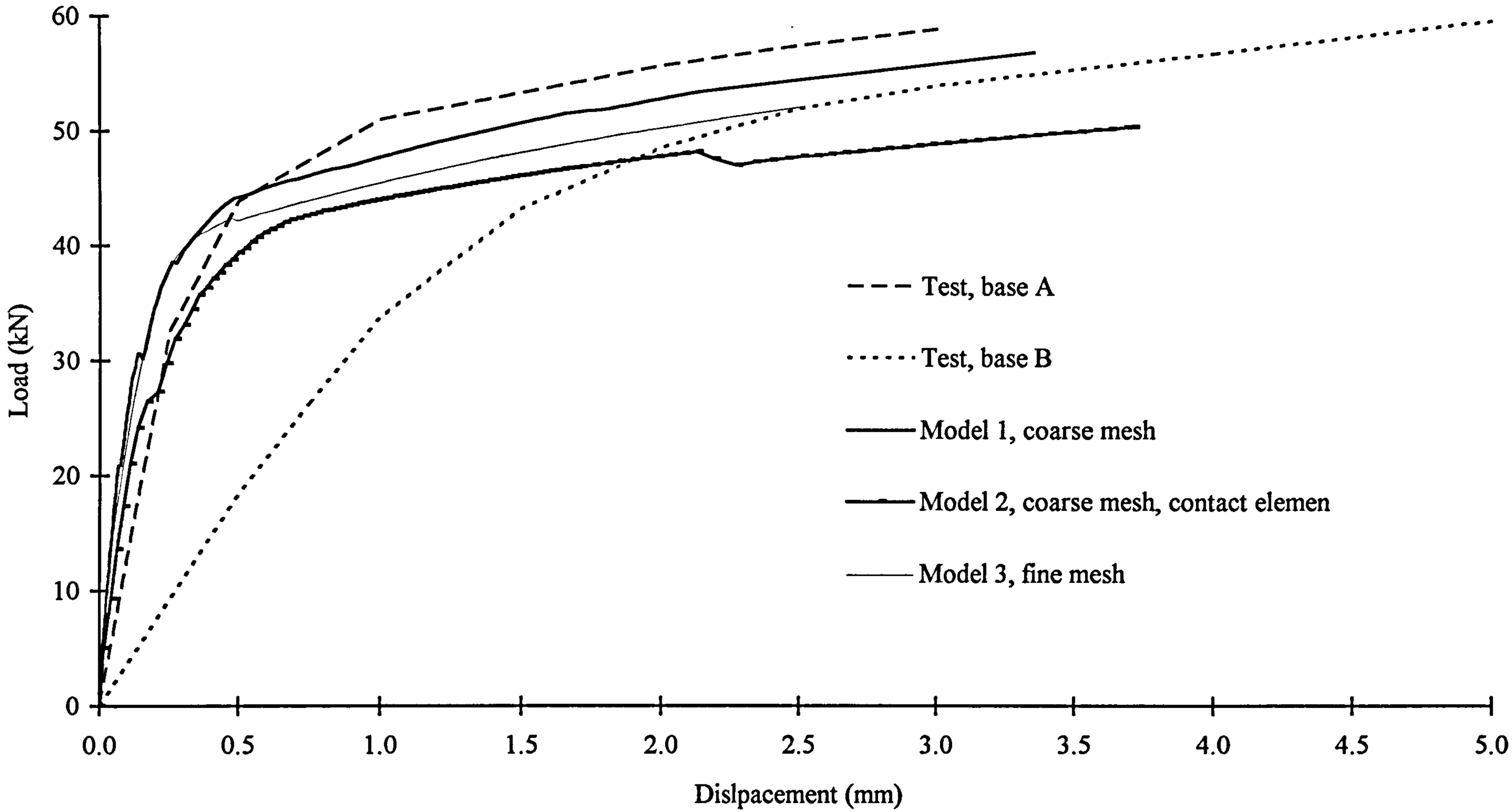

Figure 5.15 *Relationships of load-displacement at the base of the bolt*

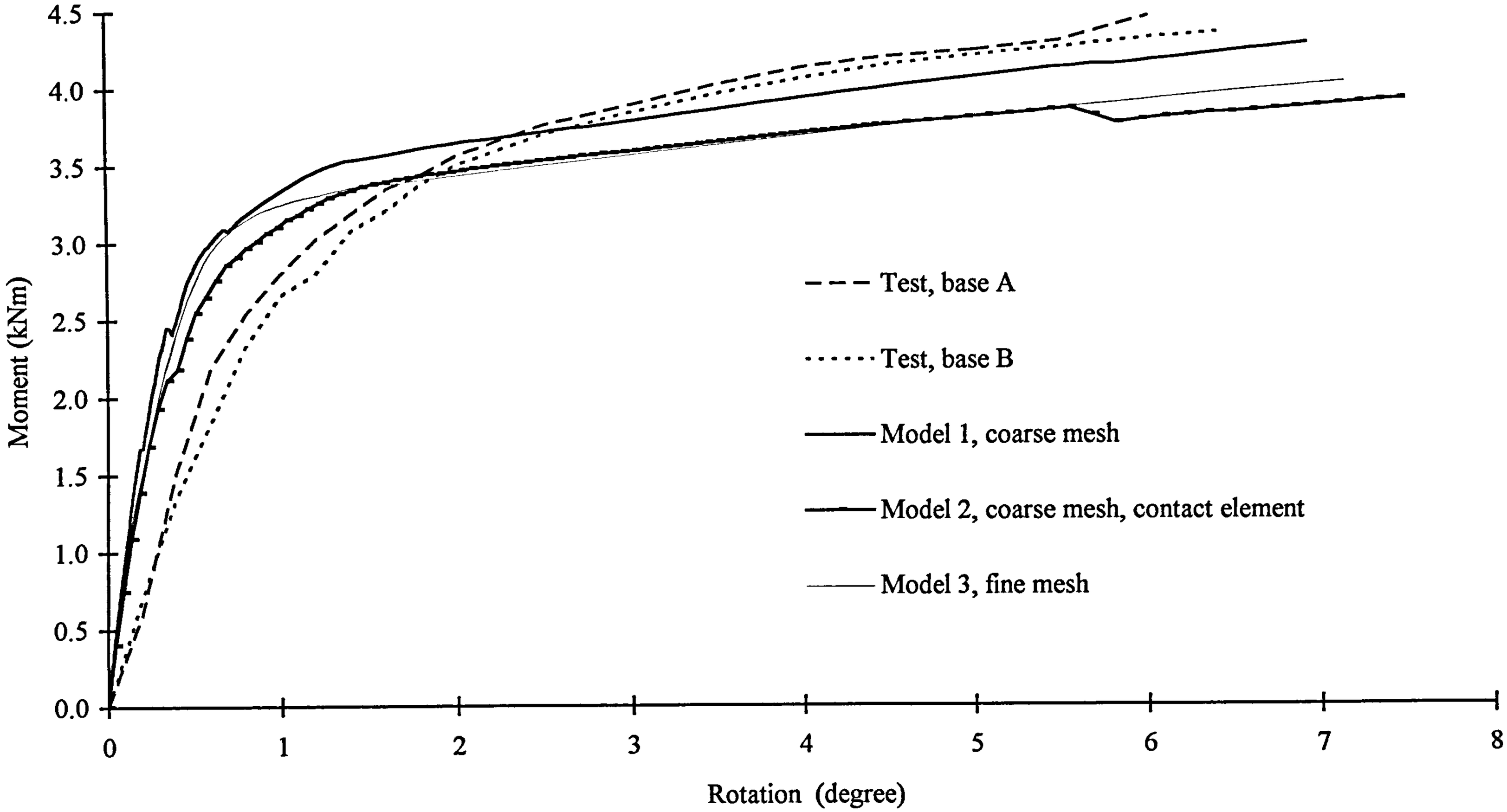

Figure 5.16 *Relationships of moment-rotation at the base of the bolt*

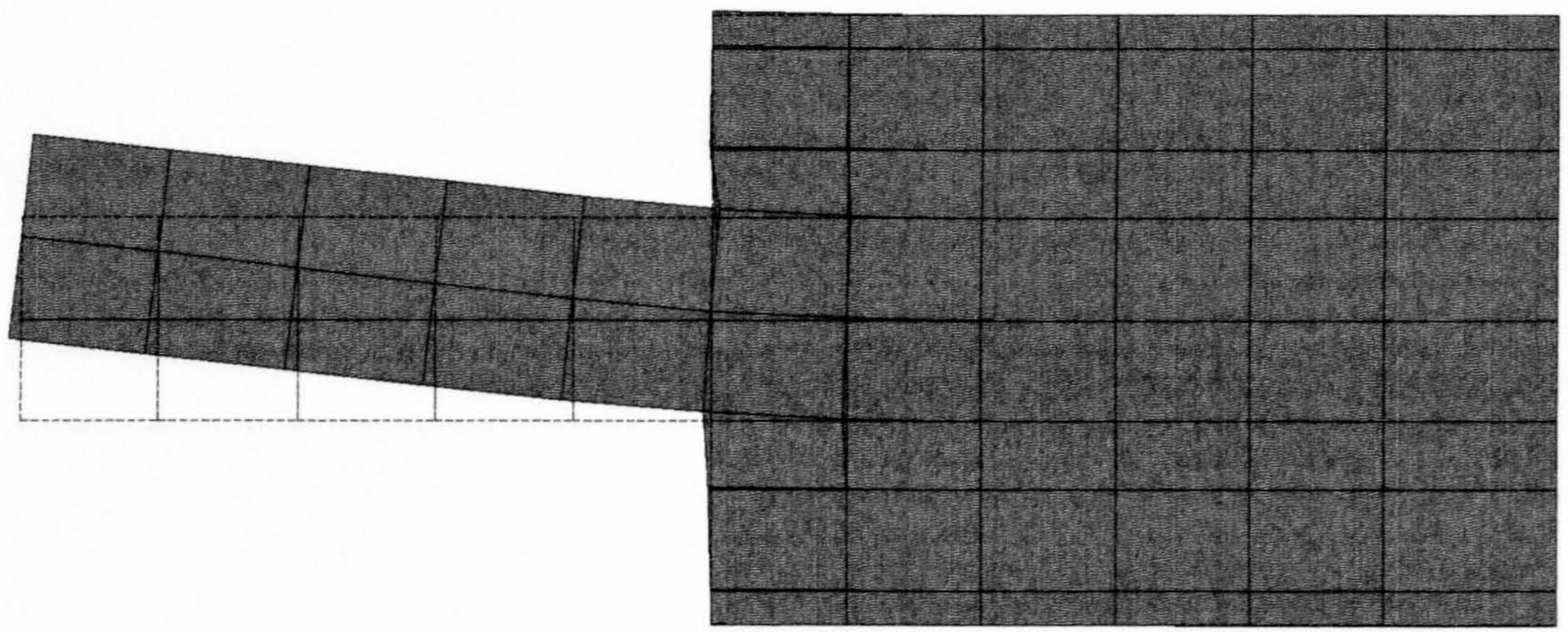

Figure 5.17 *Original position and deformed shape of model 1*

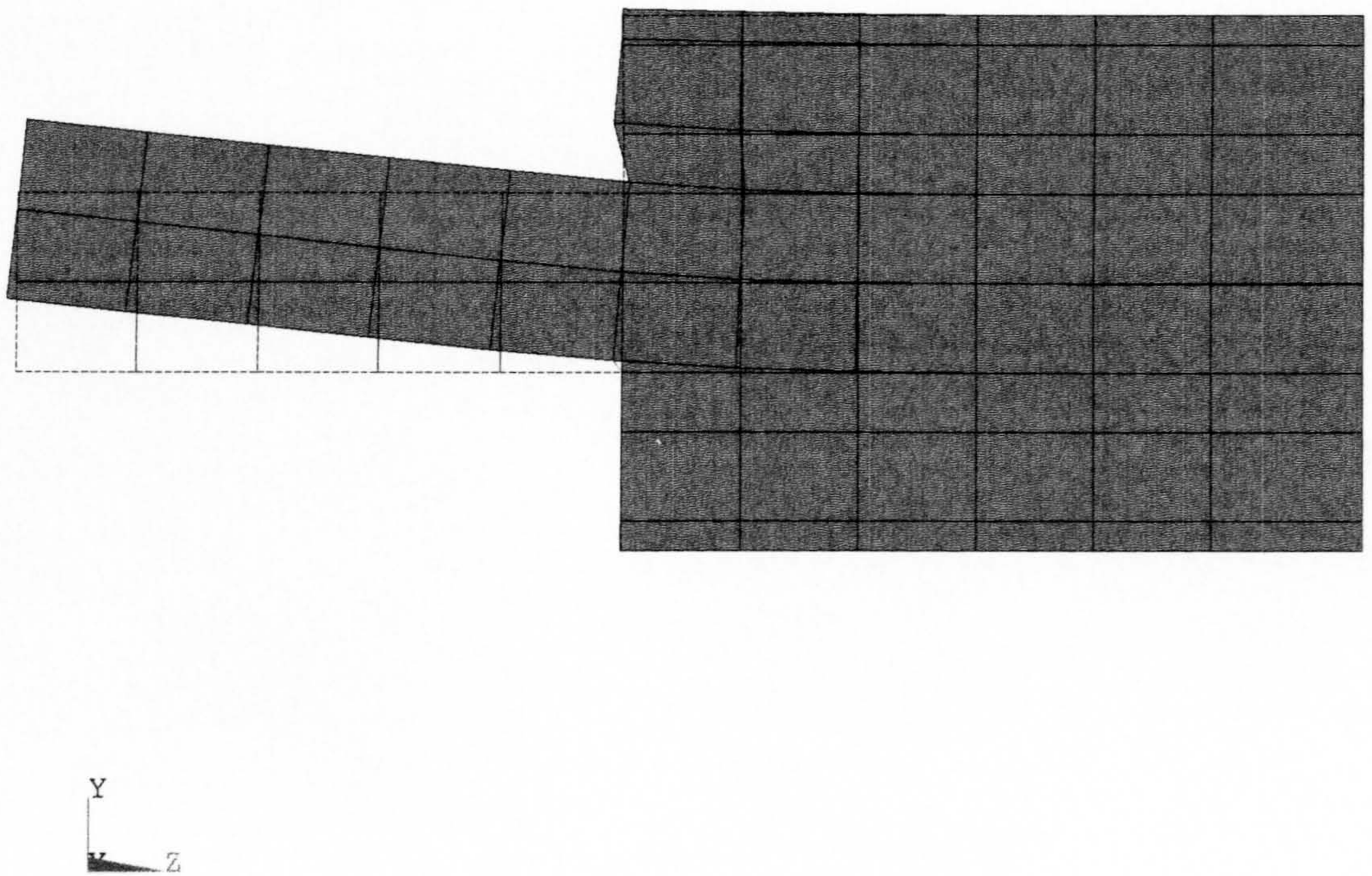

Figure 5.18 *Original position and deformed shape of model 2*

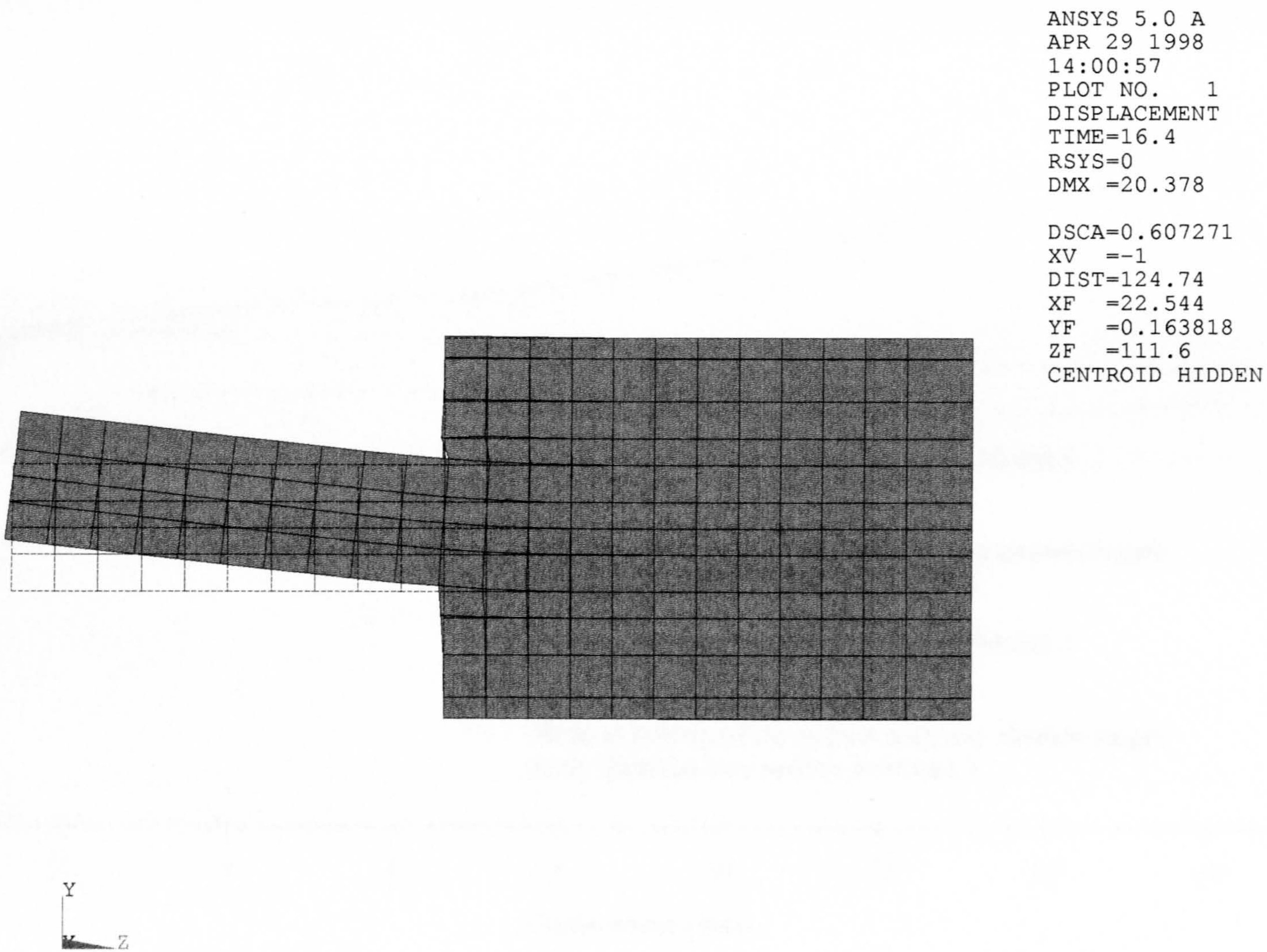

Figure 5.19 *Original position and deformed shape of model 3*

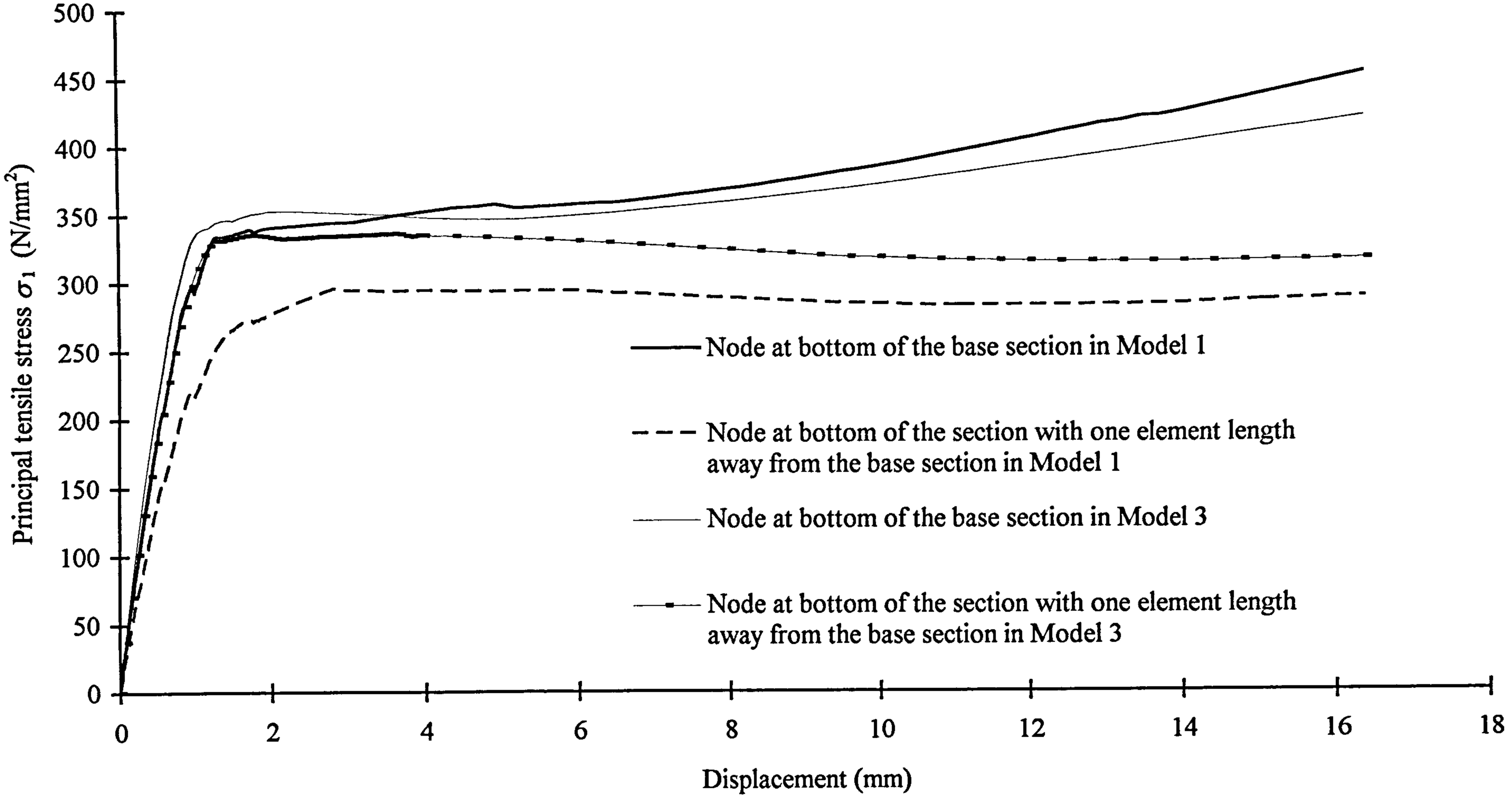

Figure 5.20 *Relationships of principal tensile stress versus displacement at the bolt head*

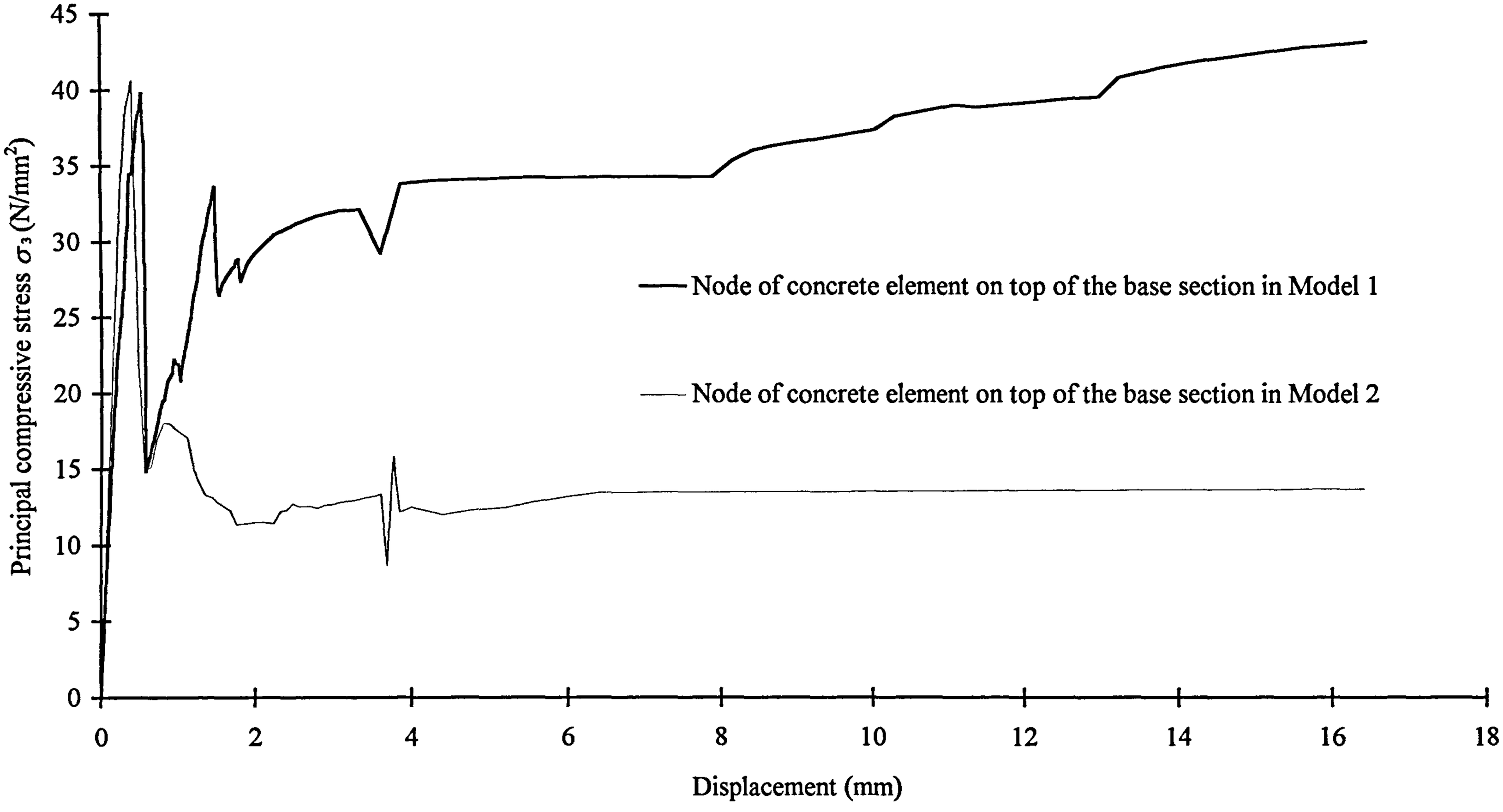

Figure 5.21 *Relationships of principle compressive stress of concrete versus displacement at the bolt head*

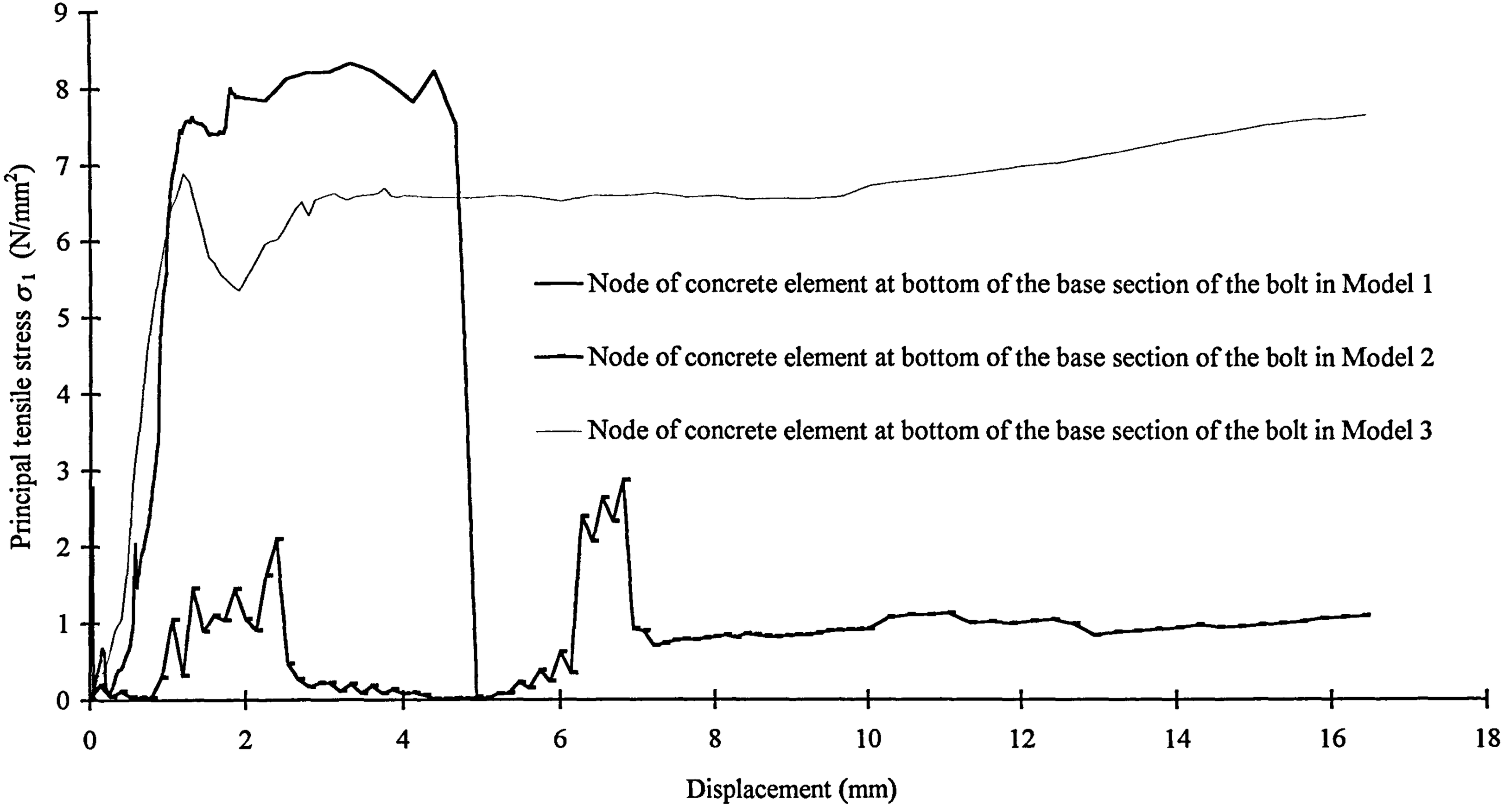

Figure 5.22 *Relationships of principal tensile stress of concrete versus displacement at the bolt head*

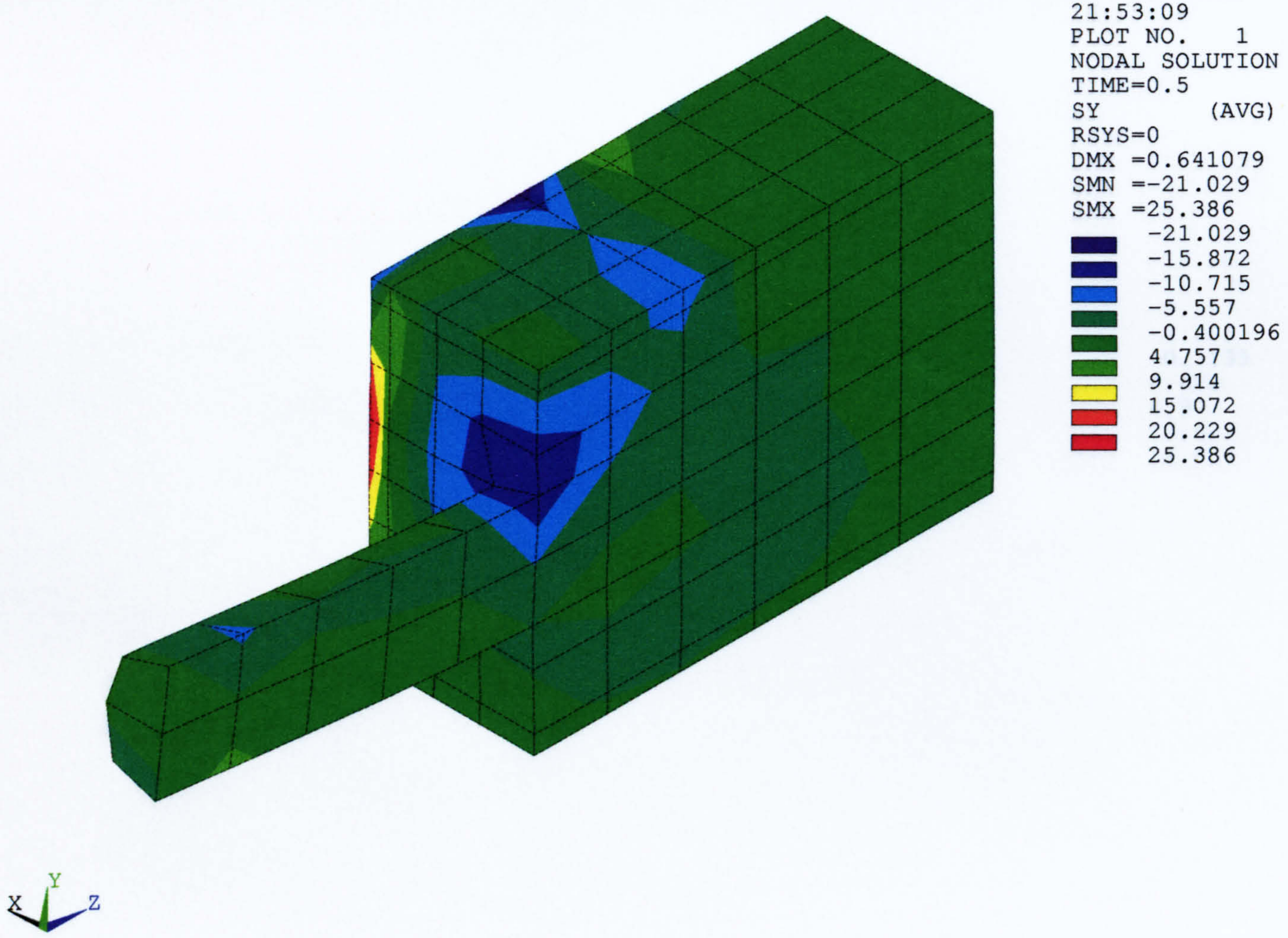

Figure 5.23 *Distribution of the vertical stress σ_y for model 1 with a 0.5mm displacement at the bolt head*

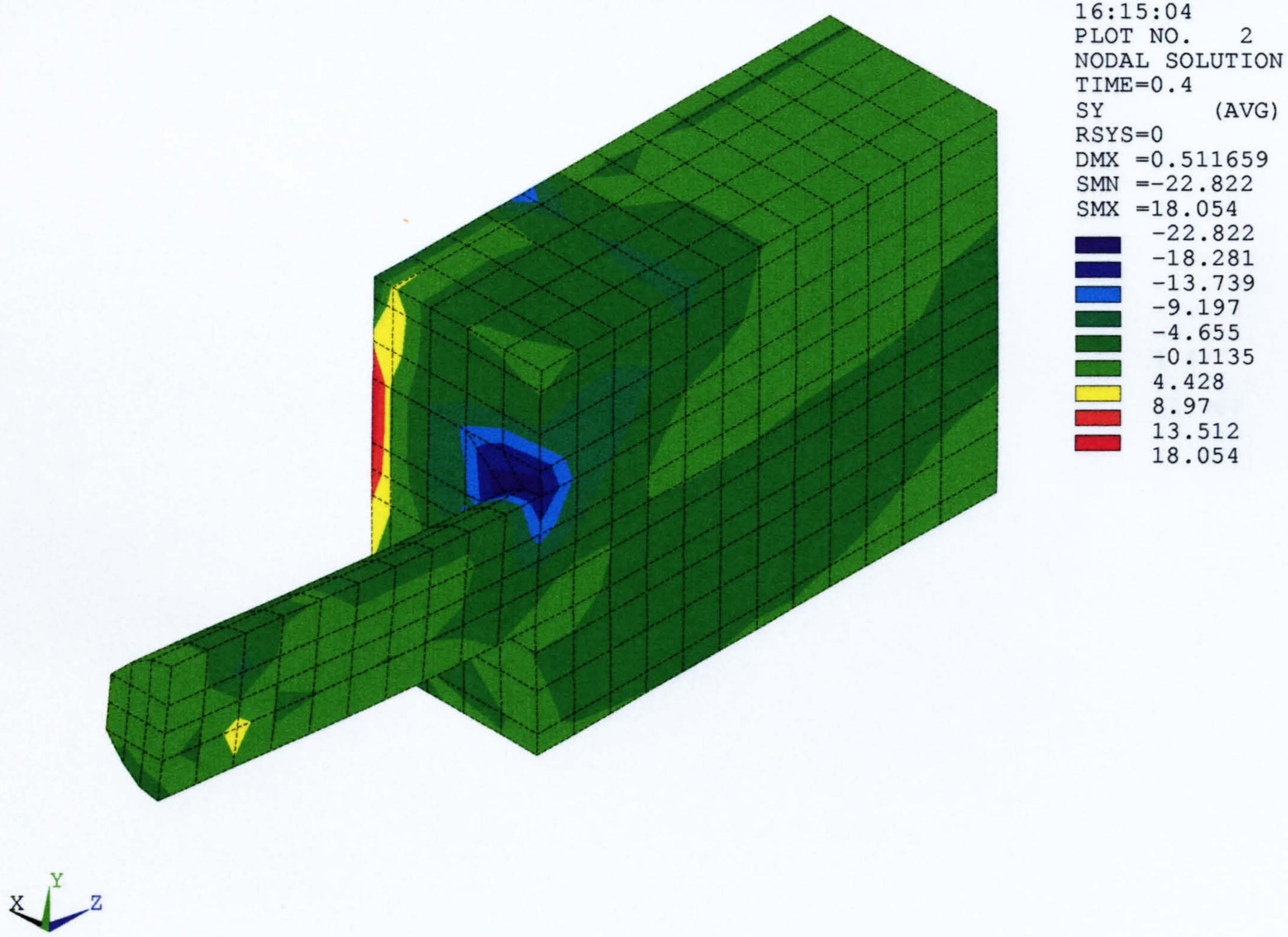

Figure 5.24 *Distribution of the vertical stress σ_y for model 3 with a 0.4mm displacement at the bolt head*

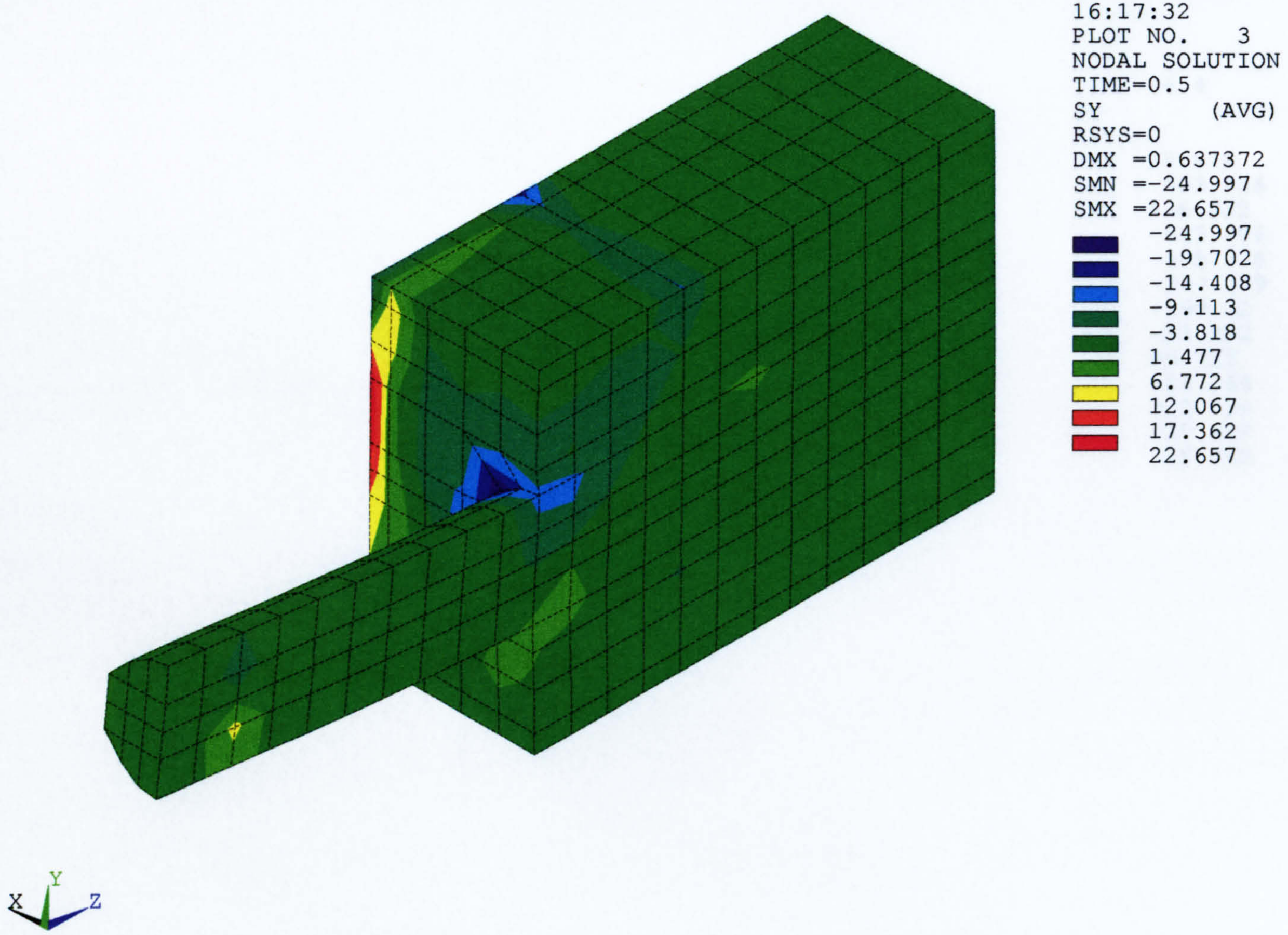

Figure 5.25 *Distribution of the vertical stress σ_y for model 3 with a 0.5mm displacement at the bolt head*

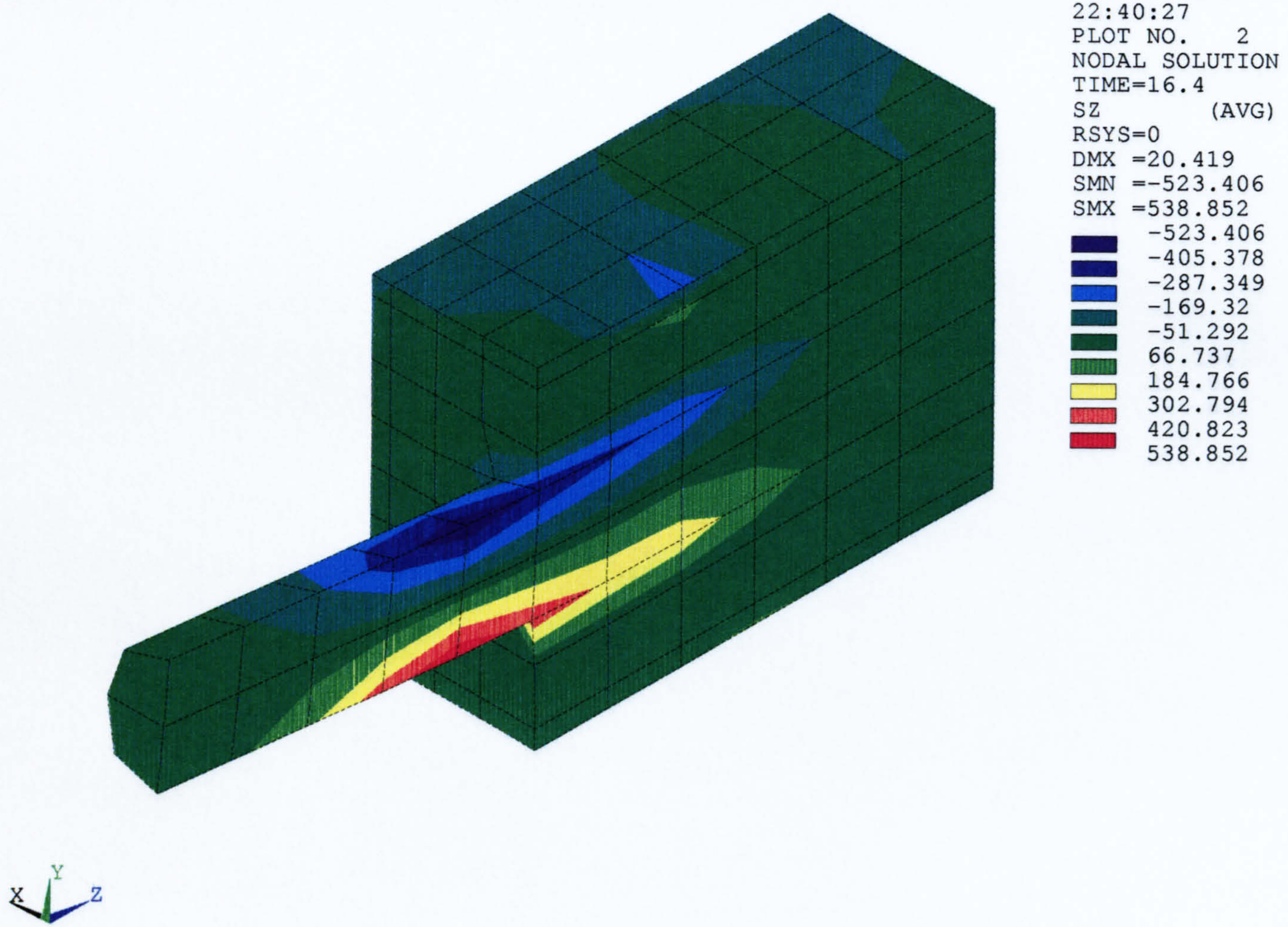

Figure 5.26 *Distribution of the bolt axis stress σ_z for model 1 with a 16.4mm displacement at the bolt head*

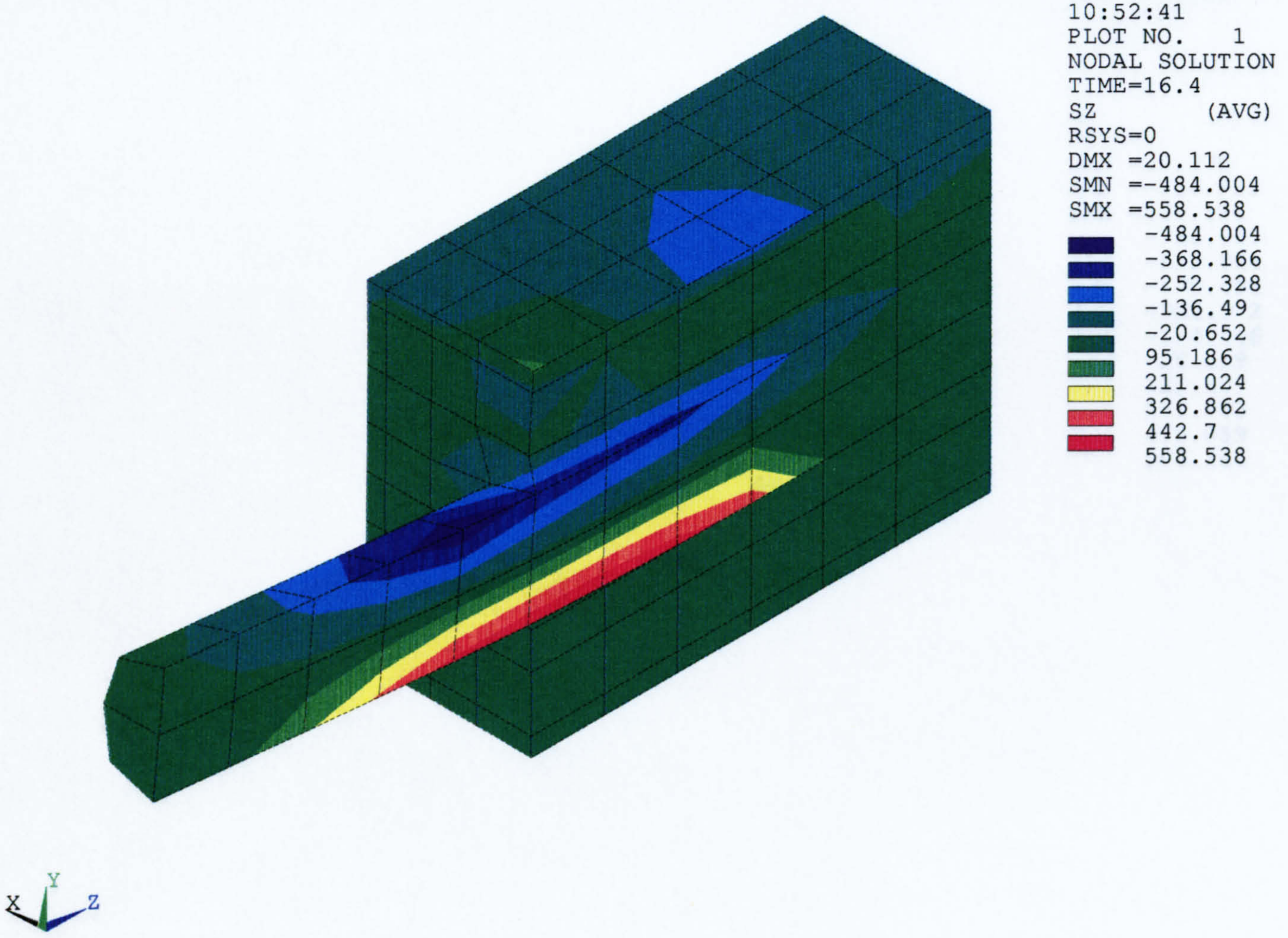

Figure 5.27 *Distribution of the bolt axis stress σ_z for model 2 with a 16.4mm displacement at the bolt head*

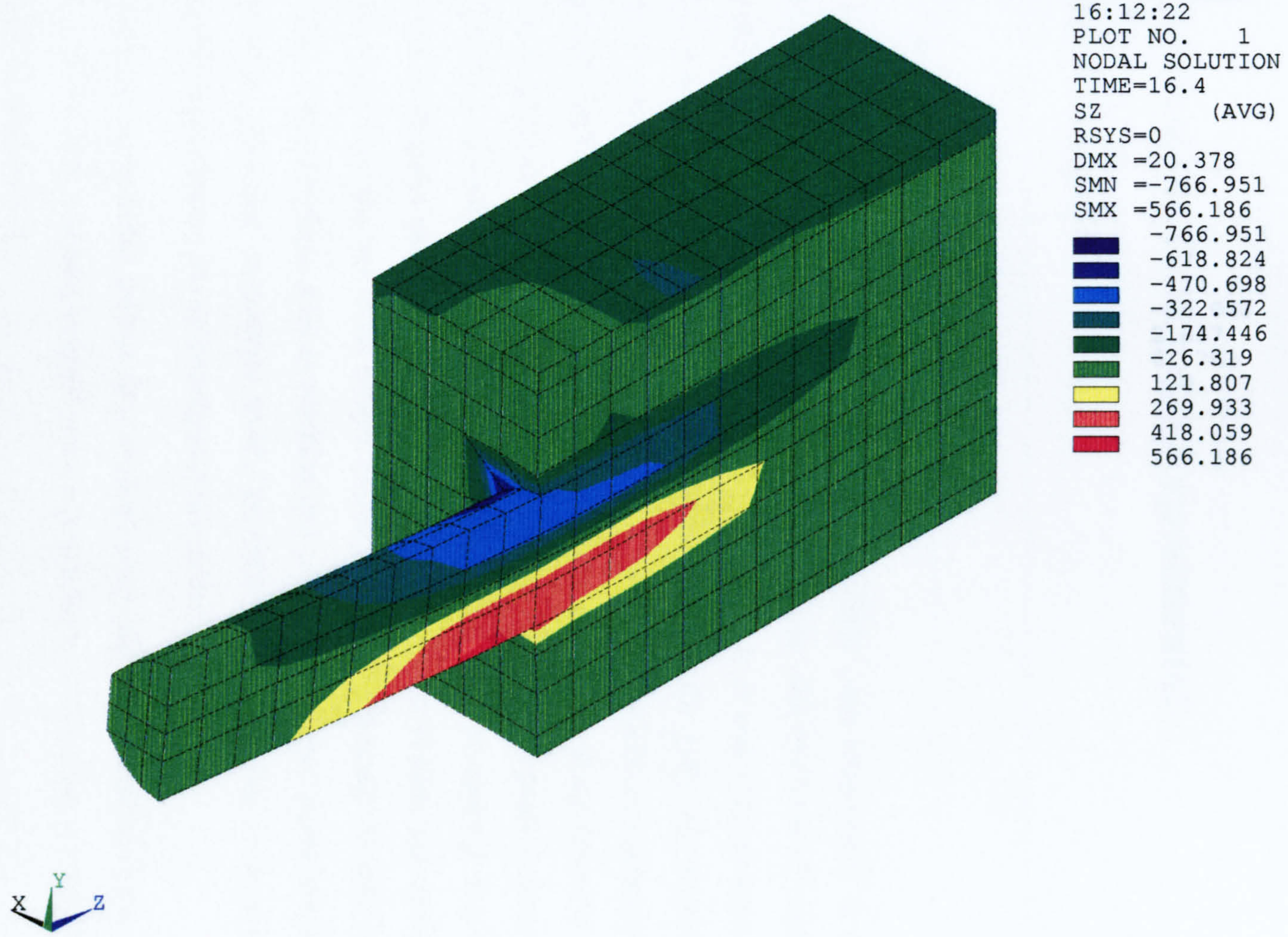

Figure 5.28 *Distribution of the bolt axis stress σ_z for model 3 with a 16.4mm displacement at the bolt head*

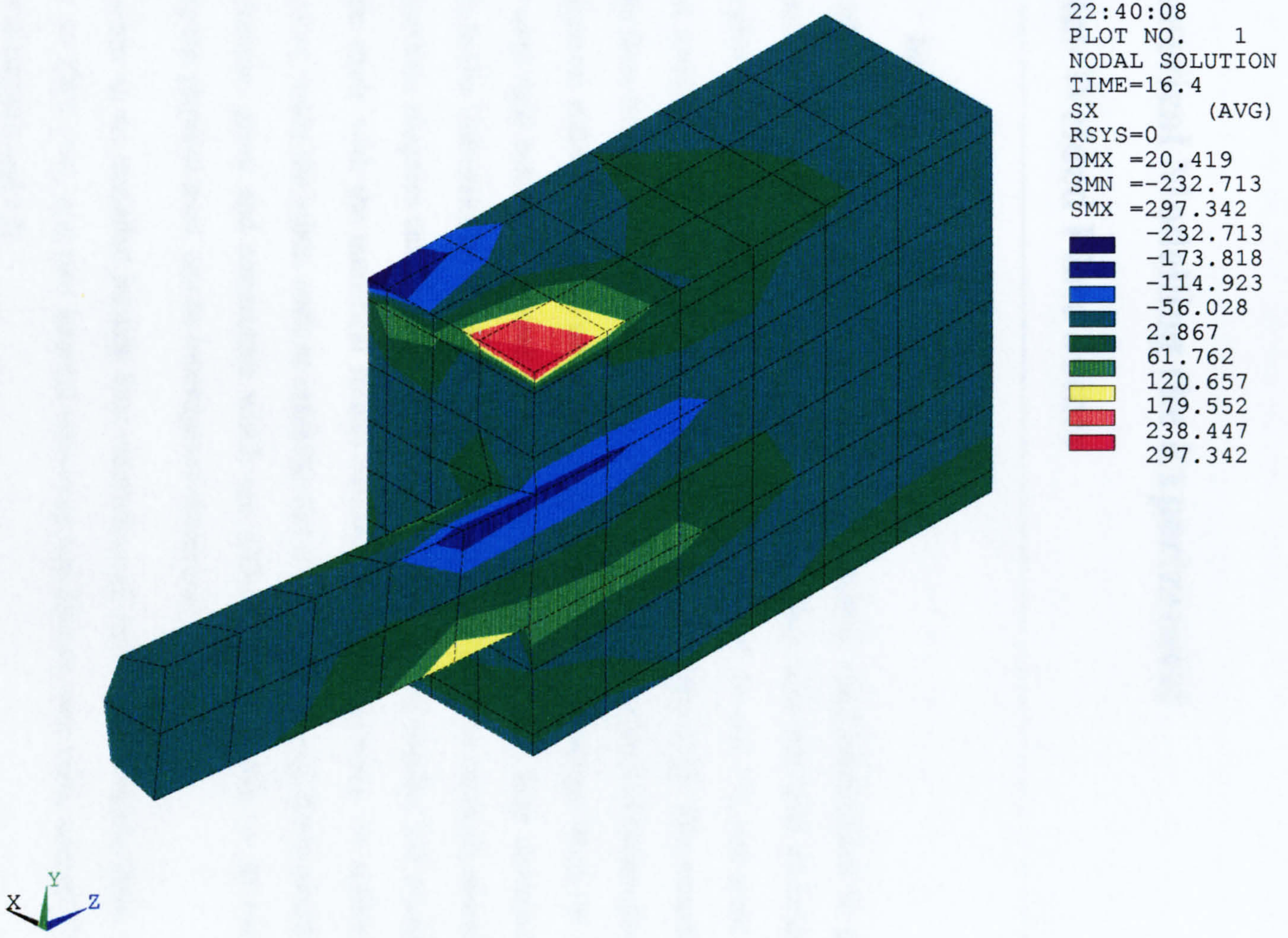

Figure 5.29 *Distribution of the horizontal stress σ_x for model 1 with a 16.4mm displacement at the bolt head*

Chapter 6

Numerical Modelling the Experimental Billet-Welded Plate Joints

6.1 Introduction

The billet with welded plate is one of the most widely used connections in precast concrete building frames in the UK. A number of joints with this kind of connection were physically tested in the University of Nottingham [14, 16 and 17], and some of the tested specimens were numerically analysed in City University [18]. The experimental results from Nottingham University indicate that joints with this kind of connection have the greatest stiffness and thus offers the greatest structural advantage from the use of their semi-rigid behaviour. Therefore, the joints with billet-welded plate connections as tested in the University of Nottingham are modelled in detail. The methods described in the previous chapters can be further calibrated against the test results, and comparison can be made with the numerical results obtained in City University. In addition, the behaviour inside the joints, such as cracking and crushing status and stress distributions of concrete, grout and connectors which are difficult or impossible to be measured during the physical tests, can be investigated numerically.

The joints to be modelled include four external sway sub-frames without slabs, named TW1 to TW4 [14], and two internal non-sway sub-frames with slabs, named TW1(A) and TW1(C)[16 and 17].

Some of the modelled joints are also scheduled in the sensitivity analyses as described in Chapter 7. This chapter addresses the general procedures and results of the numerical analyses, the effects of changing various parameters on the joint behaviour will be described in Chapter 7.

6.2 Test specimens and arrangements

The dimensions, load and constraint conditions of TW1 to TW4 are shown in Figs. 6.1 and 6.2, while TW1(A) and TW1(C) are in Figs. 6.3 and 6.4. The beams were 300 mm wide, and either 300 mm or 600 mm deep, and cast using specified grade C40 concrete. The columns were all 300*300 mm^2 in cross-sections, cast using specified grade C50 concrete. The floor slabs were 200 mm deep proprietary hollow-cored units concreted into position using grade C30 infill concrete after 2 No. T25 longitudinal tie bars were placed over the beams and through a slot in the column, and 6 T12 transverse tie bars were placed in slots in the slabs. Reinforcement details of the specimens are graphically illustrated in Figs. 6.5 and 6.6, details of the connectors are given in Fig. 6.7.

All the specimens showed the expected failure mode of flexure except TW1(C) of shear.

Although some of the specimens were loaded cyclically or reverse cyclically in the physical tests, all of the joints are loaded monotonically in these numerical analyses.

6.3 Models

All models are generated complying with the standardisation described in the previous chapters. According to the particular requirements of the specimens, however, each model possesses some individual characteristics.

6.3.1 Model geometry

The models of the joints are meshed as shown in Figs. 6.8 to 6.10 with the following geometrical features:

a. Due to the geometrical and loading symmetries in the *YZ* plane, just half of the tested specimen is modelled for TW1 to TW4, only a quarter for TW1(A) and TW1(C).

b. A finer mesh is applied to the core zone of the joint while a coarser mesh is used for the other parts. Both the finer and coarser meshes are especially designed to match the geometry demands of all the components, such as dimensions of the billet and welded plate, and positions of the reinforcing bars and links.

c. Attention is paid to maintain the comparability between the models so that

sensitivity of parameters can be more reasonably discussed. For instance, TW1 to TW4 have the same column meshes, and TW1(A) and TW1(C) have the same beam meshes as those of TW1 and TW2.

d. Gap elements are utilised in the interfaces between the connectors and the surrounding concrete or grout, such as the billet and the grout, the billet and the column concrete, the grout and the column, the grout and the beam, etc.. The billet to column concrete gap element extends only for the first element layer in from the internal face of the column. To allow for the shrinkage, 0.015 mm initial gap is assumed at the contact surfaces.

e. Both the billet and welded plate are initially meshed to connect to each other, with no additional element for the fillet weld. Herein the assumption is adopted that the fillet weld has a higher than, or the same strength as, that of the origin material.

6.3.2 Material properties

Table 6.1 lists the fundamental parameters of the material properties for the analysed joints. Stress-strain relationships of both steel and concrete derived using the mechanical models described in Chapters 3 and 4 are exhibited in Appendix Figs. A1 to A3. In order to account for the reduction of joint quality caused by the in-situ cast grout, lower grout and concrete uniaxial compressive strength was used. The calculation procedure is as follows:

$$f_{c,k} = 0.8 f_{cu} - 8 \tag{6.1}$$

$$f_c = 0.85 f_{c,k} \tag{6.2}$$

where f_{cu} is the mean value of the tested cube strength in N/mm^2

$0.8 f_{cu}$ the mean value of equivalent prism strength in N/mm^2

$f_{c,k}$ the characteristic equivalent prism strength in N/mm^2

0.85 the further reduction coefficient and

f_c the uniaxial compressive strength in N/mm^2.

6.4 Solution

The models of TW1 to TW4 were loaded at the mid-height of the lower column by adding equal increments of displacement. 60 mm total displacement was applied for all the models, since this value was just large enough to cover the whole working procedures of the joints from the beginning of loading to the stage after the whole model had crushed. This displacement was added with 120 sub-steps, thus each sub-step contained 0.5 mm increment of displacement. To save the hard disk space of the computer only every tenth solution was output, except that for TW4 every fifth solution was stored, because it would be used as the standard case in the sensitivity analyses.

As for the model of TW1(A), 50 mm total displacement was applied at the beam mid-span with 100 sub-steps. The model of TW1(C) was loaded at the location 535 mm away from the column surface. 8 mm displacement was applied with 80 sub-steps.

The accuracy of solution was controlled by nodal forces, with criterion of 10%.

6.5 Definition of the joint rotation

Several factors contribute towards the total joint deformation. Generally, it includes bending and shearing deformations of the joint core zone, and beam end(s) and column end(s) adjoining the core zone. As for the joints in precast concrete frames, bending, shearing and rigid deformation of the connectors should be additionally accounted, and furthermore they will contribute the majority of the joint deformation.

The main purpose of this research is to investigate and predict the moment-rotation properties of the semi-rigid joints. The definition of the calculation method of the rotation, however, is uncertain and a subject of much academic debates. In this chapter, results for the deformation behaviour of a typical joint will be analysed first. Then the possible methods to measure the joint rotation will be summarised and discussed. Finally the preferred method for the subsequent analyses is defined.

6.5.1 Rotational deformation performance of the joint

The deformation performance in the joint zone provides useful information for understanding and determining the rotation of the joints. Some typical deformation performances of joint TW4 are graphically displayed in Figs. 6.11 to 6.13 and will be discussed below, while the other deformation properties will be discussed together with

the strength behaviour in the following chapters.

It is observed that at the beam end the horizontal deformation does not obey the plane sections remaining plane assumptions within the full joint geometry. This is the case within the zone extending from about 300 mm at the commencement of loading to about 600 mm at the ultimate load state (Fig. 6.11). This 600 mm just covers the range from the column surface to the end of the welded plate.

There is a distinct crack between the billet and the surrounding concrete in the tension zone. This can be discovered from the shape change in the horizontal deformation of the column at the joint core zone along the vertical axis in Fig. 6.11, the gaps between the billet and the concrete on top of the billet in Fig. 6.12, and the different vertical rotations of different sections in the joint core zone in the column in Fig. 6.13.

The distribution of vertical deformation along the beam axis presents a curve and varies significantly between the beam end and the grout/billet end, the grout and the column, Fig. 6.13.

The big deformation gaps existing between the column and beam in Figs. 6.11 and 6.13 indicate that the deformation of connectors play an important role in the total joint deformation.

6.5.2 Possible rotation measurement methods and the preferred method

There are several approaches to measurement of the joint rotation. One is to measure the vertical deflections of the beam relative to the column as is normally used in physical tests, Fig. 6.14. Another way is to measure relative rotations between the beam end and the joint core zone in the column according to their vertical deflections as shown in Fig. 6.15. The third method is to measure relative rotations of the beam end and the joint core zone in the column according to their horizontal deflections, Fig. 6.16. The rotation can also be measured by the relative difference between the vertical axis rotation of the joint core zone in the column and the horizontal axis rotation of the beam, as shown in Fig. 6.17. In Figs. 6.14 to 6.17, θ_b and θ_c are the rotations of the beam end and the joint core zone in the column respectively, and $\Delta\theta$ is the relative rotation of the joint.

The first method is simple but it is not a direct method. The difficulty remaining in the second method is over which gauge length to measure the rotation at the beam end. If it

is measured over a small gauge length, the vertical displacement varies greatly from the billet to the beam end. If it is measured over a long gauge length, the vertical displacement distributes as a curve, Fig. 6.13. In the third method, the relative rotation includes the deformation of column in the height between the billet top (or bottom) and beam top (or bottom), and this value varies with the change of beam depth. Consequently, the fourth method is selected in the present research.

In the application of this method, the node positions at which the displacements will be measured must be defined precisely, because different choices of the node positions provide different results, Figs. 6.18 and 6.19. The billet rotation is measured using the vertical displacement at the nodes at the billet end (or the node at the vertical central line of column for the no-sway joint) and one element inside the internal column surface, see the marks * in Fig. 6.18. The beam end rotation is measured by the horizontal displacements of the nodes at the top and bottom surfaces of the beam (or top of slab, if applicable) at the section 600 mm away from the internal column surface. This distance is about 1~2 times of the beam depths, which approximately equals the length of *plastic hinge* for normal concrete beam analyses.

6.6 Other definitions

6.6.1 Ultimate state

The crushing characteristics of the concrete element are determined in ANSYS. If a sufficient number of integration points crush, the load capacity of the entire model will drop suddenly (Chapters 2 and 4), and a corresponding peak point will appear on the load-deformation curve. This numerical crushing is treated as a global failure of the joint, and the peak point is treated as the ultimate state, Fig. 6.20.

6.6.2 Failure mode

As in the definition for a normal concrete frame joint, if a joint fails at the beam end(s), such as by crushing of the grout, it is defined as a *weak beam end-strong column joint*. If a joint fails at the column end(s), the joint is called a *strong beam end-weak column joint*. Both cases, however, should be on the basis that the connectors and their anchorage with the surrounding concrete will not fail before either the beam end(s) or the column end(s). Otherwise the sample is termed a *weak connection joint*.

6.6.3 Beam end moment and moment resistance

The beam end moment of the joint is derived from the reaction at the beam mid-span by dividing it with the distance from the reaction location to the middle section of the grout. This definition is same as that in the experimental investigation [14]. The beam end ultimate moment resistance is equal to the peak value of the moment-rotation curve only for a *weak beam end-strong column joint*. If the joint is *strong beam end-weak column*, then the peak value on the curve represents the maximum beam end moment and not the ultimate value.

6.6.4 Rotation capacity

The rotation capacity of the joint is taken as the rotation achieved at the moment resistance, see Fig. 6.20.

6.7 Force and deformation relationships

6.7.1 The external joins without slabs

The load-displacement relationships at the column mid-height for TW1 to TW4 are shown in Figs. 6.21 to 6.24, together with the test results and the early numerical results obtained in City University . All of the curves present non-linear behaviour from the beginning of loading. The Nottingham University test results of TW3 and TW4 show an initial displacement of the column mid-height of about 5.00 mm before the joint provides a significant load resistance, and this is believed to be due to some shrinkage cracks in some interfaces in the joints and supports. These cracks are not modelled in the finite element analyses. The absence of ultimate failure criteria in the results of City University means that their models would predict the ever-increasing load-displacement responses. Comparison with the test results and the numerical results obtained in City University indicates that the models of the present research can represent the full performance of the joints. In addition, these results provide closer matches to the test results for initial stiffness and ascending slopes of the curves, the peak points/ultimate states and the descending post crushing curves.

From the moment-rotation relationships at the beam ends illustrated in Figs. 6.25 to 6.28, similar conclusions can be obtained. Furthermore, better agreements between the results have been achieved. The existence of the distinct peak points on the curves make

it convenient to determine the moment resistance and the rotation capacity for the joint.

6.7.2 The internal joints with slabs

Figs. 6.29 to 6.31 illustrate the results for TW1(A). From the beginning to the end of loading the joint experiences a typical non-linear procedure. Because of the presence of the floor slabs, a T beam section is generated. As the tie bars in the slabs resist tension, the effective depth of the beam section increases. In addition, the tie bars yielded early and subsequently performed plastically, Fig. 6.32. The crushing of the grout in the compressive zone did not cause the strength reductions in the curves as sharply as those in the models of TW1 to TW4. A longer deformation range with high load, i.e. more pseudo ductility, appears until the ultimate state. The moment resistance of the section increases about three times that of TW2.

Except for a little higher load capacity, which normally happens in the finite element modelling, the numerical results match the experimental results well, see Fig. 6.31.

The force-displacement relationships of TW1(C) in Fig. 6.33 indicates that even in the shear failure case, the joint also experiences an ascending and descending full elasto-plastic procedure. The tie bars in this joint perform a similar stress - strain response to that in TW1(A), Fig. 6.32.

The excellent agreement between the numerical and experimental results displayed in Fig. 6.34 proves that the modelling techniques proposed in the present research can also be applied for the models with shear failure mode.

6.8 Cracking status

6.8.1 The external joints without slabs

Figs. 6.35 to 6.38 show the cracking status of TW1 to TW4 at certain displacement intervals. TW1 is at 40%, 60% and 80% of the peak displacement point and the interval beyond the peak. The cracking status for TW2 to TW4 are at 25%, 50%, 75% the peak displacement intervals and the intervals beyond the peak. In order to observe the development of the cracks through the thickness of the joints, the cracking status at each pair of integration points within the element corner is presented for each of the four element layers. Beyond the joint core zone, only two element layers were used to represent the main parts of the beams and columns, Figs. 6.8 and 6.9. Thus the cracking

status of the main parts of the beams and columns shown in Figs. 6.35(a & b) to 6.38(a & b) is that in the first element layer and is repeated. The corresponding cracking status shown in Figs. 6.35(c & d) to 6.38(c & d) is that in the second element layer and is also repeated.

In the figures, each element is divided into four equal sub-elements in the *YZ* plane, and each sub-element contains two integration points. The black colour expresses that two integration points have cracked, and the grey colour expresses one.

Following cracking features have been indicated in the figures:

a. All the joints crack at very early loading stage at locations in the concrete around the billet and the plate. With increase of the displacement at the column mid-height, the cracked range extends rapidly in the three directions.

b. The developing pattern and range of the cracks significantly depend on the strength and stiffness characteristics of the joints. The higher load capacity joints, TW2 and TW4, have larger cracked range than the lower load capacity joints, TW1 and TW3. The joints with larger stiffness ratio of the beam over the columns, TW3 and TW4, have bigger cracked zones in the columns than the joints with smaller stiffness ratio of the beam to the columns, TW1 and TW2.

c. The internal forces affect the cracking pattern and range of the joints consequentially as well. The upper columns in TW2 and TW4 have the extra tensions than the lower columns as they are loaded with hogging moments at the beam ends, thus the upper columns present bigger cracked zones. Whereas, as the joints are loaded in the opposite direction, tests TW1 and TW3, the upper columns have the extra compression, and they develop relatively smaller cracked zones.

Due to the above reasons, TW4 shows the most extensive cracked zone with the upper column fully cracked after the ultimate state, whilst TW1 has the smallest cracked zone and the least cracked upper column.

The cracking characteristics of the joints indicate that special attention should be paid to the durability of the precast concrete building frames, especially when they are used in the conditions with potential corrosion.

6.8.2 The internal joints with slabs

The typical cracking patterns for TW1(A) and TW1(C) are shown in Figs. 6.39 and 6.40. Although the lower columns in the two internal joints are subjected to compression only, cracking still occurs in the concrete surrounding the billet and at the column mid-spans. TW1(C) has a higher load capacity, thus a larger cracked zone appears in the column.

The other cracked zone in TW1(A) fills not only the grout, the beam end and the slabs, but also the portion of the beam from the slab edge to the loading point, Figs. 6.39. This is due to the higher load capacity of the joint, compared with TW2, and the sudden reduction of the section from the one with the stiffening slab to the one without the slabs. The cracking of TW1(C) is limited in the zone from the internal column surface to the load point, because the shear in this part is much larger than in the part from the load point to the beam mid-span, Fig. 6.40.

The shear transferring pattern can be observed from the views of cracking status of slab tops. The non-cracked zones are located either by the interface between the adjacent slabs or on top of the hollows.

6.9 Failure mode

Figs. 6.41 to 6.46 show the distribution of equivalent stress in von-Mises failure criterion at the ultimate state for the concrete and grout elements of the joints. Figs. 6.47 to 6.52 show the corresponding equivalent stress distribution for the joint core zones. The equivalent stress, σ_e, is expressed as below [31, 51]

$$\sigma_e = \left(\frac{1}{2}\left[(\sigma_1-\sigma_2)^2+(\sigma_2-\sigma_3)^2+(\sigma_3-\sigma_1)^2\right]\right)^{\frac{1}{2}} \qquad (6.3)$$

where σ_1, σ_2 and σ_3 are the principle stresses.

The high equivalent stress concentrating location is the critical zone at which the failure of the joint may start.

The crushing status beyond the peak points of the six joints is exhibited in Figs. 6.53 to 6.57 with the similar manner to the cracking status.

6.9.1 The external joints without slabs

All the concrete components of the four joints have high equivalent stress concentrations in the compressive zones of the grout and the column ends, Figs. 6.41 to 6.44. The cube strengths of column concrete, however, are higher than those of the grout, Table 6.1. Early stage and more extension crushing predictably occurred within the grout. This has been proved by the crushing status of the joints as illustrated in Figs. 6.53 to 6.56. Thus all the four joints are *weak beam end joints*. At the ultimate state the connectors have not yielded, except possibly very locally around the welds, Figs. 6.47 to 6.50. All the column reinforcement does not yield at the column ends in both tension and compression, except the tension steel in TW4, see Fig. 6.58 for the details. Therefore the critical sections in the grout are over reinforced, and the failure of the sections belong to brittle failure.

The effect of the characteristics of joint load capacity and stiffness to the equivalent stress distribution also can be observed in Figs. 6.41 and 6.44. The joints with higher load capacities and stiffer beams, TW3 and TW4, generate bigger high stress zones, especially in the columns.

The deformed shapes of the entire joints and the gap status at the interfaces can be observed as well in the Figs. 6.41 and 6.44. Higher load capacity and larger stiffness ratio of the beam compared with the columns, as in tests TW3 and TW4, correlate with larger deformation of columns and wider opened gaps.

Figs. 6.53 to 6.56 indicate that the load capacity and stiffness characteristics further affect the crushing pattern and extend. The stronger joint, TW4 for instance, has bigger crushed zone, whereas the weaker joint, TW1, has a smaller crushed zone. The larger stiffness ratio of the beam over the columns in TW3 and TW4 associates with more crushed elements in the columns, Figs. 6.53 and 6.54. The smaller stiffness ratio joints, TW1 and TW2, are not crushed in the columns at all, Figs. 6.55 and 6.56.

At the ultimate state the shrinkage gap between the grout and the column face, which existed initially, developed so greatly that it crossed the billet and extended into the grout on the other side of the billet. Fig. 6.59 exhibits the detailed gap status for TW1 to TW4. Similar phenomenon was measured in the experimental investigations [14]. This gap status is associated with the compressive stress concentration in a relatively small

zone near the edge of the section. Typical compressive stress distributions in the middle section of the grout at the ultimate state for TW1 to TW4 are illustrated in Fig. 6.60. These stress distributions are triangular in shape.

Fig. 6.61 shows the ultimate state vertical (i.e. column axial direction) stresses at the welds for TW1 to TW4. The moment at the weld is not significant because the rotation stiffness at the weld is much smaller than that of both the plate and the billet (about 10% of the plate and 20% of the billet). The shear force is mainly transferred by the grout, not by the connector. The reason is that in the analyses only the internal forces caused by the sway at the column mid-height are considered. According to the typical geometry used and the loading conditions (Figs. 6.1 and 6.2), one unit reaction at the beam mid-span, which is the shear force in the beam, will cause about 7 (TW4) to 30 (TW1) units of compression in the grout. The static friction coefficient between concrete to concrete was taken as 0.8, Table 2.1. The friction capacity at the interface between the column and the grout will be 5.6 to 24 times higher than the applied shear force. Thus the shear force will be balanced by the friction at the interface until close to the ultimate state.

6.9.2 The internal joints with slabs

For joint TW1(A), since there is symmetry to the central line of the column, the highest equivalent stress concentrates in the grout and the beam end only, Fig. 6.45. Thus it fails at the grout and the beam end concrete, Fig. 6.57(a). Compared with TW2, this joint shows a bigger zone of high compressive stress, and no gaps observed at the interfaces. The reason is that the tie bars in the slabs contribute in tension. In addition, the tie bars have yielded before the ultimate state, Fig. 6.32, and the failure of this joint is ductile.

As for joint TW1(C), the highest equivalent stress is located at the column concrete beneath the billet for this special load condition, Figs. 6.46. It fails at the grout as well, Fig. 6.57(B). It is clear that the compressive stress flow transfers from the loading location to the grout and beam end in the compressive zone, and then into the lower column. Part of the compressive stress path also transfers to the top of the billet end within the grout.

The connectors in both TW1(A) and TW1(C) are not subject to any significant forces, Figs. 6.51 and 6.52. This is because the connectors are located at the middle depth of the sections, and the majority of the tension is taken by the tie bars.

6.10 Summary

The numerical results of the billet-welded plate joints obtained in the present research show good correlation with the experimental results and the relevant numerical results. The numerical investigation also indicate the potential internal mechanisms of the joints, such as cracking, crushing status and stress distributions, which are difficult or impossible to be measured experimentally.

Concrete cracking was initialled in the area surrounding the connectors, and resulted in extensive cracking occurring over virtually entire joint region. All the external joints without slabs were classified as *weak beam end joints*. Failure of these joints was by crushing of the grout, with stresses in the connectors remaining within elastic limits. Therefore, the failure mode of these joints is brittle. The internal joints with slab had the typical ductile flexural and shear failure as expected.

The standard FEA techniques have been further calibrated, and can be applied with a reasonable degree of confidence to the following research.

No.	Specimen	$f_{cu,\ beam}$	$f_{cu,\ column}$	$f_{cu,\ grout}$	$f_{cu,\ slab}$	$f_{y,\ main}$	$f_{y,\ link}$	$f_{y,\ billet}$	$f_{y,\ welded\ plate}$	$f_{y,\ anchor\ bar}$	$f_{y,\ tie\ bar}$	$f_{y,\ prestressed\ bar}$
1	TW1	54.5	58.4	46.2		460	460	275	275			
2	TW2	54.5	58.4	49.8		460	460	275	275			
3	TW3	63.2	62.5	47.3		460	460	275	275			
4	TW4	54.5	58.6	48.2		460	460	275	275			
5	TW1(A)	52.7	56.3	45.4	60	460	460	275	275	275	460	1500
6	TW1(C)	52.7	56.3	45.4	60	460	460	275	275	275	460	1500

Note: 1) All the strengths are in the unit of N/mm^2

2) f_{cu} is the tested mean cube strength for all the beam, column concrete and grout, while the characteristic cube strength for the slab concrete

3) f_y is the characteristic yield strength for all the steel reinforcement and the connectors.

Table 6.1 *Fundamental parameters for the material properties of the analysed joints*

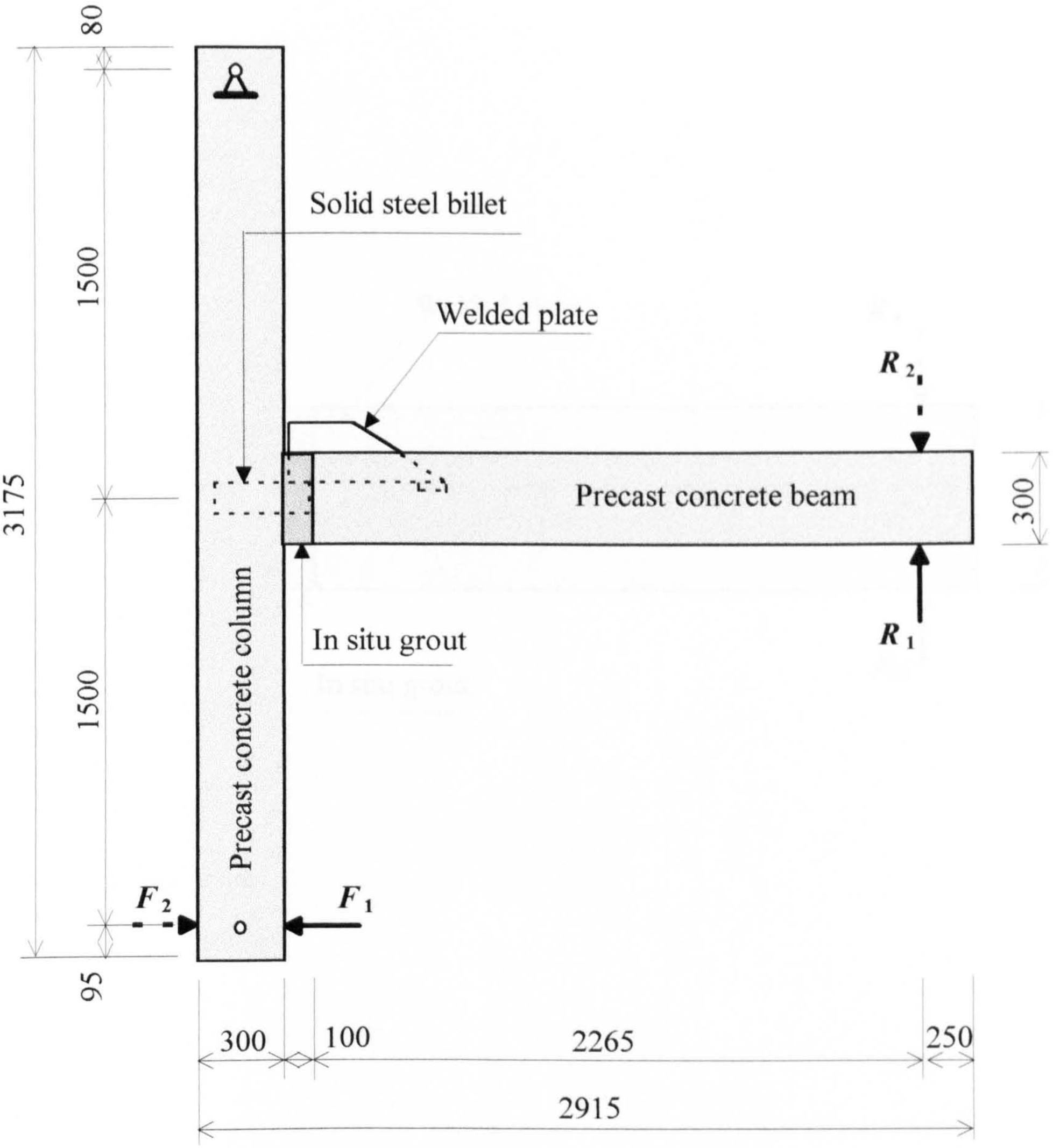

Note: F_1 and F_2 are the applied loads to TW1 and TW2 respectively and
R_1 and R_2 are the reactions of TW1 and TW2 respectively.

Figure 6.1 *Dimensions and test arrangements of TW1 and TW2*

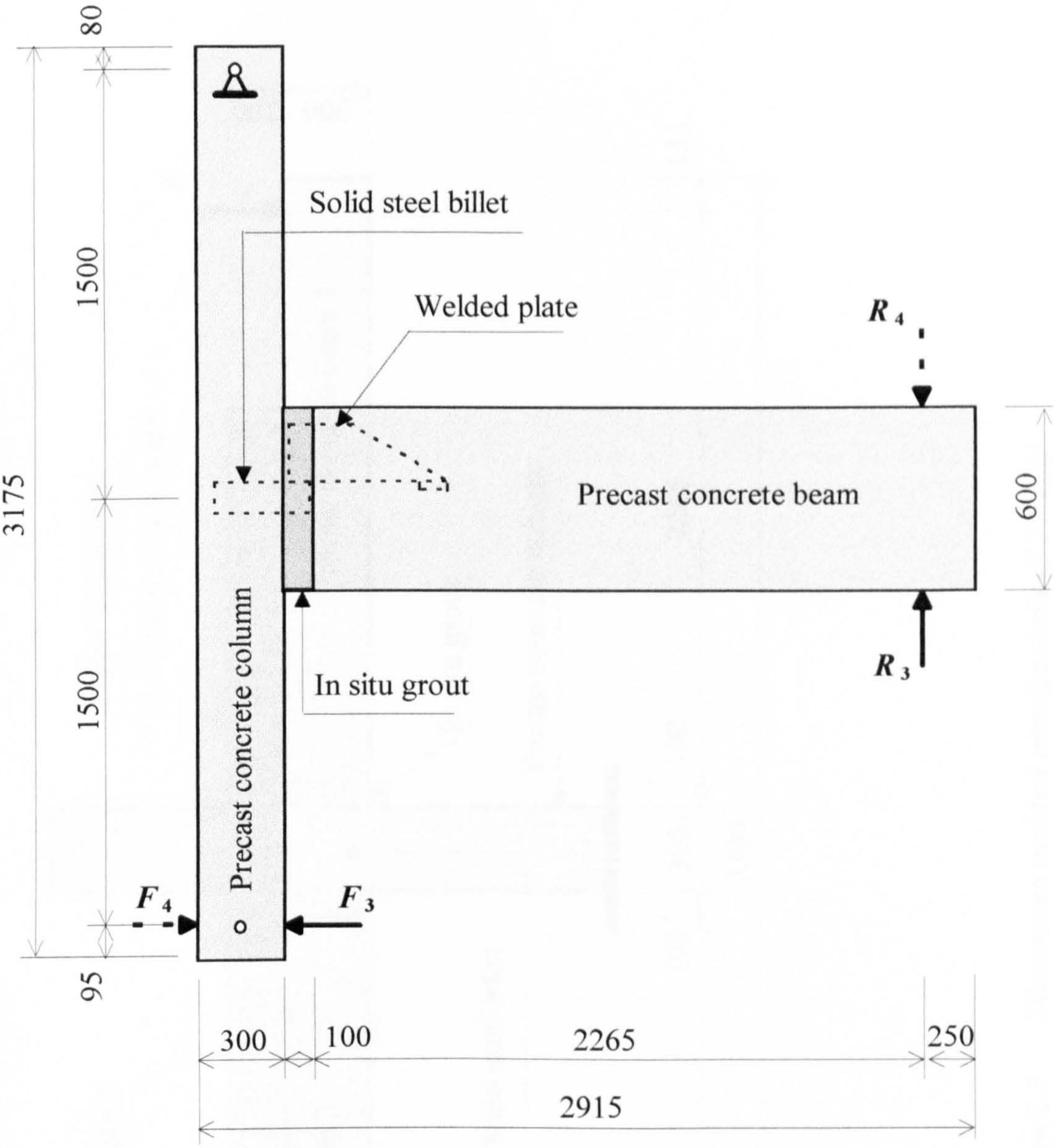

Note: F_3 and F_4 are the applied loads to TW3 and TW4 respectively and
R_3 and R_4 are the reactions of TW3 and TW4 respectively.

Figure 6.2 *Dimensions and test arrangements of TW3 and TW4*

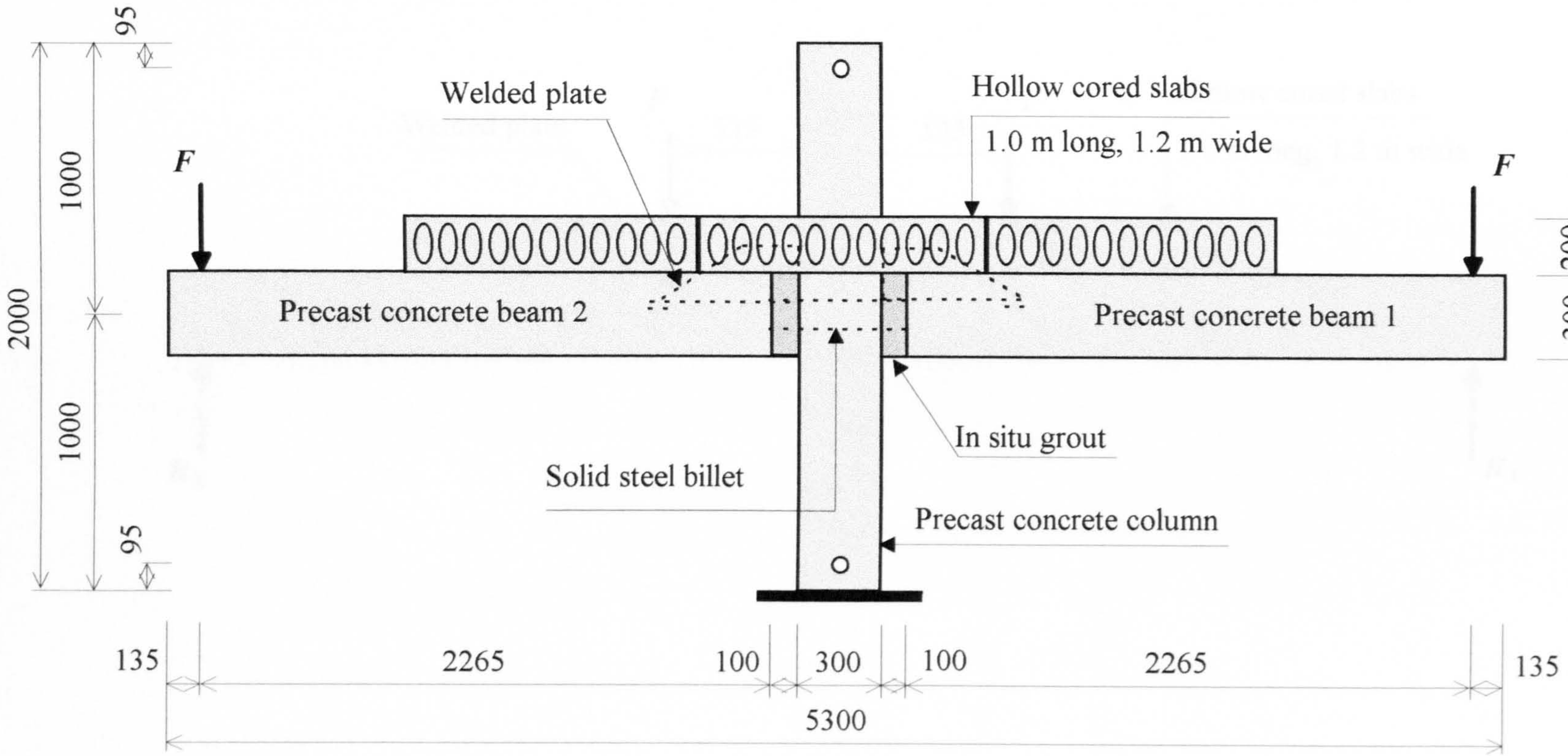

Figure 6.3 *Dimensions and test arrangements of TW1(A)*

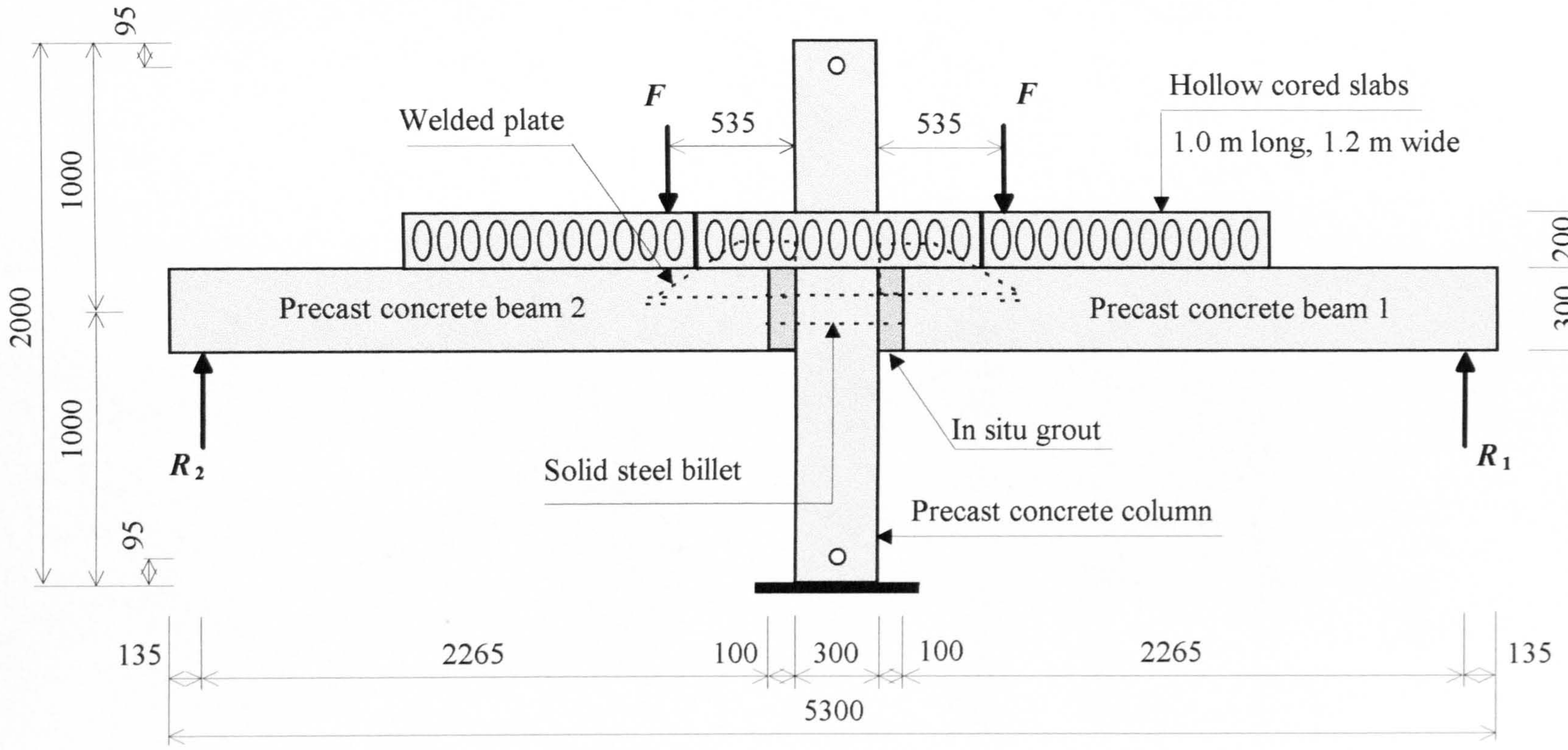

Figure 6.4 *Dimensions and test arrangements of TW1(C)*

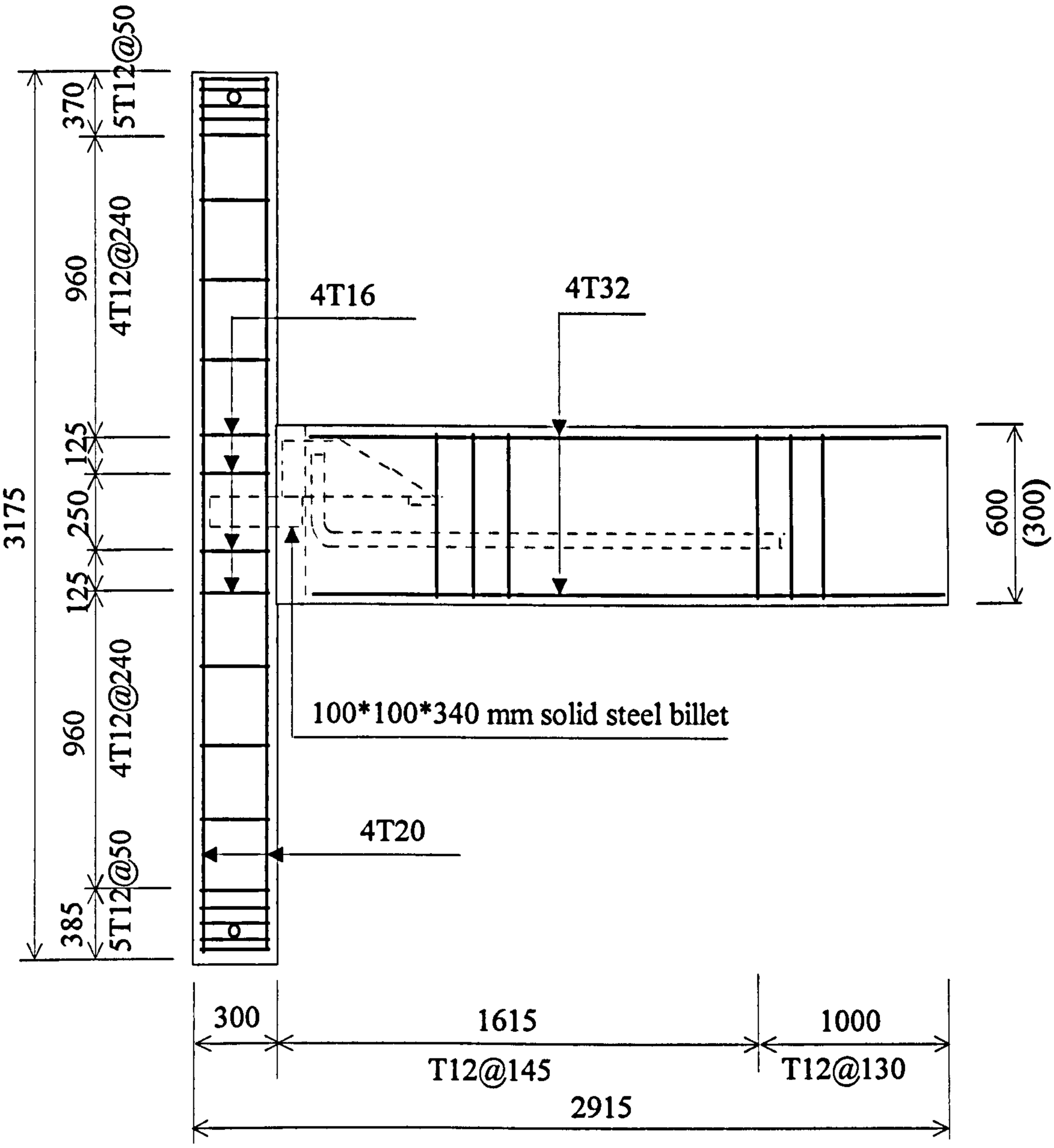

Figure 6.5 *Reinforcement details for TW1 to TW4*

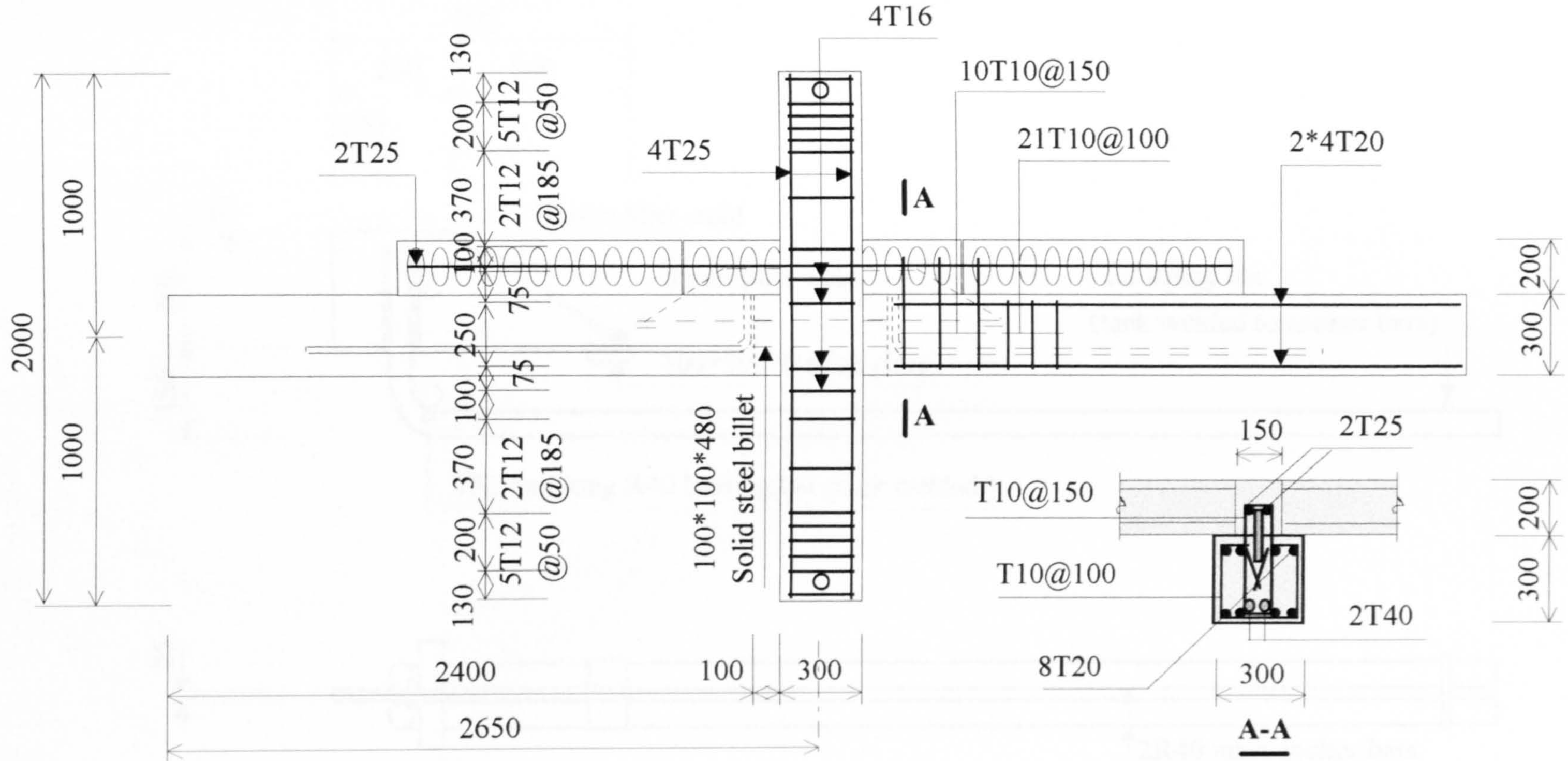

Figure 6.6 *Reinforcement details for TW1(A)and TW1(C)*

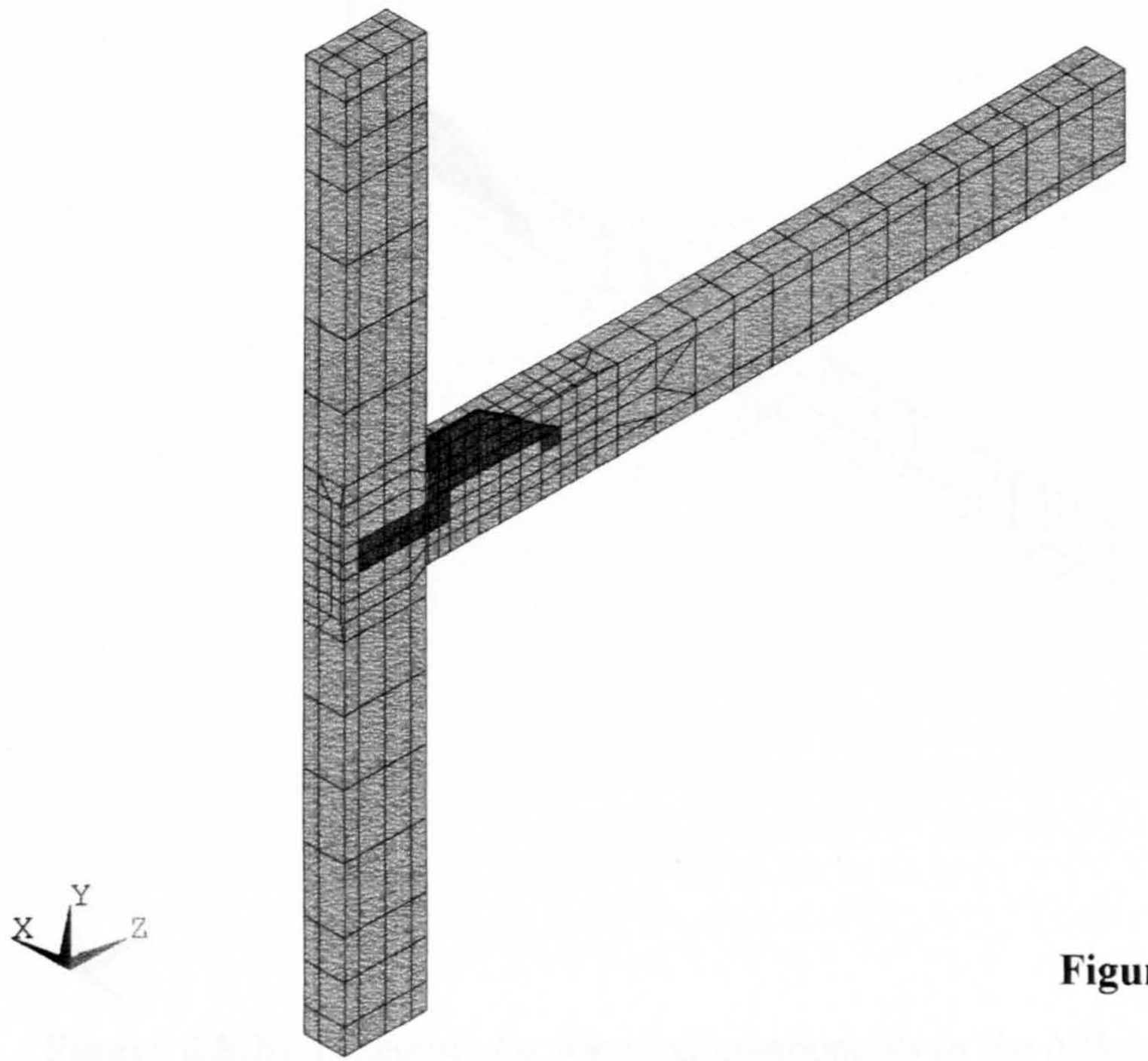

Figure 6.8(a) *Element mesh for the billet-welded plate joints TW1 and TW2*

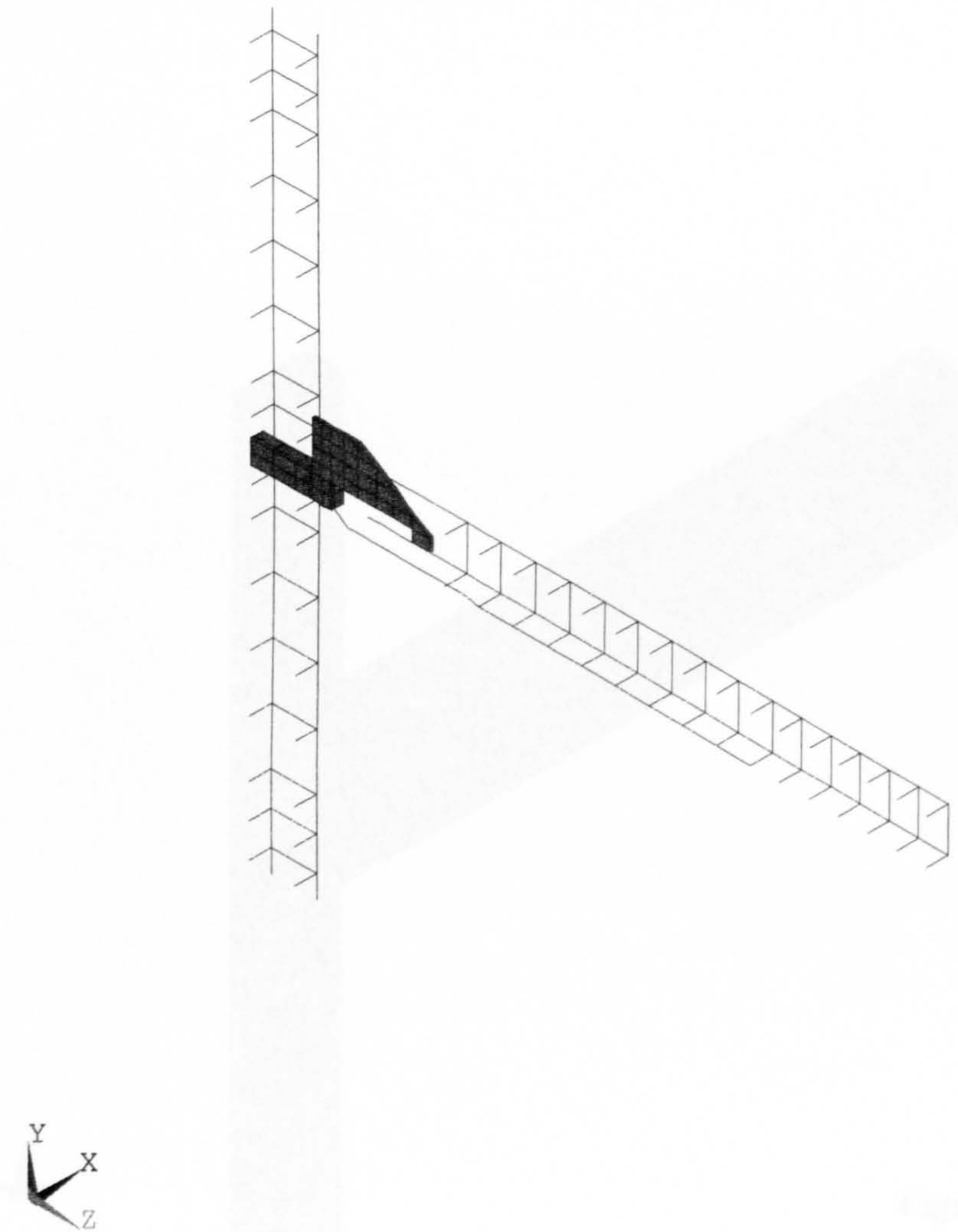

Figure 6.8(b) *Elements for the steel components in the billet-welded plate joints TW1 and TW2*

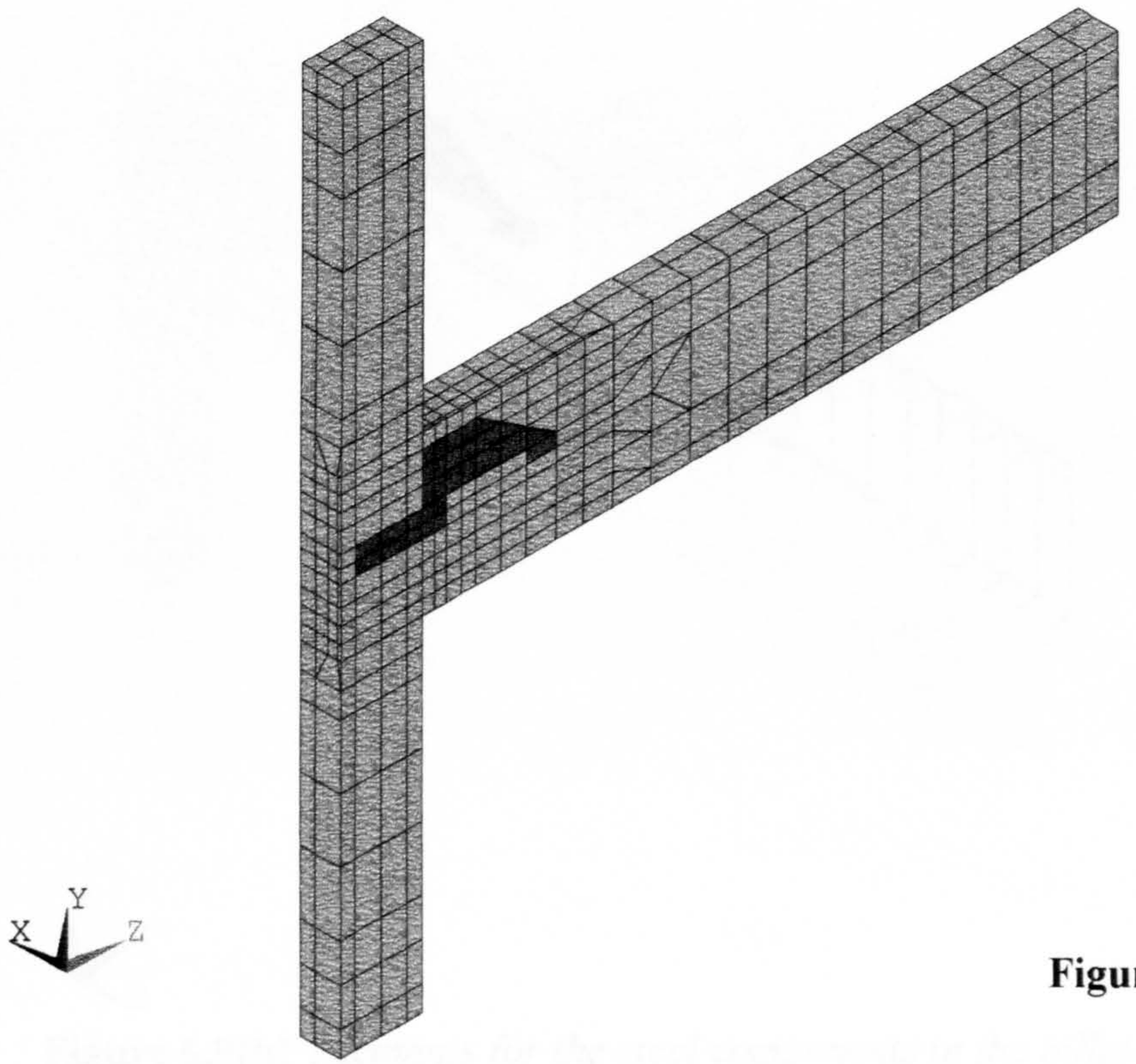

Figure 6.9(a) *Element mesh for the billet-welded plate joints TW3 and TW4*

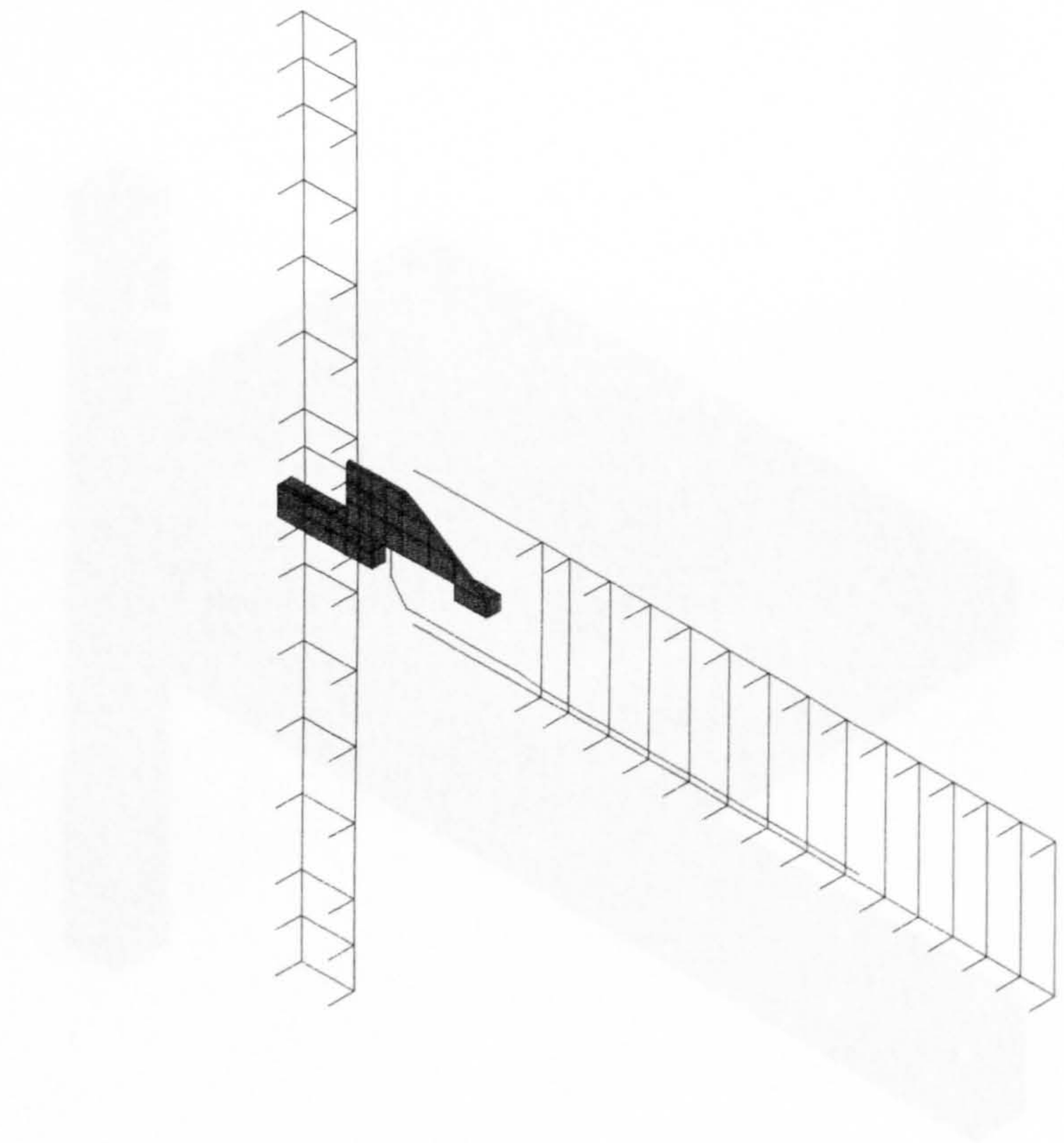

Figure 6.9(b) *Elements for the steel components in the billet-welded plate joints TW3 and TW4*

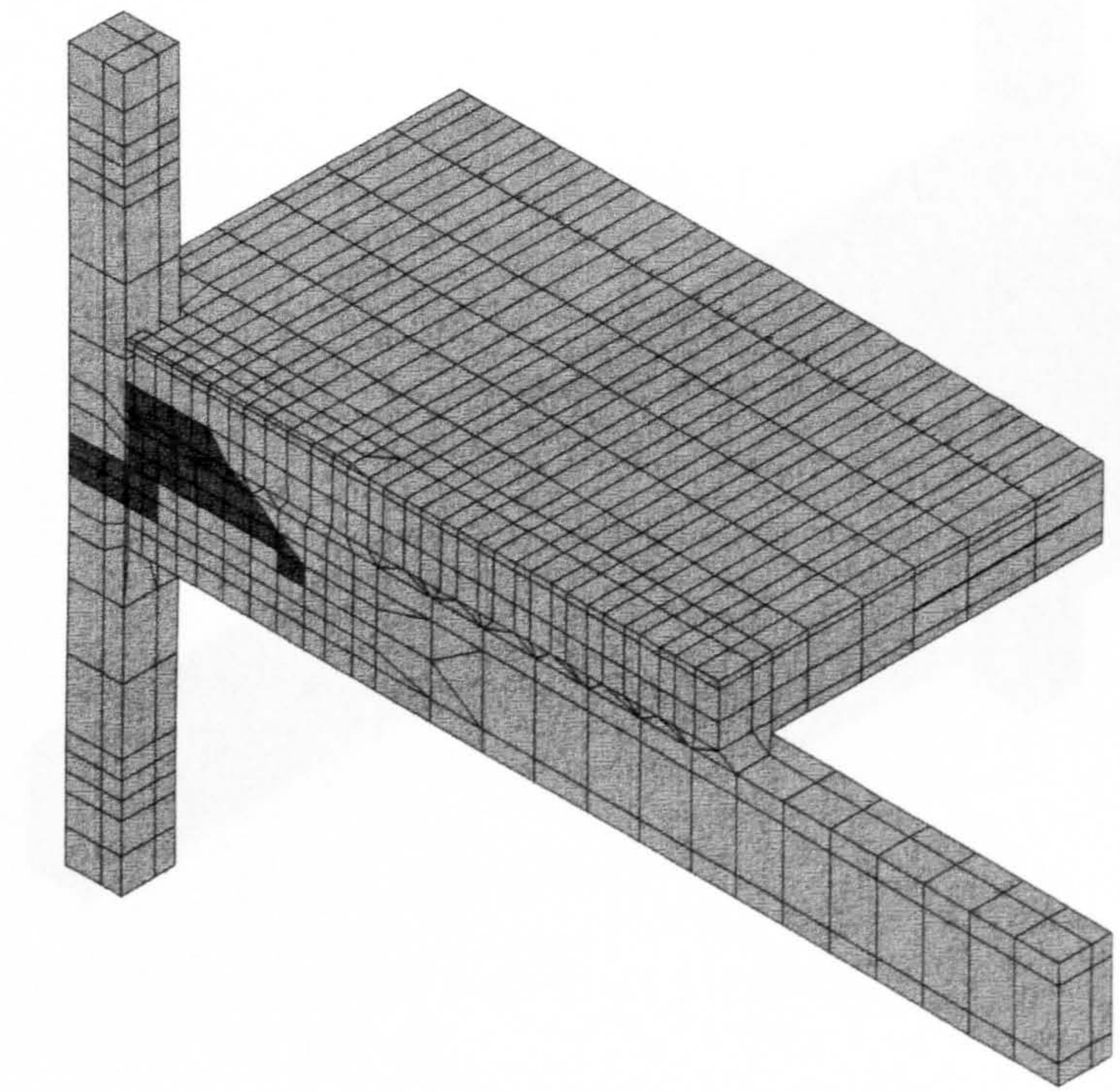

Figure 6.10(a) *Element mesh for the billet-welded plate joints TW1(A) and TW1(C)*

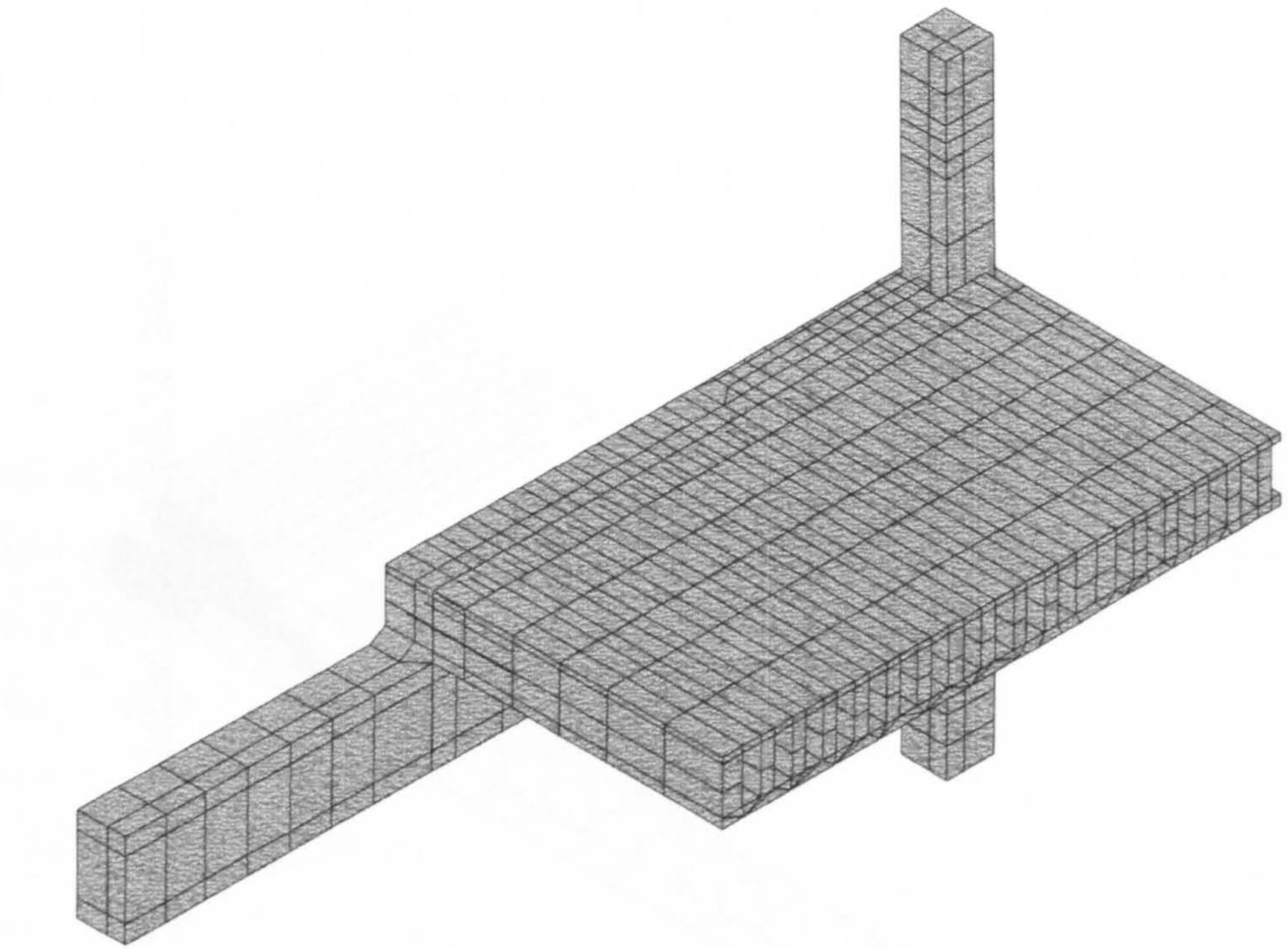

Figure 6.10(b) *Element mesh for the billet-welded plate joints TW1(A) and TW1(C)*

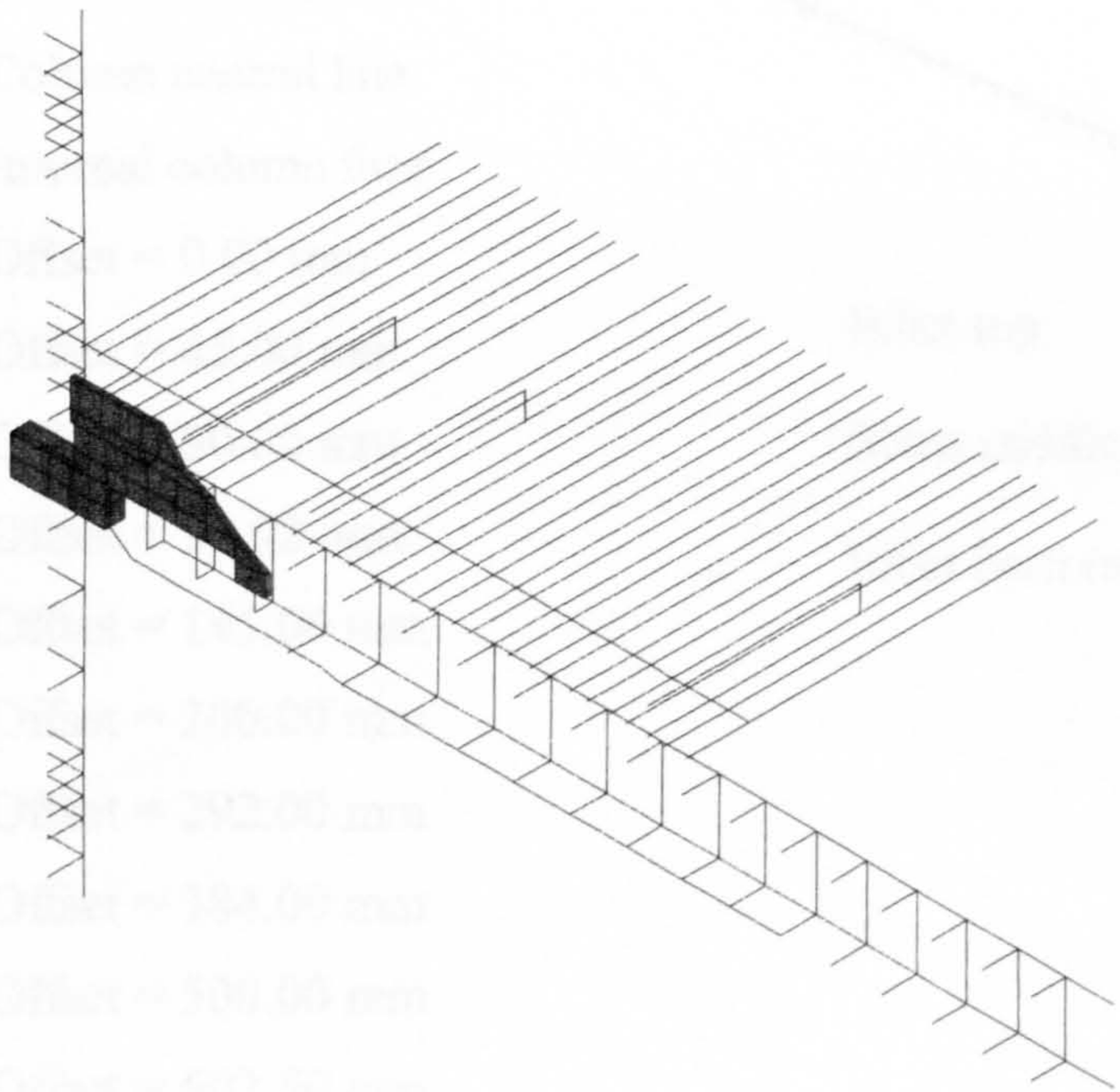

Figure 6.10(c) *Elements for the steel components in the billet-welded plate joints TW1(A) and TW1(C)*

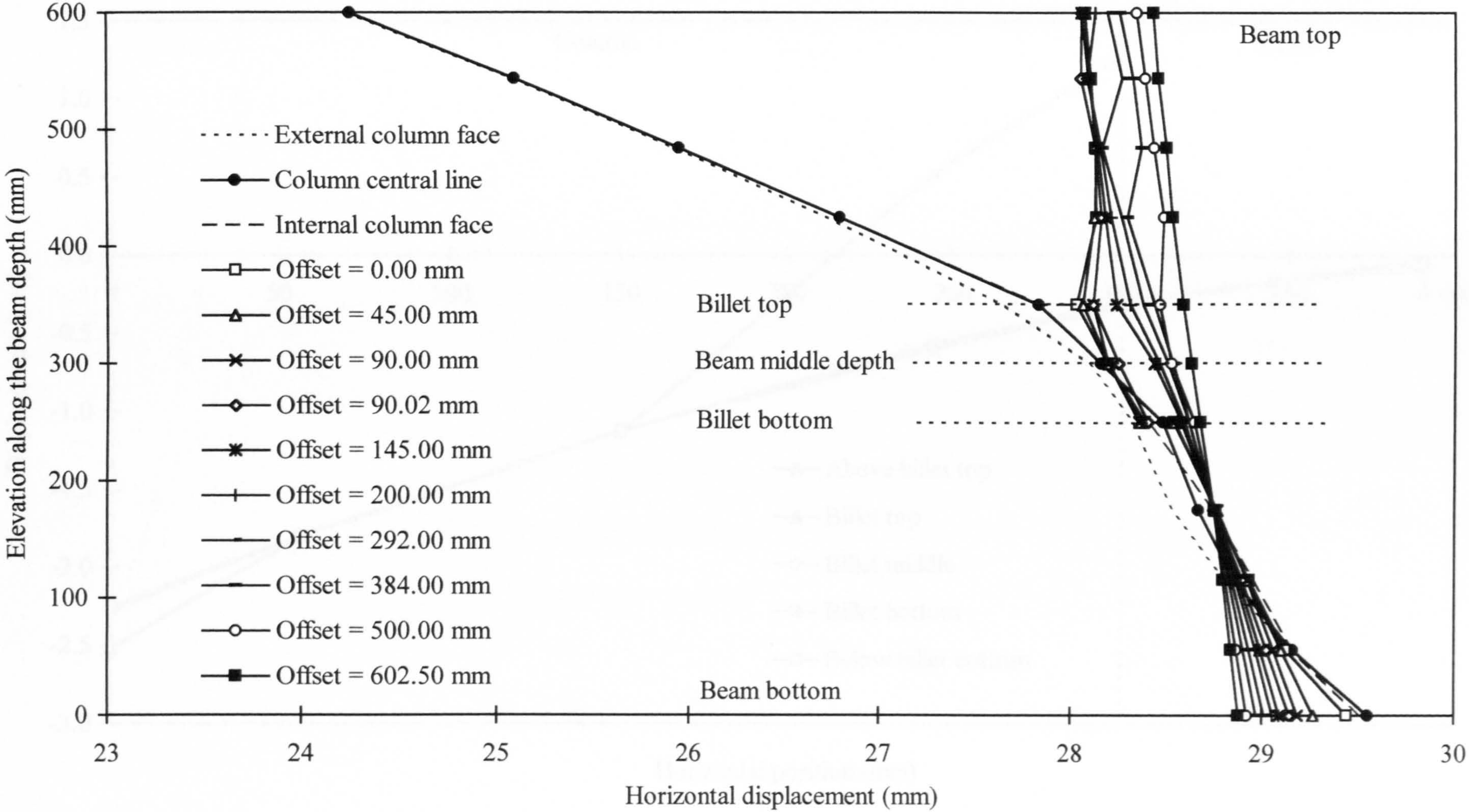

Figure 6.11 *Joint core zone horizontal displacement for TW4 with a 40 mm column mid-height displacement*

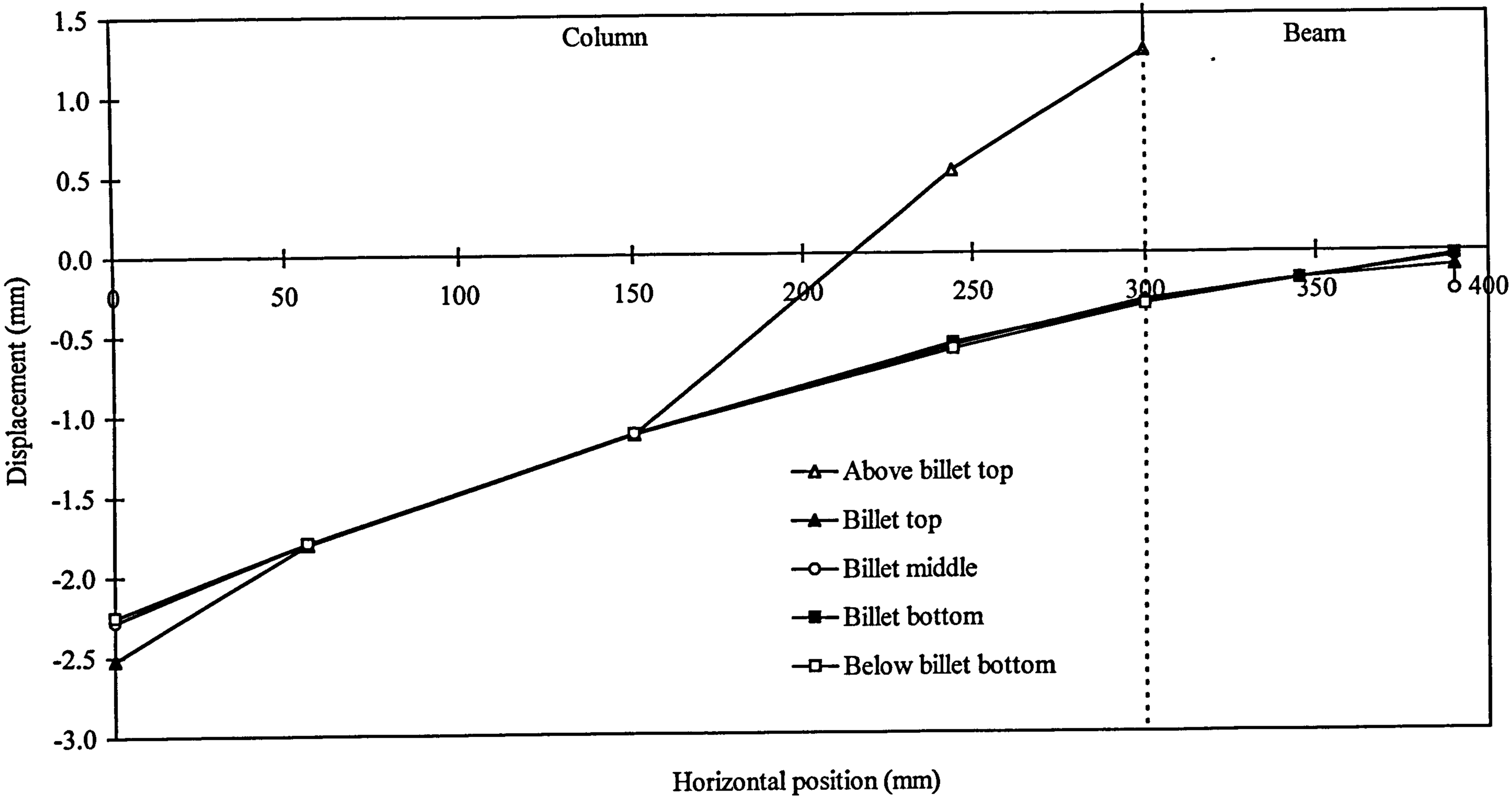

Figure 6.12 *Vertical displacement of the billet for TW4 with a 40 mm column mid-height displacement*

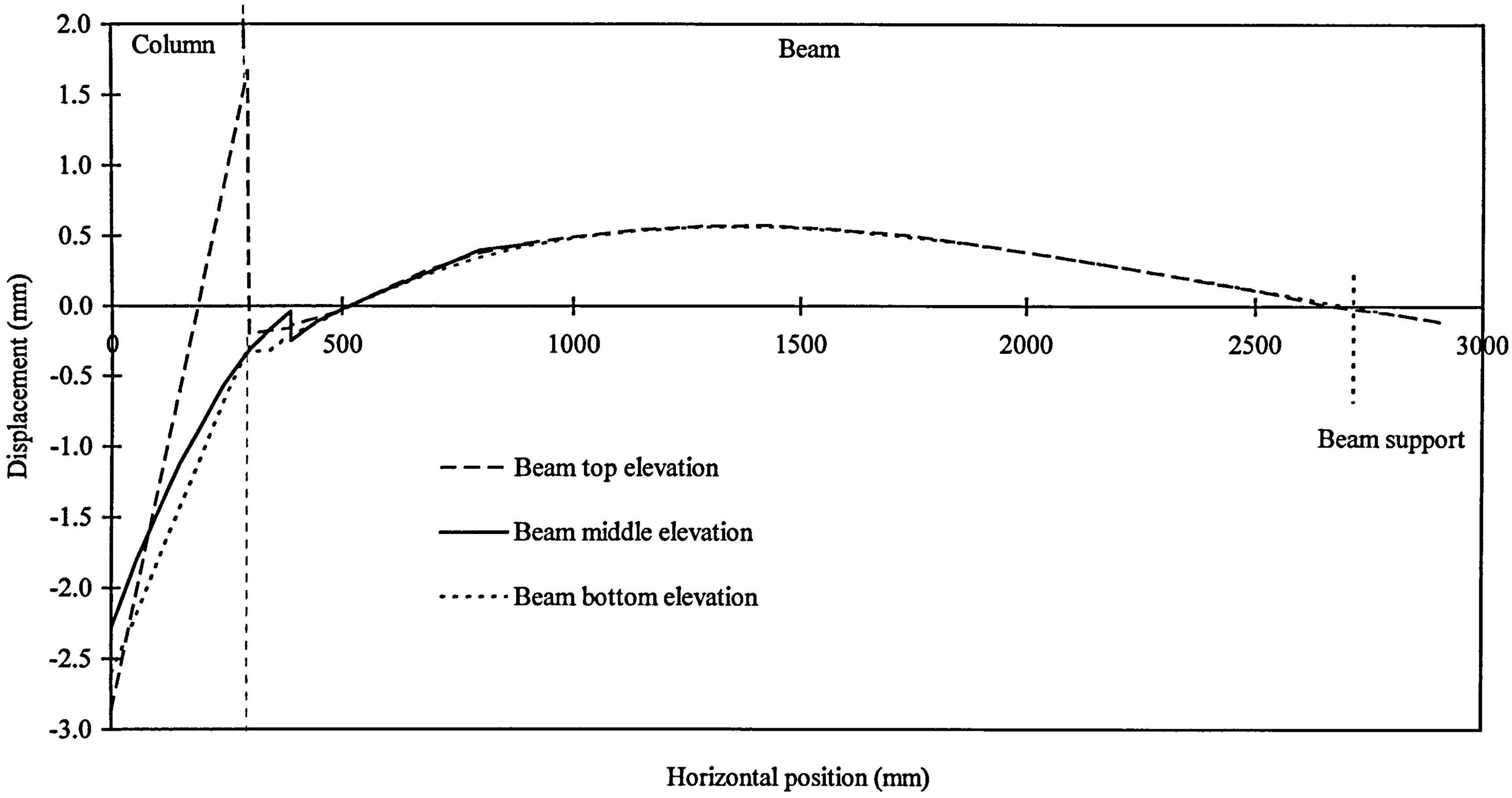

Figure 6.13 *Vertical displacement of the joint for TW4 along the longitudinal beam axis with a 40 mm column mid-height displacement*

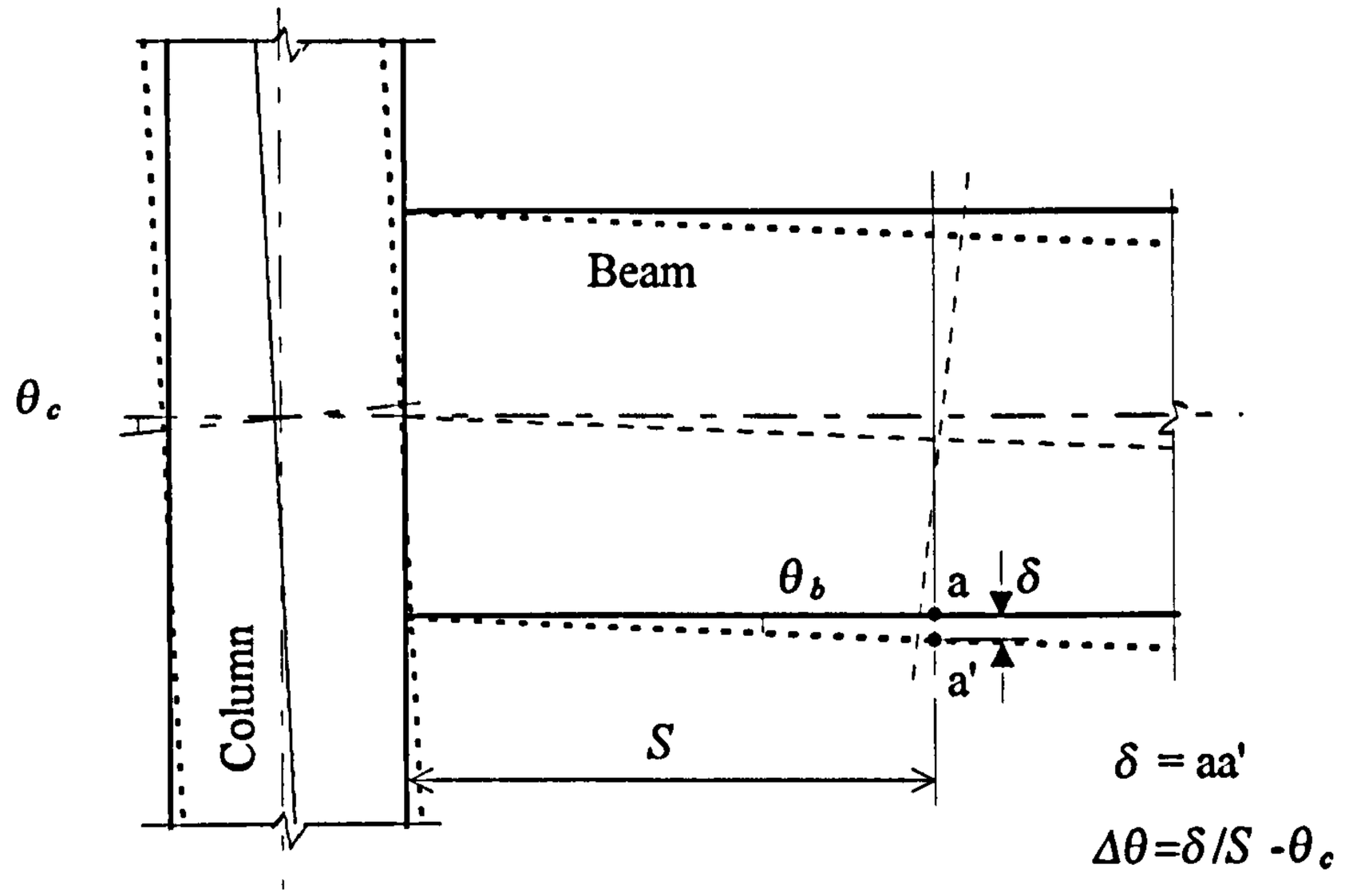

Figure 6.14 *Rotation measurement Method 1*

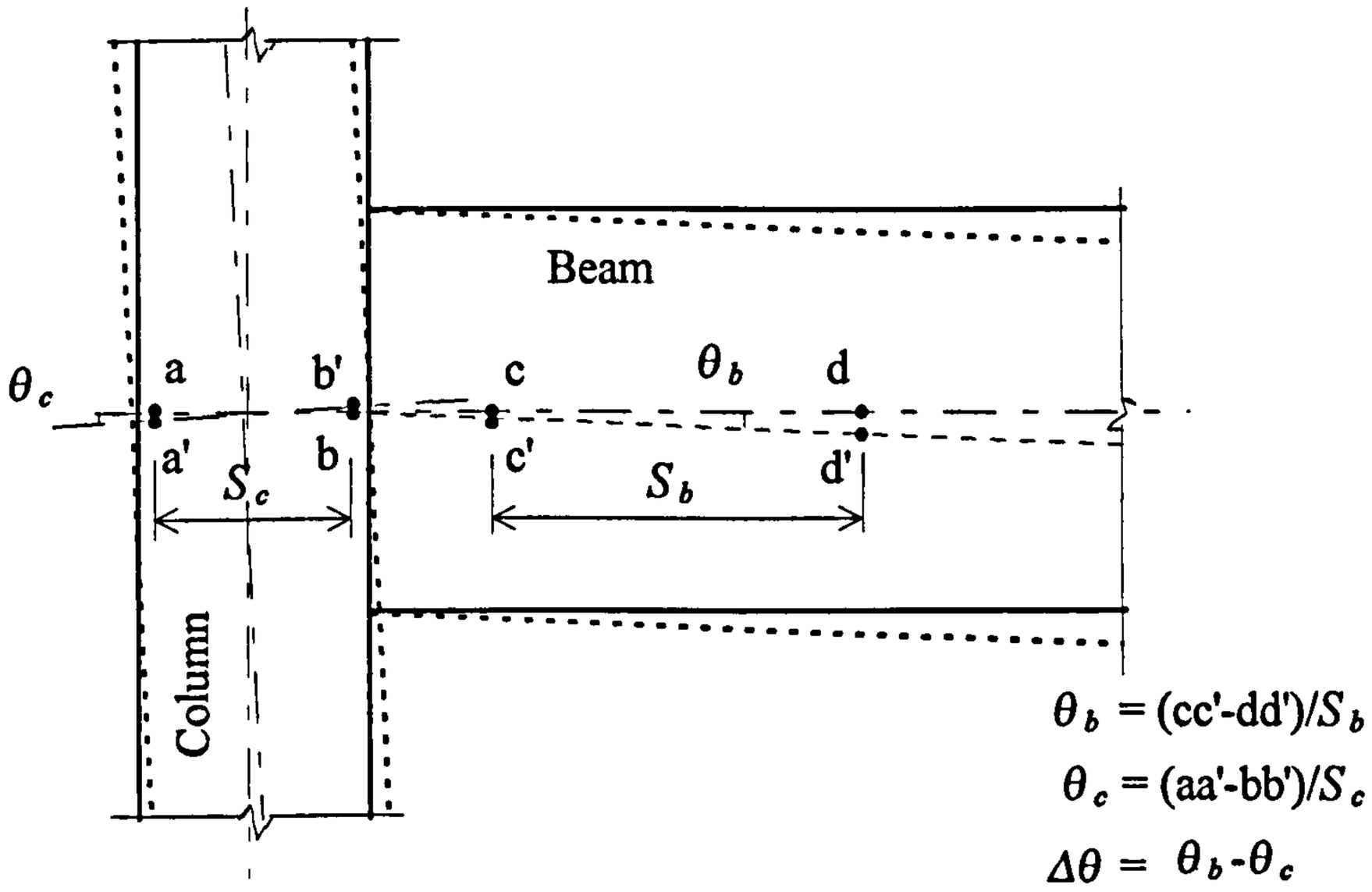

Figure 6.15 *Rotation measurement Method 2*

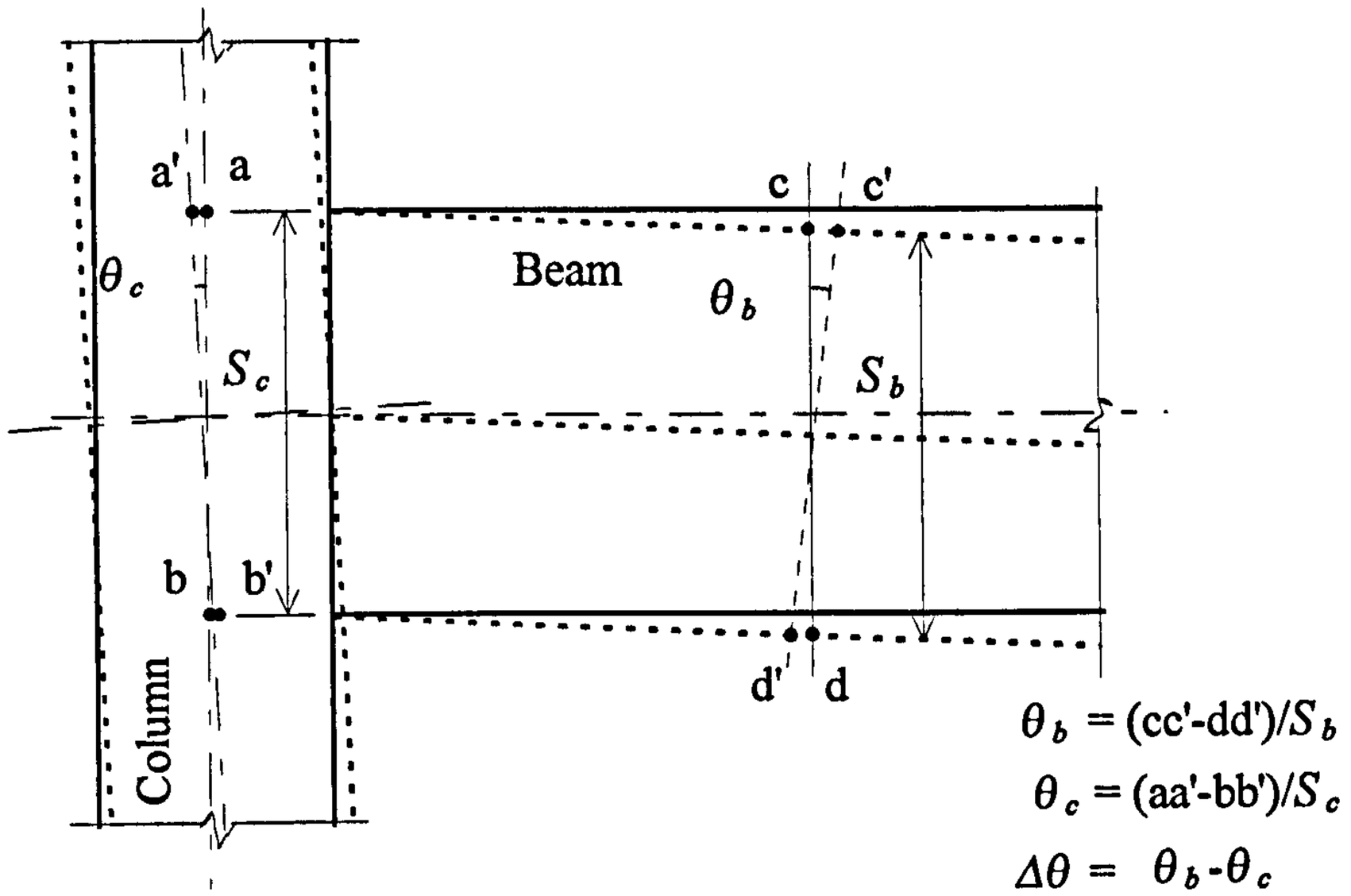

Figure 6.16 *Rotation measurement Method 3*

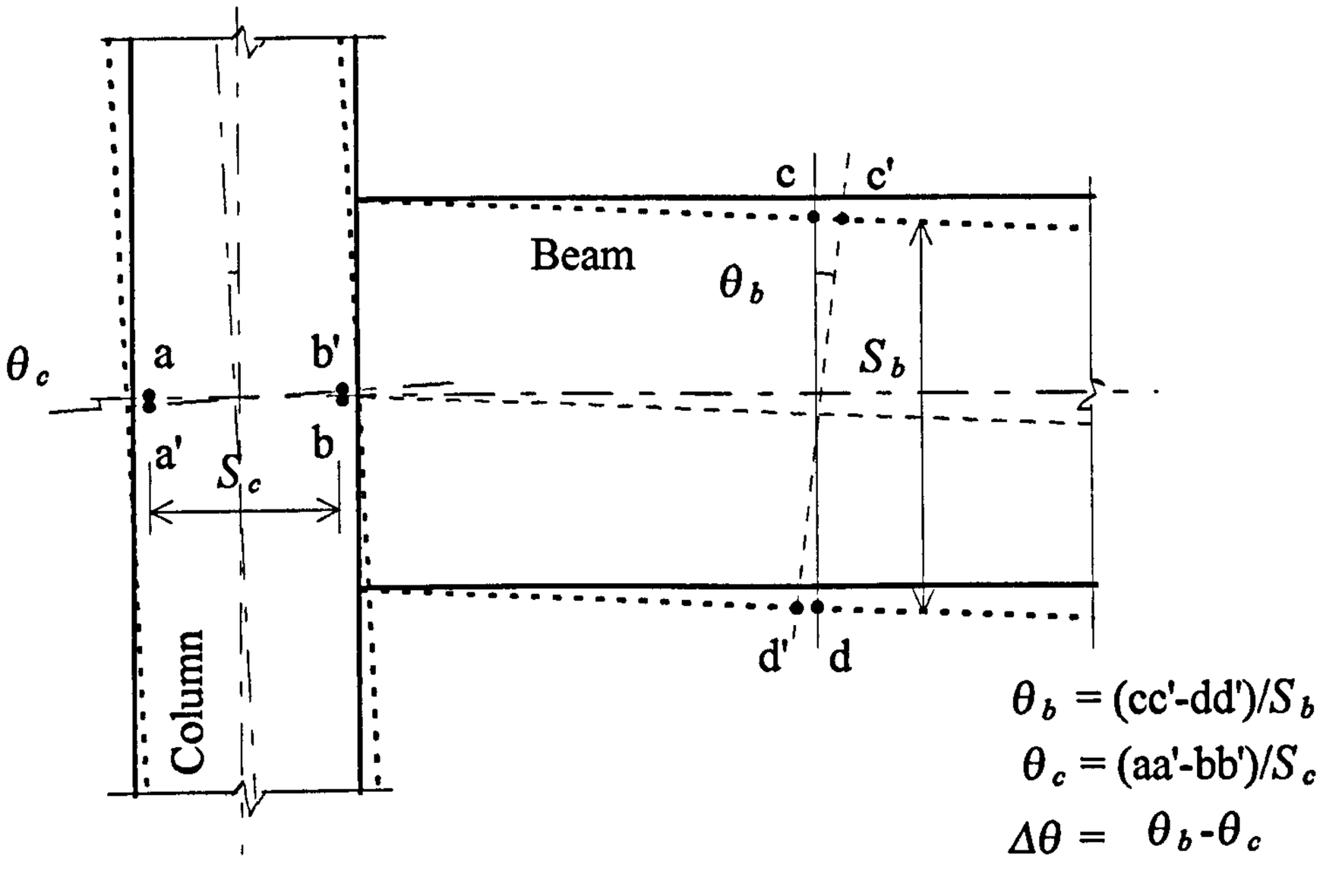

Figure 6.17 *Rotation measurement Method 4*

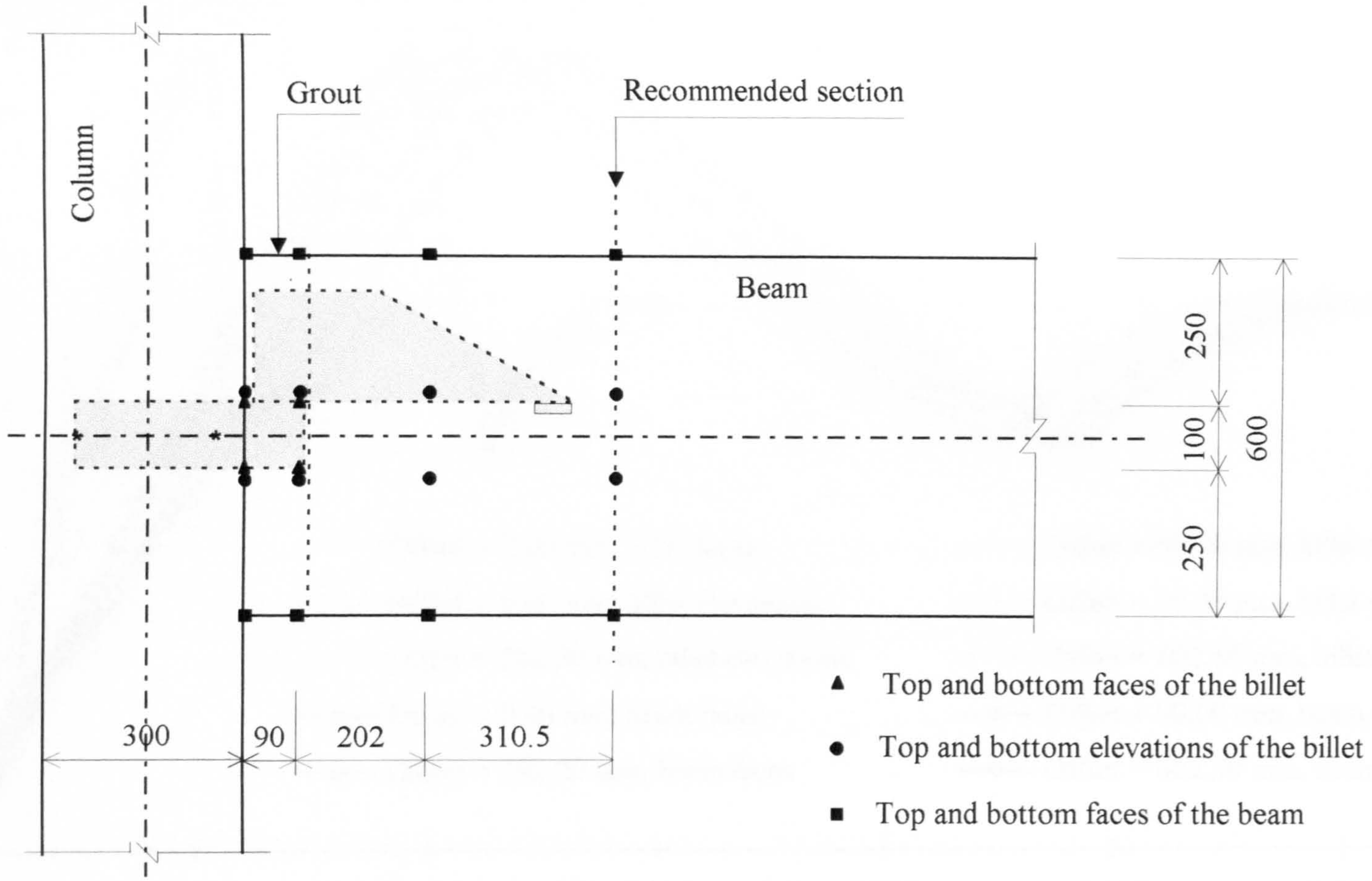

Figure 6.18 *Positions for the rotation measurement*

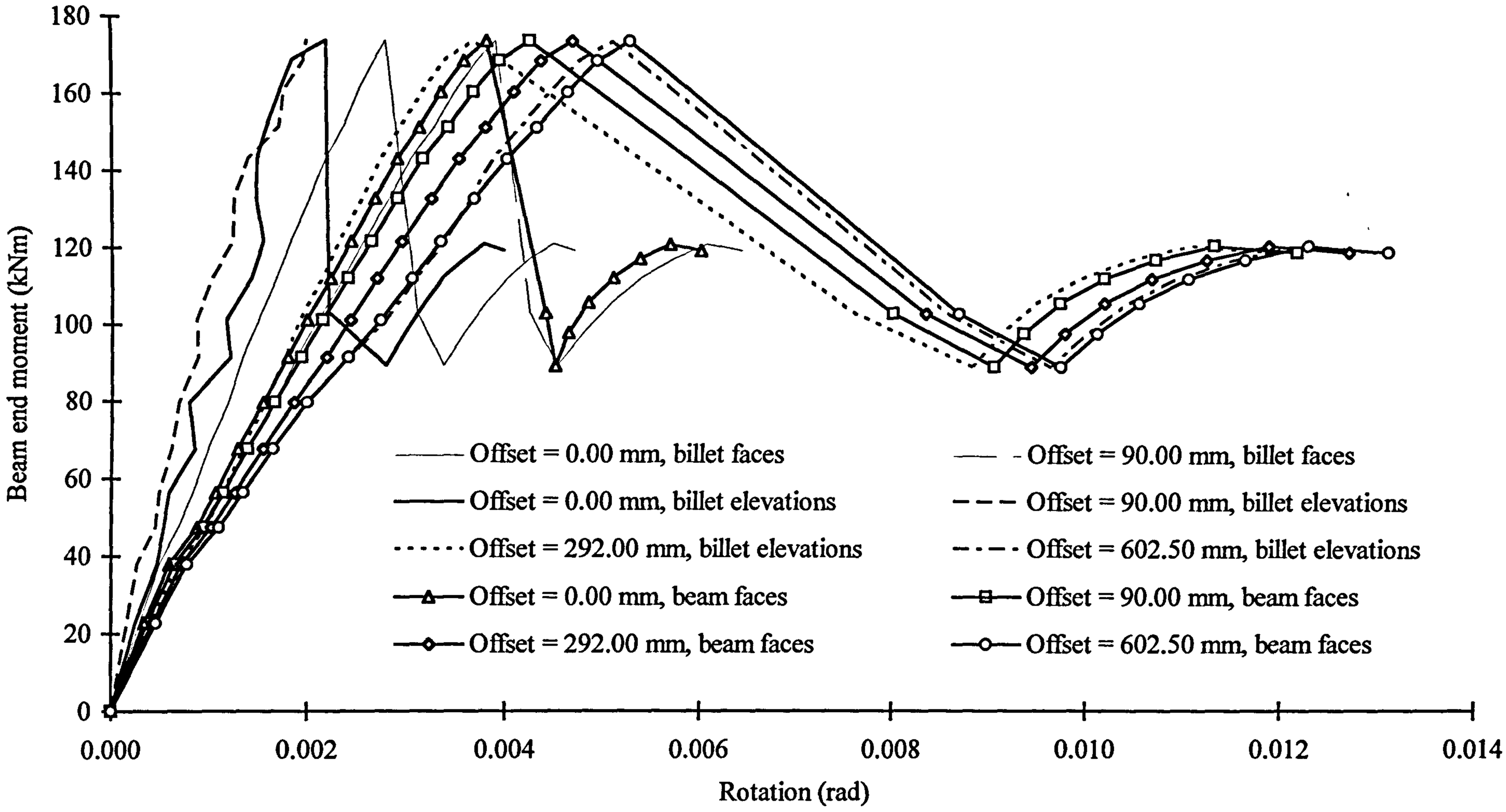

Figure 6.19(a) *Influence of the measurement positions to the rotations for TW4 with a 40 mm column mid-height displacement*

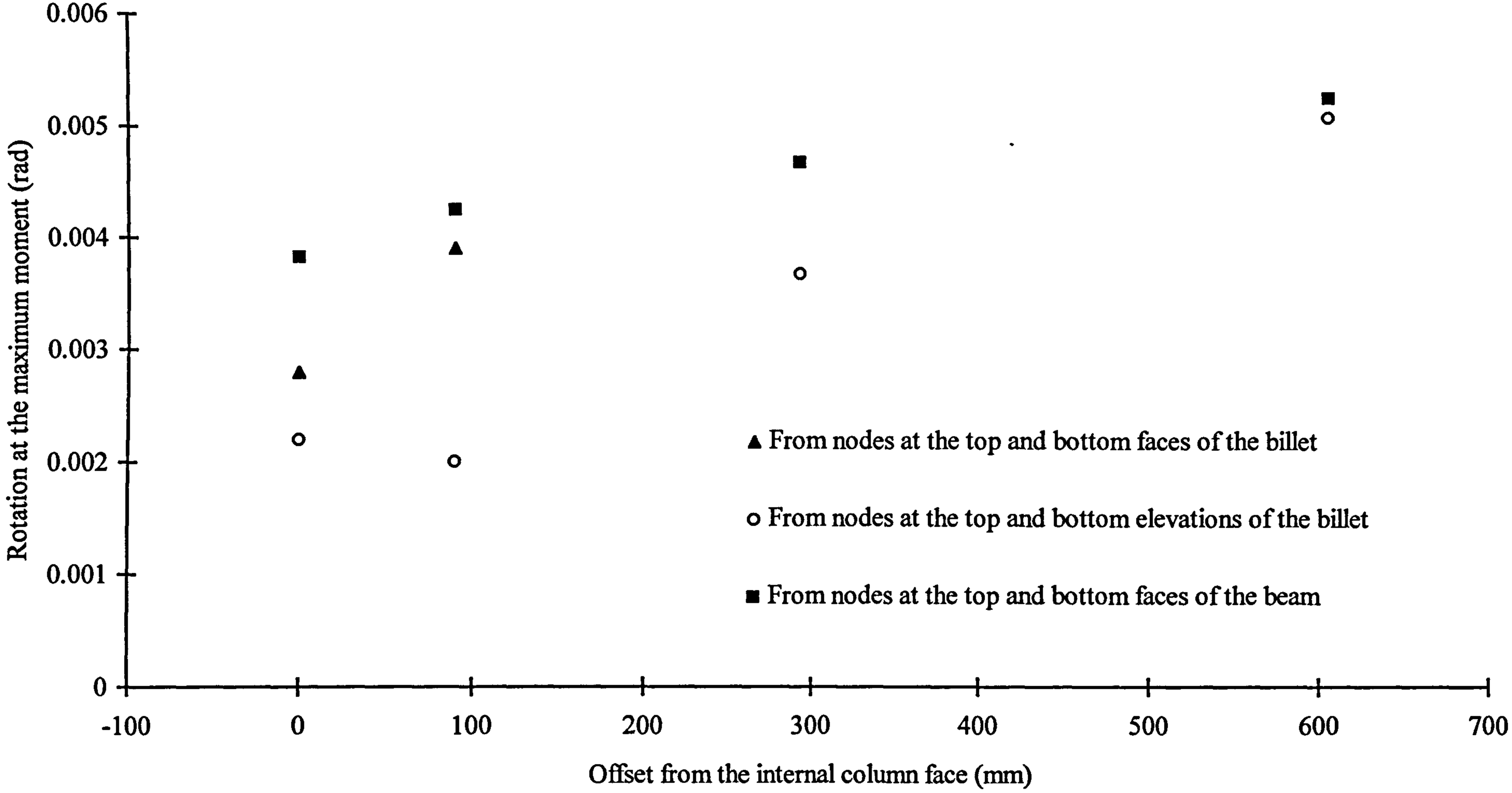

Figure 6.19(b) *Influence of the measurement positions to the rotations for TW4 with a 40 mm column mid-height displacement*

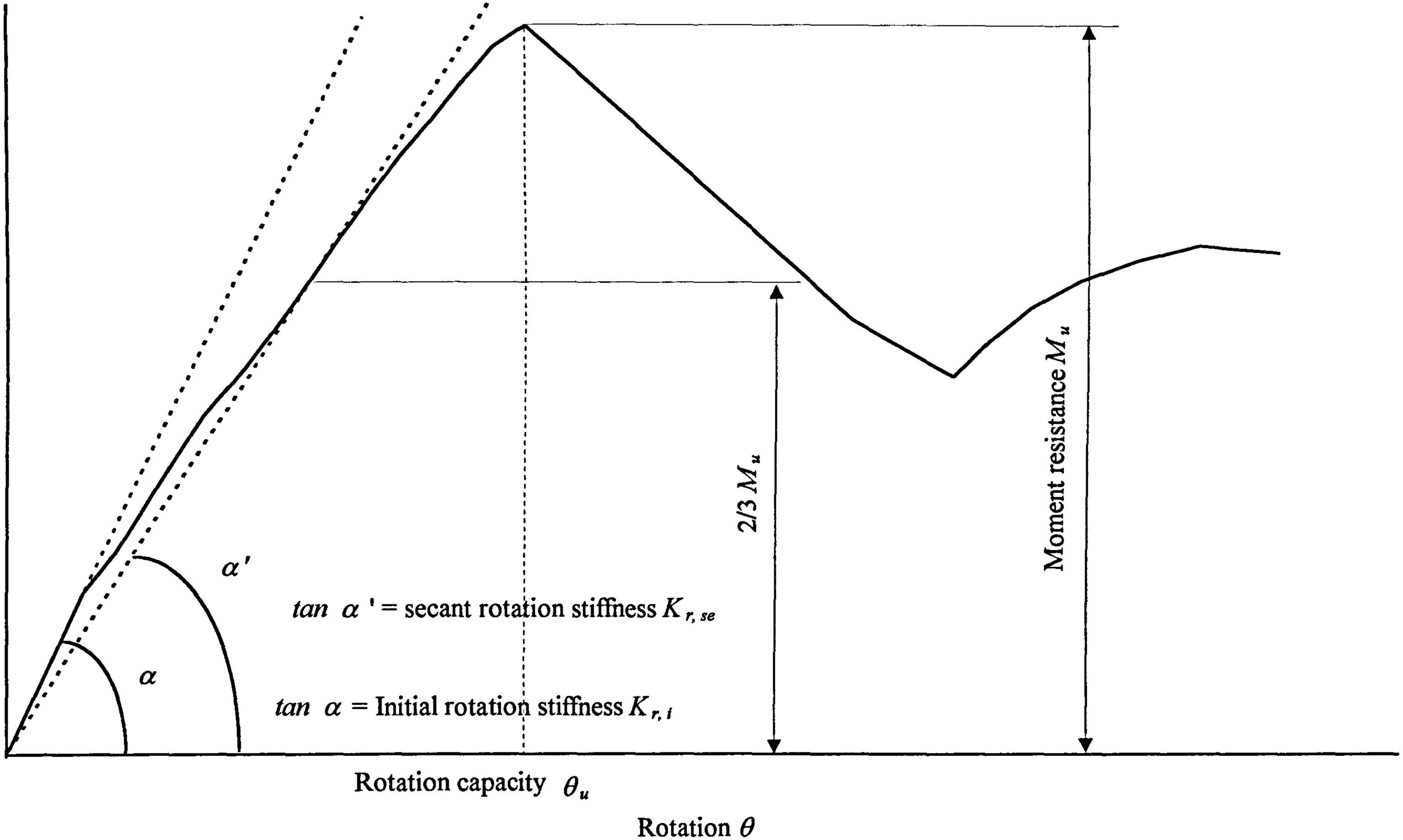

Figure 6.20 *Definition of the terms for analysing the numerical results*

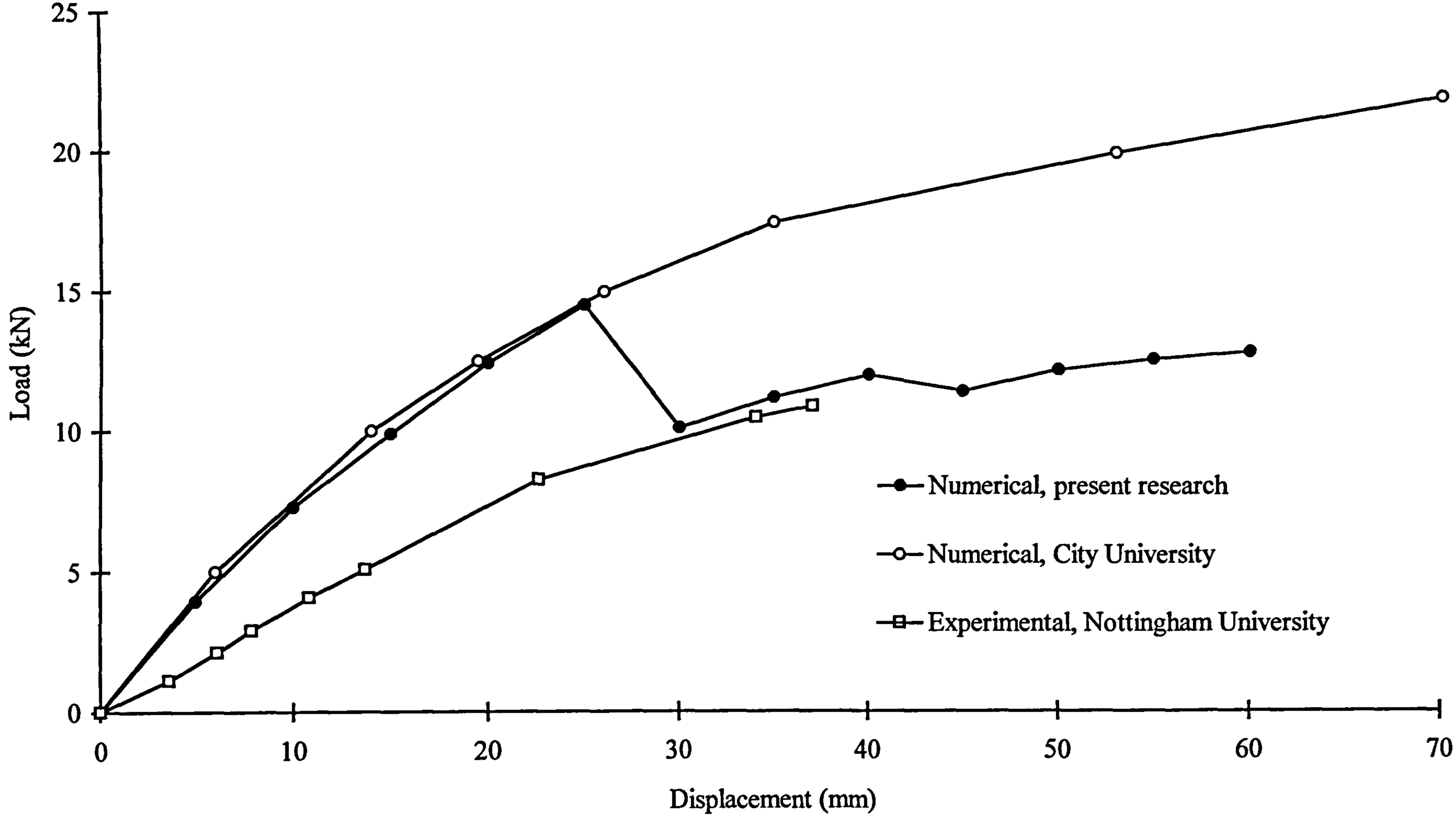

Figure 6.21 *Load-displacement relationships of the billet-welded plate joint TW1*

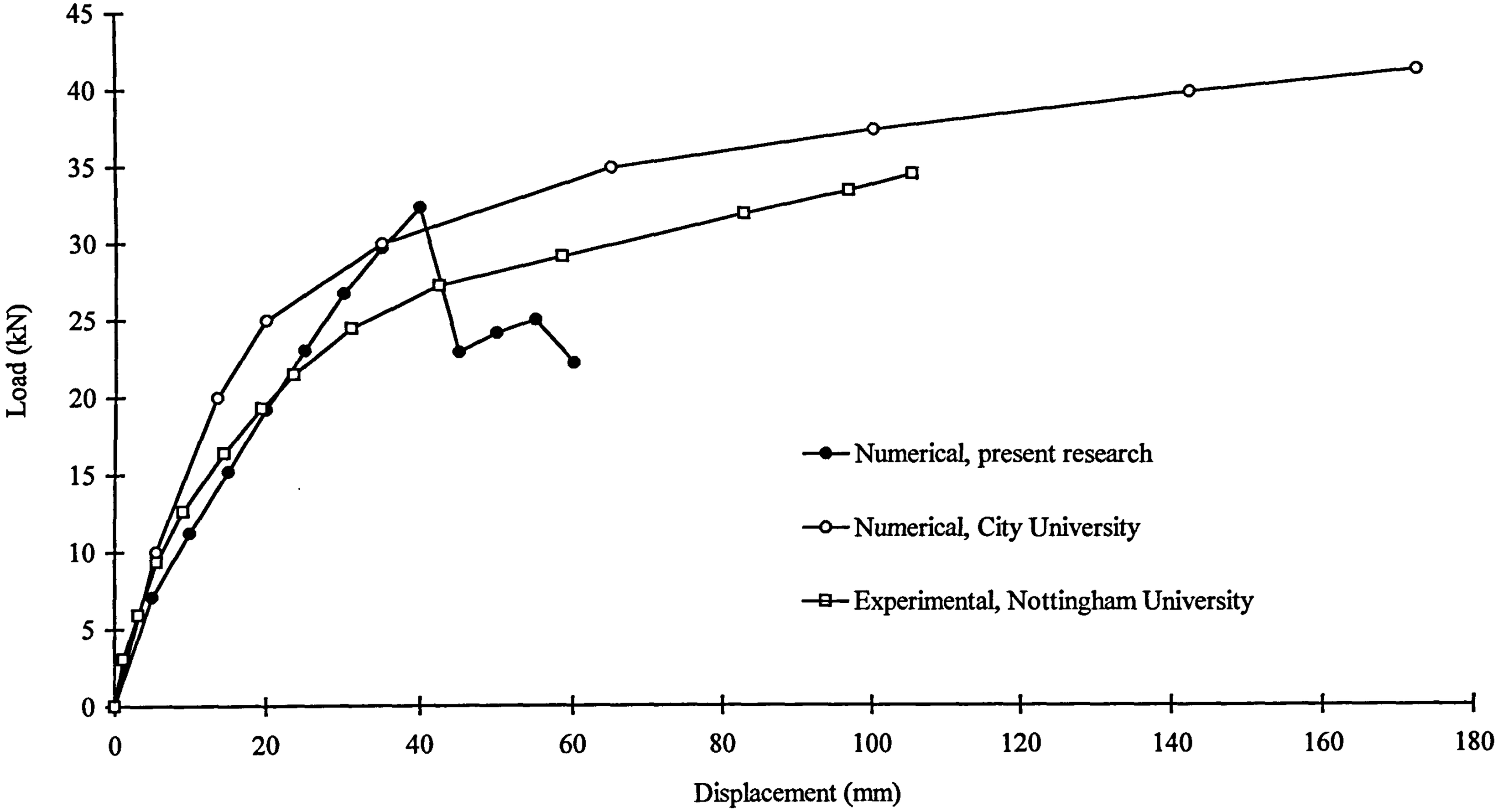

Figure 6.22 *Load-displacement relationships of the billet-welded plate joint TW2*

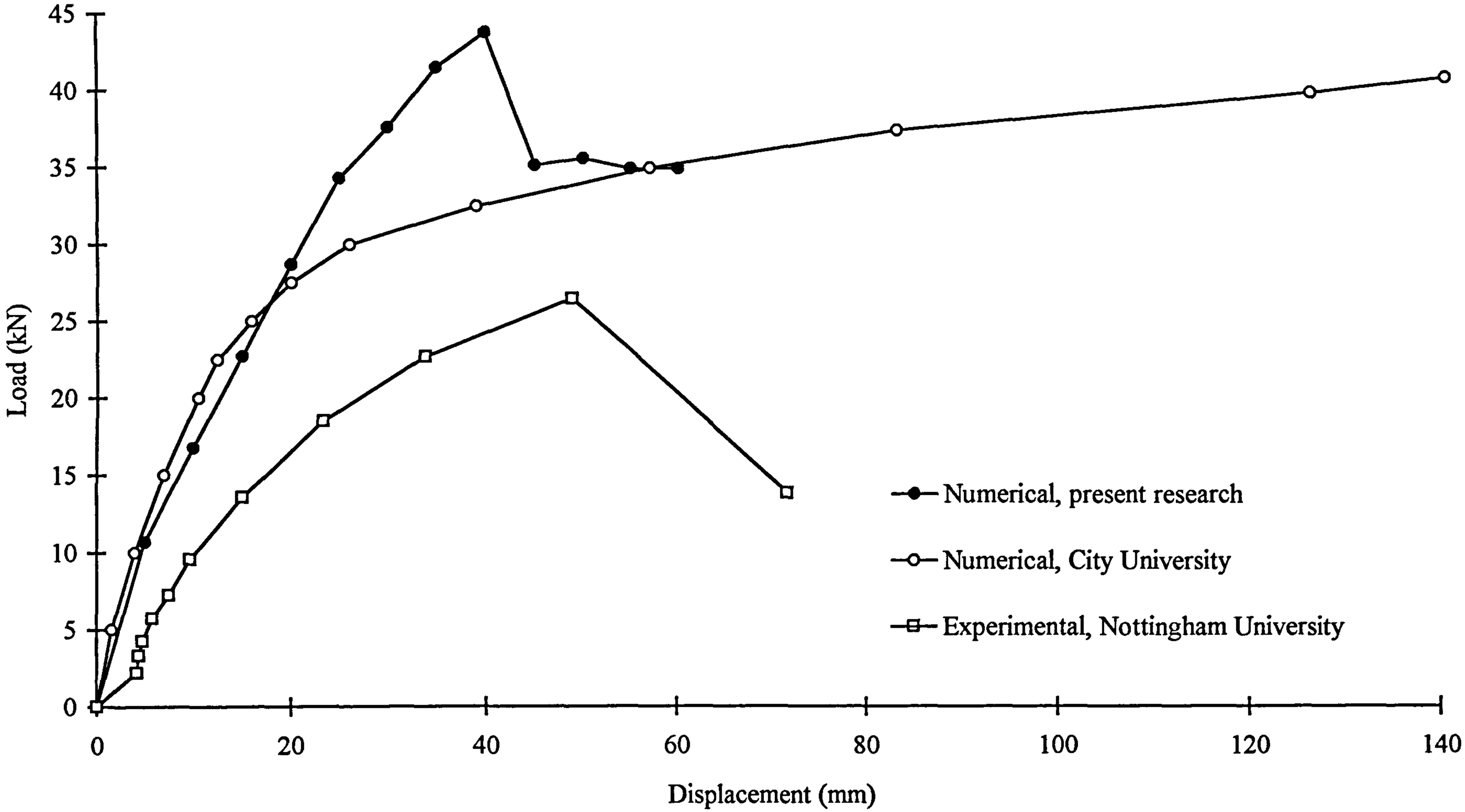

Figure 6.23 *Load-displacement relationships of the billet-welded plate joint TW3*
Note: This case is named TW4 in Reference 14

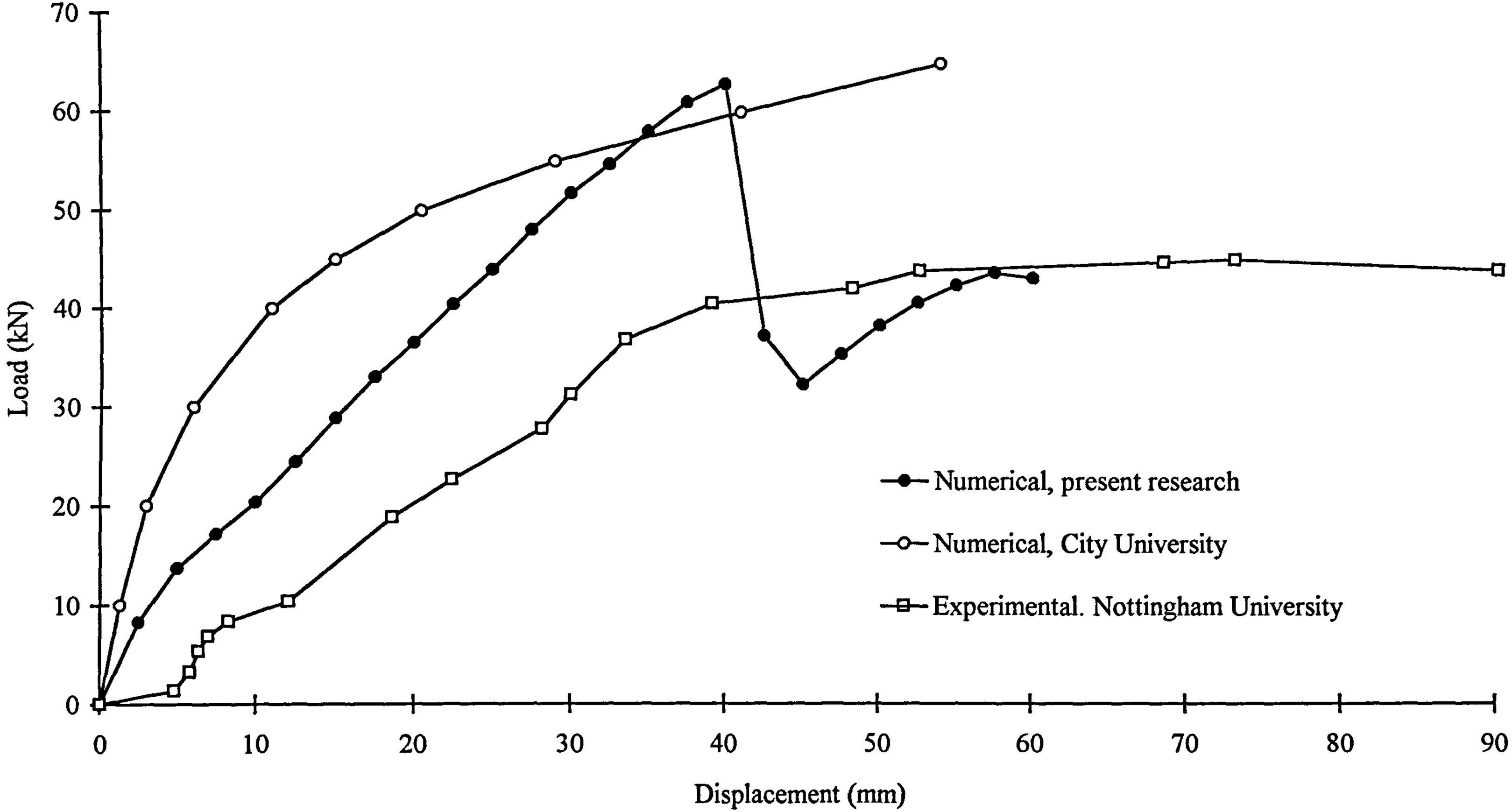

Figure 6.24 *Load-displacement relationships of the billet-welded plate joint TW4*
Note: This case is named TW3 in Reference 14

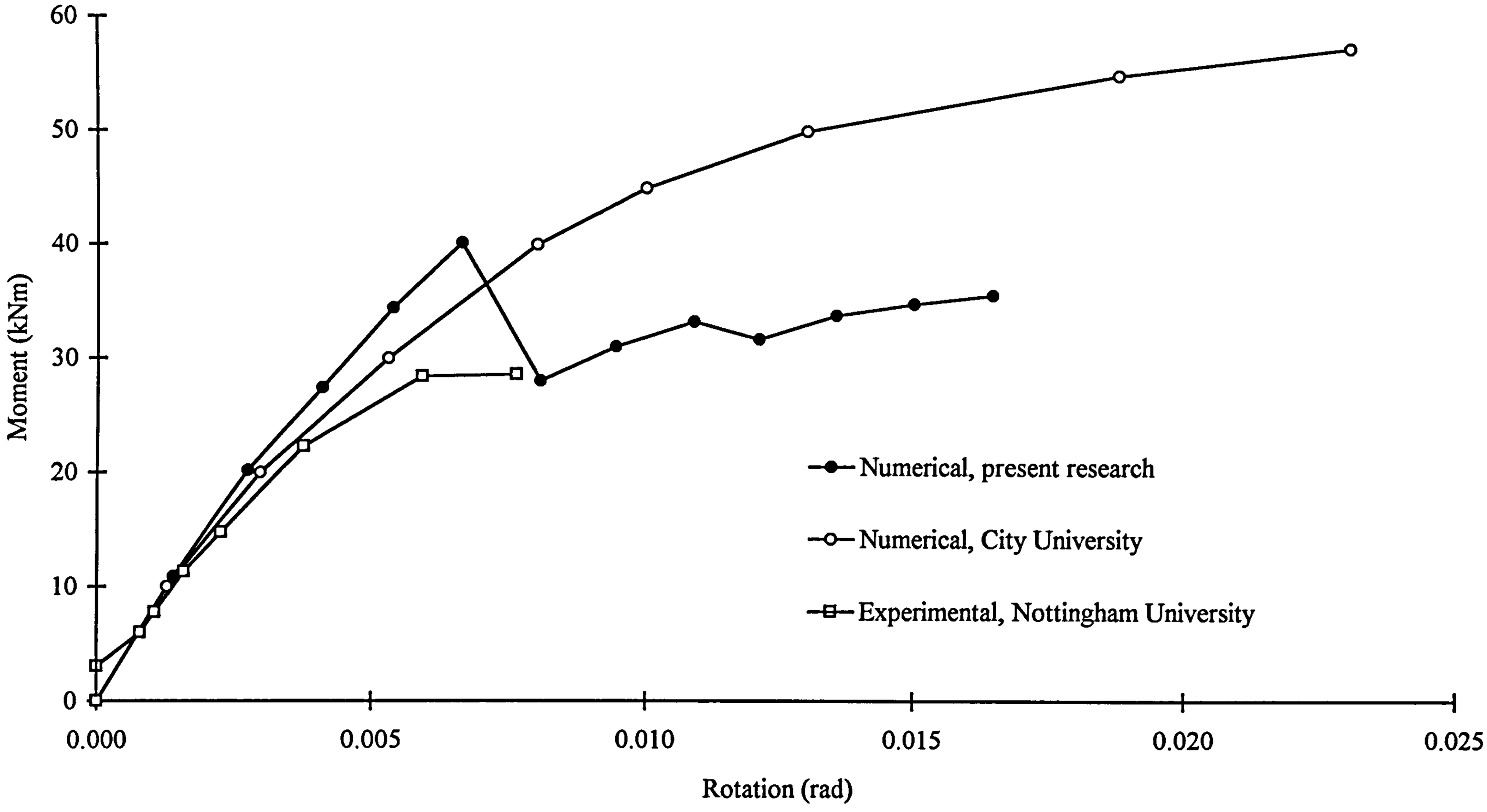

Figure 6.25 *Moment-rotation relationships of the billet-welded plate joint TW1*

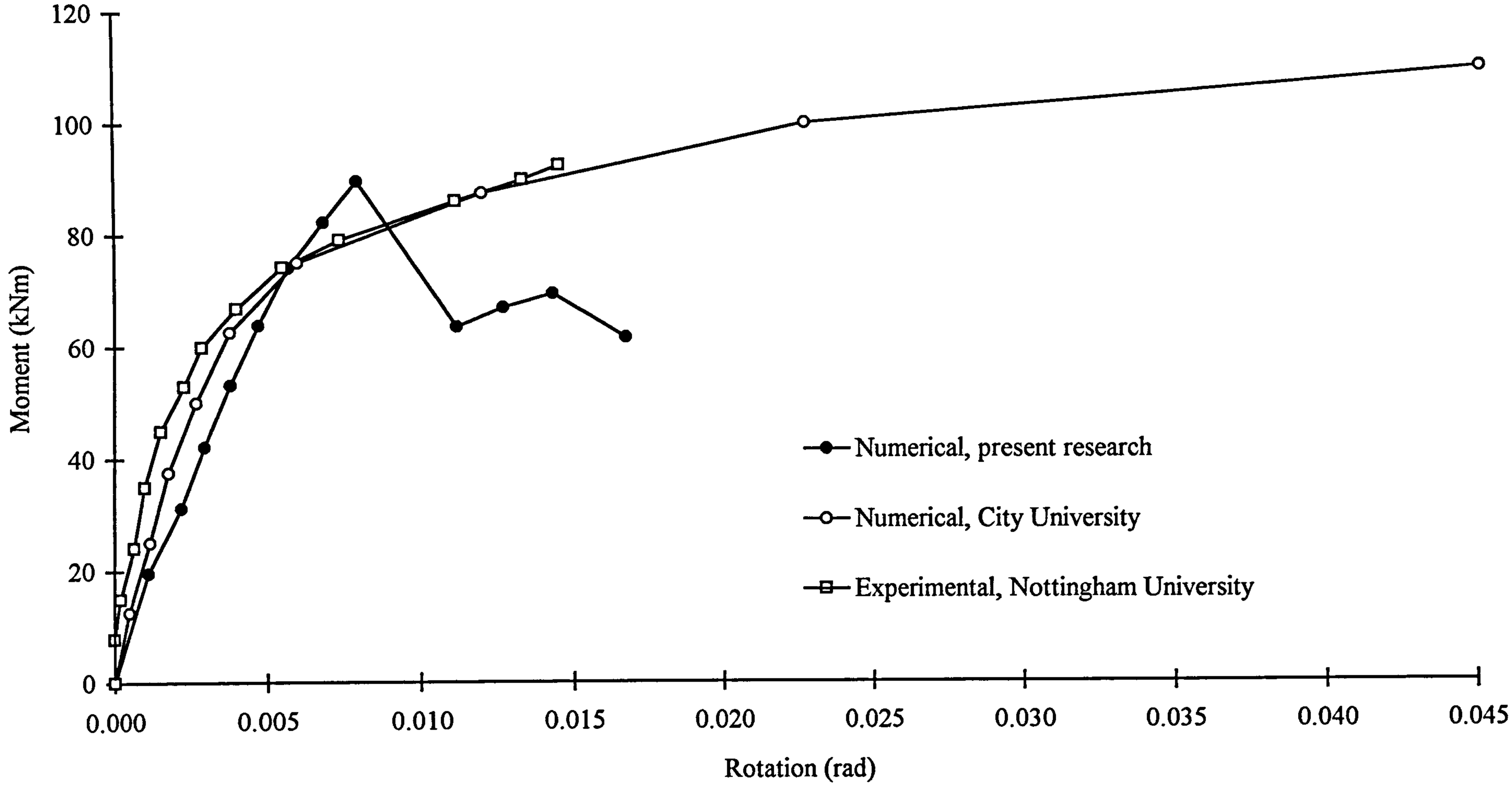

Figure 6.26 *Moment-rotation relationships of the billet-welded plate joint TW2*

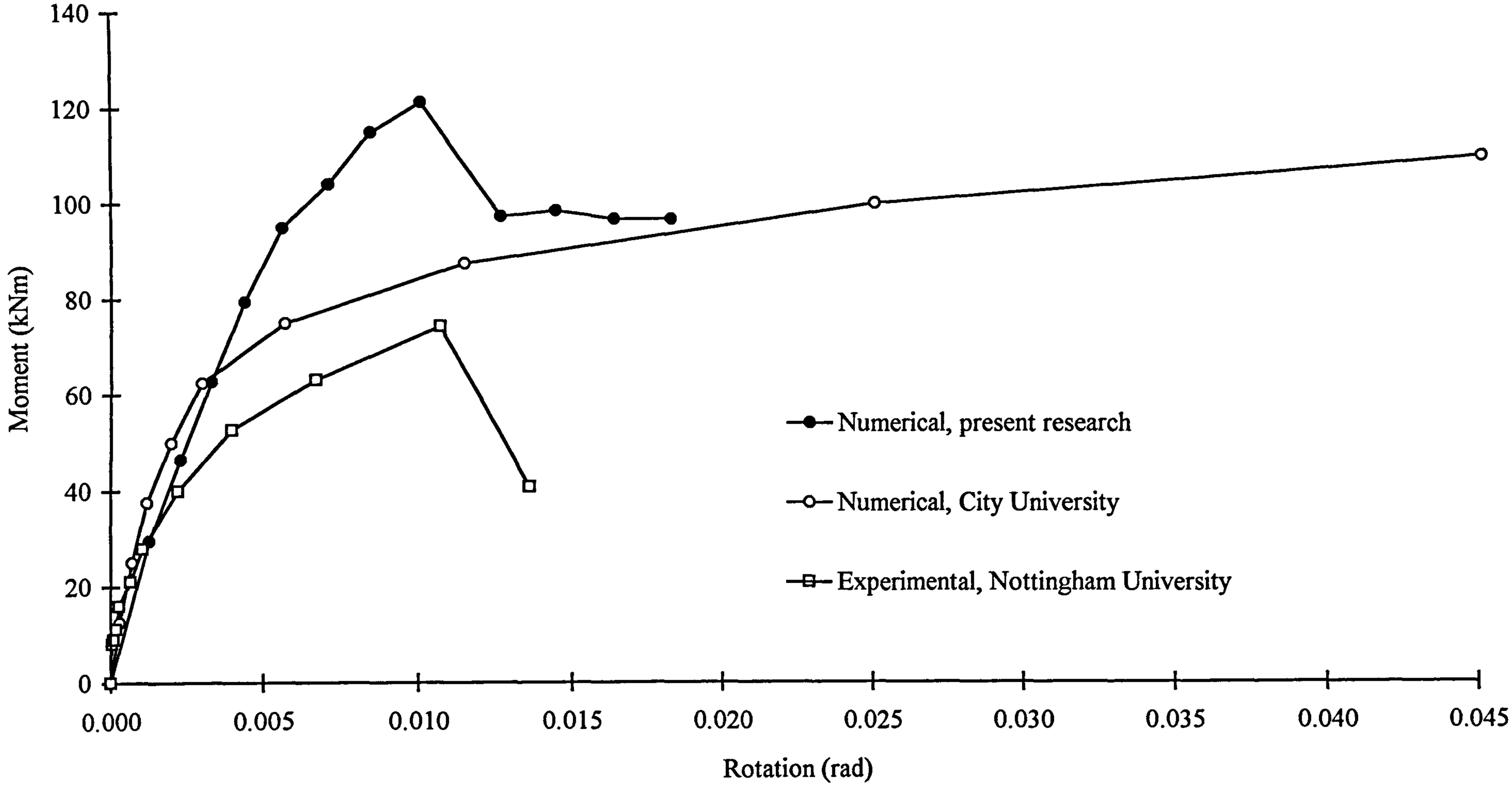

Figure 6.27 *Moment-rotation relationships of the billet-welded plate joint TW3*
Note: This case is named TW4 in Reference 14

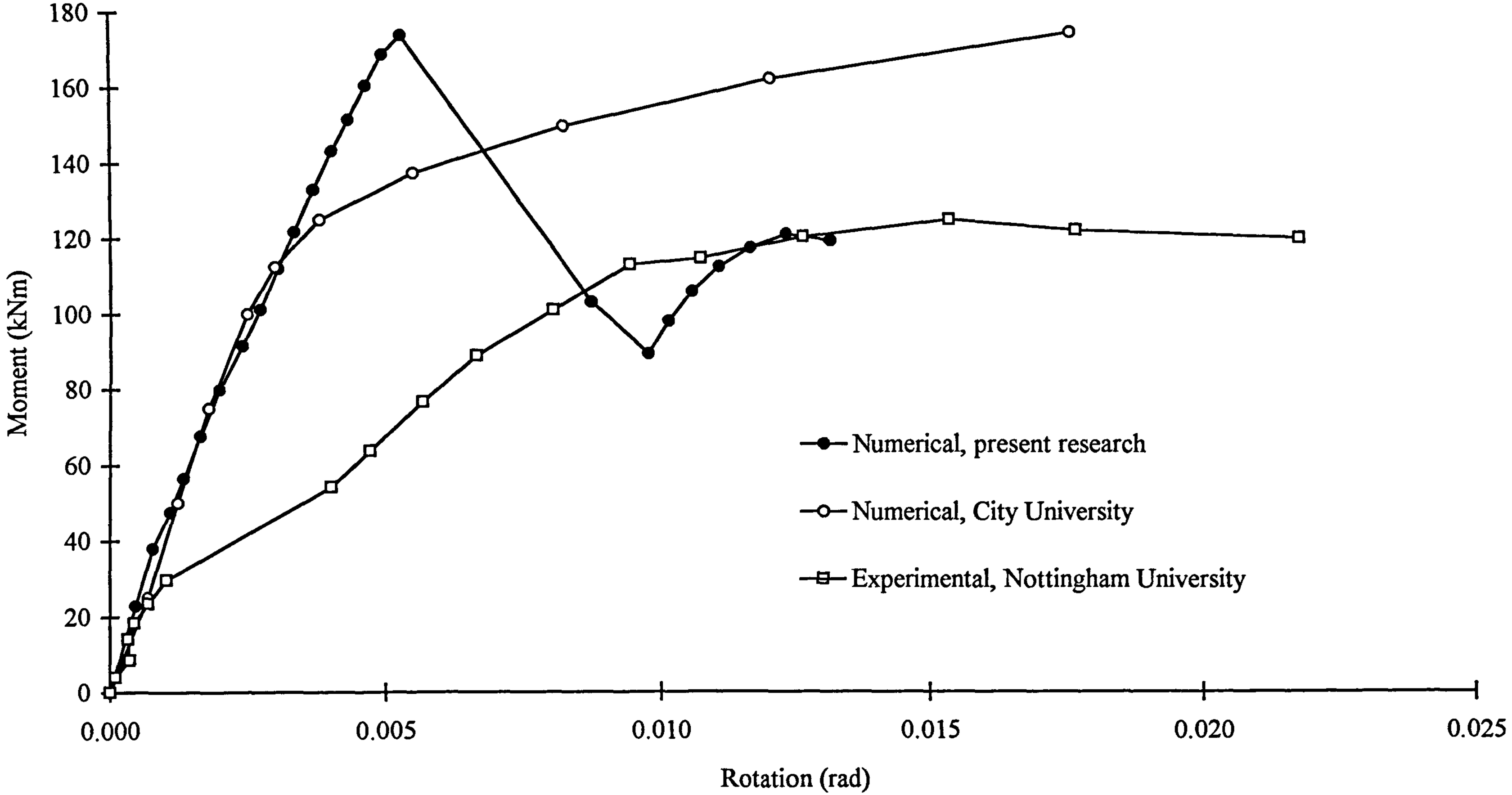

Figure 6.28 *Moment-rotation relationships of the billet-welded plate joint TW4*
Note: This case is named TW3 in Reference 14

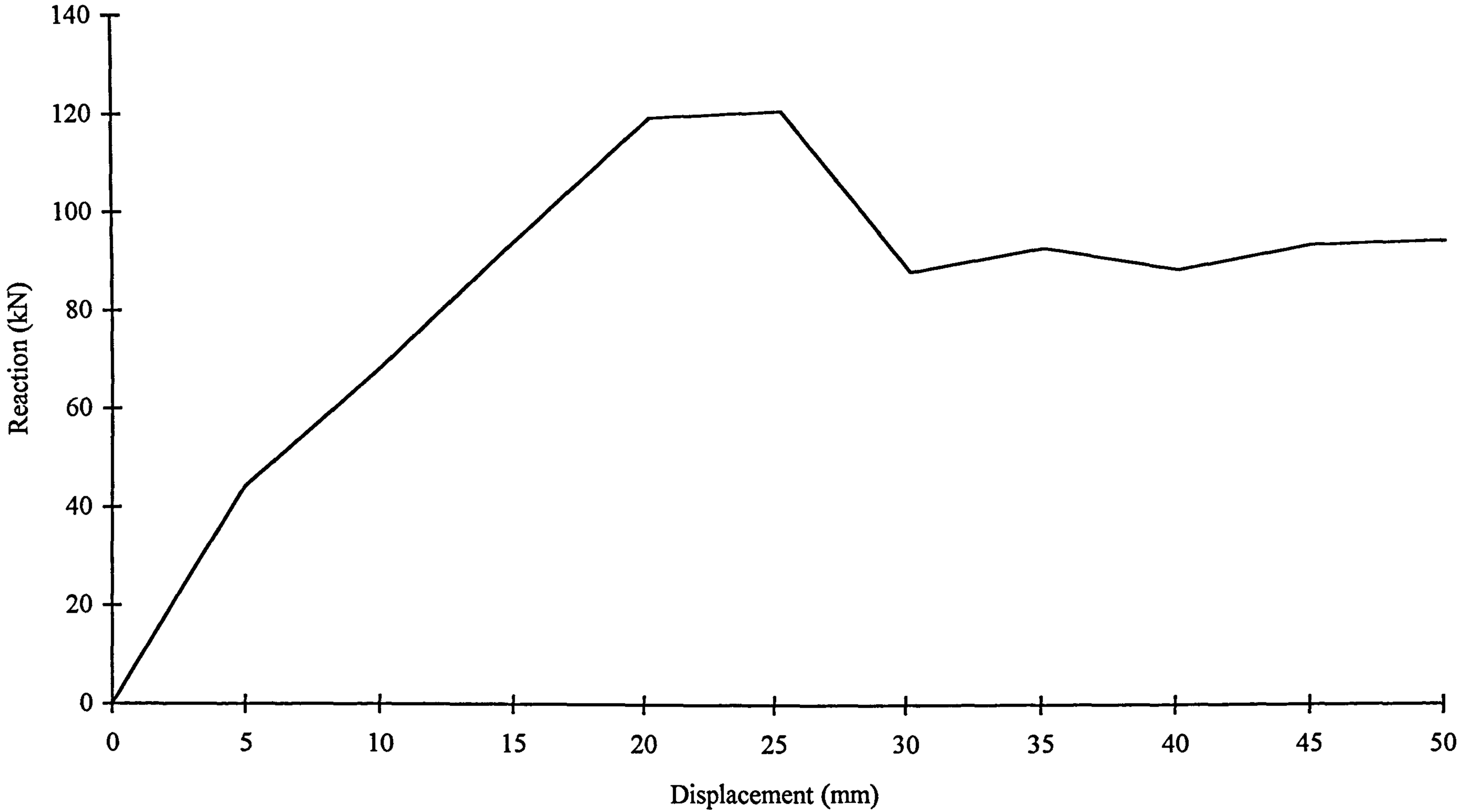

Figure 6.29 *The numerical result for the reaction at the beam mid-span versus the relevant displacement in TW1(A)*

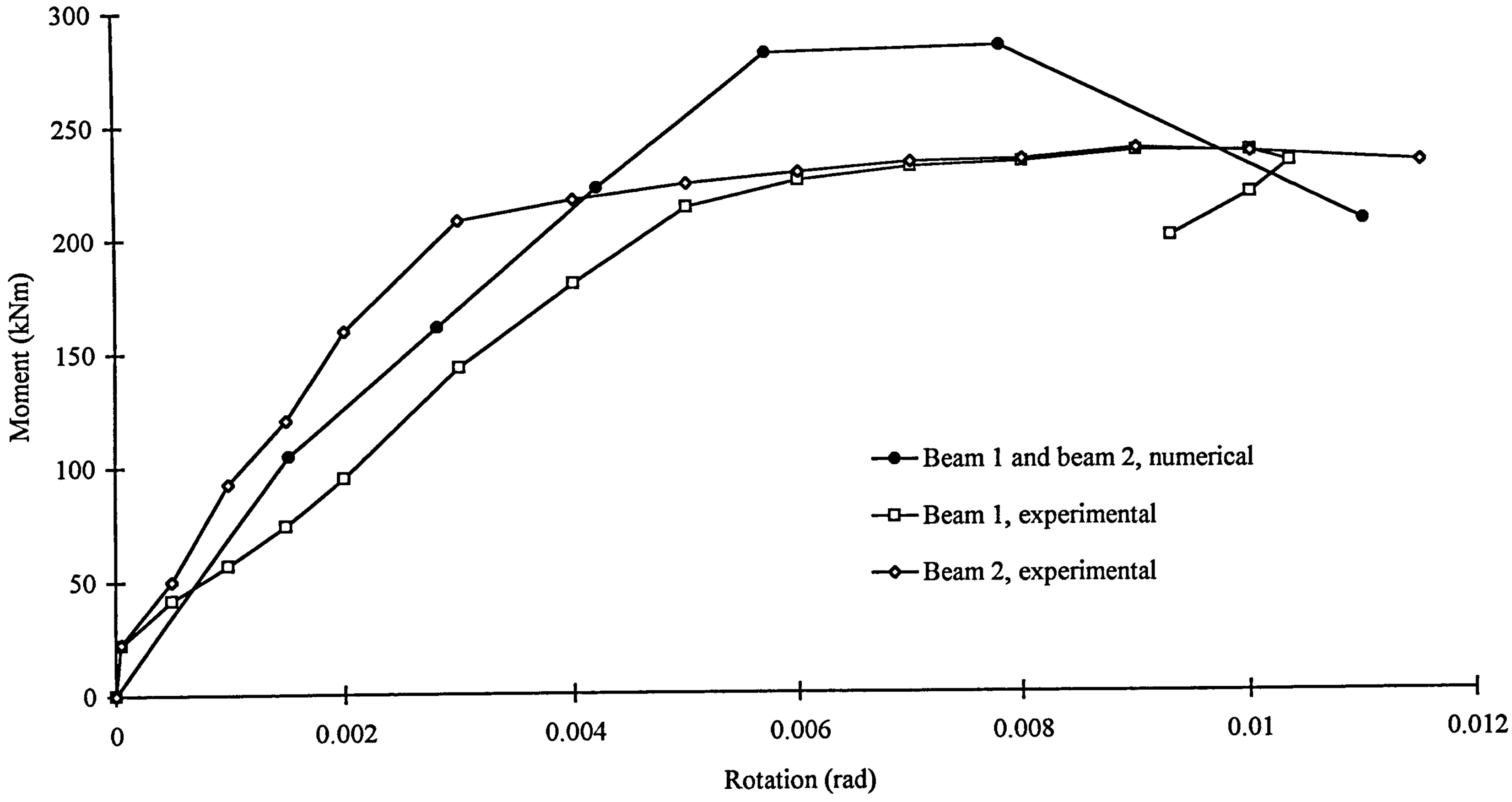

Figure 6.30 *Beam end moment versus rotation for TW1(A)*

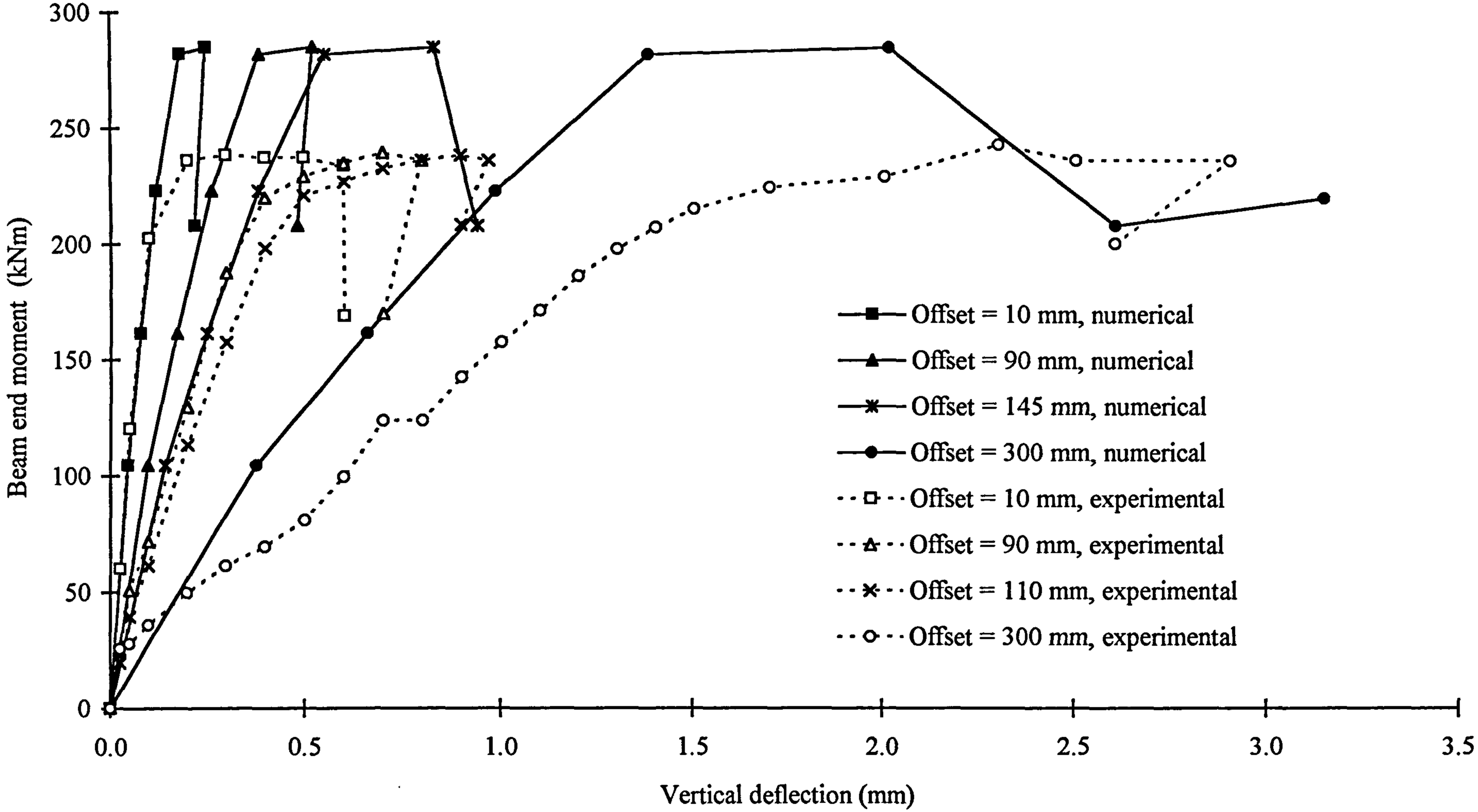

Figure 6.31 *Beam end moment versus vertical deflection in beam 1 in TW1(A)*

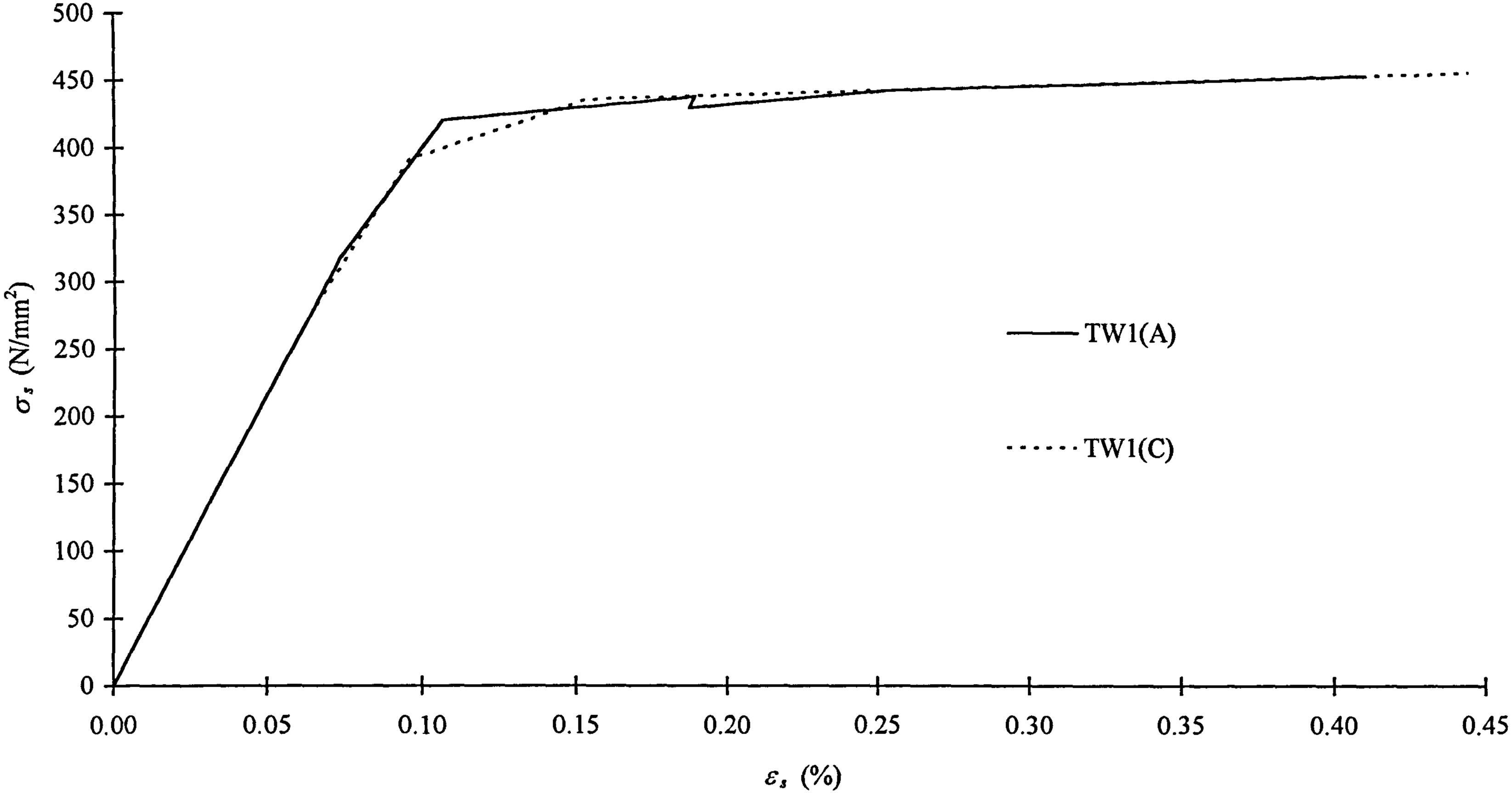

Figure 6.32 *Stress-strain responses of the tie bars in the joints with slabs*

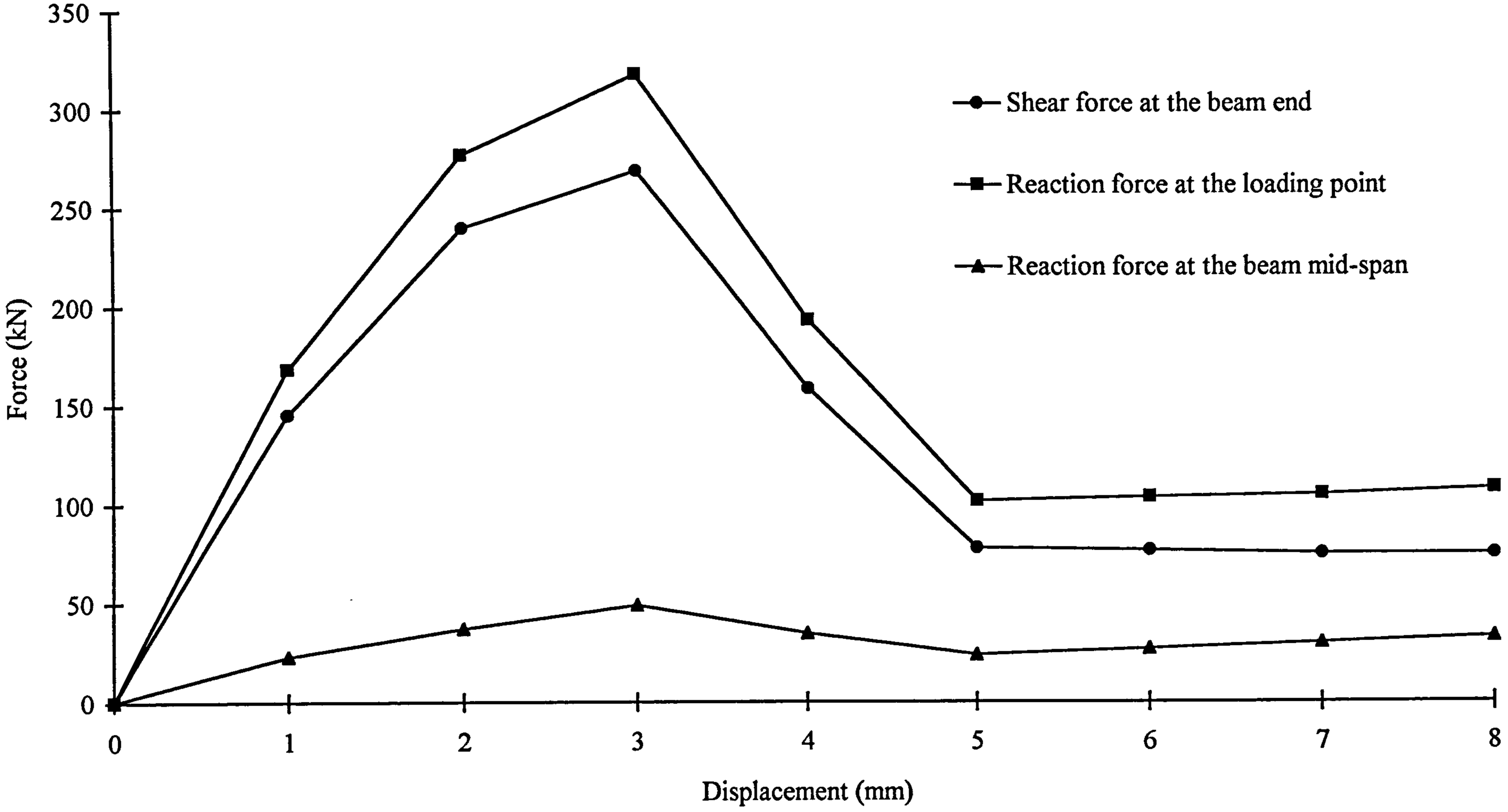

Figure 6.33 *Relationships of force versus displacement at the loading point for TW1(C)*

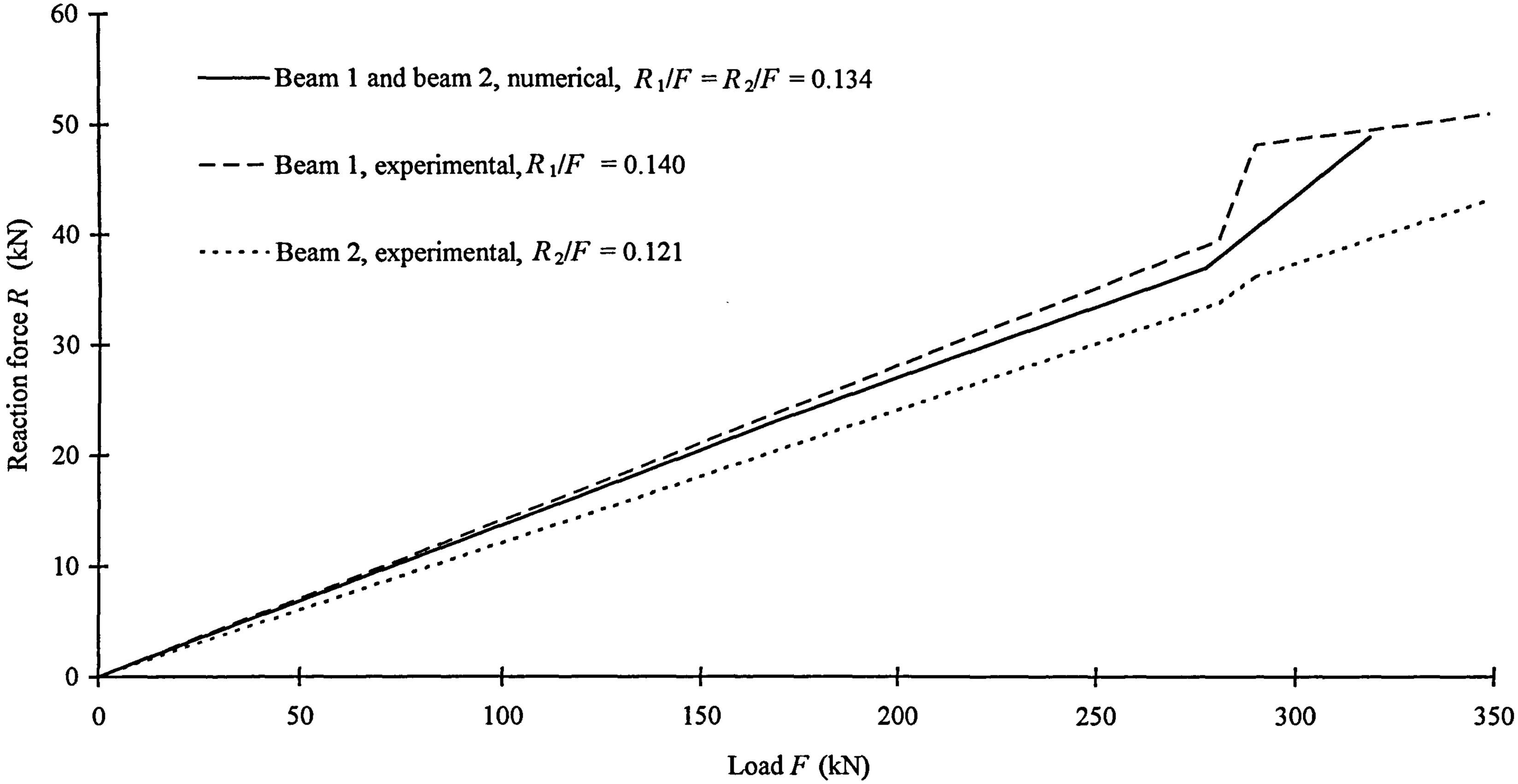

Figure 6.34 *Relationships between reaction force and load for TW1(C)*

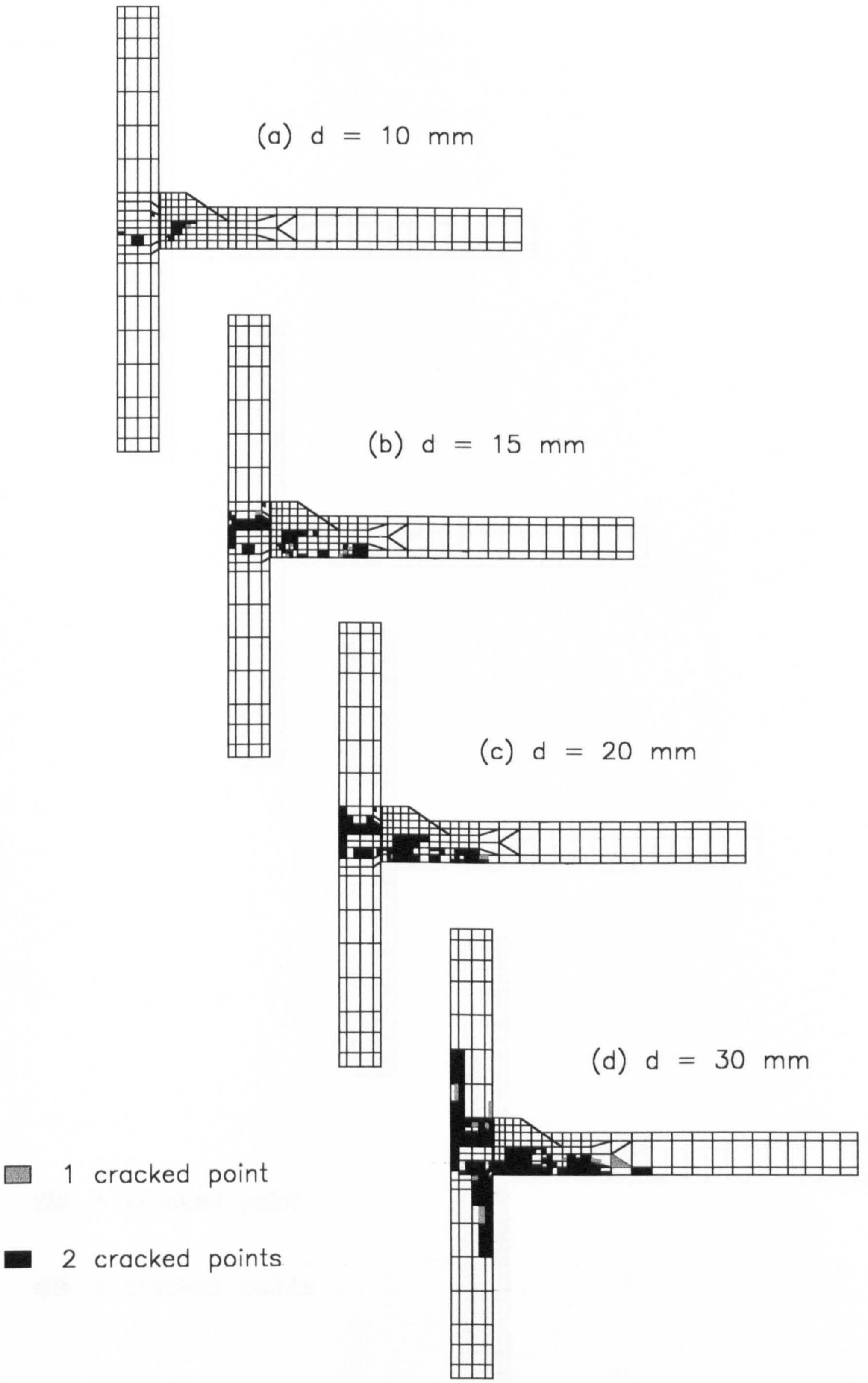

Figure 6.35(a) *Cracking status in the first (i.e. nearest to the central line) element layer of TW1*

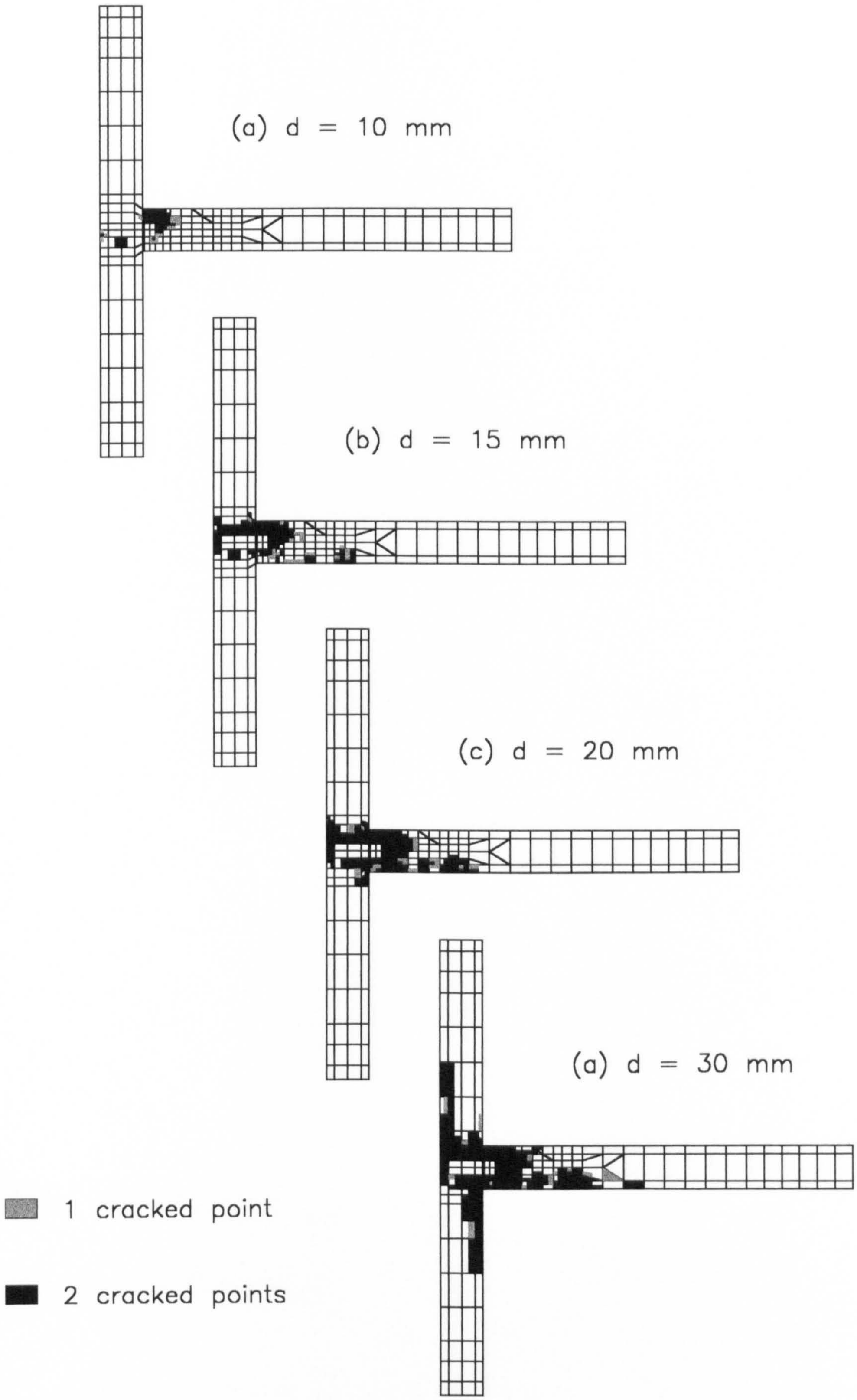

Figure 6.35(b) *Cracking status in the second element layer of TW1*

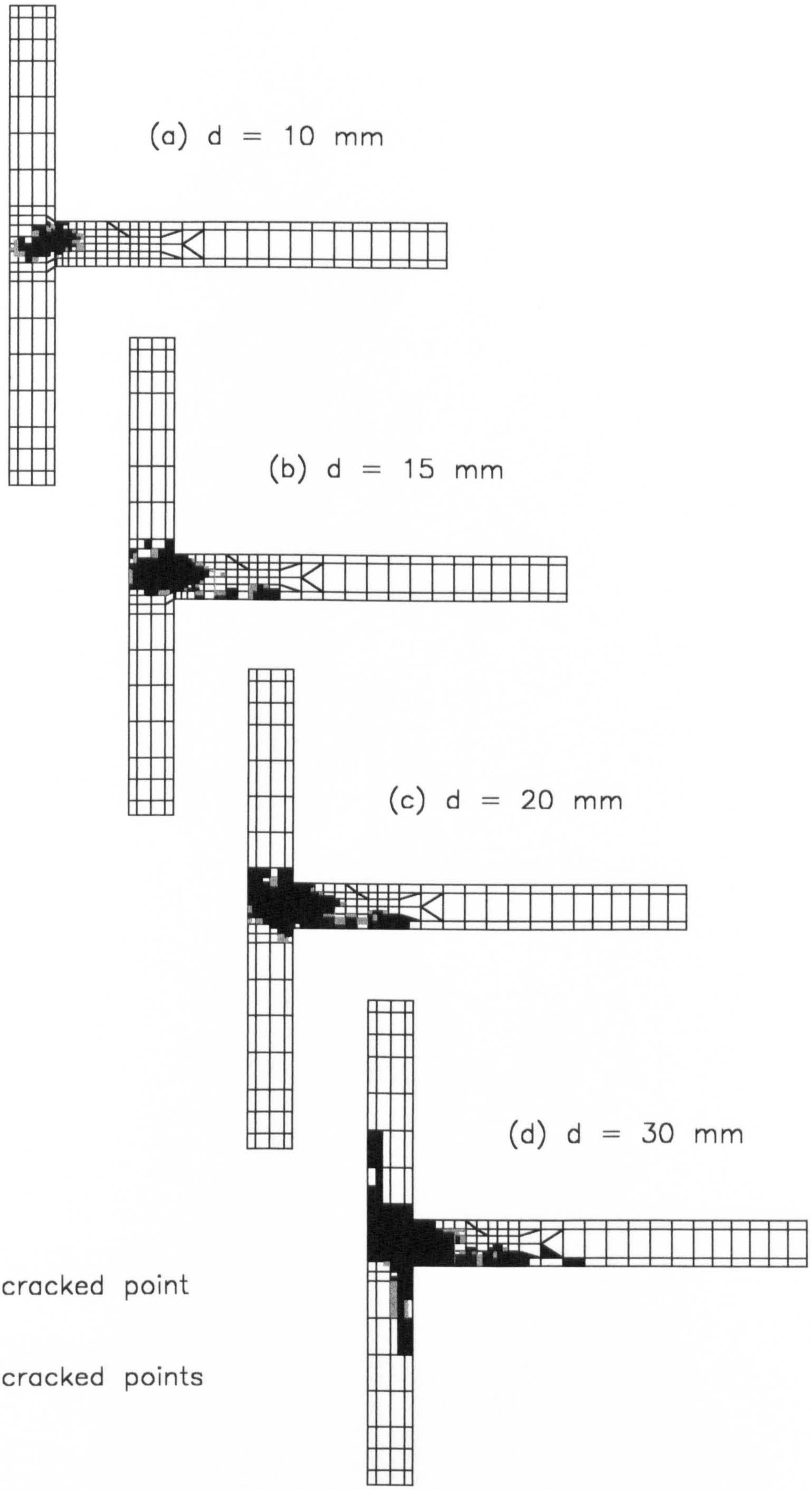

Figure 6.35(c) *Cracking status in the third element layer of TW1*

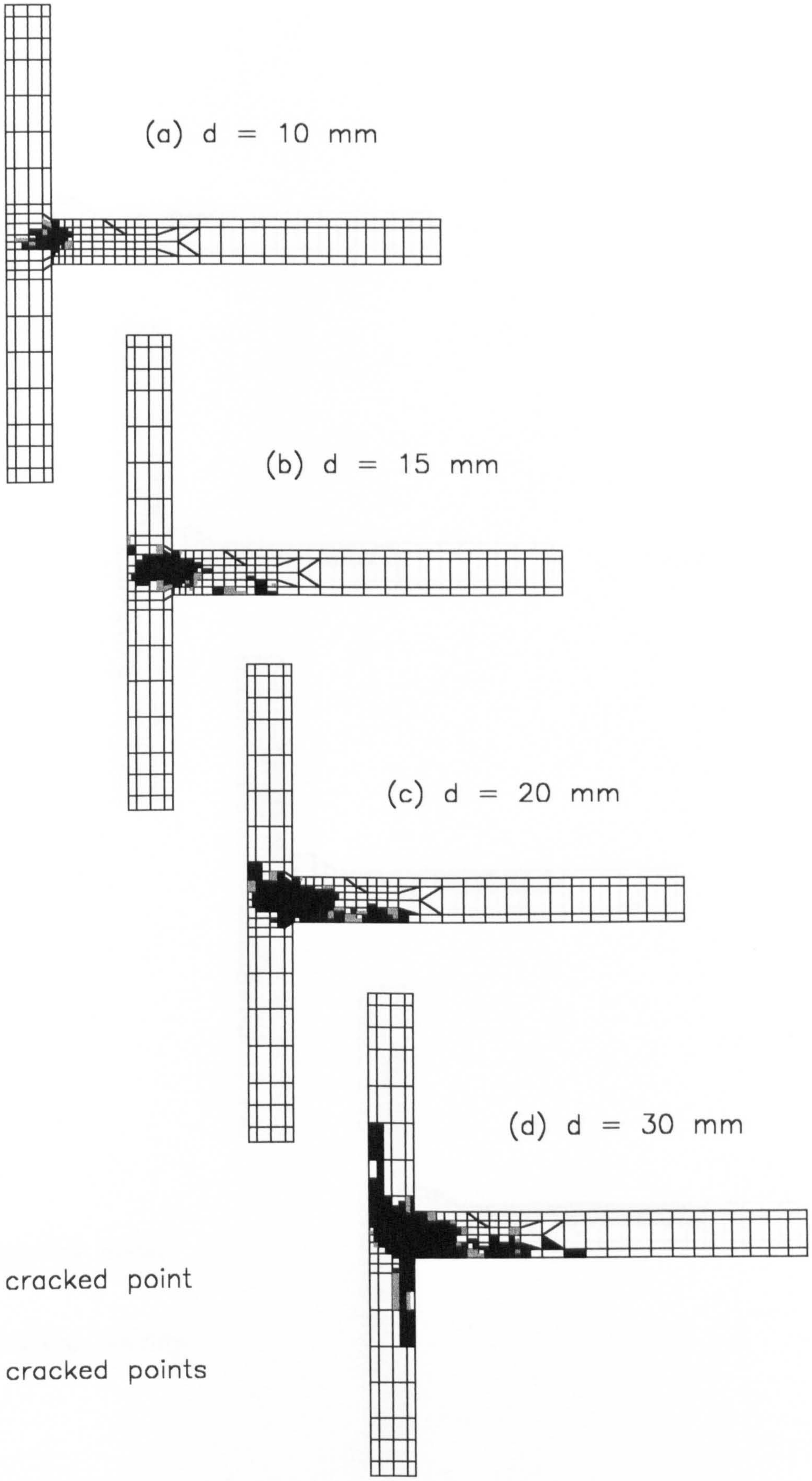

Figure 6.35(d) *Cracking status in the fourth (i.e. outside face) element layer of TW1*

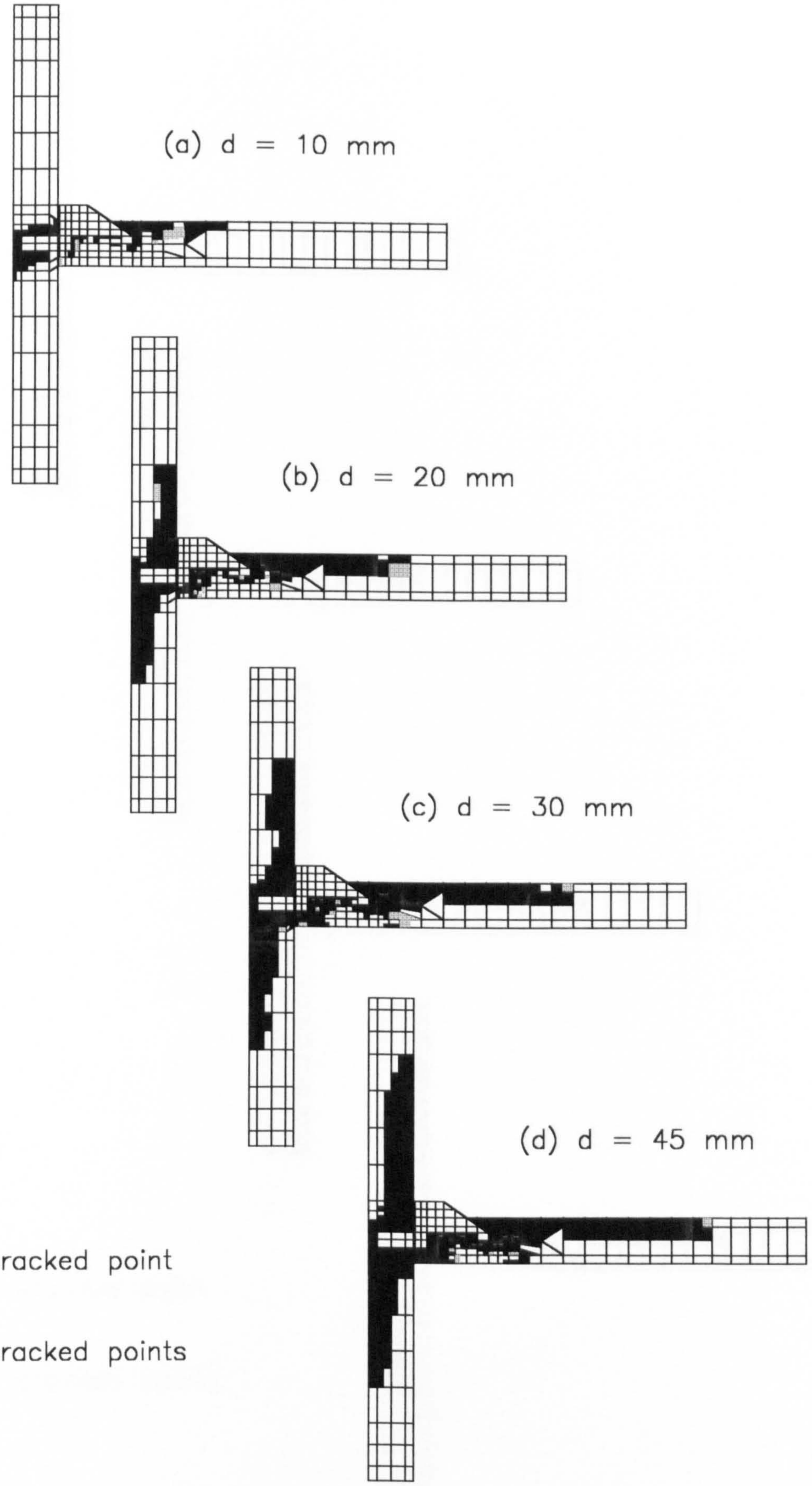

Figure 6.36(a) *Cracking status in the first (i.e. nearest to the central line) element layer of TW2*

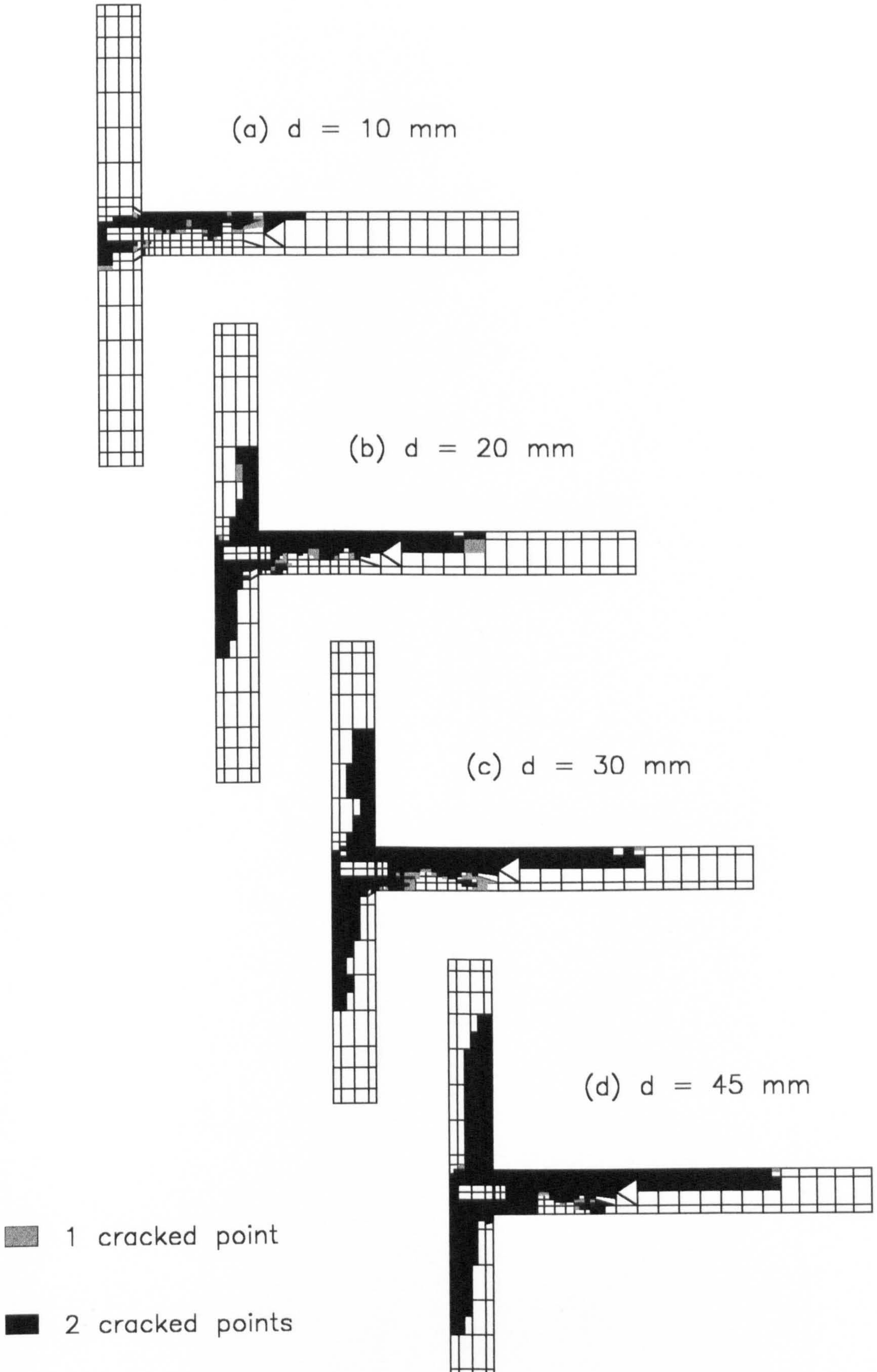

Figure 6.36(b) *Cracking status in the second element layer of TW2*

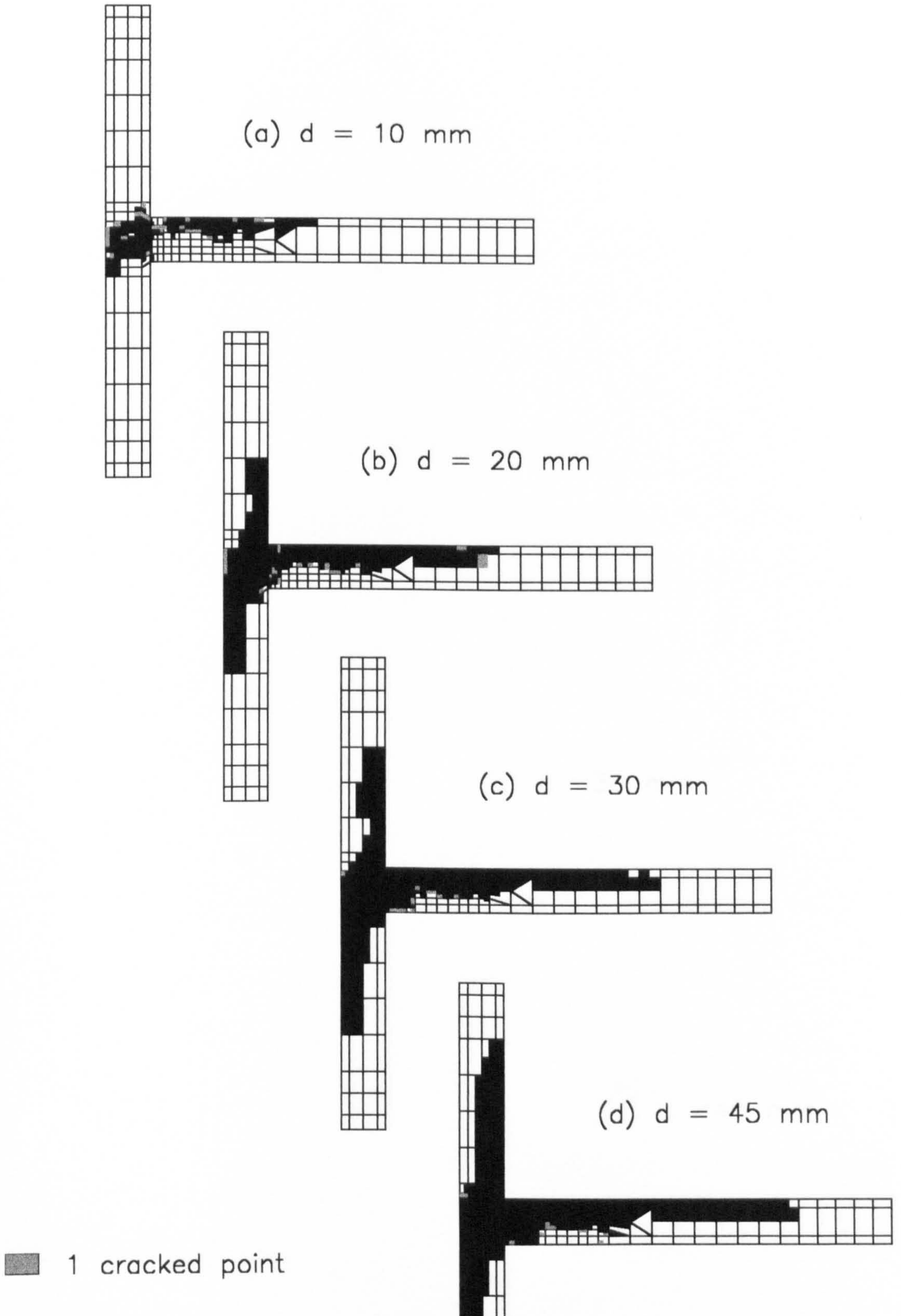

Figure 6.36(c) *Cracking status in the third element layer of TW2*

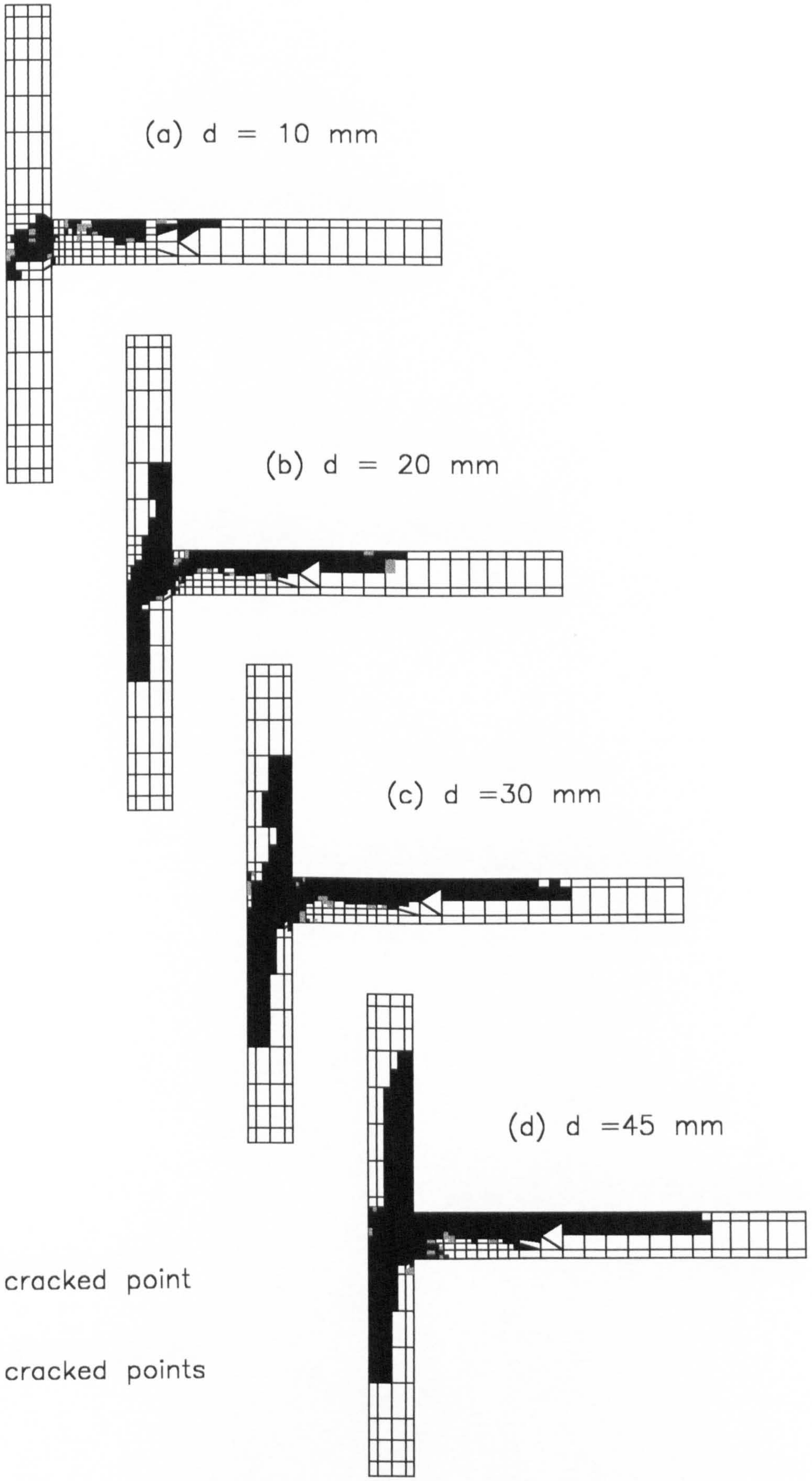

Figure 6.36(d) *Cracking status in the fourth (i.e. outside face) element layer of TW2*

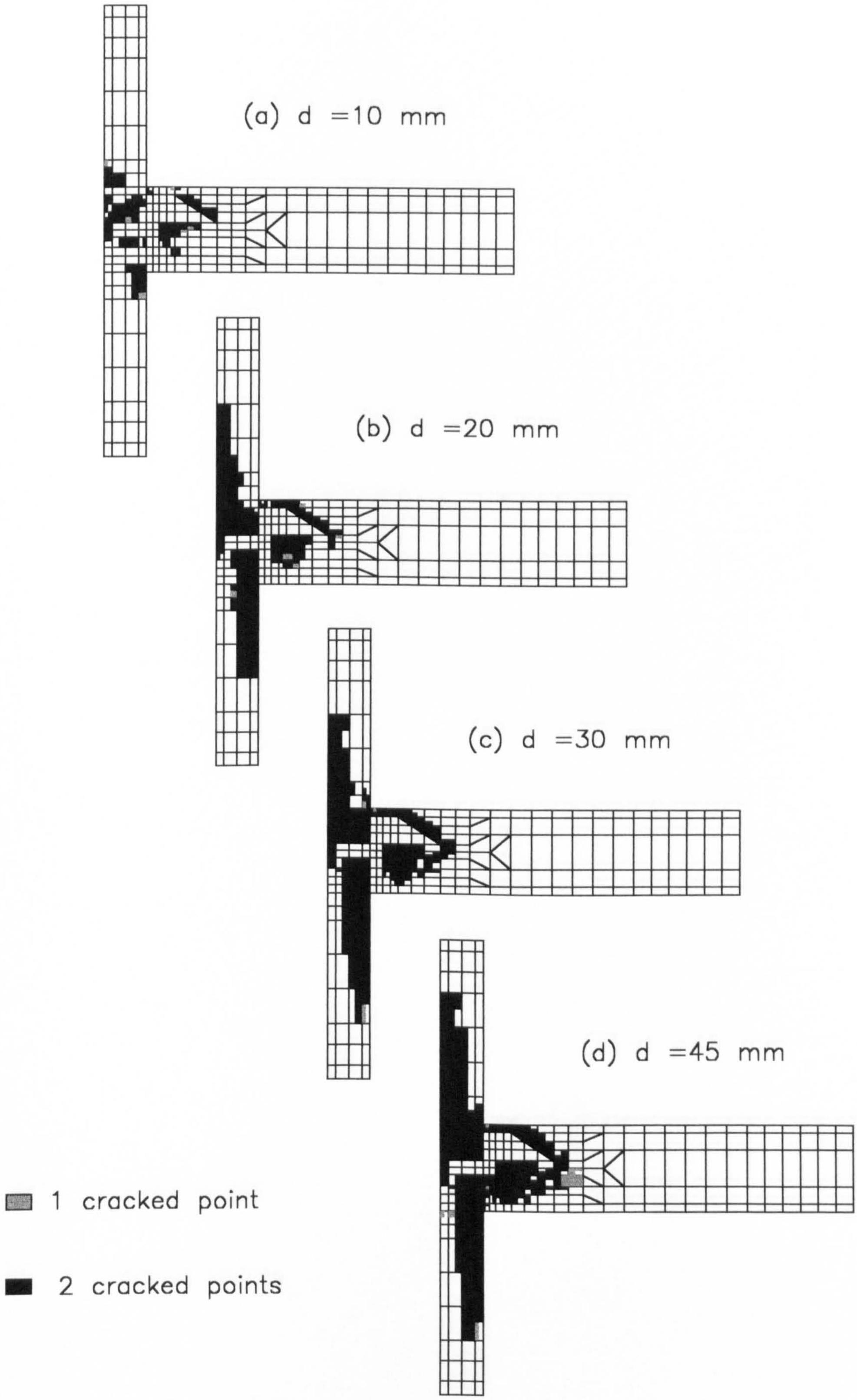

Figure 6.37(a) *Cracking status in the first (i.e. nearest to the central line) element layer of TW3*

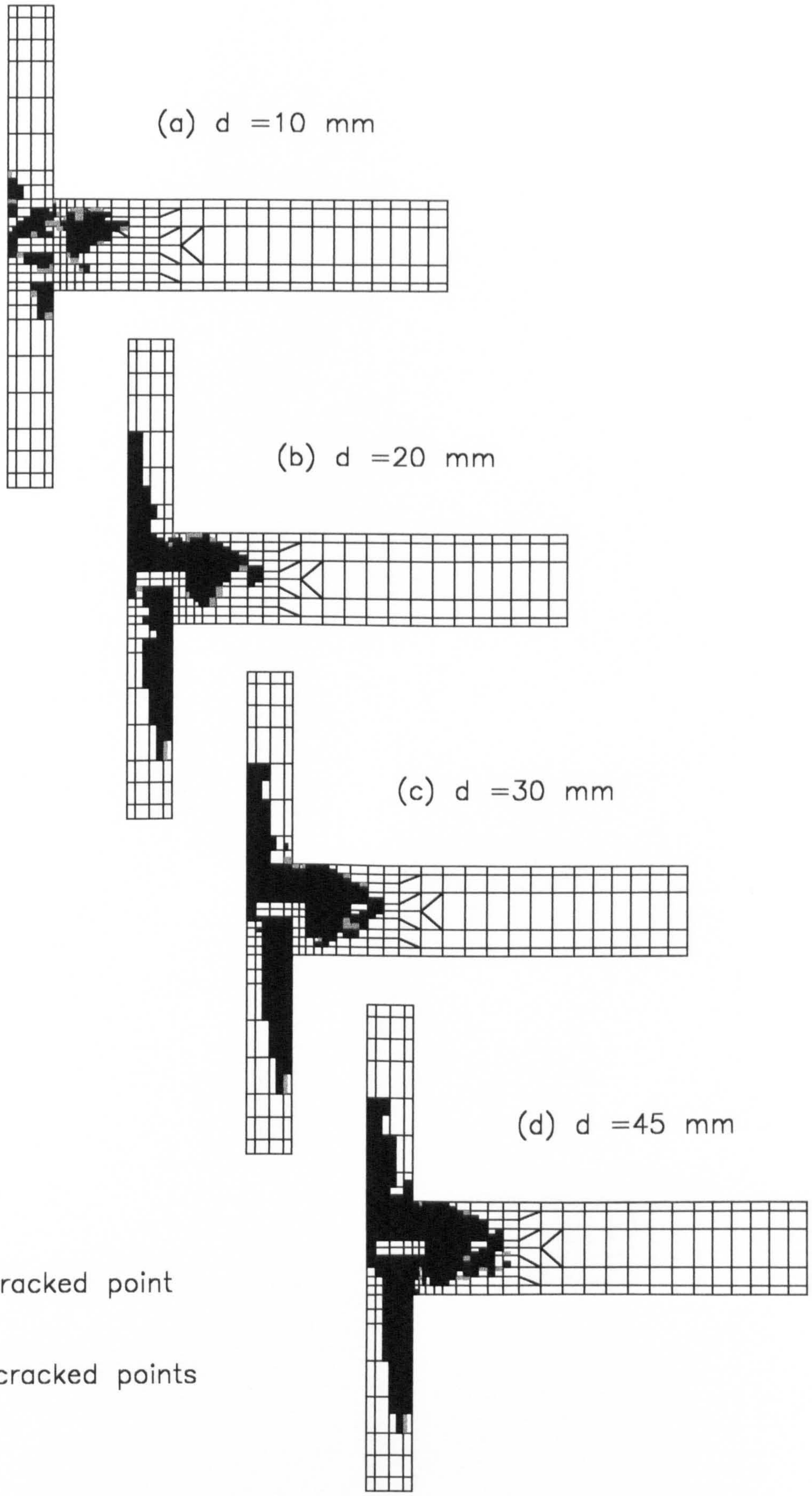

Figure 6.37(b) *Cracking status in the second element layer of TW3*

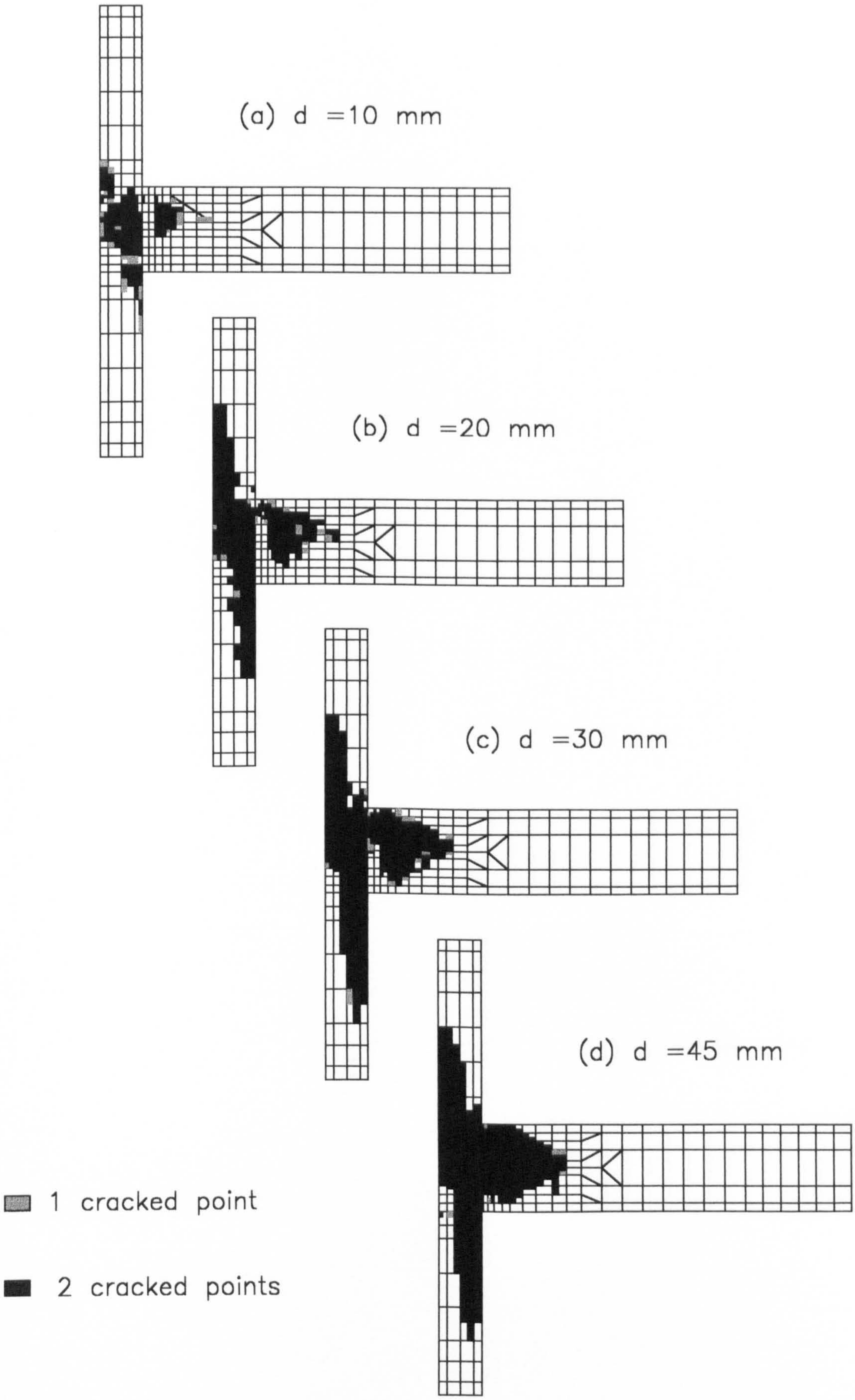

Figure 6.37(c) *Cracking status in the third element layer of TW3*

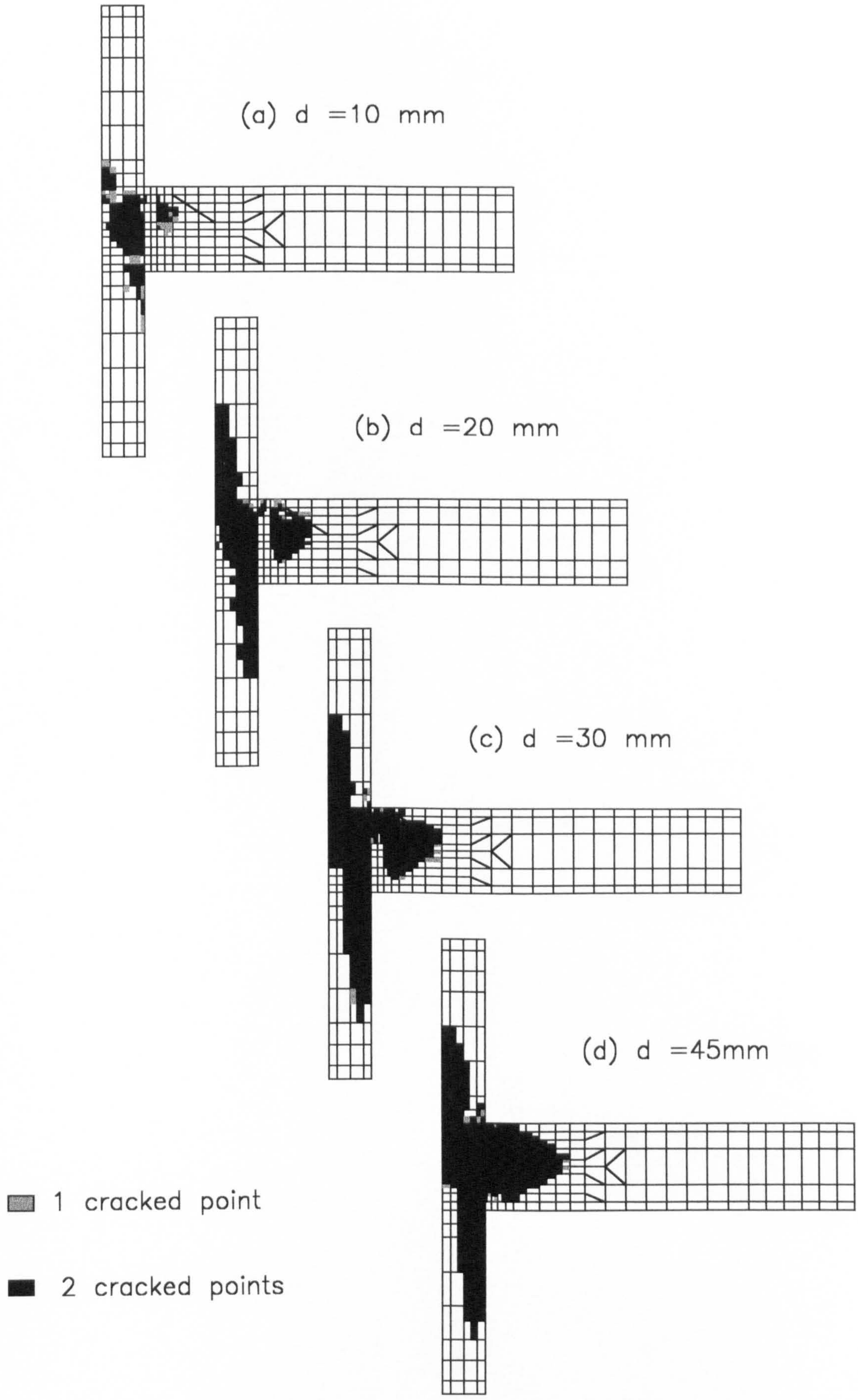

Figure 6.37(d) *Cracking status in the fourth (i.e. outside face) element layer of TW3*

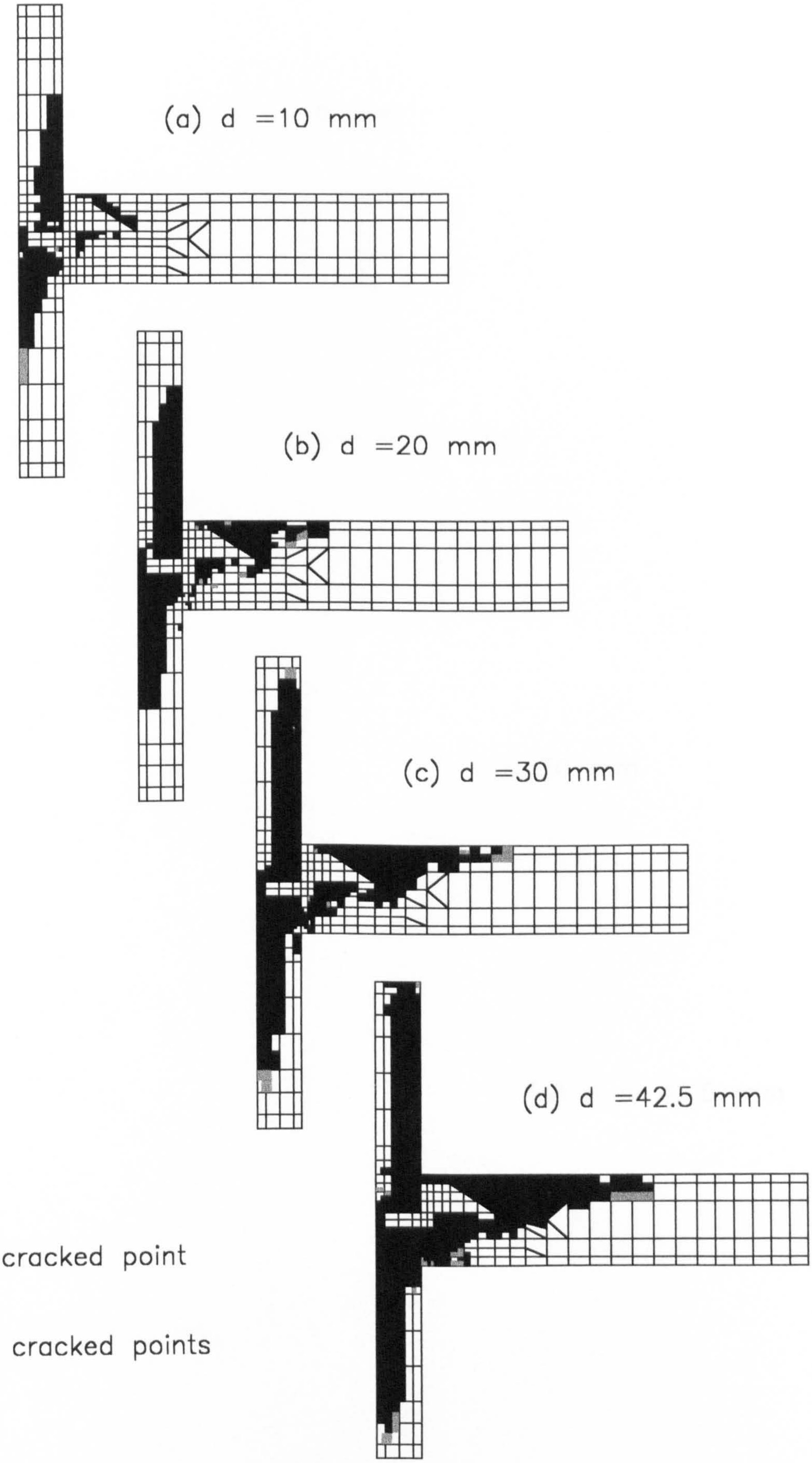

Figure 6.38(a) *Cracking status in the first (i.e. nearest to the central line) element layer of TW4*

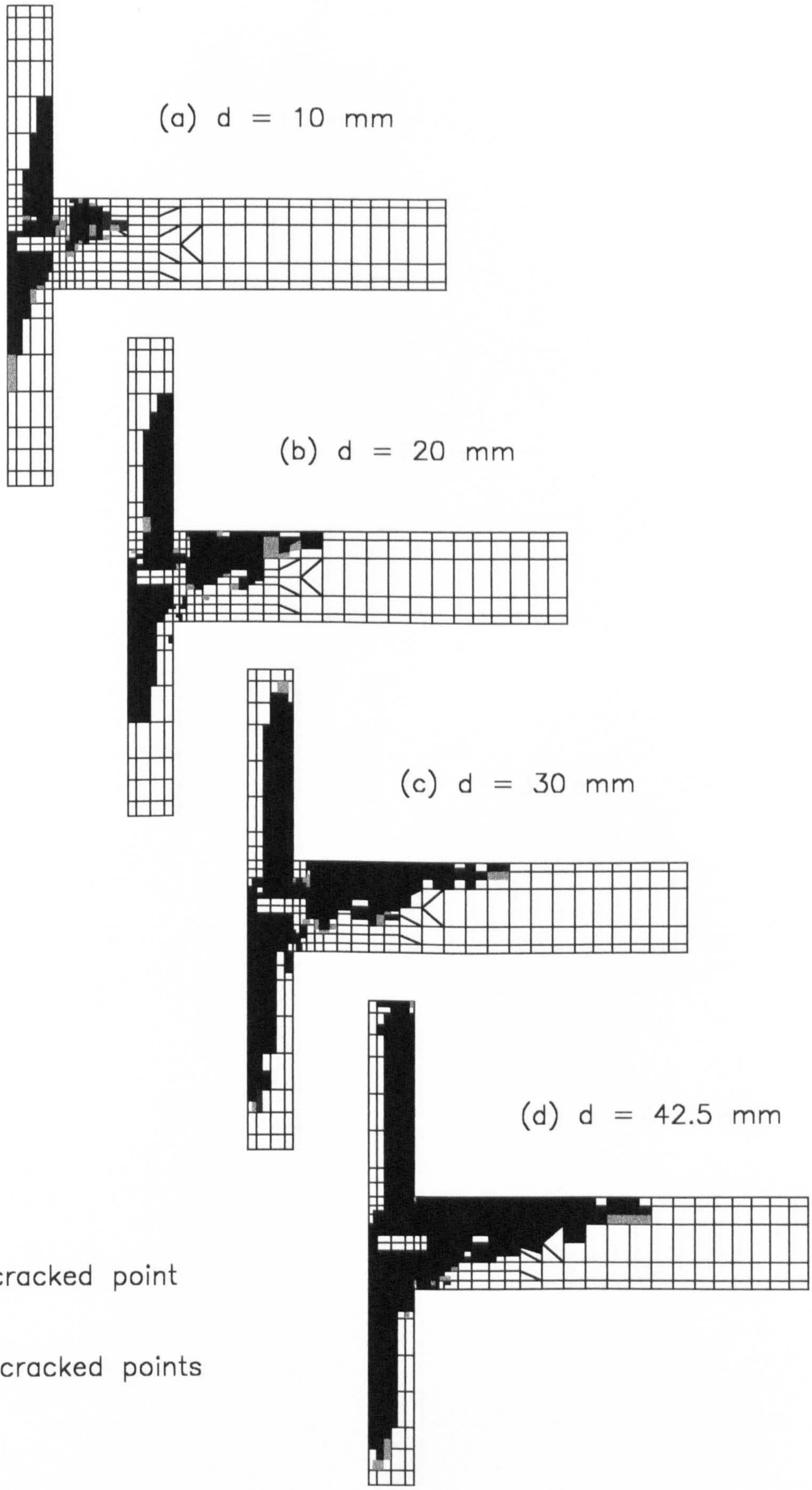

Figure 6.38(b) *Cracking status in the second element layer of TW4*

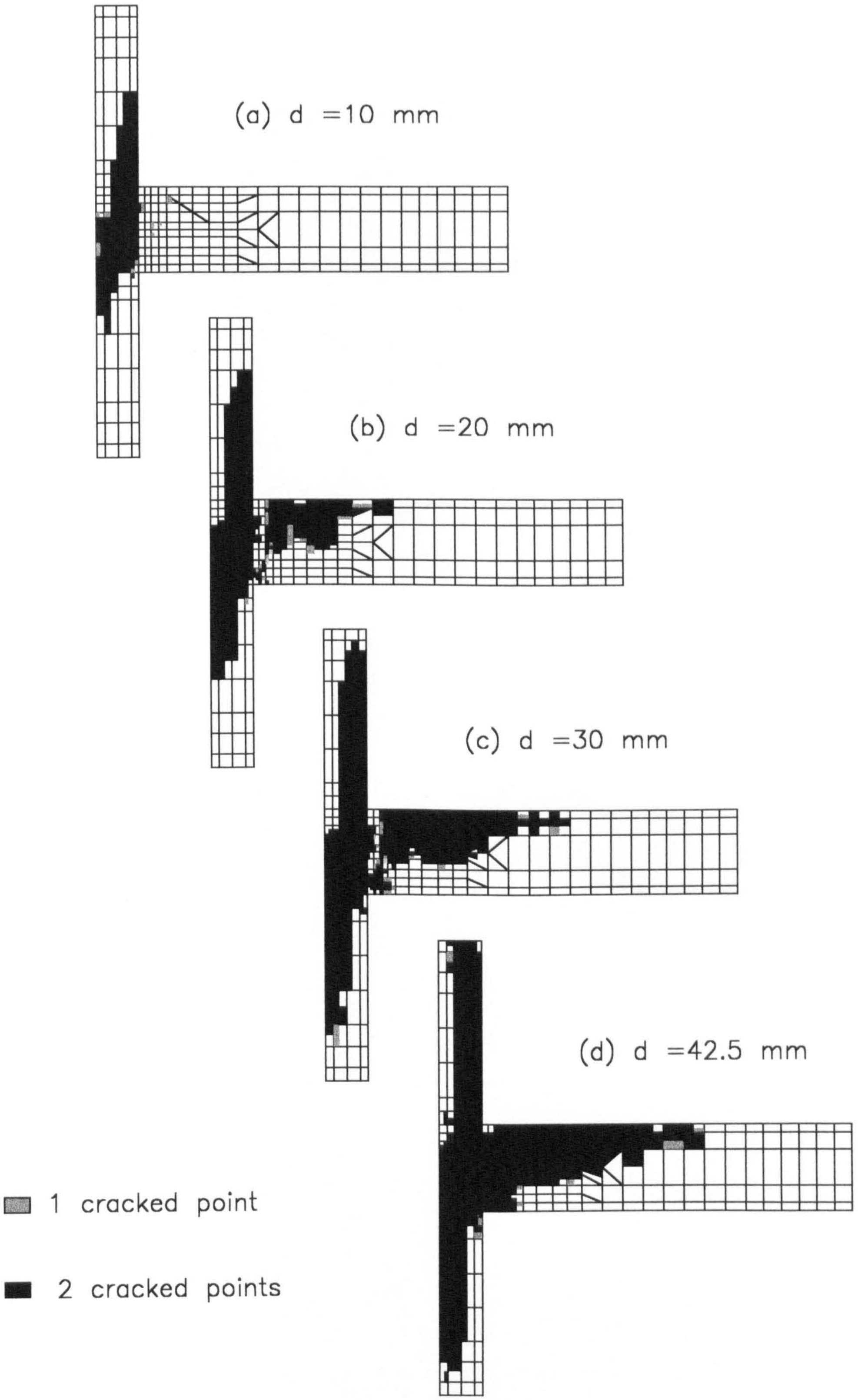

Figure 6.38(c) *Cracking status in the third element layer of TW4*

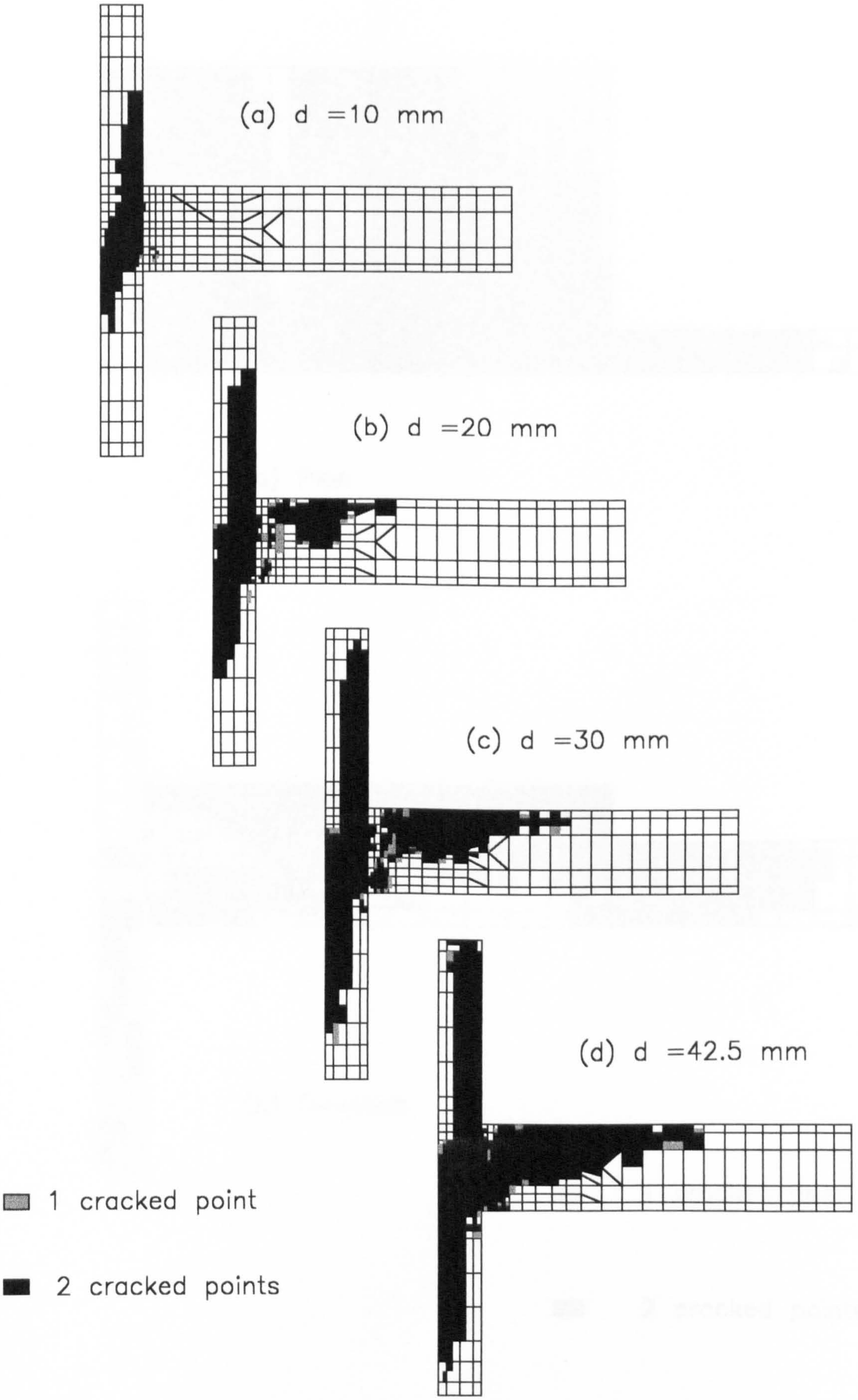

Figure 6.38(d) *Cracking status in the fourth (i.e. outside face) element layer of TW4*

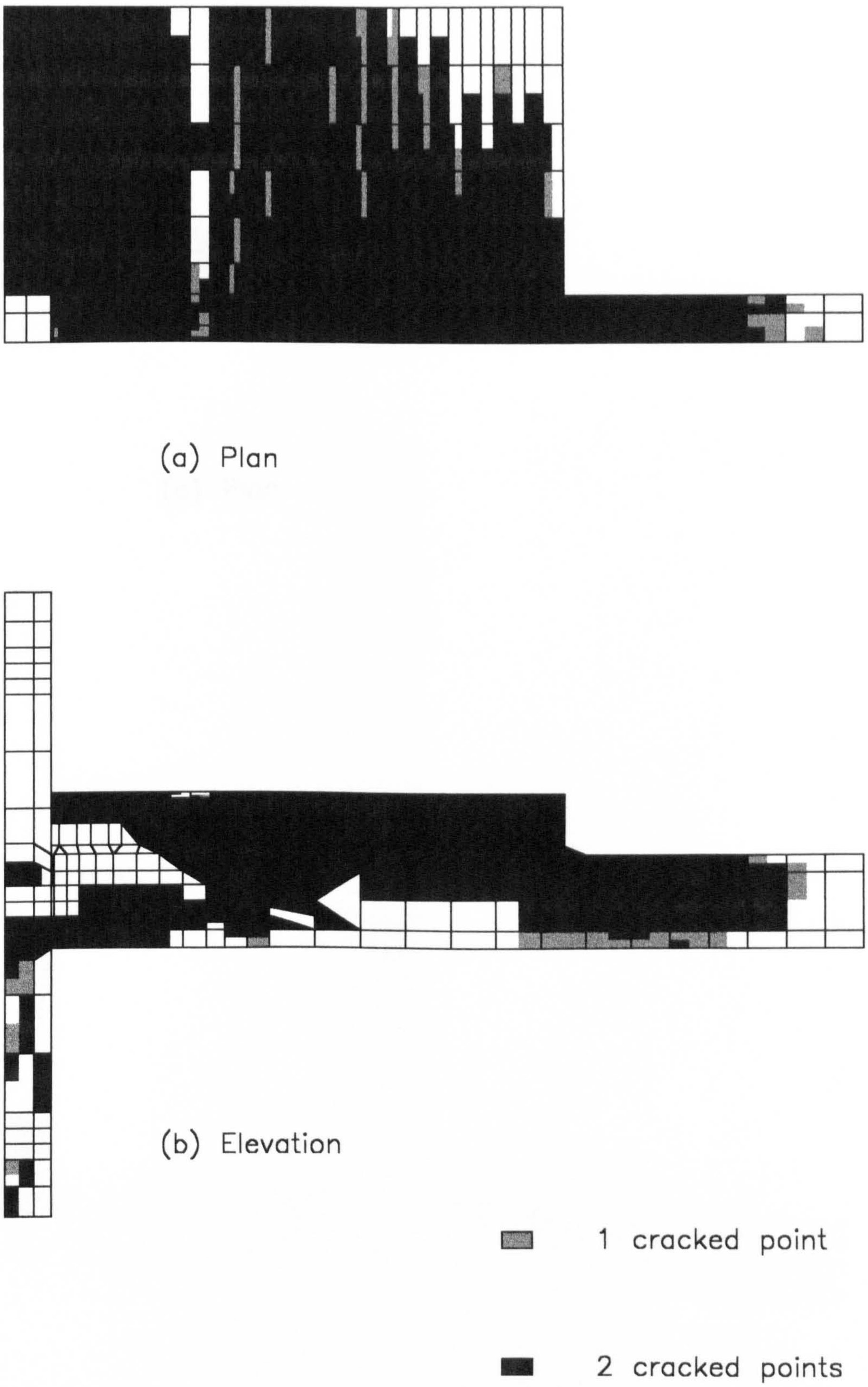

Figure 6.39 *Cracking status of TW1(A) with a 30 mm column mid-height displacement*

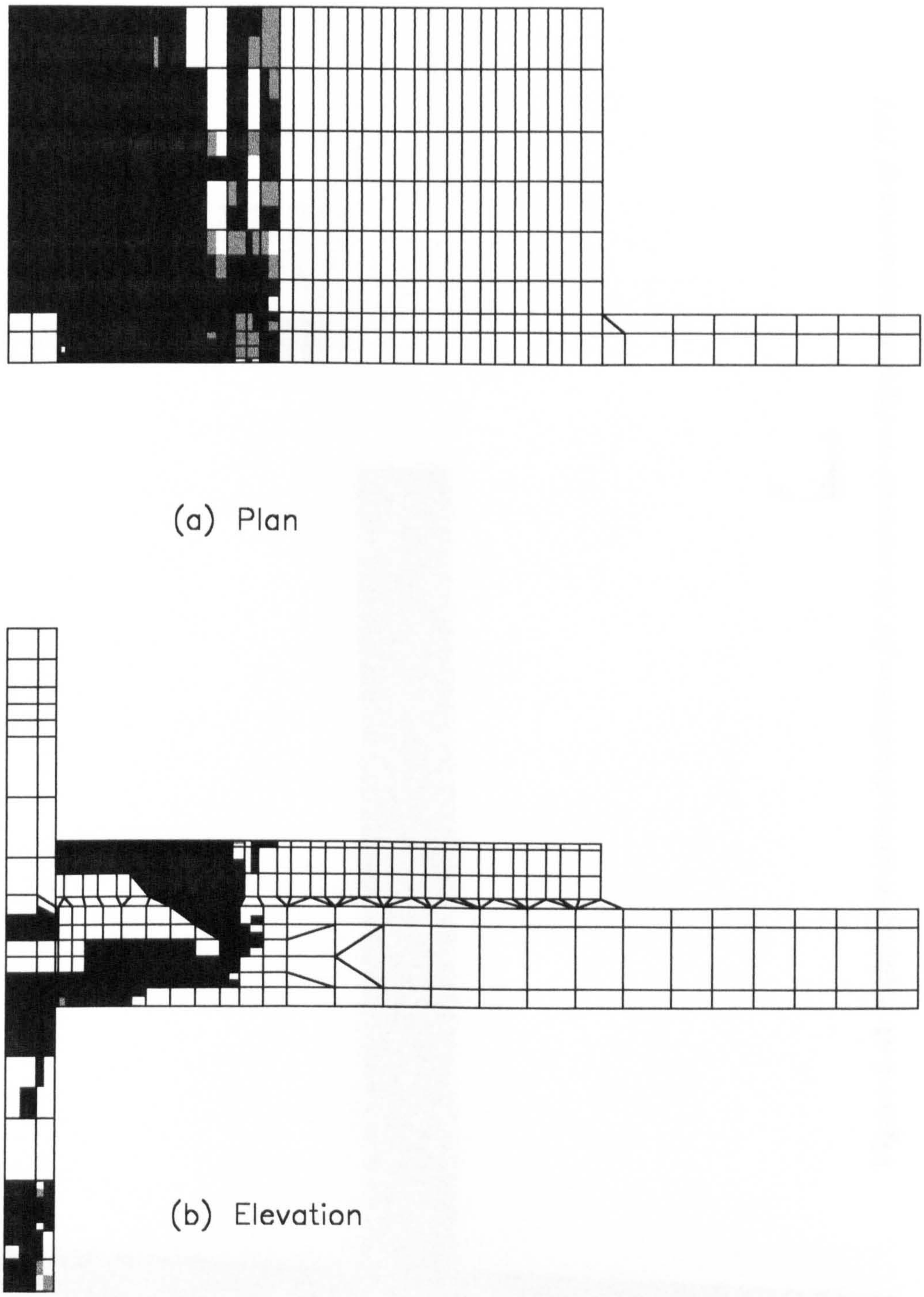

Figure 6.40 *Cracking status of TW1(C) with a 4 mm column mid-height displacement*

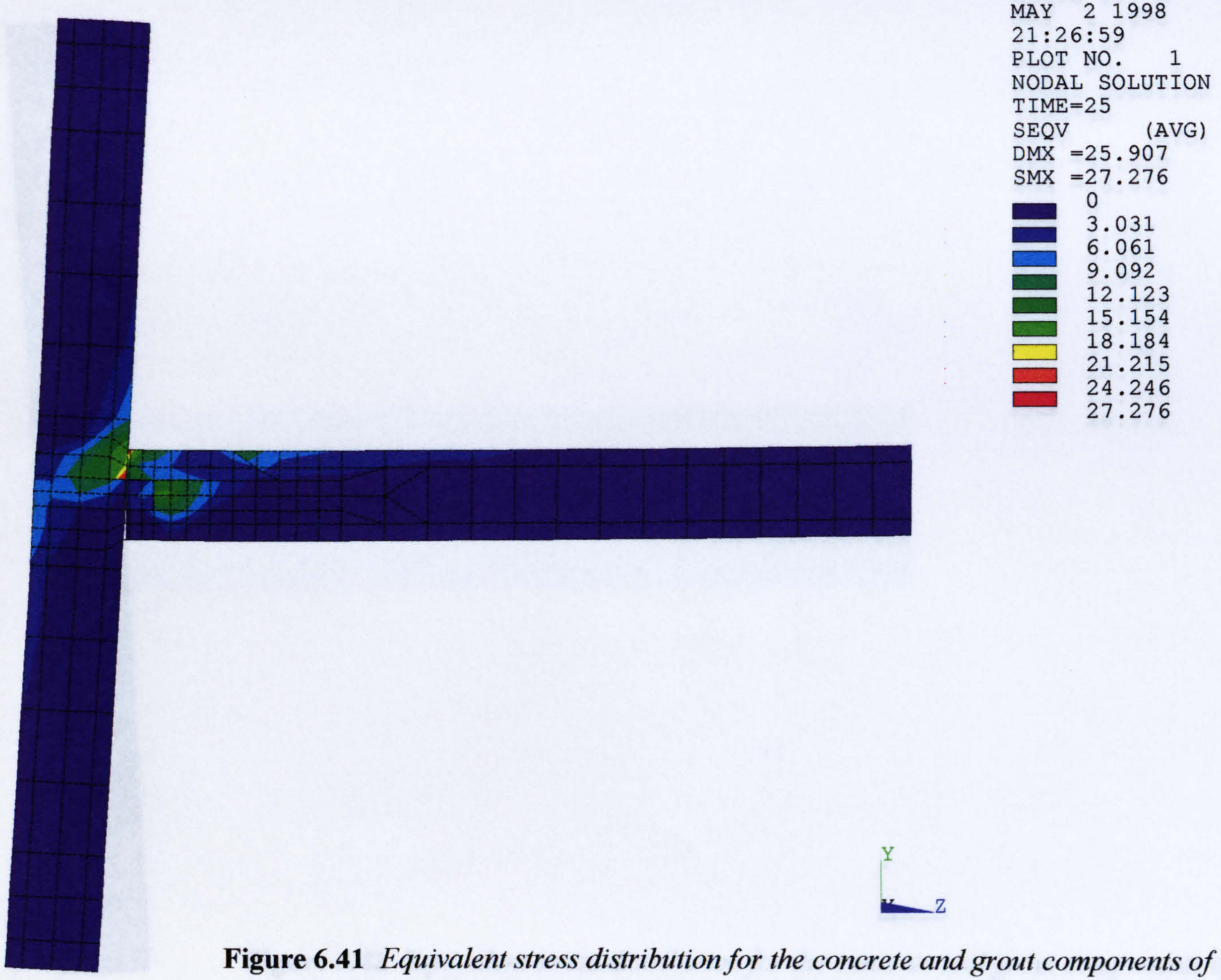

Figure 6.41 *Equivalent stress distribution for the concrete and grout components of TW1*

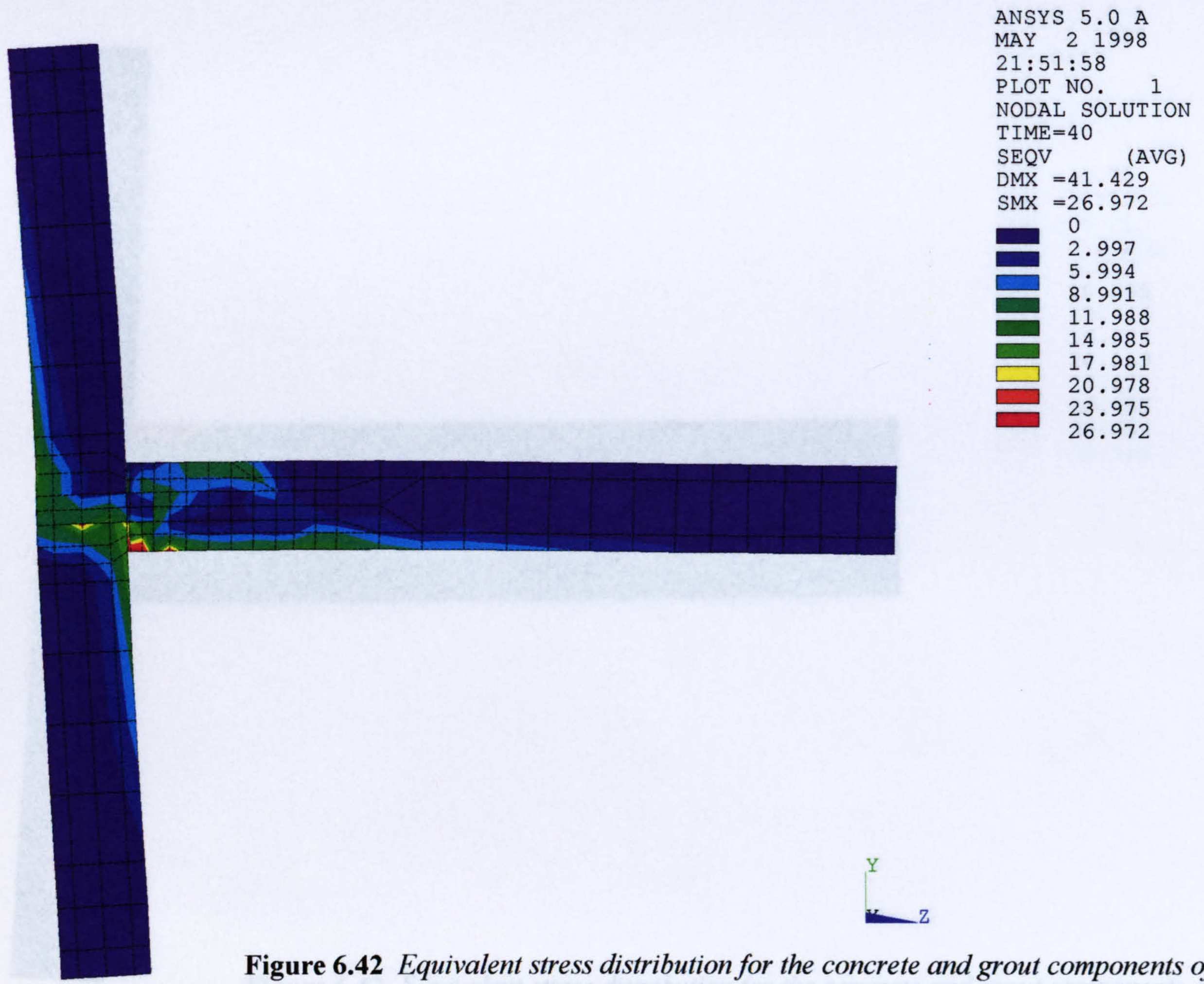

Figure 6.42 *Equivalent stress distribution for the concrete and grout components of TW2*

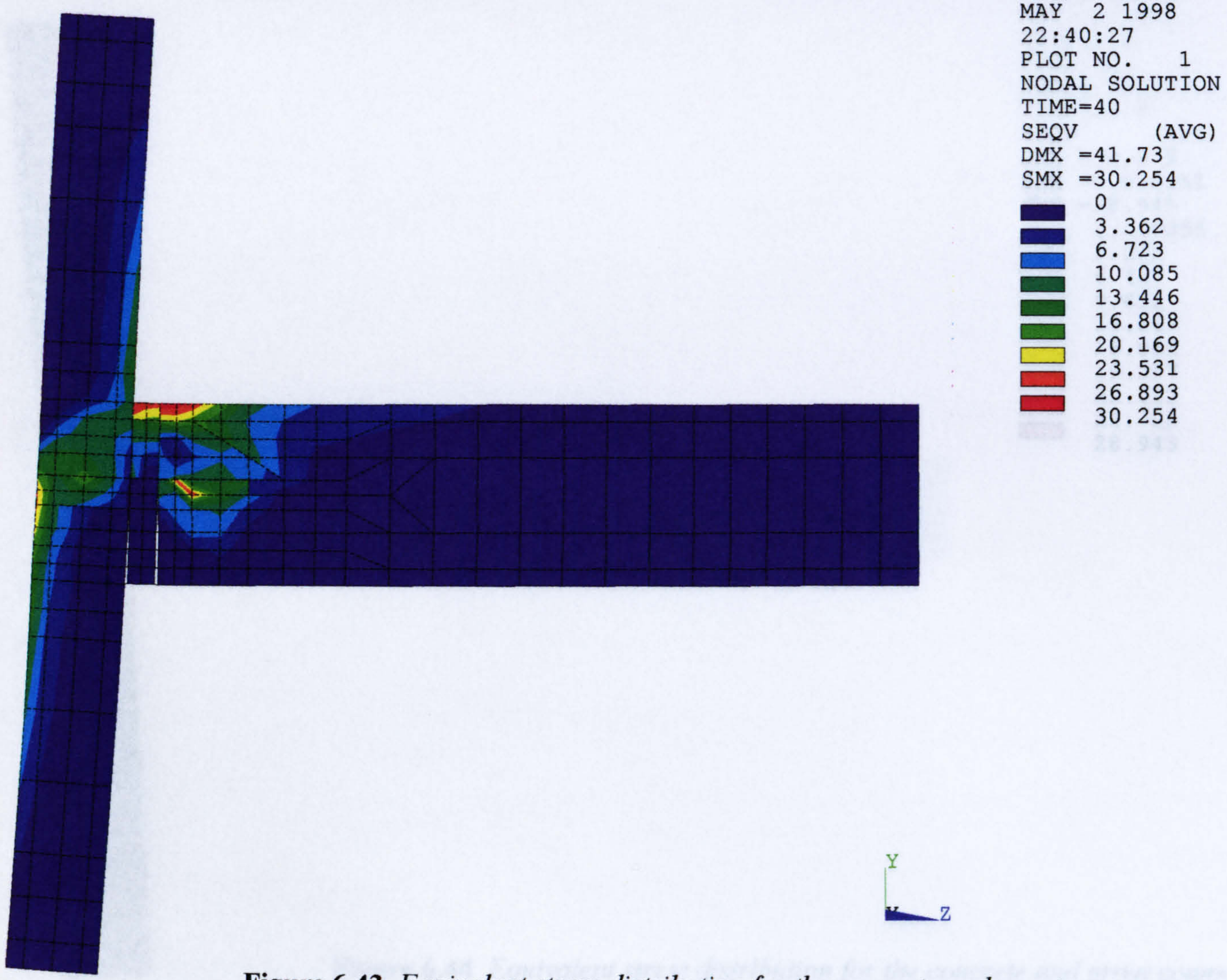

Figure 6.43 *Equivalent stress distribution for the concrete and grout components of TW3*

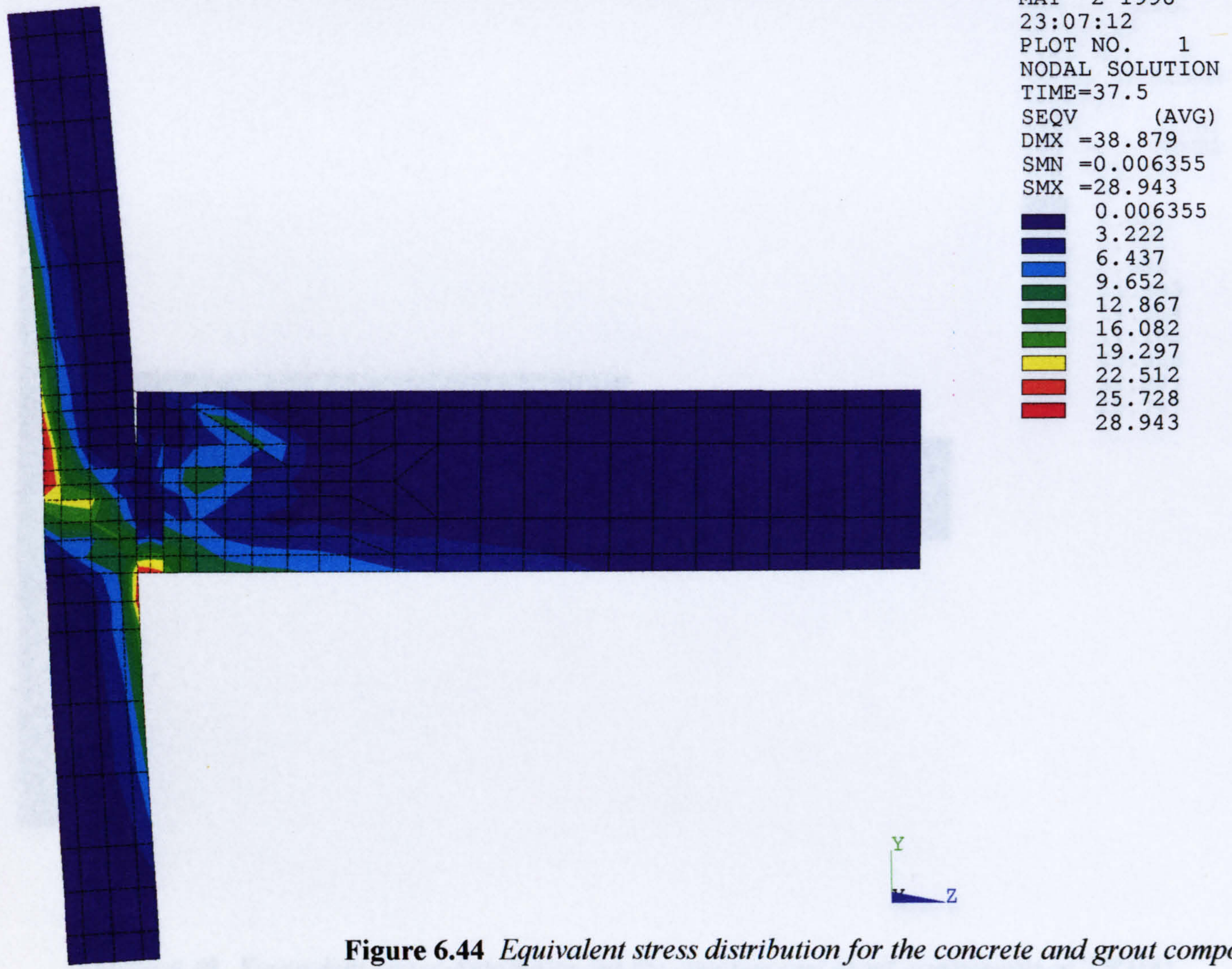

Figure 6.44 *Equivalent stress distribution for the concrete and grout components of TW4*

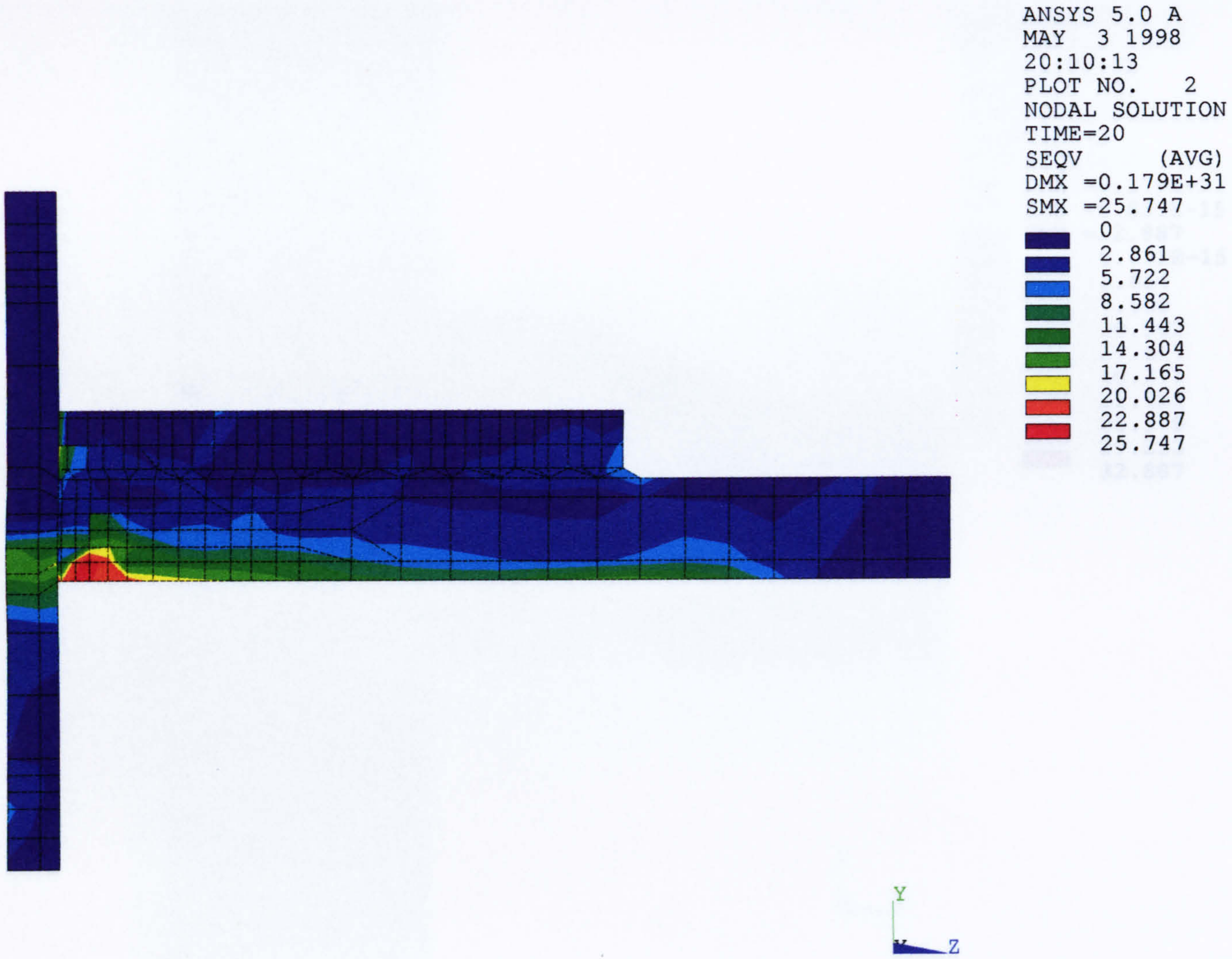

Figure 6.45 *Equivalent stress distribution for the concrete and grout components of TW1(A)*

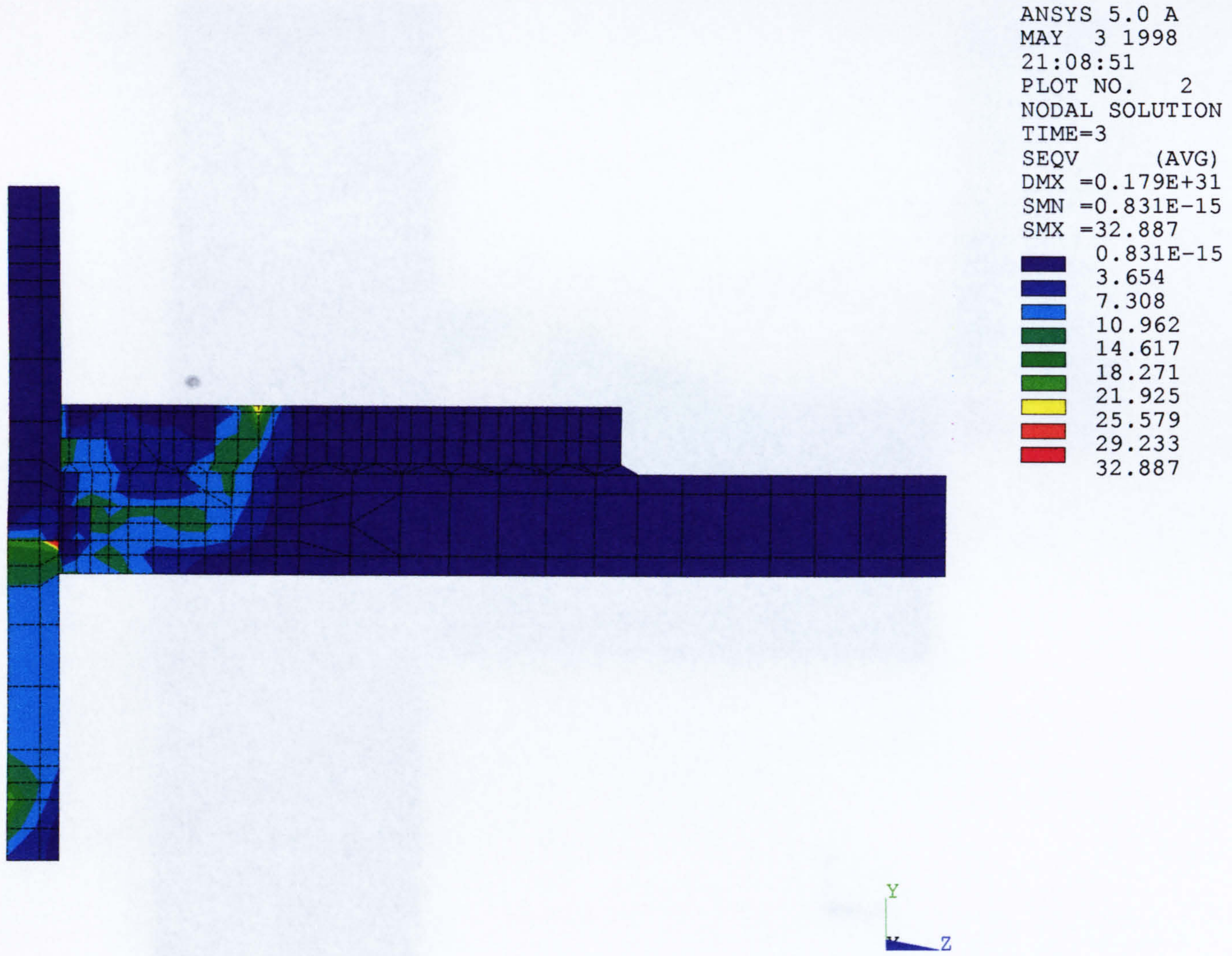

Figure 6.46 *Equivalent stress distribution for the concrete and grout components of TW1(C)*

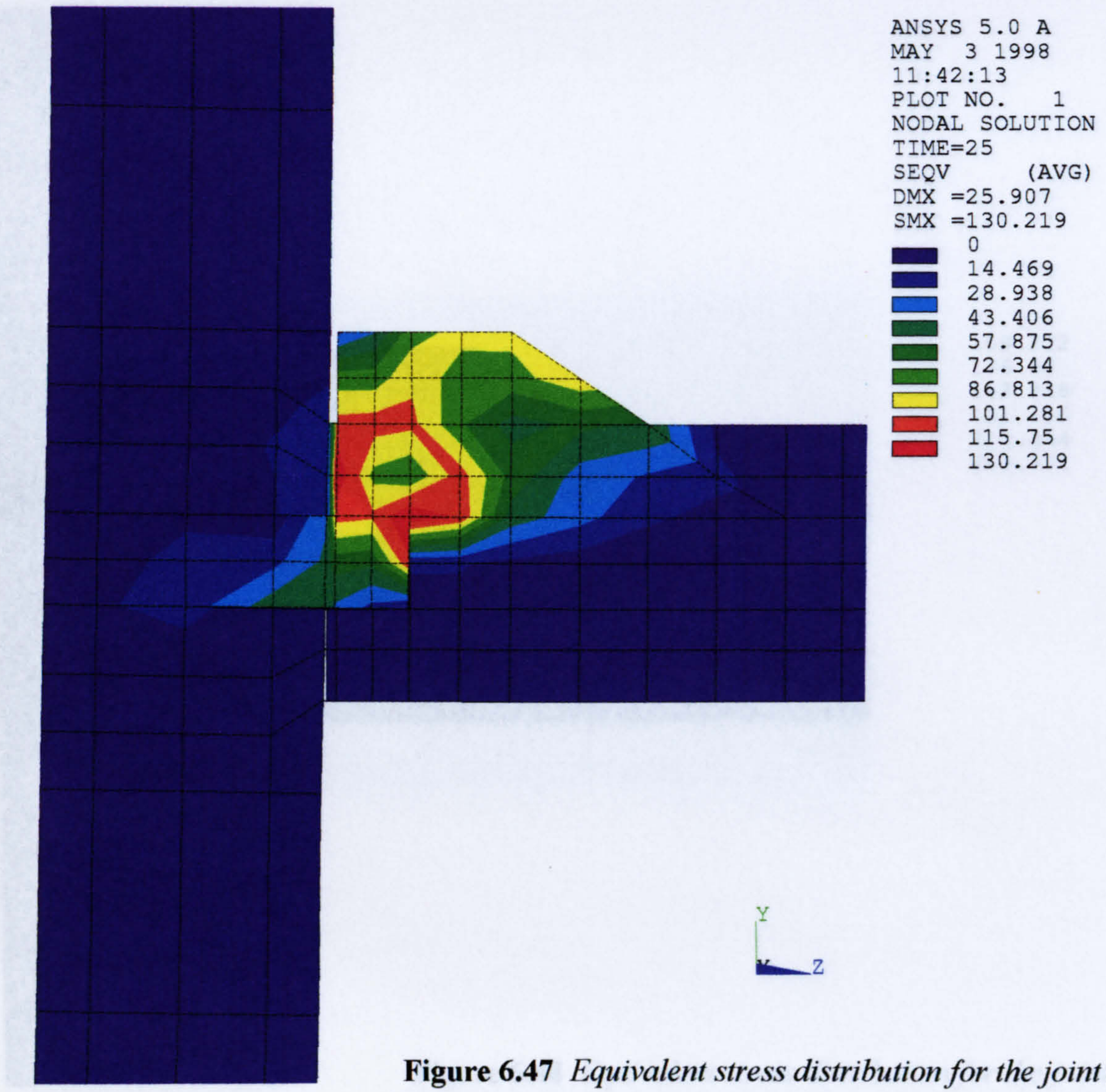

Figure 6.47 *Equivalent stress distribution for the joint core zone of TW1*

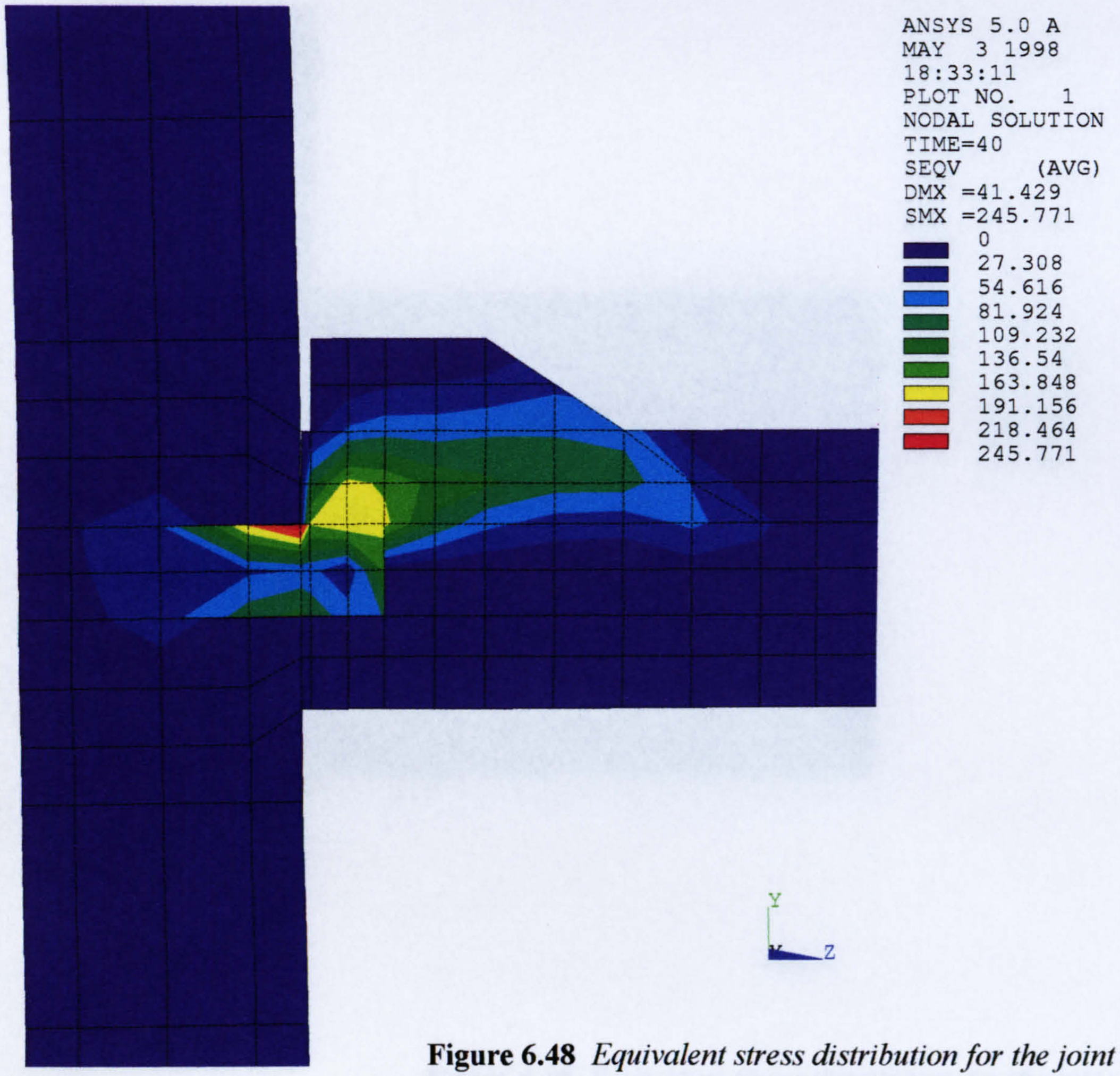

Figure 6.48 *Equivalent stress distribution for the joint core zone of TW2*

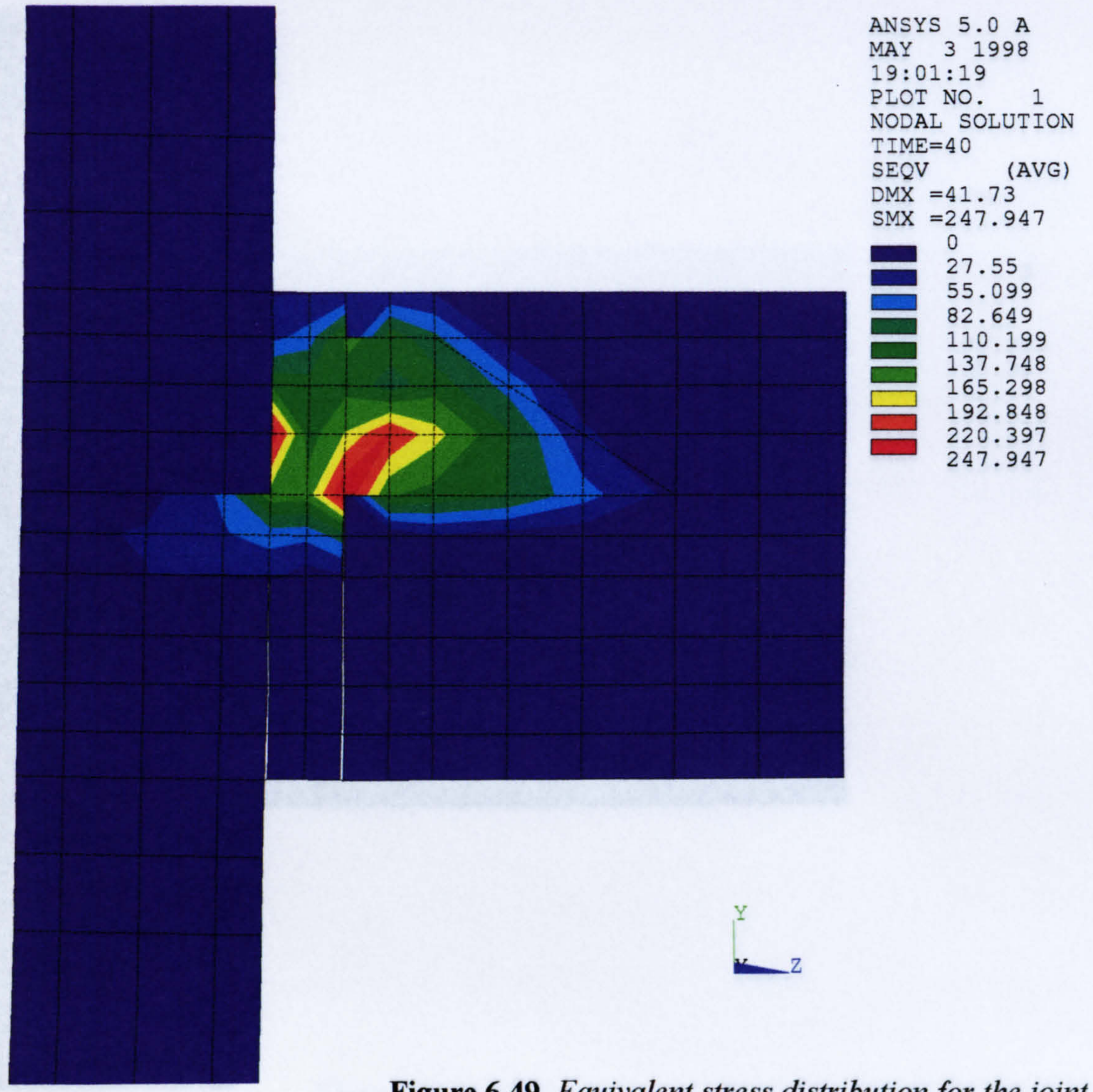

Figure 6.49 *Equivalent stress distribution for the joint core zone of TW3*

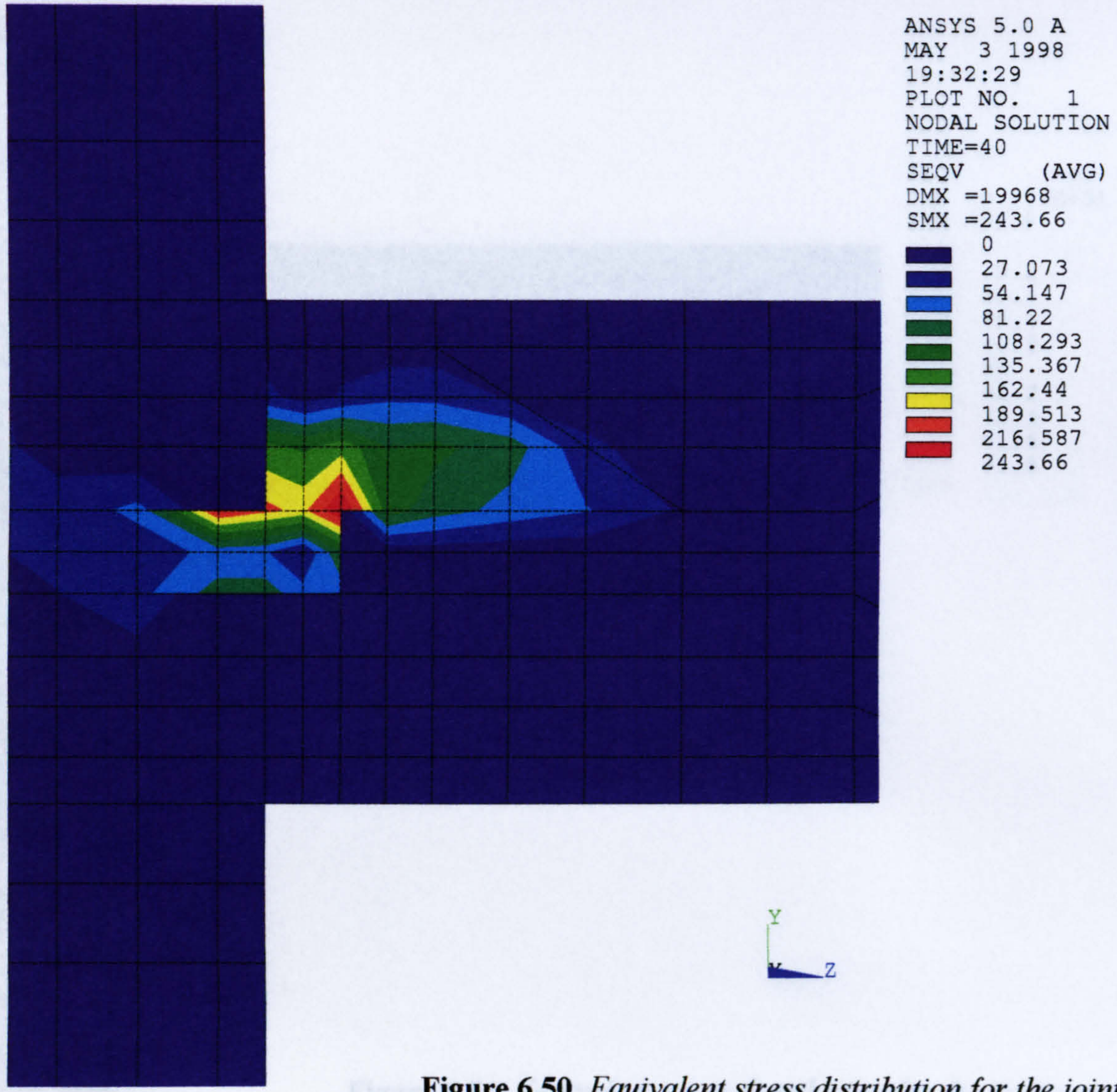

Figure 6.50 *Equivalent stress distribution for the joint core zone of TW4*

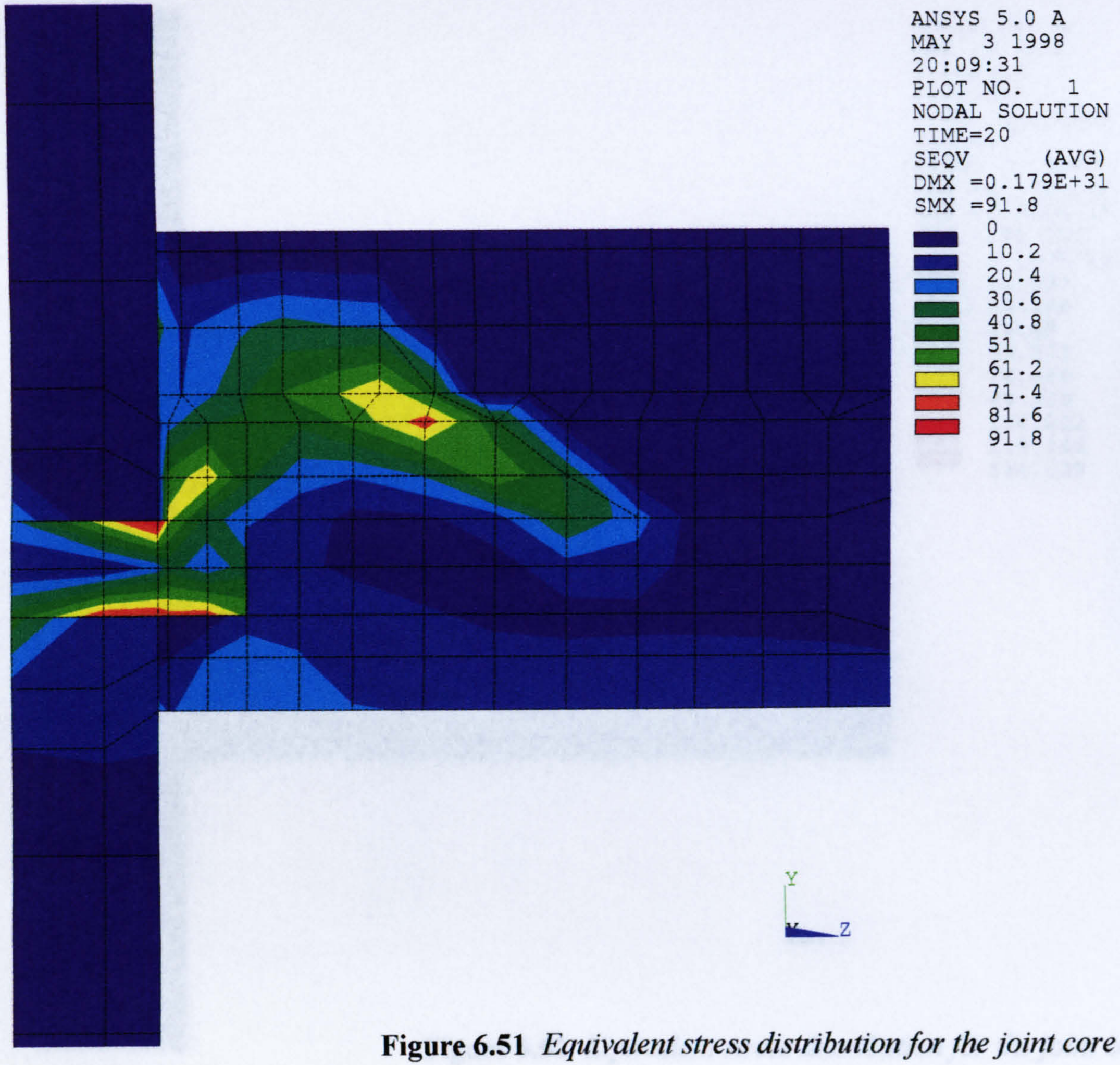

Figure 6.51 *Equivalent stress distribution for the joint core zone of TW1(A)*

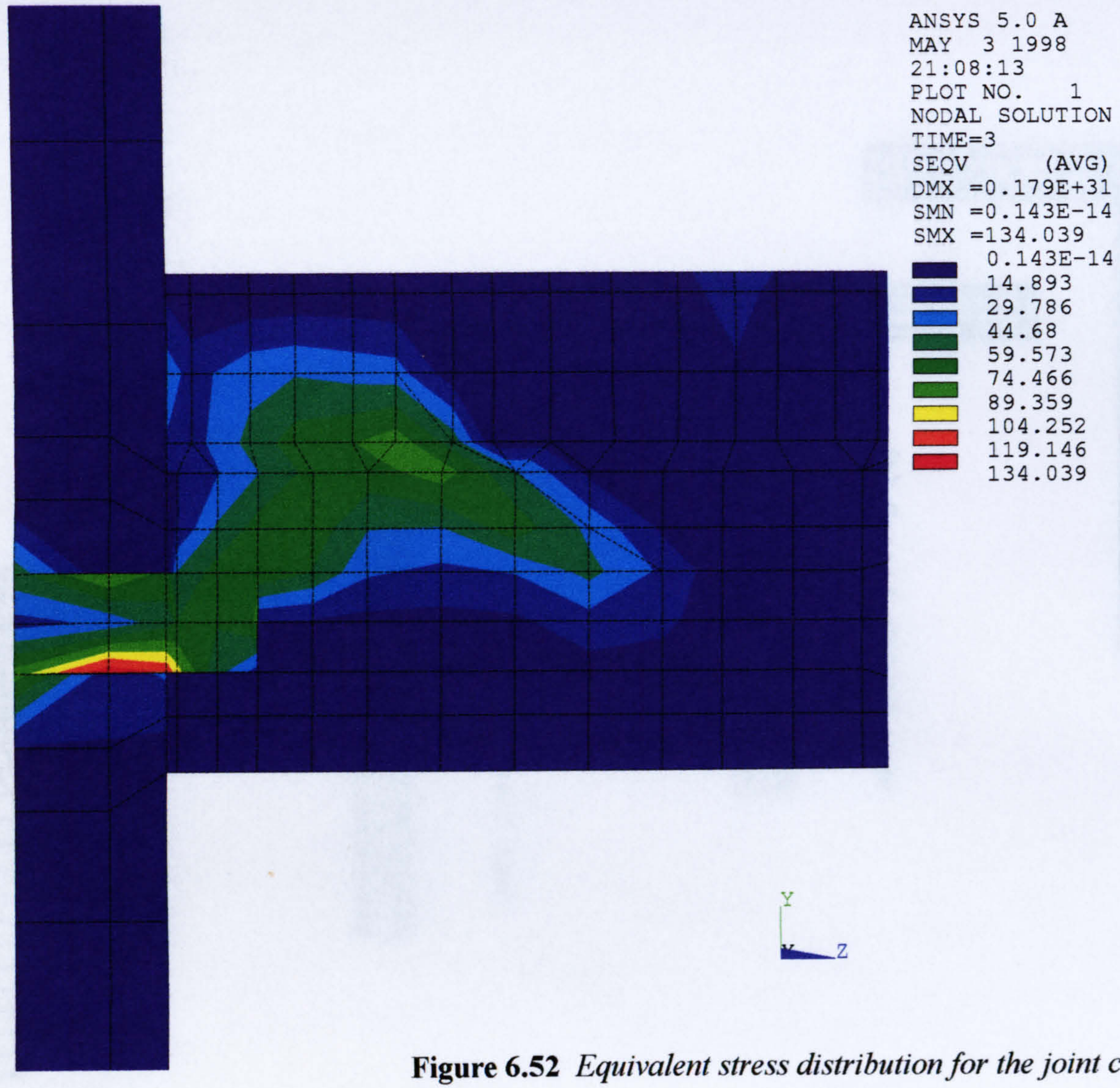

Figure 6.52 *Equivalent stress distribution for the joint core zone of TW1(C)*

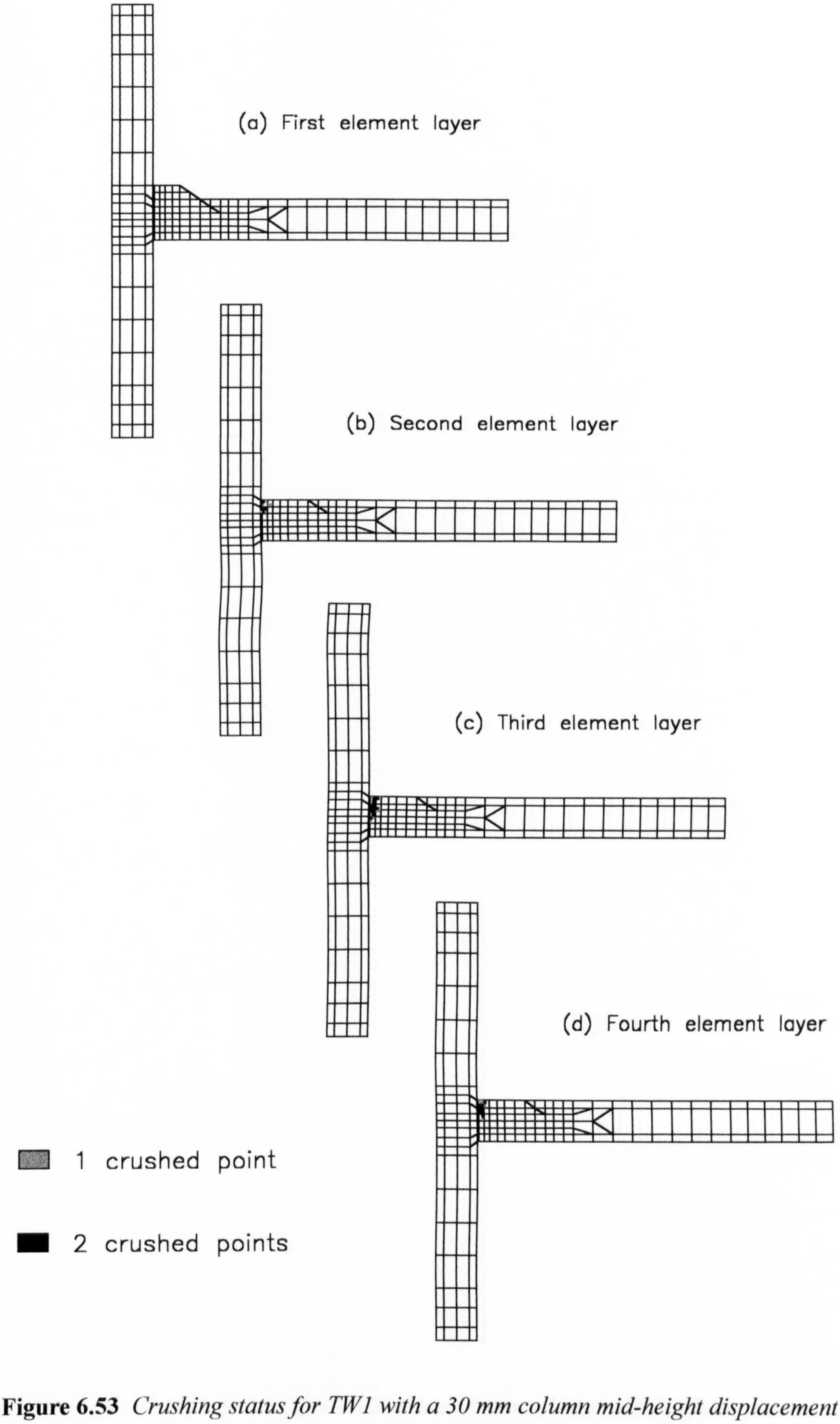

Figure 6.53 *Crushing status for TW1 with a 30 mm column mid-height displacement*

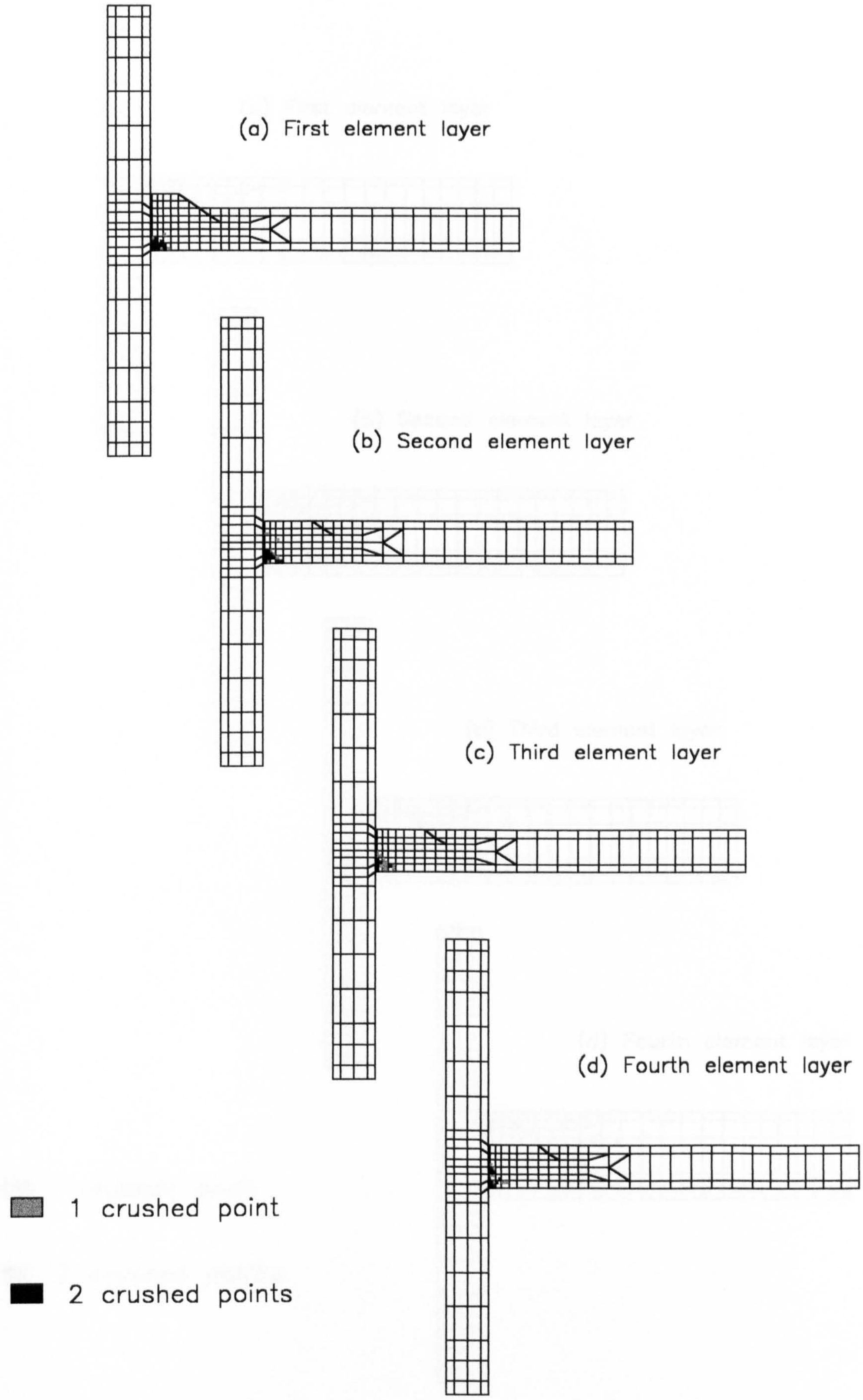

Figure 6.54 *Crushing status for TW2 with a 45 mm column mid-height displacement*

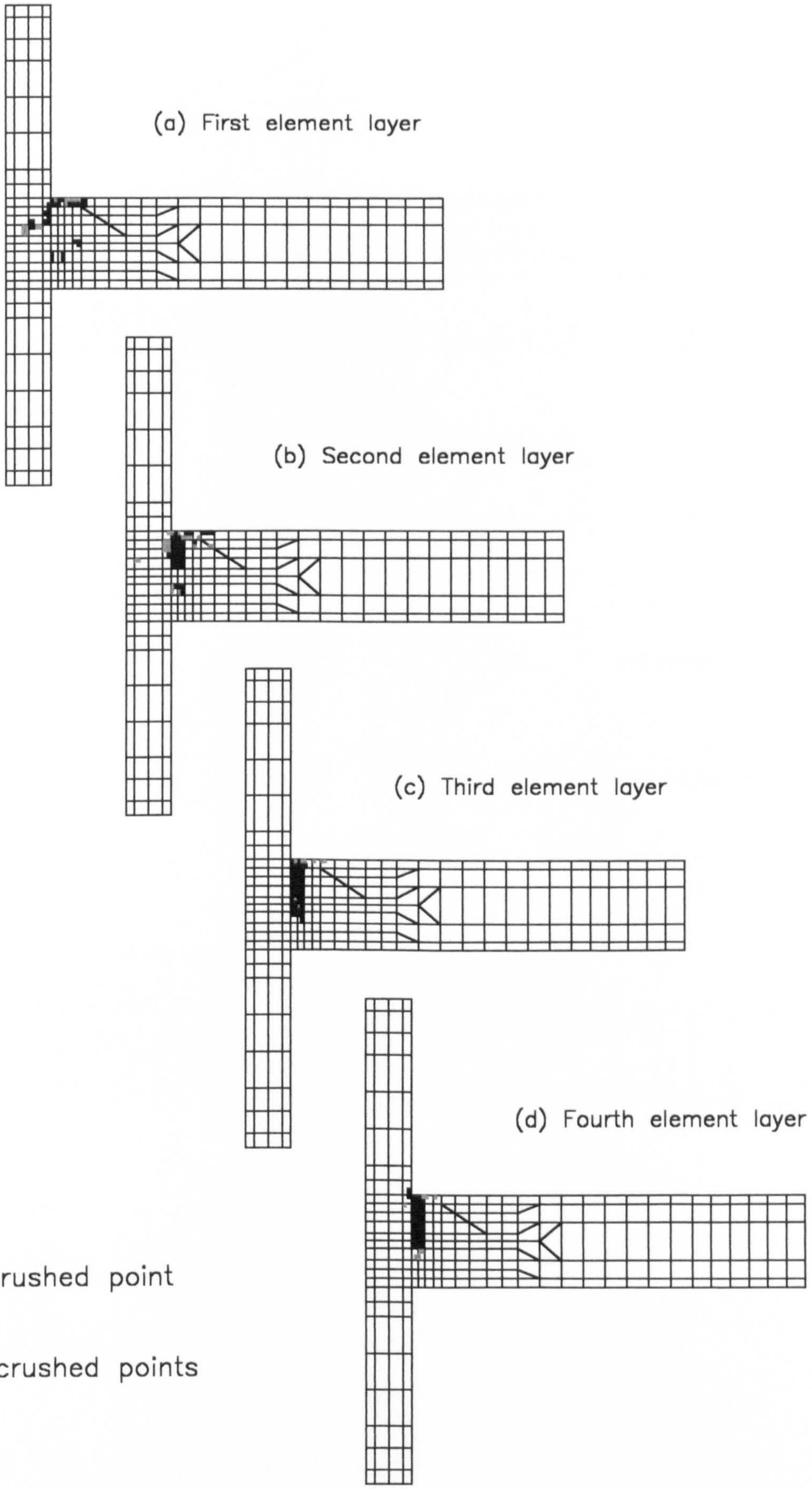

Figure 6.55 *Crushing status for TW3 with a 45 mm column mid-height displacement*

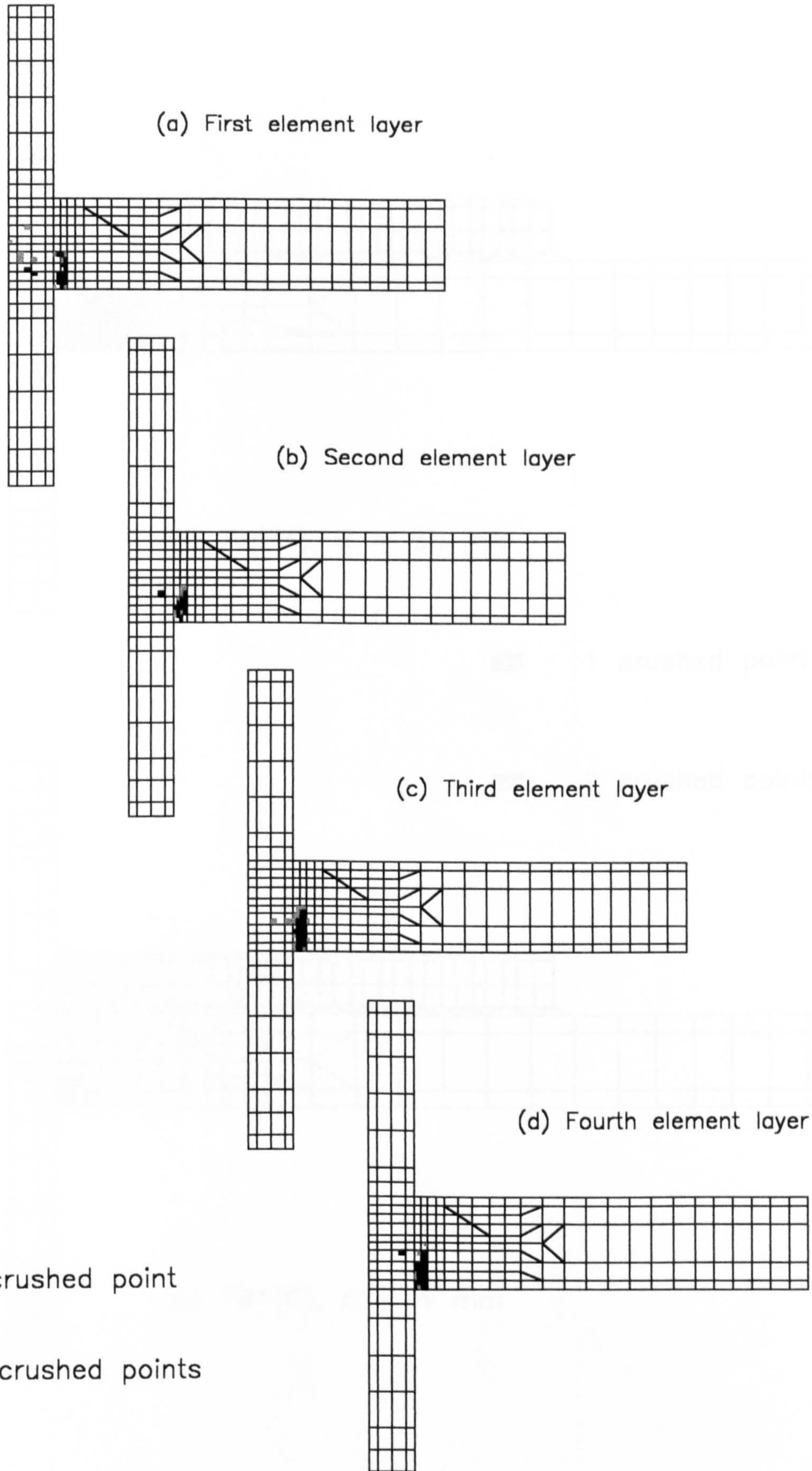

Figure 6.56 *Crushing status for TW4 with a 42.5 mm column mid-height displacement*

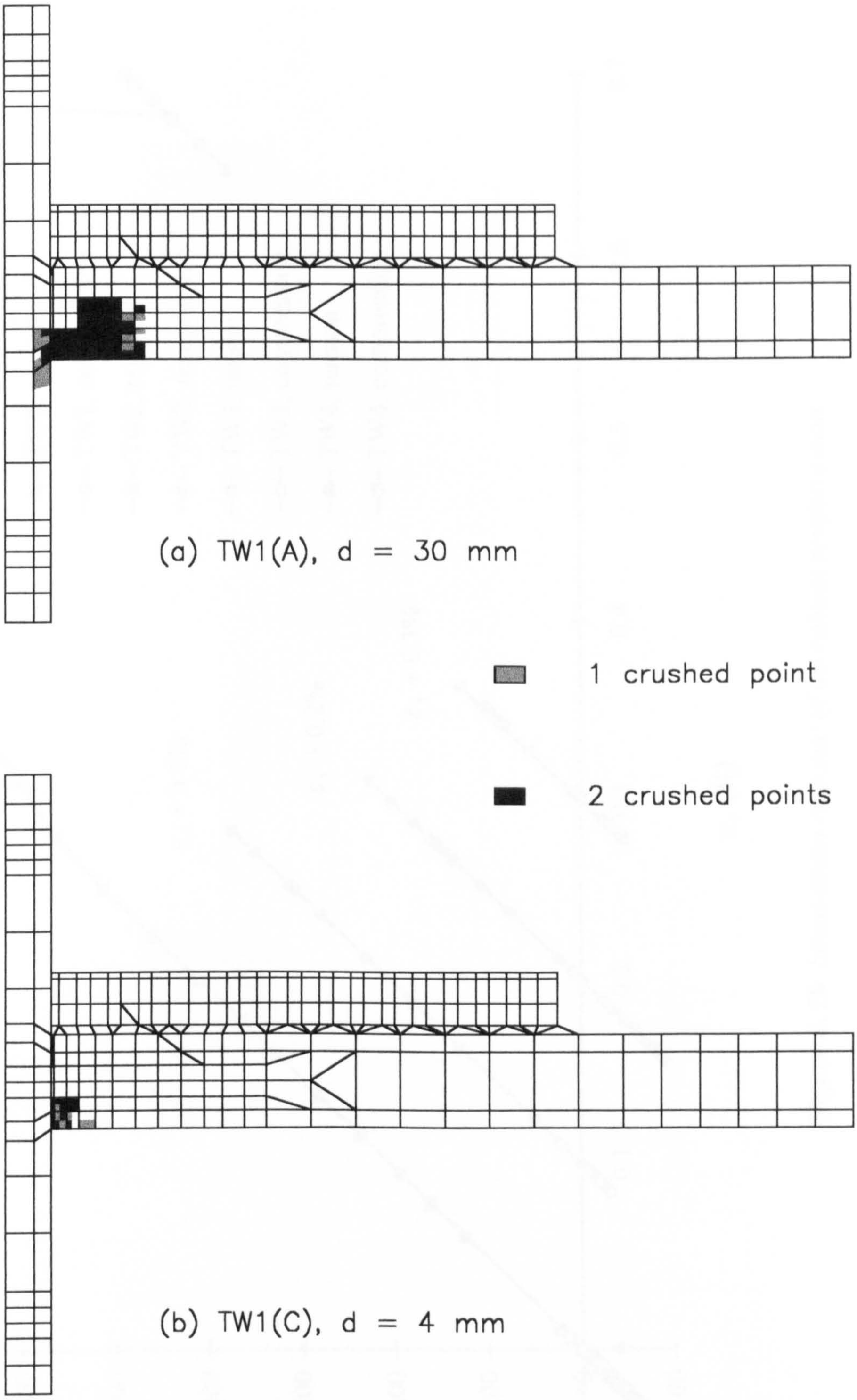

Figure 6.57 *Crushing status for TW1(A) and TW1(C) beyond the ultimate states*

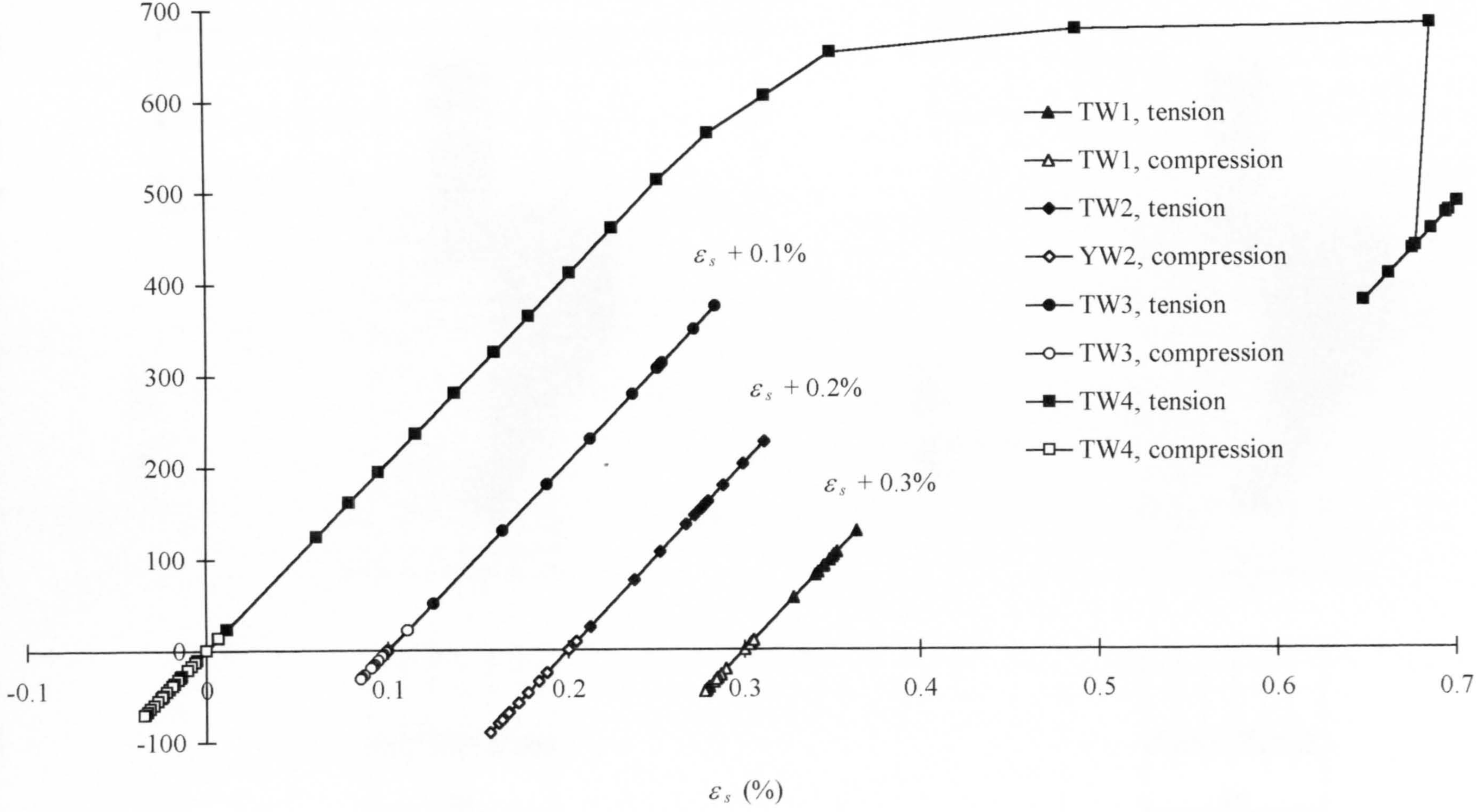

Figure 6. 58 *Stress-strain response of the column reinforcement*

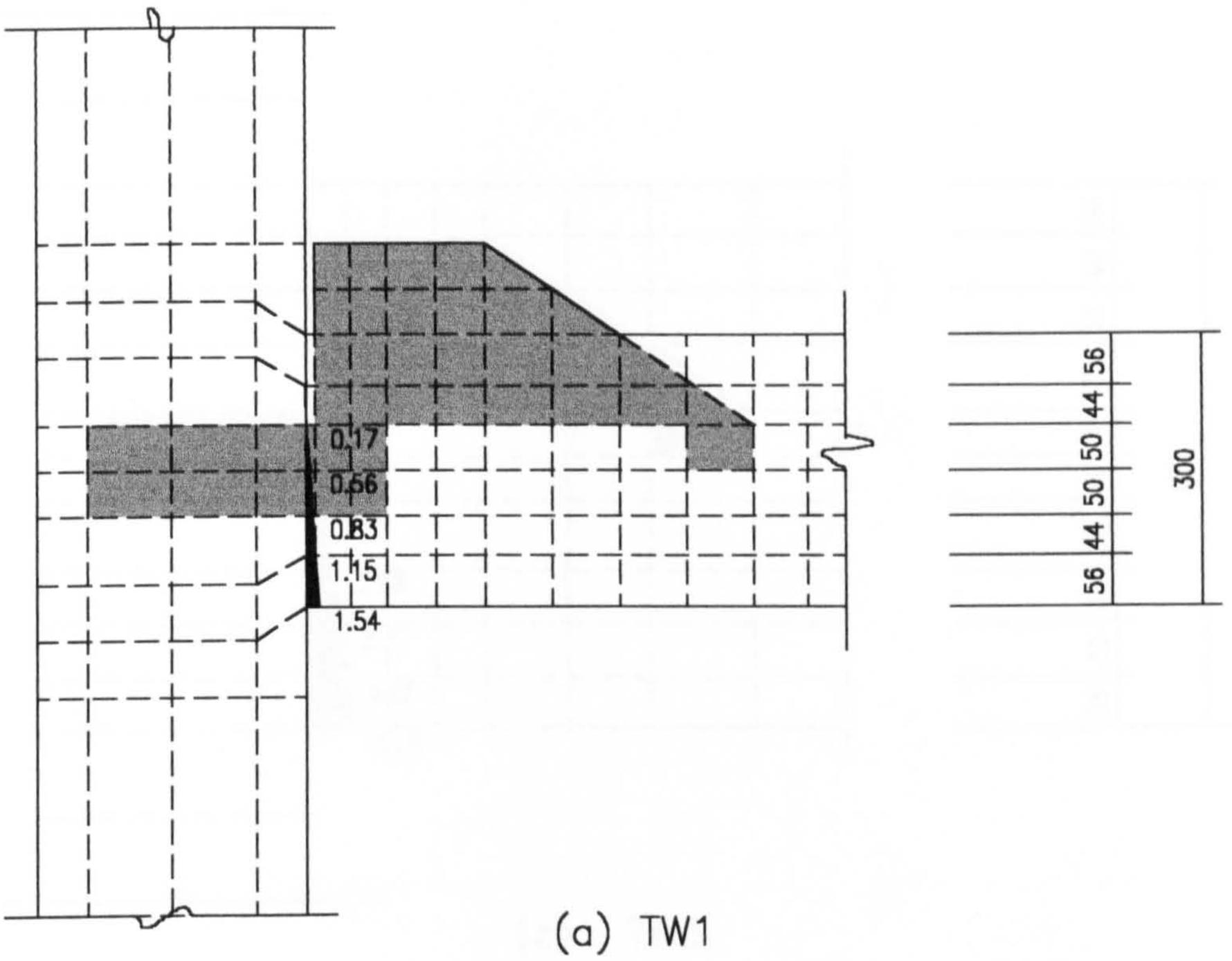

(a) TW1

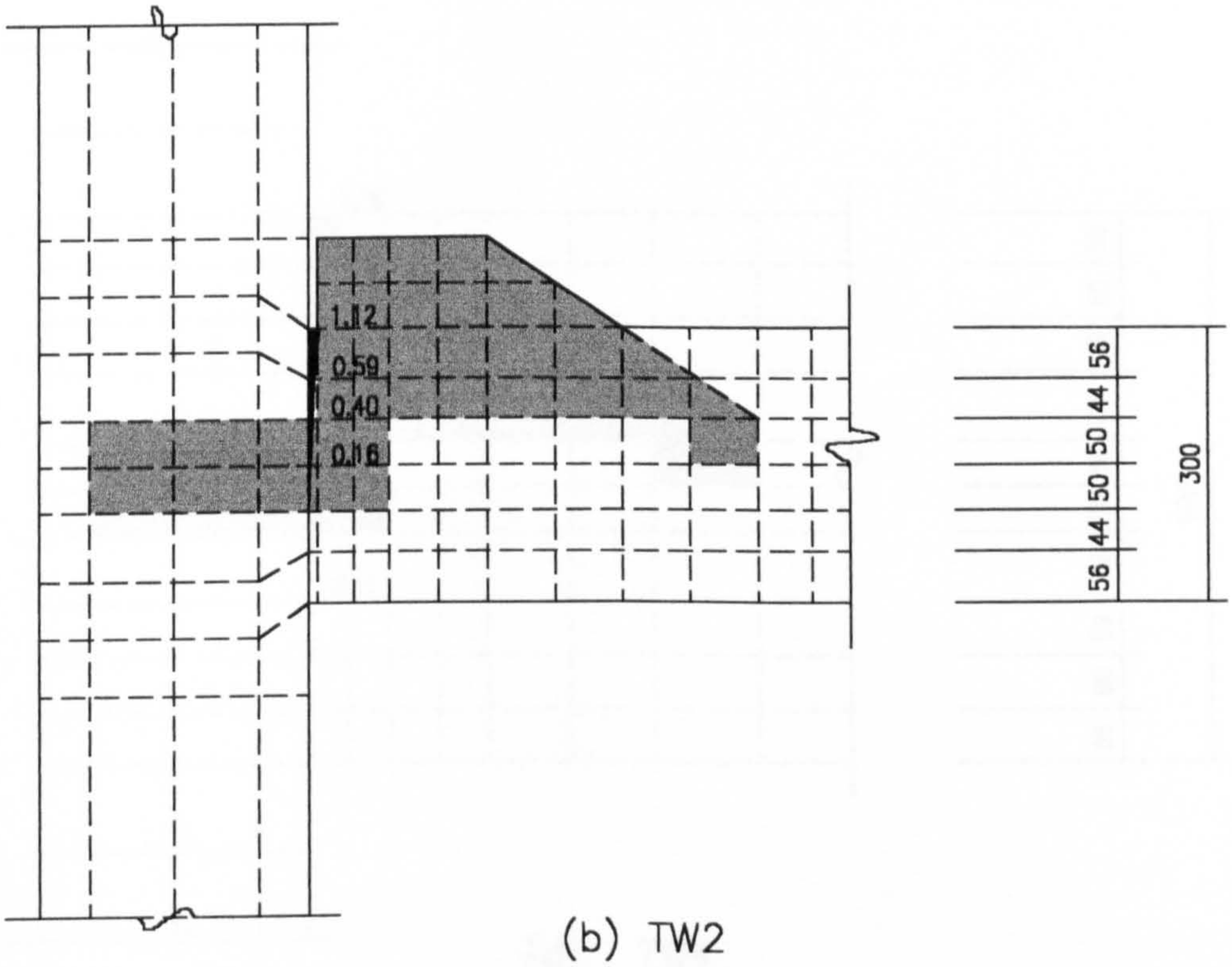

(b) TW2

Figure 6.59 *The ultimate state gap status at the beam end for TW1 to TW4 (scaled 10:1.0 in mm)*

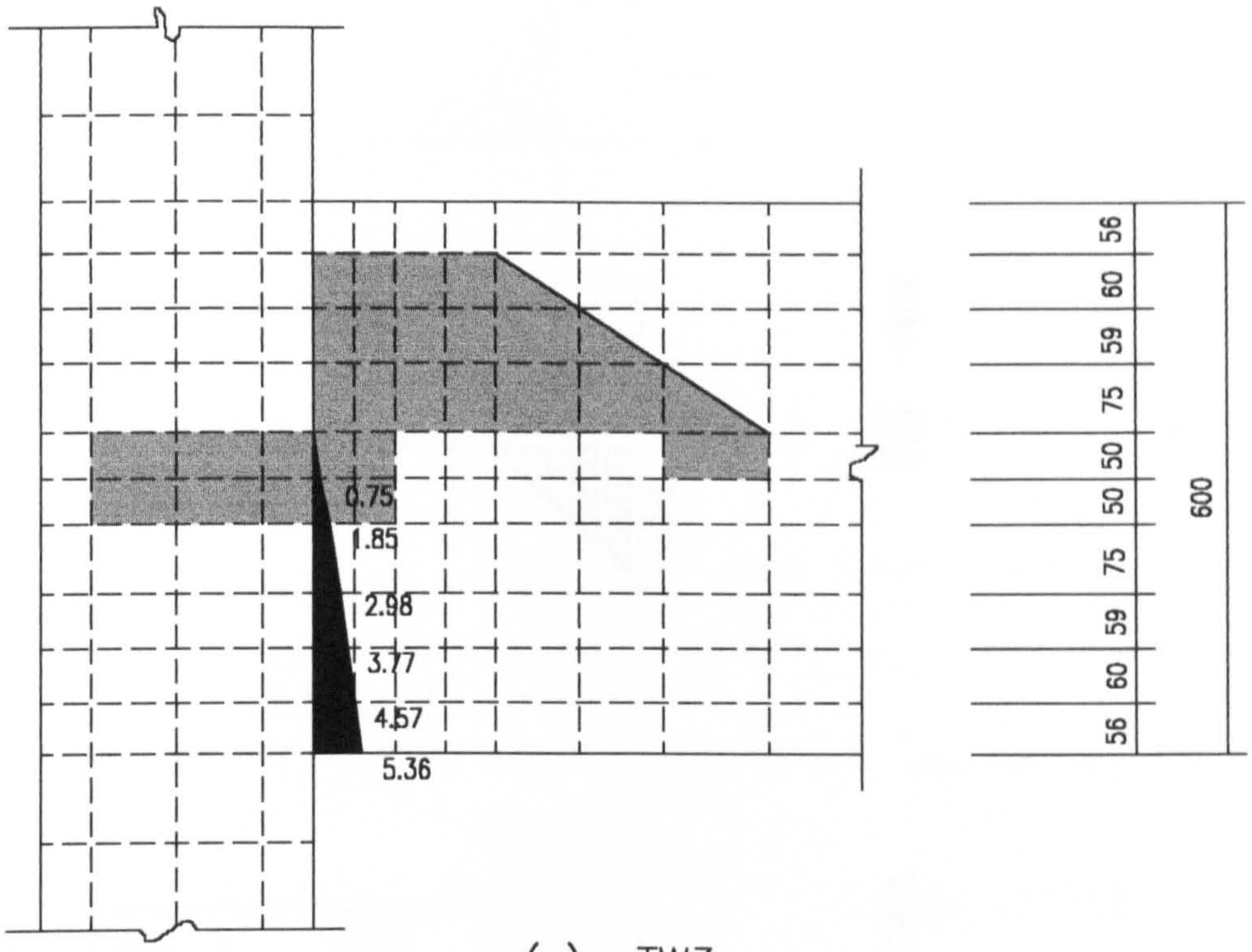

(c) TW3

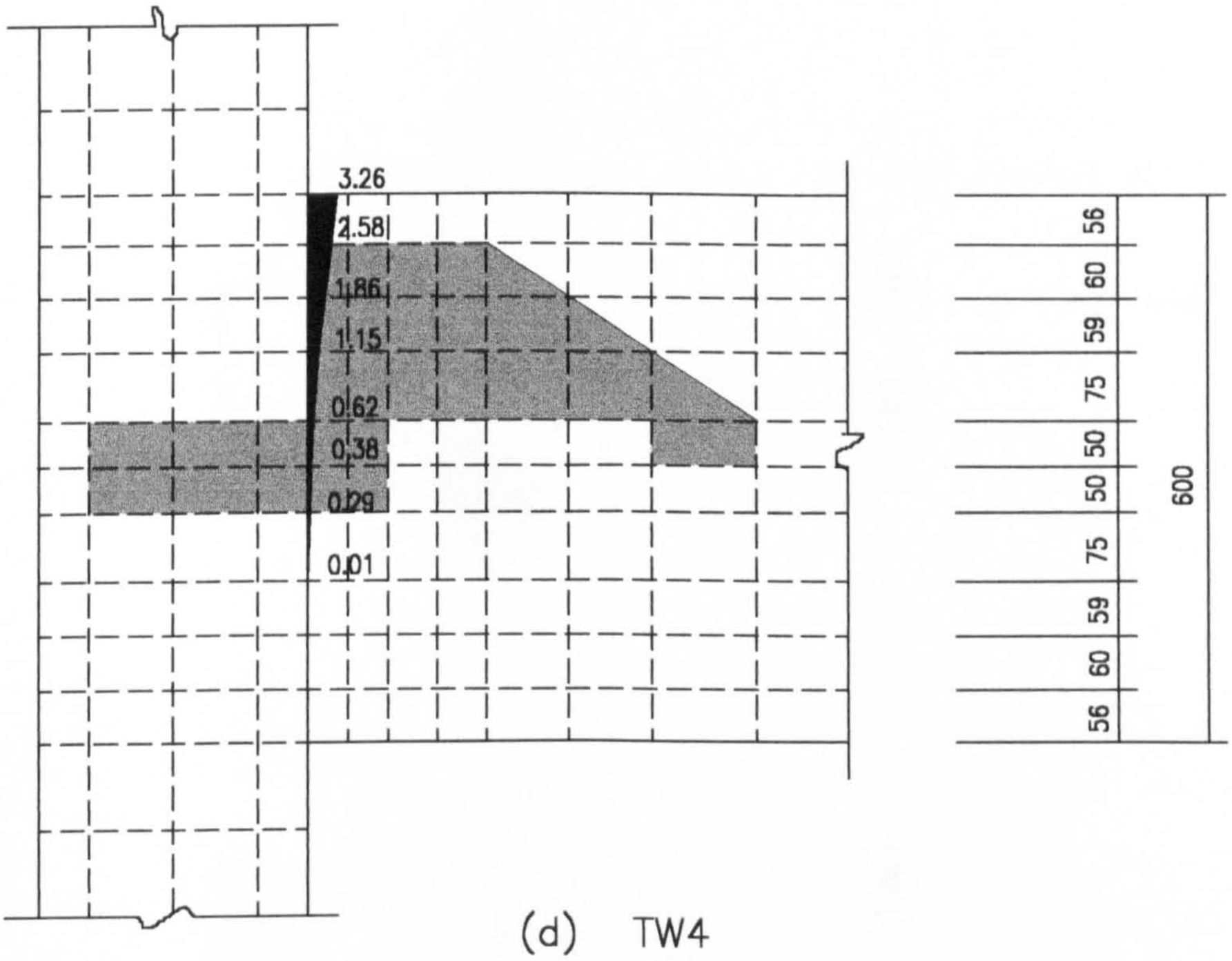

(d) TW4

Figure 6.59 *The ultimate state gap status at the beam end for TW1 to TW4 (scaled 10:1.0 in mm)*

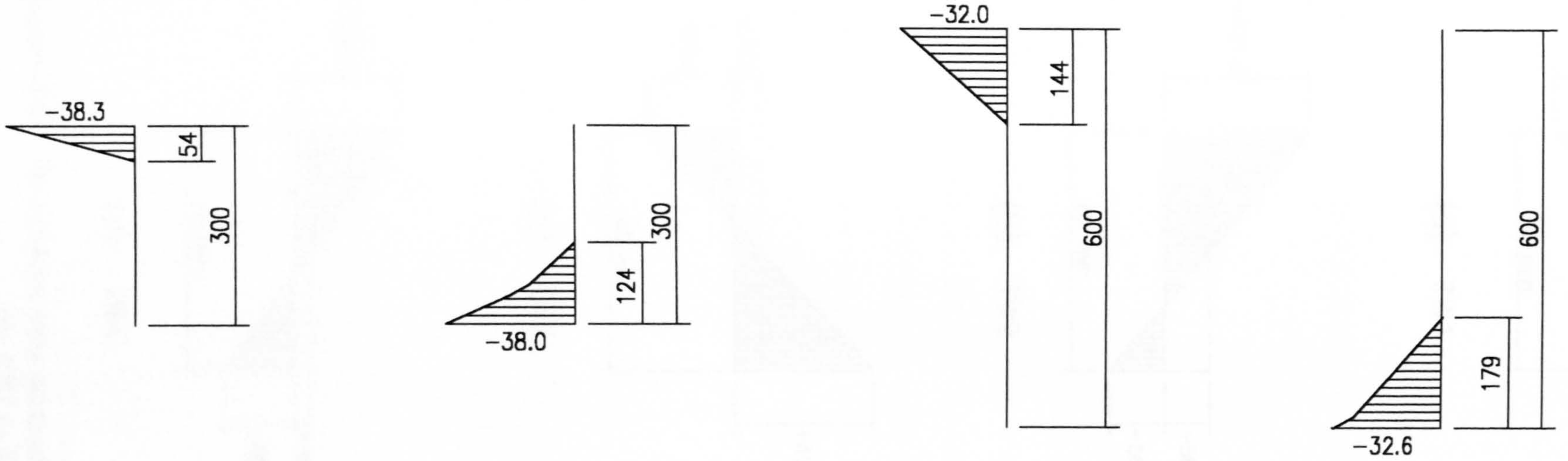

(a) TW1 (b) TW2 (c) TW3 (d) TW4

Figure 6.60 *The ultimate state compressive stress distribution in the grout middle section for TW1 to TW4 (N/mm^2)*

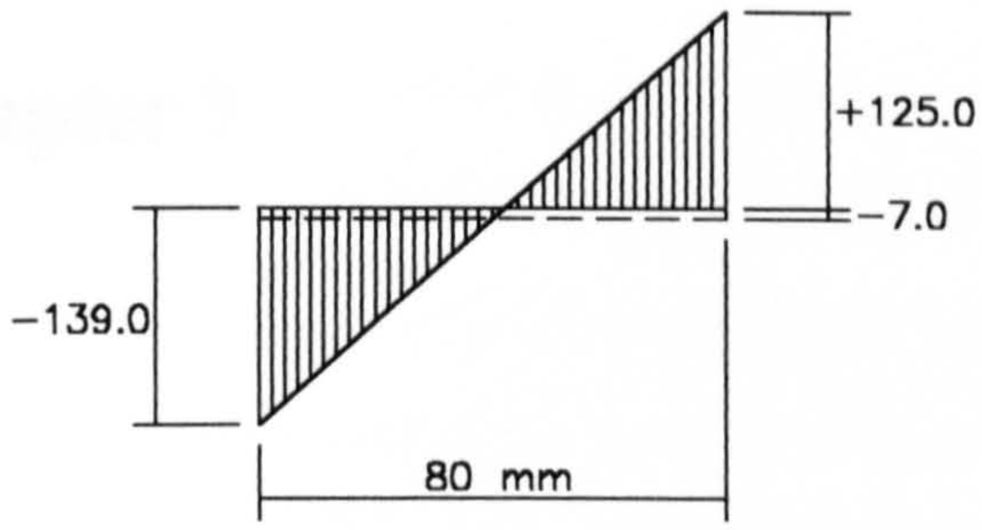

(a) TW1

Mw = 3.5 kNm

Vw = 14.0 kN

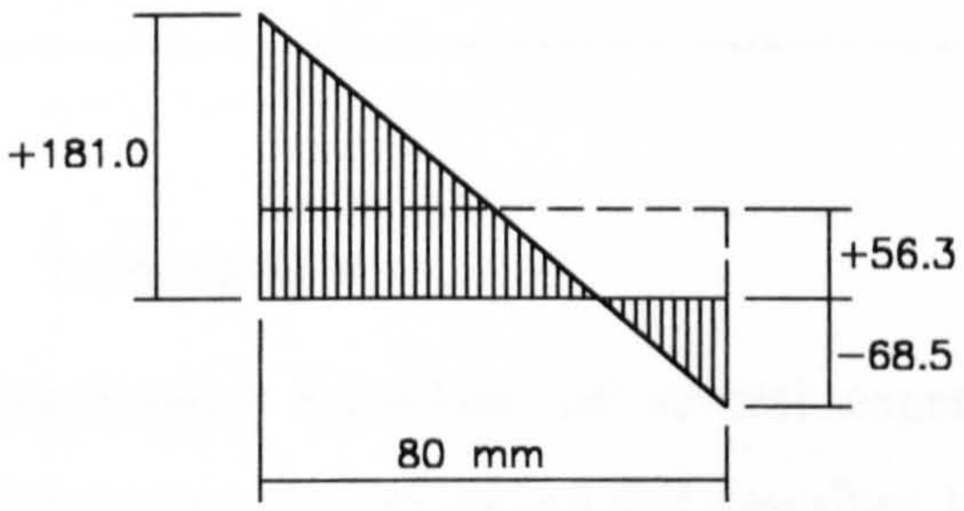

(b) TW2

Mw = 3.3 kNm

Vw = 112.5 kN

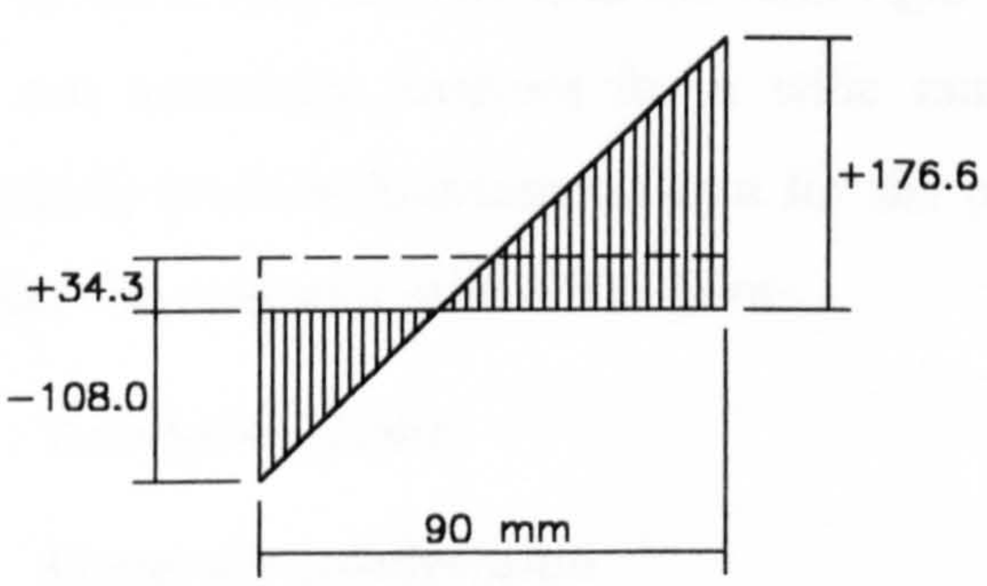

(c) TW3

Mw = 4.8 kNm

Vw = 77.0 kN

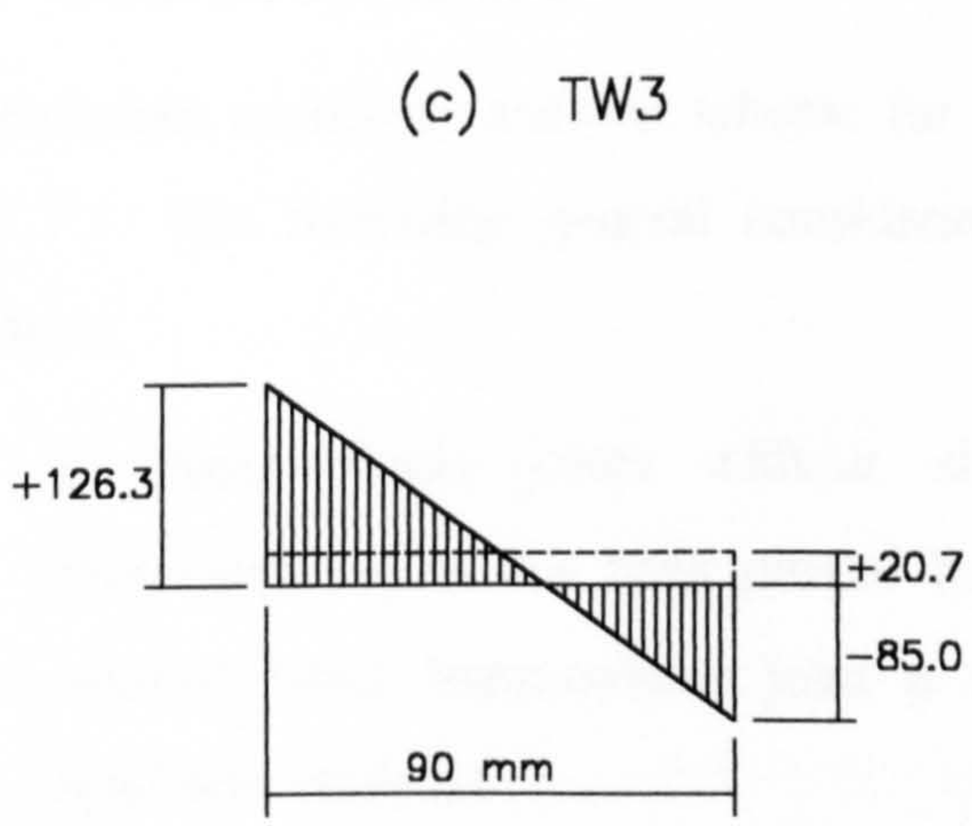

(d) TW4

Mw = 3.6 kNm

Vw = 46.5 kN

Figure 6.61 *The ultimate state vertical stress distribution at the weld position for TW1 to TW4 (N/mm^2)*

Chapter 7

Sensitivity Analyses of the Billet-Welded Plate Joints

7.1 Introduction

The mechanical behaviour of several experimental joints with billet-welded plate connections has been modelled and described in Chapter 6. However, a large number of factors affect the behaviour of the joints. These factors include not only the properties of the connectors themselves, but also the properties of the beam(s) and column(s). In order to more fully comprehend the semi-rigid behaviour of the joint, it is necessary to carry out sensitivity analyses for a wide range of parameters. These analyses will additionally provide fundamental data for the proposition of the simplified methods to calculate the characteristics of the joints.

7.2 Analysis scheme

7.2.1 General consideration

The complete sensitivity analysis scheme for the billet-welded plate joints is listed in Table 7.1. The following general considerations were used to select analyses for inclusion:

a. Beam-column joints without slabs perform with distinct semi-rigid characteristics, as has been proved by the previous investigations. Hence the external sway beam-column joint is selected as the basic joint type in the sensitivity analyses.

b. The parameters for one of the tests at Nottingham University, TW4, occur very frequently in the UK construction. Consequently, this joint is selected as a

standard case, and selected as Analysis 1 in Table 7.1. Only one change is made from this standard case in each of the other cases analysed.

c. The stress concentration within the joint will cause non-linear response throughout almost the entire loading process. Any variation of a component in the joint will be reflected by the joint behaviour. Therefore, not only are the obviously significant parameters included, such as beam depth, grout and concrete grades, but also the other detailed parameters.

d. For most parameters the possible maximum and minimum limits in the design standards or in practical engineering applications are selected, so that the sensitivities of the joints to the whole range of the parameters can be visualised.

e. Although only the external joints are scheduled, the behaviour of the joints in other positions can also be estimated according to the results of the analyses in the scheme. This is because

i. The moment resistance and rotation stiffness of the beam ends of an internal joint (╬) are approximately double that of a similar external joint (╠).

ii. The moment resistance and rotation stiffness of the column end in an internal joint on the top level (╦) are approximately half of that in a similar internal joint on the other levels (╬).

iii. The moment resistance and rotation stiffness of the beam end in an external joint on the top level (╔) are approximately half of that in an internal joint on the top level (╦).

f. Since a change of reinforcement strength has the similar effect as a change of steel/concrete ratio which develops the same reinforcement force, only the ratios of main and link reinforcement vary in the scheme.

g. The dimensions and the material properties of the connectors will not be changed frequently in practical engineering to avoid substitution errors. Therefore no variations for the connectors have been included in the scheme.

h. The welded plate is non-symmetrical to the beam end moment. Thus analyses for both the hogging and sagging beam end moments are essential for some

parameters, see analysis numbers 1 to 10 and 13 and 14 in Table 7.1. However, for some other parameters the paired analyses are not necessary, since the response to load reversal is predictably small. Thus only the case with hogging bending moment at the beam end is analysed for the joint configurations in analysis numbers 11-12 and 15 onwards in the schedule.

7.2.2 Experimental joints in the scheme

The first four analyses are of the tested external sway joints, named TW4, TW3, TW2 and TW1 respectively in Reference 14. Details of the specimens and the test arrangements can be found in Figs. 6.1, 6.2 and 6.5, 6.7. In Table 7.1 the dimensions of the specimens are the nominal design values. The first data quoted for concrete material properties are the mean values of tested cube compressive strength and the second data are the corresponding characteristic tensile strengths. The nominal value of 275 N/mm^2 is used as the characteristic yield strength for both the billet and the welded plate, while 460 N/mm^2 for both the main reinforcement and the links. The material strengths are arranged into groups with same properties when they are input into the models.

In Analysis 2 (TW3), results have been corrected as if the concrete and grout material properties have been changed to same as those in Analysis 1, because the large difference between the measured concrete cube strengths for the two beams was clearly significant. In fact, Analysis 2 is the standard case with reversed loading (with sagging moment at the beam end). In Analyses 3 and 4, the tested concrete and grout material properties are similar to those in the standard case for Analysis 1, thus they are directly applied into the analyses.

7.2.3 Beam geometry

The highest likely beam depth for a normal beam with length of 4.73 m, 1200 mm, is added and schemed as Analyses 5 and 6 for the two different loading directions. Together with Analyses 1 to 4, sensitivities of the joint behaviour to the beam depths of 300 mm, 600 mm and 1200 mm can be investigated.

Beam breadth varies in the Analyses 7, 8 and 9, 10 with values of 250 mm and 400 mm respectively.

The selected shortest and longest beam lengths are 3.15 m and 16.50 m. 3.15 m

produces a short frame beam, but with the span/effective depth ratio outside the range defined as a deep beam. 16.50 m offers a long and flexible frame beam with the span/effective depth ratio just near the largest limit for a normal beam as given in the design standards. The relevant analysis numbers of the two cases are 11 and 12 respectively.

7.2.4 Column geometry

Only one variable is made for column section, because in practical applications the dimensions of precast concrete members are normally limited to discrete regular values. The alternative value is 400*400 mm^2 as tabled in Analyses 13 and 14 for the two different loading directions.

The lowest possible and highest practical column lengths for buildings, 2.55 m and 7.00 m, are chosen as the next variables, scheduled as Analyses 15 and 16 in Table 7.1 respectively. 2.55 m is probably the lowest level height in some special structures, such as a car park. 7.00 m height associates with a slender column.

7.2.5 Concrete and grout grades

C40 and C70 are considered to be the lowest and highest concrete grades regularly applied to precast concrete components, they are therefore selected as the limiting values for both the beam and the column. In-situ cast grout, however, will normally achieve lower strength than the precast beams and columns. Thus the lowest limit grade value for concrete in the practical engineering application, C25, is used as the lowest grout grade. See Analyses 17 to 19 in Table 7.1 for the details.

7.2.6 Beam reinforcement

The beam top main reinforcement is doubled from the amount contained in the standard case. Both the minimum and maximum rates of reinforcement in the design standards are selected as the variation of beam bottom main reinforcement. The rates of 0.1% and 1.33% are chosen as the range for beam links. The associated analyses are numbered 20 to 24 in Table 7.1.

The ratios of both the top and the bottom main reinforcement in Table 7.1 were calculated using the following equation:

$$\rho_b = \frac{A_s}{b_b d_b}\% \qquad (7.1)$$

where ρ_b is the rate of beam top or bottom main reinforcement

A_s the total area of the beam top or the bottom main reinforcement

b_b the breadth of the beam section and

d_b the effective depth of the beam section, equals the height from the centre of the tensile reinforcement to the edge of compressive zone of the beam section.

The ratios of beam links in Table 7.1 were calculated using Eq. 7.2.

$$\rho_l = \frac{nA_{sv1}}{b_b s}\% \qquad (7.2)$$

where ρ_l is the rate of the beam links

n the number of links within one link space

A_{sv1} the area of one link section

b_b the breadth of the beam and

s the link space of the beam.

7.2.7 Column reinforcement

The minimum and maximum rates of column main reinforcement, 0.4% and 6.0%, are taken as the limiting variables. They are shown as Analyses 25 and 26 in Table 7.1. These rates were determined using Eq. 7.3.

$$\rho_c = \frac{A_{s,c}}{A_c}\% \qquad (7.3)$$

where ρ_c is the rate of column main reinforcement

$A_{s,c}$ the total area of the column main reinforcement and

A_c the gross area of the column section.

The varied rate of column joint links is taken as half of the value in the standard case. This case is listed as Analysis 27 in Table 7.1. The ratio was calculated using an

equation similar to Eq. 7.2.

7.2.8 Monolithic joint

In order to estimate the semi-rigid behaviour of the analysed joints based on the comparison with a rigid joint, one monolithic joint is scheduled. No billet, welded plate and in-situ grout exist in this joint, instead the beam and the column are treated as cast monolithically and both the top and the bottom beam reinforcement extends and anchors into the column. The other characteristics of this joint are similar to those in the standard case, see Analysis 28 in Table 7.1.

7.3 Models

All the models are built up using the finite element standardisation techniques described in Chapters 2 to 5. Due to the particular requirement in the scheme, however, each model has some individual features. The finite element model of the standard case acts as a basis. The models in the other cases are modified as little as possible to meet the need of the parameter variations in the scheme and to maintain the comparability with the standard model as well.

7.3.1 Model geometry

The standard cases in Analyses 1 and 2 have a common model geometry which has been graphically expressed in Fig. 6.9, while Analyses 3 and 4 in Fig. 6.8. Comparison of these two models indicates that all the differences between them are caused by the different beam depths. Detailed features of the two models have been described already in Chapter 6.3.1.

Figs. 7.1 to 7.6 exhibits the meshed models for 1200 mm beam depth (Analyses 5 and 6), variations of beam breadth (Analyses 7 to 10), larger beam length (Analysis 12), bigger column section (Analyses 13 and 14) and longer column length (Analysis 16) respectively. The models for cases with shorter beam length (Analysis 11) and shorter column length (Analysis 15) can be achieved by changing constraint and loading positions on the column and the beam of the standard model respectively. Variations in Analyses 17 to 27 do not affect the model geometry, which for these analyses is the same as the standard model.

The model of the monolithic joint in Analysis 28 contains no billet, welded plate or in-

situ grout, so no contact element is required. Both the beam top and the bottom main reinforcement extend into the column as long as the demanded anchorage length in the general design standards, Fig. 7.7.

7.3.2 Material properties

All descriptions of the material properties can be found in Chapter 6.3.2 and Figs. A.1 to A.3 in Appendix A, except those in Analyses 17 to 19. The stress-strain relationships of concrete for these three models are illustrated in Figs. A.4.

7.4 Solution

The solution method is the same as that used in the numerical analyses of the experimental joints, Chapter 6.4.

7.5 Results and analyses

Results of the schemed sensitivity analyses for the joints are illustrated in Tables 7.2 to 7.7 and Figs. 7.8 to 7.42. The numerical results in the tables are summarised in groups. Each group includes the variation and the associated responses for one parameter. For convenience of describing and reading, the groups and the associate results are numbered, and these numbers will be referenced in the following text. Tables 7.2 and 7.5 summarise the general load-displacement and moment-rotation results at the ultimate state for the cases with hogging and sagging beam end moments respectively. The derived load-displacement results are listed in Tables 7.3 and 7.6 for the two loading directions, whilst the derived moment-rotation results appear in Tables 7.4 and 7.7.

The graphic results include the equivalent stress distribution at the ultimate state, the relationships of load-displacement at the column mid-height, and the relationships of moment-rotation at the beam end. The relationships are compared within groups as well. In addition, solid symbols are used for the cases with hogging beam end moment, whereas hollow symbols represent the reversed loading direction.

The terms defined in Chapters 6.5 and 6.6 are still valid. In addition, secant rotation stiffness will be used in the analyses, which is defined as the ratio of two-third moment resistance over the associated rotation, see Fig. 6.32. In the following analyses, the failure mode of a joint is *weak beam end–strong column*, unless it is otherwise described.

7.5.1 Beam depth

As described in Chapter 6.9.1, the joints with 300 mm and 600 mm beam depths in Analyses 1 to 4 are *weak beam end-strong column joints*. The joints with 1200 mm beam depth (Analyses 5 and 6), have high stress concentrated at the column ends in both the two loading directions, Figs. 7.8 and 7.9, and they failed at the column ends. These 1200 mm deep beam joints are therefore *strong beam end-weak column joints*.

For the *weak beam end joints*, with an increase of beam depth, not only the capacities of load and moment resistance, but also the relevant stiffness are improved significantly, Figs. 7.10 to 7.13.

The numerical results in Table 7.2 indicate the following relationships: For the joints with hogging beam end moment, the 100% increase of the beam depth from 300 mm to 600 mm causes increases of 94% for the load and the moment resistance (Group 1, Columns G and H, Table 7.2), 96% for the initial sway stiffness (Group 1, Columns D and E, Table 7.3), 180% for the initial rotation stiffness (Group 1, Columns D and E, Table 7.4) and 172% for the secant rotation stiffness (Group 1, Columns G and H, Table 7.4). The rotation capacity, however, decreases by 51% (Group 1, Columns E and I, Table 7.2). For the joints with sagging beam end moment, the 100% increment of beam depth results in the increases of 297% for the load and the moment resistance (Group 1, Columns G and H, Table 7.5), 164% for the initial sway stiffness (Group 1, Columns D and E, Table 7.6), 233% for the initial rotation stiffness (Group 1, Columns D and E, Table 7.7) and 178% for the secant rotation stiffness (Group 1, Columns G and H, Table 7.7). The reduction of the rotation capacity is 18% (Group 1, Columns E and I, Table 7.5).

For the *weak column joints,* according to the stages before and after the column yields (actually the reinforcement in the column yields), the response curves in Figs. 7.10 to 7.13 distinctly contain two parts with different slopes in the ascending portions. The moment-rotation behaviour at the beam end can be analysed in the first part.

A 100% increment of beam depth from 600 mm to 1200 mm causes increases of 41% for the initial sway stiffness (Group 1, Columns D and E, Table 7.3), 159% for the initial rotation stiffness (Group 1, Columns D and E, Table 7.4) and 120% for the secant rotation stiffness (Group 1, Columns G and H, Table 7.4) for the cases with hogging

beam end moment. For the cases with sagging beam end moment, the relevant values are 86% (Group 1, Columns D and E, Table 7.6), 267% (Group 1, Columns D and E, Table 7.7) and 236% (Group 1, Columns G and H) respectively.

Fig. 7.11 shows that in the cases with hogging beam end moment, the limit case between *strong beam end* and *strong column* for the analysed joints is very close to the standard case.

The above results also indicate that the joints with sagging beam end moment respond to variation of the beam depth more sensitively than those with hogging beam end moment. The reason is that in the cases with sagging beam end moment, the effective beam depth increases more rapidly than the hogging beam end moment cases.

7.5.2 Beam breadth

As the beam breadth increases, the load, the moment resistance and the stiffness improve, Figs. 7.14 to 7.17. However, the improvement in the force responses is so small that the error permitted by the convergence criteria result in some unreasonable conclusions around the peak values.

For the deformation behaviour of the cases with hogging beam end moment, a 60% increase of beam breadth from 250 mm to 400 mm causes just 5% increase for the initial sway stiffness (Group 2, Columns D and E, Table 7.3) and 10% for the rotation stiffness (Group 2, Columns D and E, Table 7.4). Whereas, for the cases loaded in the reversed direction, the relevant increases are 12% (Group 2, Columns D and E, Table 7.6) and 32% (Group 2, Columns D and E, Table 7.6) respectively.

7.5.3 Beam length

The beam length will influence the sway stiffness of the joint, and it is shown in Fig. 7.18. The beam length, however, will not change the rotation stiffness of the joints, Fig. 7.19. The differences of moment resistance of the beam ends in Fig. 7.19 are probably caused by the different stress distributions at the beam ends.

7.5.4 Column section

The effect of the large column section stiffening the column rigidity can be clearly observed in the load-displacement relationships in Figs. 7.20 and 7.22. As the column sections vary from 300*300 mm^2 to 400*400 mm^2, which is 78% enlarged (Group 4,

Columns A and F, Table 7.2), the initial sway stiffness increases by about 70% (Group 4, Columns D and E, Table 7.3) and 27% (Group 3, Columns D and E, Table 7.6) respectively for the two opposed directions of loading.

The large column section also enhances the constraint to the grout at the beam end, thus the load and the moment resistance of the joint have been improved, Figs. 7.20 to 7.23. The 78% increase of column section results in about 22% and 5% increases of the load and moment resistance in the two loading directions, see Table 7.2 (Group 4, Columns B, D, G and H) and Table 7.5 (Group 3, Columns B, D, G and H). The large column section does not affect the initial rotation stiffness at the beam end significantly, Figs. 7.22 and 7.24, with only about 4% and 7% variation in Table 7.4 (Group 4, Columns D and E) and Table 7.7 (Group 3, Columns D and E).

7.5.5 Column length

The column length should be a very significant factor affecting the behaviour of the sway stiffness and the load at the column mid-height. These expectations are confirmed from the load-displacement relationships in Figs. 7.24. The numerical results indicate that as the column length increases 175% from 2.55 m to 7.00 m, the load reduces 71% from 79.65 kN to 23.16 kN (Group 5, Columns B and G, Table 7.2) and the sway stiffness reduces by about 9 times (Group 5, Columns D and E, Table 7.3).

The column lengths, however, change neither the failure mode nor the rotation stiffness of the joints, Fig. 7.25. Since the column lengths affect the stress distribution at the beam end, the moment resistance of the beam ends has been influenced. A short column associated with a slightly higher moment resistance, Figs. 7.24 and 7.25.

7.5.6 Concrete and grout grades

The concrete and grout grades are very important factors to the responses of the joints, Figs. 7.26 and 7.27. As the grades of the beam and column concrete and the grout increase to 70 N/mm^2, the joint becomes a *weak beam end-strong column joint*, Fig. 7.28. For the analysed joints, the critical zones are within the grouts, hence the grout grades are used as the variable parameter in the tables for comparison.

When the grout grade has a 93% increase from 25.0 N/mm^2 to 48.2 N/mm^2, the load and moment resistance gain by 87% (Group 6, Columns B, D, G and H, Table 7.2). The

rotation capacity increases by 47% (Group 6, Columns E and I, Table 2). For the deformation response, with 180% grade increase from 25 N/mm^2 to 70 N/mm^2, the initial sway, initial rotation and secant rotation stiffness increases by 39% (Group 6, Columns D and E, Table 7.3), 28% (Group 6, Columns D and E, Table 7.4) and 12% (Group 6, Columns G and H, Table 7.4) respectively.

7.5.7 Beam reinforcement

The beam top and bottom reinforcement and links are important factors to the mechanical behaviour of normal concrete joints, especially to the moment - rotation characteristics of the beam end. In the analysed precast concrete joints, however, both the beam top and bottom reinforcement is only located in the precast concrete beams, and there is no connection between this reinforcement and the column, Figs. 6.5 and 6.9(c). The links in TW1 to TW4 are located outside the joint core zone at the beam end, Fig. 6.5. Consequently, the variation of beam reinforcement does not significantly influence the behaviour of the joints, see Figs. 7.29 to 7.34.

7.5.8 Column reinforcement

The quantity and properties of column main reinforcement distinctly influence the mechanical behaviour of the column. As the amount of main reinforcement increases, both the load and the sway stiffness of the joint at the column mid-height improve, Fig. 7.35. However, the column main reinforcement is not a direct factor to the moment-rotation characteristics of the beam end. With the amount of reinforcement increases greatly, the rotation stiffness change only slightly as shown in Fig. 7.36.

For the case with 0.4% ratio of main reinforcement in the column, Analysis No. 25, the joint becomes to a *strong beam end-weak column joint*. Thus lower load and moment responses which are determined by the column resistance capacity have been achieved, Figs. 7.35 and 7.37.

The link characteristics in the joint core zone are significant factors for the normal concrete joint behaviour. The precast concrete joints analysed in the present work, however, fail in the grout at the beam end, thus variation of the column joint links does not significantly affect the joint behaviour, Figs. 7.38 to 7.39.

7.5.9 Configuration approach

The analysis results of the monolithic joint is described in this chapter. Due to symmetry of the geometry and of the materials, this joint will behave the same for the two directions of loading. For ease of comparison, the results of the two standard precast joints, Analyses 1 and No. 2 are shown simultaneously.

The effective beam depth of the monolithic joint has increased because of the connection of both the top and the bottom main reinforcement to the column. This has changed the characteristics of the joint so greatly that the joint failure mode has been converted into that of a *strong beam end-weak column,* Fig. 7.40. Both the load and the moment resistance have been enhanced significantly, Figs. 7.41 and 7.42.

The numerical results in Tables 7.2 and 7.5 show that the monolithic joint increases the load and the moment resistance by about 46% that of the precast joint with hogging beam end moment, and about 93% that with sagging beam end moment (Group 12, Columns B, D, G and H).

7.6 Summary

7.6.1 Semi-rigid behaviour of the joints

Since the monolithic joint of Analysis 28 is a *strong beam end-weak column joint*, its results can only be valid for the discussion of semi-rigid deformation behaviour at the beam ends of the joints. For the discussion of force behaviour, a fixed beam end moment resistance is required. The beam in the tested joint was equally reinforced at top and bottom of the section, Fig. 6.5. The fixed beam end moment resistance, $M_{u,\ fixed,}$ is estimated using the normal method in the standards:

$$M_{u,fixed} = A_s f_y (d_b - 0.45x) \approx A_s f_y (d_b - a') \qquad (7.4)$$

where A_s and f_y are the area and characteristic yield strength of reinforcement in tension, d_b the effective beam depth, x the depth of compressive zone and a' the distance from the centre of the compressive reinforcement to the edge of the compression zone. This moment resistance equals 139 kNm, 361 kNm and 805 kNm for the beams with depths of 300 mm, 600 mm and 1200 mm respectively.

The ratios of the moment resistance over the fixed beam end moments vary from 40% to

65% for the joints with hogging beam end moment (Co. C, Tables 7.4) and from 24% to 40% for the joints with sagging beam end moment (Co. C, Table 7.7). The moment resistance in the standard cases are 48% and 37% of the fixed beam end moment for Analyses 1 and 2 respectively.

For most precast joints which have similar geometry with the monolithic joint, the initial sway stiffness of is about 60% to 70% that of the monolithic joint in the hogging beam end moment loading condition. The initial rotation stiffness is about 30% of the monolithic joint value, see Columns D and E in Tables 7.3 and 7.4 respectively. In the loading condition with sagging beam end moment, these ratios are around 50% and 17% respectively, see Columns D and E in Tables 7.6 and 7.7.

7.6.2 Sensitivity of the force responses

The sensitivity of the load and the maximum moment of the joints to the variation of the parameters is summarised in Figs. 7.43 to 7.45. Actually, these figures are the graphic presentation of the results in Columns F to H in Tables 7.2 and 7.5. The broken line means that the joint with the parameter at the end point is a *weak column joint*. For a *weak beam end-strong column joint*, the beam end moment response value is the moment resistance. Thus for the cases of *weak column joints*, the moment responses in the figures should be smaller than the relevant moment resistance. In these figures, if a trendline of a parameter has a more vertical direction then, this parameter is more significant to the responses of the joints.

For most joints both the load and the moment respond to the variation of the parameters at same or very similar rates, see Figs. 7.43 and 7.44, because of the equilibrium relationship between the load at the column mid-height and the moment at the beam mid-span. Thus the exception is only for those joints with the beam length, the column length or the column main reinforcement having been changed. This association is also indicated in Columns G and H in Tables 7.2 and 7.5. In the sagging beam end loading condition, both the load and the moment have exactly the same responses, thus they are summarised in one chart, Fig. 7.45.

From the results shown in Figs. 7.43 to 7.45 and the analyses in the above chapters, it can be concluded that beam depth and concrete/grout grade are the most significant factors to the joint force responses. Furthermore, both of them increase the force

responses at the same rate for the cases with hogging beam end moment. About a 100% increase of the parameters causes about 100% increase of the force responses, Figs. 7.43 and 7.44, until the column failure constrains the joint capacities.

For most of the other parameters, the moment responses vary within 20% although the parameters range several hundred percentage points, Figs. 7.44 and 7.45.

7.6.3 Sensitivity of the deformation responses

The sensitivity of the secant rotation stiffness is summarised in Figs. 7.46 and 7.47, because this stiffness is frequently used in the simplified analyses. It is shown that the beam depth is the only significant factor affecting the secant rotation stiffness of the beam end.

The sensitivity of the rotation at the peak point is summarised in Figs. 7.48 and 7.49. Again it indicates that both the beam depth and concrete/grout grade are the two most important factors on the rotation responses. As the beam depth increases, the rotation capacity reduces. However, as the concrete/grout grade increases, the rotation capacity improves.

7.7 Simplified predictions for the characteristics of the beam end

The semi-rigid behaviour of the joints in precast concrete frame structures can be reached by experimental investigation or/and finite element analyses. The behaviour of the billet-welded plate joints can be estimated from the existing test results and the sensitivity analysis results. Both of the two numerical approaches have been fully described in the preceding chapters. In engineering practice, however, simplified predictions may also be required, because they are quick, economic and convenient for preliminary analysis. Therefore methods of predicting the required characteristics at the beam end in the billet-welded plate joints are proposed through a statistical approach using the sensitivity analysis results. In other words, the beam end characteristics from the sensitivity analysis already described are summarised and represented by a set of statistical equations. These characteristics include the moment resistance, the initial rotation stiffness, the secant rotation stiffness and the rotation capacity. Thus all characteristics required to define the joint performance in a full frame analysis can be estimated.

The statistical analyses also have been made for predictions of the characteristics of horizontal force, displacement and associated stiffness at the column mid-height. However it is difficult to give a set of equations with acceptable statistical accuracy. Thus this part of calculation, which is not essential for full frame analysis, is omitted.

7.7.1 General considerations

a. Only the cases of *weaker beam end-strong column* are taken into account in derivation of the equations for the characteristics of the beam end.

b. Although the numerical results provide some indications of behaviour, such as that at the ultimate state the compressive stress in the grout is triangularly distributed, the stress states of the connectors however are uncertain. Methods using equilibrium of the internal forces at the critical section are invalid. Consequently a statistical approach is adopted.

c. The significant factors taken into account in the statistical calculation include the geometry and material properties of both the beam end and the column. The properties of the column dominate the boundary conditions of the beam end. These factors will be accounted in grouped items according to their physical relationships to the characteristics.

d. Since many factors will be included, multiple linear regression statistical analyses are essential.

7.7.2 Equations

In each of the semi-empirical Eqs. 7.5 to 7.8, the coefficients for each term are statistically derived from the 23 appropriate FEA results described in the sensitivity analyses. Statistical measures (R^2) and Standard Error of Estimates (*SEE*) for each equation are quoted on the Figs. 7.50 to 7.53.

a. Beam end moment resistance $M_{u,\,cal}$

$$M_{u,cal} = 9.428*10^{-8} f_{cu} b_b d_e^{\,2} + 2.746*10^{-9} E_c I_c / L_c \qquad (7.5)$$

where f_{cu} is the mean value of the tested cube strength in N/mm^2

b_b the breadth of the beam end/grout in mm

d_e the effective depth of the beam end section in mm, taken as the distance from

the location 15 mm below the billet top to the edge of the compressive zone. The value 15 mm is defined because it gives batter statistical predictions.

E_c the modulus of elasticity of column concrete in N/mm^2, calculated using the methods described in Chapter 4.4.2

I_c the second area moment of the column section accounting the contribution of the reinforcement, in mm^4 and

L_c the height of the column in mm.

b. Beam end initial rotation stiffness $K_{r,\,i,\,cal}$

$$K_{r,i,cal} = 2.79*10^{-5} f_{cu} b_b d_e^{\,2} + 1.80*10^{-7} E_c I_c / L_c \qquad (7.6)$$

c. Beam end secant rotation stiffness $K_{r,\,se,\,cal}$

$$K_{r,se,cal} = 2.13*10^{-5} f_{cu} b_b d_e^{\,2} + 1.90*10^{-7} E_c I_c / L_c \qquad (7.7)$$

d. Beam end rotation capacity $\theta_{u,\,cal}$

$$\theta_{u,cal} = 1.80*10^{-12} f_{cu} b_b d_e^{\,2} + 1.39*10^{-13} E_c I_c / L_c - 4.022*10^{-5} d_e + 0.0152 \qquad (7.8)$$

The predicted beam end characteristics are shown in Figs. 7.50 to 7.53, against the targets of the numerical values. The associated data are listed in Table 7.8. These results show that the statistical equations can provide predictions for the beam end characteristics with acceptable accuracy, and remain functions of parameters with clear physical meaning.

No.	Force direction at the beam mid-span	Beam geometry			Column geometry			Concrete Material (N/mm^2)			Steel/concrete ratios (%)				
		Depth (mm)	Breadth (mm)	Length (mm)	Depth (mm)	Breadth (mm)	Length (mm)	Beam	Column	Grout	Beam top	Beam bottom	Beam links	Column main	Column joint links
1	⊩↓	**600**	**300**	**4730**	**300**	**300**	**3000**	**-54.50 +2.93**	**-58.60 +3.10**	**-48.20 +2.65**	**0.985**	**0.985**	**0.52**	**1.40**	**0.785**
2	⊩↑	**600**	**300**	**4730**	**300**	**300**	**3000**	**-54.50 +2.93**	**-58.60 +3.10**	**-48.20 +2.65**	**0.985**	**0.985**	**0.52**	**1.40**	**0.785**
3	⊩↓	**300**	300	4730	300	300	3000	**-54.50 +2.93**	**-58.40 +3.10**	**-49.80 +2.72**	2.196	2.196	0.52	1.40	0.785
4	⊩↑	**300**	300	4730	300	300	3000	**-54.50 +2.93**	**-58.40 +3.10**	**-46.20 +2.55**	2.196	2.196	0.52	1.40	0.785
5	⊩↓	**1200**	300	4730	300	300	3000	-54.50 +2.93	-58.60 +3.10	-48.20 +2.65	0.985	0.985	0.52	1.40	0.785
6	⊩↑	**1200**	300	4730	300	300	3000	-54.50 +2.93	-58.60 +3.10	-48.20 +2.65	0.985	0.985	0.52	1.40	0.785
7	⊩↓	600	**250**	4730	300	300	3000	-54.50 +2.93	-58.60 +3.10	-48.20 +2.65	0.985	0.985	0.52	1.40	0.785
8	⊩↑	600	**250**	4730	300	300	3000	-54.50 +2.93	-58.60 +3.10	-48.20 +2.65	0.985	0.985	0.52	1.40	0.785
9	⊩↓	600	**400**	4730	300	300	3000	-54.50 +2.93	-58.60 +3.10	-48.20 +2.65	0.985	0.985	0.52	1.40	0.785
10	⊩↑	600	**400**	4730	300	300	3000	-54.50 +2.93	-58.60 +3.10	-48.20 +2.65	0.985	0.985	0.52	1.40	0.785

Table 7.1 *Scheme for the sensitivity analysesof the billet-welded plate joints*

No.	Force direction at the beam mid-span	Beam geometry			Column geometry			Concrete Material (N/mm^2)			Steel/concrete ratios (%)				
		Depth (mm)	Breadth (mm)	Length (mm)	Depth (mm)	Breadth (mm)	Length (mm)	Beam	Column	Grout	Beam top	Beam bottom	Beam links	Column main	Column joint links
11	⊩↓	600	300	**3150**	300	300	3000	-54.50 +2.93	-58.60 +3.10	-48.20 +2.65	0.985	0.985	0.52	1.40	0.785
12	⊩↓	600	300	**16500**	300	300	3000	-54.50 +2.93	-58.60 +3.10	-48.20 +2.65	0.985	0.985	0.52	1.40	0.785
13	⊩↓	600	300	4730	**400**	**400**	3000	-54.50 +2.93	-58.60 +3.10	-48.20 +2.65	0.985	0.985	0.52	1.40	0.785
14	⊩↑	600	300	4730	**400**	**400**	3000	-54.50 +2.93	-58.60 +3.10	-48.20 +2.65	0.985	0.985	0.52	1.40	0.785
15	⊩↓	600	300	4730	300	300	**2550**	-54.50 +2.93	-58.60 +3.10	-48.20 +2.65	0.985	0.985	0.52	1.40	0.785
16	⊩↓	600	300	4730	300	300	**7000**	-54.50 +2.93	-58.60 +3.10	-48.20 +2.65	0.985	0.985	0.52	1.40	0.785
17	⊩↓	600	300	4730	300	300	3000	**-70.00 +3.58**	**-70.00 +3.58**	**-70.00 +3.58**	0.985	0.985	0.52	1.40	0.785
18	⊩↓	600	300	4730	300	300	3000	**-40.00 +2.25**	**-40.00 +2.25**	**-40.00 +2.25**	0.985	0.985	0.52	1.40	0.785
19	⊩↓	600	300	4730	300	300	3000	**-40.00 +2.25**	**-40.00 +2.25**	**-25.00 +1.72**	0.985	0.985	0.52	1.40	0.785
20	⊩↓	600	300	4730	300	300	3000	-54.50 +2.93	-58.60 +3.10	-48.20 +2.65	**1.970**	0.985	0.52	1.40	0.785

Table 7.1 continued *Scheme for the sensitivity analyses of the billet-welded plate joints*

No.	Force direction at the beam mid-span	Beam geometry			Column geometry			Concrete Material (N/mm^2)			Steel/concrete ratios (%)				
		Depth (mm)	Breadth (mm)	Length (mm)	Depth (mm)	Breadth (mm)	Length (mm)	Beam	Column	Grout	Beam top	Beam bottom	Beam links	Column main	Column joint links
21	⊩↓	600	300	4730	300	300	3000	-54.50 +2.93	-58.60 +3.10	-48.20 +2.65	0.985	**0.200**	0.52	1.40	0.785
22	⊩↓	600	300	4730	300	300	3000	-54.50 +2.93	-58.60 +3.10	-48.20 +2.65	0.985	**4.000**	0.52	1.40	0.785
23	⊩↓	600	300	4730	300	300	3000	-54.50 +2.93	-58.60 +3.10	-48.20 +2.65	0.985	0.985	**0.10**	1.40	0.785
24	⊩↓	600	300	4730	300	300	3000	-54.50 +2.93	-58.60 +3.10	-48.20 +2.65	0.985	0.985	**1.33**	1.40	0.785
25	⊩↓	600	300	4730	300	300	3000	-54.50 +2.93	-58.60 +3.10	-48.20 +2.65	0.985	0.985	0.52	**0.40**	0.785
26	⊩↓	600	300	4730	300	300	3000	-54.50 +2.93	-58.60 +3.10	-48.20 +2.65	0.985	0.985	0.52	**6.00**	0.785
27	⊩↓	600	300	4730	300	300	3000	-54.50 +2.93	-58.60 +3.10	-48.20 +2.65	0.985	0.985	0.52	1.40	**0.393**
28	⊩↓	600	300	4730	300	300	3000	-54.50 +2.93	-58.60 +3.10	-48.20 +2.65	0.985	0.985	0.52	1.40	0.785

Note: Analysis No. 28 is a monolithic joint.

Table 7.1 continued *Scheme for the sensitivity analyses of the billet-welded plate joins*

No.	Parameter p	A	B	C	D	E	F	G	H	I	J
		p value	F (kN)	d (mm)	M_u (kNm)	θ_u (rad)	p/p_s (%)	F/F_s (%)	$M_u/M_{u,s}$ (%)	$\theta_u/\theta_{u,s}$ (%)	Failure mode
1	Beam depth (mm)	300	32.40	40.00	89.67	0.0080	50.00	51.53	51.57	150.94	Weak beam end
		600	62.87	40.00	173.89	0.0053	100.00	100.00	100.00	100.00	Weak beam end
		1200	79.53	70.00	220.09	0.0026	200.00	126.50	126.57	37.74	Weak column
2	Beam breadth (mm)	250	61.05	40.00	168.95	0.0059	83.33	97.10	97.10	111.32	Weak beam end
		300	62.87	40.00	173.89	0.0053	100.00	100.00	100.00	100.00	Weak beam end
		400	59.29	35.00	164.10	0.0046	133.33	94.32	94.329	86.79	Weak beam end
3	Beam length (m)	3.15	67.75	50.00	228.90	0.0056	66.60	107.77	131.63	105.66	Weak beam end
		4.73	62.87	40.00	173.89	0.0053	100.00	100.00	100.00	100.00	Weak beam end
		16.50	65.62	55.00	192.26	0.0063	345.24	104.39	110.56	118.87	Weak beam end
4	Column section (mm^2)	90000	62.87	40.00	173.89	0.0053	100.00	100.00	100.00	100.00	Weak beam end
		160000	77.46	35.00	210.19	0.0081	177.78	123.21	120.87	152.83	Weak beam end
5	Column length (m)	2.55	79.65	30.00	177.81	0.0054	85.00	126.69	102.25	101.89	Weak beam end
		3.00	62.87	40.00	173.89	0.0053	100.00	100.00	100.00	100.00	Weak beam end
		7.00	23.16	135.00	149.55	0.0045	36.84	36.84	86.00	84.91	Weak beam end
6	Concrete/grout grade (N/mm^2)	25.00	33.64	25.00	93.11	0.0036	63.64	53.51	53.54	67.92	Weak beam end
		40.00	38.55	25.00	106.67	0.0033	72.73	61.31	61.35	62.26	Weak beam end
		48.20	62.87	40.00	173.89	0.0053	97.76	100.00	100.00	100.00	Weak beam end
		70.00	77.79	60.00	215.79	0.0095	127.27	123.74	124.10	179.24	Weak column

Table 7.2 *General results of the sensitivity analyses for the billet-welded plate joints with hogging beam end moment*

No.	Parameter p	A	B	C	D	E	F	G	H	I	J
		p value	F (kN)	d (mm)	M_u (kNm)	θ_u (rad)	p/p_s (%)	F/F_s (%)	$M_u/M_{u,s}$ (%)	$\theta_u/\theta_{u,s}$ (%)	Failure mode
7	Beam top main reinforcement	0.98%	62.87	40.00	173.89	0.0053	100.00	100.00	100.00	100.00	Weak beam end
		1.92%	59.06	35.00	163.44	0.0047	195.51	93.94	93.99	88.68	Weak beam end
8	Beam bottom main reinforcement	0.20%	64.44	47.00	178.33	0.0070	20.41	102.50	102.55	132.08	Weak beam end
		0.98%	62.87	40.00	173.89	0.0053	100.00	100.00	100.00	100.00	Weak beam end
		4.00%	63.56	40.00	175.90	0.0052	408.16	101.10	101.16	98.11	Weak beam end
9	Beam links	0.10%	65.80	45.00	182.11	0.0061	19.23	104.67	104.73	115.09	Weak beam end
		0.52%	62.87	45.00	173.89	0.0053	100.00	100.00	100.00	100.00	Weak beam end
		1.33%	62.81	40.00	173.83	0.0053	255.77	99.91	99.96	100.00	Weak beam end
10	Column main reinforcement	0.40%	49.22	50.00	141.32	0.0041	11.17	28.57	81.27	77.36	Weak column
		1.40%	62.87	40.00	173.89	0.0053	100.00	100.00	100.00	100.00	Weak beam end
		6.00%	59.75	25.00	165.36	0.0046	167.60	428.57	95.09	86.79	Weak beam end
11	Column joint links	0.39%	67.26	45.00	182.40	0.0059	49.75	106.99	104.89	111.32	Weak beam end
		0.79%	62.87	40.00	173.89	0.0053	99.37	100.00	100.00	100.00	Weak beam
12	Configuration approach	Monolithic	91.92	55.00	254.37	0.0047		146.21	146.28	88.68	Weak column
		Analysis 1	62.87	40.00	173.89	0.0053		100.00	100.00	100.00	Weak beam end
		Analysis 2	47.71	45.00	132.04	0.0092		75.89	75.93	173.58	Weak beam end

Note: d is the displacement applied at the column mid-height at the joint ultimate state, F is the relevant reaction, named load, M is the beam end moment at the joint ultimate state, θ is the relevant rotation, footnotes u and s mean *ultimate* and *standard* respectively.

Table 7.2 continued *General results of the sensitivity analyses for the billet-welded plate joints with hogging beam end moment*

No.	Parameter p	A	B	C	D	E	F	G	H	I	J
		p value	F (kN)	F/F_m (%)	$K_{d,i}$ (kNm/rad)	$K_{d,i}/K_{d,i,s}$ (%)	$K_{d,i}/K_{d,i,m}$ (%)	$K_{d,se}$ (kNm/rad)	$K_{d,se}/K_{d,se,s}$ (%)	$K_{d,se}/K_{d,se,m}$ (%)	Failure mode
1	Beam depth (mm)	300	32.40	35.25	1400.00	51.04	33.38	941.16	53.50	37.13	Weak beam end
		600	62.87	68.40	2742.68	100.00	65.39	1759.09	100.00	69.40	Weak beam end
		1200	79.53	86.52	3873.08	141.22	92.34	2697.40	153.34	106.42	Weak column
2	Beam breadth (mm)	250	61.05	66.42	2675.36	97.55	63.78	1706.11	96.99	67.31	Weak beam end
		300	62.87	68.40	2742.68	100.00	65.39	1759.09	100.00	69.40	Weak beam end
		400	59.29	64.51	2805.46	102.29	66.88	1903.36	108.20	75.09	Weak beam end
3	Beam length (m)	3.15	67.75	73.71	2761.76	100.70	65.84	1789.58	101.73	70.60	Weak beam end
		4.73	62.87	68.40	2742.68	100.00	65.39	1759.09	100.00	69.40	Weak beam end
		16.50	65.62	71.40	2380.24	86.79	56.74	1347.58	76.61	53.16	Weak beam end
4	Column section (mm^2)	90000	62.87	68.40	2742.68	100.00	65.39	1759.09	100.00	69.40	Weak beam end
		160000	77.46	84.27	4622.02	168.52	110.19	2977.27	169.25	117.46	Weak beam end
5	Column length (m)	2.55	79.65	86.65	3995.50	145.68	95.26	3081.45	175.17	121.57	Weak beam end
		3.00	62.87	68.40	2742.68	100.00	65.39	1759.09	100.00	69.40	Weak beam end
		7.00	23.16	25.20	374.36	13.65	8.93	189.83	10.79	7.49	Weak beam end
6	Concrete grade (N/mm^2)	25.00	33.64	53.51	2242.76	81.77	53.47	1740.81	96.91	67.26	Weak beam end
		40.00	38.55	41.94	2265.88	82.62	54.02	1729.52	98.32	68.23	Weak beam end
		48.20	62.87	68.40	2742.68	100.00	65.39	1759.09	100.00	69.40	Weak beam end
		70.00	77.79	84.63	3115.96	113.61	74.29	1911.95	108.69	75.43	Weak column

Table 7.3 *Derived load-displacement results of the sensitivity analyses for the joints with hogging beam end moment*

No.	Parameter p	A	B	C	D	E	F	G	H	I	J
		p value	F (kN)	F/F_m (%)	$K_{d,i}$ (kNm/rad)	$K_{d,i}/K_{d,i,s}$ (%)	$K_{d,i}/K_{d,i,m}$ (%)	$K_{d,se}$ (kNm/rad)	$K_{d,se}/K_{d,se,s}$ (%)	$K_{d,se}/K_{d,se,m}$ (%)	Failure mode
7	Beam top main reinforcement	0.98%	62.87	68.40	2742.68	100.00	65.39	1759.09	100.00	69.40	Weak beam end
		1.92%	59.06	64.25	2748.10	100.20	65.52	1862.71	105.89	73.49	Weak beam end
8	Beam bottom main reinforcement	0.20%	64.44	70.10	2731.40	99.59	65.12	1756.93	99.88	69.31	Weak beam end
		0.98%	62.87	68.40	2742.68	100.00	65.39	1759.09	100.00	69.40	Weak beam end
		4.00%	63.56	69.15	2776.66	101.24	66.20	1785.00	101.47	70.42	Weak beam end
9	Beam links	0.10%	65.80	71.59	2742.58	99.99	65.38	1772.2	100.75	69.92	Weak beam end
		0.52%	62.87	68.40	2742.68	100.00	65.39	1759.09	100.00	69.40	Weak beam end
		1.33%	62.81	68.33	2743.00	100.01	65.40	1759.92	100.05	69.43	Weak beam end
10	Column main reinforcement	0.40%	49.22	53.55	2363.02	86.16	56.34	1460.17	83.01	57.61	Weak column
		1.40%	62.87	68.40	2742.68	100.00	65.39	1759.09	100.00	69.40	Weak beam end
		6.00%	59.75	65.01	3333.92	121.56	79.48	2625.07	149.23	103.56	Weak beam end
11	Column joint links	0.39%	67.26	73.17	2739.58	99.89	65.31	1765.63	100.37	69.66	Weak beam end
		0.79%	62.87	68.40	2742.68	100.00	65.39	1759.09	100.00	69.40	Weak beam end
12	Configuration approach	Monolithic	91.92	100.00	4194.46	152.93	100.00	2534.78	144.10	100.00	Weak column
		Analysis 1	62.87	68.40	2742.68	100.00	65.39	1759.09	100.00	69.40	Weak beam end
		Analysis 2	47.71	51.91	2070.22	75.48	49.36	1337.45	76.03	52.76	Weak beam end

Note: F is the load at the column mid-height at the joint ultimate state, K is the stiffness, footnotes *m, d, i, s, se* mean *monolithic*, *displacement*, *initial*, *standard* and *secant* respectively.

Table 7.3 continued *Derived load-displacement results of the sensitivity analyses for the joints with hogging beam end moment*

No.	Parameter p	A	B	C	D	E	F	G	H	I	J
		p value	M_u (kNm)	$M_u/M_{u,\,fix}$ (%)	$K_{r,\,i}$ (kNm/rad)	$K_{r,\,i}/K_{r,\,i,\,s}$ (%)	$K_{r,\,i}/K_{r,\,i,\,m}$ (%)	$K_{r,\,se}$ (kNm/rad)	$K_{r,\,se}/K_{r,\,se,\,s}$ (%)	$K_{r,\,se}/K_{r,\,se,\,m}$ (%)	Failure mode
1	Beam depth (mm)	300	89.67	64.51	17243.36	35.76	11.62	13484.51	36.83	21.95	Weak beam end
		600	173.89	48.17	48223.13	100.00	32.49	36616.01	100.00	59.59	Weak beam end
		1200	220.09	27.34	124924.00	259.05	84.16	80657.48	220.28	131.26	Weak column
2	Beam breadth (mm)	250	168.95	46.80	44709.90	92.71	30.12	32679.96	89.25	53.18	Weak beam end
		300	173.89	48.17	48223.13	100.00	32.49	36616.01	100.00	59.59	Weak beam end
		400	164.10	45.46	49139.49	101.90	33.10	39980.65	109.19	65.07	Weak beam end
3	Beam length (m)	3.15	228.90	63.41	49321.65	102.28	33.23	36152.52	98.73	58.84	Weak beam end
		4.73	173.89	48.17	48223.13	100.00	32.49	36616.01	100.00	59.59	Weak beam end
		16.50	192.26	53.26	48902.24	101.41	32.94	35645.63	97.35	58.01	Weak beam end
4	Column section (mm^2)	90000	173.89	48.17	48223.13	100.00	32.49	36616.01	100.00	59.59	Weak beam end
		160000	210.19	58.22	50007.90	103.70	33.69	37971.38	103.70	61.80	Weak beam end
5	Column length (m)	2.55	177.81	49.25	49941.65	103.56	33.65	37122.36	101.38	60.41	Weak beam end
		3.00	173.89	48.17	48223.13	100.00	32.49	36616.01	100.00	59.59	Weak beam end
		7.00	149.55	41.43	42115.68	87.34	28.37	36689.86	100.20	59.71	Weak beam end
6	Concrete grade (N/mm^2)	25.00	93.11	25.79	40566.27	84.12	27.33	34622.06	94.55	56.34	Weak beam end
		40.00	106.67	29.55	41472.49	86.00	27.94	36113.88	98.63	58.77	Weak beam end
		48.20	173.89	48.17	48223.13	100.00	32.49	36616.01	100.00	59.59	Weak beam end
		70.00	215.79	59.78	52073.71	107.98	35.08	39116.70	106.83	63.66	Weak column

Table 7.4 *Derived moment-rotation results of the sensitivity analyses for the joints with hogging beam end moment*

No.	Parameter p	A	B	C	D	E	F	G	H	I	J
		p value	M_u (kNm)	$M_u/M_{u,fix}$ (%)	$K_{r,i}$ (kNm/rad)	$K_{r,i}/K_{r,i,s}$ (%)	$K_{r,i}/K_{r,i,m}$ (%)	$K_{r,se}$ (kNm/rad)	$K_{r,se}/K_{r,se,s}$ (%)	$K_{r,se}/K_{r,se,m}$ (%)	Failure mode
7	Beam top main reinforcement	0.98%	173.89	48.17	48223.13	100.00	32.49	36616.01	100.00	59.59	Weak beam end
		1.92%	163.44	45.27	48503.06	100.58	32.68	38058.32	103.94	61.94	Weak beam end
8	Beam bottom main reinforcement	0.20%	178.33	49.40	47661.16	98.83	32.11	35646.92	97.35	58.01	Weak beam end
		0.98%	173.89	48.17	48223.13	100.00	32.49	36616.01	100.00	59.59	Weak beam end
		4.00%	175.90	48.73	49321.95	102.28	33.23	36820.81	100.56	59.92	Weak beam end
9	Beam links	0.10%	182.11	50.45	47796.22	99.11	32.20	31298.92	85.48	50.94	Weak beam end
		0.52%	173.89	48.17	48223.13	100.00	32.49	36616.01	100.00	59.59	Weak beam end
		1.33%	173.83	48.15	48228.72	100.01	32.49	36689.35	100.20	59.71	Weak beam end
10	Column main reinforcement	0.40%	141.32	39.15	46082.14	95.56	31.05	31327.21	85.56	50.98	Weak column
		1.40%	173.89	48.17	48223.13	100.00	32.49	36616.01	100.00	59.59	Weak beam end
		6.00%	165.36	48.81	46930.52	97.32	31.62	38835.35	106.06	63.20	Weak beam end
11	Column joint links	0.39%	182.40	50.53	48230.03	100.01	32.49	36334.92	99.23	59.13	Weak beam end
		0.79%	173.89	48.17	48223.13	100.00	32.49	36616.01	100.00	59.59	Weak beam end
12	Configuration approach	Monolithic	254.37	70.47	148436.60	307.81	100.00	61446.74	167.81	100.00	Weak column
		Analysis 1	173.89	48.17	48223.13	100.00	32.49	36616.01	100.00	59.59	Weak beam end
		Analysis 2	132.04	36.58	25372.45	52.61	17.09	20229.73	55.25	32.92	Weak beam end

Note: M is the beam end moment at the joint ultimate state, K is the stiffness, footnotes *u, fix, r, i, s, m, se* mean *ultimate, fixed end, rotation, initial, standard, monolithic* and *secant* respectively.

Table 7.4 continued *Derived moment-rotation results of the sensitivity analyses for the joints with hogging beam end moment*

No.	Parameter p	A	B	C	D	E	F	G	H	I	J
		p value	F (kN)	d (mm)	M_u (kNm)	θ_u (rad)	p/p_s (%)	F/F_s (%)	$M_u/M_{u,s}$ (%)	$\theta_u/\theta_{u,s}$ (%)	Failure mode
1	Beam depth (mm)	300	12.01	40.00	33.25	0.0109	50.00	25.18	25.18	118.48	Weak beam end
		600	47.71	45.00	132.04	0.0092	100.00	100.00	100.00	100.00	Weak beam end
		1200	79.85	45.00	220.97	0.0038	200.00	167.34	167.34	41.30	Weak column
2	Beam breadth (mm)	250	42.62	40.00	117.94	0.0081	83.33	89.32	89.32	88.04	Weak beam end
		300	47.71	45.00	132.04	0.0092	100.00	100.00	100.00	100.00	Weak beam end
		400	51.88	55.00	143.58	0.0120	133.33	108.74	108.74	130.43	Weak beam end
3	Column section (mm^2)	90000	47.71	40.00	132.04	0.0092	100.00	100.00	100.00	100.00	Weak beam end
		160000	50.04	35.00	135.78	0.0087	177.78	104.87	104.87	94.57	Weak beam end

Note: d is the displacement applied at the column mid-height at the joint ultimate state, F is the relevant reaction, named load, M is the beam end moment at the joint ultimate state, θ is the relevant rotation, footnotes u and s mean *ultimate* and *standard* respectively.

Table 7.5 *General results of the sensitivity analyses for the billet-welded plate joints with sagging beam end moment*

No.	Parameter p	A	B	C	D	E	F	G	H	I	J
		p value	F (kN)	F/F_m (%)	$K_{d,i}$ (kNm/rad)	$K_{d,i}/K_{d,i,s}$ (%)	$K_{d,i}/K_{d,i,m}$ (%)	$K_{d,se}$ (kNm/rad)	$K_{d,se}/K_{d,se,s}$ (%)	$K_{d,se}/K_{d,se,m}$ (%)	Failure mode
1	Beam depth (mm)	300	12.01	13.07	785.71	37.95	18.73	694.66	50.46	27.41	Weak beam end
		600	47.71	51.91	2070.22	100.00	49.36	1376.61	100.00	54.31	Weak beam end
		1200	79.85	86.87	3855.42	186.23	91.92	2773.71	201.49	109.43	Weak column
2	Beam breadth (mm)	250	42.62	46.37	1960.11	94.68	46.73	1353.24	98.30	53.39	Weak beam end
		300	47.71	51.91	2070.22	100.00	49.36	1376.61	100.00	54.31	Weak beam end
		400	51.88	56.45	2189.00	105.74	52.19	1400.80	101.76	55.26	Weak beam end
3	Column section (mm^2)	90000	47.71	51.91	2070.22	100.00	49.36	1376.61	100.00	54.31	Weak beam end
		160000	50.04	54.44	2636.86	127.37	62.87	1984.11	144.13	78.28	Weak beam end

Note: F is the load at the column mid-height at the joint ultimate state, K is the stiffness, footnotes *m, d, i, s, se* mean *monolithic*, *displacement*, *initial*, *standard* and *secant* respectively.

Table 7.6 *Derived load-displacement results of the sensitivity analyses for the joints with sagging beam end moment*

No.	Parameter p	A	B	C	D	E	F	G	H	I	J
		p value	M_u (kNm)	$M_u/M_{u,\,fix}$ (%)	$K_{r,\,i}$ (kNm/rad)	$K_{r,\,i}/K_{r,\,i,\,s}$ (%)	$K_{r,\,i}/K_{r,\,i,\,m}$ (%)	$K_{r,\,se}$ (kNm/rad)	$K_{r,\,se}/K_{r,\,se,\,s}$ (%)	$K_{r,\,se}/K_{r,\,se,\,m}$ (%)	Failure mode
1	Beam depth (mm)	300	33.25	23.92	7627.09	30.06	5.14	7290.64	36.04	11.86	Weak beam end
		600	132.04	36.58	25372.45	100.00	17.09	20229.73	100.00	32.92	Weak beam end
		1200	220.97	27.45	93101.57	366.94	62.72	68019.05	336.23	110.70	Weak column
2	Beam breadth (mm)	250	117.94	32.67	21124.82	83.26	14.23	17195.63	85.00	27.98	Weak beam end
		300	132.04	36.58	25372.45	100.00	17.09	20229.73	100.00	32.92	Weak beam end
		400	143.58	39.77	27864.77	109.82	18.77	22116.23	109.33	35.99	Weak beam end
3	Column section (mm^2)	90000	132.04	36.58	25372.45	100.00	17.09	20229.73	100.00	32.92	Weak beam end
		160000	135.78	37.61	27184.57	107.14	18.31	23088.18	114.13	37.57	Weak beam end

Note: M is the beam end moment at the joint ultimate state, K is the stiffness, footnotes *u, fix, r, i, s, m, se* mean *ultimate, fixed end, rotation, initial, standard, monolithic* and *secant* respectively.

Table 7.7 *Derived moment-rotation results of the sensitivity analyses for the joints with sagging beam end moment*

Analysis	Parameter	A	B	C	D	E	F	G	H	I	J	K
		b_b (mm)	d_e (mm)	f_{cu} (N/mm^2)	b_c (mm)	h_c (mm)	L_c (mm)	$0.5A_{s,c}$ (mm^2)	n_c (=E_s/E_c)	I_c (mm^4)	E_c (N/mm^2)	E_cI_c/L_c (N-mm)
1	h_b = 600 mm	300	335	48.20	300	300	3000	402	7.08	7.25E+08	28960	7.00E+09
2	h_b = 600 mm, sagging	300	265	48.20	300	300	3000	402	7.08	7.25E+08	28960	7.00E+09
3	h_b = 300 mm	300	185	49.80	300	300	3000	402	7.09	7.25E+08	28927	6.99E+09
4	h_b = 300 mm, sagging	300	115	46.20	300	300	3000	402	7.09	7.25E+08	28927	6.99E+09
7	b_b = 250 mm	250	335	48.20	300	300	3000	402	7.08	7.25E+08	28960	7.00E+09
8	b_b = 250 mm, sagging	250	265	48.20	300	300	3000	402	7.08	7.25E+08	28960	7.00E+09
9	b_b = 400 mm	400	335	48.20	300	300	3000	402	7.08	7.25E+08	28960	7.00E+09
10	b_b = 400 mm, sagging	400	265	48.20	300	300	3000	402	7.08	7.25E+08	28960	7.00E+09
11	L_b = 3150 mm	300	335	48.20	300	300	3000	402	7.08	7.25E+08	28960	7.00E+09
12	L_b = 16500 mm	300	335	48.20	300	300	3000	402	7.08	7.25E+08	28960	7.00E+09
13	A_c = 400*400 mm^2	300	335	48.20	400	400	3000	402	7.08	2.25E+09	28960	2.17E+10
14	A_c = 400*400 mm^2, sagging	300	265	48.20	400	400	3000	402	7.08	2.25E+09	28960	2.17E+10
15	L_c = 2550 mm	300	335	48.20	300	300	2500	402	7.08	7.25E+08	28960	8.40E+09
16	L_c = 7000 mm	300	335	48.20	300	300	7000	402	7.08	7.25E+08	28960	3.00E+09
18	C40, grout	300	335	40.00	300	300	3000	402	8.04	7.32E+08	25502	6.22E+09
19	C25, grout	300	335	25.00	300	300	3000	402	8.04	7.32E+08	25502	6.22E+09
20	$\rho_{beam\ top}$ = 1.970%	300	335	48.20	300	300	3000	402	7.08	7.25E+08	28960	7.00E+09
21	$\rho_{beam\ bottom}$ = 0.20%	300	335	48.20	300	300	3000	402	7.08	7.25E+08	28960	7.00E+09
22	$\rho_{beam\ bottom}$ = 4.0%	300	335	48.20	300	300	3000	402	7.08	7.25E+08	28960	7.00E+09
23	$\rho_{beam\ link}$ =0.1%	300	335	48.20	300	300	3000	402	7.08	7.25E+08	28960	7.00E+09
24	$\rho_{beam\ link}$ =1.33%	300	335	48.20	300	300	3000	402	7.08	7.25E+08	28960	7.00E+09
26	$\rho_{column\ main}$ = 6.00%	300	335	48.20	300	300	3000	673	7.08	7.59E+08	28960	7.33E+09
27	$\rho_{column\ joint\ link}$ = 0.393%	300	335	48.20	300	300	3000	402	7.08	7.25E+08	28960	7.00E+09

Table 7.8 *Simplified calculations for the beam end characteristics of the billet-welded plate joints*

Analysis	L	M	N	O	P	Q	R	S	T	U	V	W
	$M_{u,\,num}$ (kN-m)	$K_{r,\,i,\,num}$ (kNm/rad)	$K_{r,\,se,\,num}$ (kNm/rad)	$\theta_{u,\,num}$ (rad)	$M_{u,\,cal}$ (kN-m)	$dM/M_{u,\,num}$ (%)	$K_{r,\,i,\,cal}$ (kNm/rad)	$dK_{r,\,i}/K_{r,\,i,\,num}$ (%)	$K_{r,\,se,\,cal}$ (kNm/rad)	$dK_{r,\,se}/K_{r,\,se,\,num}$ (%)	$\theta_{u,\,cal}$ (rad)	$d\theta/\theta_{u,\,num}$ (%)
1	173.89	48223	36616	0.0053	172.22	-0.96	46537	-3.50	35913	-1.92	0.0056	5.21
2	132.04	25372	20230	0.0092	114.96	-12.93	29592	16.63	22971	13.55	0.0073	-20.67
3	89.67	17243	13485	0.008	67.41	-24.82	15525	-9.96	12226	-9.34	0.0096	20.10
4	33.25	7627	7291	0.0109	36.49	9.74	6373	-16.44	5235	-28.19	0.0118	8.56
7	168.95	44710	32680	0.0059	146.72	-13.16	38991	-12.79	30149	-7.74	0.0051	-13.74
8	117.94	21125	17196	0.0081	99.01	-16.05	24870	17.73	19364	12.61	0.0070	-13.65
9	164.10	49139	39981	0.0046	223.22	36.03	61630	25.42	47441	18.66	0.0066	42.39
10	143.58	27865	22116	0.012	146.88	2.30	39036	40.09	30184	36.48	0.0079	-34.10
11	228.90	49322	36153	0.0056	172.22	-24.76	46537	-5.65	35913	-0.66	0.0056	-0.42
12	192.26	48902	35646	0.0063	172.22	-10.42	46537	-4.84	35913	0.75	0.0056	-11.49
13	210.19	50008	37971	0.0081	212.67	1.18	49189	-1.64	38712	1.95	0.0076	-5.89
14	135.78	27185	23088	0.0087	155.42	14.46	32244	18.61	25770	11.61	0.0093	7.41
15	177.81	49942	37122	0.0054	176.07	-0.98	46789	-6.31	36179	-2.54	0.0058	6.87
16	149.55	42116	36690	0.0045	161.23	7.81	45817	8.79	35153	-4.19	0.0050	11.57
18	106.67	41472	36114	0.0033	144.06	35.05	38694	-6.70	29882	-17.26	0.0050	50.65
19	93.11	40566	34622	0.0036	96.44	3.58	24604	-39.35	19120	-44.78	0.0041	12.84
20	163.44	48503	38058	0.0047	172.22	5.37	46537	-4.05	35913	-5.64	0.0056	18.65
21	178.33	47661	35647	0.007	172.22	-3.43	46537	-2.36	35913	0.75	0.0056	-20.34
22	175.90	49322	36821	0.0052	172.22	-2.09	46537	-5.65	35913	-2.46	0.0056	7.24
23	182.11	47796	31299	0.0061	172.22	-5.43	46537	-2.63	35913	14.74	0.0056	-8.58
24	173.83	48229	36689	0.0053	172.22	-0.93	46537	-3.51	35913	-2.12	0.0056	5.21
26	165.36	46931	38835	0.0046	173.12	4.69	46596	-0.71	35975	-7.36	0.0056	22.21
27	182.40	48230	36335	0.0059	172.22	-5.58	46537	-3.51	35913	-1.16	0.0056	-5.49

Table 7.8 continued *Simplified calculations for the beam end characteristics of the billet-welded plate joints*

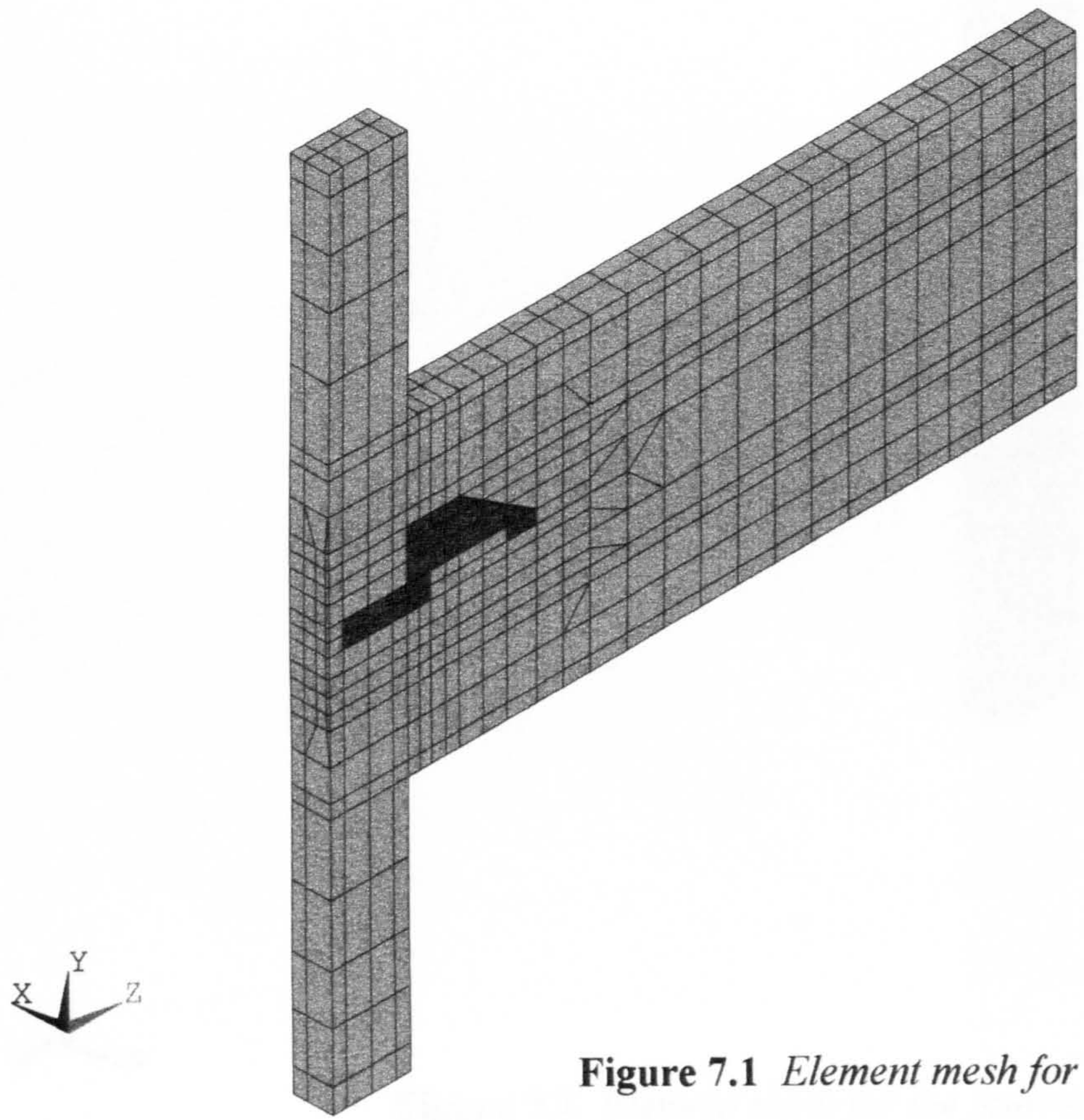

Figure 7.1 *Element mesh for the joint with a 1200 mm beam depth (Analyses 5 and 6)*

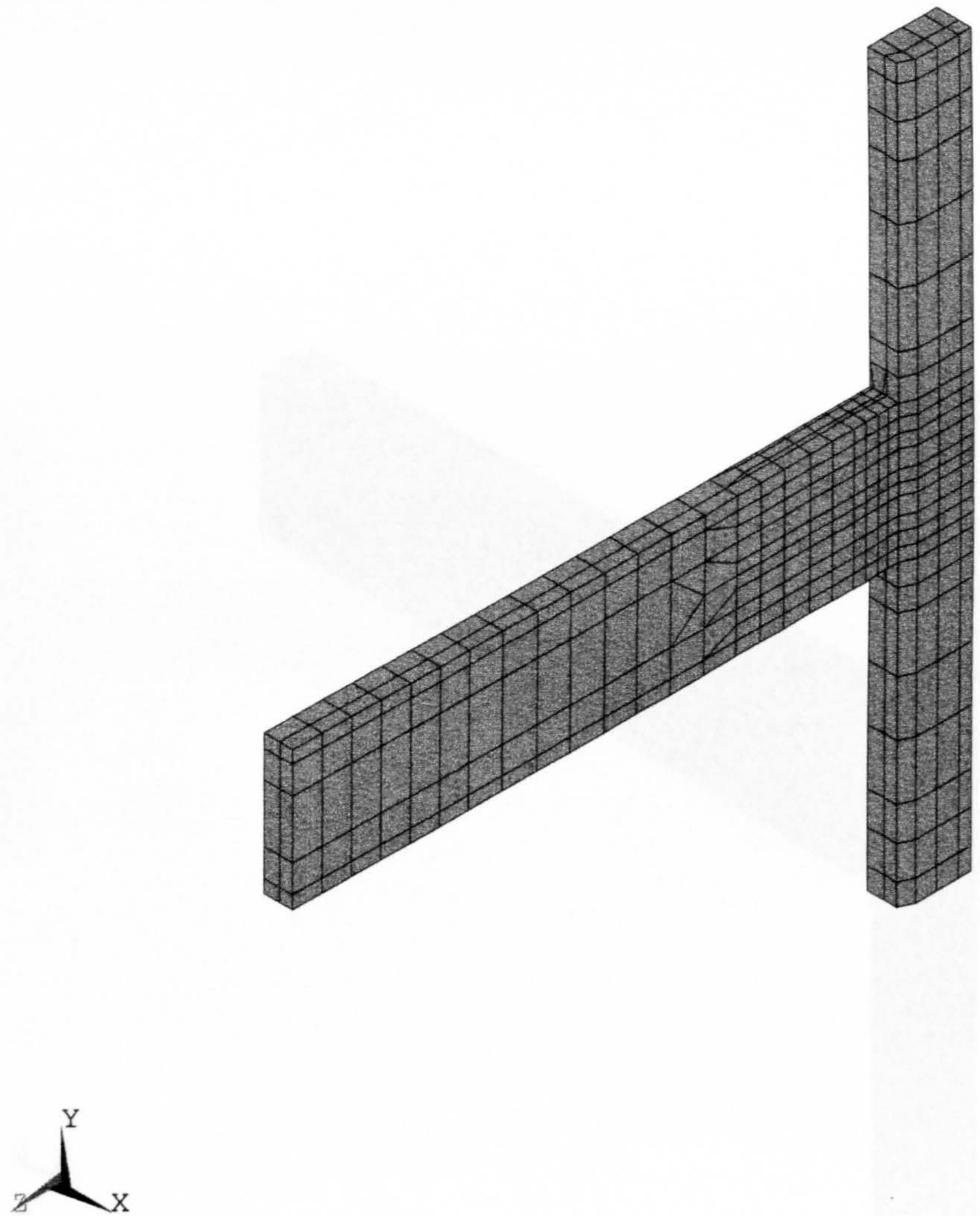

Figure 7.2 *Element mesh for the joint with a 250 mm beam breadth (Analyses 7 and 8)*

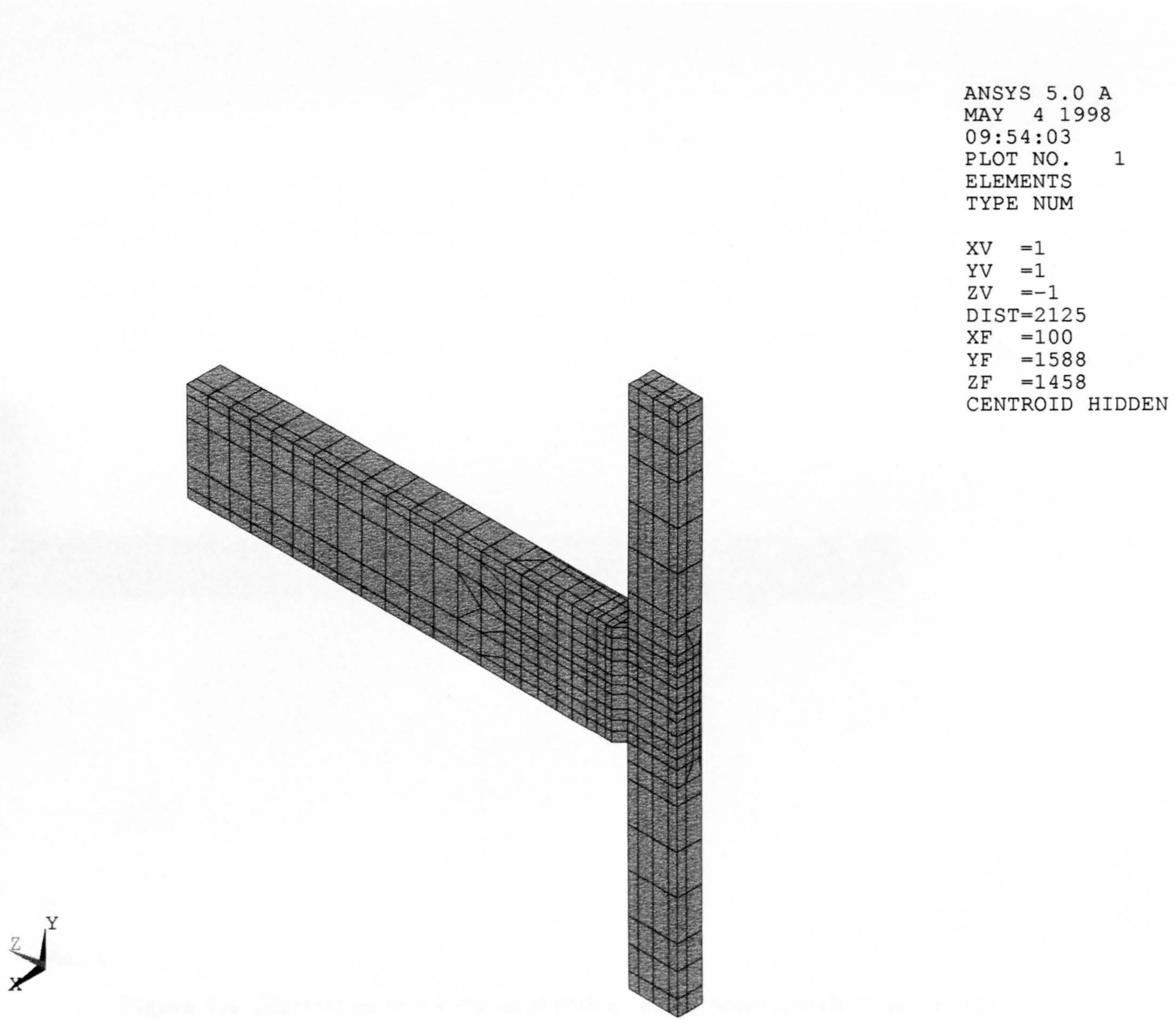

Figure 7.3 *Element mesh for the joint with a 400 mm beam breadth (Analyses 9 and 10)*

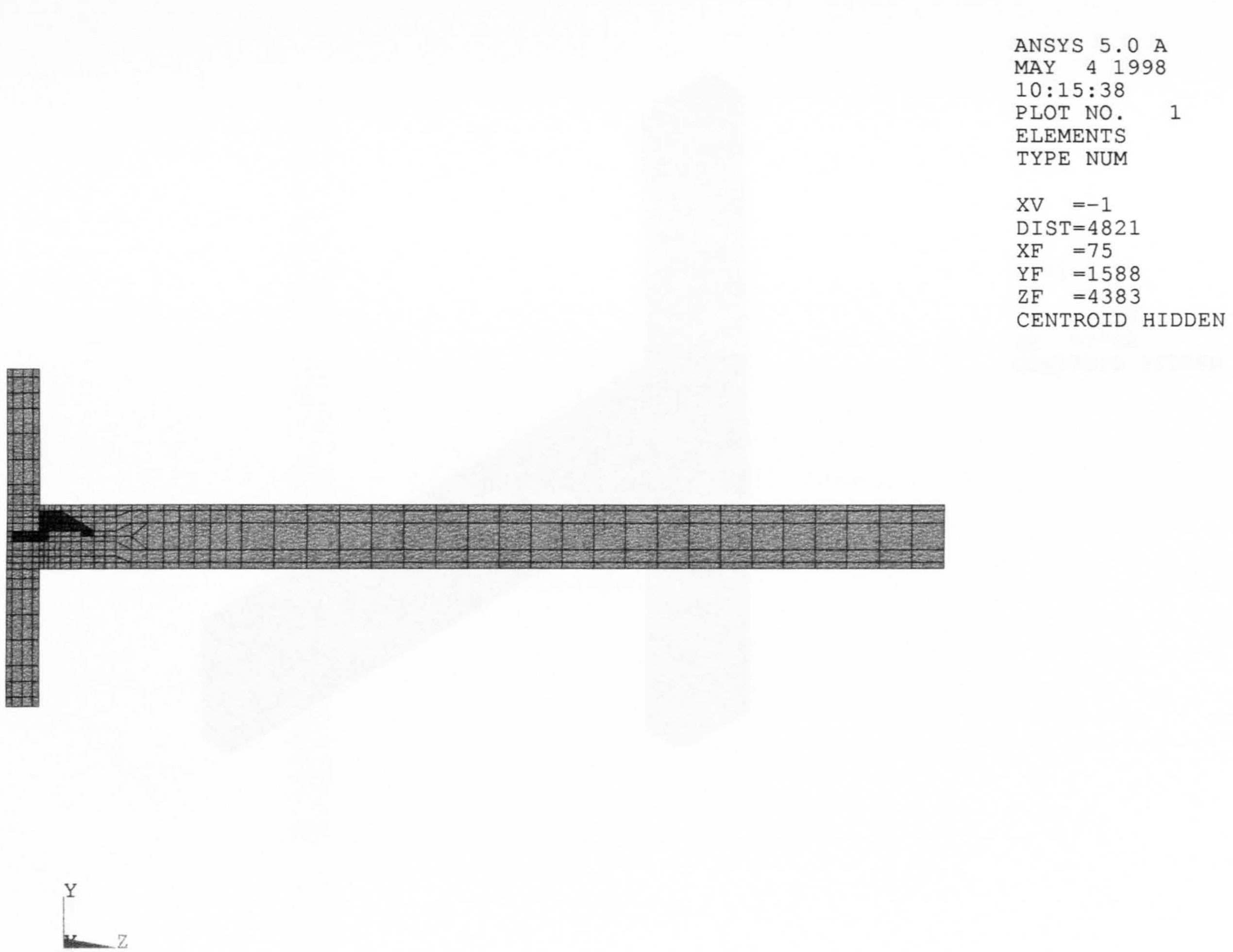

Figure 7.4 *Element mesh for the joint with a 16.5 m beam length (Analysis 12)*

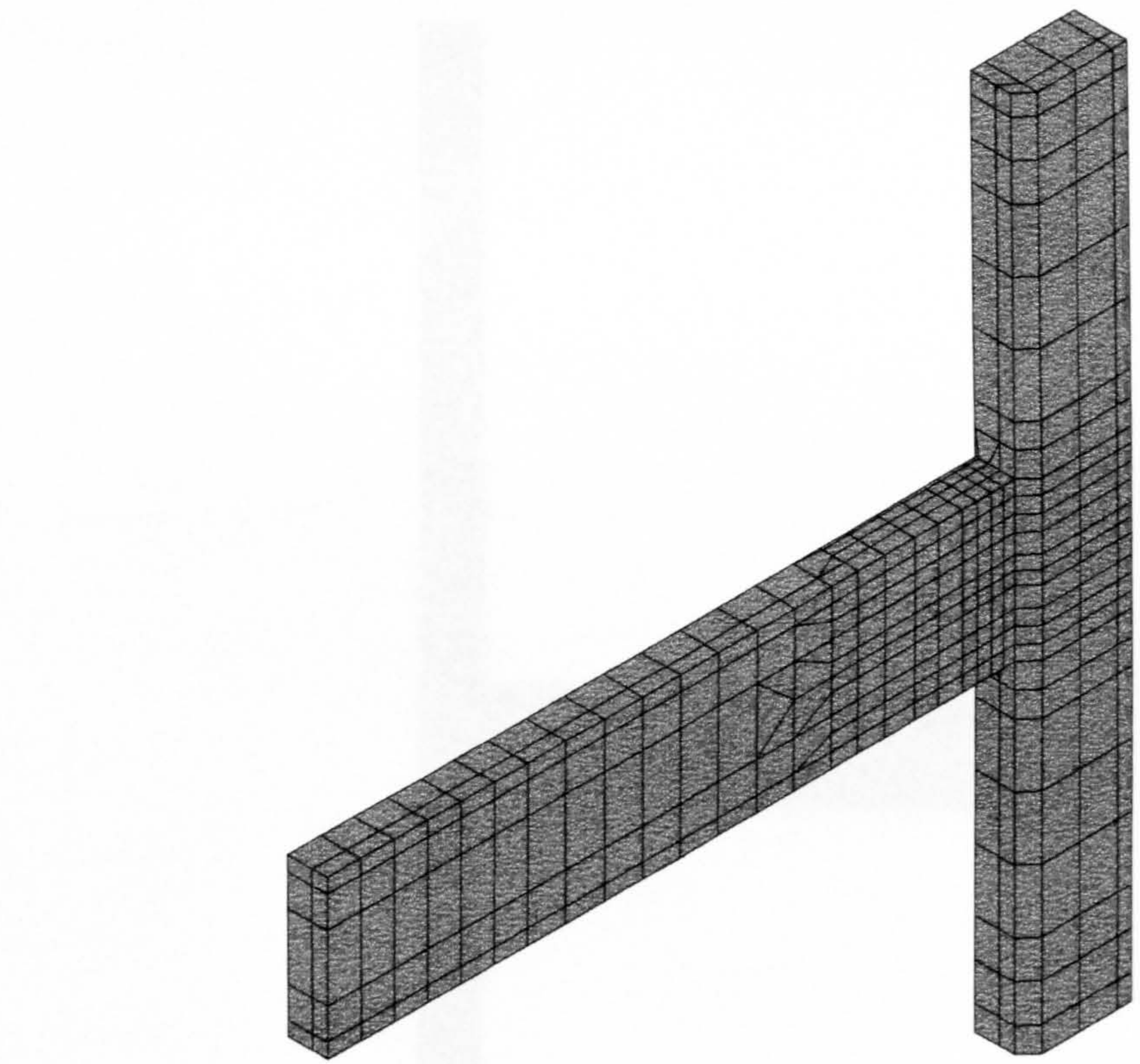

Figure 7.5 *Element mesh for the joint with a 400*400 mm^2 column section (Analyses 13 and 14)*

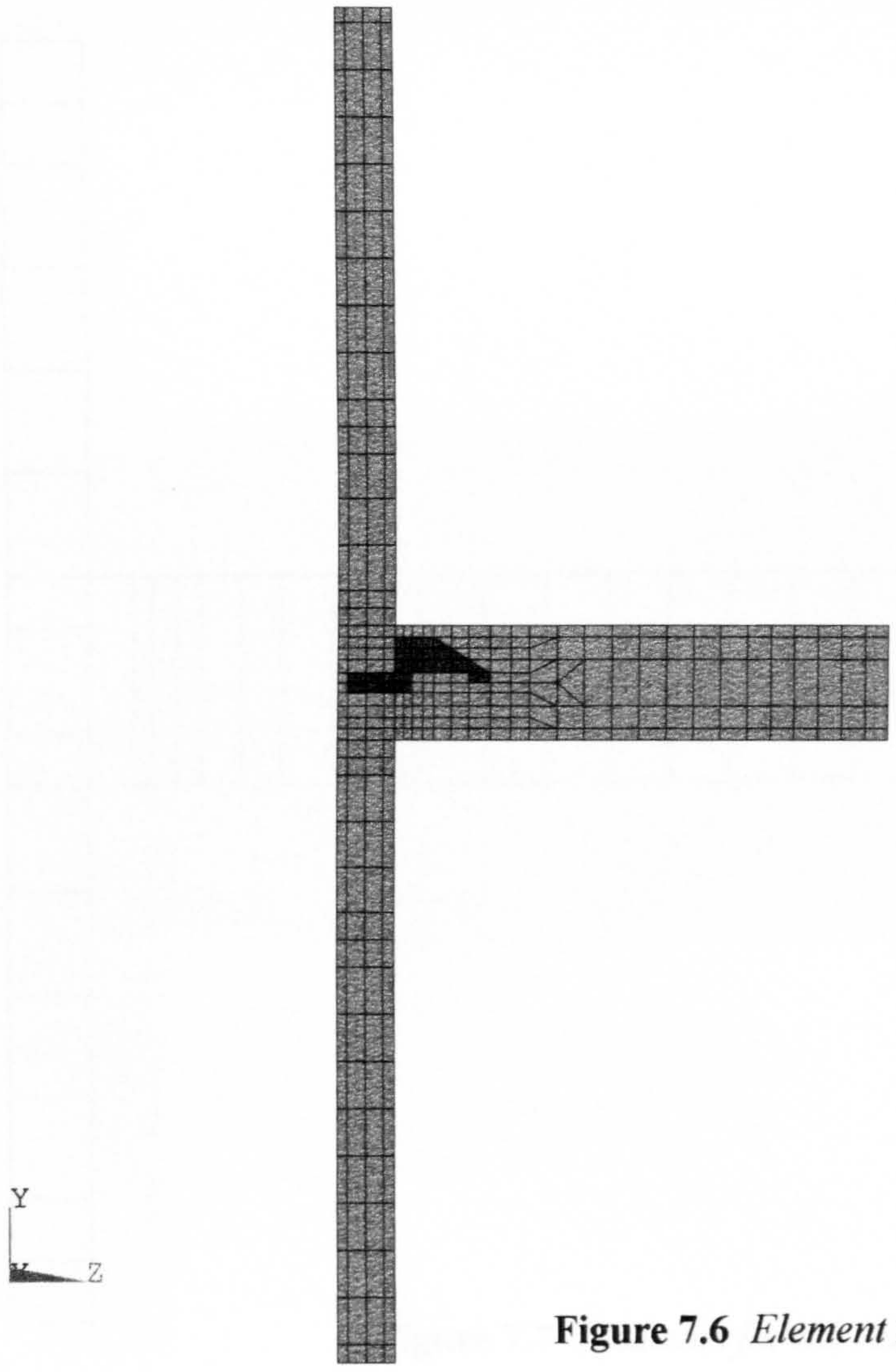

Figure 7.6 *Element mesh for the joint with a 7.0 m column height (Analysis 16)*

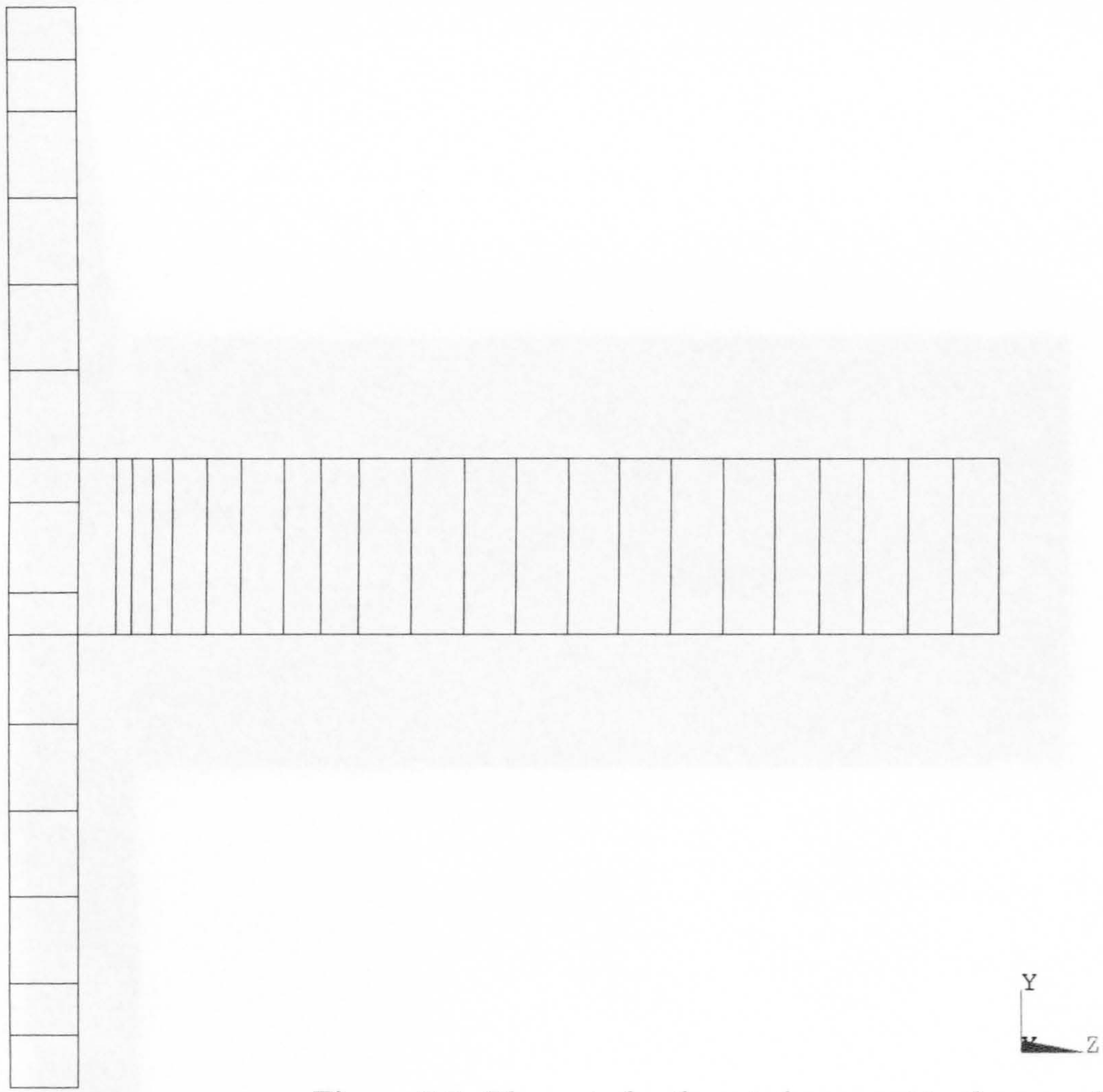

Figure 7.7 *Elements for the reinforcement in the monolithic joint (Analysis 28)*

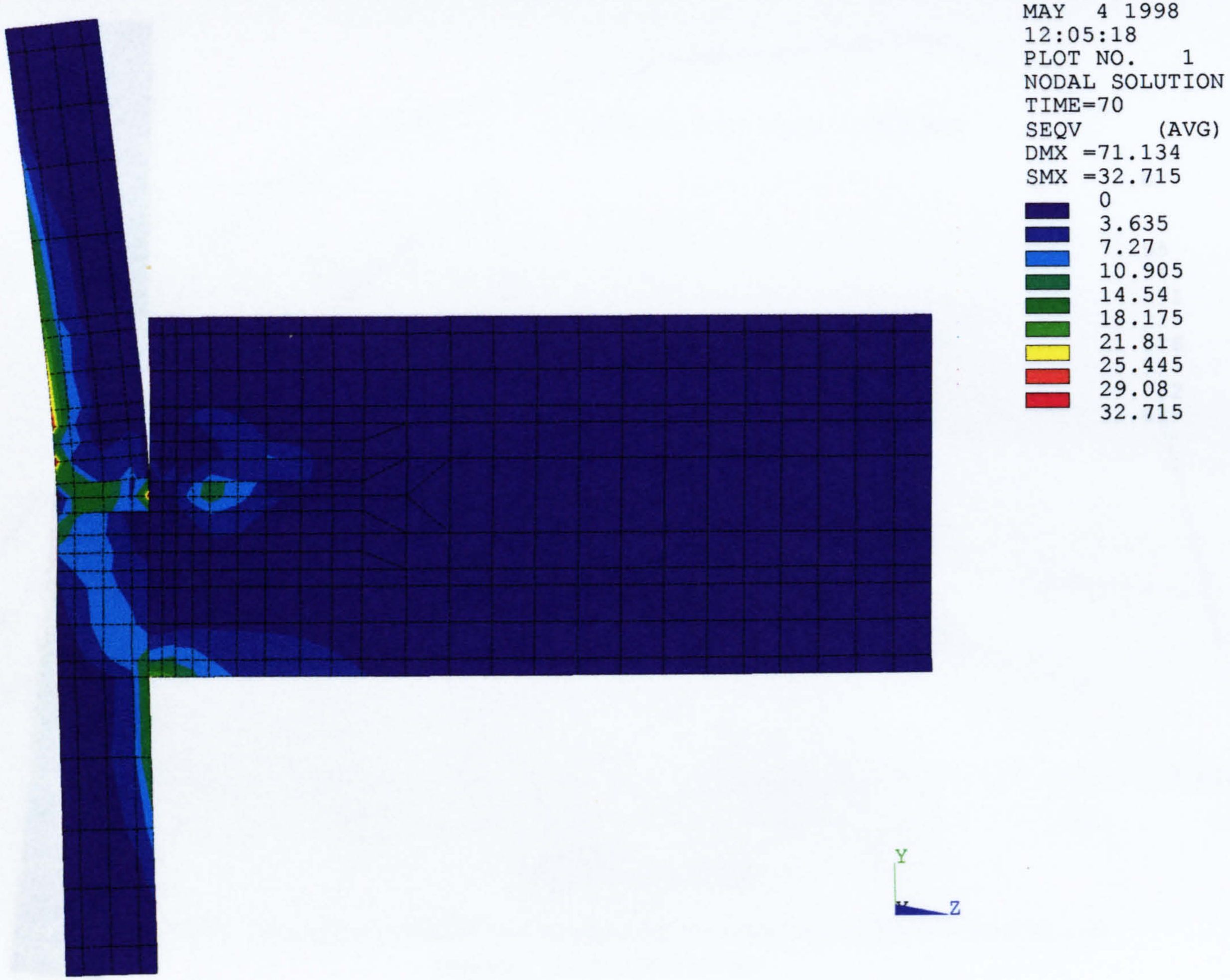

Figure 7.8 *Ultimate equivalent stress distribution for the 1200 mm beam depth joint with a hogging beam end moment (Analysis 5)*

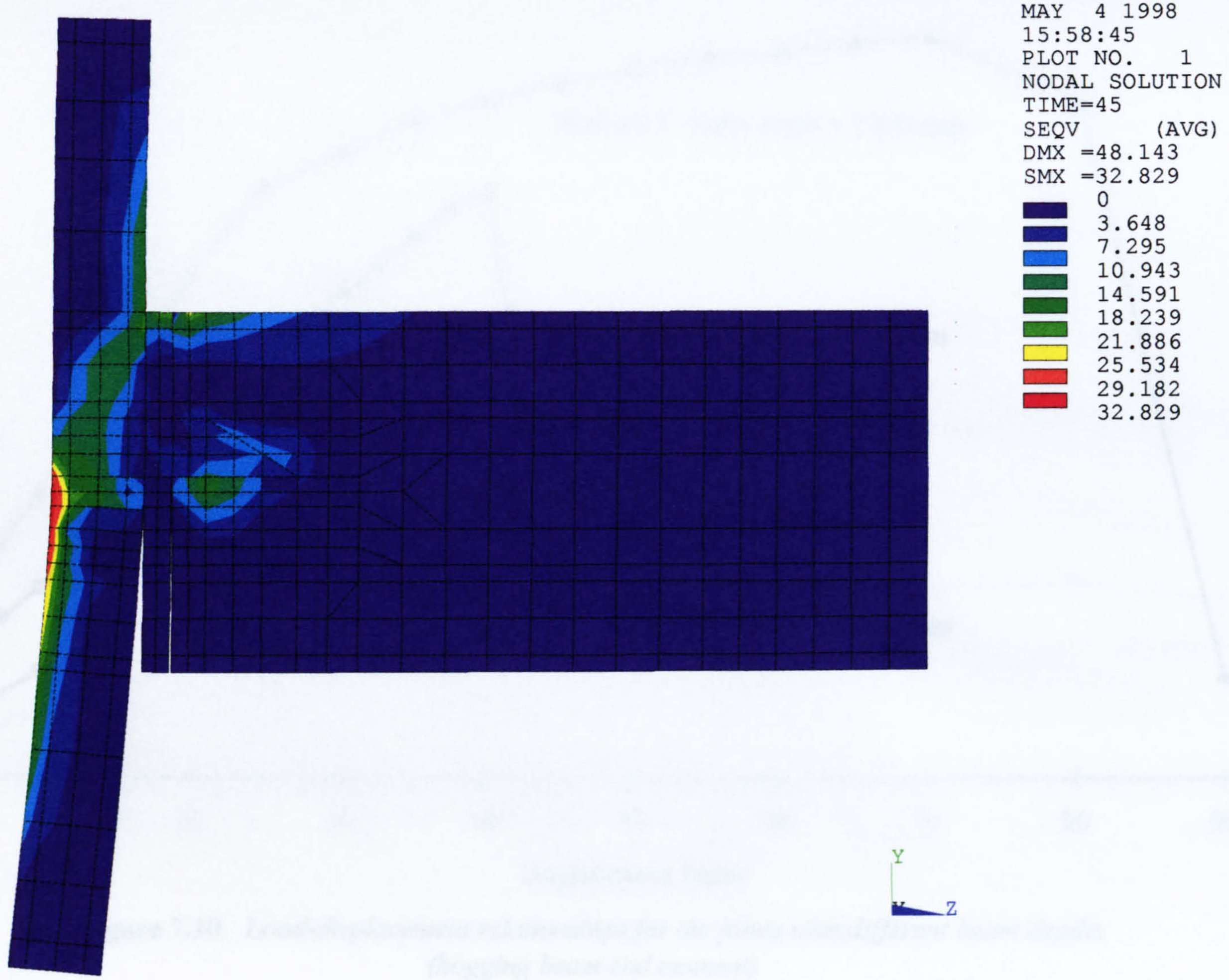

Figure 7.9 *Ultimate equivalent stress distribution for the 1200 mm beam depth joint with a sagging beam end moment (Analysis 6)*

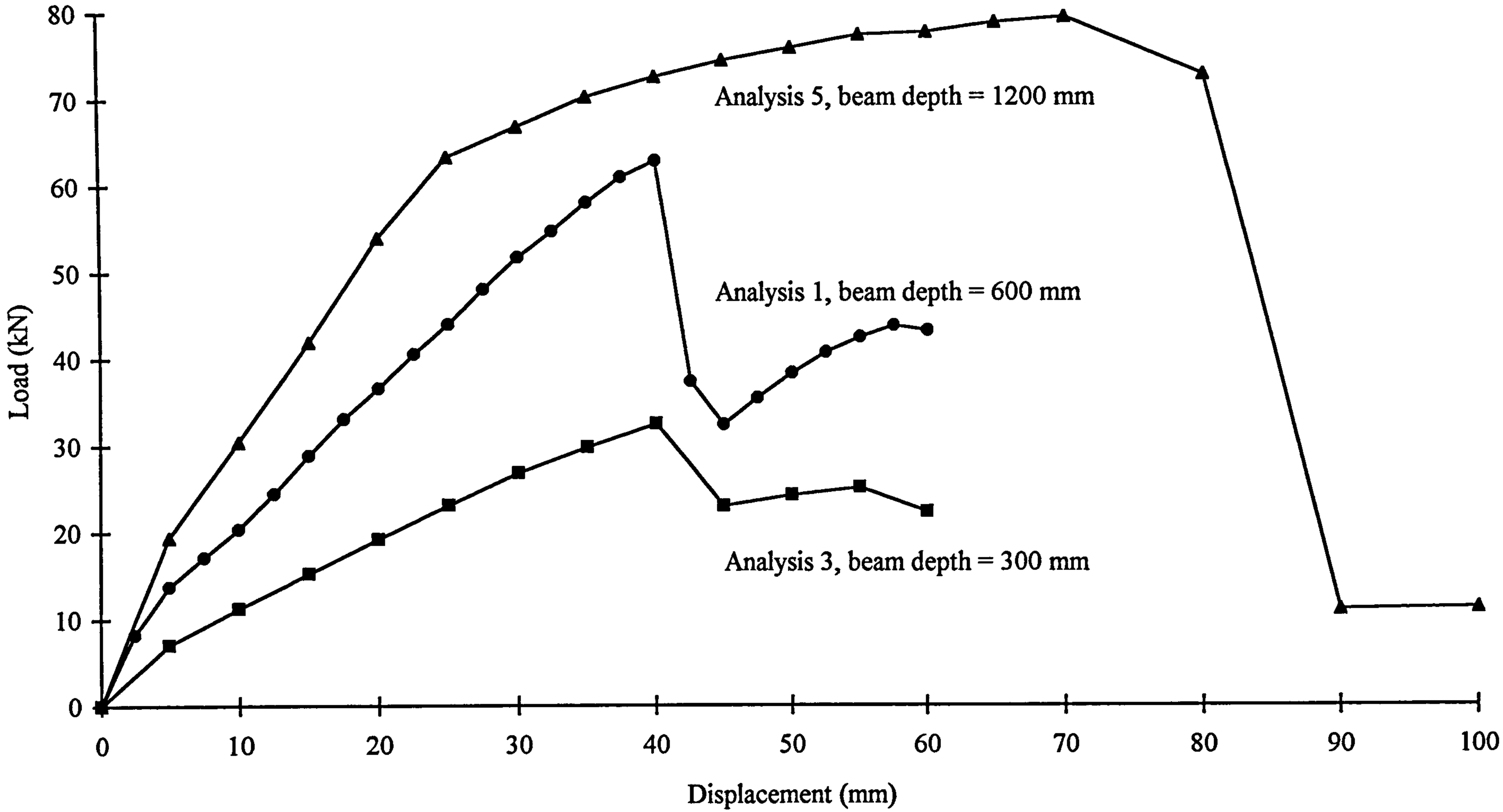

Figure 7.10 *Load-displacement relationships for the joints with different beam depths (hogging beam end moment)*

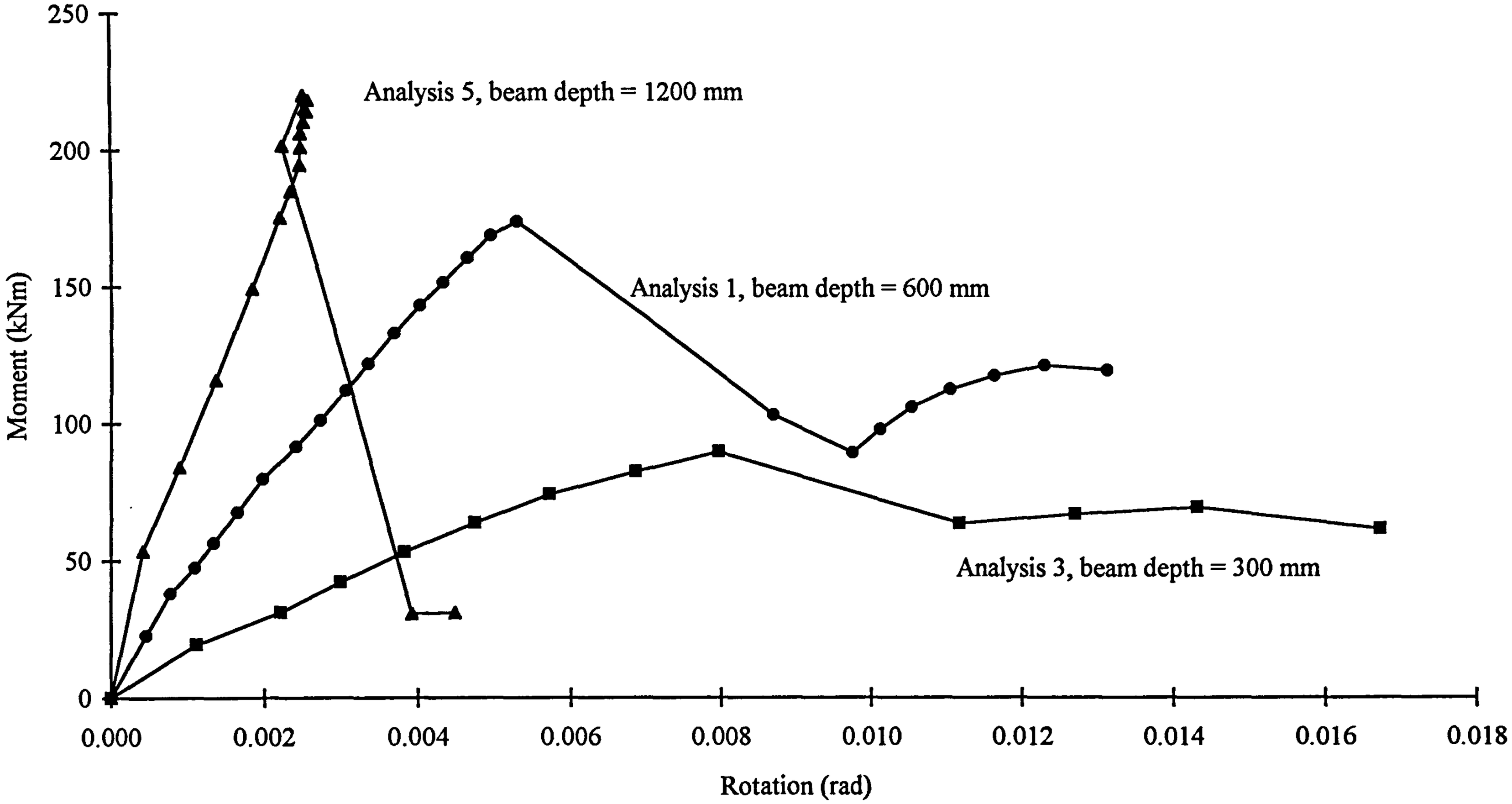

Figure 7.11 *Moment-rotation relationships for the joints with different beam depths (hogging beam end moment)*

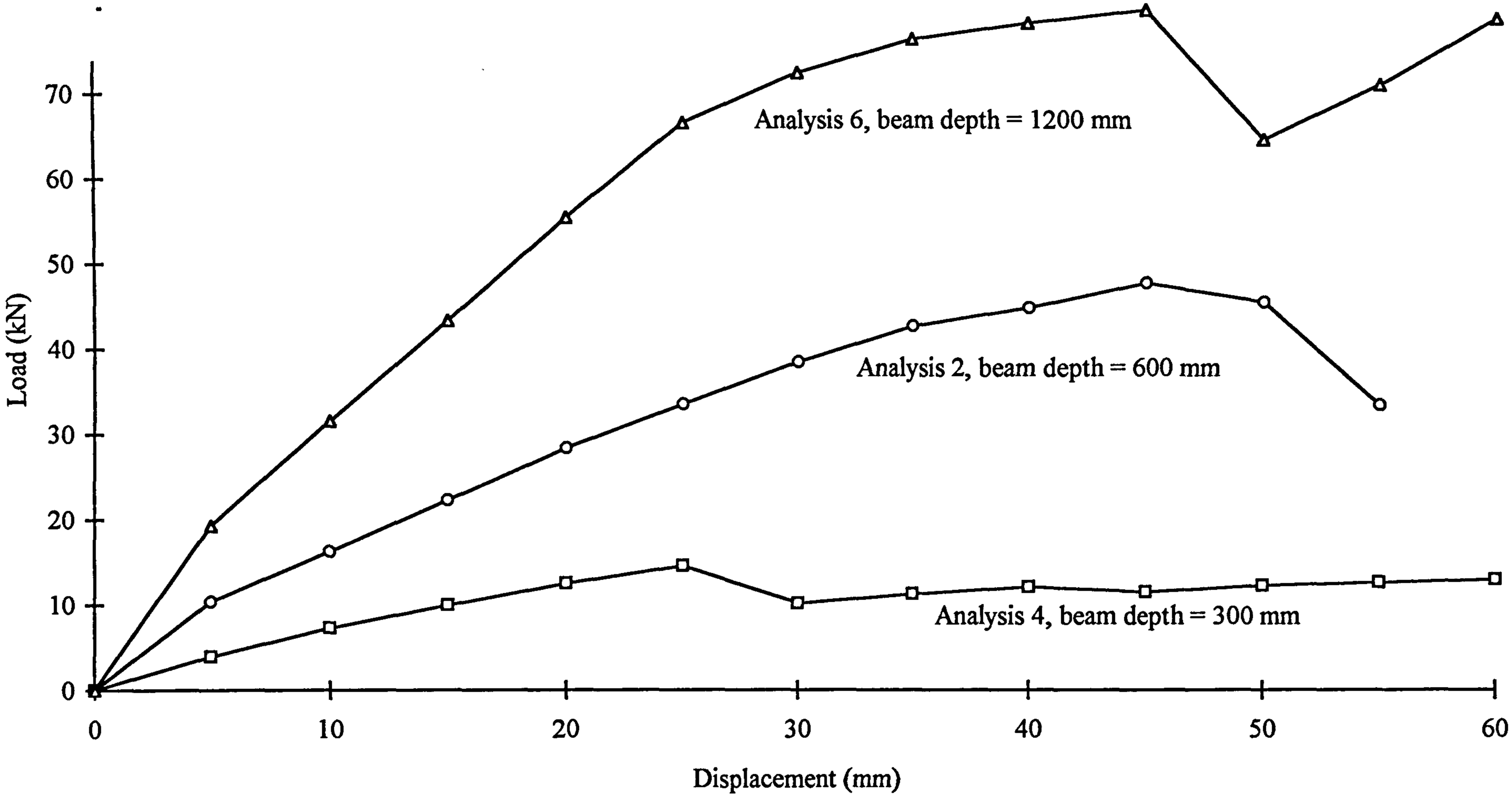

Figure 7.12 *Load-displacement relationships for the joints with different beam depths (sagging beam end moment)*

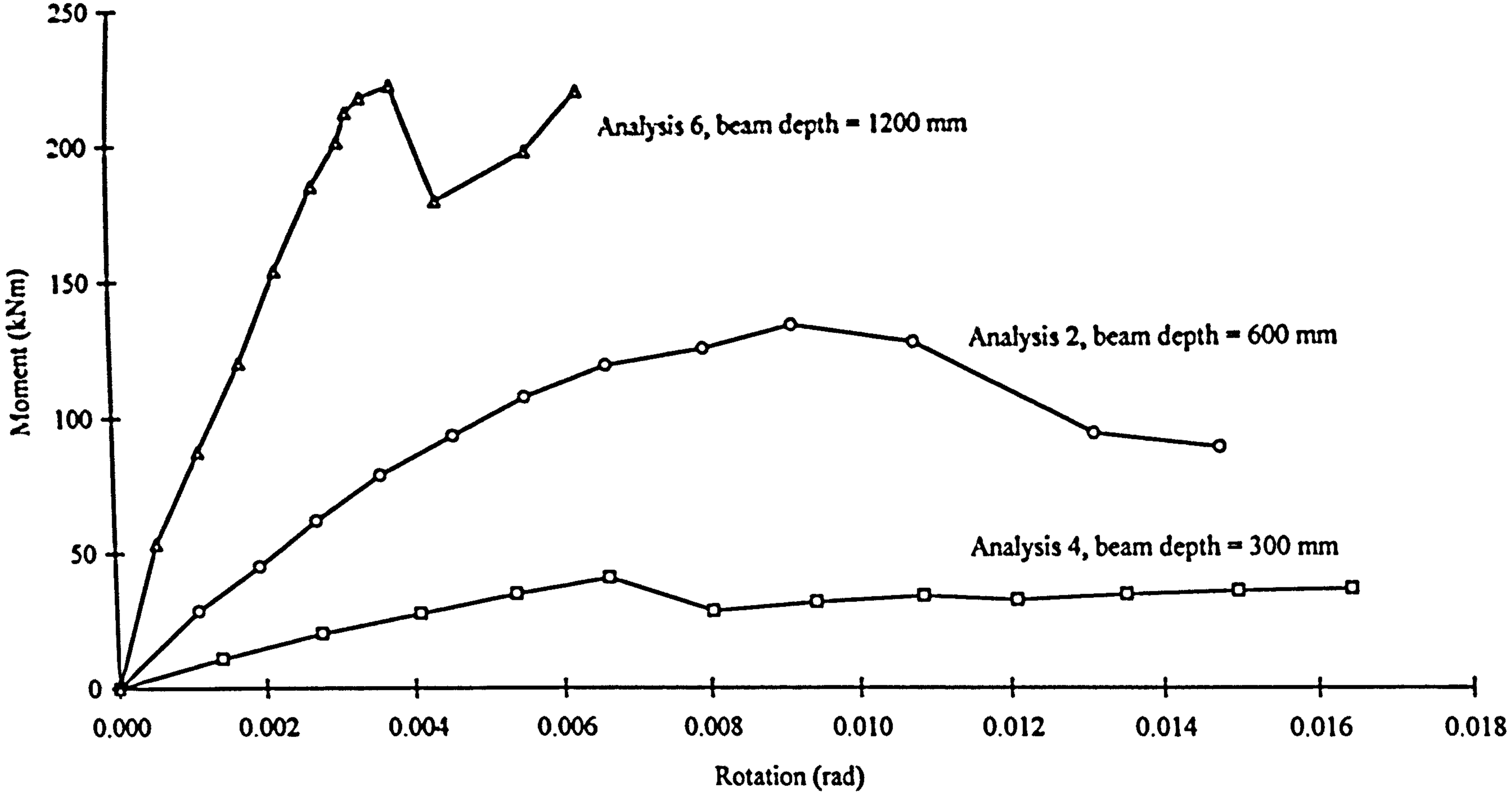

Figure 7.13 *Moment-rotation relationships for the joints with different beam depths (sagging beam end moment)*

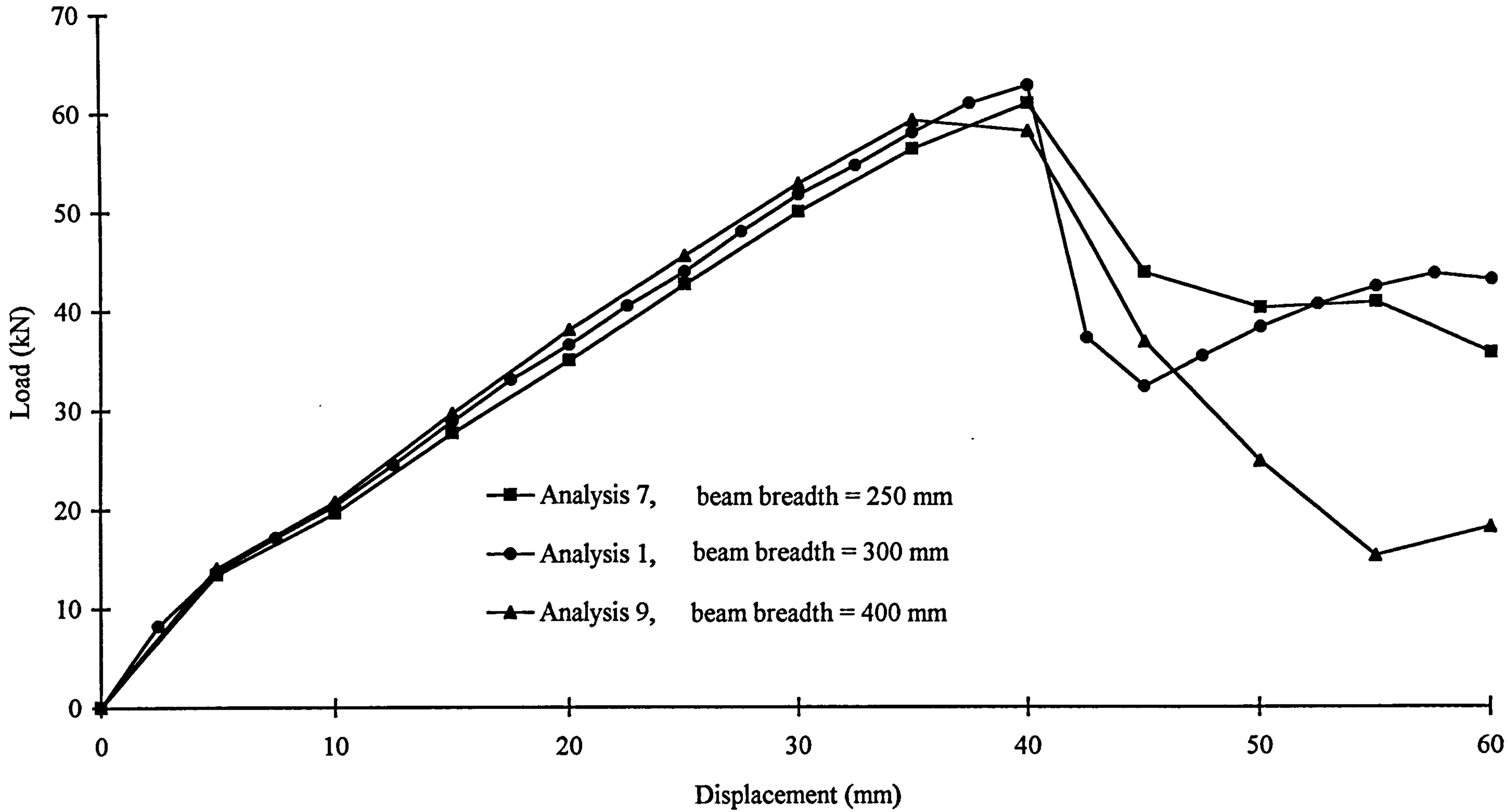

Figure 7.14 *Load-displacement relationships for the joints with different beam breadths (hogging beam end moment)*

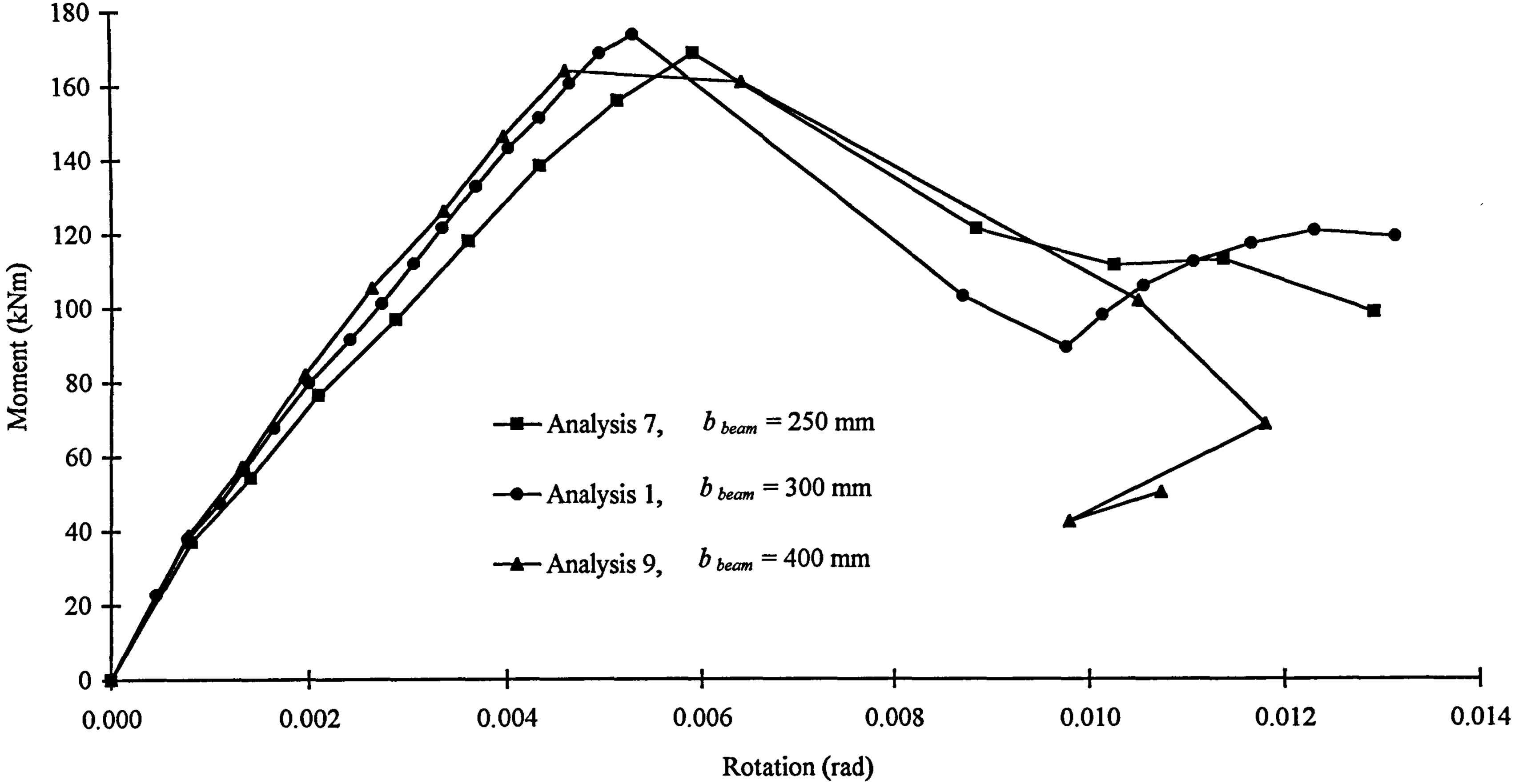

Figure 7.15 *Moment-rotation relationships for the joints with different beam breadths (hogging beam end moment)*

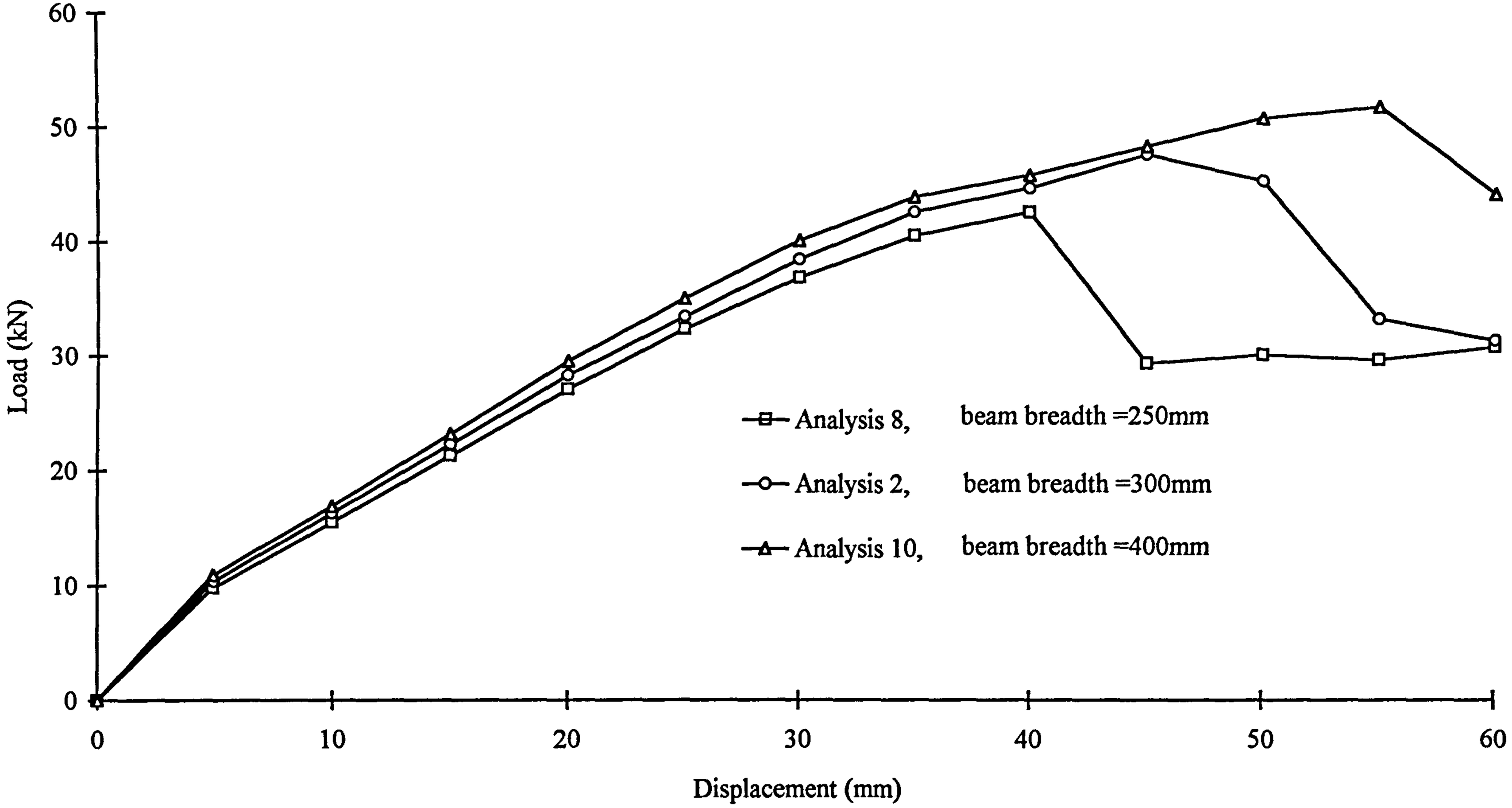

Figure 7.16 *Load-displacement relationships for the joints with different beam breadths (sagging beam end moment)*

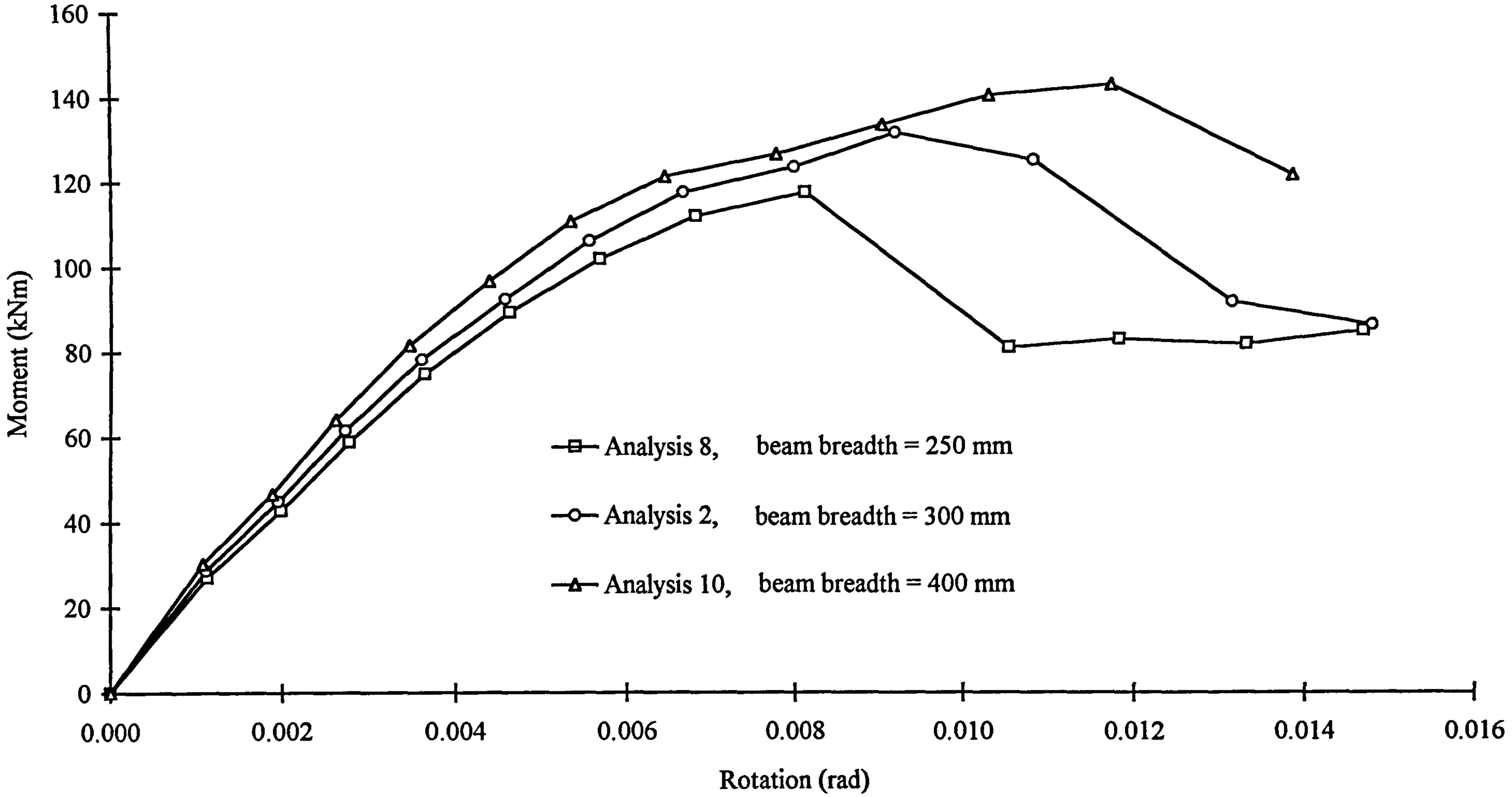

Figure 7.17 *Moment-rotation relationships for the joints with different beam breadths (sagging beam end moment)*

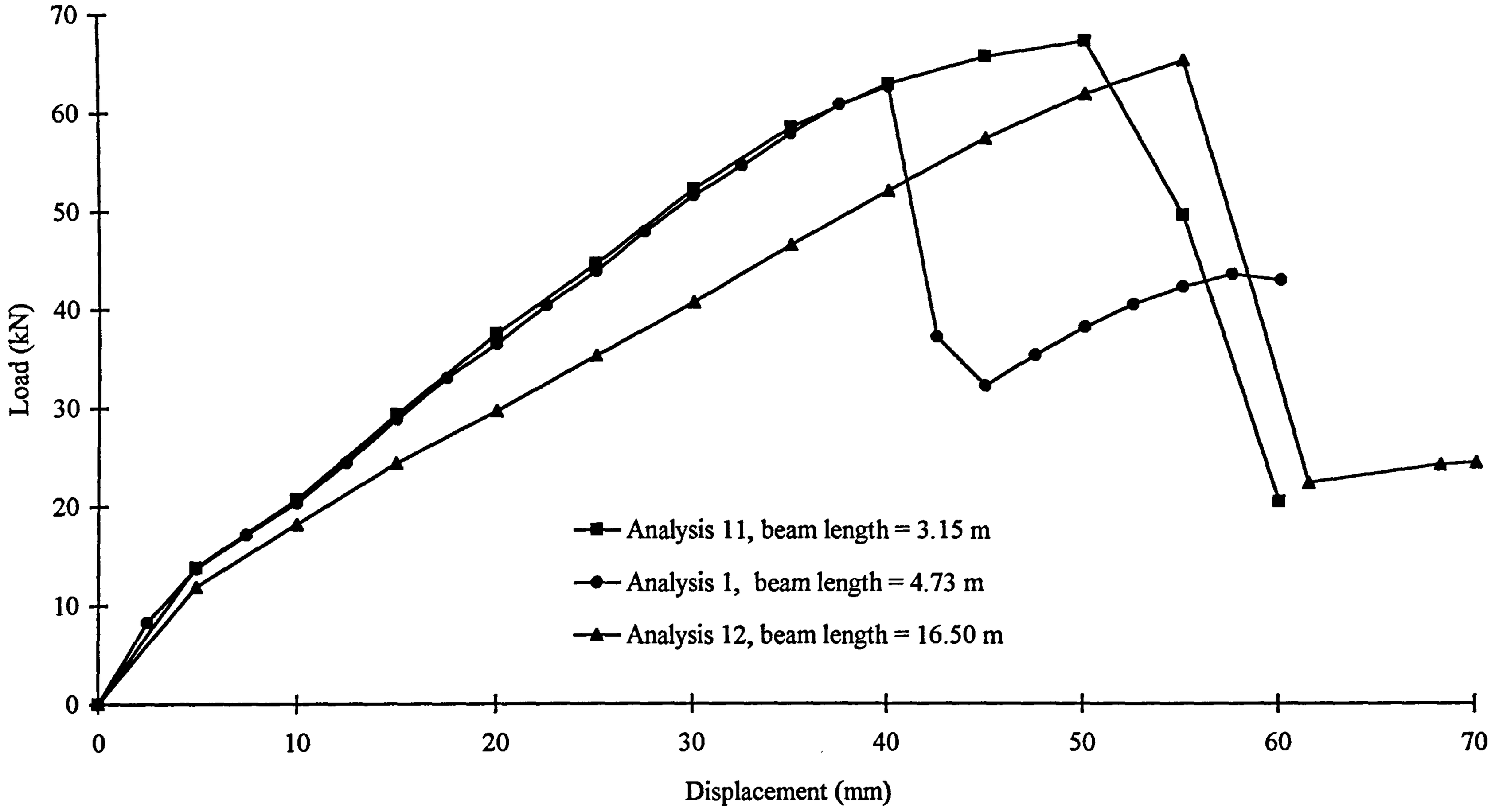

Figure 7.18 *Load-displacement relationships for the joints with different beam lengths (hogging beam end moment)*

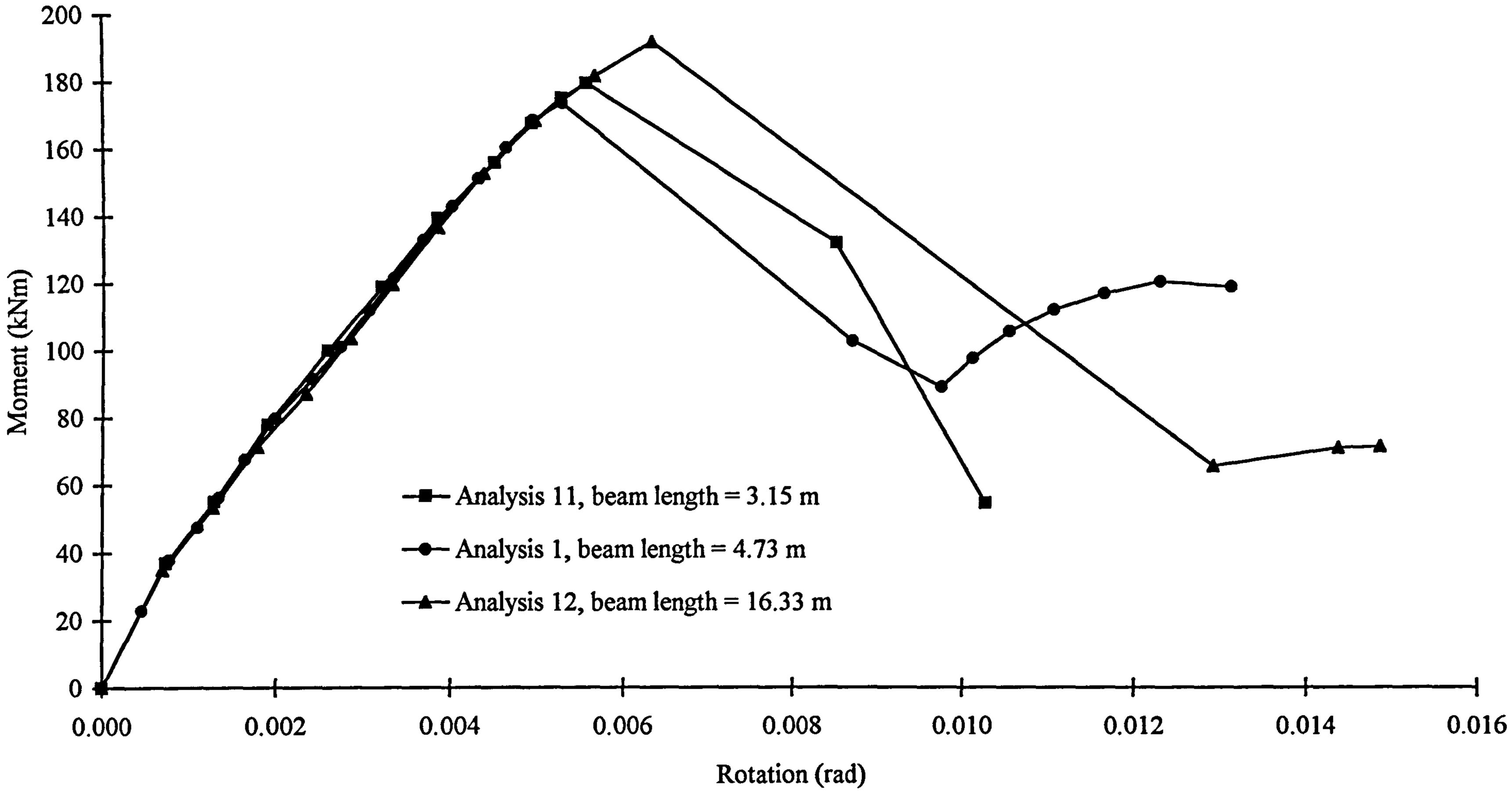

Figure 7.19 *Moment-rotation relationships for the joints with different beam lengths (hogging beam end moment)*

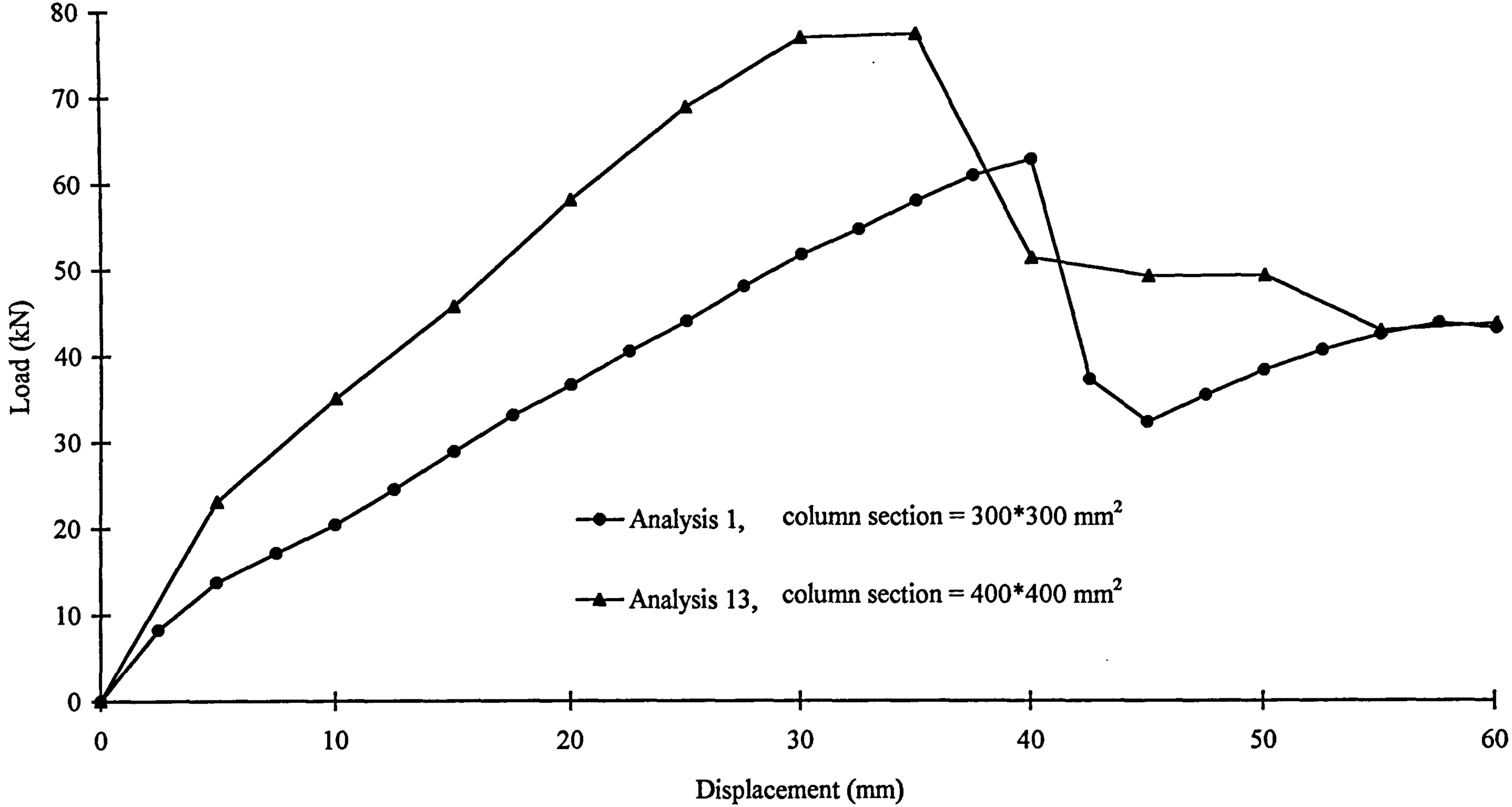

Figure 7.20 *Load-displacement relationships for the joints with different column sections (hogging beam end moment)*

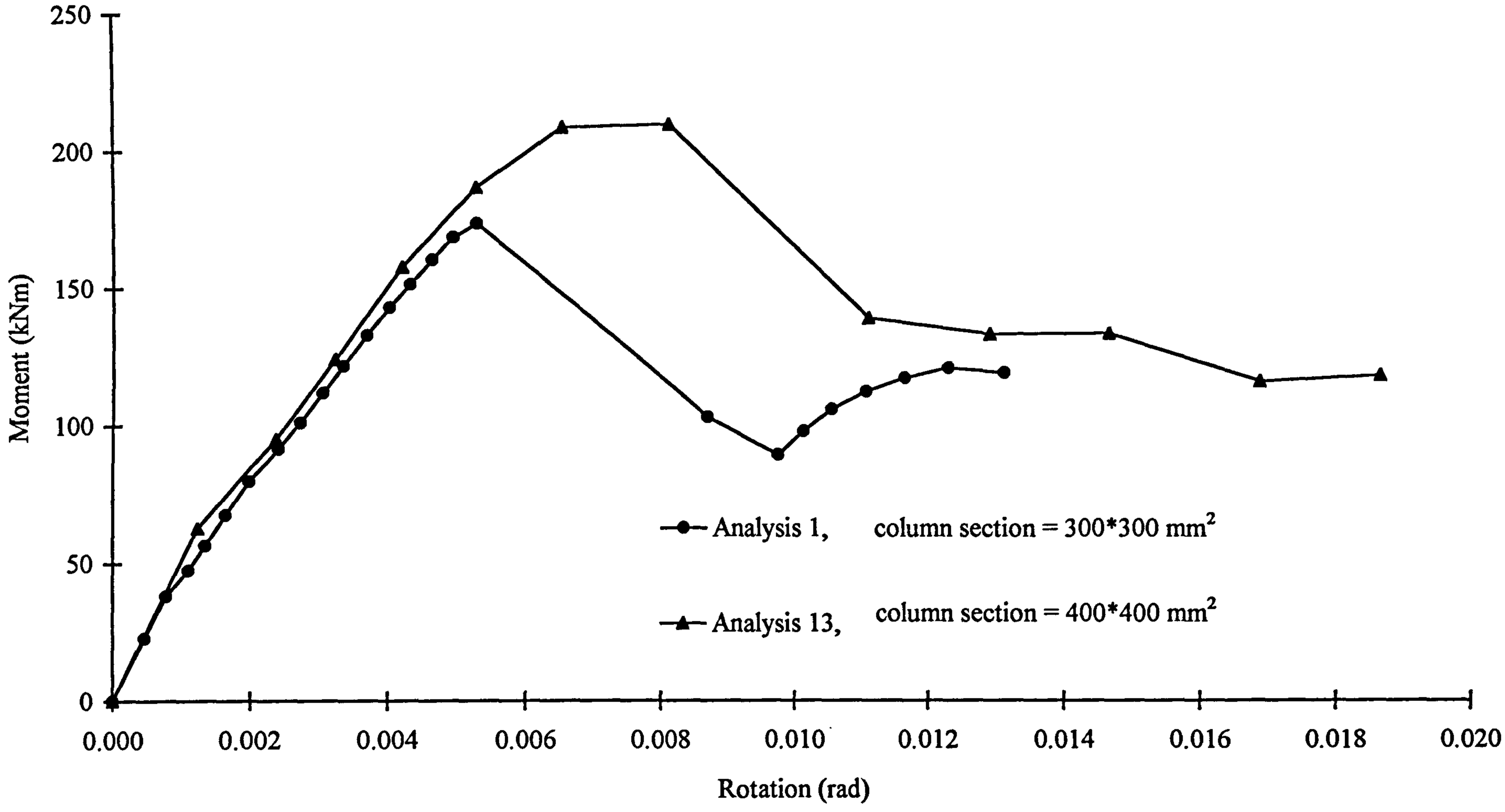

Figure 7.21 *Moment-rotation relationships for the joints with different column sections (hogging beam end moment)*

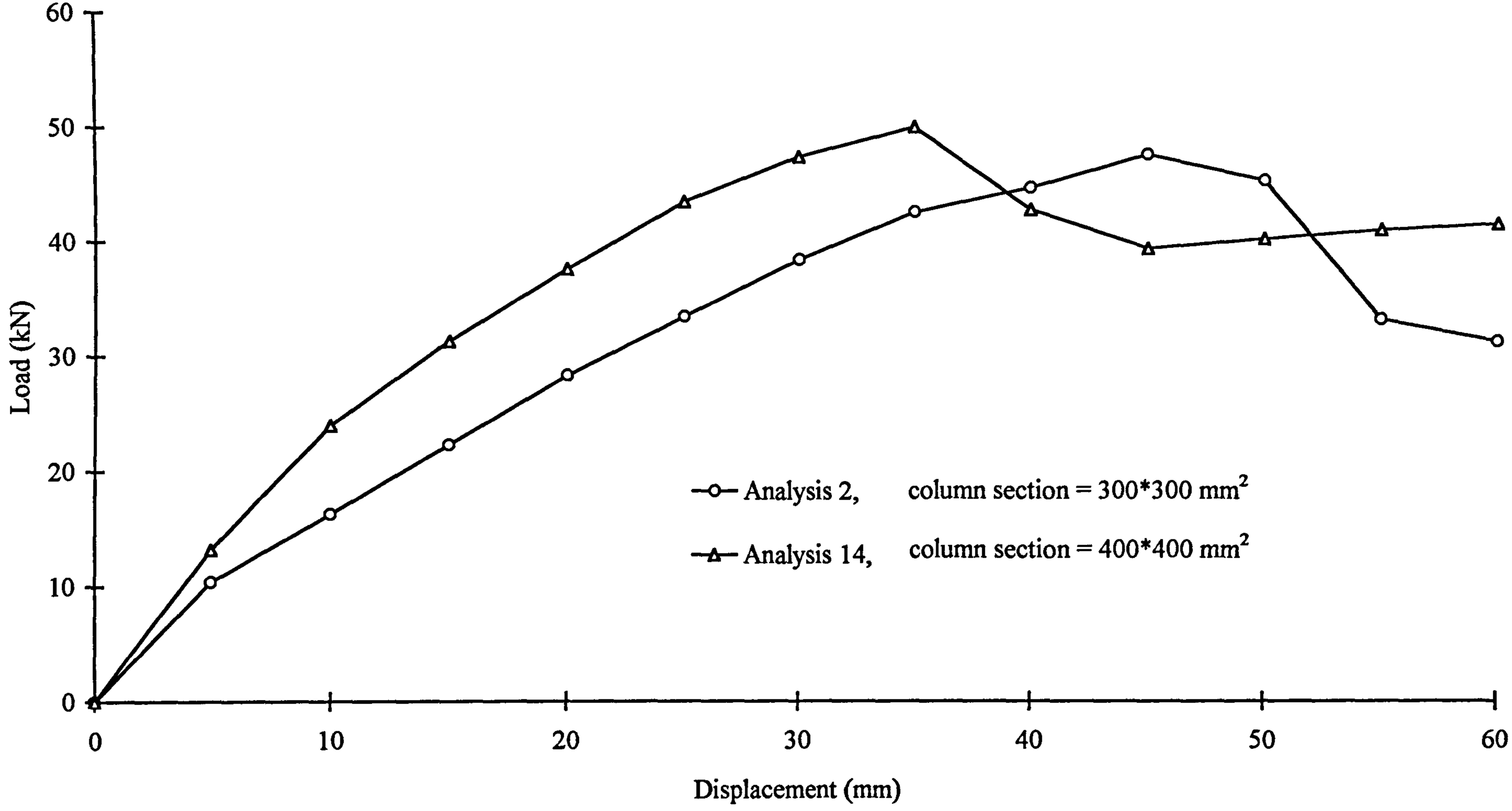

Figure 7.22 *Load-displacement relationships for the joints with different column sections (sagging beam end moment)*

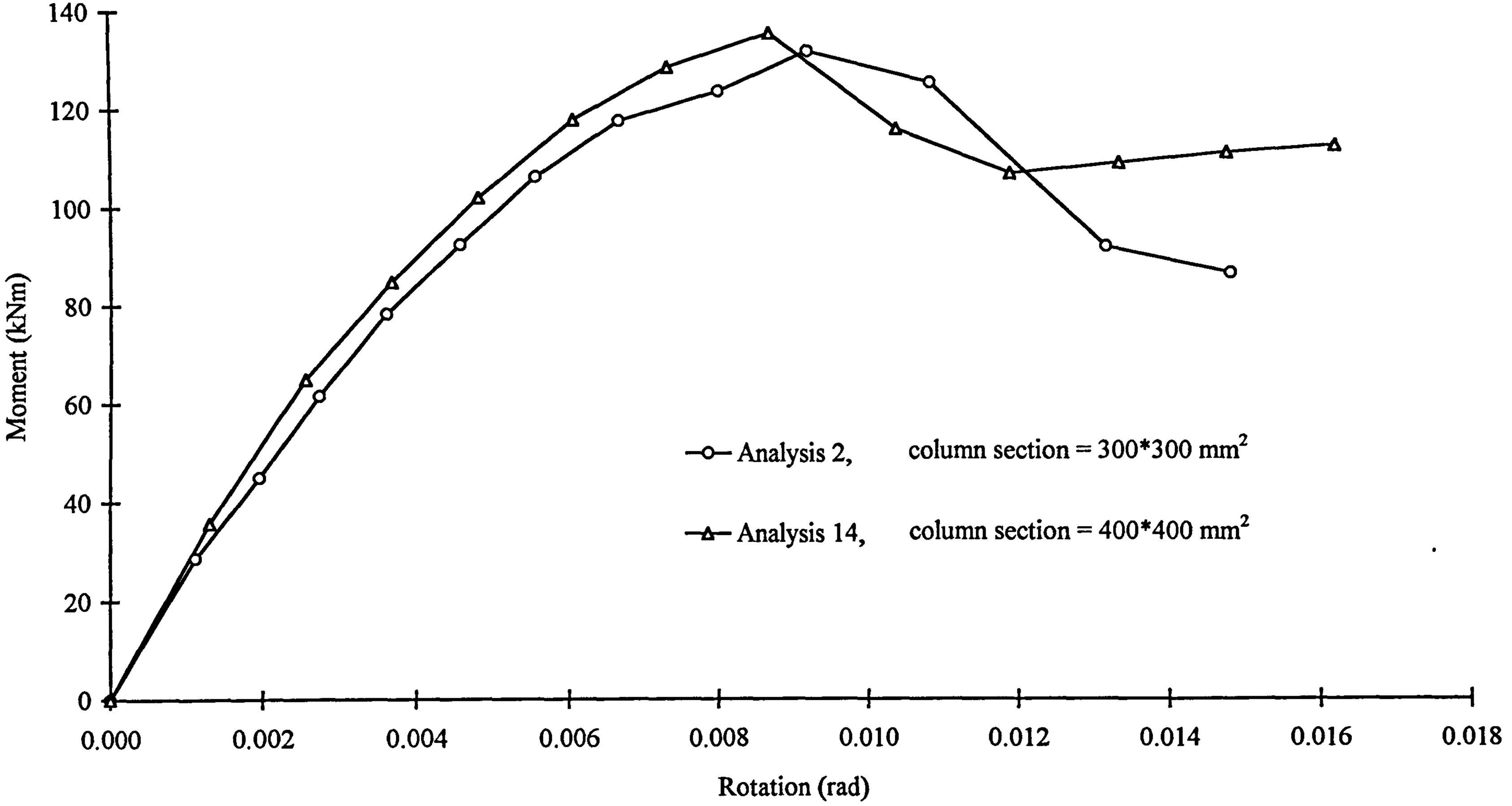

Figure 7.23 *Moment-rotation relationships for the joints with different column sections (sagging beam end moment)*

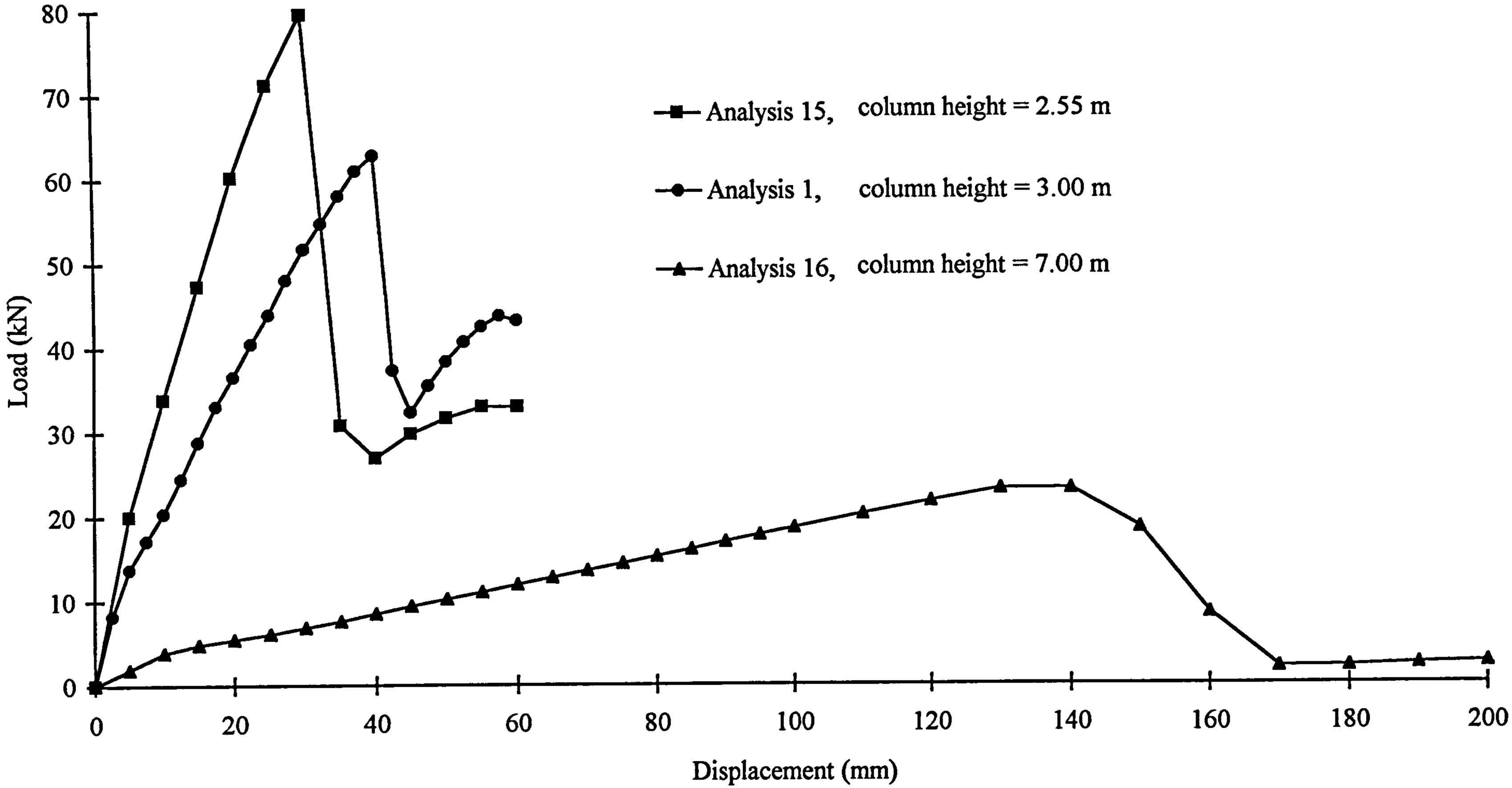

Figure 7.24 *Load-displacement relationships for the joints with different column heights (hogging beam end moment)*

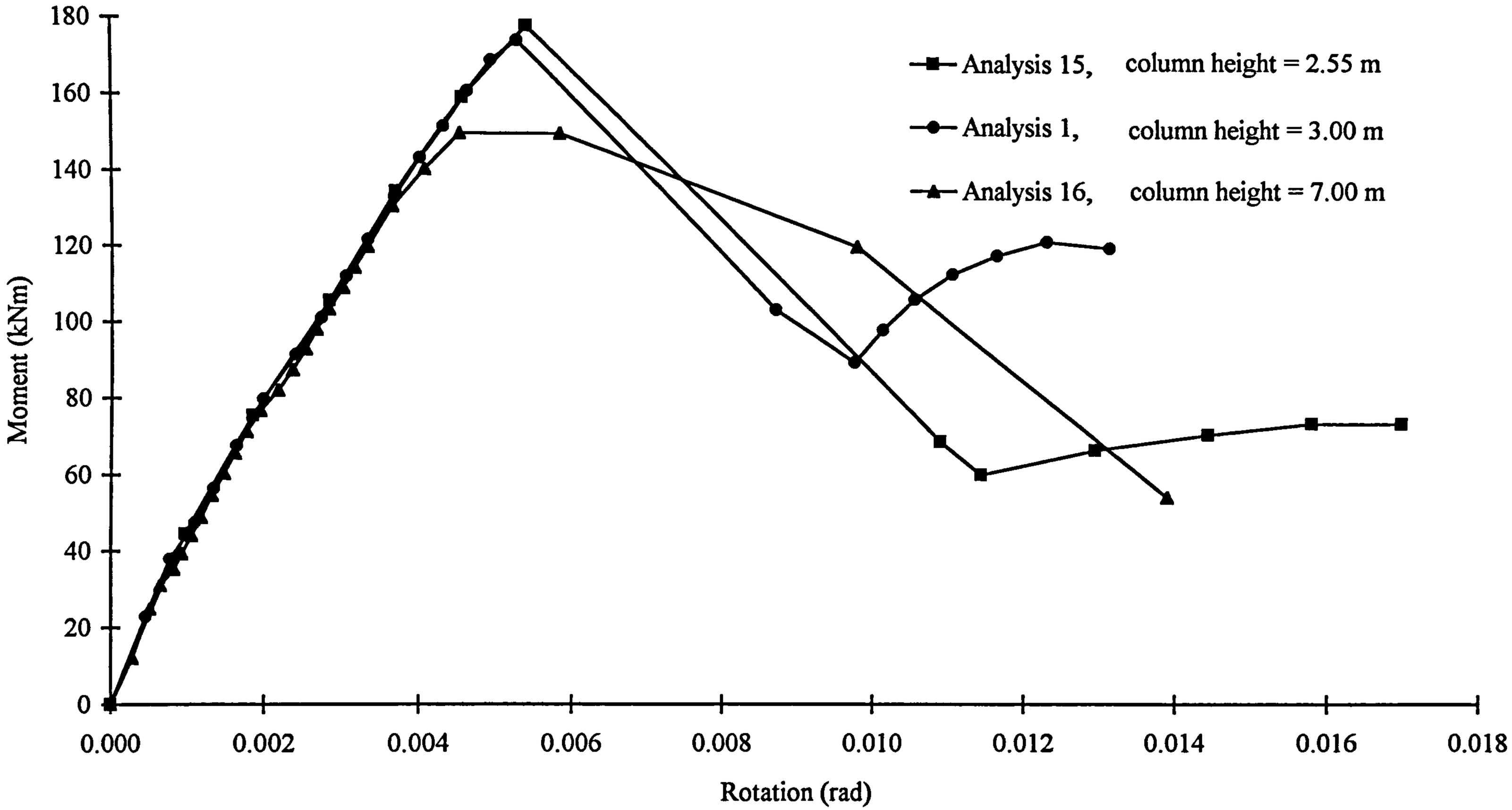

Figure 7.25 *Moment-rotation relationships for the joints with different column heights (hogging beam end moment)*

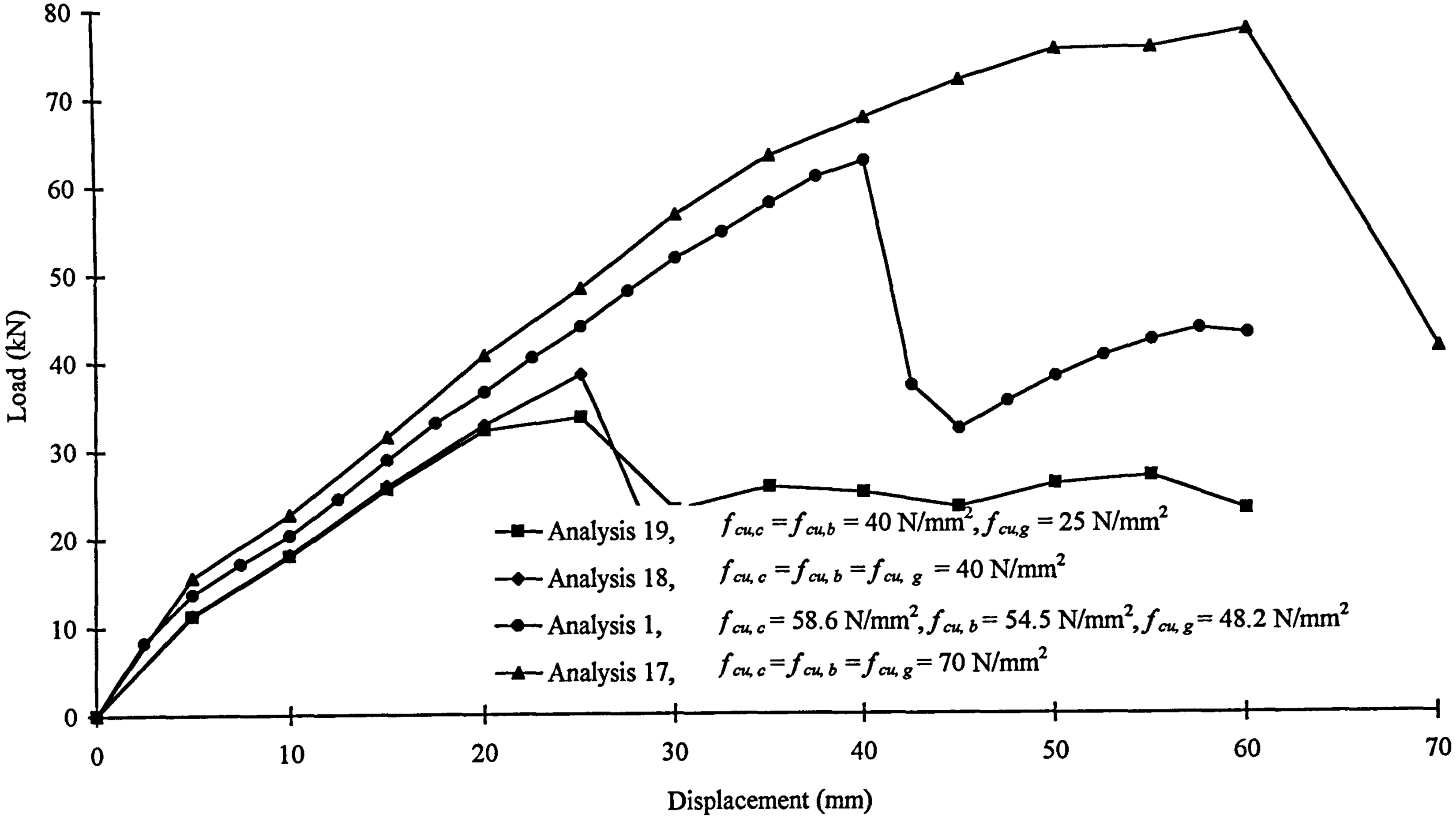

Figure 7.26 *Load-displacement relationships for the joints with different concrete and grout grades (hogging beam end moment)*

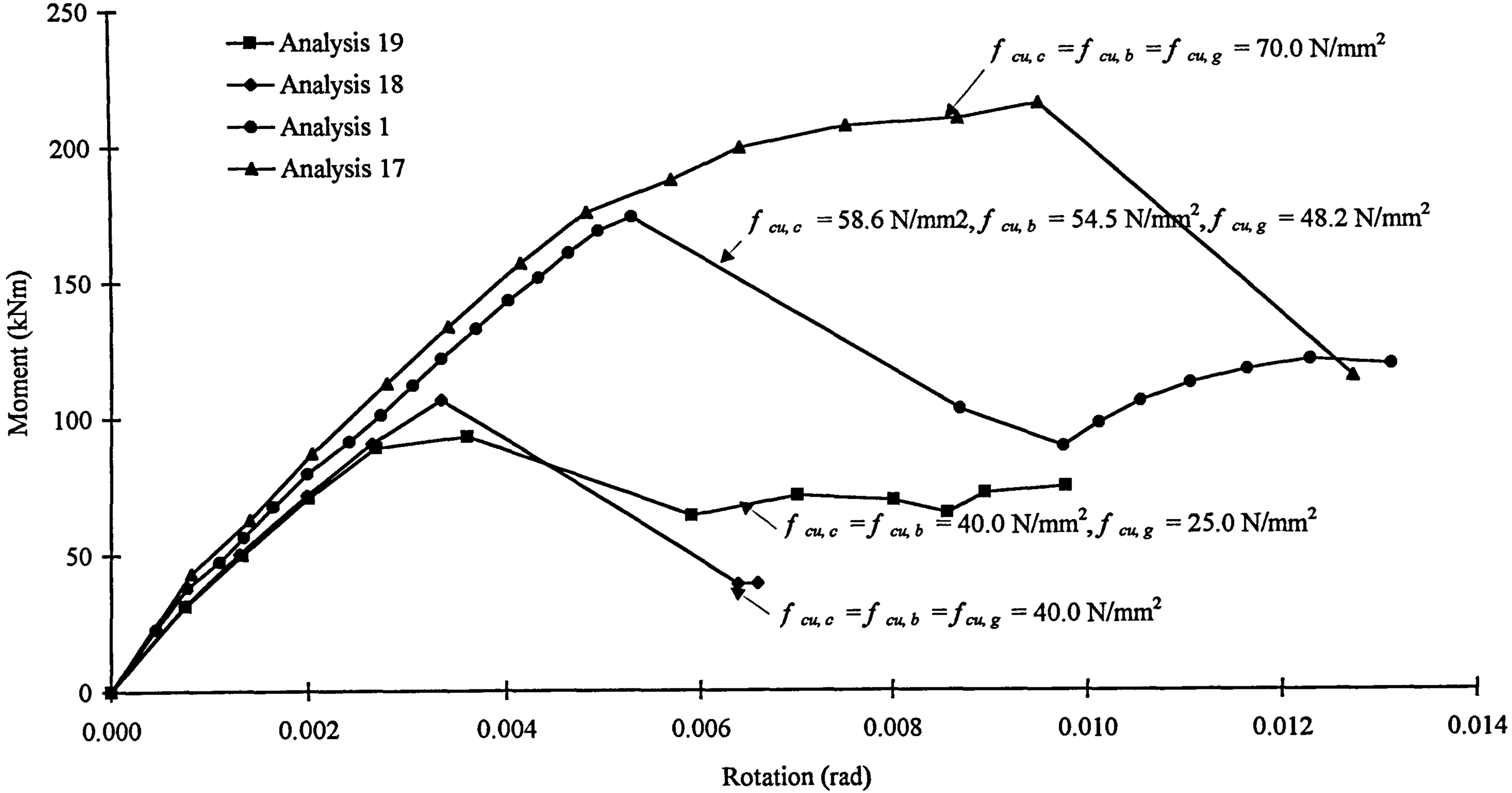

Figure 7.27 *Moment-rotation relationships for the joints with different concrete and grout grades (hogging beam end moment)*

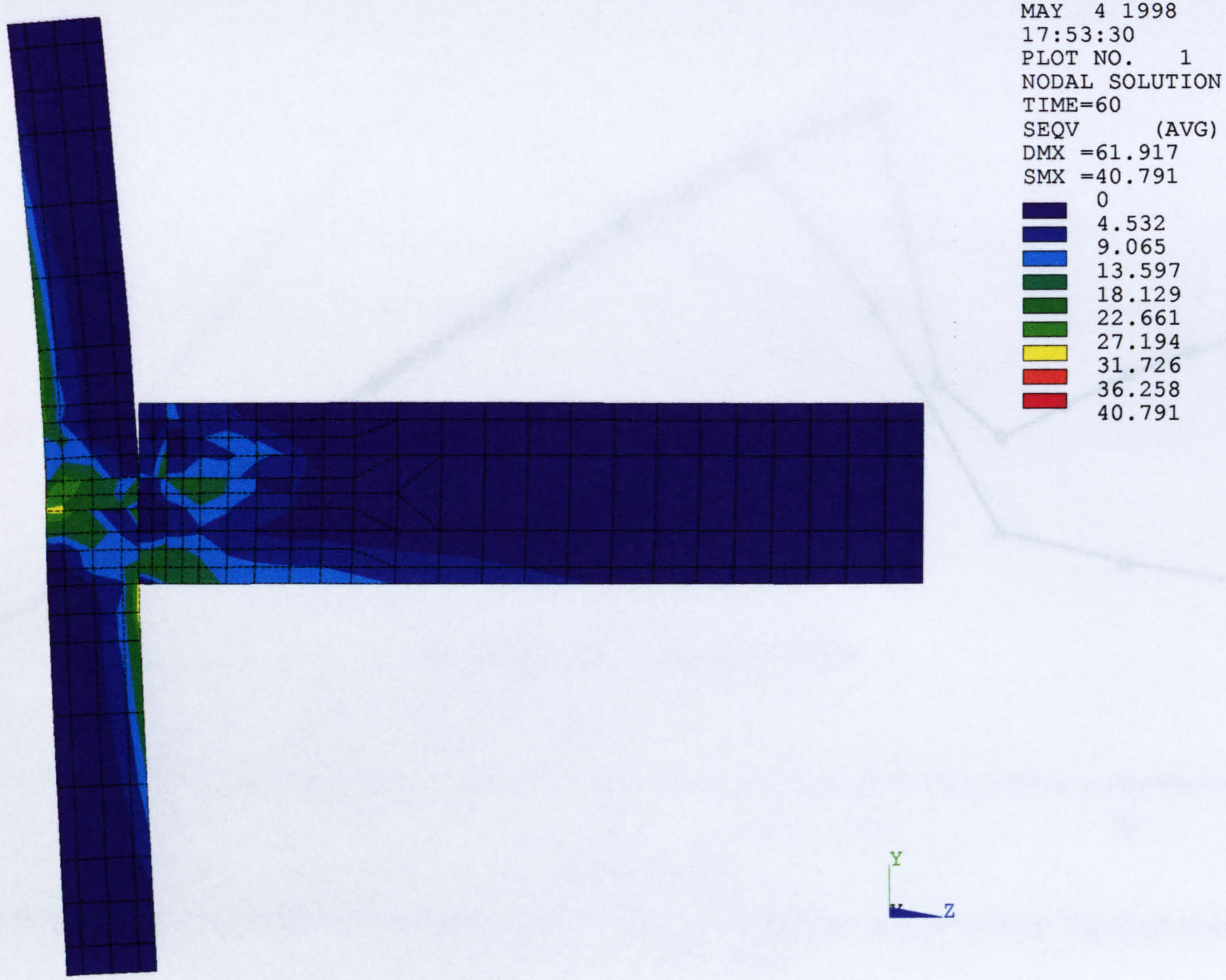

Figure 7.28 *Ultimate equivalent stress distribution for the concrete and grout components of grade C70 (Analysis 17)*

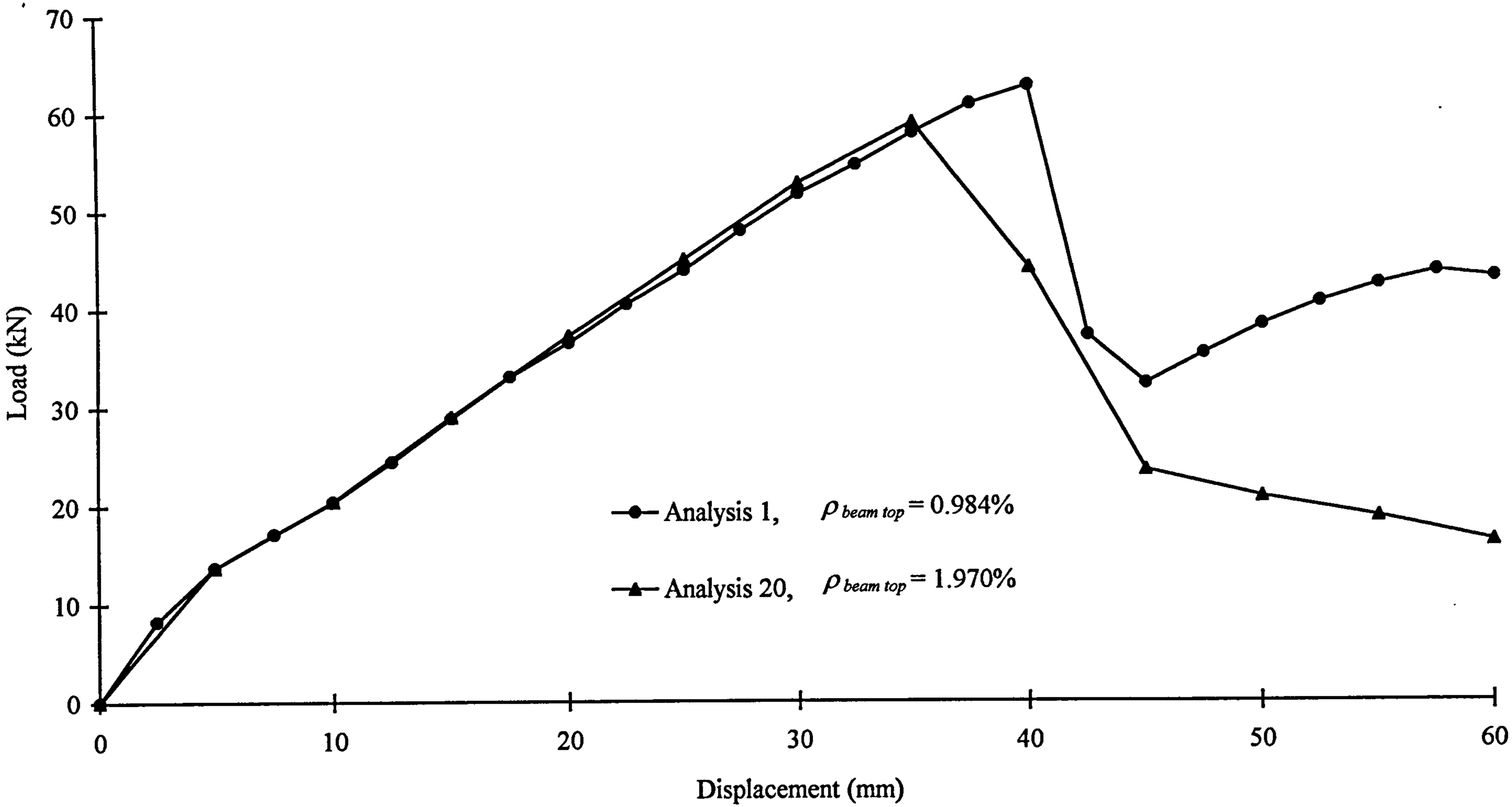

Figure 7.29 *Load-displacement relationships for the joints with different amount of beam top reinforcement (hogging beam end moment)*

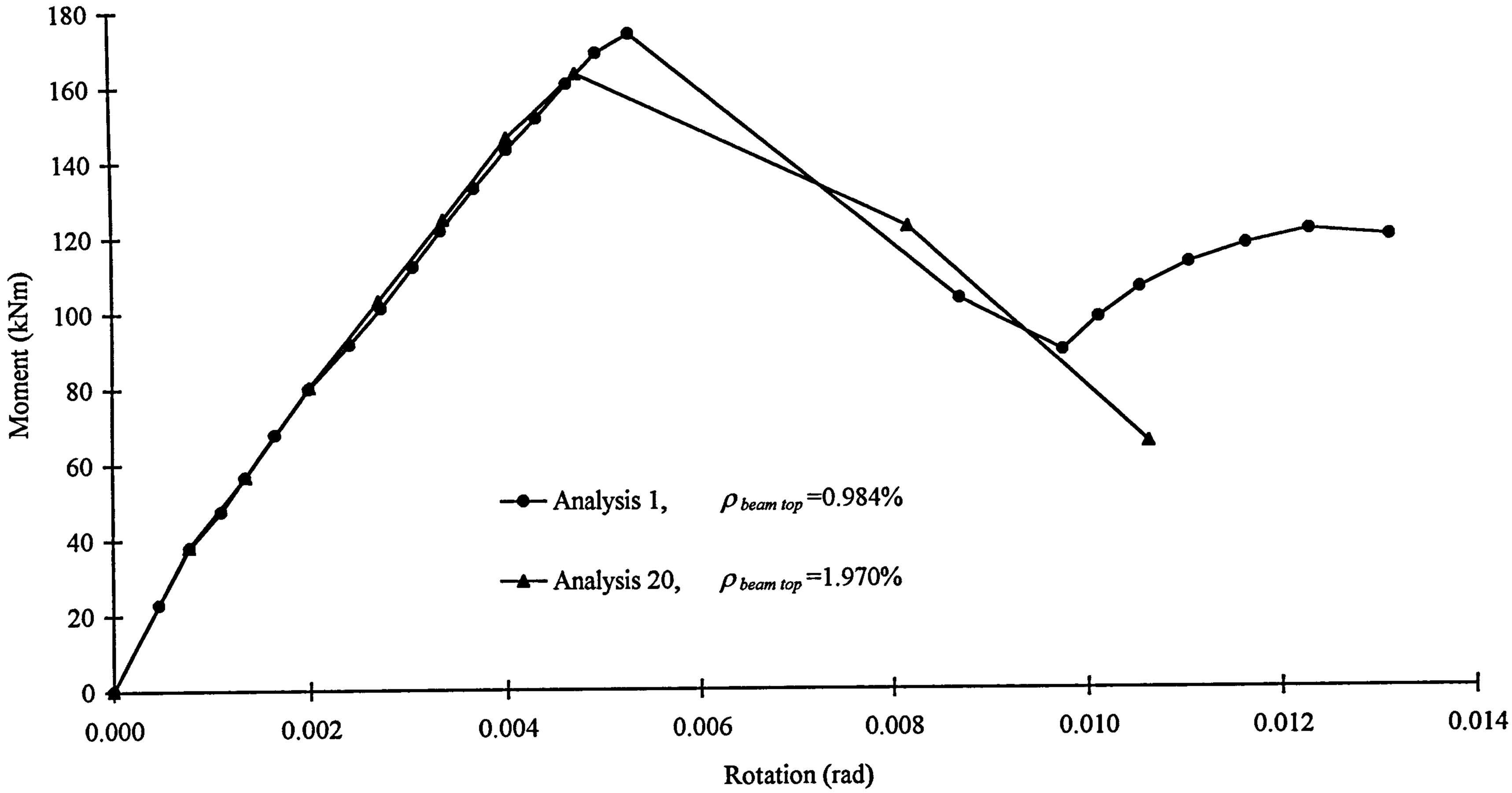

Figure 7.30 *Moment-rotation relationships for the joints with different amount of beam top reinforcement (hogging beam end moment)*

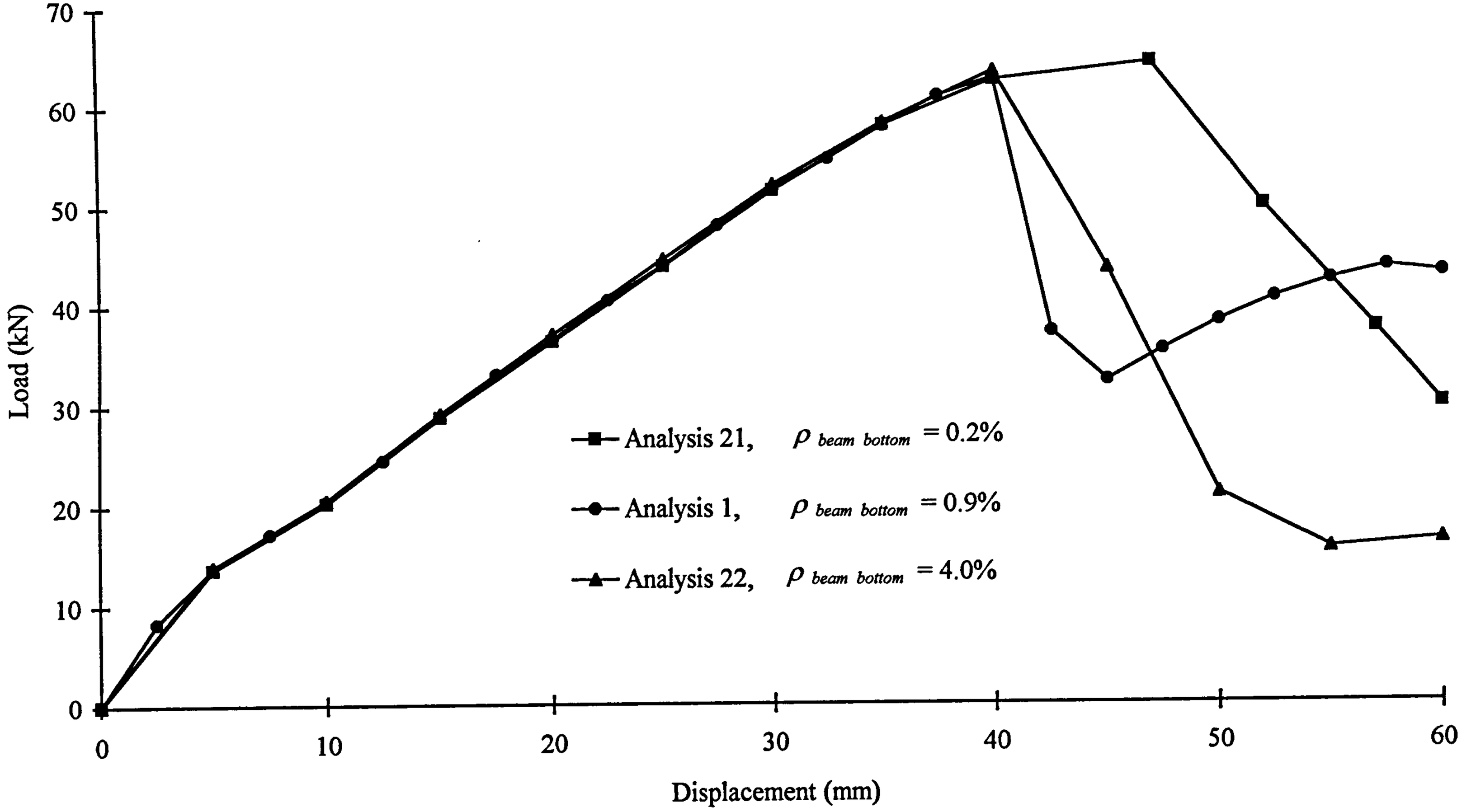

Figure7.31 *Load-displacement relationships for the joints with different amount of beam bottom reinforcement (hogging beam end moment)*

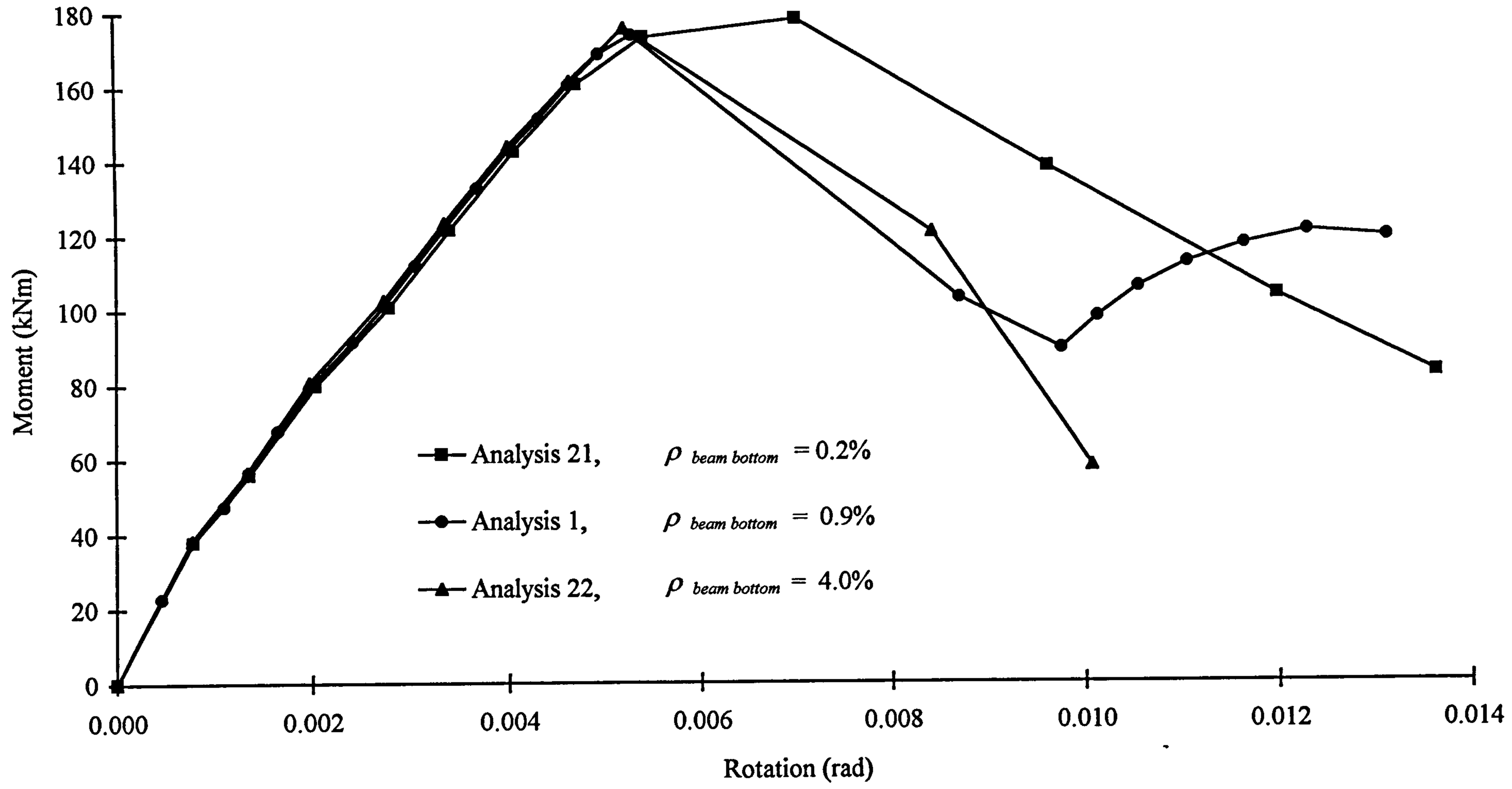

Figure 7.32 *Moment-rotation relationships for the joints with different amount of beam bottom reinforcement (hogging beam end moment)*

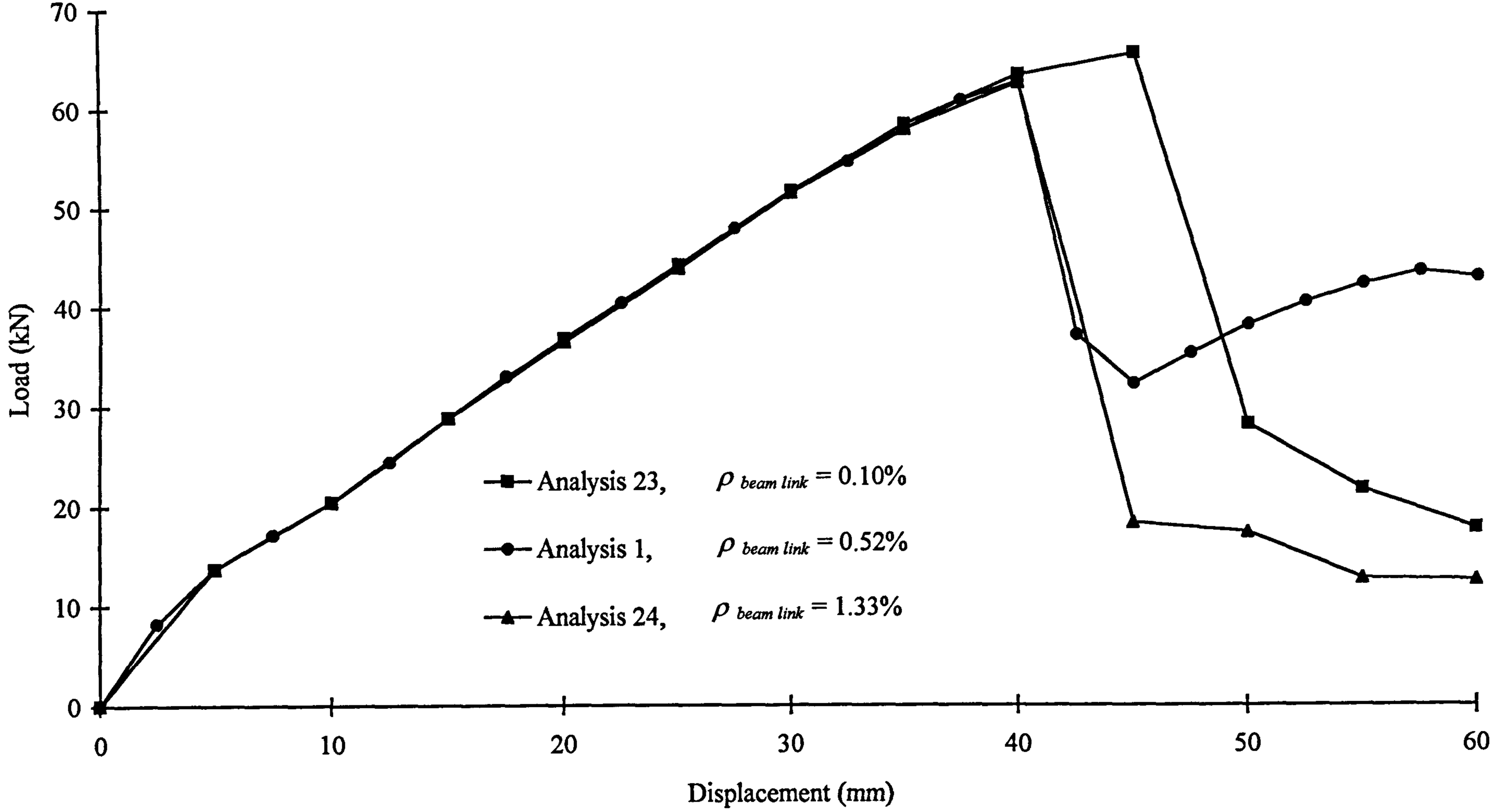

Figure 7.33 *Load-displacement relationships for the joints with different amount of beam links (hogging beam end moment)*

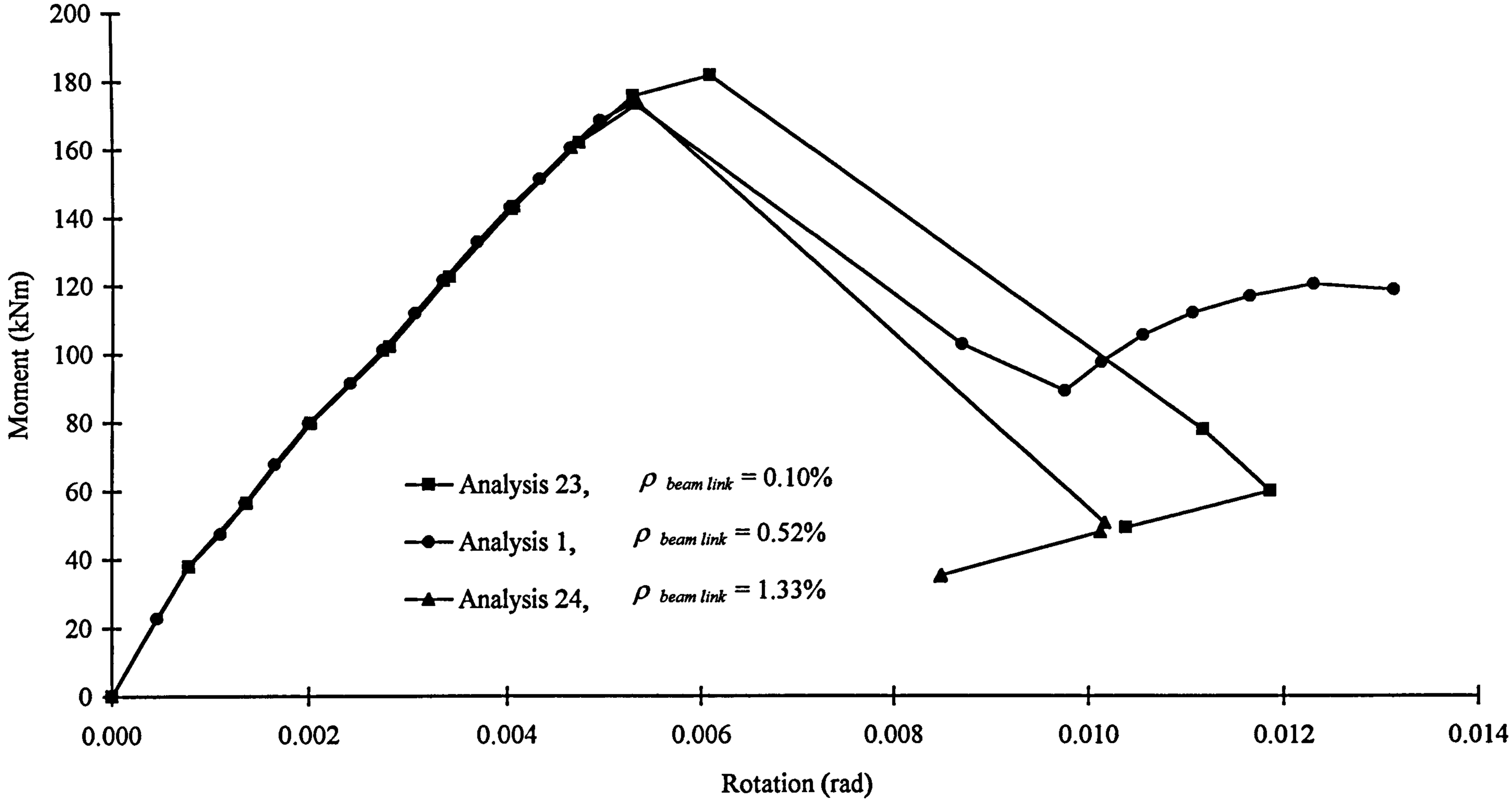

Figure 7.34 *Moment-rotation relationships for the joints with different amount of beam links (hogging beam end moment)*

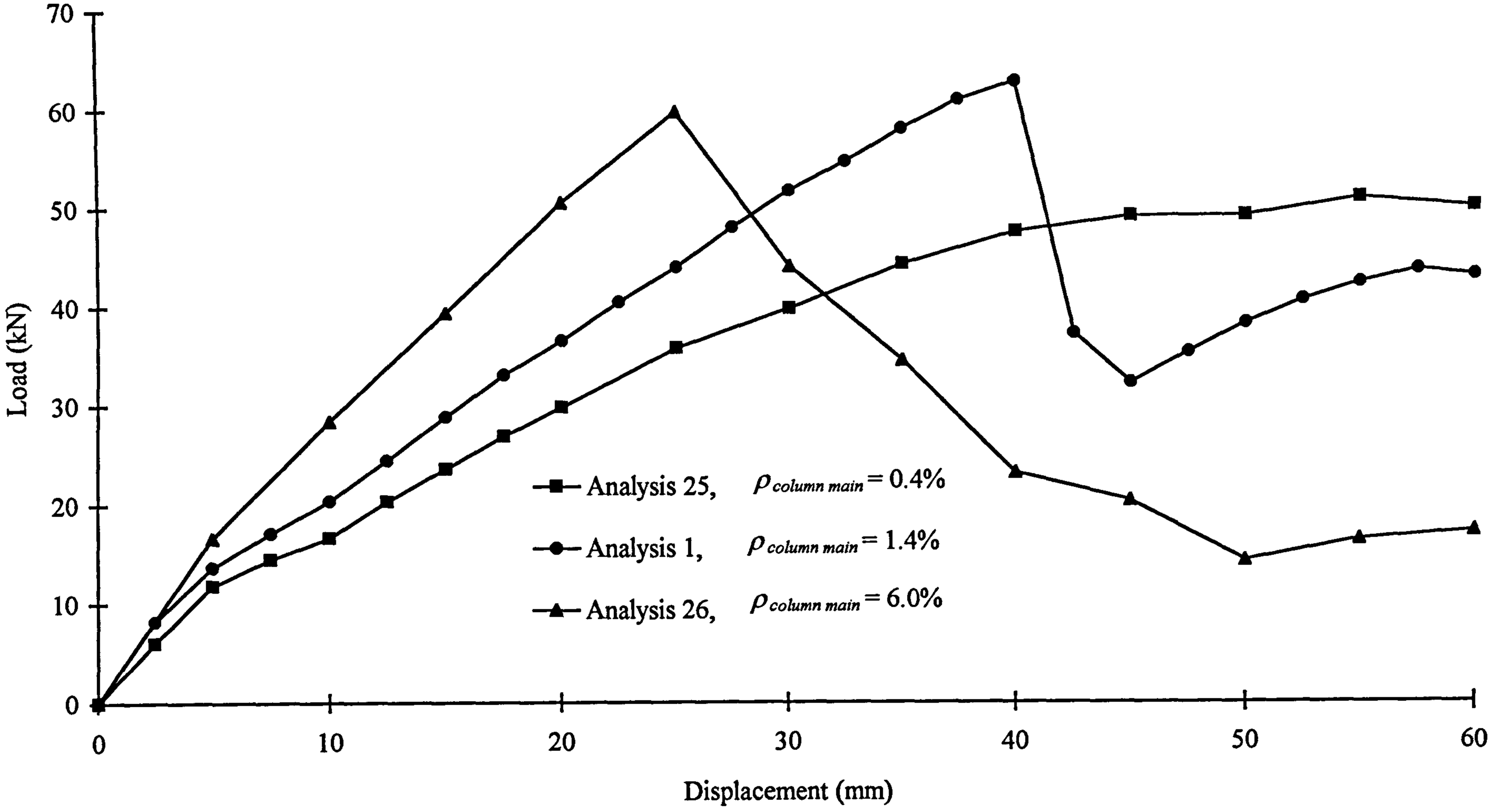

Figure 7.35 *Load-displacement relationships for the joints with different amount of column main reinforcement (hogging beam end moment)*

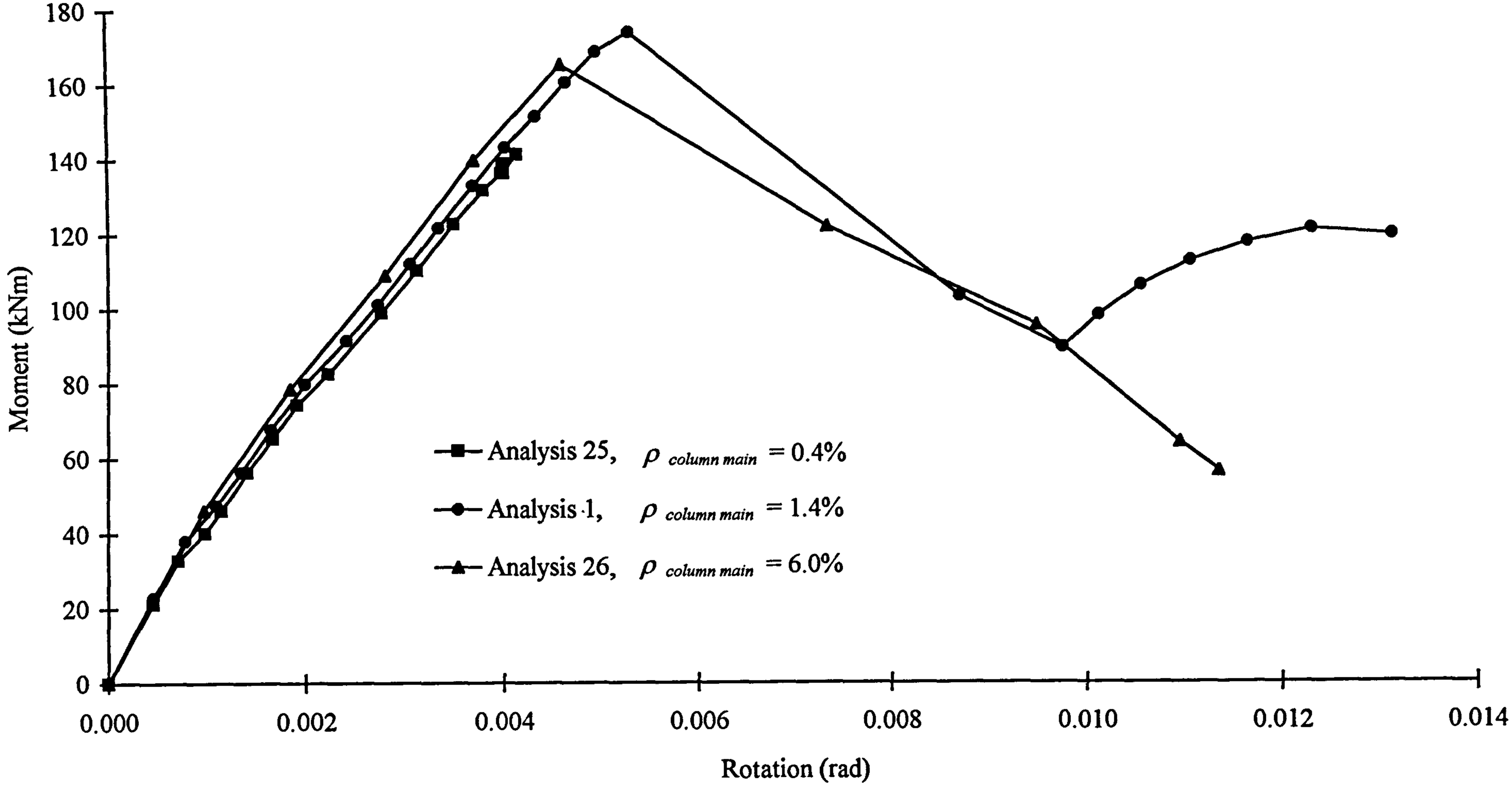

Figure 7.36 *Moment-rotation relationships for the joints with different amount of column main reinforcement (hogging beam end moment)*

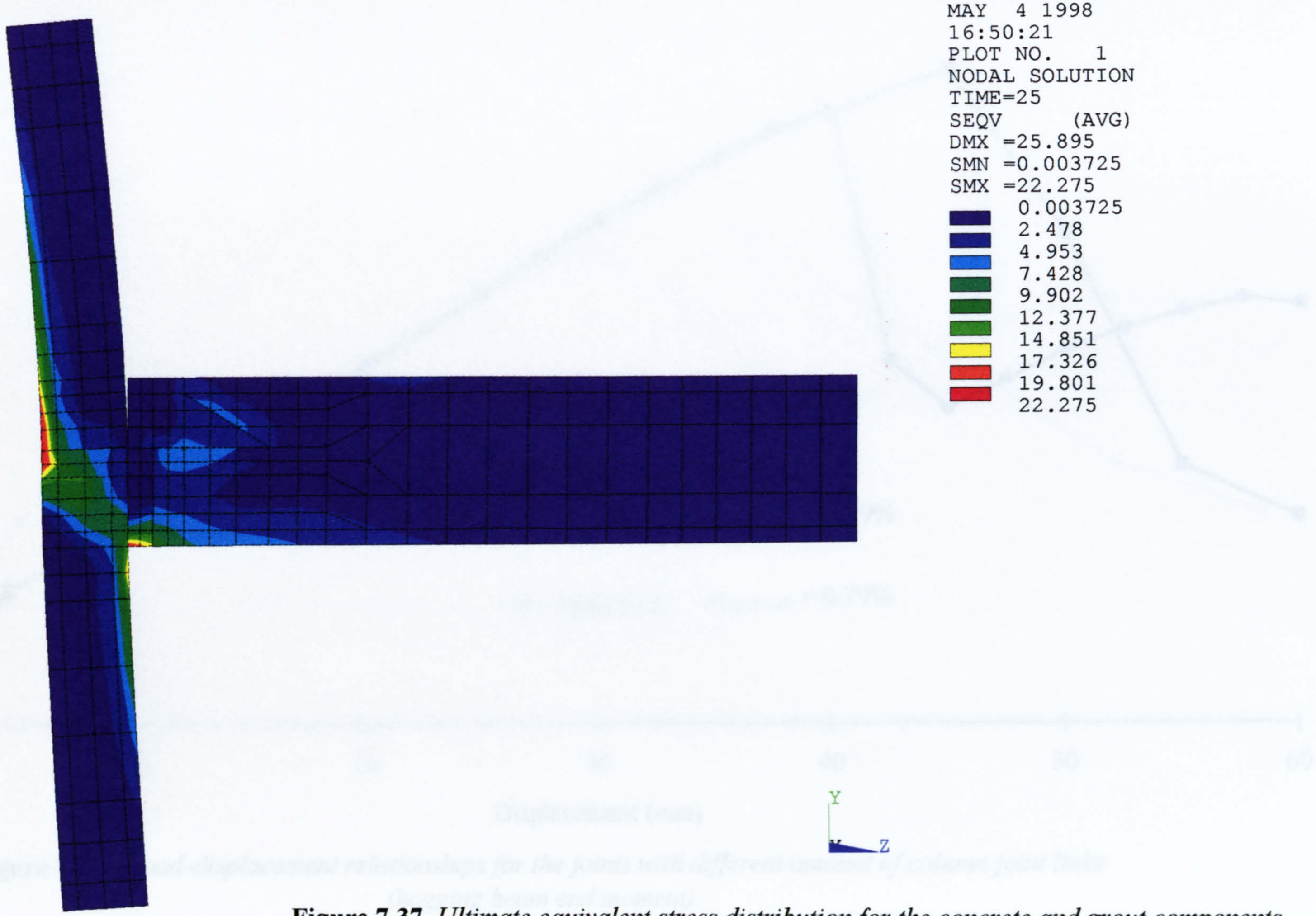

Figure 7.37 *Ultimate equivalent stress distribution for the concrete and grout components in the joint with 0.4% column main reinforcement (Analysis 25)*

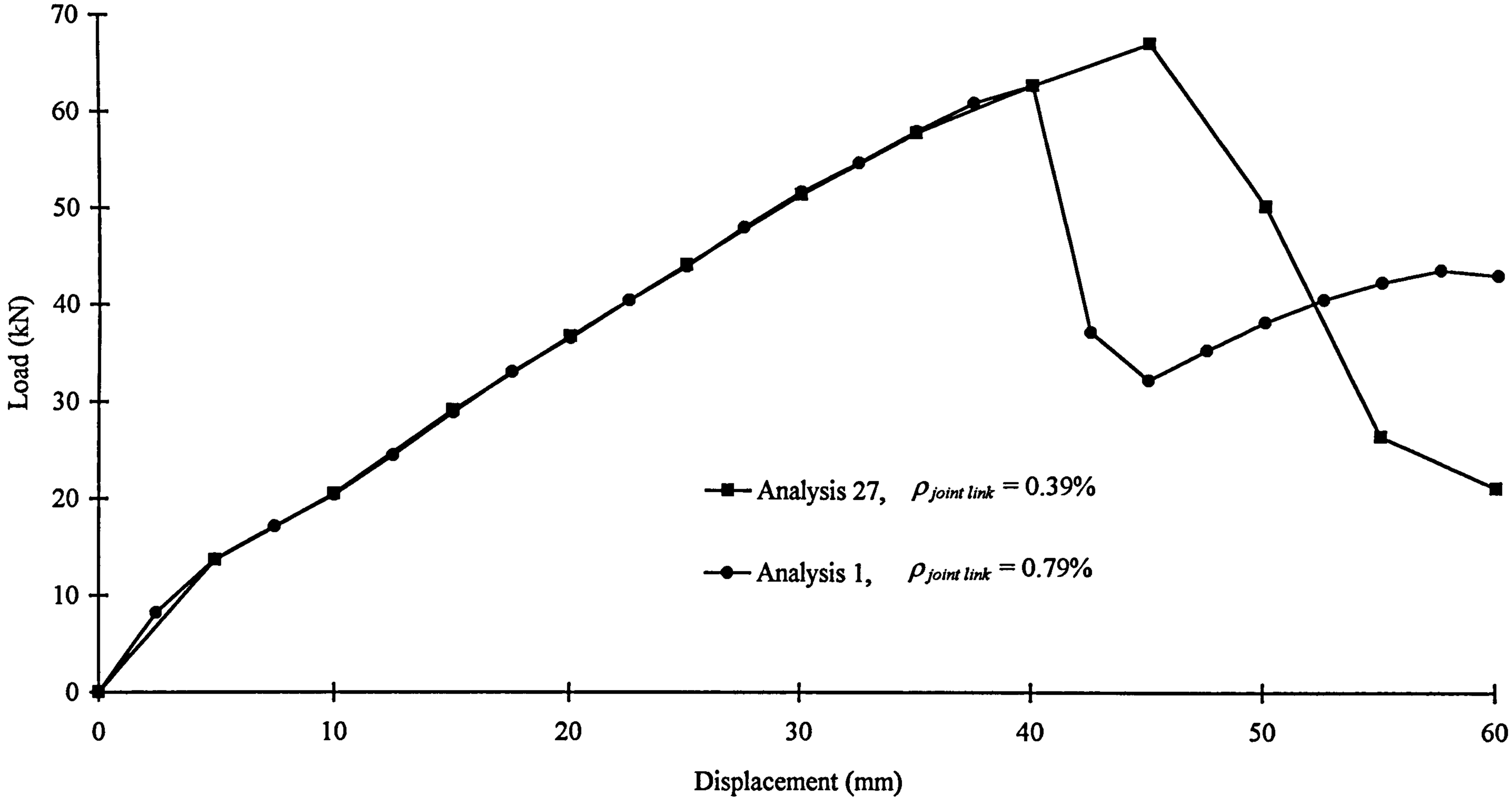

Figure 7.38 *Load-displacement relationships for the joints with different amount of column joint links (hogging beam end moment)*

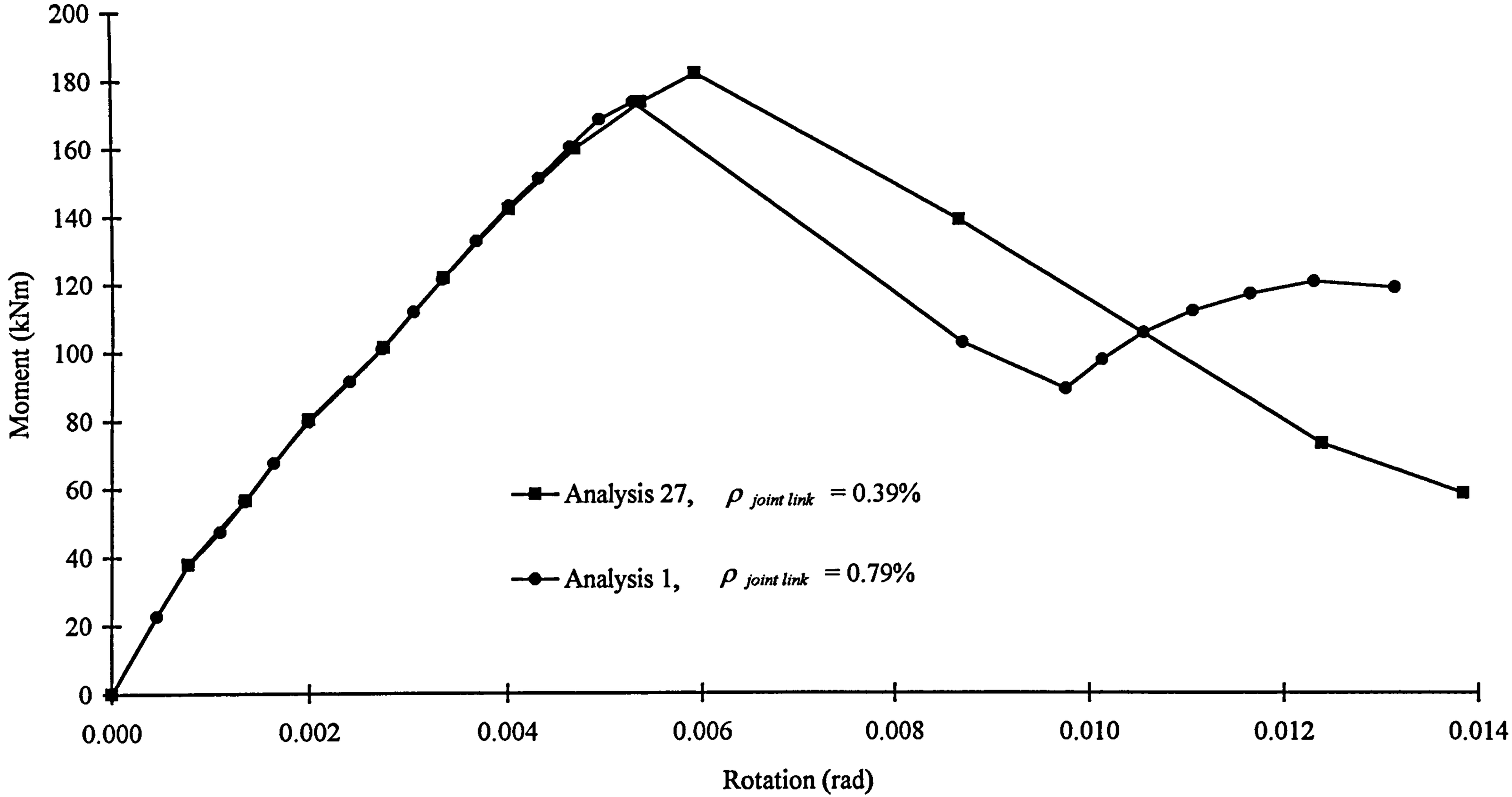

Figure 7.39 *Moment-rotation relationships for the joints with different amount of column joint links (hogging beam end moment)*

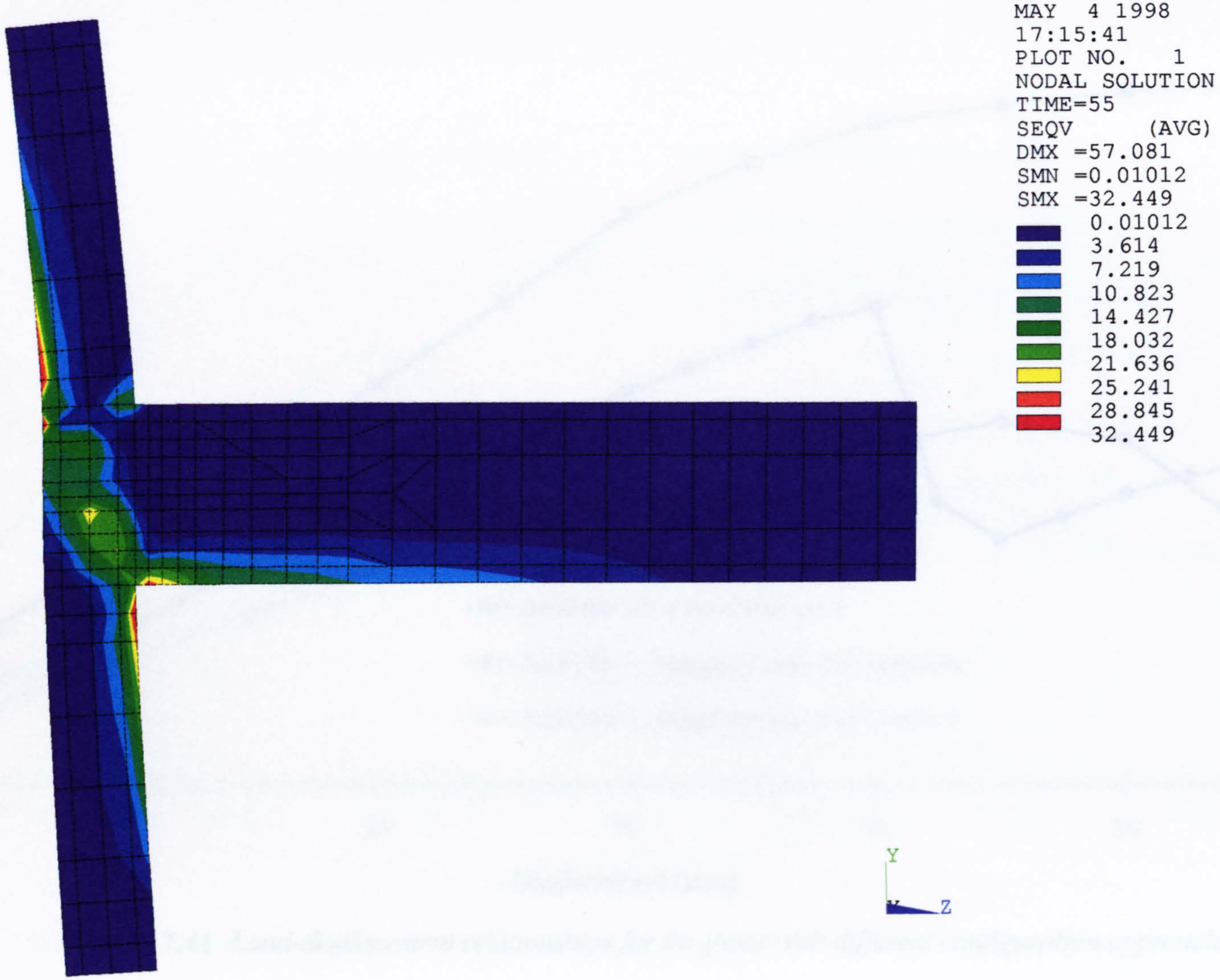

Figure 7.40 *Ultimate equivalent stress distribution for the monolithic joint (Analysis 28)*

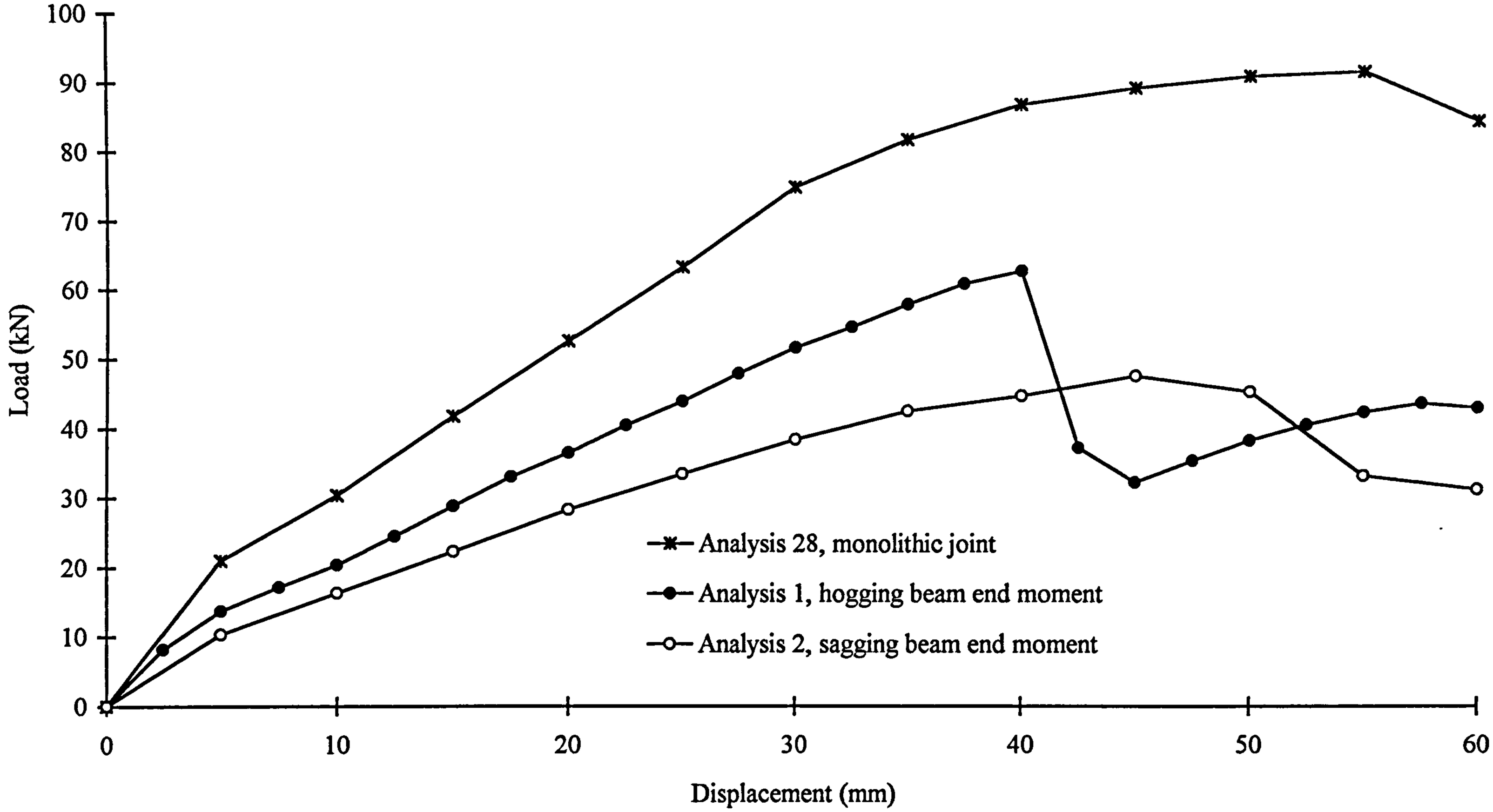

Figure 7.41 *Load-displacement relationships for the joints with different configuration approache* s

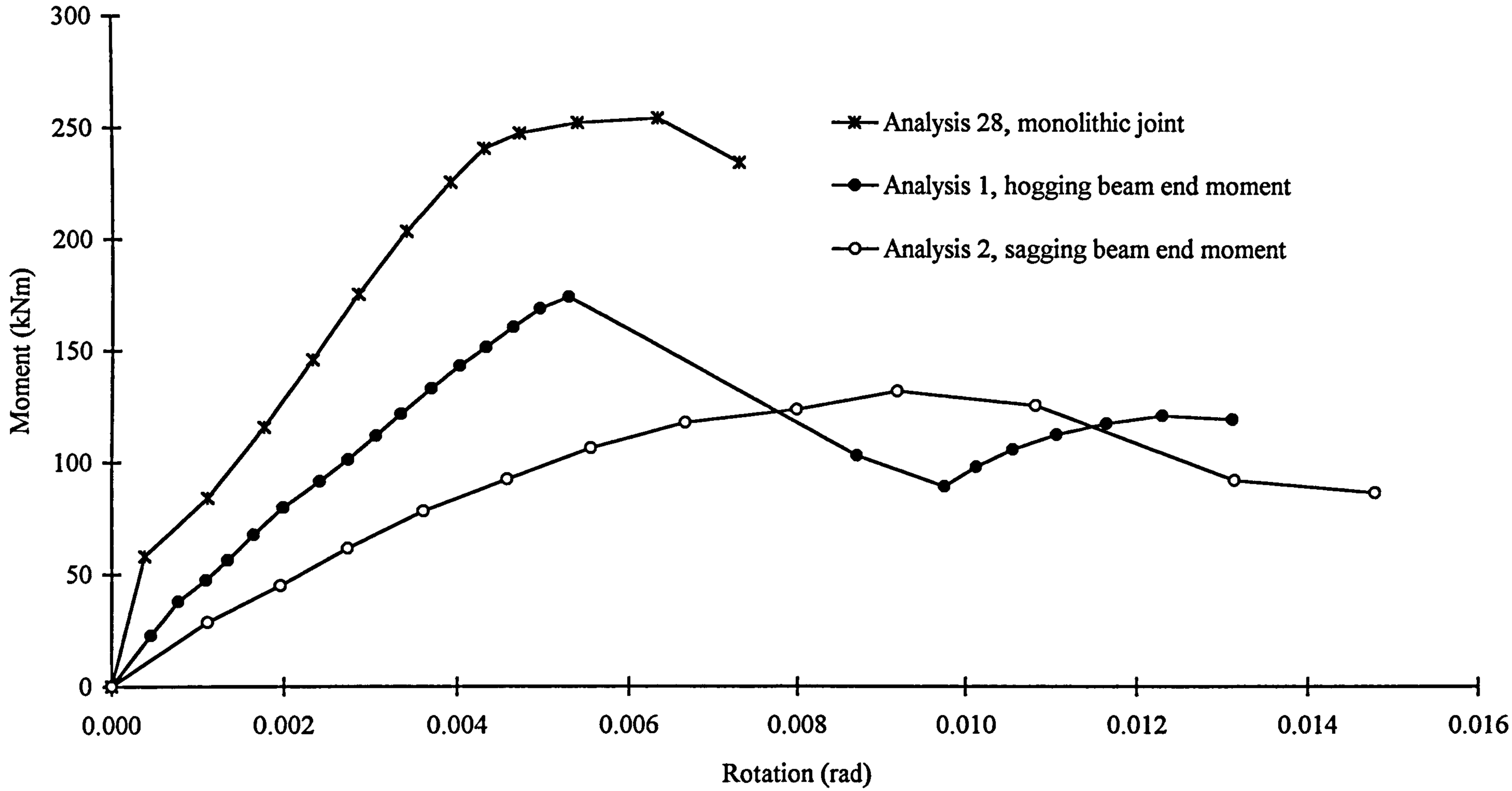

Figure 7.42 *Moment-rotation relationships for the joints with different configuration approaches*

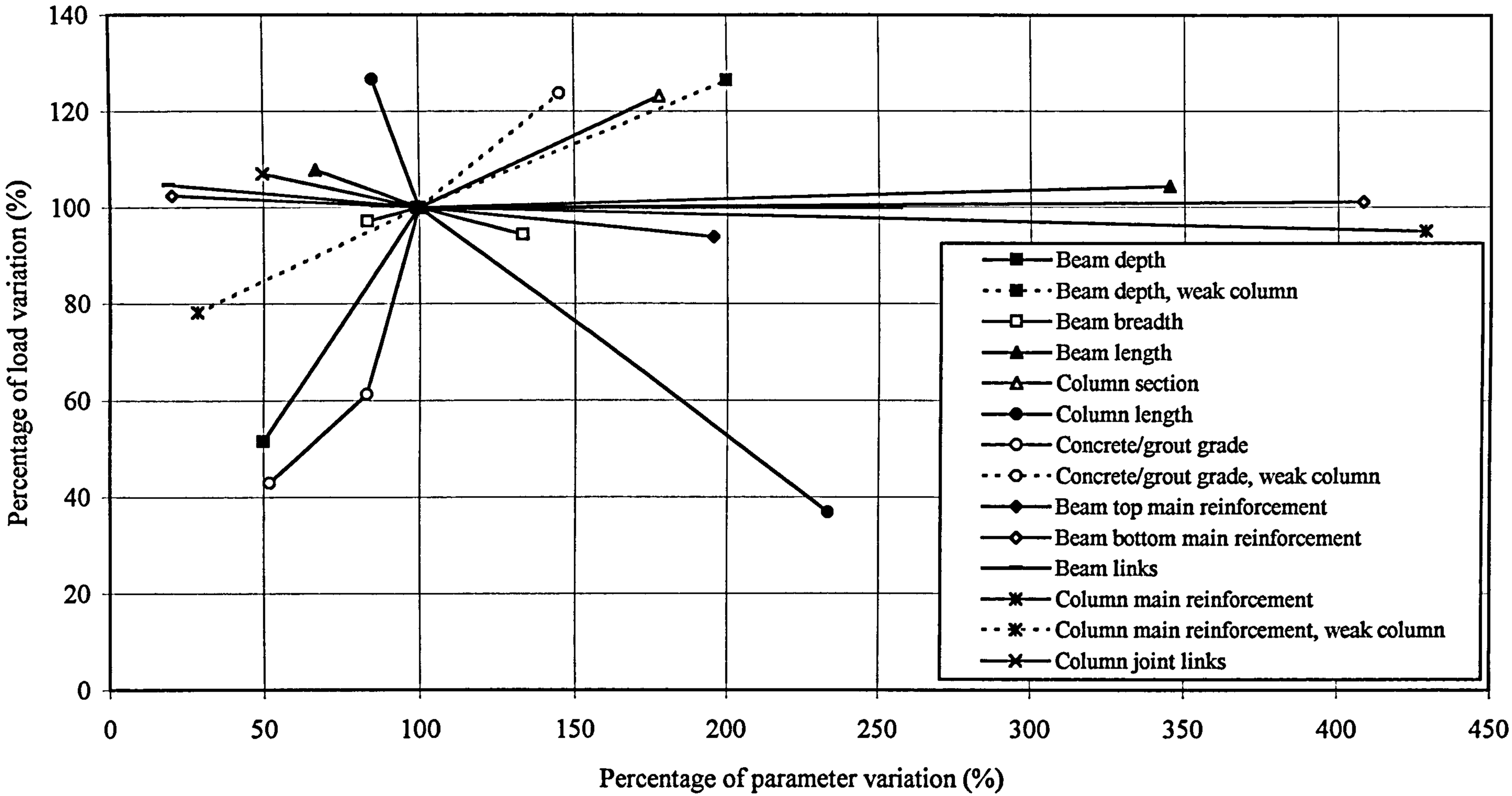

Figure 7.43 *Sensitivity of the load for the joints with hogging beam end moment*

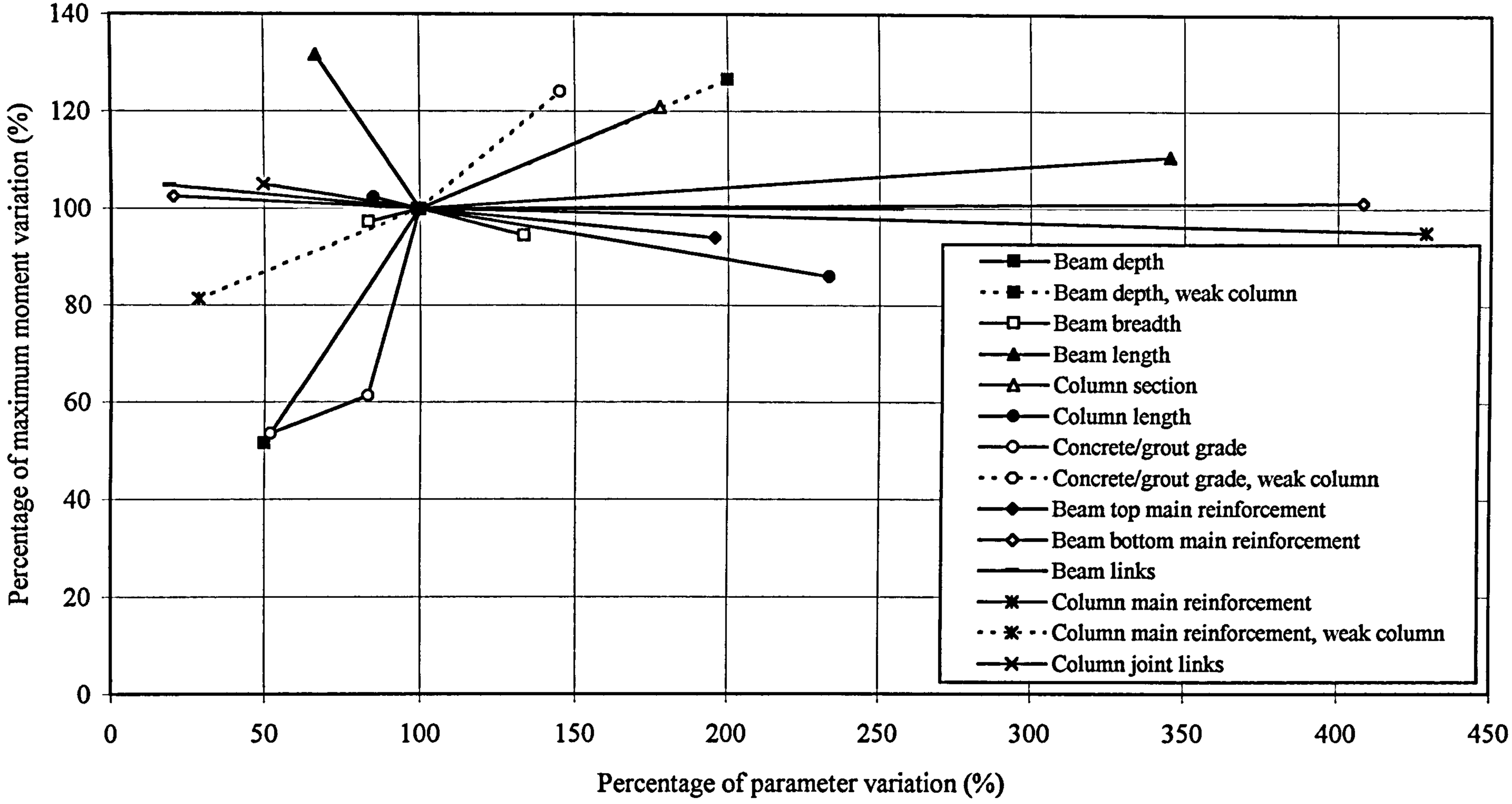

Figure 7.44 *Sensitivity of the maximum moment for the joints with hogging beam end moment*

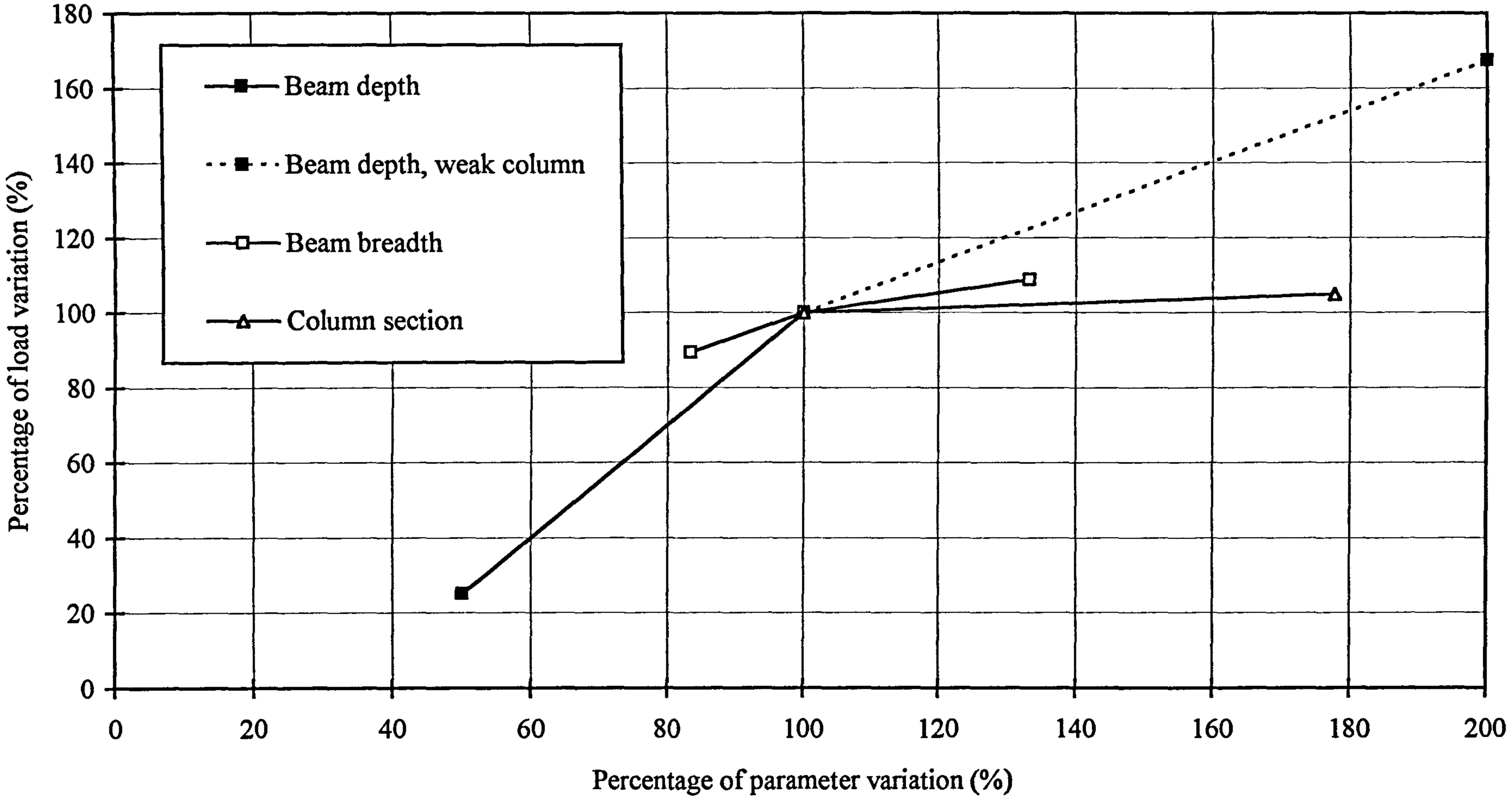

Figure 7.45 *Sensitivity of the load and the maximum moment for the joints with sagging beam end moment*

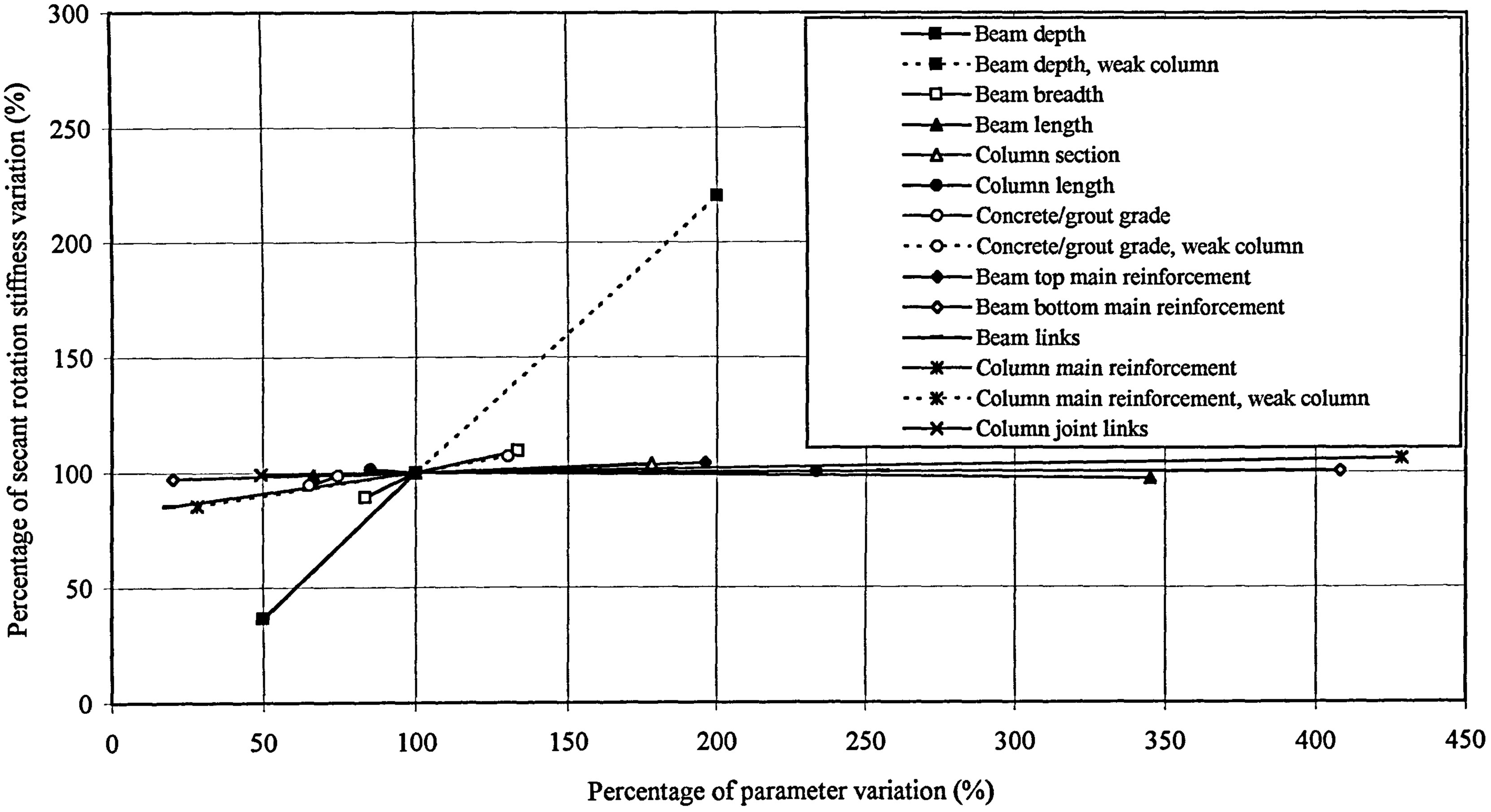

Figure 7.46 *Sensitivity of the secant rotation stiffness for the joints with hogging beam end moment*

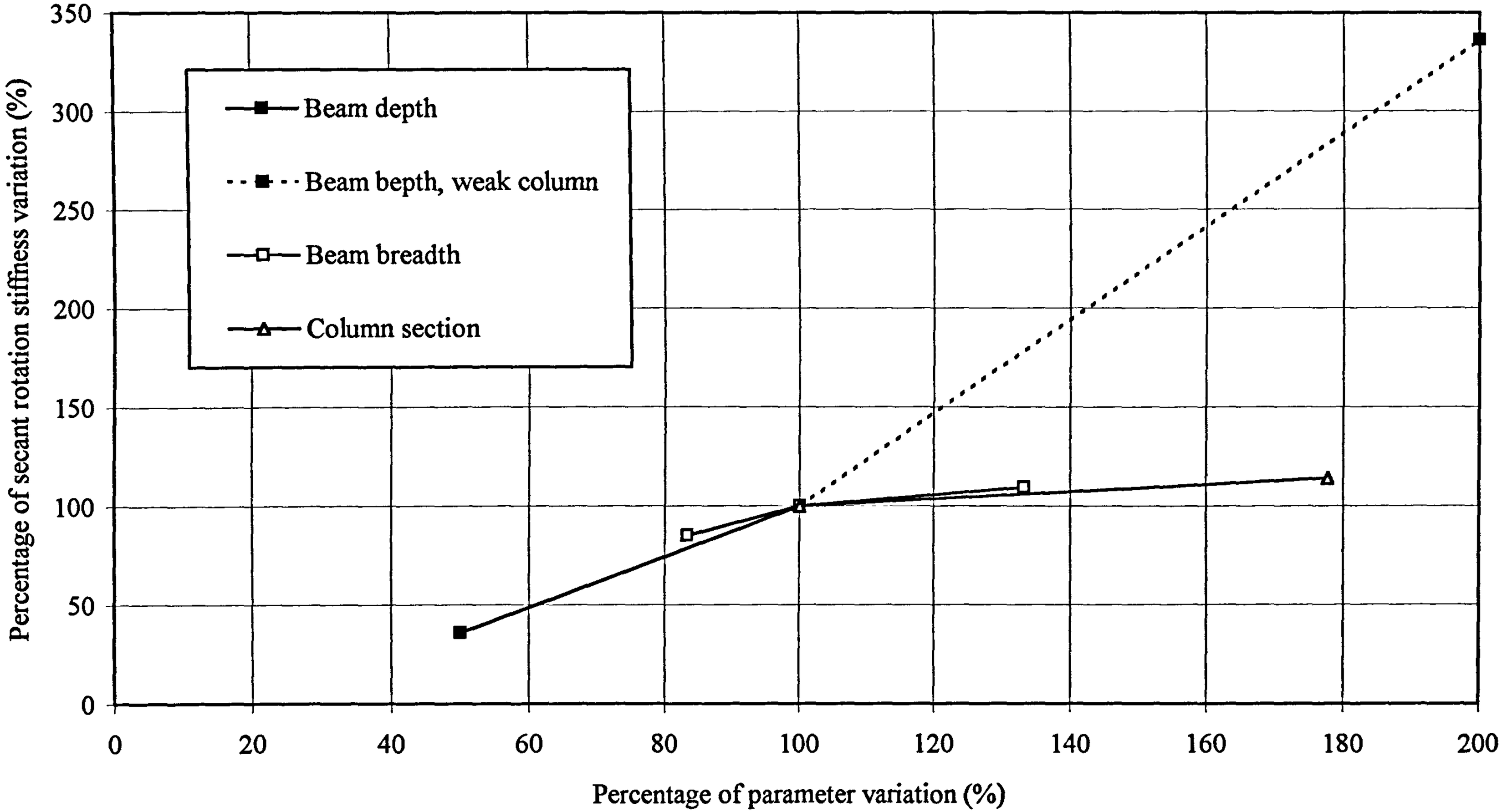

Figure 7.47 *Sensitivity of the secant rotation stiffness for the joints with sagging beam end moment*

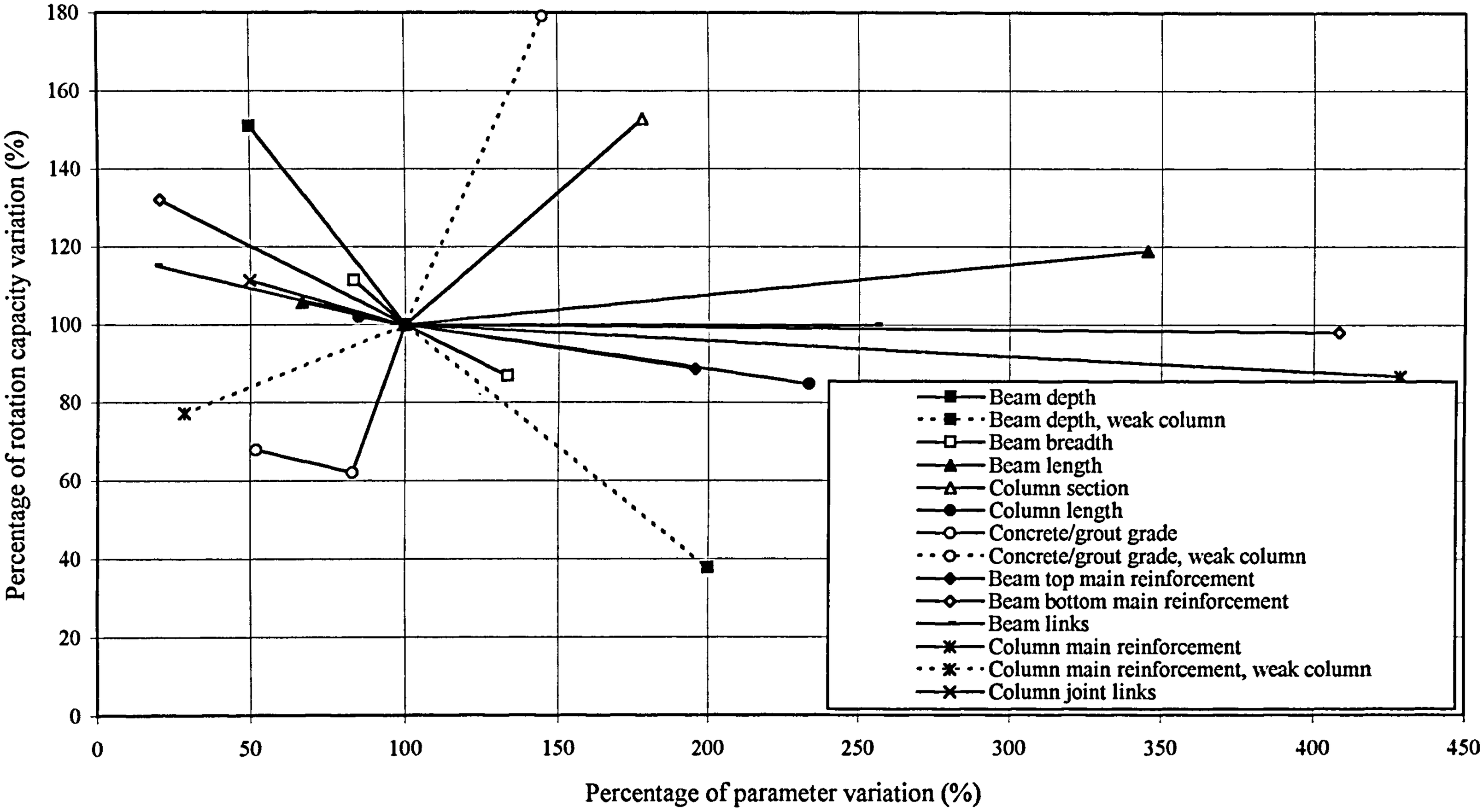

Figure 7.48 *Sensitivity of the rotation capacity for the joints with hogging beam end moment*

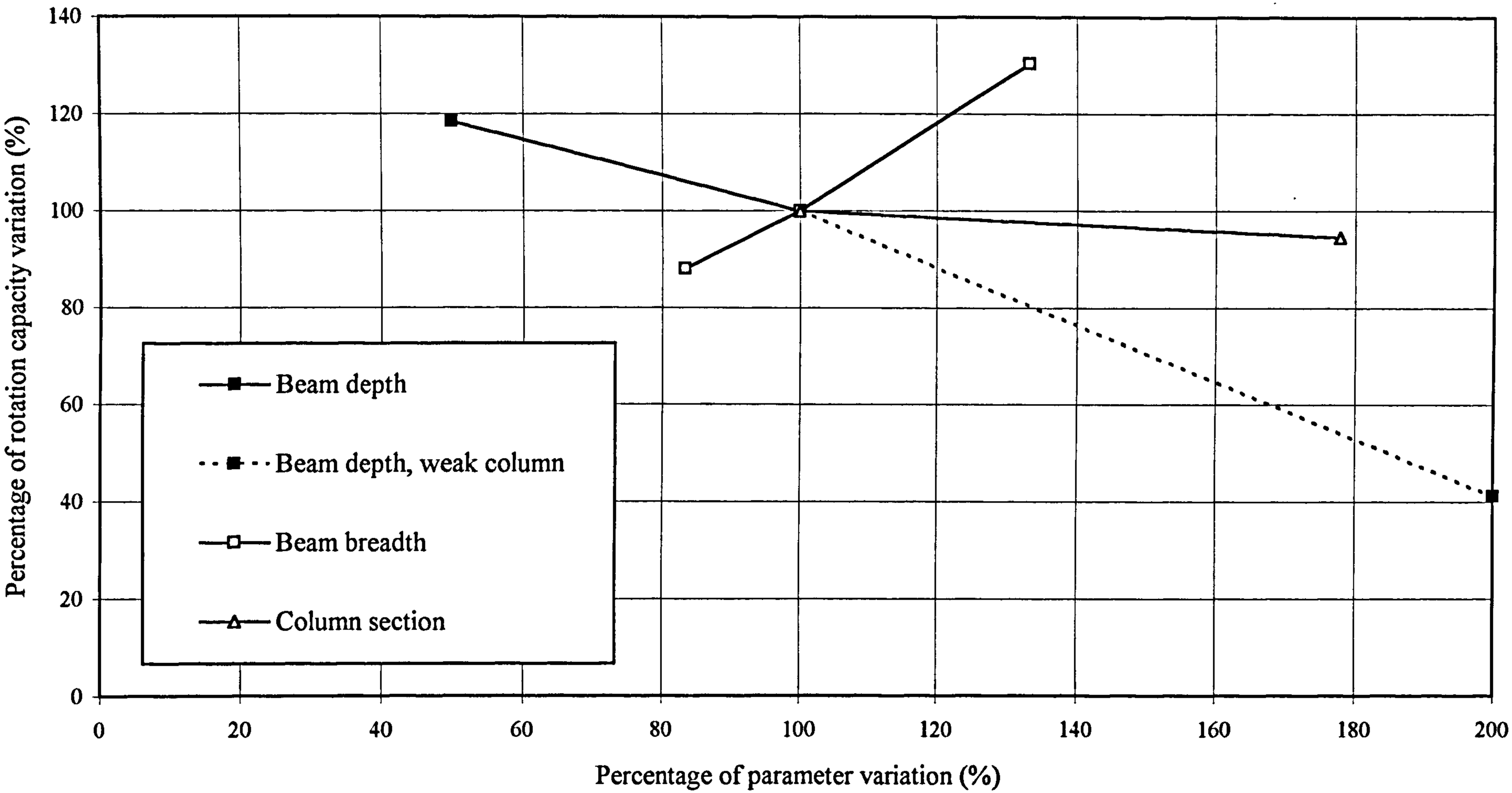

Figure 7.49 *Sensitivity of the rotation capacity for the joints with sagging beam end moment*

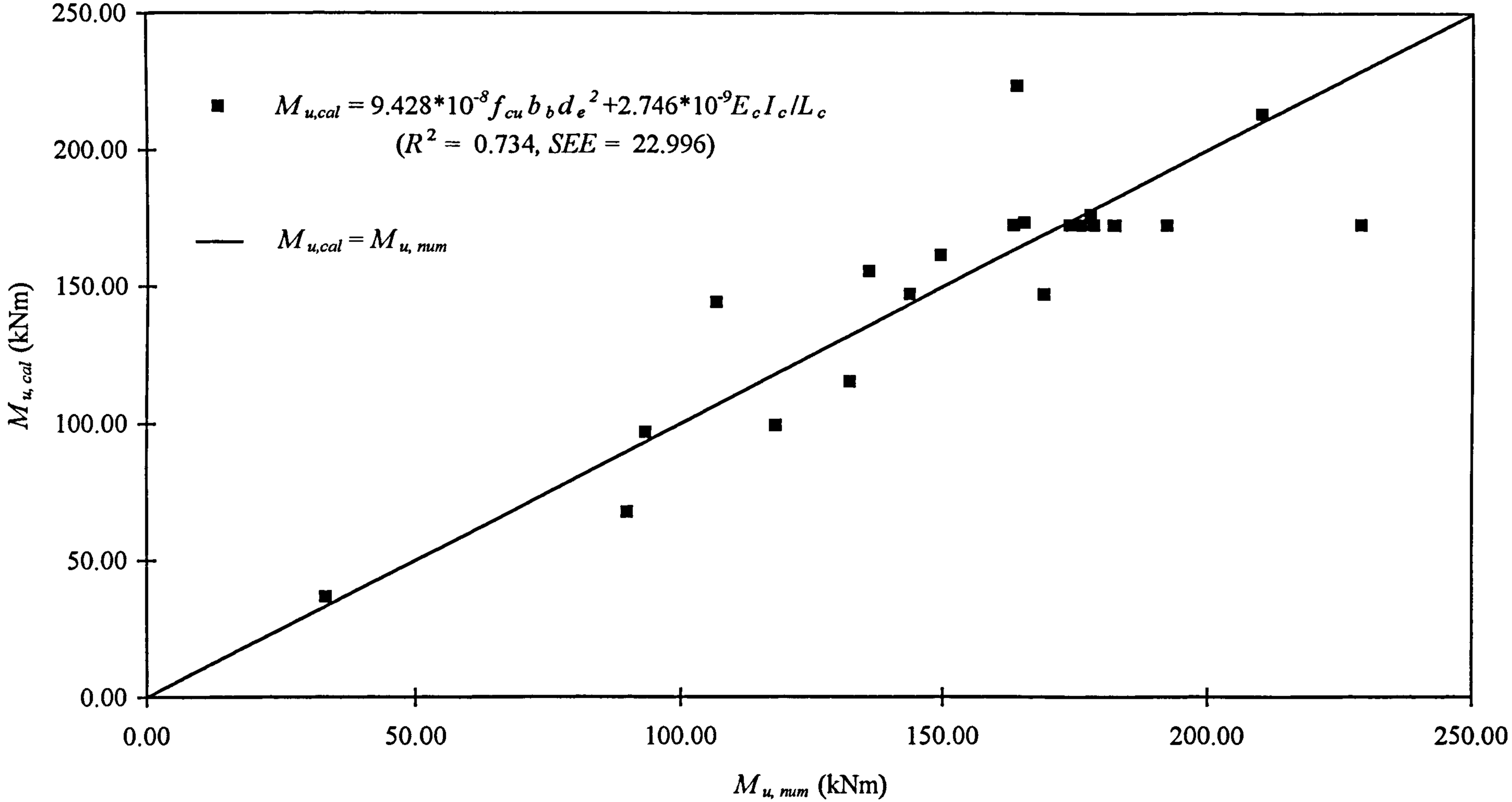

Figure 7. 50 *The calculated beam end moment resistance $M_{u,cal}$ versus the numerical value $M_{u,num}$*

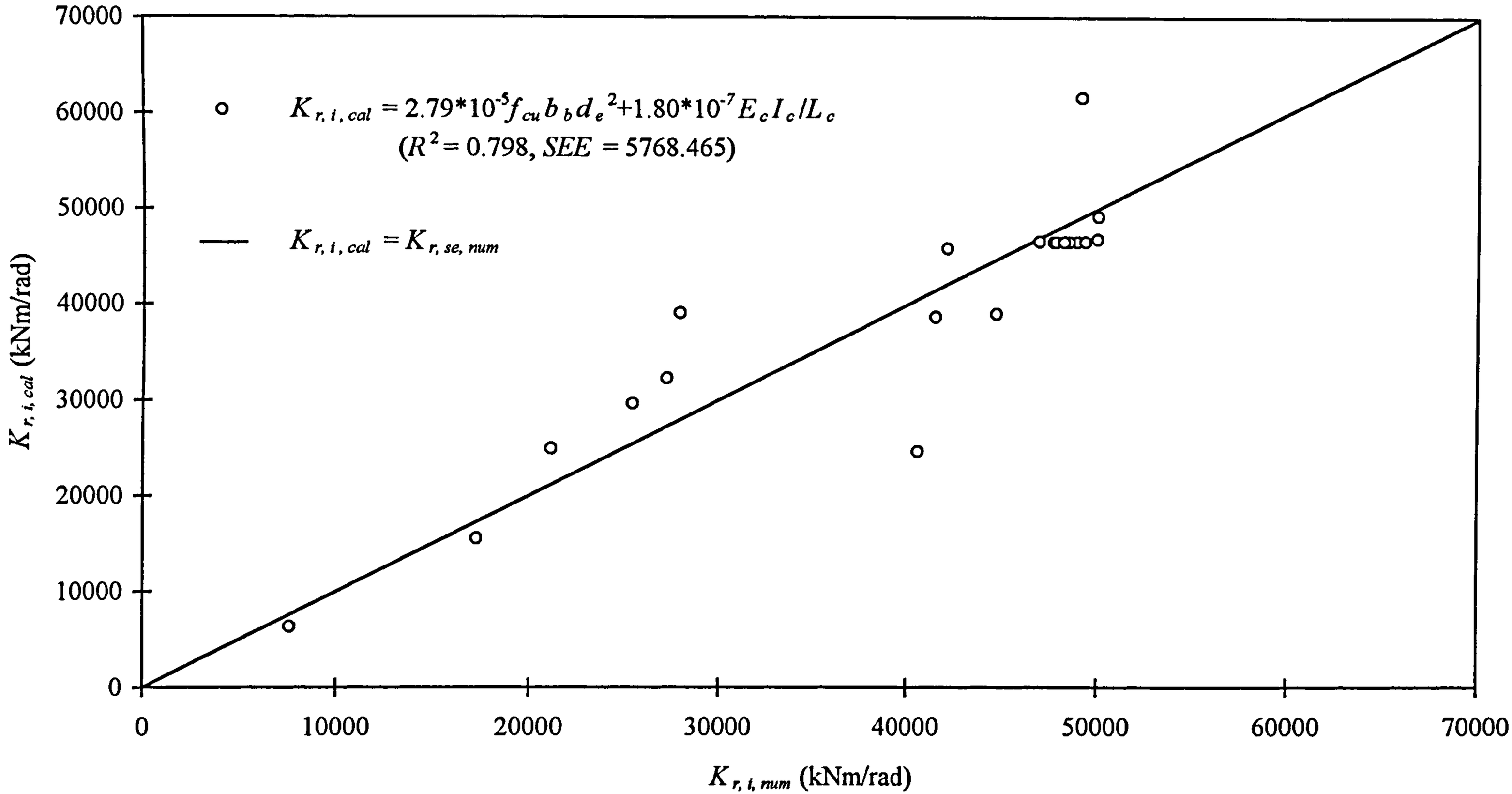

Figure 7.51 *The calculated beam end initial rotation stiffness $K_{r,i,cal}$ versus the numerical value $K_{r,i,num}$*

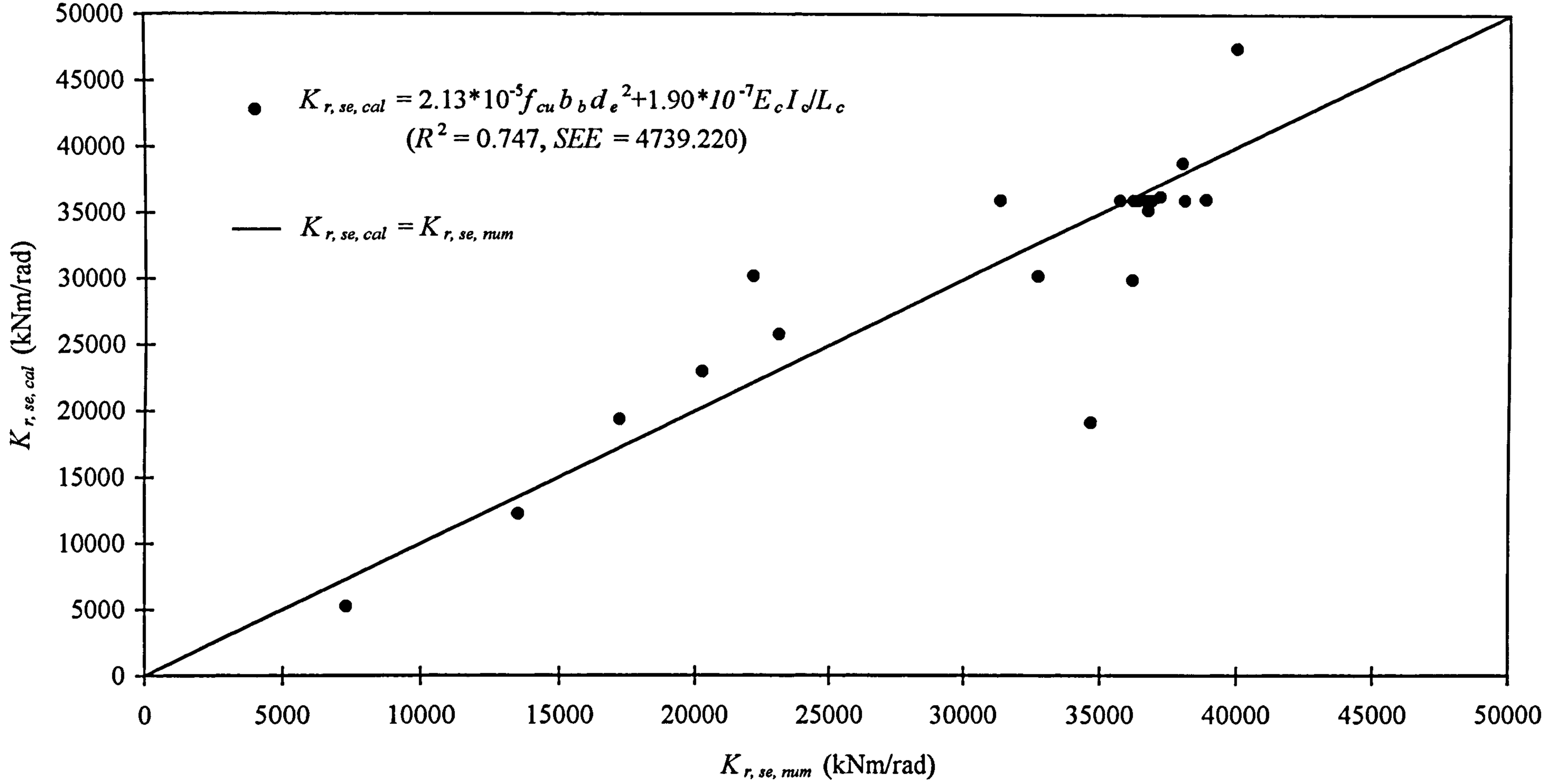

Figure 7.52 *The calculated beam end secant rotation stiffness $K_{r,se,cal}$ versus the numerical value $K_{r,se,num}$*

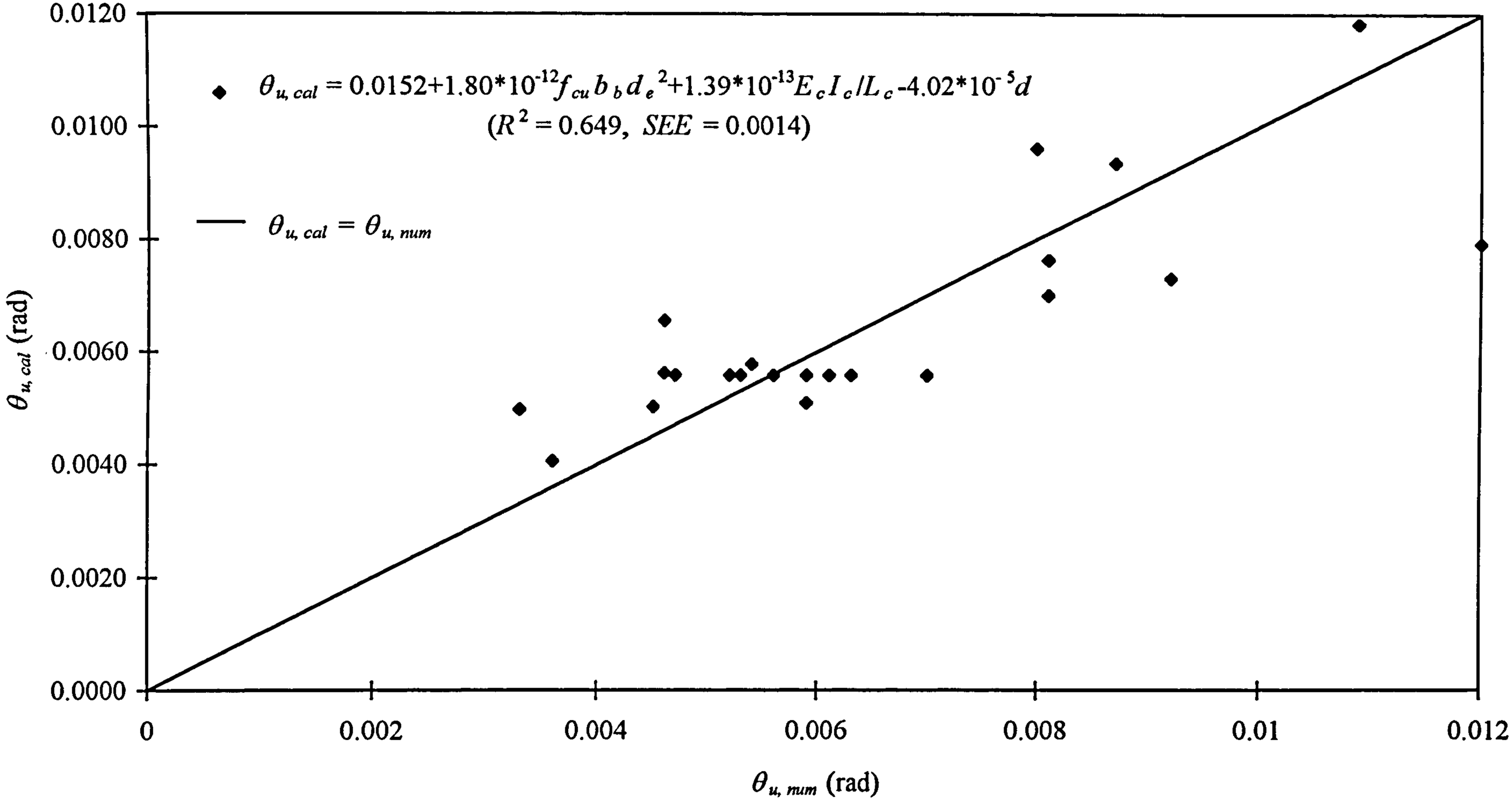

Figure 7.53 *The calculated beam end rotation capacity* $\theta_{u,cal}$ *versus the numerical value* $\theta_{u,num}$

Chapter 8

A Finite Element Model for FRP Tube Confined Concrete Circular Columns

8.1 Introduction

Fibre reinforced plastics (FRP) are widely used composite materials in many fields, such as aircraft structures, automobiles, and many consumer products, due to their superior potential for high ratios of strength to weight and stiffness to weight. In building engineering they are primarily utilised as non-ferrous reinforcement particularly, for the purpose of avoiding corrosion and environmental degradation[61, 62]. The FRP tube confined concrete circular column is an innovative application of the composites to concrete structures. A series of experimental investigations for the columns, funded by EPSRC, has been carried out by the Structures Research Group at the University of Southampton[63~67].

The column is formed by casting concrete into the prefabricated filament wound FRP tube which serves as both permanent formwork and circumferential reinforcement, Fig. 8.1. The study includes variations of the reinforcing material using glass or carbon fibre, concrete strength, column diameter and slenderness ratio. Efficiency of using additional axial glass or carbon FRP reinforcement was also investigated. The columns were loaded either axially or eccentrically. The test results indicate that confinement of the FRP tubes has significantly enhanced both load and deformation capacities of the concrete columns. Subsequently, a design methodology for the columns has been proposed.

The connections of the columns to beams, slabs and foundations, however, also need to be studied in detail before practical application of the columns is possible. Combined experimental and numerical investigations provide an efficient research approach. Therefore a finite element model for the combination of FRP and concrete is essential, and it is built up in the present research. The model must be effective for the columns first. Thus it will be based on the previously derived standardised finite element techniques for reinforced concrete structures, including the modelling method for the composite FRP, and modified to consider the individual features of the columns. A number of typical tested columns will be analysed so that the efficiency and applicability of the model can be verified using the experimental results. Furthermore, some internal mechanism of the columns can be investigated during the modelling.

8.2 Mechanical properties of an unidirectional lamina

The filament wound FRP tube used in the tested column is a typical *laminate*. Performance of a laminate will be dominated by the characteristics and configurations of the individual *laminae*. Material properties of a laminate can be predicted by knowing the properties of its constituent laminae. Thus the mechanical properties of an unidirectional lamina is essential in analyses and applications. An unidirectional lamina is normally treated as an *orthotropic* material. Its mechanical properties are governed by the mechanical properties of constituent fibre and matrix and the amount of fibre embedded in the matrix.

Stress-strain relationships of an unidirectional lamina in the lamina co-ordinate system coinciding with the symmetrical axes of the material as shown in Fig. 8.2 are

$$\begin{Bmatrix} \varepsilon_1 \\ \varepsilon_2 \\ \varepsilon_3 \\ \varepsilon_{12} \\ \varepsilon_{23} \\ \varepsilon_{13} \end{Bmatrix} = \begin{bmatrix} \frac{1}{E_1} & \frac{-\nu_{12}}{E_2} & \frac{-\nu_{13}}{E_3} & 0 & 0 & 0 \\ \frac{-\nu_{21}}{E_1} & \frac{1}{E_2} & \frac{-\nu_{23}}{E_3} & 0 & 0 & 0 \\ \frac{-\nu_{31}}{E_1} & \frac{-\nu_{32}}{E_2} & \frac{1}{E_3} & 0 & 0 & 0 \\ 0 & 0 & 0 & \frac{1}{G_{12}} & 0 & 0 \\ 0 & 0 & 0 & 0 & \frac{1}{G_{23}} & 0 \\ 0 & 0 & 0 & 0 & 0 & \frac{1}{G_{13}} \end{bmatrix} \begin{Bmatrix} \sigma_1 \\ \sigma_2 \\ \sigma_3 \\ \sigma_{12} \\ \sigma_{23} \\ \sigma_{13} \end{Bmatrix} \tag{8.1}$$

where E_1 is Young's modulus of the lamina in the longitudinal lamina direction, G_{12} the shear modulus of the lamina in lamina 1-2 plane, ν_{12} Poisson's ratio of the lamina in 1-2 plane, etc.

As for an orthotropic material the *elastic compliance matrix* is presumed to be symmetric, so that in the above equation,

$$\frac{\nu_{21}}{E_1}=\frac{\nu_{12}}{E_2}, \qquad \frac{\nu_{31}}{E_1}=\frac{\nu_{13}}{E_3}, \qquad \frac{\nu_{32}}{E_2}=\frac{\nu_{23}}{E_3} \tag{8.2}$$

All the elastic constants in the above equations and the uniaxial strengths of the unidirectional lamina, which will be used in the failure criterion, should be determined in advance. Many methods are available to measure these properties[68~71]. The equations selected in the present research are based on the unified set of composite micromechanics equations[71], whilst the methods in other literature are also referenced. In the equations the matrix is assumed to be *isotropic*.

8.2.1 Elastic constants

a. Longitudinal modulus E_1

Using the *Law of Mixture*,

$$E_1 = k_f E_{f1} + k_m E_m \tag{8.3}$$

where E_{f1} and E_m are the longitudinal modulus of fibre and modulus of matrix respectively, k_f and k_m the volume ratios of fibre and matrix, determined by

$$k_f = \frac{V_f}{V}, \qquad k_m = \frac{V_m}{V}$$

in which V_f, V_m and V are the volumes of fibre, matrix and total lamina respectively.

b. Transverse module E_2 and E_3

$$E_2 = \frac{E_m}{1-\sqrt{k_f}(1-E_m / E_{f2})} = E_3 \tag{8.4}$$

where E_{f2} is the transverse modulus of fibre.

c. Shear module G_{12} and G_{13}

$$G_{12} = \frac{G_m}{1-\sqrt{k_f}(1-G_m / G_{f12})} = G_{13} \tag{8.5}$$

where G_m and G_{f12} are the shear module of matrix and fibre in 1-2 plane respectively.

d. Shear modulus G_{23}

$$G_{23} = \frac{G_m}{1-k_f(1-G_m / G_{f23})} \tag{8.6}$$

where G_{f23} is the shear modulus of fibre in 2-3 plane.

e. Poisson's Ratios ν_{12} and ν_{13}

$$\nu_{12} = k_f \nu_{f12} + k_m \nu_m = \nu_{13} \tag{8.7}$$

In ANSYS the constants in the *elastic compliance matrix* at the symmetrical positions in Eq. 8.1 are all given in the forms of ν_{12}/E_2 and ν_{13}/E_3 [31]. Thus, using the relations in Eq. 8.2, translated values $\nu_{12}E_2/E_1$ and $\nu_{13}E_3/E_1$ should be used as the input Poisson's Ratios. Hereafter ν_{12} and ν_{13} are the values defined by Eq. 8.7.

f. Poisson's Ratio ν_{23}

$$\nu_{23} = k_f \nu_{f23} + k_m (2\nu_m - \frac{\nu_{12}}{E_1} E_2) \tag{8.8}$$

In ANSYS the similar translation should be made for ν_{23}. Since $E_2 = E_3$, the translated value equals the one defined by Eq. 8.8.

8.2.2 Uniaxial strengths

a. Longitudinal tensile strength f_{1t}

$$f_{1t} = k_f f_{f_t} \tag{8.9}$$

where f_{ft} is the tensile strength of fibre.

b. Longitudinal compression strength f_{1c}

As a conservative approach, the smallest value predicted using the following three equations is used.

Fibre compression: $$f_{1c} = k_f f_{fc} \tag{8.10a}$$

Delamination/shear: $$f_{1c} = 10 f_{12s} + 2.5 f_{mt} \tag{8.10b}$$

Microbuckling: $$f_{1c} = \frac{G_m}{1 - k_f (1 - \frac{G_m}{G_{f12}})} \tag{8.10c}$$

where f_{fc} is the fibre compressive strength, if it is not known, $f_{fc} = 0.9 f_{ft}$ can provide a good approximation, f_{12s} the intralaminar shear strength, calculated with Eq. 8.13, f_{mt} the tensile strength of matrix.

c. Transverse tensile strength f_{2t}

$$f_{2t} = (1 - (\sqrt{k_f} - k_f)(1 - \frac{E_m}{E_{f2}})) f_{mt} \tag{8.11}$$

In the thickness direction the tensile strength f_{3t} is taken as equal f_{2t}.

d. Transverse compressive strength f_{2c}

$$f_{2c} = (1 - (\sqrt{k_f} - k_f)(1 - \frac{E_m}{E_{f2}})) f_{mc} \tag{8.12}$$

where f_{mc} is the compressive strength of the matrix.

In the thickness direction the compressive strength f_{3c} is taken as equal f_{2c}.

e. Intralaminar shear strengths f_{12s}, f_{13s} and f_{23s}

The shear strengths in the three directions can be estimated with the following equations:

$$f_{12s} = (1 - (\sqrt{k_f} - k_f)(1 - \frac{G_m}{G_{f12}})) f_{ms} = f_{13s} \tag{8.13}$$

$$f_{23s} = \left[\frac{1 - \sqrt{k_f}(1 - G_m / G_{f23})}{1 - k_f (1 - G_m / G_{f23})} \right] f_{ms} \tag{8.14}$$

where f_{ms} is the matrix shear strength.

8.3 Finite element modelling of the FRP laminate

8.3.1 Methods

Three possible approaches exist for modelling the FRP laminate. One is to use the normal solid element, and the mechanical properties of the composite laminate should be established first, normally using elastic mechanics methods [68~70]. However, it is not easy to do these calculations manually. The second approach is to use the specified layered elements provided in ANSYS, and the material properties are input in matrix form. That is, all the constants in the *stiffness matrix* in the force-strain and moment-curvature relationships are computed outside the ANSYS programme [31]. The third approach is again using the specified layered elements, but the material properties are input by layer form. The required mechanical properties in the layers are just those of the unidirectional lamina, so that they can be easily established with the existing equations. The method using layered element with layer form input of the material properties was selected.

8.3.2 Element types

Three layered structural element types are provided in ANSYS, SOLID46, SHELL91 and SHELL99. All of them are 8-node 3-dimension elements. SHELL91 allows up to 16 different material layers, while in SOLID46 and SHELL99 up to 100 uniform-thickness different material layers are permitted. In the modelling of the FRP tube confined concrete columns, the element type for FRP will be used simultaneously with the concrete element SOLID65. To maintain compatibility between the element types for the two different materials, SOLID46 is chosen as the element type for the FRP laminate.

8.3.3 Failure criteria

There are three predefined failure criterion options in ANSYS, the *maximum strain*, the *maximum stress* and *Tsai-Wu* failure criteria. The maximum stress failure criteria is selected because it gives a direct indication of the stress status.

These failure criteria can only be used to obtain an indication as to whether a lamina has failed due to the applied loads. The lamina will behave linearly during the whole loading

process, and a manual check must be made to determine whether the constituents have ruptured or not.

8.4 Special features of the columns and the associated methods

8.4.1 Stress state of concrete

The average confined compressive stress of concrete at the ultimate state in the tested cylinder increased up to about 10 times that of the unconfined concrete compressive strength f_c, and the strain increased about 10 to 20 times that of the peak point strain ε_{c0} [63~67](Figs. 8.9 and 8.10). The stress of the concrete at this stage is much higher than the stress limit for the concrete element given in ANSYS, Chapter 2.8.2 and Reference 31. Thus when the standard FEA techniques described in the previous chapters are directly applied to the modelling of the column, good prediction can be reached only while both the stress and strain ratios are smaller, less than 2 for instance. After the ratios become larger, the numerical result will underestimate load/stress, and the full solution will be unacceptable, see the example shown in Fig. 8.3 (details of the modelling are described in Chapter 8.5).

Consequently, it is necessary to turn off the cracking and crushing capabilities of the concrete element, because this will simultaneously remove the stress limit for the concrete element. Also, the added smeared material is removed from the element.

8.4.2 Poisson's ratio of concrete

For plain concrete, Poisson's ratio is a constant, about 0.2, only while the compressive stress is under about 80% of the compressive strength. After the compressive stress is above this value, an *apparent Poisson's ratio* develops because the development of the micro-cracks results in voids in the specimen. As the compressive stress reaches the compressive strength, the apparent Poisson's ratio usually exceeds 0.2. In some cases values even in excess of 1.0 have been measured, Chapter 4.2.

For the tested columns, at the later loading stage the concrete has seriously cracked. It is because of the confinement of the FRP tube that the concrete can still bear such a high stress. The circumferential strain of the cylinder depends on the circumferential stiffness of the laminate. This circumferential stiffness is directly influenced by the winding angles of the laminae. From the cylinder test results the following relations can be derived

[63~65]: At the ultimate state the average value of circumferential strain at the mid-height is about 1.1 times the axial strain for the lamina with 45^0 nominal fibre winding angle to the vertical direction, 0.6 for 67.5^0, and 0.4 for 90^0. This phenomenon intimates that the concrete at the later loading stage has changed its material state from solid into a granular "soil". The ratio of circumferential strain to axial strain ν of the concrete can then be larger than 1.1.

As for the confined columns, the bigger the Poisson's ratio of concrete, the more significant the confinement. In the ANSYS programme, however, Poisson's ratio is limited to 0.5 as it is in solid mechanics. Thus the effect of a larger Poisson's ration has to be achieved by some equivalent approaches.

One approach is achieved by redefining the relations between the confining/radiate stress, Poisson's ratio of concrete and modulus of the composite.

By equilibrium between the hoop tensile force T_{th} and the radial confining stress σ_r in an unit height tube as shown in Fig. 8.4,

$$\begin{aligned} 2T_{th} &= \int_{\frac{\pi}{2}}^{\frac{\pi}{2}} \sigma_r \frac{D}{2} \cos\phi d\phi \\ &= D\sigma_r \end{aligned} \tag{8.15}$$

where D is the internal diameter of the tube. The following relationships also exist,

$$\begin{aligned} T_{th} &= \sigma_{th} t \\ &= \varepsilon_{th} E_{th} t \\ &= \varepsilon_{ch} E_{th} t \\ &= \nu_c \varepsilon_{cz} E_{th} t \end{aligned} \tag{8.16}$$

where σ_{th}, ε_{th} and E_{th} are the hoop stress, strain and elastic modulus of the tube, t the thickness of the tube, ε_{ch} the hoop strain of concrete, ν_c the Poisson's ratio of concrete, and ε_{cz} the axial/vertical strain of concrete. In Eq. 8.16 following relations are assumed and used, both the tube and concrete have a same strain in the hoop direction, $\varepsilon_{th} = \varepsilon_{ch}$, and the concrete hoop strain equals the axial strain times Poisson's ratio of concrete, $\varepsilon_{ch} = \nu_c \varepsilon_{cz}$.

Substituting T_{th} into Eq. 8.15,

$$\sigma_r = \frac{2}{D} \nu_c \varepsilon_{cz} E_{th} t \tag{8.17}$$

This equation shows that σ_r is proportional to both ν_c and E_{th}. The short-fall of the input ν_c value can be complemented by an equivalent increase of the E_{th} value. This relationship is used to maintain adequate confinement in the columns with lower input of concrete Poisson's ratio.

For the tube with 90^0 fibre winding angle laminae, E_{th} can be approximately taken as the longitudinal modulus of a lamina E_1. Since the ratio of circumferential strain over axial strain of the concrete in the column was measured to be over 1.1, yet the maximum allowed input Poisson's ratio for concrete is 0.5, and the real fibre winding angles of the lamina are close to 90^0, an input value of $2.5E_1$ is selected.

From the typical experimental and the numerical results (see Chapter 8.5 for the details) shown in Fig. 8.5 some useful results can be obtained. All the experimental and numerical curves give the stress-strength ratios σ/f_c' near to 1.0 as the strain ratio $\varepsilon/\varepsilon_{c0}$ equals 1.0. Here σ is the average compressive stress equalling the total load divided by the area of concrete cylinder section, and f_c' is the concrete cylinder compressive strength taken as 0.83 times the mean value of cube strength f_{cu}. The result indicates that the effects of confinement are significant only after the compressive stress is over the unconfined cylinder compressive strength f_c'. The numerical results with E_1 and $2.5E_1$ associating with similar responses as the ratios σ/f_c' and $\varepsilon/\varepsilon_{c0}$ are smaller than 1 confirms that $2.5E_1$ input value will not directly affect the results before the compressive stress exceeds the unconfined compressive strength. Whereas, after the compressive stress exceeds the unconfined compressive strength, the numerical curve with $2.5E_1$ input value increases its slope and matches the tested curve well. This shows that the proposed method works effectively.

For the tubes with other fibre winding angle laminae, further studies are required to determine the enhanced hoop modulus E_{th}.

8.5 Numerical modelling of the experimental columns

8.5.1 Specimens

Two sets of tested columns are analysed using the proposed model, so that the applicability of the model can be verified. The first set includes four short columns/cylinders, two with 80 mm diameter and 160 mm height, and the other two with 150 mm diameter and 300 mm height. These are loaded axially.

The second set includes four columns, two are 80 mm diameter and are 800 mm in height, and the other two are 150 mm diameter and 1500 mm in height. They are loaded eccentrically with 4 mm and 7.5 mm eccentricity respectively. Concrete strengths vary between the coupled specimens with the same geometry and loading condition. E-glass FRP tubes are used for all the specimens. The nominal thickness of the tubes is 2.5 mm, and the nominal fibre winding angle is 90^0. Geometry and material details of the specimens are listed in Table 8.1.

8.5.2 Models

Due to the symmetrical conditions, only one eighth of the cylinders and a quarter of the columns are meshed. The meshed models are illustrated in Figs. 8.6 and 8.7 respectively.

The element SOLID65 is used for the concrete without cracking and crushing capabilities and the smeared material in it. Poisson's ratio of the concrete is taken as 0.5. Since it is the modelling of cylinders and columns, the compressive strength of concrete f_c is taken as $0.8f_{cu}$, where f_{cu} is the mean value of the tested cube strengths. The measured peak point strain of concrete ε_{c0} are utilised in the analyses. Other properties are determined using the standard methods as described in the previous chapters. The derived parameters for the concrete in the modelled specimens are listed in Table 8.2.

The layered element SOLID46 is used for the FRP tubes. According to the configuration of the laminated tubes [63~67], 8 uniform-thickness layers are designed within the tube thickness, Figs. 8.6 and 8.8. The mechanical properties of the E-glass and the Epoxy resin used in the tested specimens are summarised in Table 8.3. The elastic constants and uniaxial strengths of a lamina are established with the equations in Chapter 8.2, and listed in Table 8.4. Due to the considerations explained in Chapter 8.4,

$2.5E_1$ is input for the longitudinal modulus of the laminae. The corresponding Poisson's ratios ν_{12} and ν_{13} are also recalculated with the value of $2.5E_1$.

The gap element CONTACT52 is applied to the interface between the concrete and the FRP tube.

8.5.3 Solution

Using the solution method in the standardisation, the displacement is applied by substeps which are determined with strain rate about 300$\mu\varepsilon$/substep.

8.5.4 Results and analyses

a. Cylinders

The numerical stress-strain curves of the cylinders are presented in Figs. 8.9 and 8.10 together with the relevant experimental curves. Generally, the numerical results match the experimental results for the full loading progress. However, since the mechanical properties of the FRP laminae are treated linearly even after rupture of the constituents, the numerical results give higher stresses around the ultimate state of the cylinder, and provide no ultimate loads. The stress-strain curves exhibit typical bilinear relationships. The slopes of the curves change where the strain ratios $\varepsilon/\varepsilon_{c0}$ are around 1.0.

The equivalent stress distribution at the end point of the solution in Fig. 8.11 shows that high stress concentrates at the two-thirds middle height of the cylinder. The stress here already exceeds the uniaxial tensile strength of the lamina.

b. Columns

The numerical load-compressive strain and load-deflection relationships for the columns and the associated experimental results are illustrated in Fig. 8.12 to 8.19. The numerical results again match the test results even after the curves have distinctly changed their slopes. However, with further loading, the numerical results give higher load because a limiting fibre rupture criterion cannot be defined. At this stage, the FRP tubes started rupturing in the tests, but they still behaved linearly in the numerical analyses.

Figs. 8.20(a & b) show the stress distribution status and the deformed shape of the column. The high equivalent stress is concentrated towards the middle height of the column as well as the loading location.

8.6 Summary

A finite element analysis model for the FRP tube confined concrete columns has been developed and applied to the modelling of typical tested columns. This model is based on the standard FEA methods for reinforced concrete structures, modified to be applicable to the high stress and large deformation found in these components.

The numerical results indicate that the standard FEA method can predict the behaviour of the FRP tube confined column up to the stage with stress-strength and strain ratios roughly equalling 2, Fig. 8.3. After the cracking and crushing capabilities and the smeared material have been removed, the numerical results can match the test results up to the stage with stress-strength and strain ratios roughly equalling 1. Afterwards, the two models give lower stress responses. As the equivalent longitudinal lamina modulus $2.5E_1$ is input , the model can provide a prediction fully matching the test results but with higher and never failing results around the tested ultimate state, Figs. 8.9 to 8.19. Therefore the model is applicable whilst the strain is limited to twice the unconfined concrete ultimate uniaxial compressive strain. However, further development is required.

No.	D (mm)	H (mm)	t (mm)	α (degree)	f_{cu} (N/mm^2)	ε_{c0} (%)	k_f	e (mm)
1	79.88	158.82	2.43	78.10	23.43	0.23	0.63	0.00
2	79.88	158.11	2.40	78.10	35.17	0.23	0.63	0.00
3	150.48	299.87	2.40	83.60	27.43	0.30	0.61	0.00
4	150.44	300.14	2.49	83.60	46.30	0.27	0.61	0.00
5	79.71	797.90	2.52	78.10	25.60	0.24	0.63	4.00
6	79.84	799.70	2.48	78.10	31.23	0.28	0.63	4.00
7	150.56	1500.00	2.47	83.60	28.37	0.22	0.61	7.50
8	150.18	1499.95	2.50	83.60	37.83	0.18	0.61	7.50

Note: D, H and t are the internal diameter, height and thickness of the FRP tube, α the fibre winding angle to the vertical direction, f_{cu} and ε_{c0} the tested cube strength and peak point strain of concrete, e the eccentricity of loading, and k_f the fibre valume fraction.

Table 8.1 *Parameters for the modelled FRP tube confined concrete specimens*

Specimen No.	f_c (N/mm^2)	f_c' (N/mm^2)	E_c (kN/mm^2)
1	18.74	19.44	22.99
2	28.14	29.20	26.33
3	22.00	22.83	24.23
4	37.00	38.39	28.85
5	20.48	21.25	23.68
6	25.00	25.94	25.30
7	22.70	23.55	24.51
8	30.30	31.44	26.98

Table 8.2 *Derived parameters for the concrete in the modelled specimens*

No.	Property	E-glass	Epoxy resin
1	Specific Gravity (kN/m^3)	25.60	12.00
2	Tensile strength f_1 (N/mm^2)	3448	85
3	Elastic modulus E_1 (kN/mm^2)	75.90	2.35
4	Elastic modulus E_2 (kN/mm^2)	75.90	2.35
5	Shear modulus G_{12} (kN/mm^2)	31.11	0.89
6	Shear modulus G_{23} (kN/mm^2)	31.11	0.89
7	Poisson's ratio ν_{12}	0.22	0.32
8	Poisson's ratio ν_{23}	0.22	0.32

Table 8.3 *Mechanical properties for the constituents of the lamina*

		$k_f = 0.61$	$k_f = 0.63$
Elastic constant of lamina	E_1 (kN/mm^2)	47.62	48.69
	E_2, E_3 (kN/mm^2)	9.66	10.18
	ν_{12}, ν_{13}	0.053	0.054
	ν_{23}	0.363	0.356
	G_{12}, G_{13} (kN/mm^2)	3.69	3.89
	G_{23} (kN/mm^2)	2.18	2.29
Uniaxial strength of lamina	f_{1t} (N/mm^2)	2103	2172
	f_{1c} (N/mm^2)	-923	-928
	f_{2t}, f_{3t} (N/mm^2)	71	72
	f_{2c}, f_{3c} (N/mm^2)	-71	-72
	f_{12}, f_{13} (N/mm^2)	71	72
	f_{23} (N/mm^2)	174	184

Table 8.4 *Elastic constants and uniaxial strengths of the laminae*

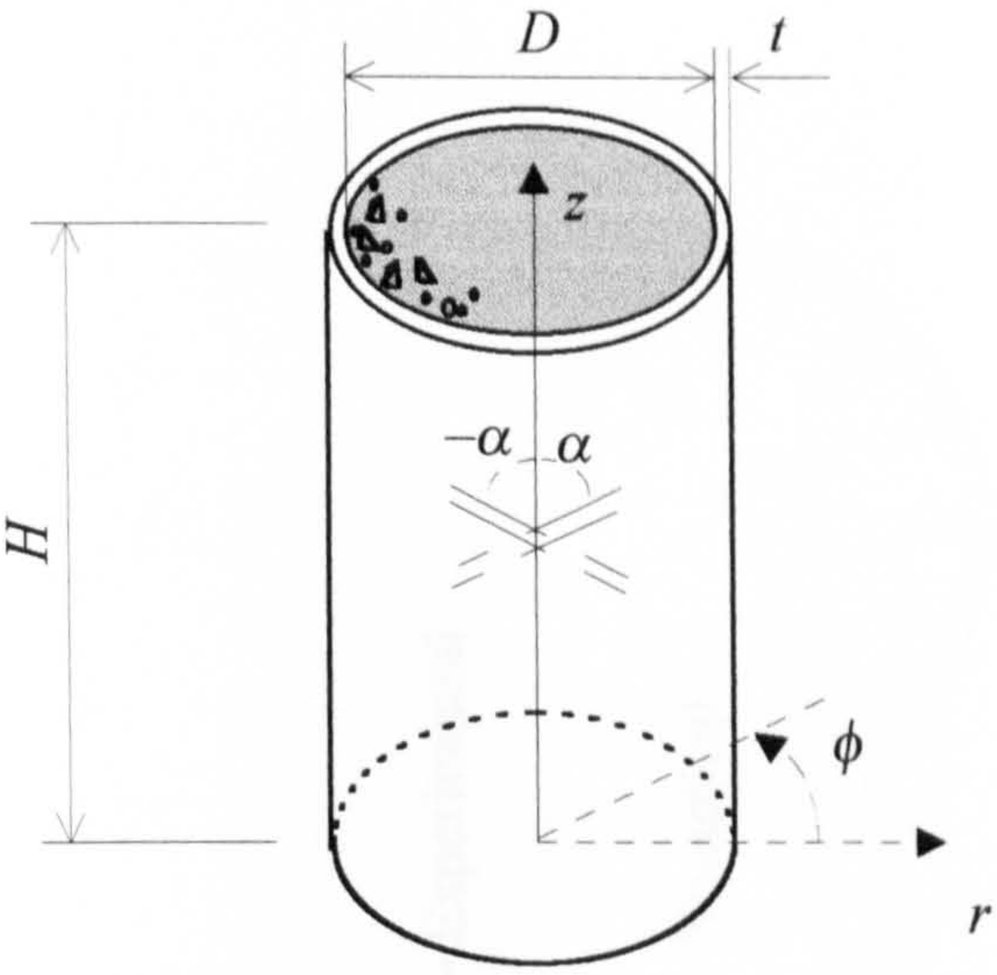

Figure 8.1 *Schematric representation of the tested specimens*

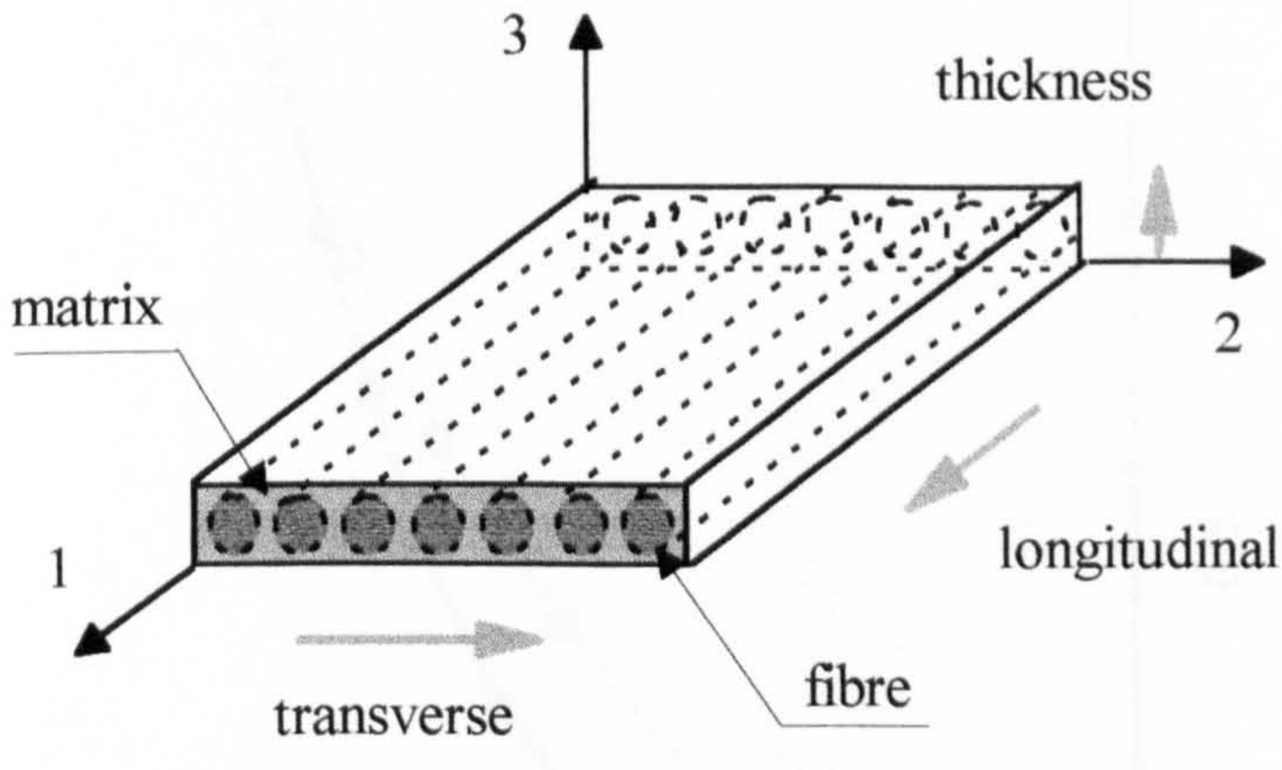

Figure 8.2 *Typical geometry of the unidirectional composite*

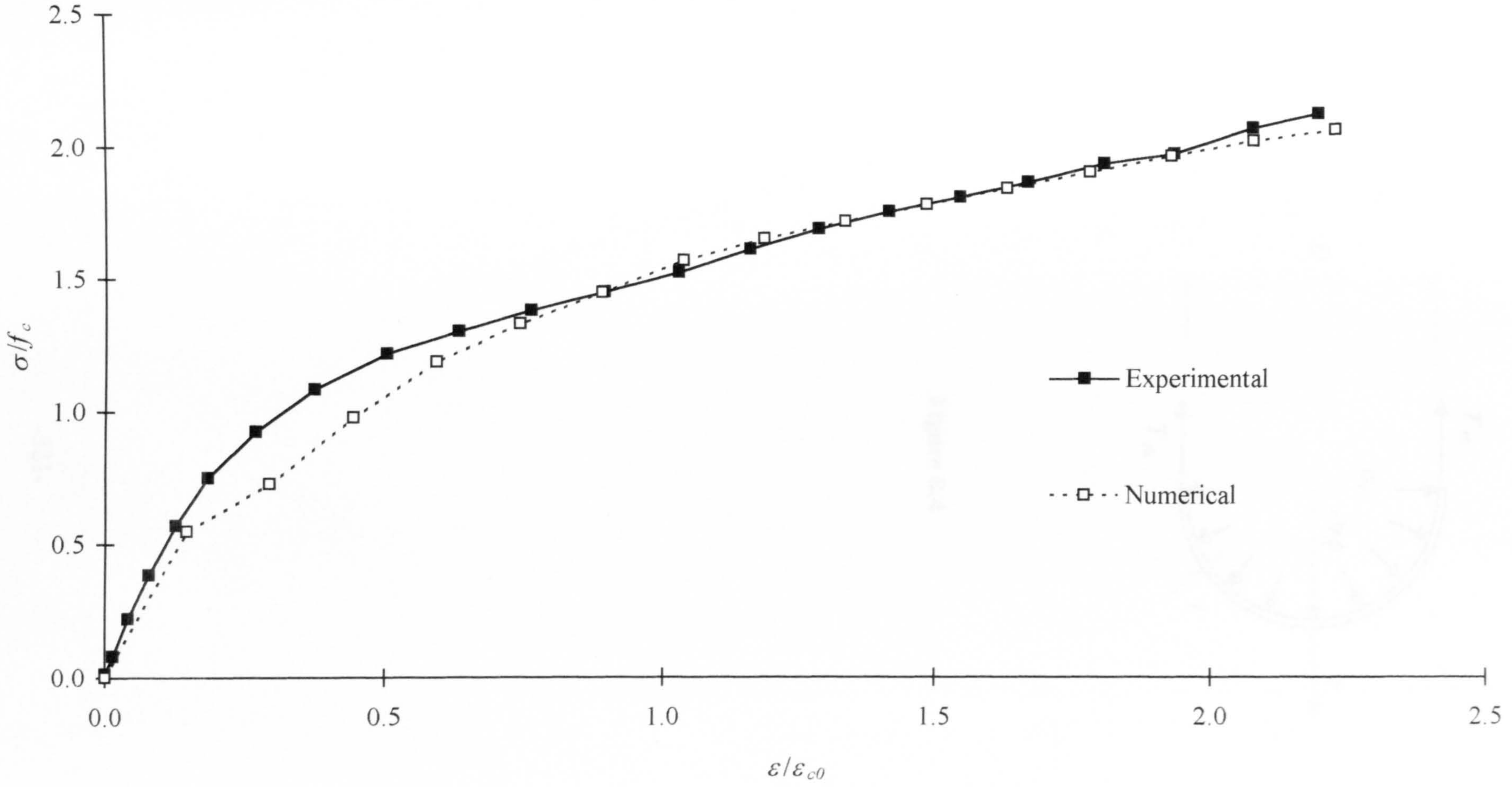

Figure 8.3 *Typical stress-strain curves of the cylinder derived using the standard FEA methods (D = 150 mm, H = 300 mm, f_{cu} = 27.4 N/mm^2)*

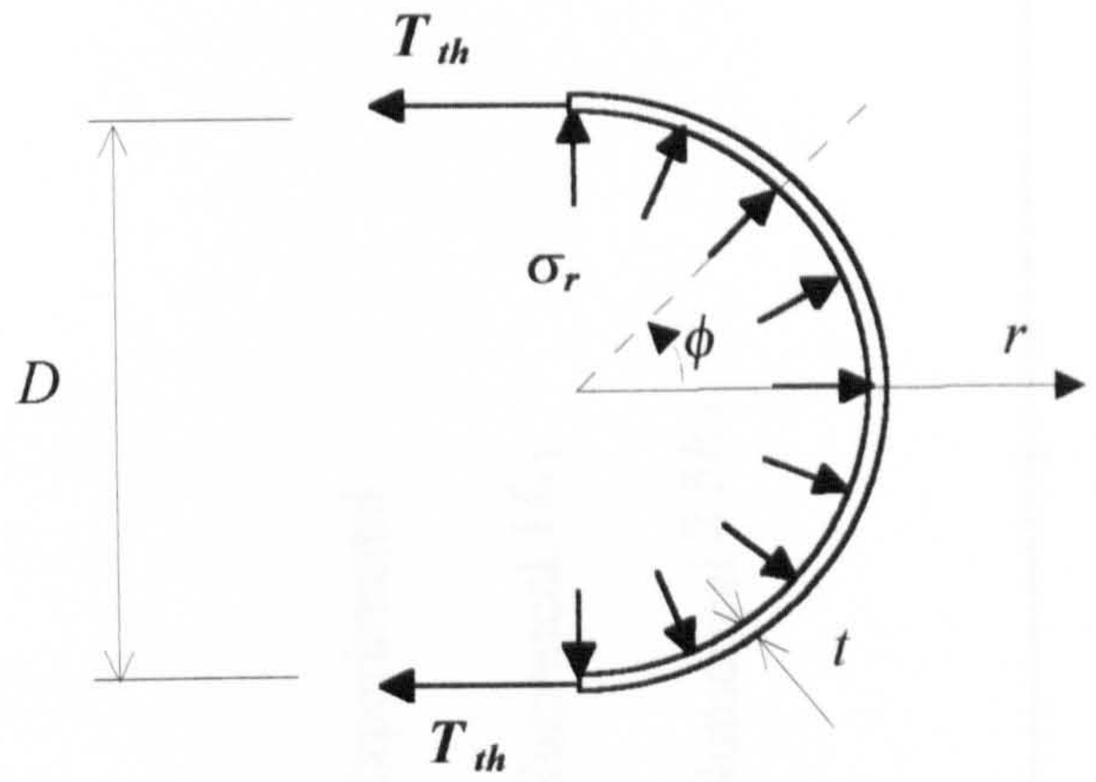

Figure 8.4

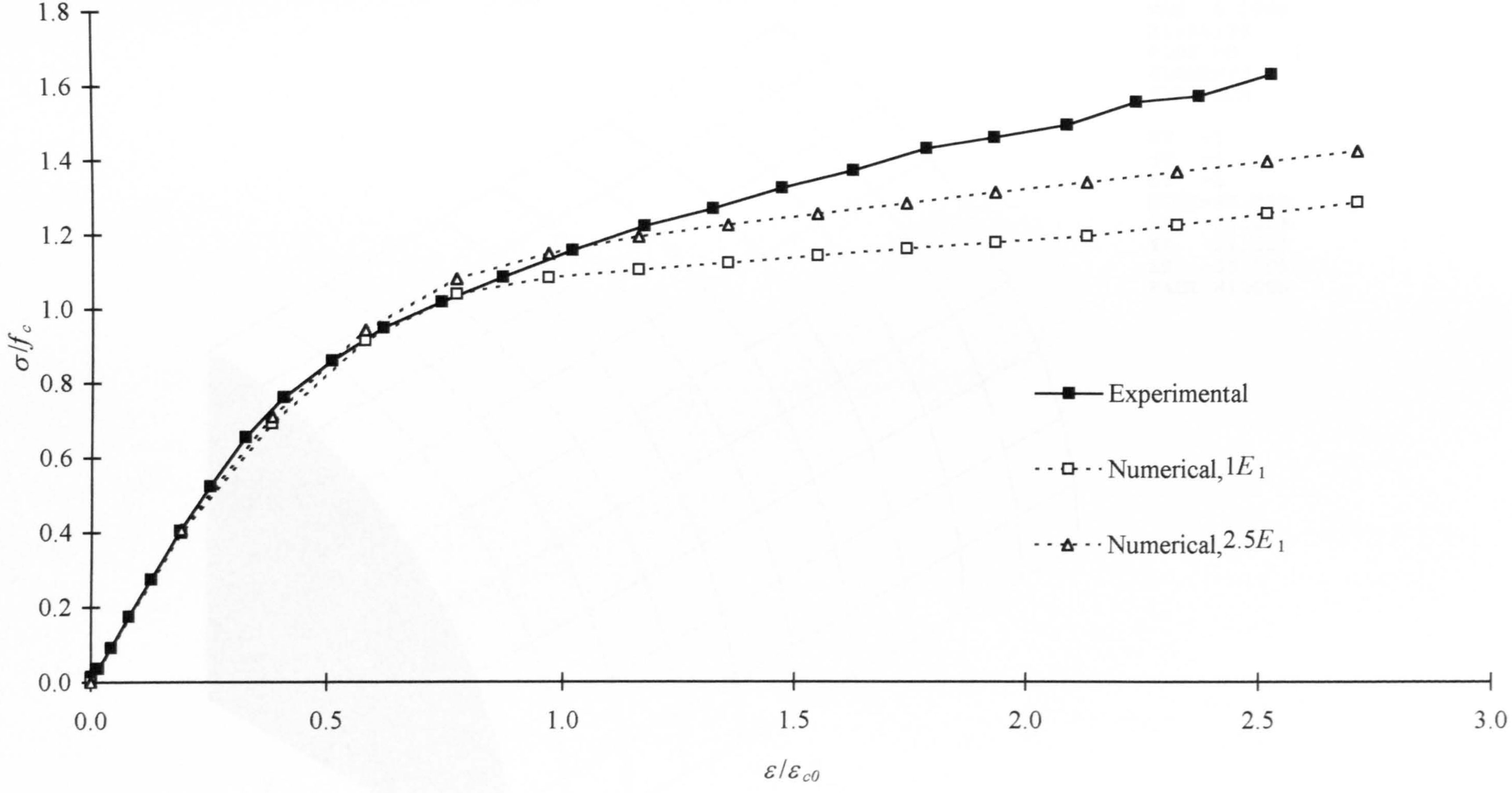

Figure 8.5 *Typical stress-strain curves of the cylinder with removing cracking and crushing capabilities for the concrete element (D = 150 mm, H = 300 mm, f_{cu} = 46.3 N/mm^2)*

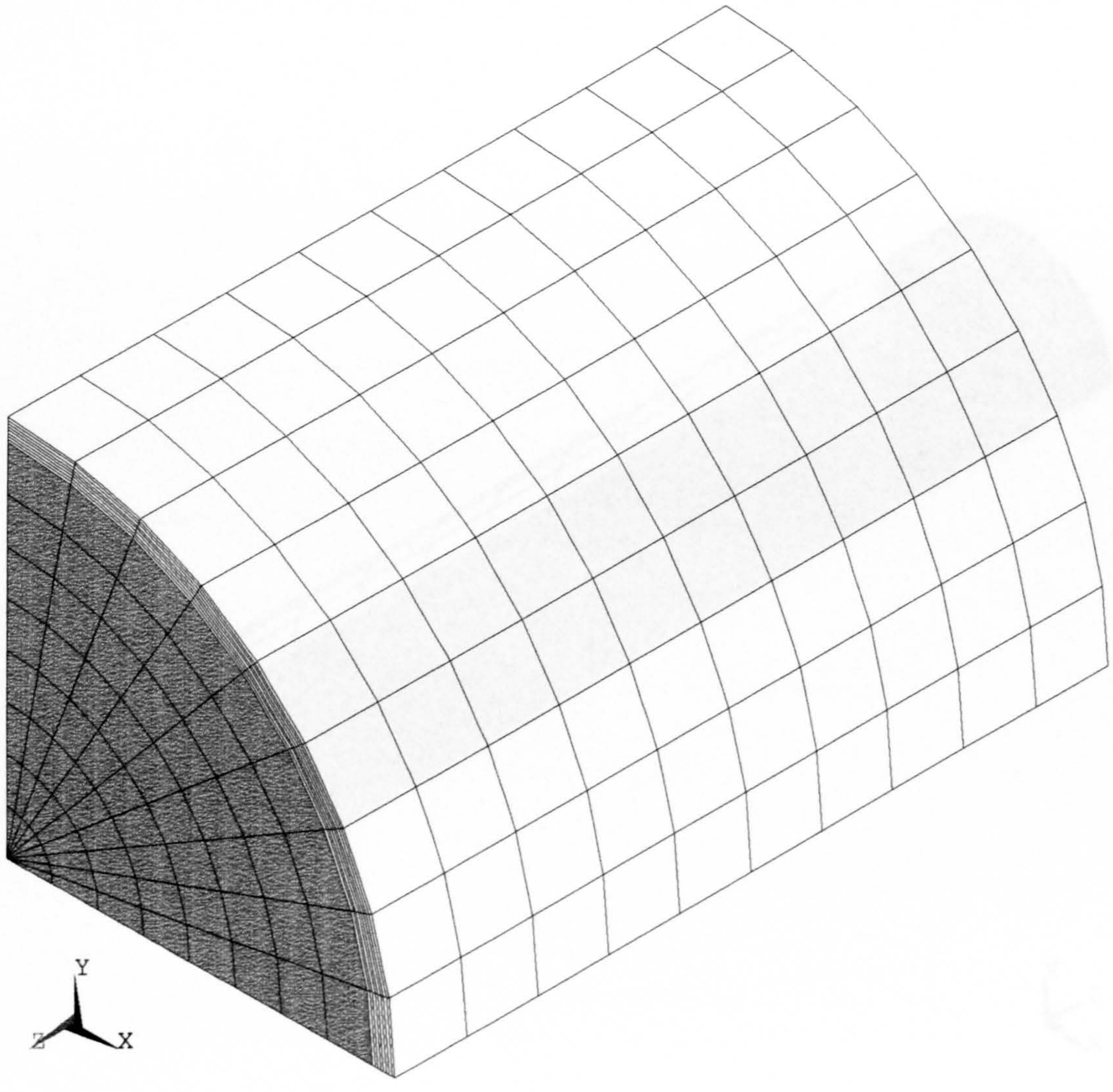

Figure 8.6 *Typical element mesh for the FRP tube confined concrete cylinders*

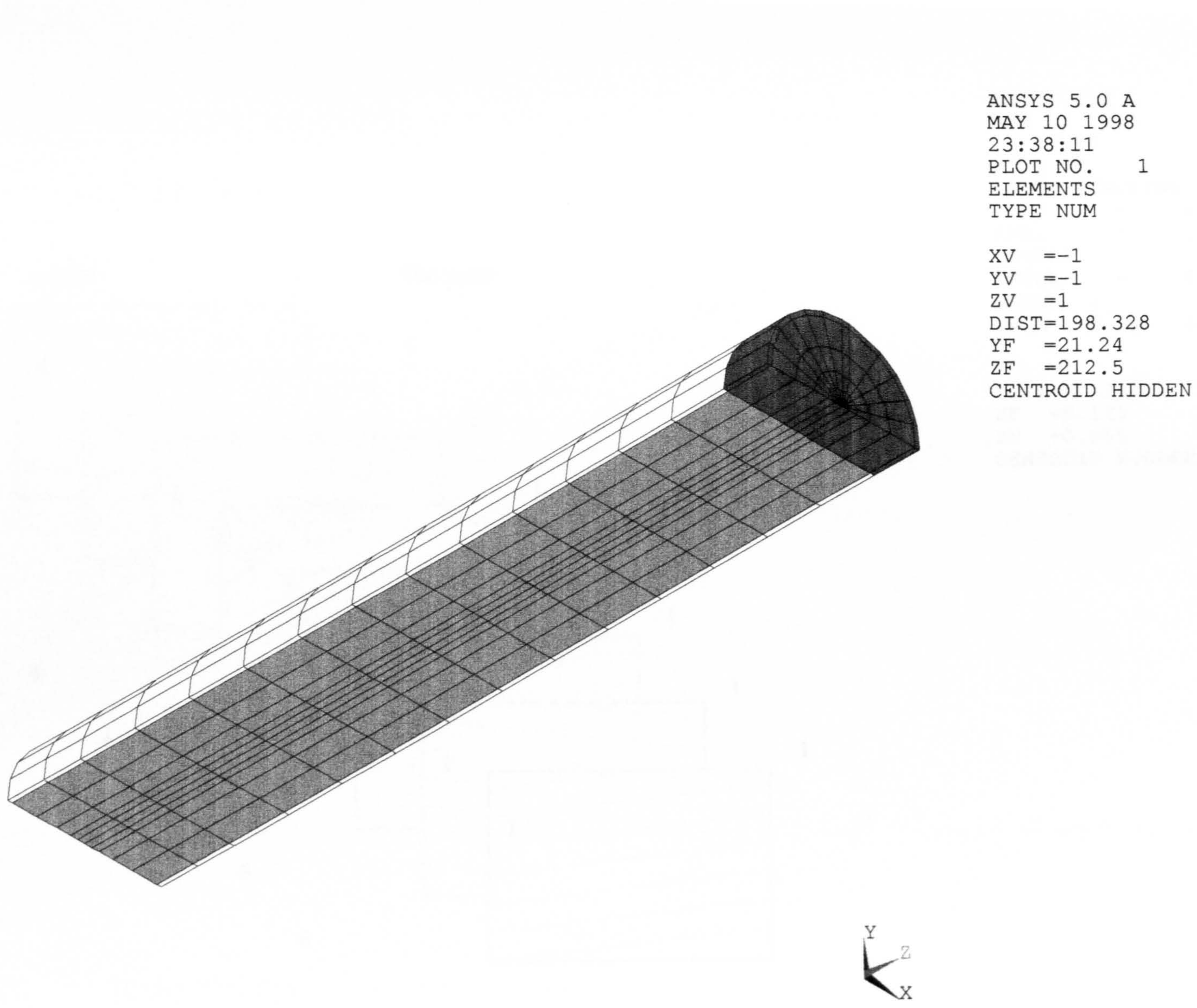

Figure 8.7 *Typical element mesh for the FRP tube confined concrete columns*

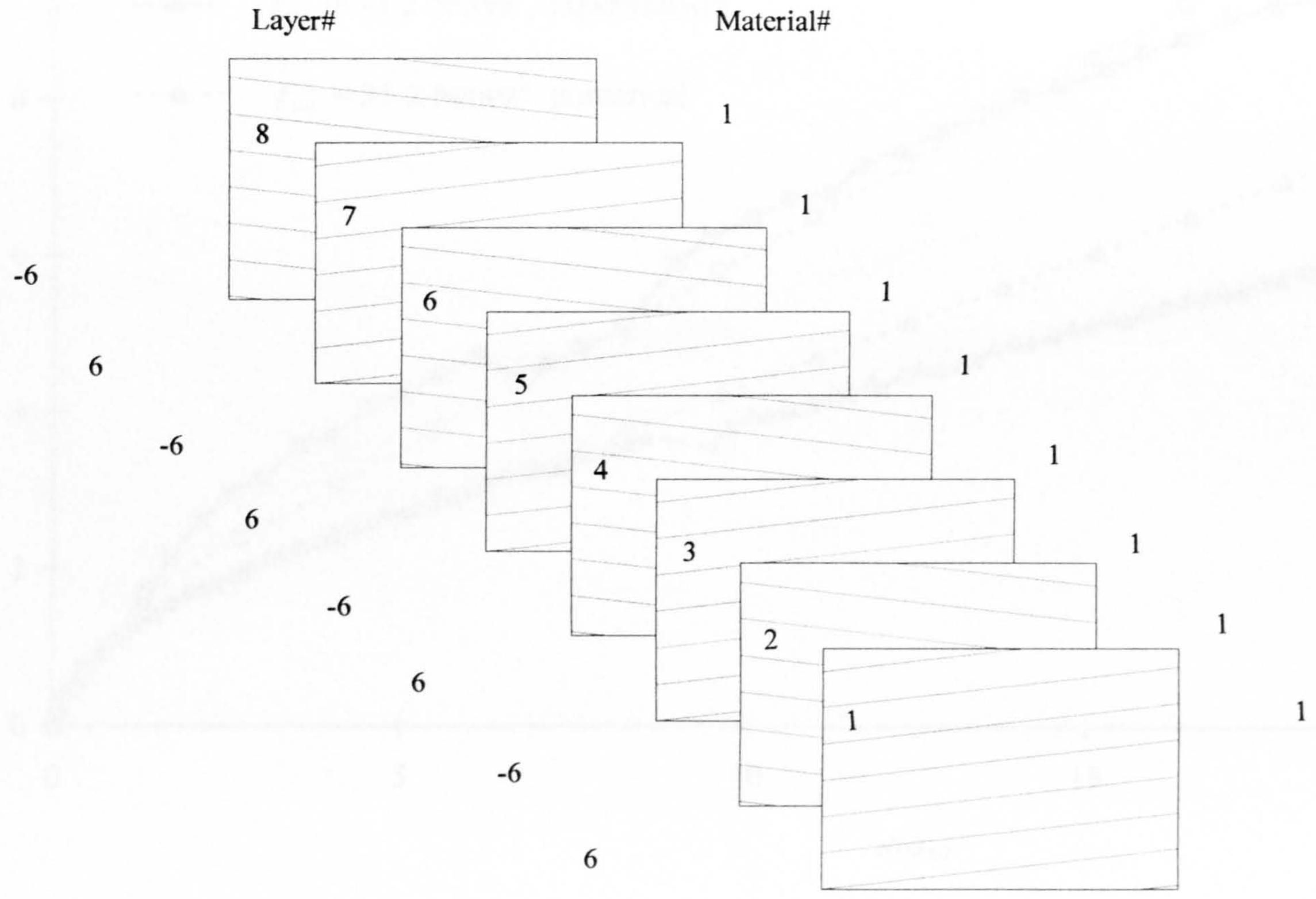


```
ANSYS 5.0 A
APR 16 1998
18:39:36
PLOT NO.   1
LAYER STACKING
TYPE     =    1
REAL     =    1
LAYERS :
TOTAL    =    8
SHOWN  :
FROM   8 TO   1

ZV  =1
DIST=0.523961
XF  =0.125
YF  =0.055
CENTROID HIDDEN
```

Figure 8.8 *Layer stacking for the FRP laminate element*

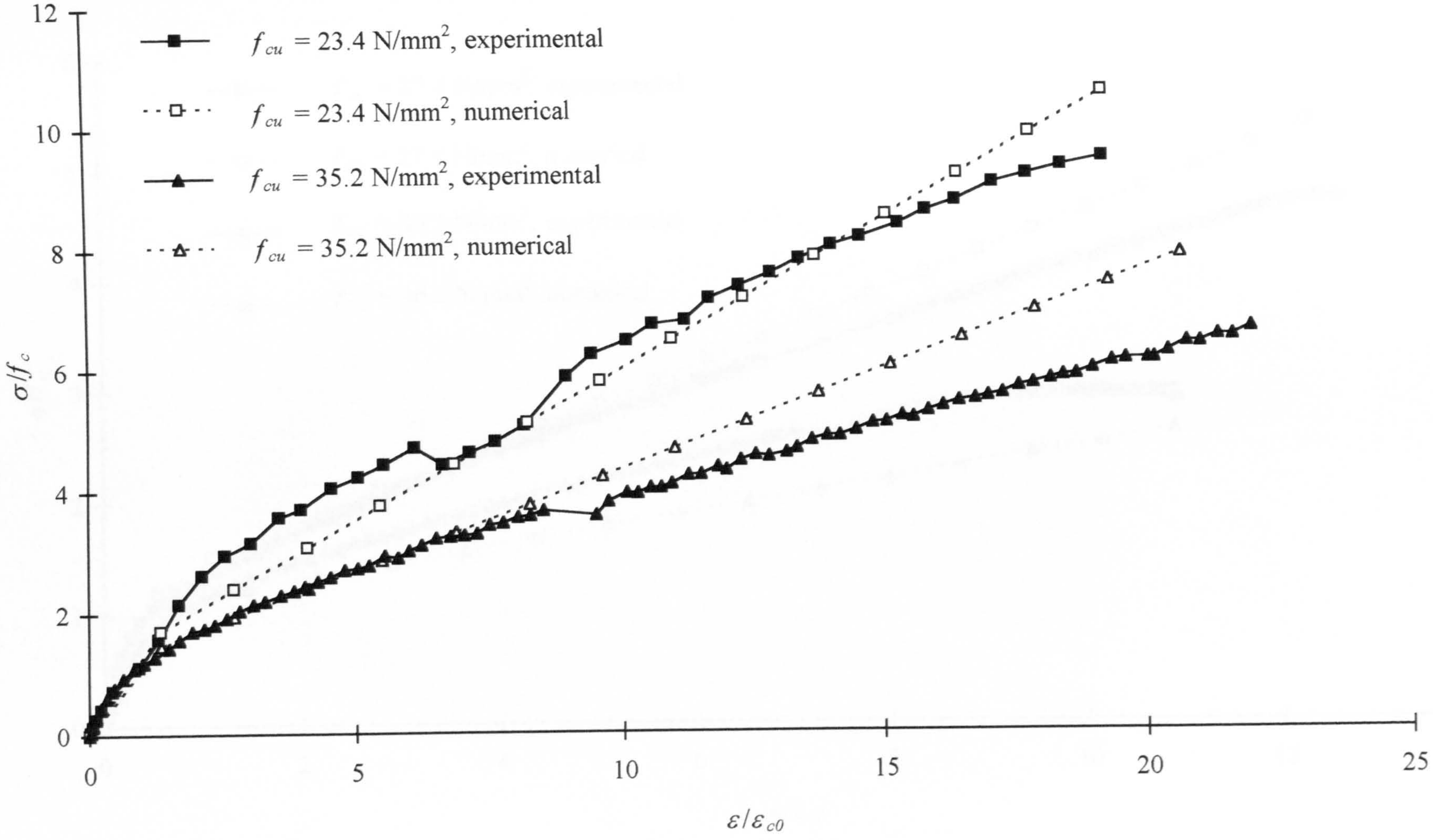

Figure 8.9 *Stress-strain relationships for the cylinders under uniaxial compression (D = 80 mm, H = 160 mm)*

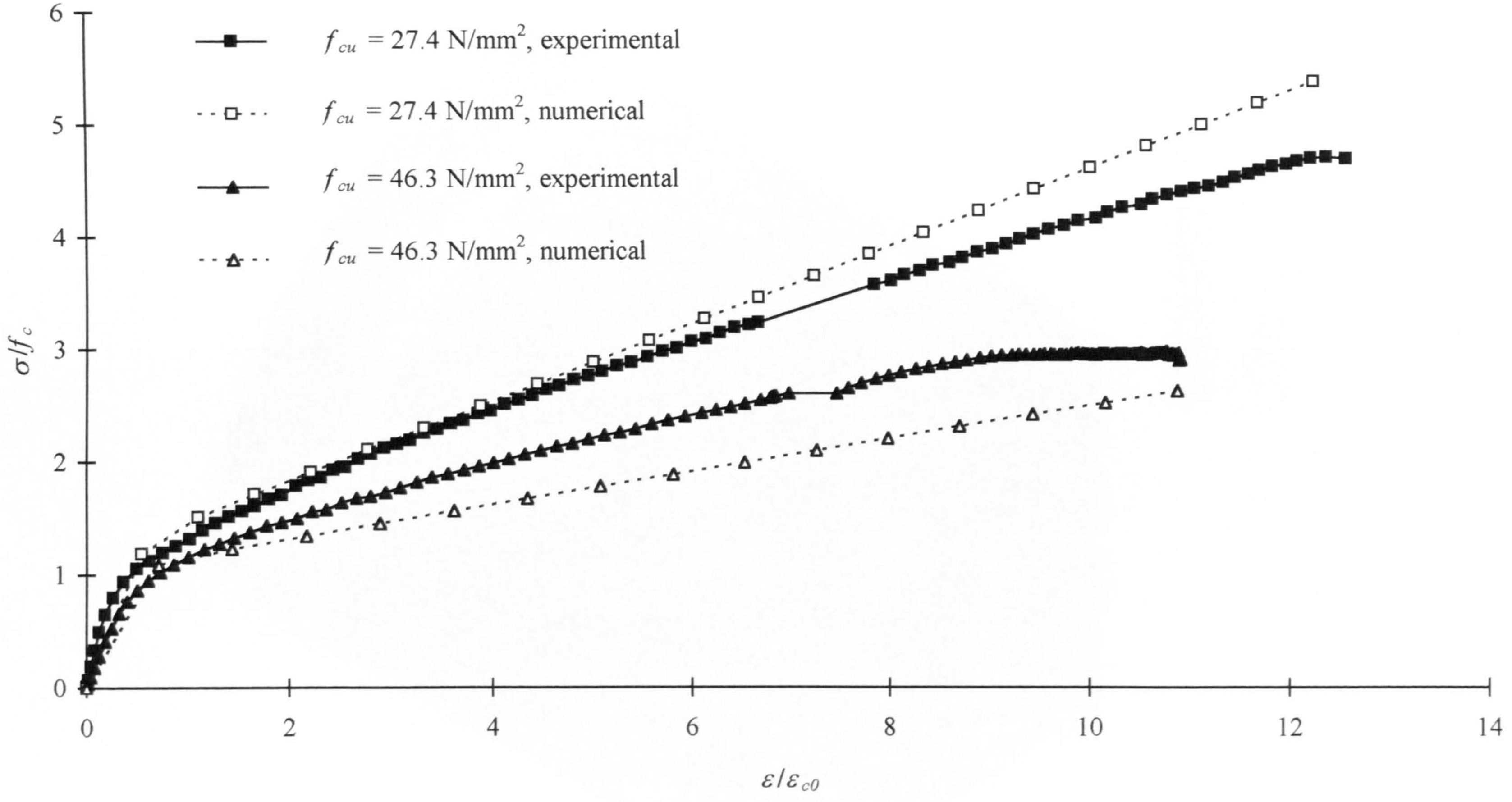

Figure 8.10 *Stress-strain relationshipds of the cylinders under uniaxial compression (D = 150 mm, H = 300 mm)*

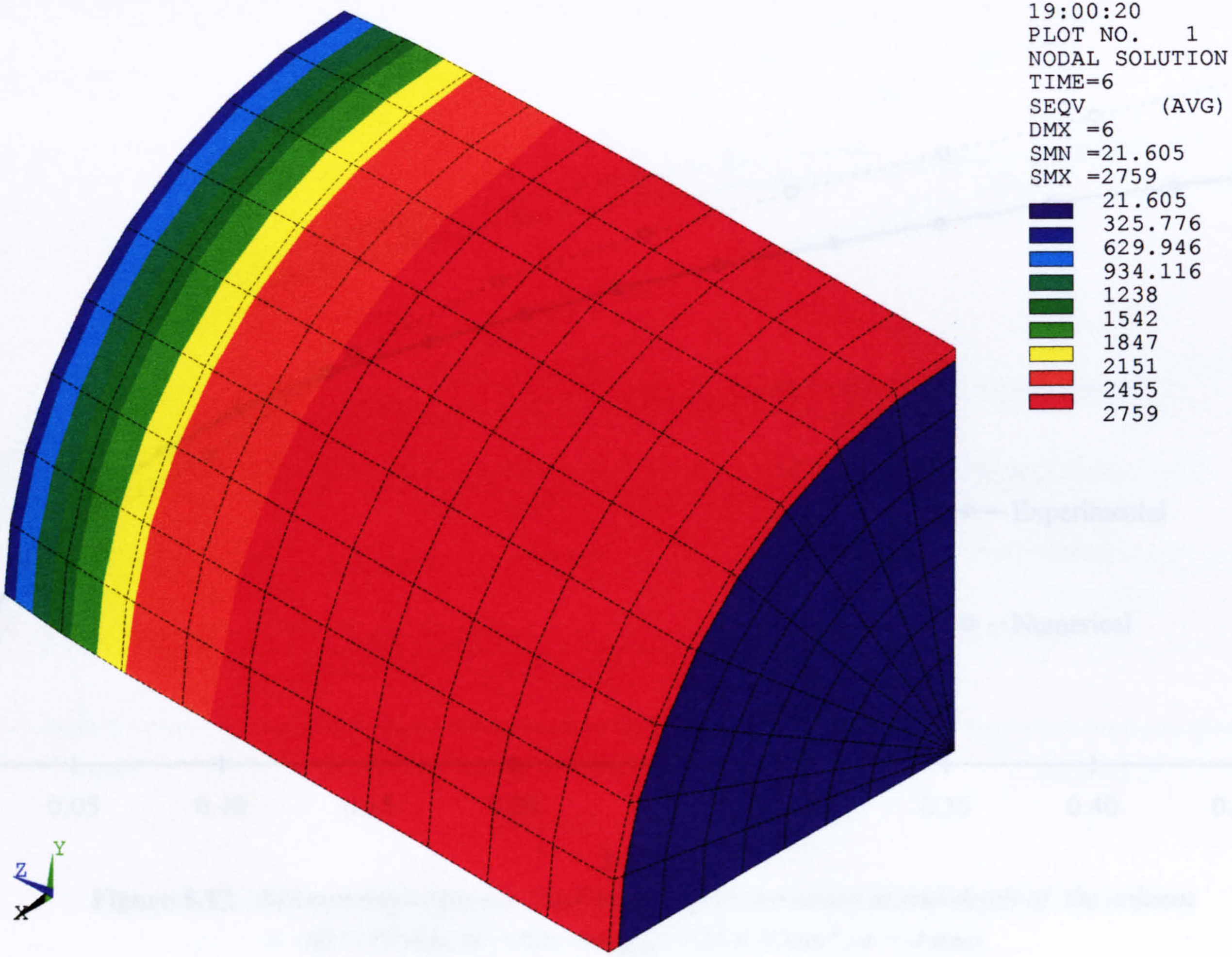

Figure 8.11 *Typical equivalent stress distribution for the FRP tube confined concrete cylinder (D = 150 mm, H = 300 mm, f_{cu} = 27.4 N/mm^2)*

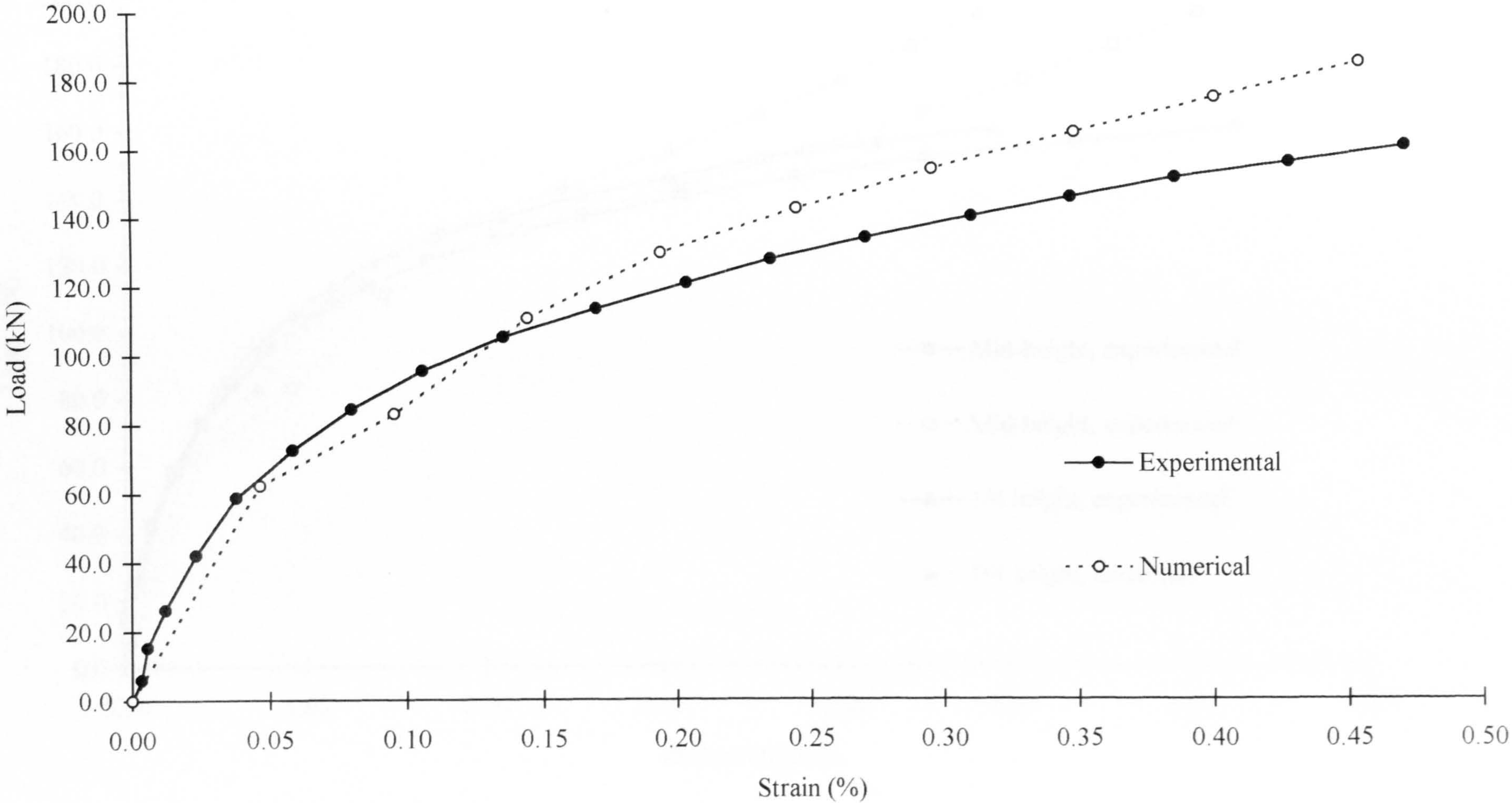

Figure 8.12 *Relationships between load and compressive strain at mid-depth of the column (D = 80 mm, H = 800 mm, f_{cu} = 25.6 N/mm^2, e = 4 mm)*

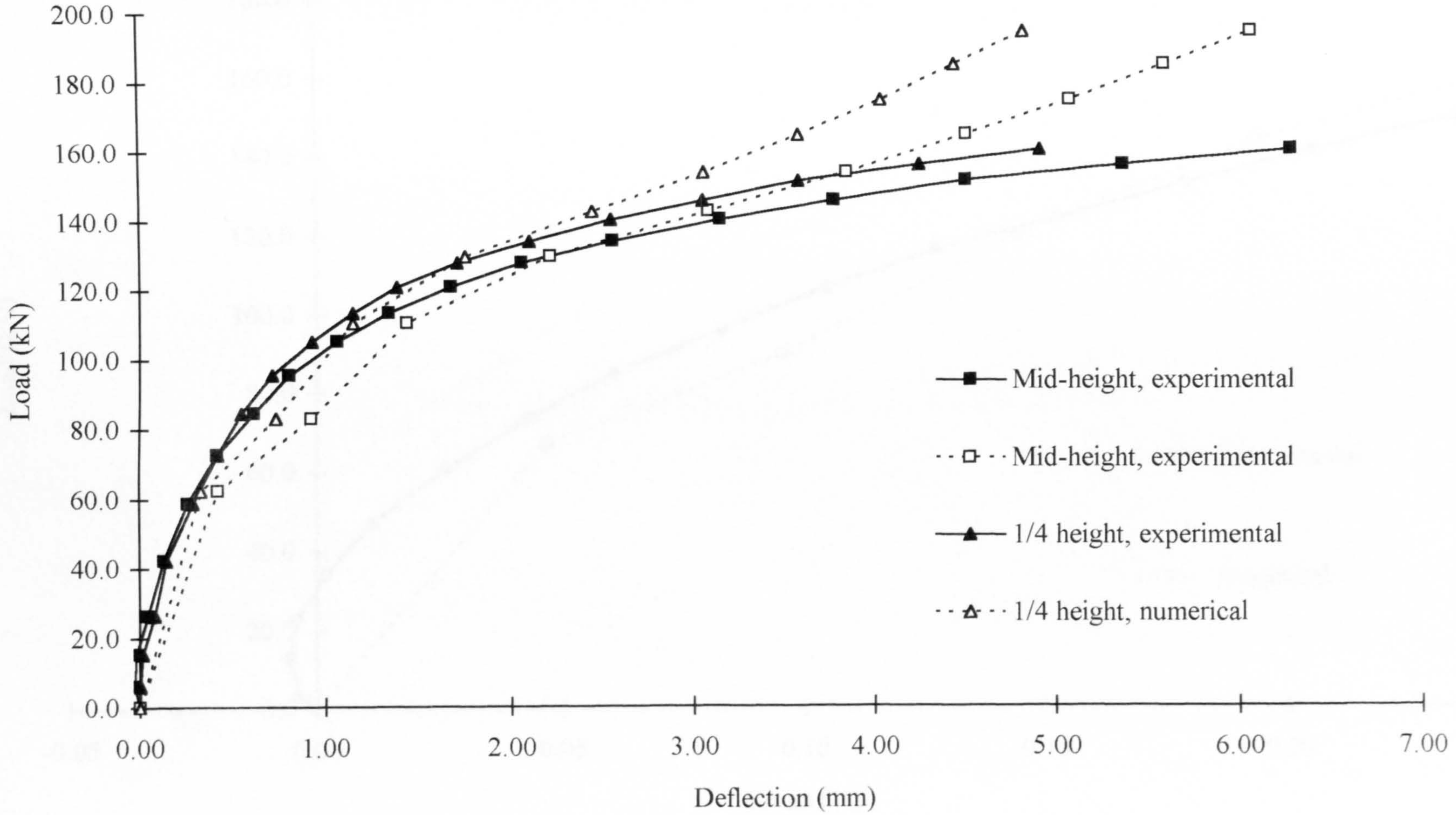

Figure 8.13 *Relationships between load and deflection of the column*
(D = 80 mm, H = 800 mm, f_{cu} = 25.6 N/mm^2, e = 4 mm)

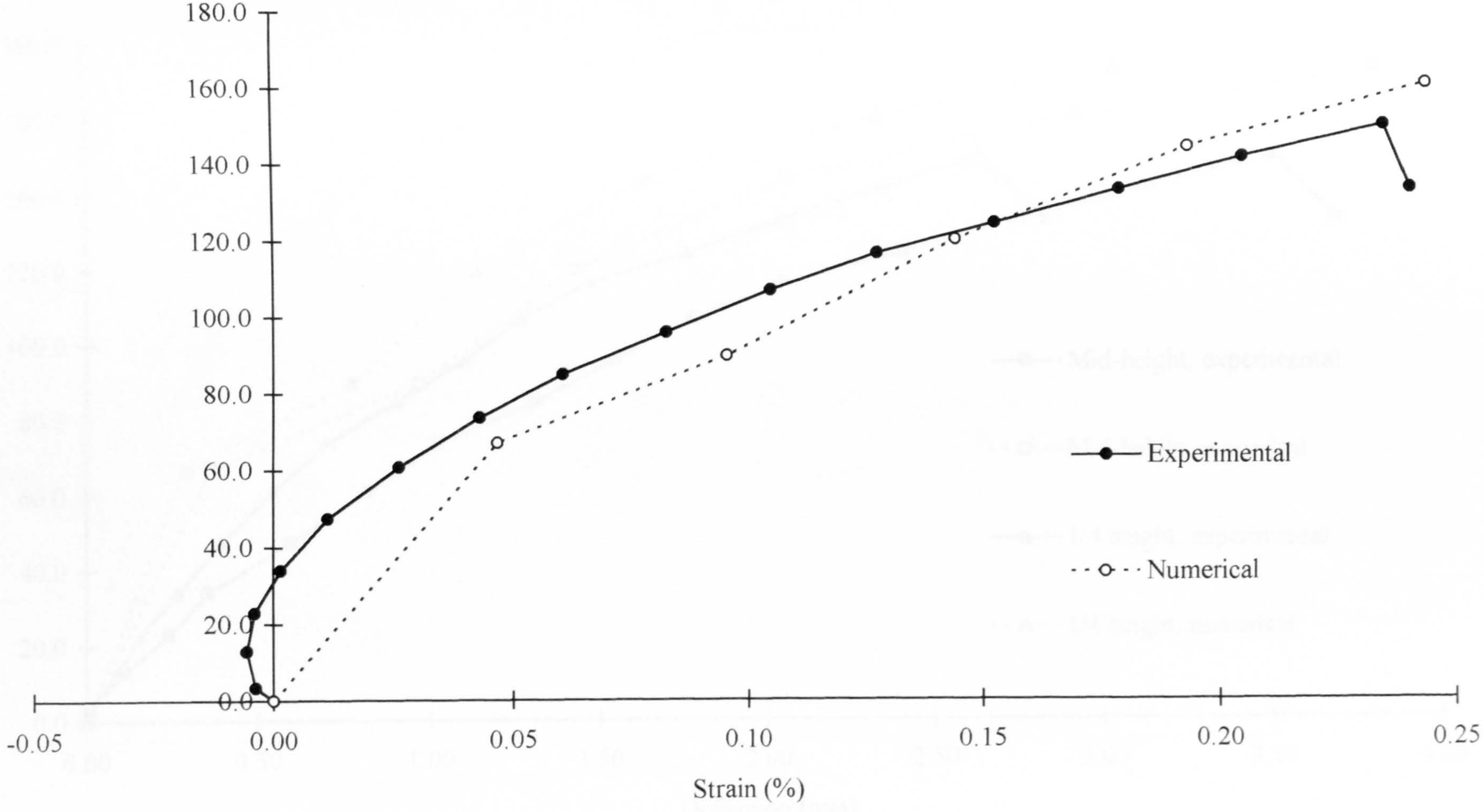

Figure 8.14 *Relationships between load and compressive strain at mid-depth of the column (D = 80 mm, H = 800 mm, f_{cu} = 31.2 N/mm^2, e = 4 mm)*

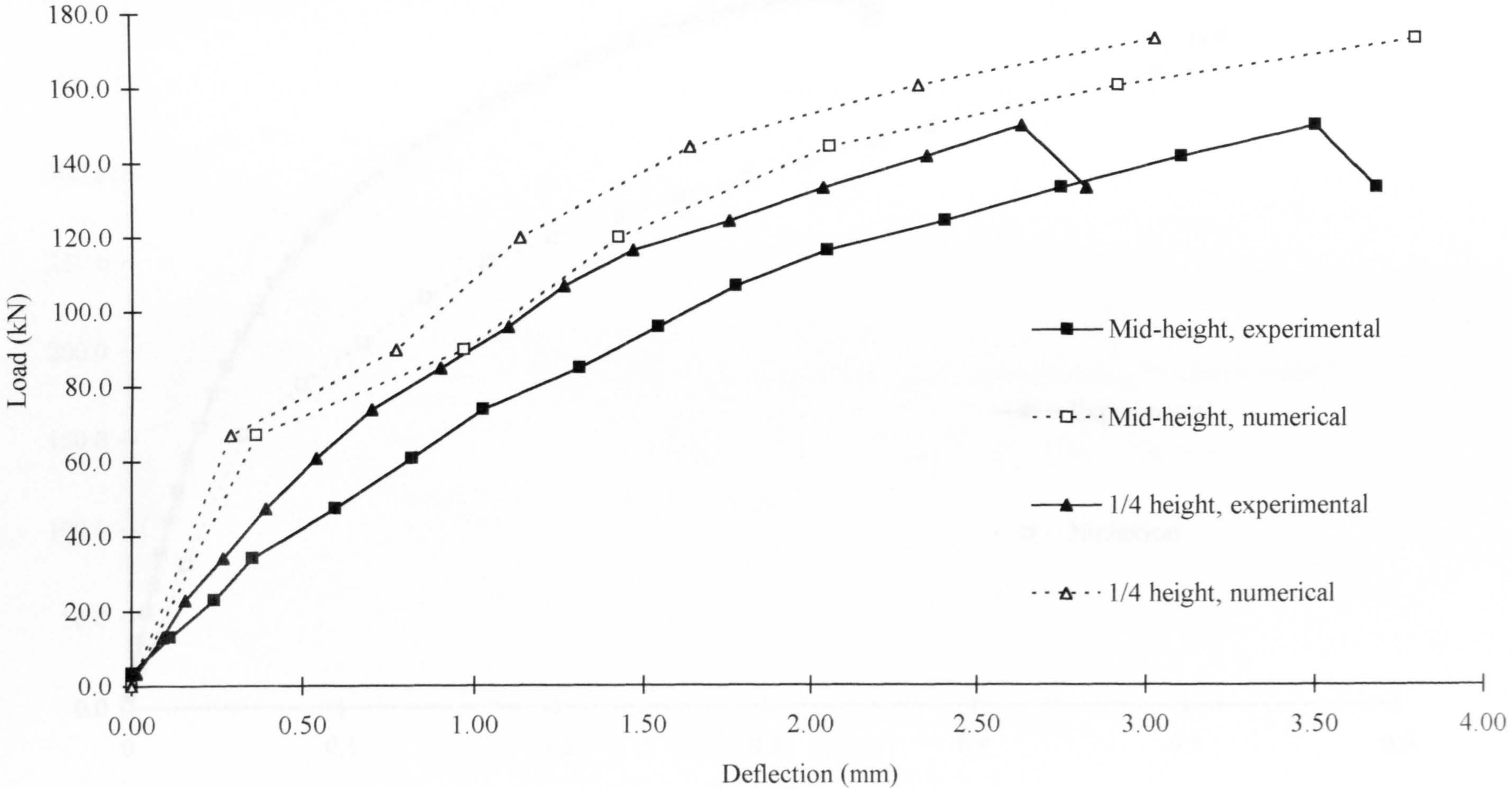

Figure 8.15 *Relationships between load and deflection of the column*
(D = 80 mm, H = 800 mm, f_{cu} = 31.2 N/mm^2, e = 4 mm)

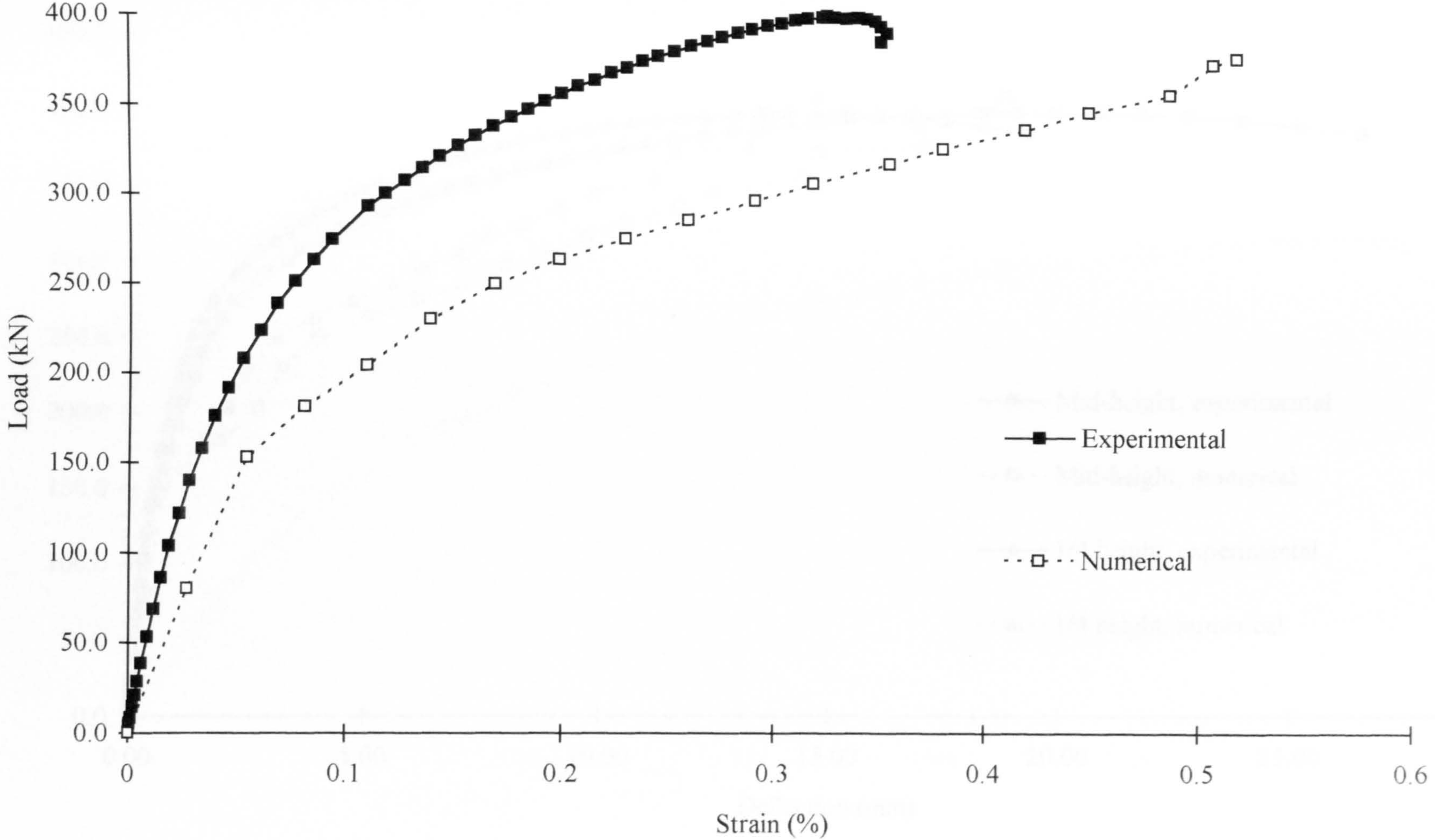

Figure 8.16 *Relationships between load and compressive strain at mid-depth of the column (D = 150 mm, H = 1500 mm, f_{cu} = 28.4 N/mm^2, e = 7.5 mm)*

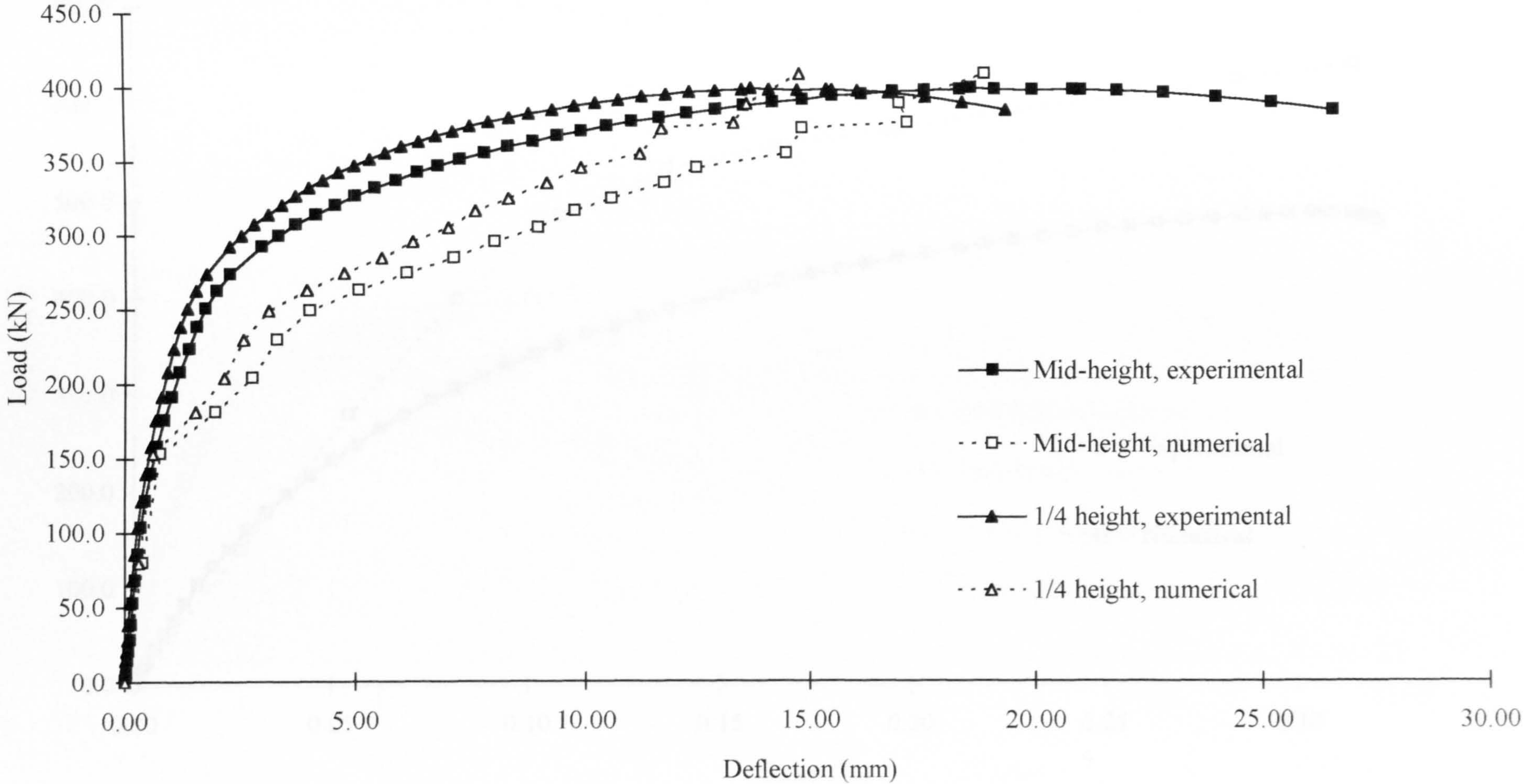

Figure 8.17 *Relationships between load and deflection of the column (D = 150 mm, H = 1500 mm, f_{cu} = 28.4 N/mm^2, e = 7.5 mm)*

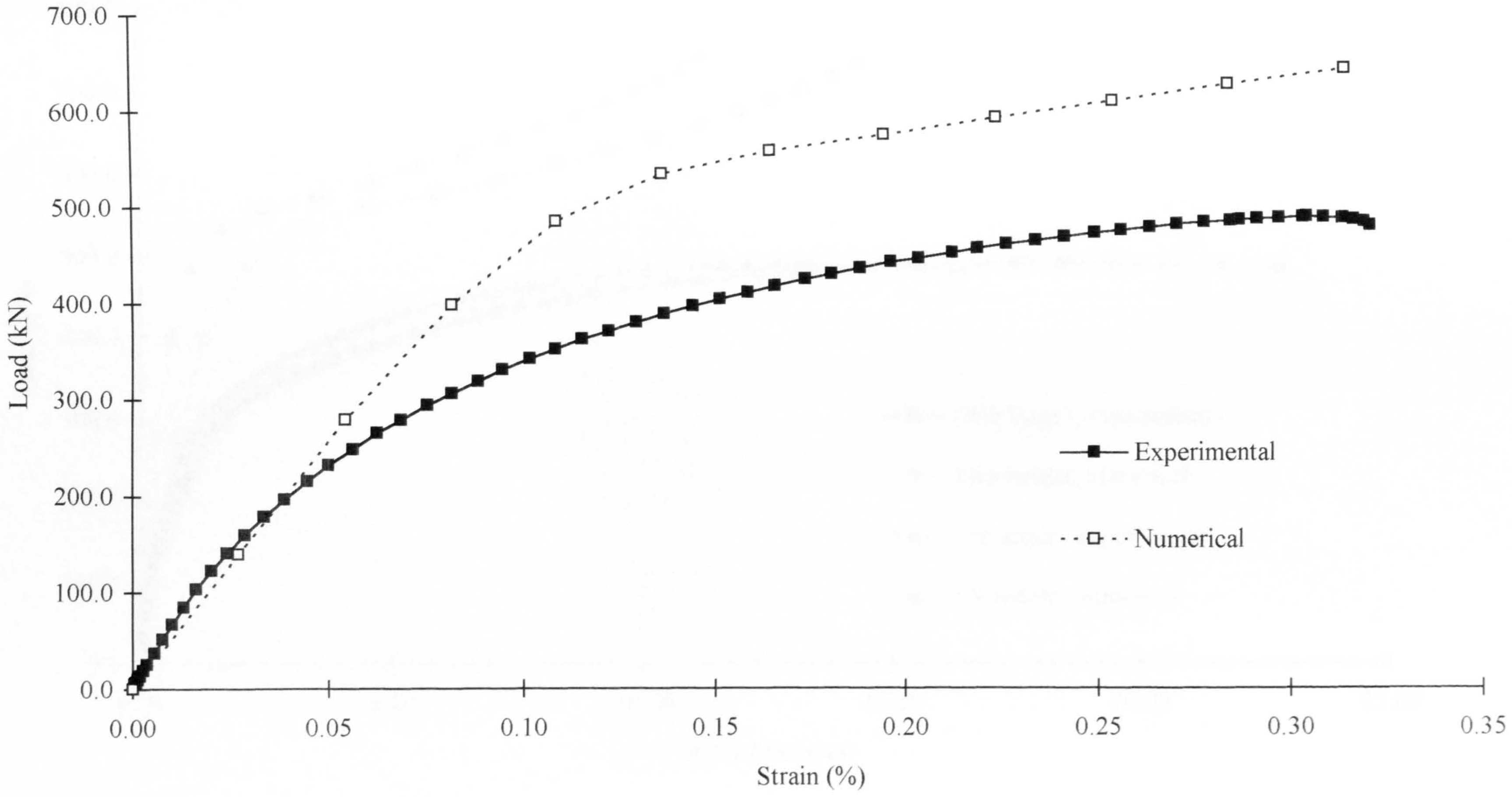

Figure 8.18 *Relationships between load and compressive strain at mid-depth of the column (D = 150 mm, H = 1500 mm, f_{cu} = 37.8 N/mm^2, e = 7.5 mm)*

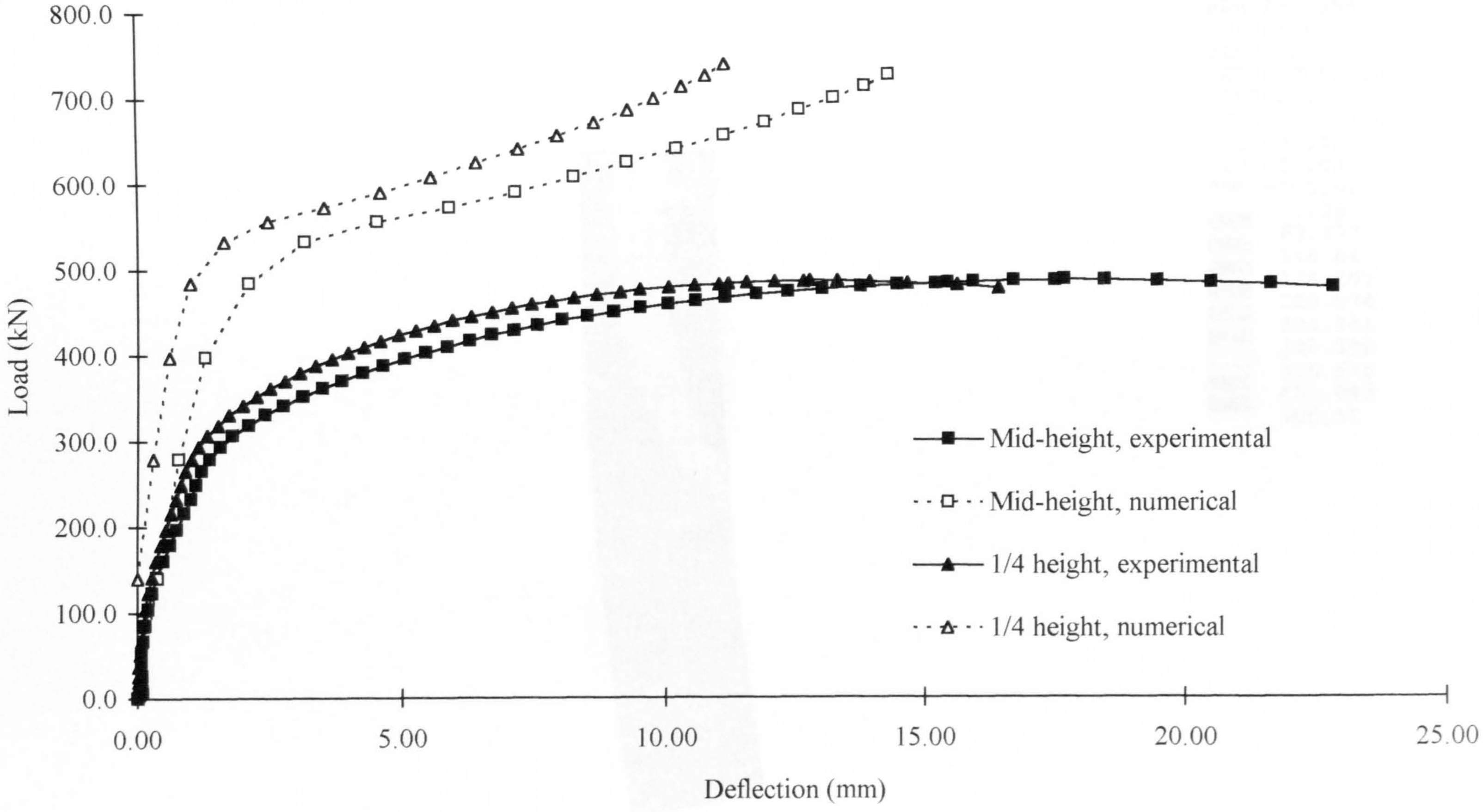

Figure 8.19 *Relationships between load and deflection of the column (D = 150 mm, H = 1500 mm, f_{cu} = 37.8 N/mm^2, e = 7.5 mm)*

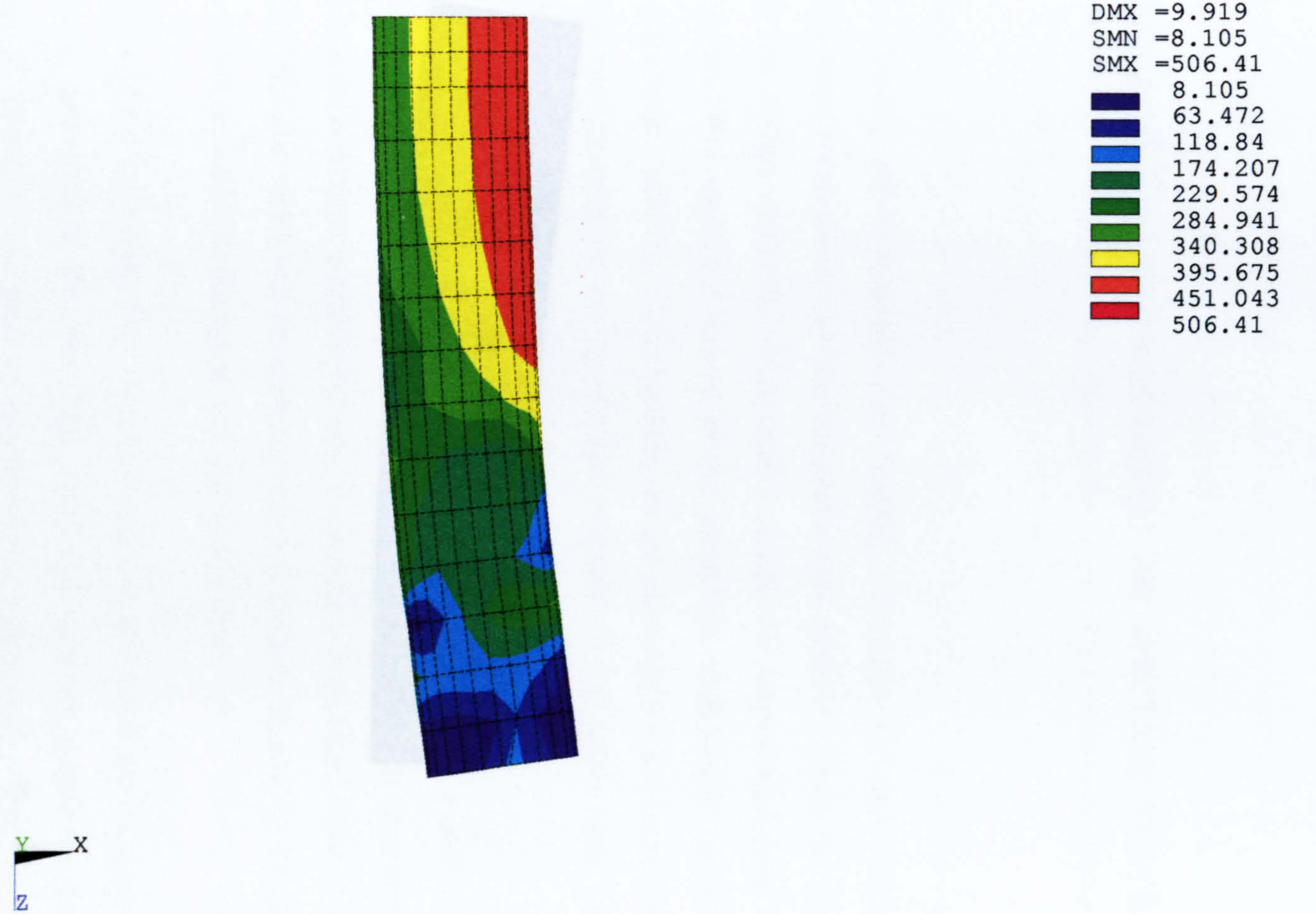

Figure 8.20(a) *Typical equivalent stress distribution for the FRP tube confined concrete column (D = 80 mm, f_{cu} = 25.6 N/mm^2)*

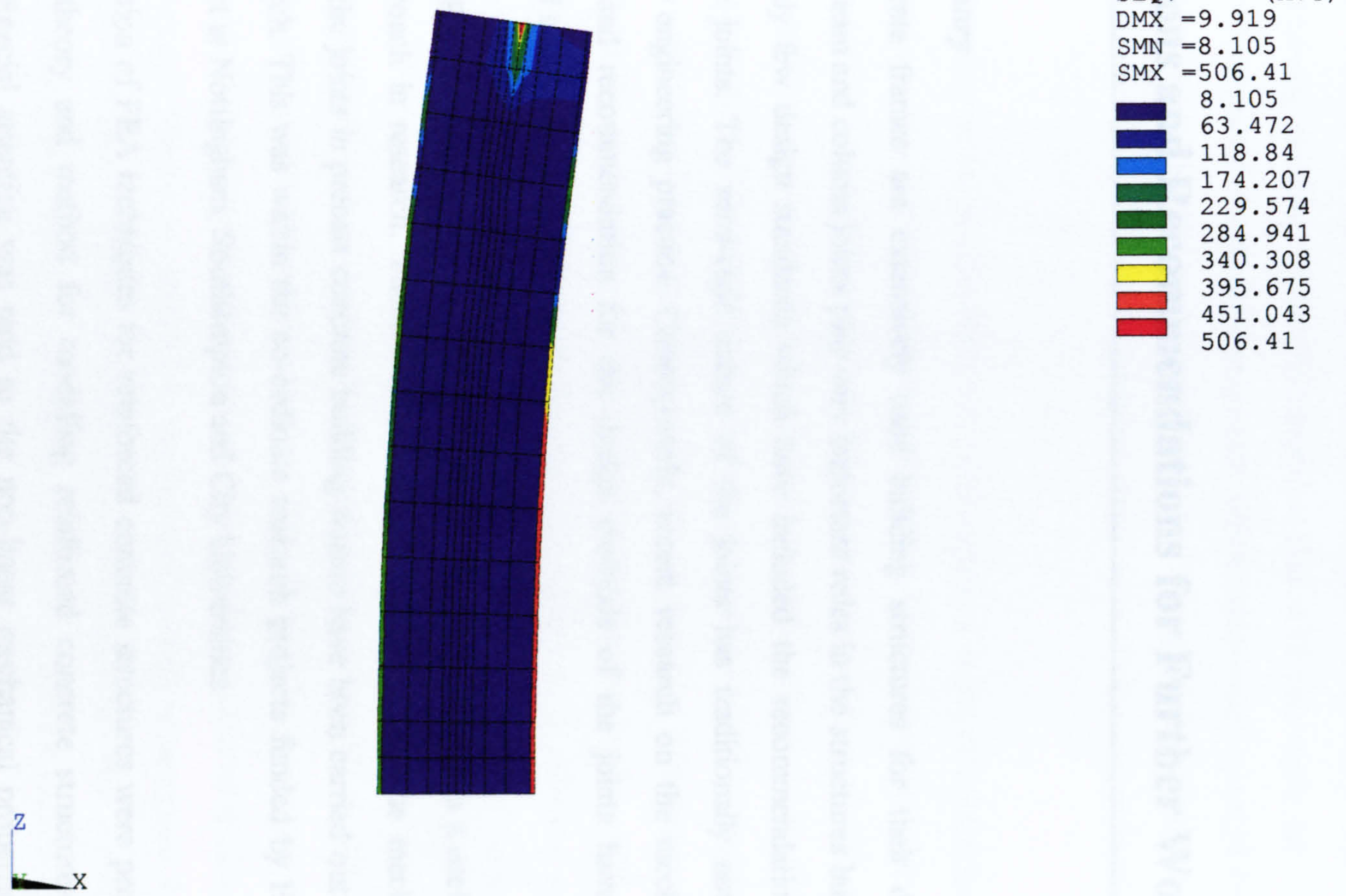

Figure 8.20(b) *Typical equivalent stress distribution for the FRP tube confined concrete column (D = 80 mm, f_{cu} = 25.6 N/mm^2)*

Chapter 9

Conclusions and Recommendations for Further Work

9.1 Summary

Precast concrete frames are extensively used building structures for their distinct advantages. Beam and column joints play very important roles in the structures but there have been only few design standards which have included the recommendations for design of the joints. The semi-rigid nature of the joints has traditionally not been considered in engineering practice. Consequently, recent research on the mechanical performance and recommendation for the design methods of the joints have been significant and necessary.

Due to the expense of physical testing of full scale specimens, FEA acts as a useful and effective approach in research. Therefore, numerical investigation of the mechanical behaviour of the joints in precast concrete building frames have been carried out in the present research. This was within the co-ordinate research projects funded by EPSRC and carried out at Nottingham, Southampton and City Universities.

A standardisation of FEA techniques for reinforced concrete structures were proposed firstly. FEA theory and method for modelling reinforced concrete structures were summarised. Special attention was paid to the non-linear mechanical properties and numerical presentations of both steel and concrete. A simplified mechanical model for steel was proposed, based on a statistical analysis of existing data. For concrete also, constitutive equations for the parameters required by the elastic constants and failure criteria in the ANSYS programme were proposed and analysed. Many numerical tests on standard prisms and cubes were carried out to define the effect of several factors on

the mechanical performance of the concrete element. The factors include the element aspect ratio and the properties required for the smeared material which was added into the concrete element to solve the earlier crushing problem which precluded solution of the analysis. A method to modify the strength reduction caused by the slender element shape, 0.33 to 1.0 element aspect ratio, is recommended. An optimum value of the smeared material was provided under the condition that with this value the standard prism test model produced a concrete stress-strain relationship which matched the input uniaxial compression curve. To apply this value into the general analyses in which concrete elements would work in the multiaxial stress state, further consideration was made.

To calibrate accuracy of the standardised FEA techniques, a series of connections and joints in precast concrete structures tested in European Union countries through the COST initiative were numerically modelled. These range from the simple tensile bar, through the T-stub connector and the bolt embedded in joint concrete, to the full scale billet-welded plate joints. The joints were tested in the University of Nottingham, and some of them had also been numerically modelled in the City University. In the numerical analyses the mechanical performance and the internal mechanism of the joints were investigated and comparison made between the results from different research teams. The internal mechanism includes the cracking and crushing status of the concrete components, stress distribution of the connectors and failure mode of the joints.

Subsequently, sensitivity analyses on the mechanical behaviour of the billet-welded plate joints to a wide range parameters were carried out. Variations of the parameters covered the beam and column geometry, concrete and grout grades and amount of reinforcement in beam and column. The range extended to the limits of realistic construction for such frame structures. The altered loading orientations and the comparison with a monolithic joint were also investigated. Based on the analysis results, simplified calculation methods were proposed for estimating the moment resistance, the initial rotation stiffness, the secant rotation stiffness and the rotation capacity of the joints.

Finally, as an extensive application of the standardisation of FEA techniques, a finite element model for the FRP tube confined concrete columns was developed. The model was based on the standard FEA methods developed earlier in this research, were

supplemented with additional FEA method for the FRP laminate, and calibrated using typical specimens tested as part of a separate study in the University of Southampton.

9.2 Conclusions

1. The standardisation of FEA techniques has provided predictions close to the experimental data for a wide range of many joint types, thus it can be applied with confidence to other structure configurations in which concrete is locally and fully confined. The sensitivity analysis of the joints supplies the opportunity to comprehend the impact of semi-rigid behaviour in any realistic frame connected with billet-welded plate joint types, so that full frame analyses can be made.

2. The simplified mechanical model for steel was derived through a statistical approach using the data from test results carried out in the University of Southampton and in various other standard publications. Comparison with the test results and application to the numerical analyses show that this model can accurately represent the mechanical properties of steel both with or without a definite yield point and so improve the accuracy of the finite element analyses.

3. The parameters required by the elastic constants and the failure criteria for the concrete element, such as elastic modules, uniaxial compressive strength and tensile strength, are chosen from a number of proposals published in the design standards. Therefore they possess higher reliability. The recommended simplified mechanical model for concrete in uniaxial compression is created from the constitutive equations in the general form used in most design standards. It accurately represents the properties of concrete, and is also convenient for use in commercial versions of FEA packages.

4. The addition of smeared material is a successful approach to avoid the early failure of the models during post crushing behaviour of the concrete element. The optimum volume of smeared material recommended for an accurate solution is about 9.7%. The compressive strength of the smeared material is suggested to be 1.725 times the uniaxial compressive strength of concrete, so that the increased failure strength of concrete in multiaxial compression can be approximated.

5. Slender elements of the mesh require their input compressive strength to be modified to compensate for the loss of strength due to numerical inaccuracies resulting from the element aspect ratio.

6. The numerical test of the tensile steel bar indicates that a more accurate input stress-strain relationship will result in a more accurate solution being obtained, because the output curve can more accurately match the input one. The numerical modelling of the bolt in joint concrete shows that utilising contact elements at the interface between steel bolt and concrete is an effective and necessary way to simulate the bond feature of the materials when debonding is anticipated.

7. All the modelling of the general connectors prove that coarser meshed models can also give solutions with acceptable accuracy if the models are carefully designed. This is a significant conclusion for the modelling of large and complex components or structures, such as precast concrete joints.

8. The numerical analyses of the experimental billet-welded plate joints provide good agreement with the test results and the relevant modelling results. Furthermore, prediction of the global failure mechanism of the joints is included in the model. All the joints cracked early in the concrete surrounding the connectors, and at the ultimate state cracked zones have extended into most parts of the joints, which matches the experimental phenomena. Additional configurations are recommended for the joint core zone, such as adding more links at the beam end, to lessen the cracking. All the joints with flexible failure are *weak beam end-strong column joints*, and they fail by crushing of the grout with the connectors not yielding. Thus, the beam ends are over reinforced.

9. All the numerical modelling results of the experimental billet-welded plate joints indicate that the standard FEA techniques for reinforced concrete structures proposed in the present research, including the general FEA methods, mechanical models of the materials and the solution methods, are successful and accurate. Consequently, the techniques can confidently be used in the further research.

10. The sensitivity analyses show that the billet-welded plate joints have certain potential of force resistance and stiffness. The hogging beam end moment resistance ranges from

40% to 65% of the fixed beam end moment, while the sagging beam end moment resistance ranges from 24% to 40%. The initial sway stiffness of the precast joints is about 60% to 70% that of the monolithic joint in the hogging beam end moment loading condition. The secant rotation stiffness is about 60% of the monolithic joint value. In the reversed loading condition, these stiffness values are around 50% and 33% respectively.

11. The sensitivity analyses also indicate that beam depth and concrete/grout grade are the most significant factors to the joint force responses. For the joints with hogging beam end moments, a 100% increase of the parameters cause about 100% increase of the force responses, until the column failure constrains the joint capacities. For most of the other parameters the moment responses vary within 20% although the parameters change several hundred percentage points. For the deformation sensitivity, the beam depth is the only significant factor affecting the rotation stiffness of the beam end.

12. The simplified equations can provide acceptable predictions of the moment-rotation characteristics for the billet-welded plate joints with the parameter ranges used in the sensitivity analyses. Thus full frame analysis can be conveniently made.

13. The finite element model for the FRP tube confined concrete columns is a successful and extended application of the standardised FEA techniques. It can reliably predict the mechanical behaviour of the columns for the full loading processes, but requires manual supervision to determine the ultimate loads.

14. All the FEA techniques and results can be confidently used to improve engineering design methodology for structures with locally and fully confined concrete.

9.3 Recommendations for further research

At the moment the research has only investigated the semi-rigid behaviour of the existing joint types for which the configuration is designed as a pin connection. The characteristics of the joints are achieved passively. To effectively improve the joints characteristics, research into active changes to this configuration is essential. The following aspects are recommended for further research of the joints in precast concrete frames:

1. For the analysed billet-welded plate joint, a common joint type in the engineering practice provides a *weak beam end-strong column joint*, and has the beam end over-reinforced. Thus the ductility of the joint should be improved if the semi-rigid potential of the joint can be utilised for the moment redistribution design of the frame structures. Additionally, the other force resistance capacities which ensure the beam end moment resistance is fully developed, such as the bond strength of the billet embedded in the column concrete and the strength of the welds connecting the billet and the plate, also need to be particularly studied.

2. The joints crack early, and long before the ultimate state is reached the cracks develop extensively. Thus special attention should be paid to the durability of the joints when its semi-rigid potential will be used in the design.

3. In the finite element analysis complete bond between rebar and concrete was assumed. Where concrete to steel connection hardware, and concrete to grout interfaces, have the ability to separate, gap elements were used. In other concrete analyses these assumptions may not be adequate. Anchorage and dowel action of the rebars in shear may need to be included, and warrant further investigations.

4. No account has been made for experimental error in the data used to calibrate the finite element analysis techniques. The significance of lack of squareness or lack of alignment in the joint as it is assembled also warrant further research.

5. The simplified calculation method appears to have large error margins on the predictions. These error margins are significantly less than they appear, because the statistical analysis is based (in most cases) on one central value plus the two extremes rather than a more realistic distribution of parameter variations. Further work is needed to correct the coefficients in these equations and make them appropriate for direct application to full-frame analysis.

The FEA model for the FRP tube confined concrete columns needs further calibrated to predict the failure features of the FRP laminate. Extensive research on the composite structures of FRP and concrete should be carried out, using FEA as one of the research approaches.

References

1. J. H. J. A. Vambersky, *"Precast Concrete in Buildings Today and in the Future"*, The Structural Engineer, Volume 72, No. 15, August 1994.

2. F. E. Bljuger, *"Design of Precast Concrete Structures"*, ELLIS HORWOOD LIMITED, 1988.

3. Prestressed Concrete Institute, *"PCI Design Handbook, Precast Prestressed Concrete"*, Second Edition, 1980.

4. C. W. Glover, *"Structural Precast Concrete"*, C. R. BOOKS LIMITED, 1964.

5. K. Billig, *"Precast Concrete"*, MACMILLAN & CO LTD, 1955.

6. M. Holmes and L. H. Martin, *"Analysis and Design of Structural Connections: Reinforced Concrete and Steel"*, ELLIS HORWOOD LIMITED, 1983.

7. J. H. Bickford, *"An Introduction to the Design and Behaviour of Bolted Joints"* , MARCEL DEKKER, INC. New York and Basel, 1981.

8. Institution of Structural Engineers, *"Manual on Structural Joints in Precast Concrete"*, London, 1978.

9. P. W. Birkeland and H. W. Birkeland, *"Connections in Precast Concrete Construction"*, Journal of the American Concrete Institute, Vol. 63, No. 3, March 1966, pp. 345-368.

10. S. A. M. Mohamed and C. K. Jolly, *"An Experimental Study of the Behaviour of Sleeved Bolt Connections in Precast Concrete Frame"*, Magazine of Concrete Research, 1995, 47, No. 171, June, 119-127.

11. S. A. M. Mohamed, *"Behaviour of Sleeved Bolt Connections in Precast Concrete Building Frames"*, PhD Thesis, University of Southampton, February 1992.

12. C. K. Jolly, *"Sleeve-Bolted Joint Constraints on Precast Concrete Beams"*, Report of University of Southampton, 1995.

13. C. K. Jolly, *"Three-Bolt Cleated Precast Concrete Beam Joints with Improved Reinforcement Details"*, Report on the Results of Tests Performed on Behalf of Composite Structures Ltd., Southampton University, June 1995.

14. A. A. Mahdi, *"Moment Rotation Effects on the Stability of Columns in Precast Concrete Structures"*, PhD thesis, University of Nottingham, 1992.

15. P. Ragupathy, *"Non-linear Behaviour of Precast Concrete Frames"*, PhD thesis, City University, February 1994.

16. K. S. Elliott and G. Davies, *"Semi-Rigid Connections in Precast Concrete Frames"*, EPSRC Research Grant Final Report, University of Nottingham, 1996.

17. H. Gorgun, *"Semi-Rigid Behaviour of Connections in Precast Concrete Structures"*, Progress Report, University of Nottingham, February 1996.

18. K. S. Virdi, *"Design of Precast Concrete Frames with Semi-Rigid Joints"*, EPSRC Research Grant Final Report, City University, December 1996.

19. C. K. Jolly, *"Finite Element Analyses of Joints in Precast Concrete Frames"*, EPSRC Research Grant Final Report, University of Southampton, May 1997.

20. C. K. Jolly, and M. Guo, *"Sensitivity Analysis of Precast Concrete Billet-Welded Plate Joints"*, European Co-operation in the field of Scientific and Technical Research COST Project C1 Precast Concrete Working Group, Paper C1/WD1/96-04, Coimbra, December 1996, 1-7.

21. C. K. Jolly, and M. Guo, *"Finite Element Models for the Ultimate State Analysis of Reinforced Concrete"*, European Co-operation in the field of Scientific and Technical Research COST Project C6 Numerical Simulation Working Group, Paper C1/WD6/96-05, LERMES, Clermont-Ferrand, November 1996, 1-16.

22. C. K. Jolly, and M. Guo, *"Finite Element Modelling on the Behaviour of a Bolt in Joint Concrete"*, European Co-operation in the field of Scientific and Technical Research COST Project C6 Numerical Simulation Working Group, Paper C1/WD6/96-04, LERMES, Clermont-Ferrand, November 1996, 1-34.

23. M. Guo, and C. K. Jolly, *"Finite Element Models for the Analysis of Steel and Concrete in Construction"*, Advances in Computational Techniques for Structural Engineering, (Edited by B. H. V. Topping), Civil-Comp Press, 1996, 283-294.

24. C. K. Jolly, and M. Guo, *"Finite Element Models for the Analysis of Concrete in Construction"*, European Co-operation in the field of Scientific and Technical Research COST Project C1 Precast Concrete Working Group, Paper C1/WD1/96-05, CERIB, Paris, May 1996, 1-24.

25. C. K. Jolly, and M. Guo, *"Numerical Simulation of a T-stub Connection Implications for More General Simulations"*, European Co-operation in the field of Scientific and Technical Research COST Project C6, Numerical Simulation Working Group, Paper C1/WD6/95-12, June 1995.

26. H. A. El-Ghazaly and H. S. Al-Zamel, *"An Innovative Detail for Precast Concrete Beam-Column Moment Connections"*, Canadian Journal of Civil Engineering, Vol. 18, No. 4, August 1991, pp. 690-710.

27. S. U. Pillai and D. W. Kirk, *"Ductile Beam-Column Connection in Precast Concrete"*, Journal of the American Concrete Institute, Vol. 78, No. 6, November - December 1981, pp. 480-487.

28. P. Bhatt and D. W. Kirk, *"Tests on an Improved Beam Column Connection for Precast Concrete"*, Journal of the American Concrete Institute, Vol. 82, No. 6, November - December 1985, pp. 834-843.

29. J. R. Tang, *"Seismic Resistance of Joints in Reinforced Concrete Frames"*, Press of Dongnan University, P. R. China, October 1989.

30. B. P. Hughes and N. I. Fattuhi, *"Reinforced Steel and Polypropylene Fibre Concrete Corbel Tests"*, The Structural Engineer, Vol. 67, No. 4, February 1989, pp. 67-72.

31. Swanson Analysis System Inc, *"ANSYS, Engineering Analysis System User's Manual"*, Vol. 1-4, Version 5.0, Houston, Pennsylvania, U. S. A., 1989.

32. M. Mazurkiewicz and W. Ostachowicz, *"Theory of Finite Element Method for Elastic Contact Problems of Solid Bodies"*, Computer & Structures, Vol. 17, No. 1, pp. 55-59, 1983.

33. P. J. Dowling, P. Knowles and G. W. Owens, *"Structural Steel Design"*, The Steel Construction Institute, Butterworths, 1988.

34. F. K. Kong and R. H. Evans, *"Reinforced and Prestressed Concrete"*, 3rd edition, Van Nostrand Reinhold (UK) Co. Ltd, 1987.

35. E. X. Ma, et al, *"Material Mechanics"*, Advanced Education Press, 1987 (in Chinese).

36. American Society of Civil Engineers, *"Finite Element Analysis of Reinforced Concrete"*, New York, U. S. A., 1982.

37. C. Z. Wang and Z. M. Teng, *"Theory of Reinforced Concrete Structures"*, Building Industry Press of China, 1985 (In Chinese).

38. C. O. Harris, *"Statics and Strength of Materials"*, John Wiley and Sons, 1982.

39. L. H. Van Vlack, *"Materials for Engineering: Concepts and Application"*, The University of Michigan, Ann Arbor, Michigan, 1983.

40. A. W. Judge, *"Engineering Materials"*, Sir Isaac Pitman and Sons Ltd., 1930.

41. P. Desayi and S. Krishnan, *"Equation for the Stress-Strain Curve of Concrete"*, ACI Journal, Proceedings V. 61, No. 3, March 1964, pp. 345.

42. British Standards Institution, *"BS8110, The Structural Use of Concrete: Part 1: Code of Practice for Design"*, BSI, London, 1985.

43. Comite Euro-international du Beton, *"CEB-FIP Model Code 1990"*, CEB-FIP, 1993.

44. Ministry of Construction, The People's Republic of China, *"Design Code for Structural Concrete, GBJ 10-89"*, Building Industry Press of China, 1989 (In Chinese).

45. *"Eurocode No. 2 Design of Concrete Structures Part 2: General Rules for Buildings"*, Commission of the European Communities, 1993.

46. Norges Byggstandardiseringsrad, *"Concrete Structures Design Rules, NS 3473E"*, NSF, November 1992.

47. E. Hognestad et al.. *"Concrete Stress Distribution in Ultimate Strength Design"*, Journal of ACI, December 1955.

48. British Standards Institution, *"BS8110, The British Standard, Structural Use of Concrete, Part 2, Code of Practice for Special Circumstances"*, BSI, London 1985.

49. American Concrete Institute, *"Building Code Requirements for Reinforced Concrete (ACI318-89) and Commentary-ACI 318R-89"*, ACI, Michigan, 1989.

50. M. Y. H. Bangash, *"Concrete and Concrete Structures: Numerical Modelling and Applications"*, Elsevier Science Publishers Ltd, 1989.

51. W. F. Chen and A. F. Saleeb, *"Constitutive Equations for Engineering Materials, Volume 1: Elasticity and Modelling"*, Elsevier, 1994.

52. W. F. Chen, *"Constitutive Equations for Engineering Materials, Volume 2: Plasticity and Modelling"*, Elsevier, 1994.

53. J. P. Jaspart, "*Numerical Simulation of a T-stub Experimental Data*", European Co-operation in the Field of Scientific and Technical Research COST Project C1, Numerical Simulation Working Group, Paper C1/WD6/94-09, July 1994.

54. P. Ragupathy and K. S. Virdi, *"Numerical Simulation of a T-stub Connection using ANSYS"*, European Co-operation in the Field of Scientific and Technical Research COST Project C1, Numerical Simulation Working Group, Paper C1/WD6/95, 15-17 June 1995.

55. O. S. Bursi and J. P. Jasrart, *"A Refined Finite Element Model for Tee-Stub Steel Connections"*, European Co-operation in the Field of Scientific and Technical Research COST Project C1, Numerical Simulation Working Group, Paper C1/WD6/95-07, 15-17 June 1995.

56. H. I. Sakellariadou, C. D. Bisbos, K. Thomopoulos and P. D. Panabiotopoulos, *"A 3-D Numerical Study of the T-Stub Problem Taking into Account the Interfacial Unilateral Contact Effects"*, Advances in Computational Methods for Simulation, (Edited by B. H. V. Topping), Civil-Comp Press, 1996, 115-124.

57. L. Dunai, S. Adany, F. Wald and Z. Sokol, *"Numerical Modelling of Column-Base Connections"*, Advances in Computational Techniques for Structural Engineering, (Edited by B. H. V. Topping), Civil-Comp Press, 1996, 171-177.

58. B. N. Nemati and D. Le Houedec, *"The Analysis and the 3D Finite Element Simulation of Steel Bolted End-Plate Connections"*, Advances in Computational Techniques for Structural Engineering, (Edited by B. H. V. Topping), Civil-Comp Press, 1996, 179-187.

59. J. Balogh and M. Ivanyi, *"Analysis of Steel Frames with Semi-Rigid Column-Base Connections"*, Advances in Computational Techniques for Structural Engineering, (Edited by B. H. V. Topping), Civil-Comp Press, 1996, 159-164.

60. Laasonen, M. And Suonketo, J., *"A Bolt in Joint Concrete"*, Test Details and Results, Private Communication, May 1996.

61. Edited by A. G. Gibson, *"FRC'98"*, Proceedings of the 7th International Conference on Fibre Reinforced Composites, University of Newcastle upon Tyne, UK, 15-17 April 1998.

62. J. L. Clarke and P. Waldron, *"The Reinforcement of Concrete Structures with Advanced Composites"*, The Structural Engineer, 74(17), 1996, p283-288.

63. C. K. Jolly, *"Development of a Design Methodology for Non-Ferrous Compositely Reinforced Concrete Columns"*, EPSRC Research Grant Final Report, University of Southampton, January 1998.

64. C. K. Jolly and D. Lillistone, *"Concrete-Filled FRP Circular Columns Under Eccentric Loading"*, FRC'98, Proceedings of the 7th International Conference on Fibre Reinforced Composites, University of Newcastle upon Tyne, UK, 15-17 April 1998, p506-513.

65. D. Lillistone and C. K. Jolly, *"Concrete-Filled Fibre Reinforced Plastic Circular Columns"*, Composite Construction - Conventional and Innovative, Innsbruck, IABSE, 1997, p759-764.

66. C. K. Jolly and D. Lillistone, *"Large Scale Testing of Concrete-Filled FRP Tubes"*, BRE Report, 1997.

67. C. K. Jolly and D. Lillistone, *"Innovative Concrete Column Reinforcement using Advanced Composites"*, submitted to The Structural Engineer.

68. B. D. Agarwal and L. J. Broutman, *"Analysis and Performance of Fibre Composites"*, A Wiley-Interscience Publication, 1980.

69. S. K. Garg, V. Svalbonas and G. A. Gurtman, *"Analysis of Structural Composite Materials"*, Marcel Dekker, INC, New York, 1973.

70. N. L. Lu, *"Mechanics of Composite Materials"*, Chongching University Publication, 1992 (in Chinese).

71. C. C. Chamist, *"Simplified Composite Micromechanics Equations for Mechanical, Thermal, and Moisture-Related Properties"*, Engineer's Guide to Composite Materials, American Society for Material, 1987.

Additional References:

72. K. J. Willam and E. P. Warnke, *"Constitutive Model for the Triaxial Behaviour of Concrete"*, Seminar on Concrete Structures Subjected to Triaxial Stresses, 17th-19th May, 1974 - ISMES - BERGAMO (ITALY).

73. C. K. Jolly and M. Guo, *"Finite Element Modelling the Semi-rigid Behaviour of Billet-Welded Plate Joints in Precast Concrete Building Frames"*, European Co-operation in the field of Scientific and Technical Research COST Project C6, Numerical Simulation Working Group, Southampton, December 1997.

74. M. Guo, *"Finite Element Analyses of Joints in Precast Concrete Building Frames"*, MPhil/PhD Transfer Thesis, University of Southampton, May 1997.

75. K. S. Elliott, *"Multi-Storey Precast Concrete Framed Structures"*, Blackwell Science, 1996.

Appendix A

Stress-Strain Relationships for the Materials in the Modelling of the Experimental Billet-Welded Plate Joints and the Sensitivity Analyses

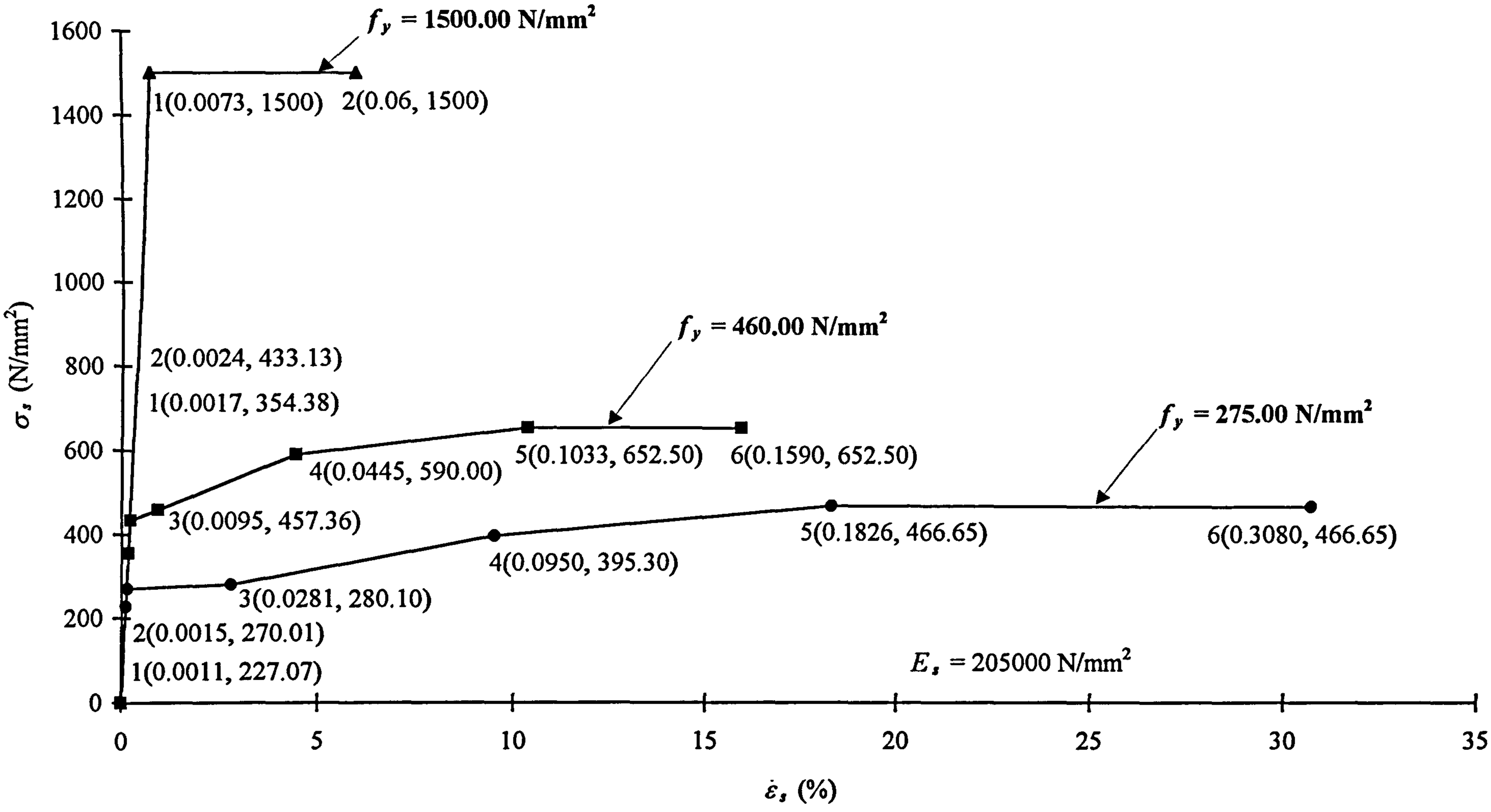

Figure A.1 *Stress-strain relationships of steel for the analyzed specimens*

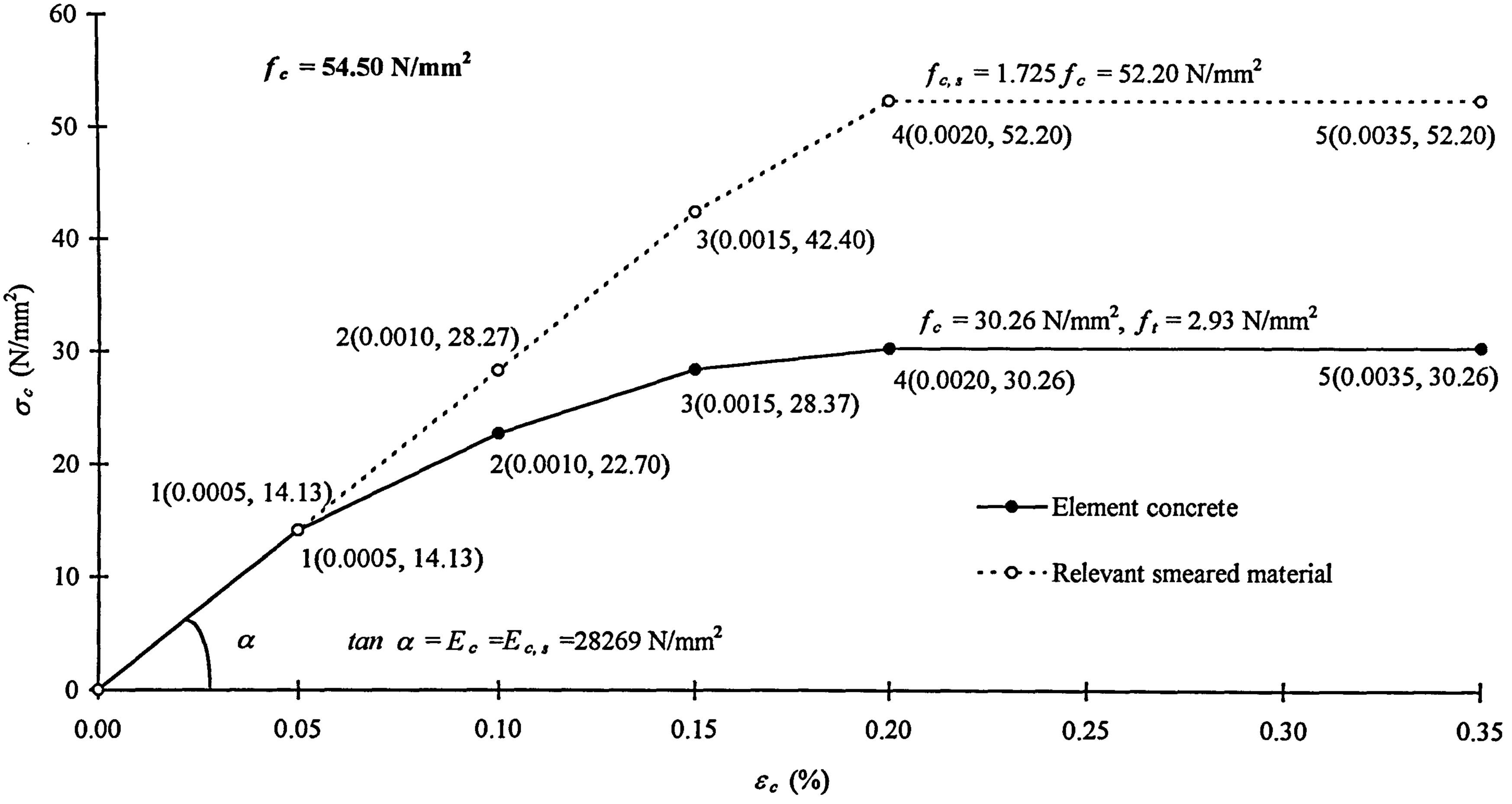

(a) Beam concrete of TW1, TW2 and TW3

Figure A.2 *Stress-strain relationships of concrete for the analyzed specimens*

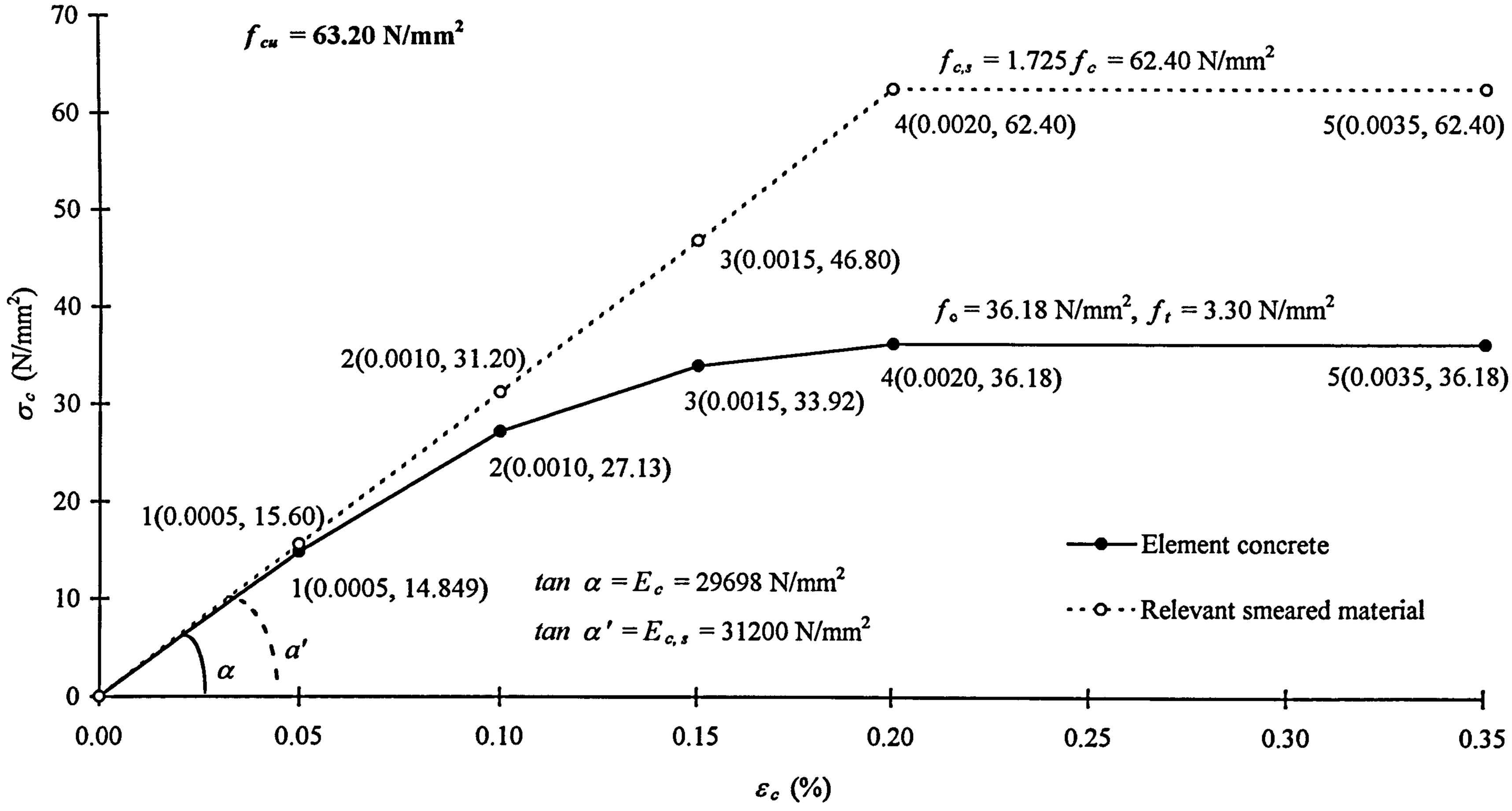

(b) Beam concrete of TW4

Figure A.2 *Stress-strain relationships of concrete for the analyzed specimens*

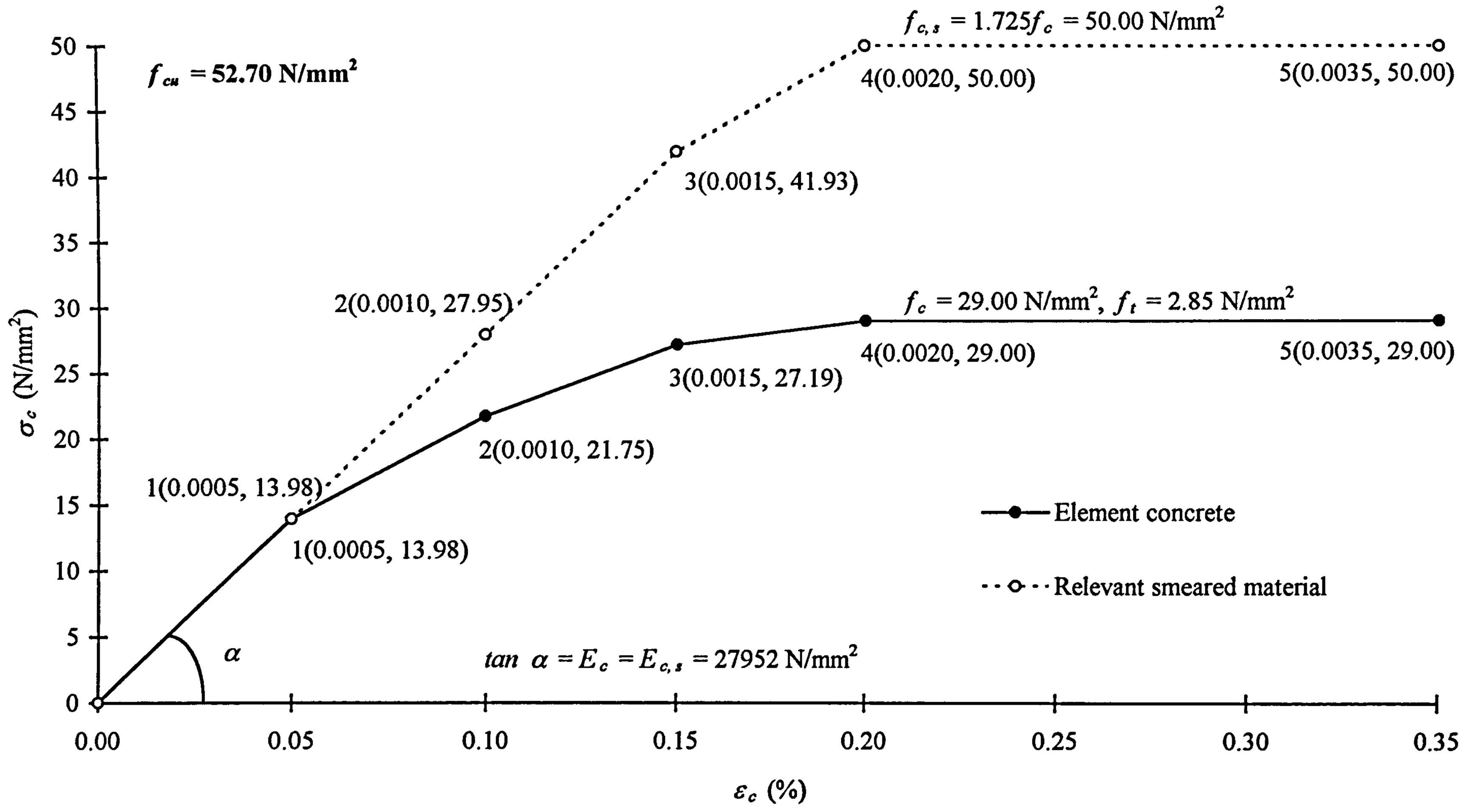

(c) *Beam concrete of TW1(A) and TW1(C)*

Figure A.2 *Stress-strain relationships of concrete for the analyzed specimens*

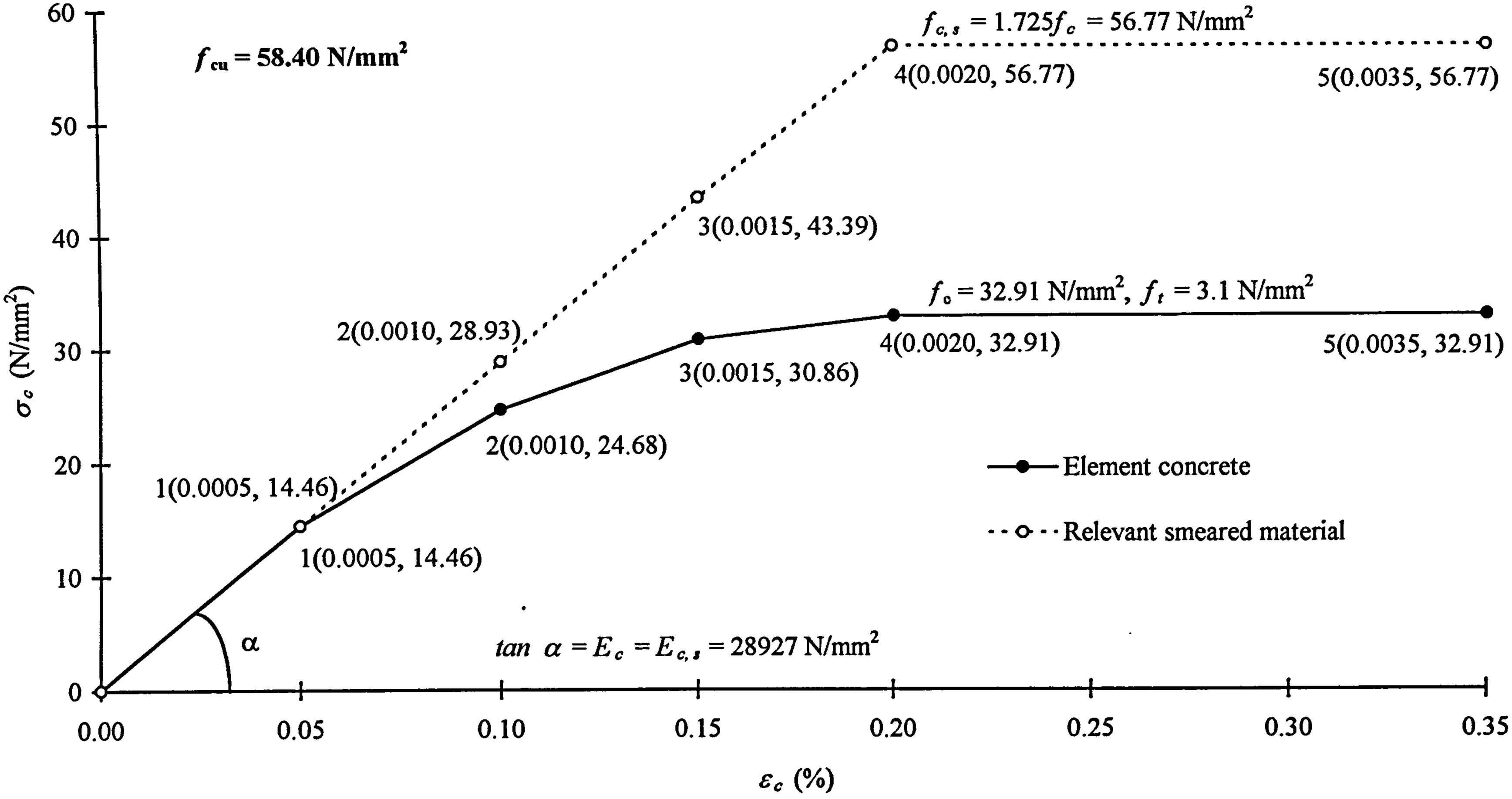

(d) Column concrete of TW1 and TW2

Figure A.2 *Stress-strain relationships of concrete for the analyzed specimens*

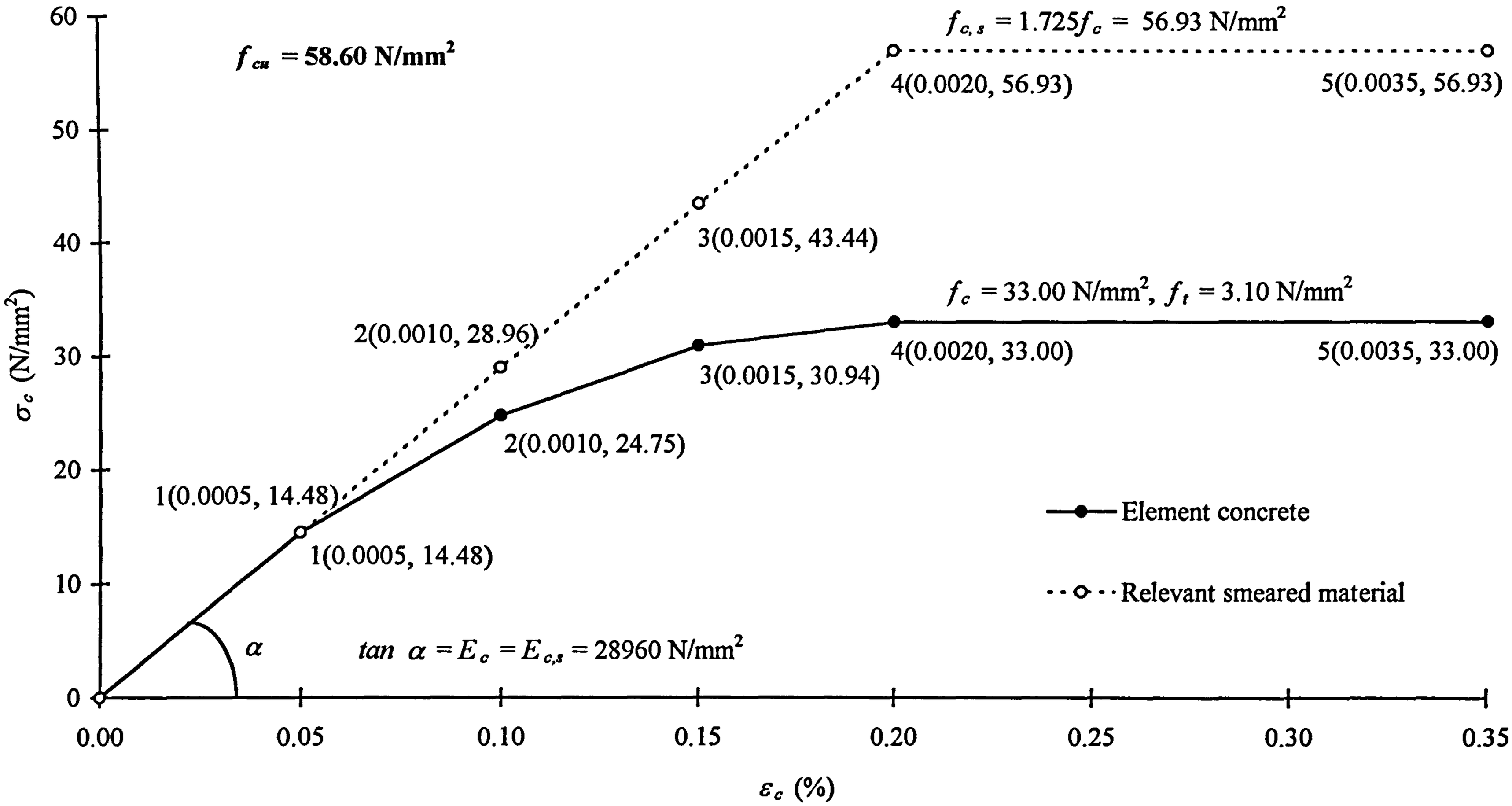

(e) Column concrete of TW3

Figure A.2 *Stress-strain relationships of concrete for the analyzed specimens*

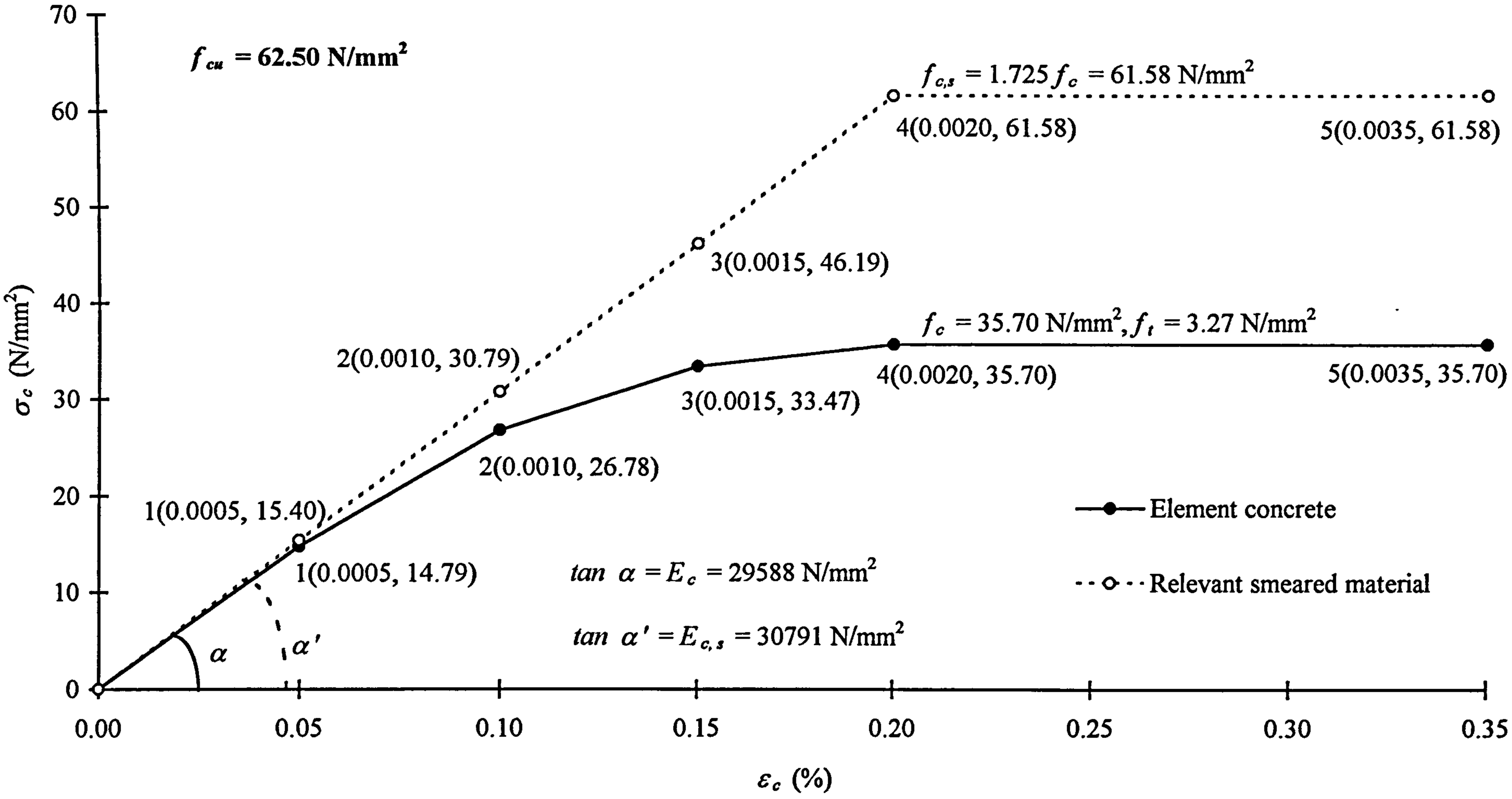

(f) Column concrete of TW4

Figure A.2 *Stress-strain relationships of concrete for the analyzed specimens*

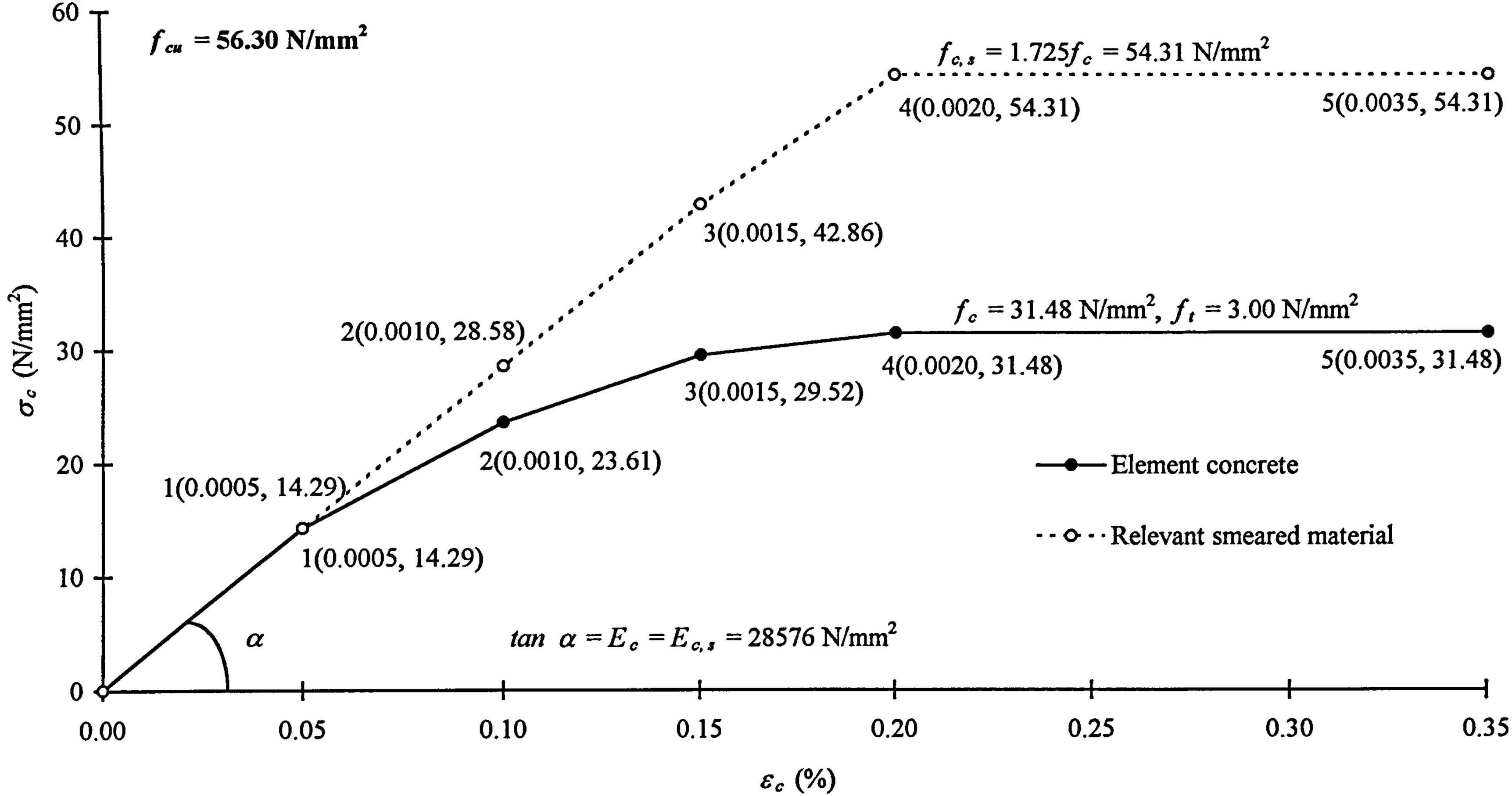

(g) Column concrete of TW1(A) and TW1(C)

Figure A.2 *Stress-strain relationships of concrete for the analyzed specimens*

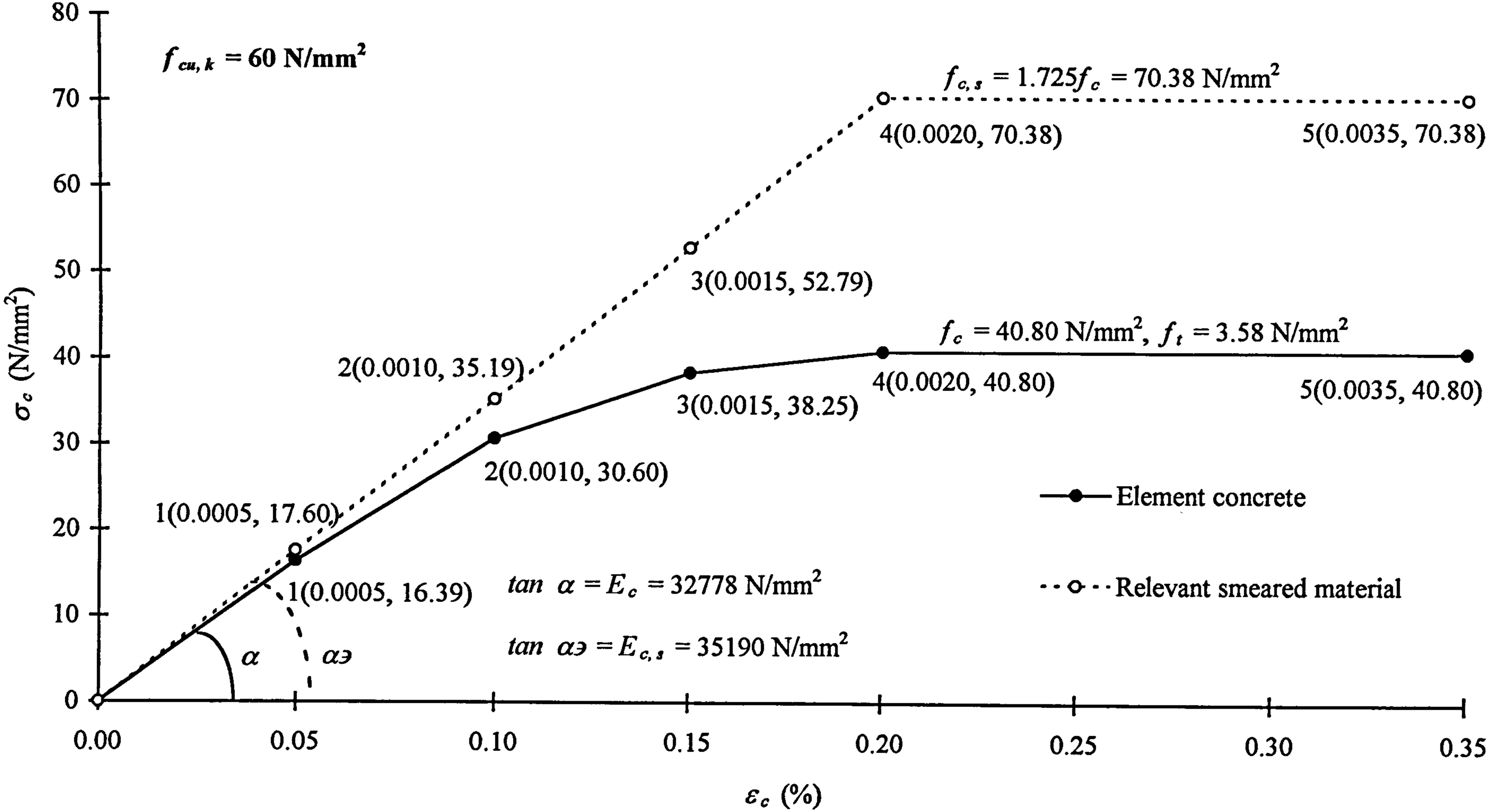

(h) Slab concrete of TW1(A) and TW1(C)

Figure A.2 *Stress-strain relationships of concrete for the analyzed specimens*

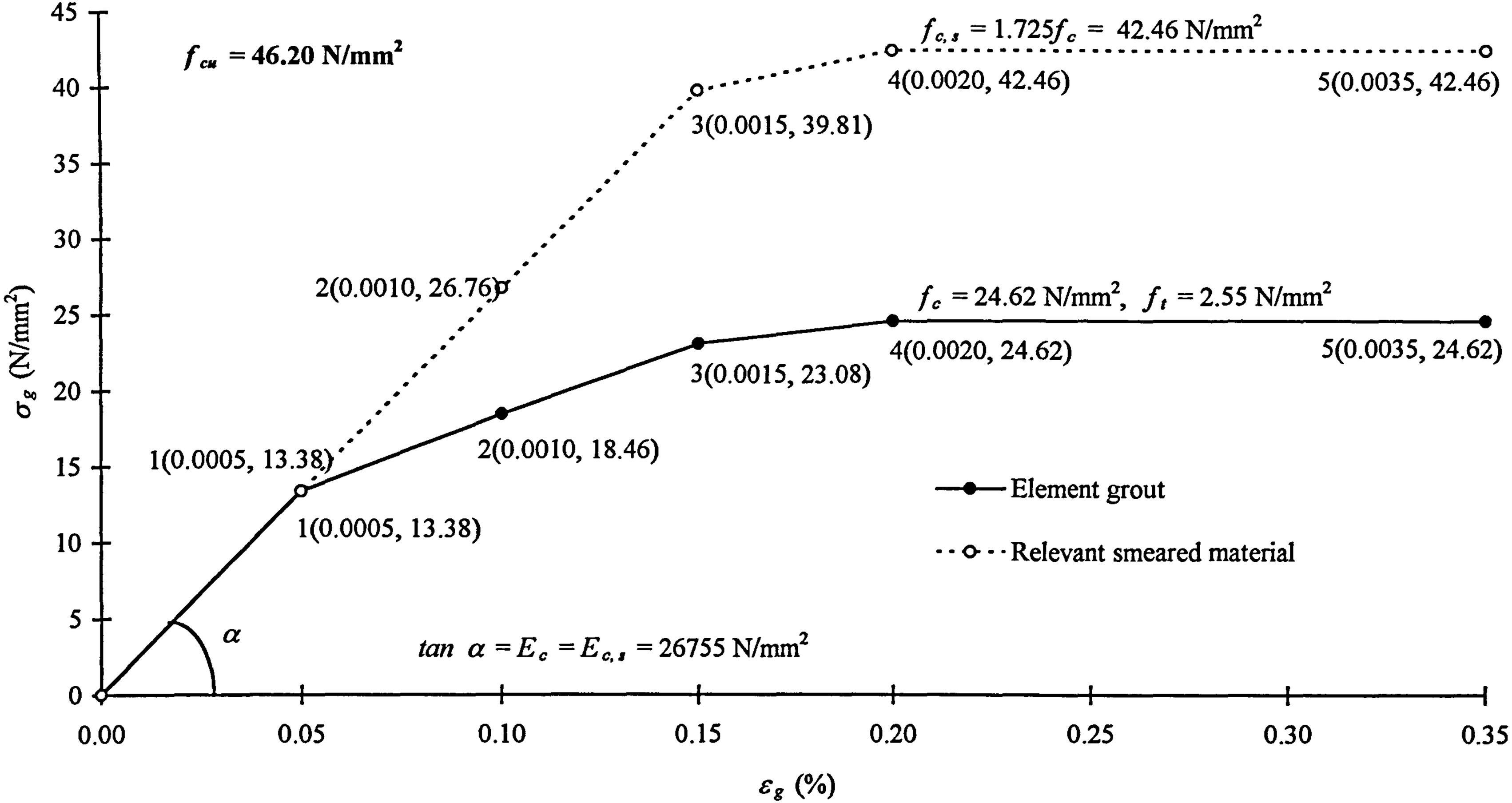

(a) Grout of TW1

Figure A.3 *Stress-strain relationships of grout for the analyzed specimens*

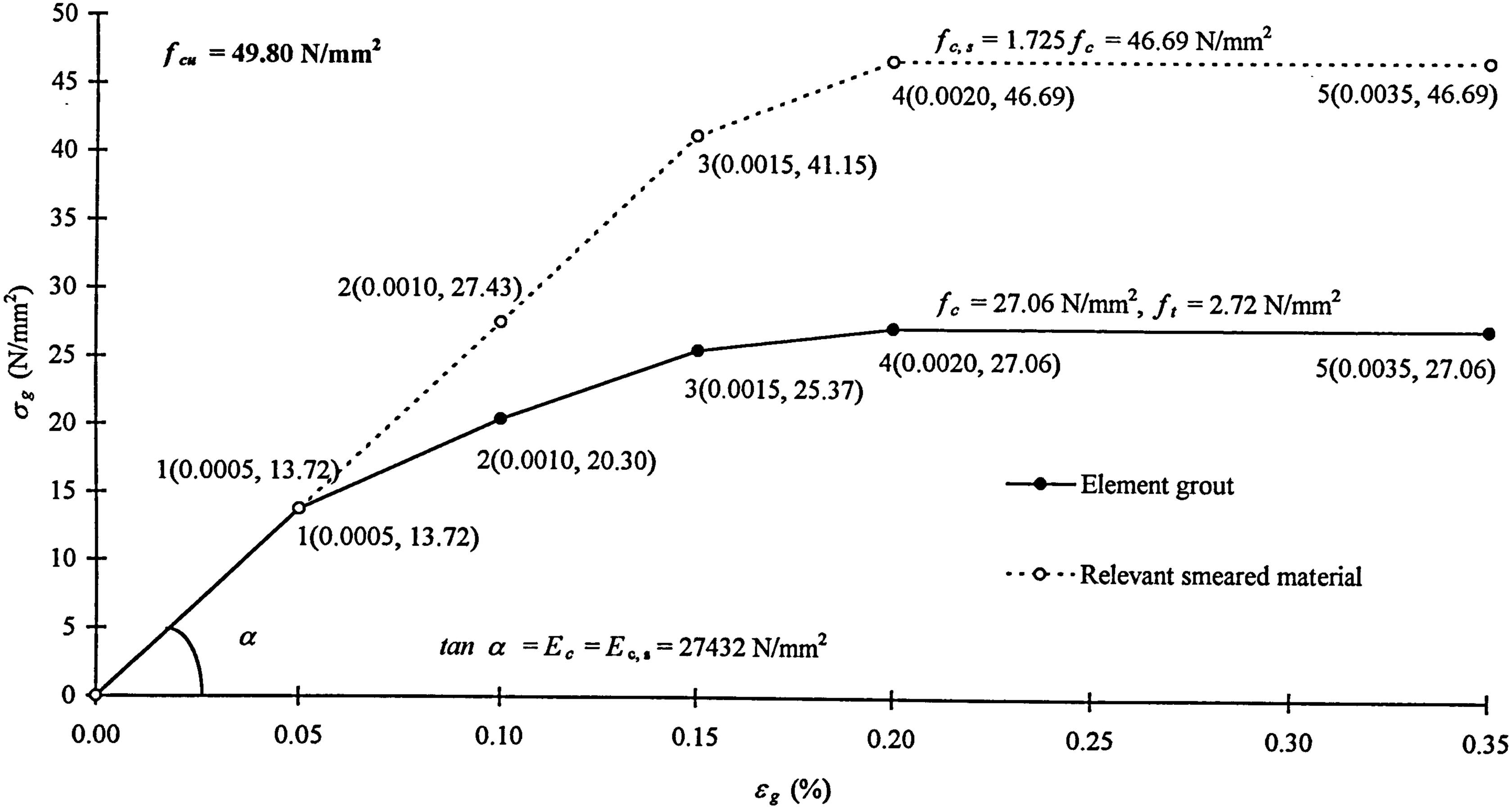

(b) Grout of TW2

Figure A.3 *Stress-strain relationships of grout for the analyzed specimens*

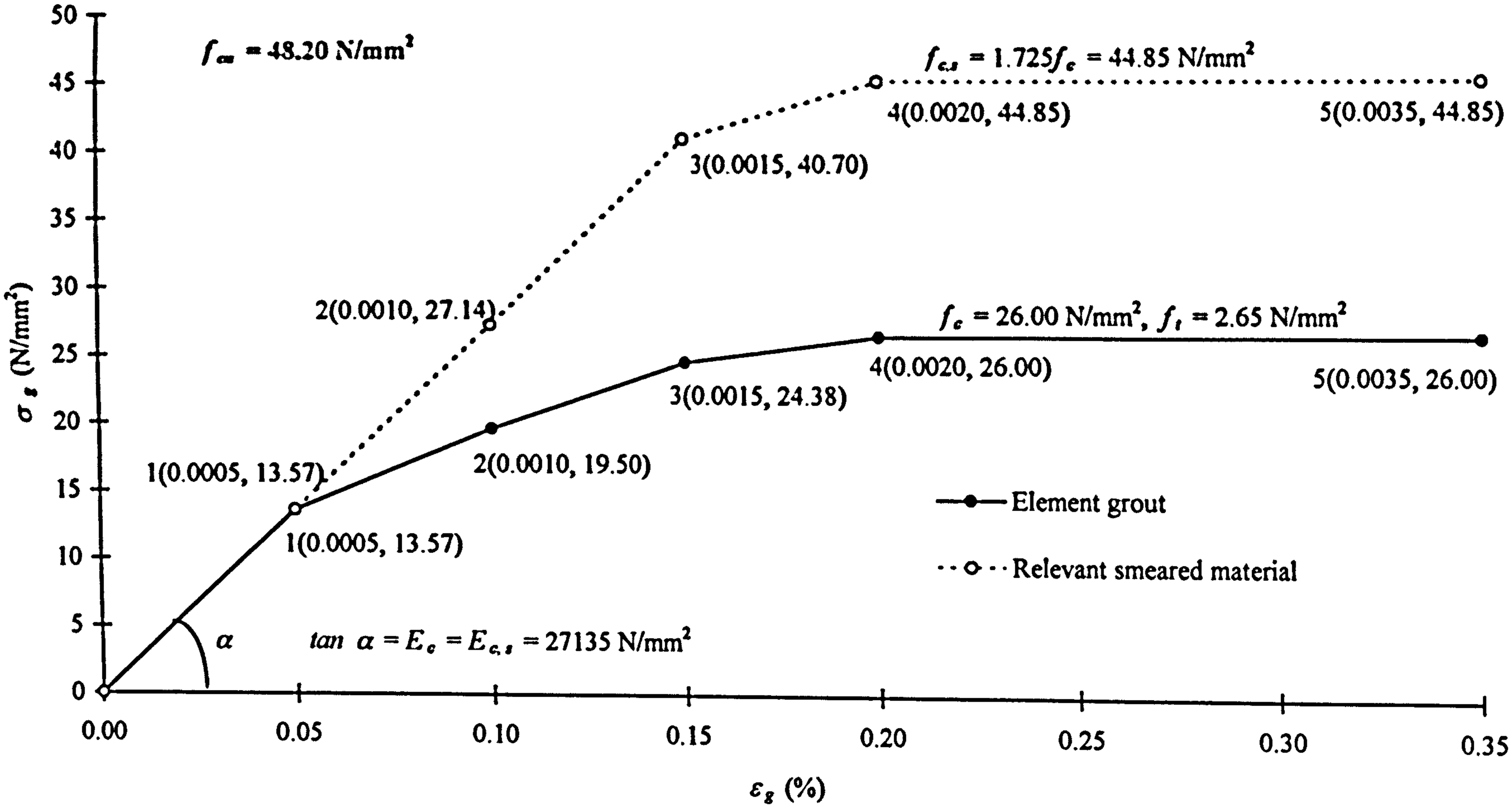

(c) Grout of TW3

Figure A.3 *Stress-strain relationships of grout for the analyzed specimens*

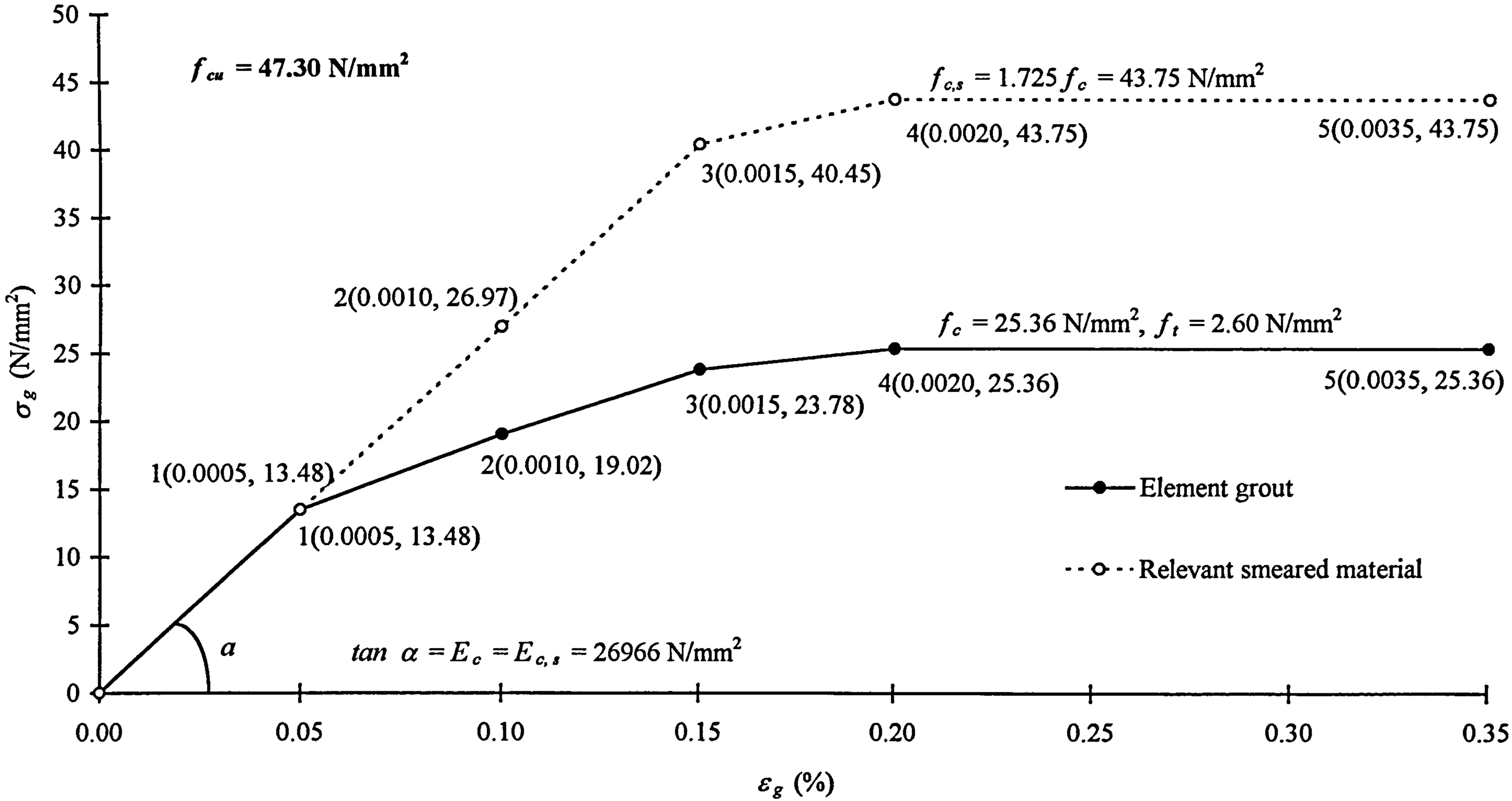

(d) Grout of TW4

Figure A.3 *Stress-strain relationships of grout for the analyzed specimens*

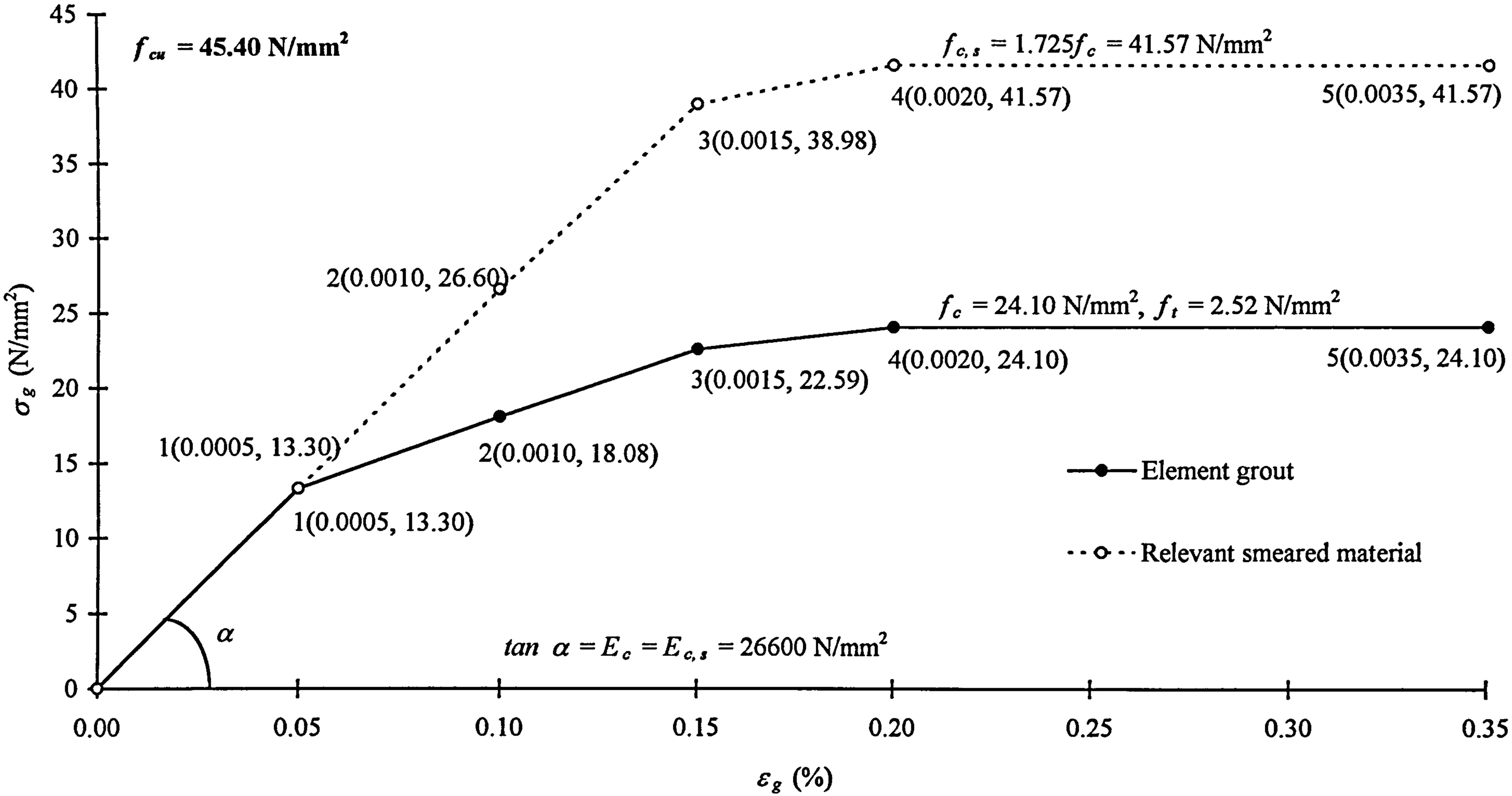

(e) Grout of TW1(A) and TW1(C)

Figure A.3 *Stress-strain relationships of grout for the analyzed specimens*

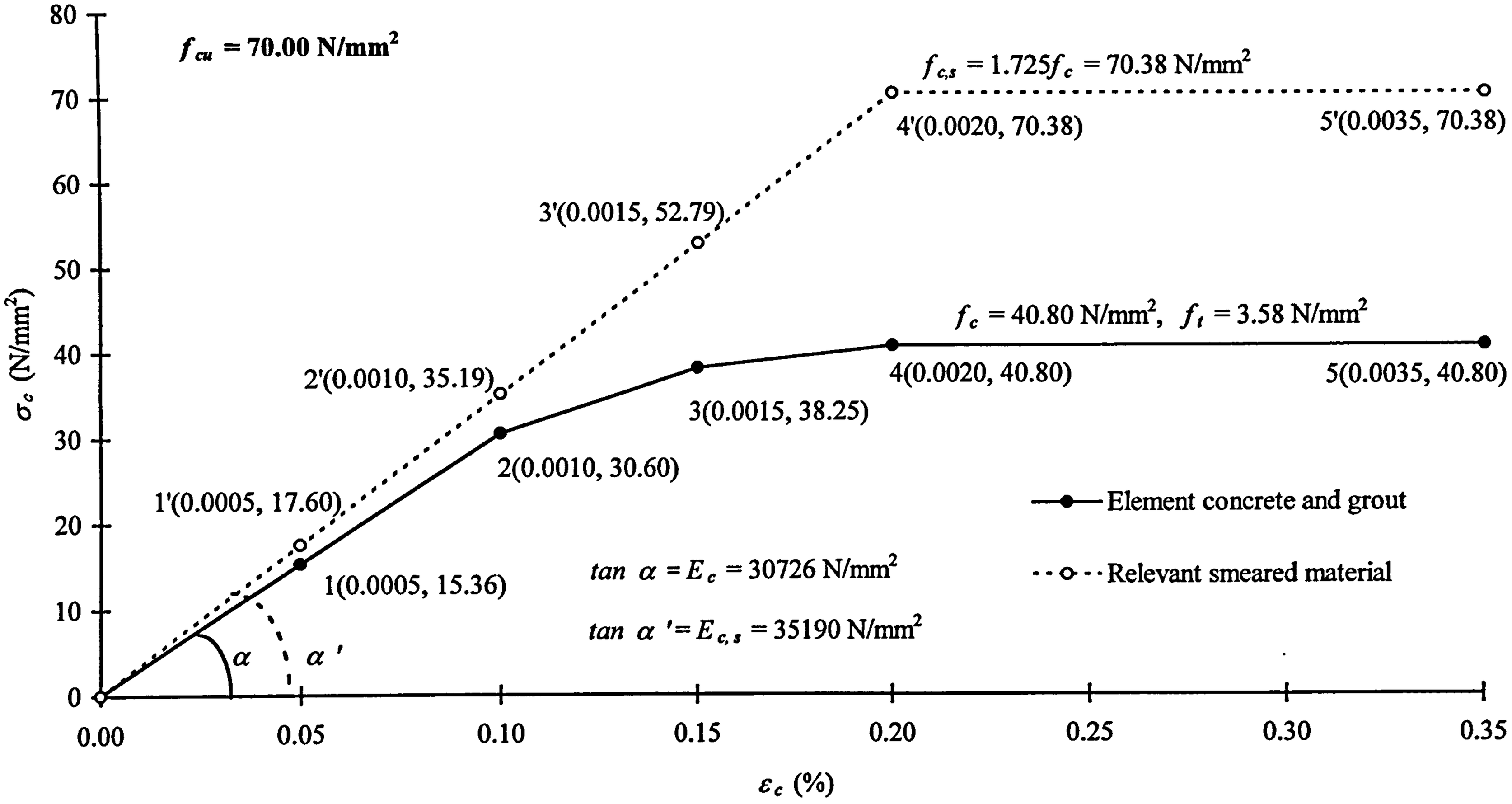

(a) Concrete in Analysis 17

Figure A.4 *Stress-strain relationships of concrete/grout for the joints in the sensitivity analyses*

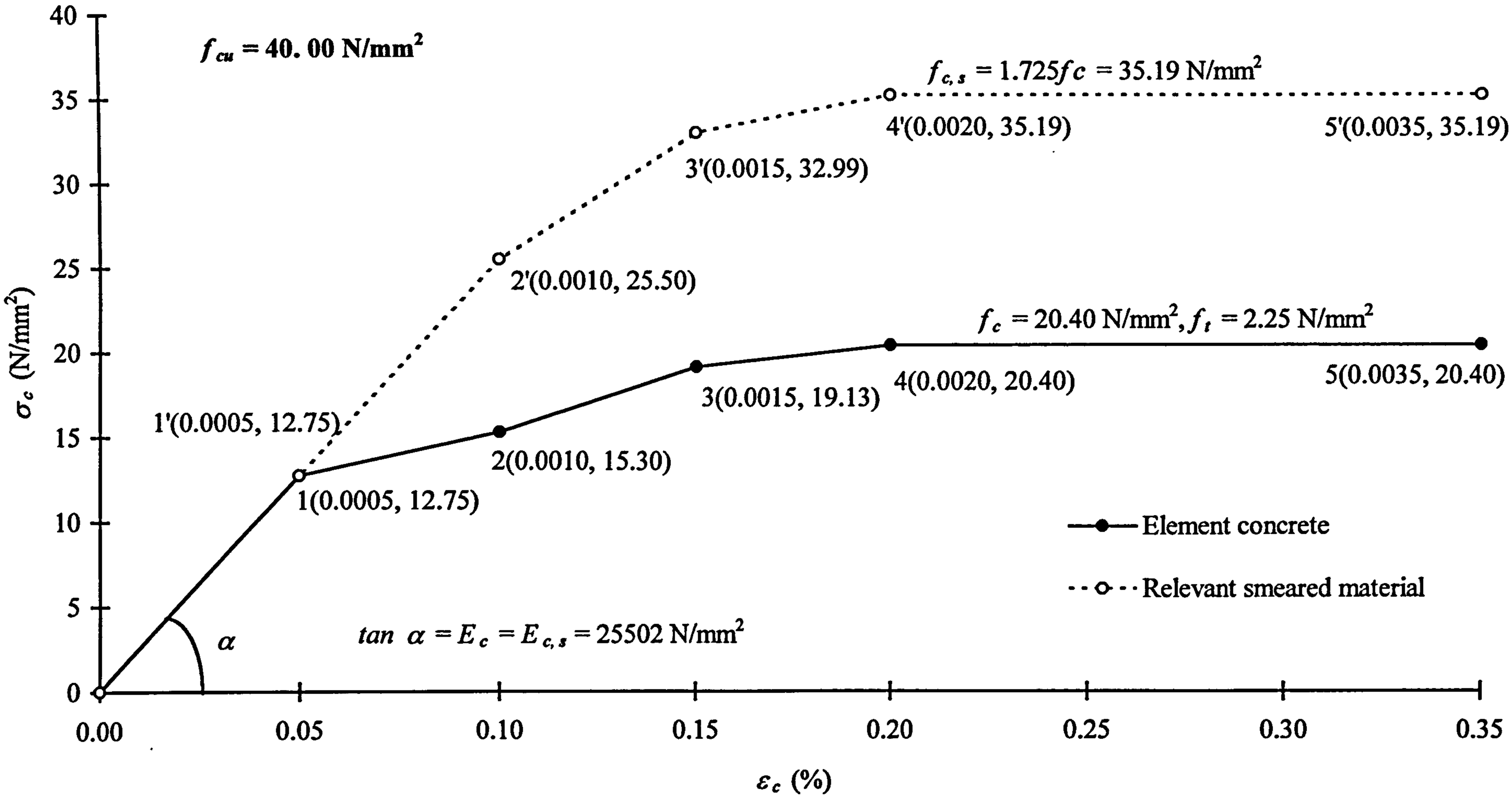

(b) Concrete in Analyses18 and 19

Figure A.4 *Stress-strain relationships of concrete/grout for the joints in the sensitivity analyses*

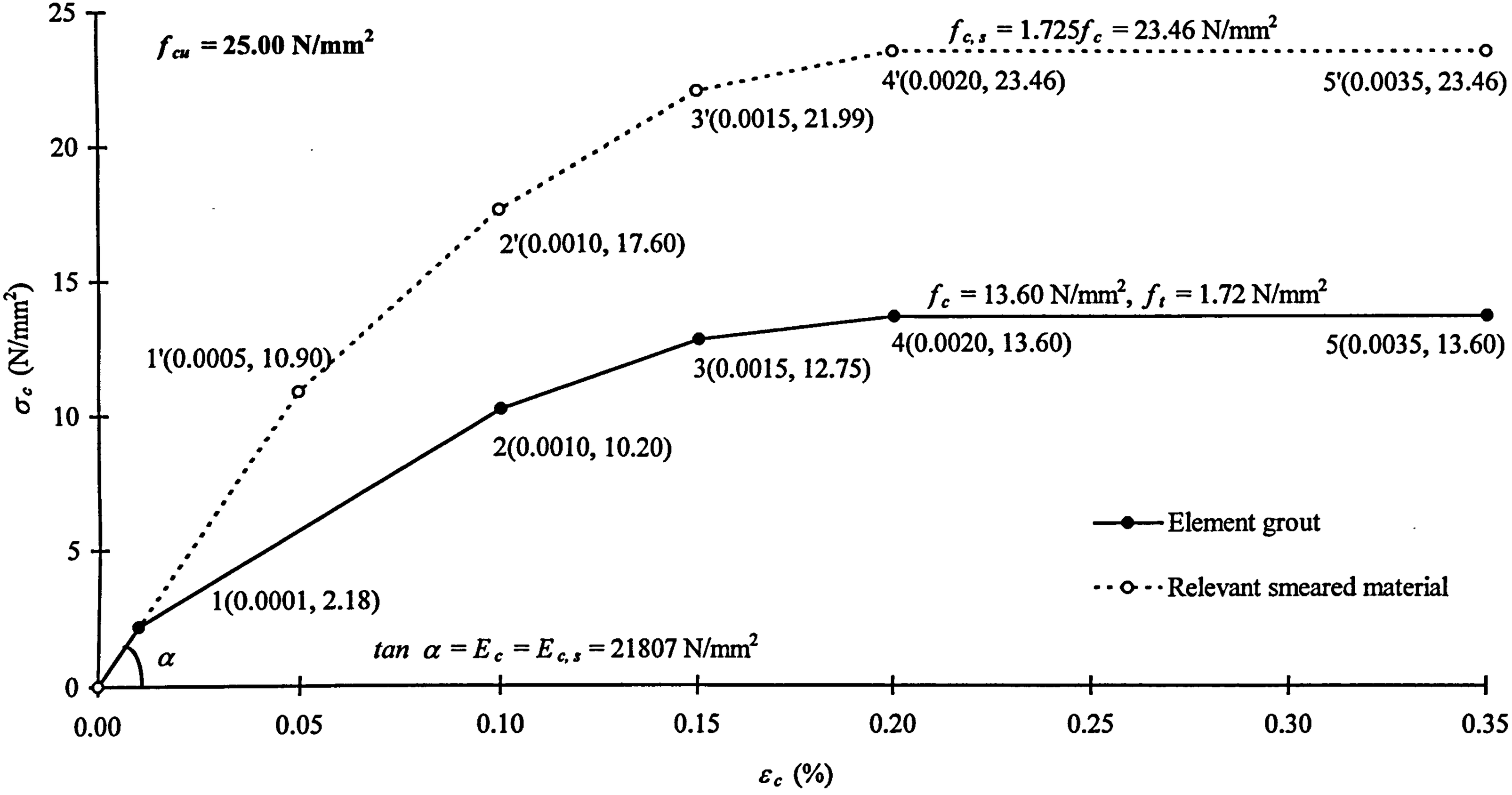

(c) Grout in Analysis 19

Figure A.4 *Stress-strain relationships of concrete/grout for the joints in the sensitivity analyses*